Physics of Atomic Nuclei, Vol. 63, No. 6, 2000, pp. 1002–1006. From Yadernaya Fizika, Vol. 63, No. 6, 2000, pp. 1077–1081.
Original English Text Copyright © 2000 by Mikaélyan, Sinev.

REACTOR NEUTRINOS

Neutrino Oscillations at Reactors: What Is Next?*

L. A. Mikaélyan and V. V. Sinev

Russian Research Centre Kurchatov Institute, pl. Kurchatova 1, Moscow, 123182 Russia

Abstract—We briefly review previous and future reactor experiments aimed at searches for neutrino masses and mixing. We also consider the new idea to seek small mixing-angle oscillations in the atmospheric-neutrino-mass-parameter region at Krasnoyarsk. © *2000 MAIK “Nauka/Interperiodica”.*

1. INTRODUCTION

The first long-baseline reactor experiment CHOOZ’97 [1] successfully reached the atmospheric-neutrino-mass-parameter region $\delta m^2_{\rm atm} \sim 10^{-3}$ eV^2 and tested there a large portion of the area of interest in the δm^2–$\sin^2 2\theta$ plane. No evidence for oscillations has been found. Thus, oscillations of electron neutrinos cannot dominate in the atmospheric-neutrino anomaly.

The Super-Kamiokande data on atmospheric neutrinos provide strong evidence for intensive $\nu_\mu \longrightarrow \nu_x$ ($x \neq e$) transitions [2]. In the three-active-neutrino (ν_e, ν_μ, ν_τ) oscillation model considered here, we have $\nu_x = \nu_\tau$.

We wish to emphasize, however, that both experiments, CHOOZ’97 and SuperKamiokande, do not rule out $\nu_e \longleftrightarrow \nu_\mu$ oscillations as a subdominant mode in the $\delta m^2_{\rm atm}$ region [3, 4].

The results of recent experiments have attracted much attention to the problem of neutrino oscillations. New physical ideas and projects of new large-scale experiments at accelerators are being vigorously discussed [4].

What new contributions can be made with reactor electron antineutrinos for exploring the problems of the electron-neutrino mass and mixing?

One line of future studies has already been announced. To probe the large-mixing-angle (LMA) MSW solution ($\delta m^2_{\rm sol} \simeq 10^{-4}$–$10^{-5}$ eV^2, $\sin^2 2\theta \sim 0.7$) [5] of the solar-neutrino puzzle, the projects KamLAND at Kamioka [6] and BOREXINO at Gran Sasso [7] plan to detect neutrinos from reactors operating hundred kilometers away from the detector sites.

In this article, we consider another possibility. We find that, with two-detector techniques, the sensitivity to the mixing parameter in the $\delta m^2_{\rm atm}$ region can be substantially increased in relation to that achieved in CHOOZ. We propose a new study of the problem at the Krasnoyarsk underground (600 mwe) laboratory with detectors situated 1100 and 250 m from the reactor. The main goals of the proposed experiment are (1) to obtain deeper insight into the role of the electron neutrino in the atmospheric neutrino anomaly, (2) to obtain new information about neutrino mixing (the U_{e3} element of the neutrino mixing matrix can be measured), and (3) to ensure normalization for future long-baseline experiments at accelerators.

2. OSCILLATIONS OF REACTOR ANTINEUTRINOS

A nuclear reactor generates antineutrinos at a rate of $N_\nu \sim 1.8 \times 10^{20}$ s^{-1} per 1 GW of thermal power. A typical reactor-$\bar\nu_e$ energy spectrum normalized to one fission event is presented in Fig. 1.

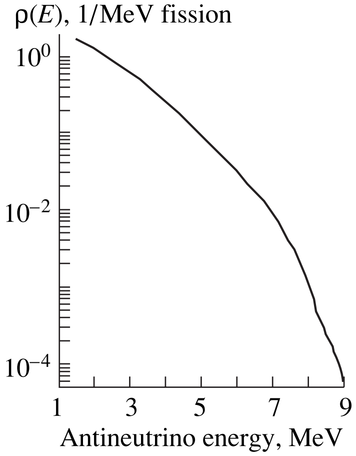

Fig. 1. Energy spectrum of reactor antineutrinos.

These electron antineutrinos are detected via the inverse beta-decay reaction

$$\bar\nu_e + p \longrightarrow e^+ + n. \qquad (1)$$

The positron kinetic energy T is related to the electron-antineutrino energy E as

$$T = E - 1.804 \text{ MeV}. \qquad (1a)$$

---

[*] This article was submitted by the authors in English.

1063-7788/00/6306-1002$20.00 © 2000 MAIK “Nauka/Interperiodica”

The signature of electron-antineutrino absorption in a liquid-scintillator target is a spatially correlated delayed coincidence of the prompt positron and the signal from the neutron-capture gamma rays.

The probability $P(\bar{\nu}_e \longrightarrow \bar{\nu}_e)$ for $\bar{\nu}_e$ to survive at a distance R (m) from the source is given by the expression

$$P(\bar{\nu}_e \longrightarrow \bar{\nu}_e) = 1 - \sin^2 2\theta \sin^2\left(1.27\delta m^2 \frac{R}{E}\right), \quad (2)$$

where E(MeV) is the neutrino energy, δm^2 is the mass parameter in eV^2, and $\sin^2 2\theta$ is the mixing parameter. The distortion of the positron energy spectrum and the deficit of the total electron-antineutrino-detection rate relative to the no-oscillation case are signatures for oscillations that are sought experimentally. The deficit of the total rate is the strongest for $(R\delta m^2)_{\max} \approx 5m\ \mathrm{eV}^2$.

In pressurized water reactors (PWR), the electron-antineutrino spectrum and the total cross section for reaction (1) vary with the nuclear-fuel composition, (the burnup effect). The current fuel composition is provided by reactor services. When the fuel composition is known, the no-oscillation cross section σ_{V-A} can be calculated within the uncertainty of 2.7%. (For more information see, for example, [8] and references therein.) With the aid of an integral-type detector, the CdF–KURCHATOV–LAPP group measured accurately the cross section at a distance of 15 m from the Bugey-5 reactor [9]:

$$\sigma_{\mathrm{expt}} = 5.750 \times 10^{-43}\ \mathrm{cm}^2/\mathrm{fission} \pm 1.4\%. \quad (3)$$

This highly accurate value σ_{expt} can be used in other experiments with reactor antineutrinos as a no-oscillation metrological reference. When it is used in practice, one must consider the differences in the fuel compositions and take into account the number of "small effects." This increases the error up to about 2%.

3. PAST, CURRENT, AND FUTURE EXPERIMENTS

Intensive searches for neutrino oscillations with detectors located at distances from reactors in the range between about 10 and 230 m were performed from 1980 to 1995. These "short-baseline" experiments are listed in Fig. 2 (left panel). The highest sensitivity to the mixing parameter ($\sin^2 2\theta \approx 0.02$) was achieved by the Bugey-3 group in the measurements with two identical detectors located at distances of 15 and 40 m from the reactor [9] (Fig. 3).

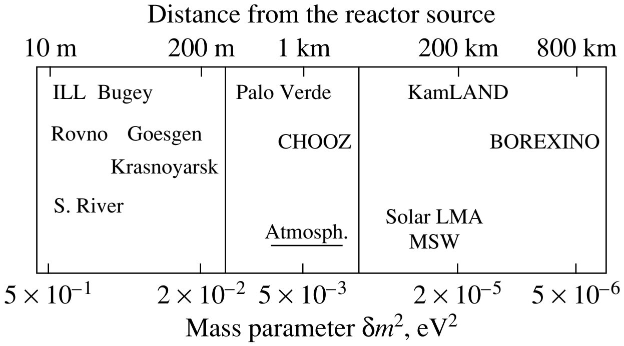

Fig. 2. Reactor oscillation experiments: (left panel) past short-baseline experiments, (middle panel) current long-baseline experiments, and (right panel) future ultralong-baseline experiments. New Krasnoyarsk project is not included.

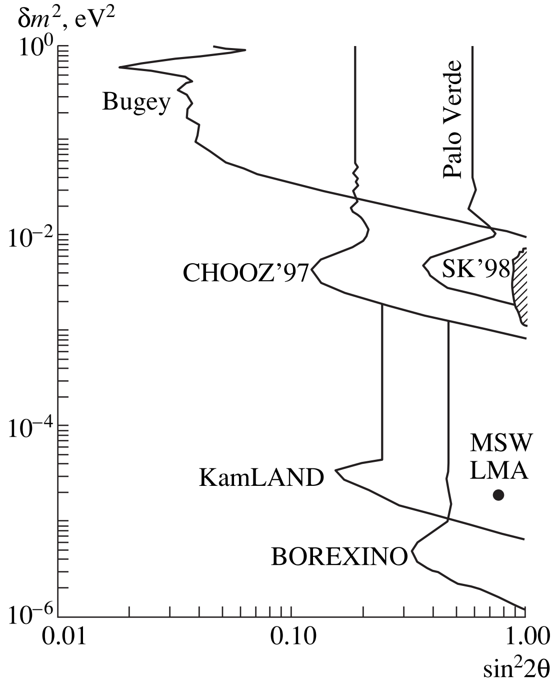

Fig. 3. Plots of reactor oscillation parameters. Bugey [10], CHOOZ'97 [1], and Palo Verde [11] are the 90% C.L. antineutrino-disappearance limits; KamLAND [6] and BOREXINO [7] are the expected $\bar{\nu}_e$ disappearance sensitivities; SK'98 [2] is the allowed $\nu_\mu \longrightarrow \nu_\tau$ oscillation region; and MSW LMA [5] is the solar ν_e solution.

The CHOOZ detector used a 5-t liquid scintillator (Gd) target. It was located in an underground laboratory (300 mwe) at a distance of about 1 km from the neutrino source. The ratio R of the measured neutrino-detection rate to that expected in the no-oscillation case was (November 1997)

$$R = 0.98 + 0.04(\mathrm{stat.}) + 0.04(\mathrm{syst.}). \quad (4)$$

The systematic errors come mainly from the reactor properties and the absolute values of neutrino-detection efficiencies. The 90% C.L. exclusion plot CHOOZ'97 for $\bar{\nu}_e$ disappearance channel is presented in Fig. 3, along with the allowed $\nu_\mu \longrightarrow \nu_\tau$ oscillation channel SK'736d [2] (shaded area). The experiment was contin-

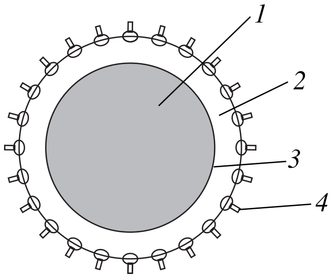

Fig. 4. Layout of the detector: (*1*) neutrino target (50 t of mineral oil + PPO), (*2*) mineral oil, (*3*) transparent film, and (*4*) photomultiplier tubes.

ued until June 1998 in order to achieve better statistics and to improve systematics. The final CHOOZ results will appear soon. The Palo Verde oscillation experiment deployed at a distance of 800 m from three reactors has been taking data since October 1998. The first 70-day results are now available [11]. Past and current experiments cover now the distances from the reactor of up to 1 km. The extension to about 200 and to about 800 km is expected from the forthcoming KamLAND and BOREXINO ultralong-baseline projects (Fig. 2). They will use liquid scintillator targets of 1000 and 300 t, respectively. The large-mixing-angle solar MSW solution [7] is well inside the area planned for the investigation (Fig. 3).

The experimental goal of the new search at Krasnoyarsk is to extend studies to the white-spot area left by the CHOOZ limits in Fig. 3.

4. NEW PROJECT FOR KRASNOYARSK

4.1 Detectors

Two identical liquid scintillation spectrometers positioned at the Krasnoyarsk underground site (600 mwe) at the distances of $R_1 = 1100$ m and $R_2 = 250$ m from the reactor source simultaneously detect (e^+, n) pairs produced in reaction (1). A simplified version of the BOREXINO detector composition is chosen for the design of the spectrometers (Fig. 4). Targets of weight 50 t each positioned at the center of the detectors (mineral oil + PPO) are viewed by photomultiplier tubes (~20% coverage, ~120 ph.e./MeV) through a nonscintillating-oil layer of thickness about 1 m. The computed neutrino detection rates can be seen in the middle of Table 1. For the sake of comparison, the parameters of the CHOOZ and the future KamLAND and BOREXINO detectors are also included.

4.2. Background

The CHOOZ experiment showed radical improvements of the reactor-neutrino techniques. A background level lower than that in previous reactor experiments by a factor of 500 to 1000 has been achieved (see the first three columns in Table 2). It is important to note that, with the CHOOZ experience and with the detailed studies at the BOREXINO CTF detector [7], the main features of the background suppression are now well understood, at least at the level we need. They are the following:

(1) In order to reduce the flux of cosmic muons—the main source of background in experiments of this type—a detector should be located underground at sufficiently large depth.

(2) In order to reduce the accidental background, the photomultipliers, with their highly radioactive glass, should be separated from the central scintillator volume by a sufficiently thick layer of oil (“BOREXINO geometry,” Fig. 4).

We estimate the total background rate as 0.1 per day per ton of the target. It is 2.5 times lower than the back-

Table 1. Antineutrino detection rates $N(e^+, n)\ d^{-1}$

Detector	CHOOZ’97	This project		KamLAND	BOREXINO
Mass of the target, t	5	50	50	1000	300
Distance from the source, km	1	0.25	1.1	~200	~800
$N(e^+, n)\ d^{-1}$	12	1000	55	2	0.08

Table 2. Neutrino signal $N(e^+, n)$ and background N_{BKG} rates (per day per ton of scintillator target)

Detector	Rovno	Bugey*	CHOOZ’97	This project**	KamLAND	BOREXINO
MWE***	30	~10	300	600	2700	3200
$N(e^+, n)$	1700	370	2.4	1.1	2×10^{-3}	3×10^{-4}
N_{BKG}	220	160	0.24	~0.1	<10	<10

* Detector at a distance of 40 m.
** Detector at a distance of 1100 m.
*** Overburden in meters of water equivalent.

ground measured at CHOOZ; this seems reasonable for a detector located twice as deep underground (Table 2).

4.3. Data Analysis

In three years of data taking, 40×10^3 (800×10^3) neutrino events with the signal-to-background ratio of 10 : 1 can be accumulated at a distance of 1100 m (250 m) from the reactor. Two types of analysis can be used. Neither is affected by the value of the absolute $\bar{\nu}_e$ flux and $\bar{\nu}_e$ energy spectrum, the reactor power, the burnup effects, and the absolute values of the detector efficiencies.

Analysis I is based on the ratio $X_{\text{rate}} = N_1/N_2$ of the neutrino detection rates measured at two distances:

$$X_{\text{rate}} = \frac{R_2^2 \epsilon_1 V_1}{R_1^2 \epsilon_2 V_2} F(\delta m^2, \sin^2 2\theta). \qquad (5)$$

Here, $\epsilon_{1,2}$ and $V_{1,2}$ are the neutrino detection efficiencies and the scintillator volumes, respectively. Thus, the absolute values of the detection efficiencies are virtually canceled—only their small relative differences are to be considered here.

Analysis II is based on a comparison of the shapes of the positron spectra $S(E_e)$ measured simultaneously in two detectors. Small deviations of the ratio $X_{\text{shape}} = S_1/S_2$,

$$X_{\text{shape}} = C(1 - \sin^2 2\theta \sin^2 \phi_1)(1 - \sin^2 2\theta \sin^2 \phi_2)^{-1}, \qquad (6)$$

from a constant value are sought as an indication of the oscillations ($\phi_{1,2}$ stands for $1.27\delta m^2 R_{1,2} E^{-1}$). No knowledge of the constant C in (6) is needed for this analysis, so that the details of geometry, the ratio of the target volumes, and the efficiencies are excluded from the consideration.

4.4. Detector Calibrations

Calibrations of the detectors are of crucial importance. The difference between the response functions for the two detectors, which is difficult to avoid, can produce some modulation of the ratio in (6), thereby mimicking the oscillation effect. The differences can be measured, and relevant corrections can be found. This can be done by a global comparison of the scales at many energy points by using the sources of gamma rays shown in Fig. 5.

An additional approach is also considered. The spectrometers can be tested periodically with the source that is provided by spontaneous fission of ^{252}Cf and which can produce a broad spectrum due to prompt gamma rays and neutron recoils (Fig. 5). The ratio of these spectra should be constant; if the instrumental modulation is observed, it can be measured and used to find corrections to (6).

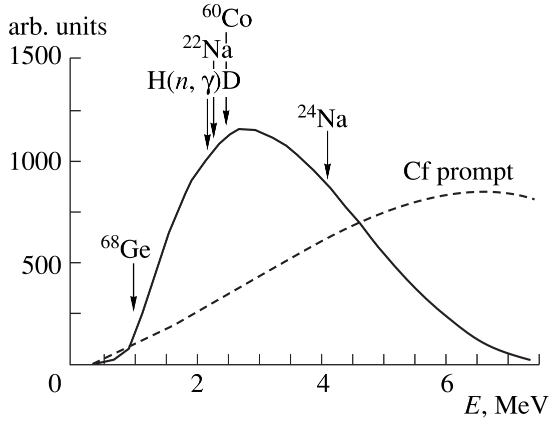

Fig. 5. Sources for detector calibrations. The solid line is the positron energy spectrum.

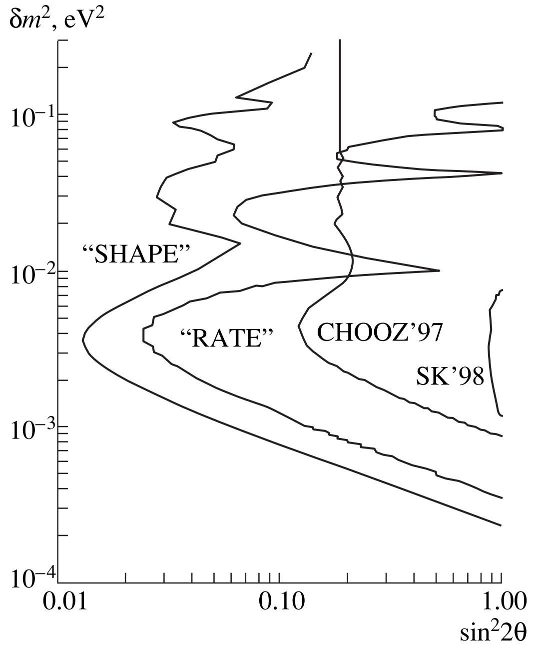

Fig. 6. Expected 90% C.L. oscillation-parameter limits: ("RATE") analysis I and ("SHAPE") analysis II.

4.5. Expected Constraints on the Oscillation Parameters

We hope that the ratio $\epsilon_1 V_1/\epsilon_2 V_2 \approx 1$ (5) can be controlled to within 0.8%. From Analysis I, we then expect the 90% C.L. limits shown in Fig. 6 (curve labeled "RATE"). We believe that the spurious effects in (6) can be controlled down to a level of 0.5%. The relevant 90% C.L. limits are presented in Fig. 6 (curve "SHAPE").

5. DISCUSSION AND CONCLUSIONS

By using the methods for data analysis that are mentioned in Section 4, we have obtained limits on the oscillation parameters free from the main sources of systematic uncertainties, which limit the sensitivity of experiments based on an absolute comparison of the measured and expected no-oscillation rates and positron spectra. Nevertheless, the systematic errors that remain reduce significantly the sensitivity to the mixing parameter $\sin^2 2\theta$. The curve "SHAPE" (Fig. 6) is about two times less restrictive in relation to the statistical limits found for an ideal detector with no systematic effects.

We return to the main question of what contributions to the neutrino physics can be expected from new oscillation experiments at reactors.

Long-baseline (LBL) experiments with detectors positioned at a distance of about 1 km from the reactor seek the mixing parameter $\sin^2 2\theta_{\mathrm{LBL}}$, which is expressed, in this case, as

$$\sin^2 2\theta_{\mathrm{LBL}} = 4U_{e3}^2(1 - U_{e3}^2), \tag{7}$$

where U_{e3}^2 is the contribution of the heaviest mass eigenstate ν_3 to the flavor electron neutrino state:

$$\nu_e = U_{e1}\nu_1 + U_{e2}\nu_2 + U_{e3}\nu_3. \tag{8}$$

From CHOOZ'97 results, we already know that U_{e3}^2 is not large: $U_{e3}^2 < (3–5) \times 10^{-2}$. The future 1-km experiment considered here can measure U_{e3}^2 or set a much smaller upper limit. Therefore, a better understanding of the neutrino mixing can be achieved. New information about U_{e3} can be useful for an analysis of atmospheric neutrinos and can give hints for future long-baseline experiments at accelerators.

The ultralong-baseline (ULBL) experiments KamLAND and BOREXINO will seek $\sin^2 2\theta_{\mathrm{ULBL}}$, which depends on the contributions of the ν_1 and ν_2 mass states:

$$\sin^2 2\theta_{\mathrm{ULBL}} = 4U_{e1}^2 U_{e2}^2. \tag{9}$$

We conclude that the experiments at reactors discussed here can provide full information about the mass structure of the electron neutrino, at least in the three-neutrino oscillation model.

ACKNOWLEDGMENTS

We greatly appreciate stimulating discussions with S. Bilenky, E. Lisi, and A. Smirnov. We thank our colleagues V. Martemyanov, Yu. Kozlov, and V. Vyrodov for many discussions.

This work was supported by the Russian Foundation for Basic Research.

REFERENCES

1. M. Apollonio *et al.*, Phys. Lett. B **420**, 397 (1998); CHOOZ Collab., hep-ex/9711002.
2. Y. Fukuda *et al.*, Phys. Rev. Lett. **81**, 1562 (1998); Super-Kamiokande Collab. (K. Scholberg), hep-ex/9905016.
3. G. Fogli, E. Lisi, A. Marrone, and G. Scioscia, hep-ph/9904465.
4. S. Bilenky, C. Giunti, and W. Grimus, Prog. Part. Nucl. Phys. (in press); hep-ph/9812360.
5. J. Bachall, P. Krastev, and A. Smirnov, Phys. Rev. D **58**, 096016 (1998); hep-ph/9905220.
6. F. Suekane, in *Proceedings of Workshop NOW'98, Amsterdam, September 1998*, http://www.nikhef.nl/pub/conferences/now98; G. Gratta, hep-ex/9905011.
7. BOREXINO Collab. (L. Oberauer), http://www-sk.icrr.u-tokyo.ac.jp/nu98; http://almime.mi.infn.it/html/papers/index.html
8. V. Kopeĭkin, L. Mikaélyan, and V. Sinev, Yad. Fiz. **60**, 230 (1997) [Phys. At. Nucl. **60**, 172 (1997)].
9. V. Vyrodov *et al.*, Pis'ma Zh. Éksp. Teor. Fiz. **61**, 3 (1995) [JETP Lett. **61**, 163 (1995)]; Y. Declay *et al.*, Phys. Lett. B **338**, 383 (1994).
10. B. Achkar *et al.*, Nucl. Phys. B **434**, 503 (1995).
11. Palo Verde Collab. (F. Boehm), http://citnp.caltech.edu/PV/Palo-Verde/html

Physics of Atomic Nuclei, Vol. 63, No. 6, 2000, pp. 1007–1011. From Yadernaya Fizika, Vol. 63, No. 6, 2000, pp. 1082–1086.
Original English Text Copyright © 2000 by Avignone III, Anderso, Awes, Berridge, Bilpuch, Britton, Bryan, Bugg, Burman, Busenitz, Carter, Chatterjee, Cianciolo, Cochran, Cohn, Danilov, De-Brackeleer, Degtiarenko, Efremenko, Elaasar, Fazely, Frank, Gabriel, Gould, Gudkov, Gunasingha, Handler, Hart, Imlay, Jagadish, Kamyshkov, Khosrovi, Koetke, Lane, Manweiler, Metcalf, Mezzacappa, Mo, Nosik, Nummaker, Nussinov, Piepke, Plasil, Reidy, Rosenfeld, Smith, Stancu, Stanislaus, Steinberg, Svoboda, Tashakkori, Tornow, Van Dalen, Walker, Watson, Wintenberg, Wolf, Wright, Zel'dovich, Zhang.

REACTOR NEUTRINOS

ORLaND: A Proposed Neutrino Facility at the Oak Ridge National Laboratory*

F. T. Avignone III1), B. D. Anderso2), T. C. Awes, S. Berridge3), W. Bilpuch4), C. Britton, W. Bryan, W. M. Bugg3), R. L. Burman5), J. Busenitz6), K. Carter7), L. Chatterjee3), V. Cianciolo, A. K. Cochran8), H. O. Cohn3), M. V. Danilov9), L. De-Brackeleer4), P. Degtiarenko10), Yu. V. Efremenko3), M. A. Elaasar11), A. R. Fazely8), S. Frank, T. A. Gabriel, C. R. Gould12), V. Gudkov1), R. Gunasingha8), T. Handler3), E. L. Hart3), R. L. Imlay13), U. Jagadish, Yu. A. Kamyshkov3), E. Khosrovi8), D. D. Koetke14), C. Lane15), R. W. Manweiler14), W. J. Metcalf13), A. Mezzacappa, L. W. Mo16), V. Z. Nosik9), T. A. Nummaker16), S. Nussinov17), A. Piepke18), F. Plasil, J. Reidy19), C. Rosenfeld1), D. Smith20), I. Stancu21), T. D. S. Stanislaus14), R. Steinberg15), R. Svoboda13), R. Tashakkori8), W. Tornow4), G. Van Dalen21), J. Walker, J. W. Watson2), A. Wintenberg, J. Wolf6), D. H. Wright22), O. Ya. Zeldovich9), and W.-M. Zhang2)

Oak Ridge National Laboratory, Tennessee, USA

Abstract—Oak Ridge National Laboratory, Tennessee, USA, ORLaND is a collaboration proposing a major neutrino physics facility at the Spallation Neutrino Source (SNS) at the Oak Ridge National Laboratory. An underground bunker is proposed adjacent to the first target station of the SNS. The bunker is designed to house one large detector (2000 t) and a number of smaller (200 t) detectors. A comprehensive program of neutrino experiments is being developed that could span the lifetime of the Spallation Source. *© 2000 MAIK "Nauka/Interperiodica".*

1. INTRODUCTION

The study of neutrino properties is one of the most important probes of physics beyond the standard model. Searching for the effects of neutrino mass and flavor mixing, the determination of the Dirac or Majorana character of neutrinos, searching for the neutrino magnetic moment, and accurate measurement of neutrino-nucleus cross sections, all have potentially significant impact on particle physics, astrophysics, and cosmology.

The recent excitement over the potential discovery of $\bar{\nu}_\mu \longrightarrow \bar{\nu}_e$ flavor oscillation by the Large Scintillation Neutrino Detector (LSND) at Los Alamos [1] and the recent report of evidence for ν_μ, $\bar{\nu}_\mu \longrightarrow \nu_\tau$, $\bar{\nu}_\tau$ oscillation by the Super-Kamiokande collaboration [2] provide strong motivation to plan new next generation accelerator experiments. Experiments of this calibre should be about two orders of magnitude more sensitive to $\bar{\nu}_\mu \longrightarrow \bar{\nu}_e$ oscillations than LSND or KARMEN and should be capable of accurately measuring δm^2 and $\sin^2 2\theta$ if the LSND signal is confirmed. In addition, such experiments should be capable of observing with ease the signal from the KARMEN time anomaly, attributed to a new and exotic decay branch $\pi^+ \longrightarrow \mu^+ + X$ [3, 4], and capable of very accurate mea-

---

* This article was submitted by the authors in English.
1) University of South Carolina, South Carolina, USA.
2) Kent State University, Kent, Ohio, USA.
3) University of Tennessee, Knoxville, Tennessee, USA.
4) Duke University, and TUNL, Durham, North Carolina, USA.
5) Los Alamos National Laboratory, Los Alamos, New Mexico, USA.
6) University of Alabama, Tuscaloosa, Alabama, USA.
7) Oak Ridge Associated Universities, Oak Ridge, Tennessee, USA.
8) Southern University, Baton Rouge, Louisiana, USA.
9) Institute for Theoretical and Experimental Physics, Moscow, Russia.
10) Jefferson Laboratory, Newport News, Virginia, USA.
11) Southern University at New Orleans, New Orleans, Louisiana, USA.
12) North Carolina State University, Raleigh, North Carolina, USA.
13) Louisiana State University, Baton Rouge, Louisiana, USA.
14) Valparaiso University, Valparaiso, Indiana, USA.
15) Drexel, Philadelphia, Pennsylvania, USA.
16) Virginia Tech, Blacksburg, Virginia, USA.
17) Tel Aviv University, Tel Aviv, Israel.
18) California Institute of Technology, Pasadena, California, USA.
19) University of Mississippi, Oxford, Mississippi, USA.
20) Embry Riddle Aeronautical University, Prescott, Arizona, USA.
21) University of California, Riverside, California, USA.
22) TRIUMF, Vancouver, B.C., Canada.

1063-7788/00/6306-1007$20.00 © 2000 MAIK "Nauka/Interperiodica"

surements of $e^-\nu$ scattering, $\nu_e{}^{12}C \longrightarrow {}^{12}N^*e^-$, $\nu_e{}^{12}C \longrightarrow {}^{12}N_{g.s}e^-$, $\nu_e{}^{12}C \longrightarrow {}^{12}C^* + 15.11$ MeV γ.

While planning an experimental facility to accomplish these goals, one should also consider designs which allow simultaneous housing other detectors to measure a number of neutrino nucleus cross sections in order to tune theoretical models used to calculate other cross sections inaccessible to experiment but which are important in stellar evolution models, for example, in supernovae collapse models. The construction of the high powered Spallation Neutron Sources (SNS) provides such opportunities. This paper addresses these insues in the context of the recently approved construction of the 2 MW SNS at the Oak Ridge National Laboratory.

2. SPALLATION NEUTRON SOURCES

Spallation Neutron Sources, optimized to produce neutrons by spallation of nucleons by high energy protons, are also prolific sources of π^+ and π^- mesons. These mesons decay as follows: $\pi^+ \longrightarrow \mu^+ + \nu_\mu$ and $\mu^+ \longrightarrow e^+ + \nu_e + \bar{\nu}_\mu$; $\pi^- \longrightarrow \mu^- + \bar{\nu}_\mu$ and $\mu^- \longrightarrow e^- + \bar{\nu}_e + \nu_\mu$. In heavy (high Z) targets, however, most of the π^- and μ^- particles are rapidly absorbed by the nuclei of the target and shielding prior to decaying, and the neutrino population is dominated by ν_μ, ν_e, and $\bar{\nu}_\mu$, with very little admixture of $\bar{\nu}_e$. This makes them ideal for searches for oscillations with $\bar{\nu}_e$ appearance experiments.

Thus far, two spallation neutron sources, namely, the LANCE (previously LAMPF) facility at the Los Alamos National Laboratory (LANL) and the ISIS facility at the Rutherford–Appleton Laboratory in the United Kingdom, have been successfully used as intermediate energy neutrino sources. Accordingly, the energy spectra and intensities of the neutrinos are well known.

The ISIS facility is powered by 200 μA of 0.8 GeV protons on a lead target. The accelerator is a rapid cycling synchrotron with a pulsed beam. The KARMEN detector is a 56-t segmented detector, the center of which is 17.5 m from the source. The detector is well shielded but is above ground.

The LANCE facility is driven by an 800 μA, 800-MeV proton Linear Accelerator, but with a long beam spill. The lack of a good pulse structure like that of ISIS prevents one from discriminating against the majority of background due to cosmic rays. In addition short pulses (500–600 ns) are required to separate the ν_μ flux from decay $\pi^+ \longrightarrow \mu^+ + \nu_\mu$ (26 ns) and fluxes of $\bar{\nu}_\mu$ and ν_e from the slower decay $\mu^+ \longrightarrow e^+ + \nu_e + \bar{\nu}_\mu$ (2.2 μs). The LSND detector was a 167-t scintillating Cerenkov detector, the center of which was 30 m from the beam stop.

The SNS at ORNL will combine the advantages of a large beam current and short pulse duration. This provides an excellent opportunity to build an intermediate energy neutrino facility that would be superior to any other for the foreseeable future.

The SNS will consist of a 1 GeV proton linear accelerator (LINAC) feeding an accumulator ring. A proton beam of 2 mA will impinge on a water cooled mercury target producing copious quantities of pions as well as neutrons. The mesons and their daughter muons decay as described above producing fluxes of neutrinos: 2×10^{16} ν/s in the full solid angle. This is five times the intensity of that at LANCE and more than 10 times that at ISIS. Some of these advantages would be lost because the center of a 2000-t detector, for example, would be 45.7 m from the source. Smaller detectors (100–200 t) could be as close as 38 m.

The ORLaND collaboration is developing a detailed plan that proposes to build an underground bunker close to the target station that could house a 2000-t scintillating Cherenkov detector and several detectors of ~200 t each and of various designs. These smaller detectors would be designed to measure a variety of ν-nucleus cross sections, some to calibrate existing and future solar neutrino and supernovae detection experiments and some to calibrate or "tine" nuclear models used to calculate many cross sections used in stellar evolution models as mentioned above.

It now appears that the National Science Foundation might build a second target station about 140 m from the center of the planned ORLaND bunker. This would change the effective flux by a factor of 0.8 as the first target station would be pulsed at 50 Hz instead of 60 Hz, and the second station would be pulsed at 10 Hz. This would result in a unique neutrino facility with different distances from the two sources pulsed at different times.

3. ORLaND'S LARGE SCINTILLATING CHERENKOV DETECTOR

One of the main motivations of the ORLaND project is the creation of a next generation neutrino oscillation experiment capable of detecting $\bar{\nu}_\mu \longrightarrow \bar{\nu}_e$ oscillations with a sensitivity 100 times superior to that of LSND and 10 times greater than MiniBooNE or I-216. In addition it should be capable of accurately measuring δm^2 and $\sin^2 2\theta$ if nature has them within the sensitivity of the facility.

The proposed scintillating Cherenkov detector is a vertical cylindrical tank with internal dimensions (r = 7.2 m; h = 14.3 m) lined with 6730, 20-cm diameter photomultiplier tubes that cover about 25% of the total area. The design fiducial volume contains 1540 metric tons of mineral oil scintillator, which is a factor of 18 larger than the 85-metric-ton fiducial mass of LSND.

The 1 GeV protons will produce twice as many pions as the 800 MeV protons at LANCE; the SNS proton beam intensity of 2 mA is 2.5 times more intense than the 0.8 mA available at LANCE.

The distance from the center of the SNS target station to the center of the ORLaND detector at the proposed site is 45.7 m, compared to 30 m in the case of LSND. This reduces the data collection efficiency of ORLaND compared to LSND by a factor of 0.43.

The LSND collaboration had a total of 15.5 months of running over the 72 months from 1993 through 1998. ORLaND would be strictly parasitic and could collect data over the planned running time of 36 weeks per year. As a result, the running time efficiency of ORLaND would be a factor of 3.1 higher than that of LSND.

The superior pulse structure of the proton beam at the SNS will allow the use of less stringent data cuts to eliminate cosmic ray backgrounds. This will result in a factor of approximately 2.2 increase in the data collection efficiency of ORLaND relative to that of LSND.

Combining all of these factors, the count rate of neutrino events in the 2000-t ORLaND detector relative to that in LSND, for an equal time period, is 264, with a significantly lower background projected. This definitely meets the criteria of a "next generation" experiment.

4. SENSITIVITY LIMITATIONS AT SPALLATION NEUTRON SOURCES

There is one unavoidable background for any $\bar{\nu}_e$ appearance experiment searching for $\bar{\nu}_\mu \longrightarrow \bar{\nu}_e$ oscillations at spallation neutron sources. In all experiments that utilize ν_μ, ν_e, and $\bar{\nu}_\mu$ fluxes from the decay chain of pions produced in reactions of protons on nuclei, there will always be a small fraction of π^- that will decay before they are captured, which is also true for the resulting μ^-. The uncaptured muons decay according to $\mu^- \longrightarrow e^- + \bar{\nu}_e$, thereby producing an unavoidable $\bar{\nu}_e$ background. The LSND experiment was simulated in detail, and the resulting ratio $\bar{\nu}_e/\bar{\nu}_\mu$ was calculated to be 7.5×10^{-4} [5]. Calculations made by the same authors resulted in the corresponding ratio of 2.4×10^{-4} at the SNS target station. This value was independently verified in a calculation performed at ORNL.

Although the production ratio π^+/π^- is almost five times larger for a water cooled target than for the pure mercury target of the SNS, the probability that the π^- and μ^- will decay prior to capture is 15 times smaller in the SNS target station.

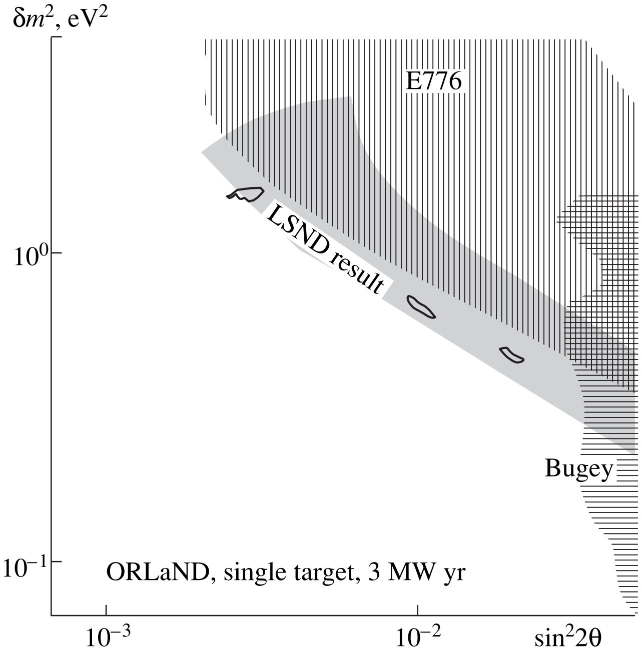

Fig. 1. The accuracy of measurement of the oscillation parameters in the LSND region for a 2-kt detector, for 6 MW yr.

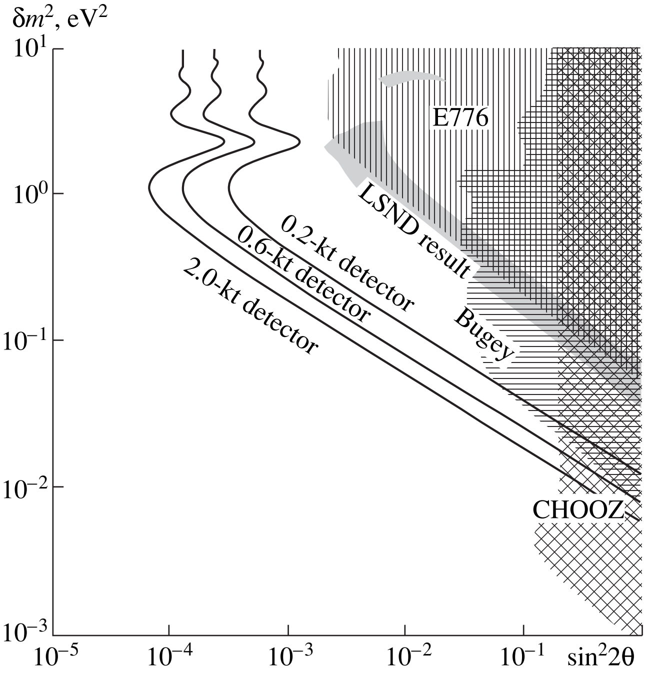

Fig. 2. Discovery potential at SNS for several detector sizes. Statistics, is for a one year of running time with 1-MW beam.

The fact that there are any $\bar{\nu}_e$'s in the neutrino flux that result from a process other than that of $\bar{\nu}_\mu \longrightarrow \bar{\nu}_e$ oscillations dictates that there is a fundamental limit to how sensitive this class of experiments can be. The large ORLaND detector at the SNS at ORNL is designed to reach that limit so that no significantly "improved" experiment would be possible. The accuracy with which the parameters δm^2 and $\sin^2 2\theta$ can be constrained (determined) if the LSND signal is real is shown in Fig. 1. The sensitivity of neutrino oscillation

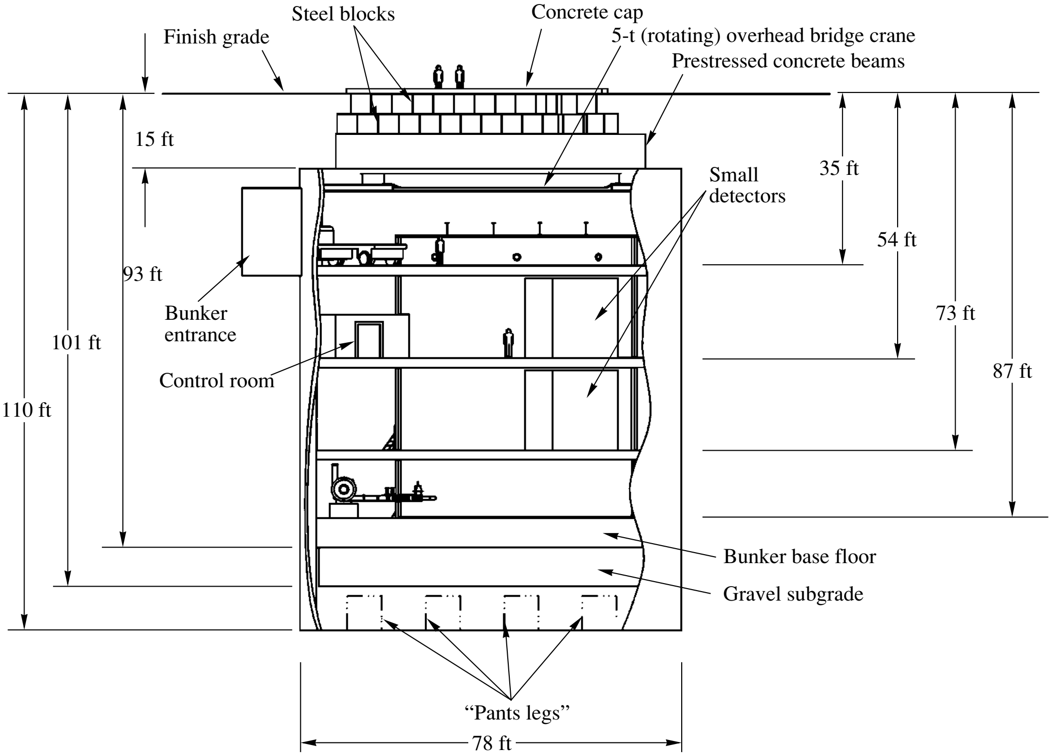

Fig. 3. Detail view of ORLaND detector bunker.

experiments for various detector masses is shown in Fig. 2.

5. BUNKER AND SHIELDING DESIGN

The bunker is designed to provide a protective environment for the neutrino detectors, providing some shielding from cosmic rays and adequate shielding from scattered neutrinos. It is a reinforced concrete structure totally underground and immediately adjacent to the SNS target building. A "slurry wall" of alternate technology will be used that constructs the bunker straight down without disturbing the adjacent structure. The bunker itself would be a cylindrical structure with a 24-m inside diameter and 22 m from floor to ceiling with 0.9-m-thick walls and a base floor 2.5 m thick. It would have four mezzanine levels, each with bearing strength to accommodate several 200-t detectors. The three upper levels would have large, off center, circular openings to accommodate the large steel tank of the main 2-kt scintillating Cherenkov detector. The inner wall of the tank will have 15.2 cm of lead outside with the outer wall a radial distance of 1.0 m further out. This outer volume will contain a liquid scintillator live veto. The bunker would be covered by precast concrete beams 0.3 m wide and 2.1 m high. On top would be two layers of steel blocks approximately 1.3 m thick. The entire structure would be covered by a concrete cap level with the ground. Details of the bunker with detectors inside can be seen in Fig. 3.

Access to the bunker will be provided by a tunnel 4.3×4.3 m, large enough to accommodate medium size trucks; it will be inclined at 15 degrees and will enter the upper mezzanine. The bunker is designed to contain a large 2000-t detector and up to six 200-t detectors for neutrino–nucleus cross sections mainly to support astrophysics. These measurements are also of interest to the field of weak interactions in nuclei.

6. IMPLICATION FOR ASTROPHYSICS

Current supernova theory revolves around the "delayed shock mechanism." Briefly, infalling matter during the collapse reaches supernuclear densities, at which point Fermi repulsion and nucleon–nucleon hard-core interactions give rise to a shock wave [6]. Various energy loss mechanisms, including neutrino escape, cause the shock to small. Theoretical simulations of these processes are very sensitive to the neutrino transport scenario assumed.

Of importance here is the fact that ν_e and $\bar{\nu}_e$ interact with the stellar core via charge currents and neutral currents, while the other flavors can only interact via neutral currents. The latter then decouple at a higher core density and, therefore, at higher temperatures, and accordingly have harder spectra. The heating of the core by charged current interactions of ν_e and $\bar{\nu}_e$ could revive the stalled shock wave. Therefore, the oscillations of the harder spectra of ν_μ, $\bar{\nu}_\mu$, ν_τ, and $\bar{\nu}_\tau$ to ν_e and $\bar{\nu}_e$ can have a significant influence.

Furthermore, ORLaND covers most of the region of the parameter space of relevance to supernova models and can accurately pin down the oscillation parameters. Finally, accurate knowledge of the vacuum oscillation parameters would allow the identification of resonance regions for MSW matter oscillations [7], which might also be important in stellar collapse.

7. MEASUREMENT OF NEUTRINO–NUCLEUS CROSS SECTIONS

Accurate measurements of neutrino–nucleus cross sections are needed to validate theoretical predictions before they are used in theoretical stellar collapse models. Supernovae involve such a large number of neutrino–nucleus reactions, some involving radioactive nuclei, that laboratory measurements of all of them are impossible. Accordingly, random phase approximation models are used [8], which themselves have parameters. It is important to experimentally test and tune these models in a few important cases. We plan to make such measurements using the small segmented detectors planned for the ORLaND facility. In these detectors, materials foreign to the scintillator can be introduced in a variety of ways.

The similarity of the neutrino spectra from π^+ and μ^+ decay at rest at neutron spallation sources and those produced during supernovae core collapse is striking. This, coupled with the intensity and pulse structure at the SNS, makes the proposed ORLaND facility ideal for making measurements that directly support theoretical nuclear astrophysics.

8. NEUTRINO OSCILLATION SENSITIVITY

The sensitivity of ORLaND to neutrino oscillations compares very favorably with other existing and proposed experiments, as may be seen in Fig. 4. It is expected that MiniBooNE will be able to either confirm or rule out the possible $\bar{\nu}_\mu \longrightarrow \bar{\nu}_e$ oscillation signal reported by LSND before ORLaND comes into operation in 2005. If MiniBooNE observes neutrino oscillations, then ORLaND will have the important role of confirming and providing an independent and more precise measurement of the oscillation parameters. If MiniBooNE does not see a signal, ORLaND will still be able to explore a substantial region of oscillation parameter space not covered by MiniBooNE or any other experiment. In particular, ORLaND will be sensitive for $\sin^2 2\theta$ down to 3×10^{-5} for $\delta m^2 > 0.3$ eV^2. For lower values of δm^2, ORLaND will also be more sensitive than MiniBooNE, as shown in Fig. 4.

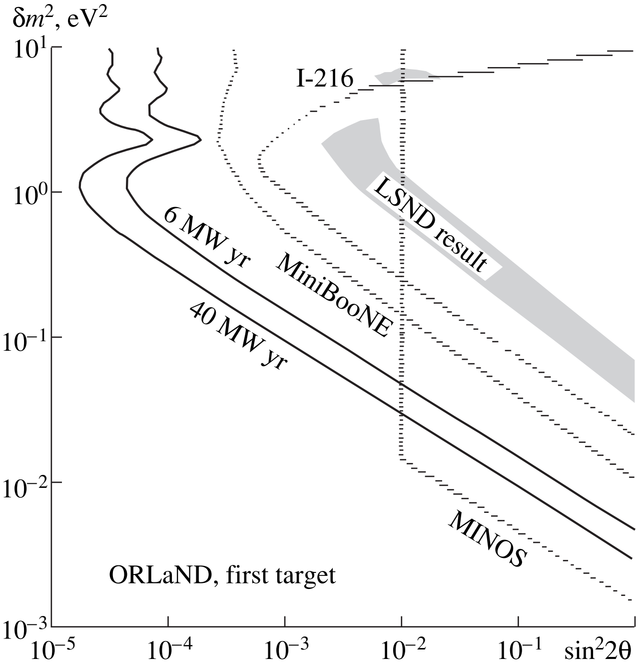

Fig. 4. Limits from the ORLaND experiment compared with those of MiniBooNE, MINOS, and I-216 proposals.

REFERENCES

1. C. Athanassopoulos *et al.*, Phys. Rev. Lett. **81**, 1774 (1998).
2. Y. Fukuda *et al.*, Phys. Lett. B **433**, 9 (1998).
3. B. Armbruster *et al.*, Phys. Lett. B **348**, 19 (1995).
4. V. Barger, R. J. N. Phillips, and S. Sarkar, Phys. Lett. B **352**, 365 (1995).
5. R. L. Burman and P. Plischke, Nucl. Instrum. Methods Phys. Res. **398**, 147 (1997).
6. J. R. Wilson, in *Numerical Astrophysics* (Jones & Bartlett, Boston, 1985), p. 422.
7. J. N. Bahcall, *Neutrino Astrophysics* (Cambridge, University Press Cambridge, 1989).
8. E. Kolbe, K.-H. Langanke, S. Krewald, and F.-K. Thielemann, Nucl. Phys. A **540**, 599 (1992).

Physics of Atomic Nuclei, Vol. 63, No. 6, 2000, pp. 1012–1015. From Yadernaya Fizika, Vol. 63, No. 6, 2000, pp. 1087–1090.
Original English Text Copyright © 2000 by Kopeĭkin, Mikaélyan, Sinev.

REACTOR NEUTRINOS

Search for the Neutrino Magnetic Moment in the Nonequilibrium Reactor-Antineutrino Energy Spectrum*

V. I. Kopeĭkin, L. A. Mikaélyan, and V. V. Sinev
Russian Research Centre Kurchatov Institute, pl. Kurchatova 1, Moscow, 123182 Russia

Abstract—We study the time evolution of a typical reactor-antineutrino energy spectrum during the reactor operating period and the decay of the residual-antineutrino spectrum after the reactor is stopped. We find that relevant variations in the spectra of soft recoil electrons produced via weak and magnetic $\bar{\nu}_e e$ scattering can play a significant role in current and planned searches for the neutrino magnetic moment at reactors. © *2000 MAIK “Nauka/Interperiodica”.*

1. INTRODUCTION

Efforts are currently being made to observe the neutrino magnetic moment μ_ν below the limit of $2 \times 10^{-10}\,\mu_B$ found in previous experiments at the Savannah River, Krasnoyarsk, and Rovno reactors [1]. The KURCHATOV–PNPI (Petersburg Nuclear Physics Institute, Gatchina) collaboration is planning new studies of low-kinetic-energy recoil electrons in a $\bar{\nu}_e e$ experiment with a Si semiconductor multidetector at the Krasnoyarsk reactor. The MUNU collaboration experiment at BUGEY with a gas TPC chamber is in the final stage of preparation [2]. At the Institute of Theoretical and Experimental Physics (ITEP, Moscow), preparations to use a HPGe detector for this purpose are also under way [3].

A dominant contribution to soft recoil electrons produced in $\bar{\nu}_e e$ scattering comes from the low-energy section of the reactor-$\bar{\nu}_e$ energy spectrum. This section of the spectrum is strongly time-dependent: it never comes to a saturation during the reactor operating period and does not vanish after the reactor is shut down, the time when the background is usually measured.

Here, we consider the time evolution of a typical reactor-$\bar{\nu}_e$ energy spectrum and discuss relevant variations in the spectra of recoil electrons from $\bar{\nu}_e e$ scattering.

2. TIME VARIATION IN THE REACTOR-ANTINEUTRINO SPECTRUM

Three components contribute to the reactor-$\bar{\nu}_e$ energy spectrum $\rho(E)$/(MeV fission event):

$$\rho(E) = \rho_F(E) + \rho_U(E) + \Delta\rho(E). \tag{1}$$

Here, the term $\rho_F(E)$ represents the radiation of the ^{235}U, ^{239}Pu, ^{238}U, and ^{241}Pu fission fragments. The second term stems from the chain of beta decays that follow neutron radiative capture in ^{238}U:

$$^{238}\mathrm{U}(n,\gamma)^{239}\mathrm{U}\frac{\beta}{23.5\ \mathrm{min}} \longrightarrow {}^{239}\mathrm{Np}\frac{\beta}{2.36\ \mathrm{d}} \longrightarrow {}^{239}\mathrm{Pu}. \tag{2}$$

The last term in (1) takes into accounts antineutrinos (and neutrinos) induced by neutron interactions with other materials in the reactor core. As was discussed in [4], this term contributes no more than 1% to the total reactor-$\bar{\nu}_e$ flux and is disregarded here.

Until recently, the term ρ_F was traditionally identified with the reactor-$\bar{\nu}_e$ spectrum. The contribution of antineutrinos from chain (2) is, however, quite sizable for all reactors where neutrino experiments are running or planned. In the Rovno, Bugey, and Chooz PWR-type reactors, about $1.2\bar{\nu}_e$ per fission event come from this source.

For each of the four isotopes ^{235}U, ^{239}Pu, ^{238}U, and ^{241}Pu, the evolution of the neutrino spectra $\rho(E, t)$ was calculated as a function of the time t from the beginning of the fission process. The subsequent decay of the spectra during the reactor shutdown period was followed. These calculations employed data on 571 fission fragments, data on nuclear isomers, and data on delayed neutron emission.

The calculations show that, in PWR reactors, about two-thirds of all antineutrinos belong typically to the energy region below $E = 1.5$ MeV. This section of the $\bar{\nu}_e$ spectrum $\rho_F(E, 330)$ and its component due to fission fragments, $\rho(E, 330)$, at the end of the 3.30-d reactor operating period are presented in Fig. 1*a*. In Fig. 1*b*, one can see the hard part of the reactor-antineutrino spectrum that was previously measured directly in Rovno [5].

---

* This article was submitted by the authors in English.

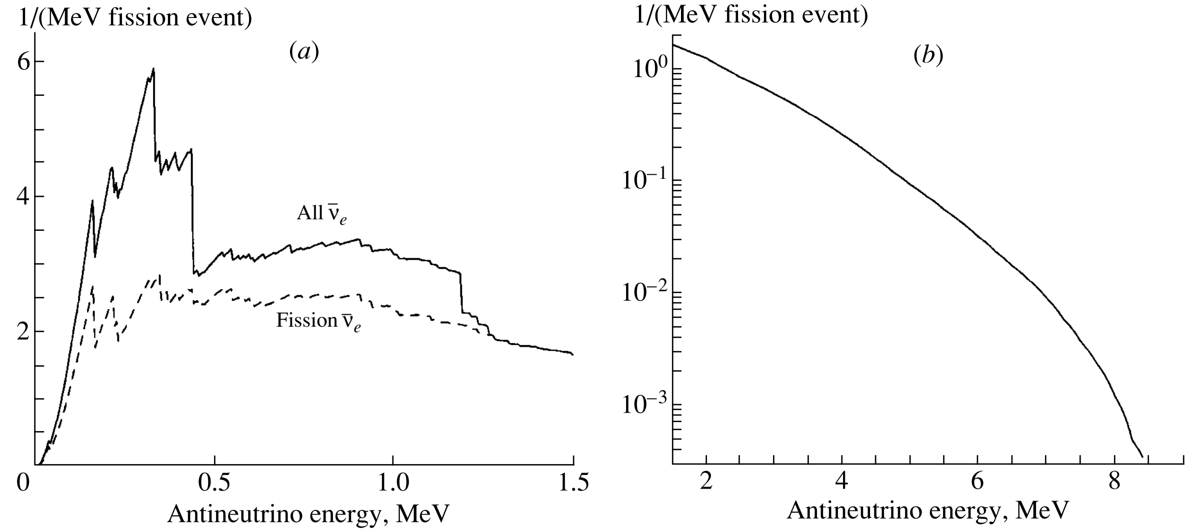

Fig. 1. Typical energy spectrum of electron antineutrinos from a PWR reactor at the end of the 330-d run: (*a*) soft section and (dashed line) fission $\bar{\nu}_e$ only; (*b*) high-energy section.

The evolution of the $\bar{\nu}_e$ spectrum during the PWR reactor operating period and its decay after the reactor is shut down is illustrated in Fig. 2.

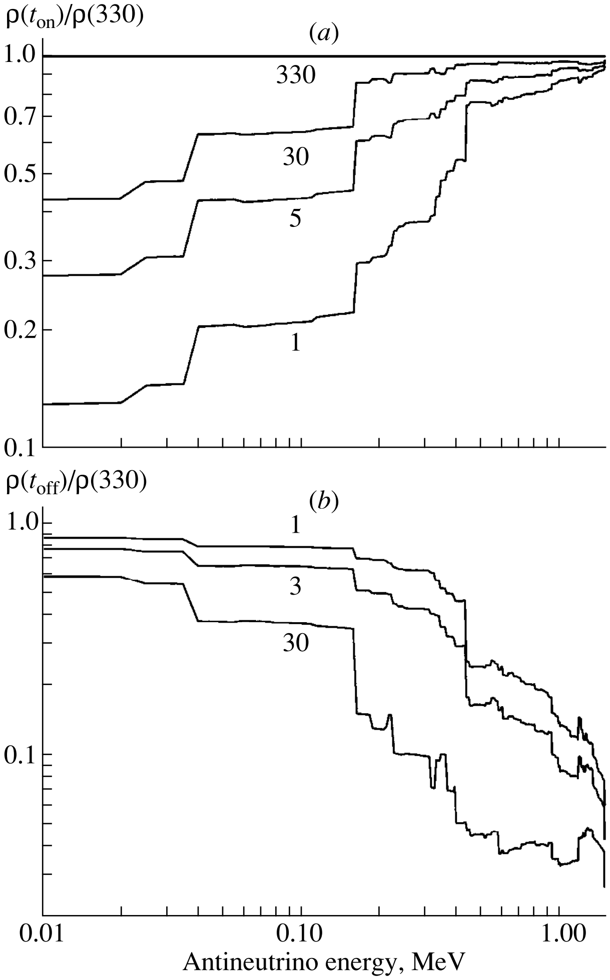

Fig. 2. Ratios of the current $\bar{\nu}_e$ spectra to that at the end of the 330-d run of the reactor (*a*) operating and (*b*) shutdown periods. The numbers indicate days from the beginning of the (*a*) period and (*b*) days after reactor shutdown.

3. RECOIL-ELECTRON ENERGY SPECTRA

The recoil-electron spectra $S^W(T)$ and $S^M(T)$ in cm^2/(MeV fission event) units (T is the recoil-electron kinetic energy) for weak (W) and magnetic (M) scattering of reactor antineutrinos are found as the convolution of the $\bar{\nu}_e$ spectra $\rho(E)$ with the differential cross sections for monoenergetic antineutrinos:

$$\frac{d\sigma^W}{dT} = g_F^2\frac{m}{2\pi}\left[4x^4 + (1+2x^2)^2\left(1-\frac{T}{E}\right)^2 - 2x^2(1+2x^2)\frac{mT}{E^2}\right], \tag{3}$$

$$\frac{d\sigma^M}{dT} = \pi r_0^2\frac{\mu_\nu^2}{\mu_B^2}\left(\frac{1}{T}-\frac{1}{E}\right). \tag{4}$$

Here, m is the electron mass, $g_F^2\frac{m}{2\pi} = 4.31 \times 10^{-45}$ cm^2/MeV, $x^2 = \sin^2\theta_W = 0.232$ is the Weinberg parameter, and $\pi r_0^2 = 2.495 \times 10^{-25}$ cm^2.

The calculated recoil-electron spectra $S^W(t, 330)$ and $S^M(t, 330)$ at the end of the reactor operating period are shown in Fig. 3. In searches for the neutrino magnetic moment, weak $\bar{\nu}_e e$ scattering plays the role of the reactor correlated background. We note that, in order to keep this background at a sufficiently low level, one should try to study recoil electrons at not overly high energies. For example, the recoil-electron energies

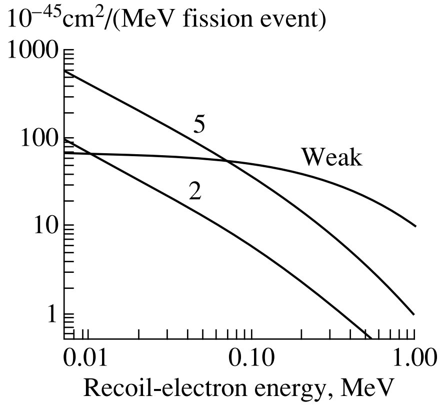

Fig. 3. Kinetic-energy spectra of recoil electrons for weak and magnetic $\bar{\nu}_e e$ scattering in the reactor-antineutrino spectrum at the end of a 330-d run. The numbers on the curves indicate the values of the moment in 10^{-11} μ_B.

$T > 100$ keV seem too "high" to seek $\mu_\nu = 2 \times 10^{-11}$ μ_B, while the range $T < 700$ keV is tolerably low for $\mu_\nu = 5 \times 10^{-11}$ μ_B.

The calculated time variations of the recoil-electron spectra during the PWR reactor operating and shutdown periods for weak and magnetic scattering are presented in Figs. 4*a* and 4*b*.

The recoil-electron energies below approximately 10 keV should be studied in order to observe the neutrino magnetic moment at a level of $\mu_\nu \simeq 10^{-11}$ μ_B (Fig. 3). For the reactor source, the differential cross sections for (2) and (3) do not depend here on the energy of the incident antineutrino and can be written as

$$\frac{d\sigma^W}{dT} = 10.16 \times 10^{-45} \text{ cm}^2/\text{MeV}, \tag{5}$$

$$\frac{d\sigma^M}{dT} = 2.495 \times 10^{-47}/T \text{ cm}^2 \text{ (for } 10^{-11}\mu_B). \tag{6}$$

We can therefore see that, in the limit considered here, the recoil-electron spectra $S^{W,M}$ can be expressed in terms of the total number of antineutrinos emitted per fission event, $N_\nu(t) = \int \rho(E, t) dE$:

$$S^W = 10.16 \times 10^{-45} N_\nu(t) \text{ cm}^2/\text{MeV fission event}, \tag{7}$$

$$S^M = 2.495 \times 10^{-47} N_\nu(t)/T \text{ cm}^2/\text{fission event}, \quad (\text{for } 10^{-11}\mu_B). \tag{8}$$

Typical time variations of the weak-scattering spectrum during the reactor operating and shutdown periods are illustrated in Fig. 5.

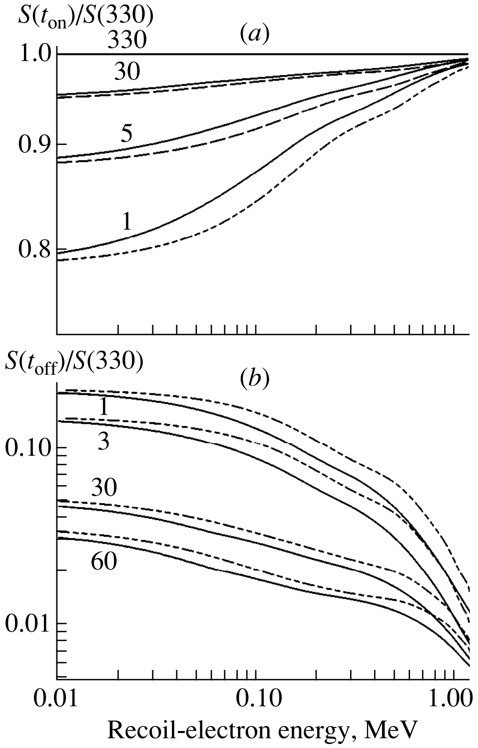

Fig. 4. Ratios of the current recoil-electron spectra to those at the end of the 330-d run for the reactor (*a*) operating and (*b*) shutdown periods. The solid (dashed) lines represent weak (magnetic) scattering.

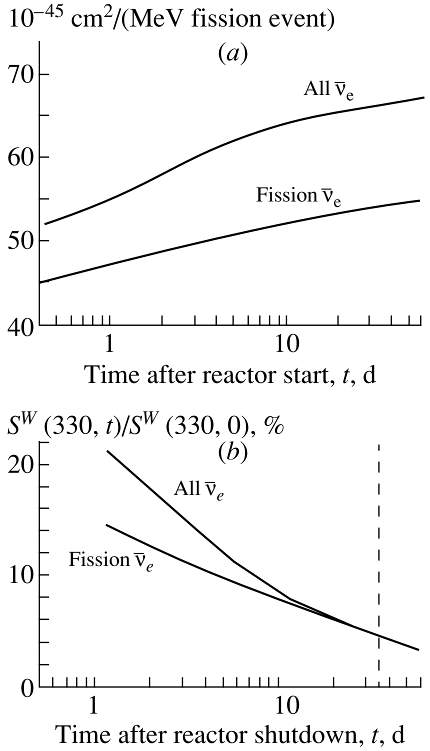

Fig. 5. Time variation in the cross section for weak $\bar{\nu}_e e$ scattering at a very low recoil, electron energy during the reactor (*a*) operating and (*b*) shutdown periods.

4. DISCUSSION AND CONCLUSIONS

In practice, the situation is not as simple as that presented above. There occur deviations from the standard operating schedule: the reactor can be stopped for a few days, or it can operate at a reduced level of power, etc. For each particular experiment, a comprehensive analysis of the reactor-operation data should be carried out with allowance for all details.

The main result of this study is that effects due to neutrino relaxation are not negligible in sensitive searches for the neutrino magnetic moment at reactors.

ACKNOWLEDGMENTS

This work was supported by Russian Foundation for Basic Research (project nos. 97-02-16031 and 00-15-96708).

REFERENCES

1. A. V. Derbin, Yad. Fiz. **57**, 236 (1994) [Phys. At. Nucl. **57**, 222 (1994)]; G. S. Vidyakin, V. N. Vyrodov, I. I. Gurevich, *et al.*, Pis'ma Zh. Éksp. Teor. Fiz. **55**, 212 (1992) [JETP Lett. **55**, 206 (1992)]; F. Reines, H. S. Gurr, and H. W. Sobel, Phys. Rev. Lett. **37**, 315 (1976).
2. The MUNU Collab. (C. Broggini), Nucl. Phys. B (Proc. Suppl.) **70**, 188 (1999).
3. A. Starostin, private communication.
4. A. M. Bakalyarov, V. I. Kopeĭkin, and L. A. Mikaélyan, Yad. Fiz. **59**, 1225 (1996) [Phys. At. Nucl. **59**, 1171 (1996)]; V. I. Kopeĭkin, L. A. Mikaélyan, and V. V. Sinev, Yad. Fiz. **61**, 2222 (1998) [Phys. At. Nucl. **61**, 2109 (1998)].
5. V. I. Kopeĭkin, L. A. Mikaélyan, and V. V. Sinev, Yad. Fiz. **60**, 230 (1997) [Phys. At. Nucl. **60**, 172 (1997)].

Physics of Atomic Nuclei, Vol. 63, No. 6, 2000, pp. 1016–1019. From Yadernaya Fizika, Vol. 63, No. 6, 2000, pp. 1091–1094.
Original English Text Copyright © 2000 by Kozlov, Khaltourtcev, Machulin, A. Martemyanov, V. Martemyanov, Sukhotin, Tarasenkov, Turbin, Vyrodov.

Antineutrino–Deuteron Experiment at the Krasnoyarsk Reactor*

Yu. V. Kozlov, S. V. Khaltourtcev, I. N. Machulin, A. V. Martemyanov, V. P. Martemyanov, S. V. Sukhotin, V. G. Tarasenkov, E. V. Turbin, and V. N. Vyrodov**

Russian Research Centre Kurchatov Institute, pl. Kurchatova 1, Moscow, 123182 Russia

Abstract—The investigation of antineutrino interaction with matter at the Krasnoyarsk reactor is described. The characteristics of the “Deuteron” detector, the results obtained, and prospects are discussed. *© 2000 MAIK “Nauka/Interperiodica”.*

1. INTRODUCTION

This article presents the results of some experiments that were performed at the neutrino underground laboratory of the Krasnoyarsk nuclear plant. First of all, it is necessary to describe the specific conditions at the Krasnoyarsk reactors. This unique complex of industrial nuclear reactors is housed inside a rock, and the passive shielding from cosmic muons corresponds to 600 mwe; therefore, the muon flux is suppressed by a factor of 1000. The reactor operating period is equal to approximately 50 d; therefore, one is able to measure the background every two months, in contrast to an interval of 1–1.5 yr at a power nuclear plant. The composition of nuclear fuel in the reactor allows the difference between the real antineutrino spectrum and the ^{235}U spectrum to be less than 1%.

A new experiment for studying antineutrino–deuteron interaction with the improved detector “Deuteron” is now under way. The interaction of antineutrinos ($\bar{\nu}_e$) with deuterons occurs via neutral current on deuteron (NCD) and charged current on deuteron (CCD),

$$\bar{\nu}_e + d \longrightarrow p + n + \bar{\nu}'_e,$$

$$\bar{\nu}_e + d \longrightarrow p + n + e^+.$$

Investigation of these reactions can furnish information about the weak-coupling constants for the charged and neutral currents, about the strength of the neutron–neutron interaction, and about neutrino oscillations. The results of the previous experiments that studied the antineutrino–deuteron interaction are shown in Table 1.

2. DETECTOR DESIGN

The upgraded detector “Deuteron” (Fig. 1) is situated in the underground laboratory at a distance of 34.0 m from the reactor. The neutrino flux is about $10^{12}\ \bar{\nu}_e/\mathrm{cm}^2$. The target volume is 513 l of D_2O (H_2O) placed in a stainless-steel tank surrounded by 30 cm of Teflon for neutron reflections, 0.1 cm of Cd, 8 cm of steel shots, 20 cm of graphite, and 16 cm of boron polyethylene (CH_2 + 3%B) for gamma and neutron shielding. The entire setup is pierced to make 169 holes (81 holes through the tank and Teflon, the others through Teflon alone). These holes house 169 proportional ^{3}He neutron counters with a reduced intrinsic alpha background. These counters are used to record neutrons. They are arranged in a square lattice 10 cm in size. The active shielding protects the main assembly against cosmic muons.

The neutron counters used in the experiment can record only neutrons, so that this is an integral-type detector. The counter consists of a stainless-steel tube 1 m long and 31 mm in diameter with walls 0.5 mm thick. A 20-μm wire is stretched along the counter. The wire is made from tungsten and coated with gold. The inner surface of the counter is covered with a 60-μm Teflon layer to reduce the natural alpha-particle back-

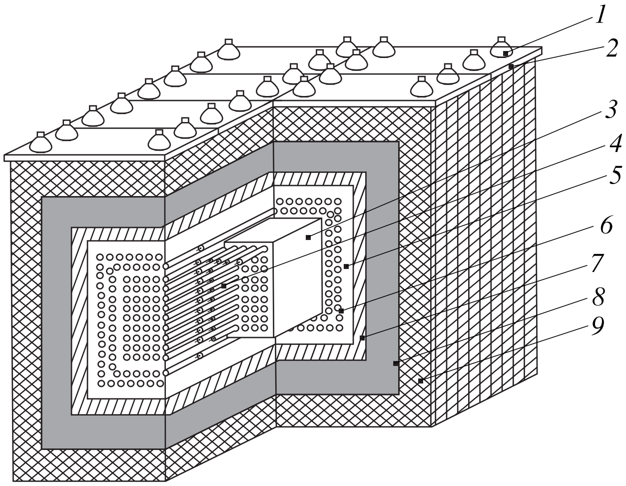

Fig. 1. Layout of the Deuteron detector: (*1*) photomultipliers, (*2*) muon veto system, (*3*) tank with water (target), (*4*) ^{3}He proportional counters, (*5*) Teflon, (*6*) channel for counters, (*7*) steel shots, (*8*) graphite, and (*9*) boron polyethylene.

---

[*] This article was submitted by the authors in English.

[**] e-mail: andrew@dnuc.polyn.kiae.su

Table 1

Savannah River [1] σ, $\times 10^{-45}$ cm$^2/\nu_e$	$\sigma^{\mathrm{NCD}} = 3.8 \pm 0.9$	$\dfrac{\sigma^{\mathrm{NCD}}_{\mathrm{expt.}}}{\sigma^{\mathrm{NCD}}_{\mathrm{theor}}} = 0.8 \pm 0.2$
	$\sigma^{\mathrm{CCD}} = 1.5 \pm 0.4$	$\dfrac{\sigma^{\mathrm{CCD}}_{\mathrm{expt.}}}{\sigma^{\mathrm{CCD}}_{\mathrm{theor}}} = 0.7 \pm 0.2$
	$\dfrac{\sigma^{\mathrm{CCD}}_{\mathrm{expt.}}}{\sigma^{\mathrm{NCD}}_{\mathrm{expt.}}} = 0.40 \pm 0.14$	$\dfrac{\sigma^{\mathrm{CCD}}_{\mathrm{theor}}}{\sigma^{\mathrm{NCD}}_{\mathrm{theor}}} = 0.353$
Krasnoyarsk [2] σ, $\times 10^{-44}$ cm^2/(^{235}U fission event)	$\sigma^{\mathrm{NCD}} = 3.0 \pm 1.0$	$\dfrac{\sigma^{\mathrm{NCD}}_{\mathrm{expt.}}}{\sigma^{\mathrm{NCD}}_{\mathrm{theor}}} = 0.95 \pm 0.33$
	$\sigma^{\mathrm{CCD}} = 1.1 \pm 0.2$	$\dfrac{\sigma^{\mathrm{CCD}}_{\mathrm{expt.}}}{\sigma^{\mathrm{CCD}}_{\mathrm{theor}}} = 0.98 \pm 0.18$
	$\dfrac{\sigma^{\mathrm{CCD}}_{\mathrm{expt.}}}{\sigma^{\mathrm{NCD}}_{\mathrm{expt.}}} = 0.37 \pm 0.14$	$\dfrac{\sigma^{\mathrm{CCD}}_{\mathrm{theor}}}{\sigma^{\mathrm{NCD}}_{\mathrm{theor}}} = 0.353$
Rovno [3] σ, $\times 10^{-44}$ cm^2/PWR-440	$\sigma^{\mathrm{NCD}} = 2.71 \pm 0.46 \pm 0.11$	$\dfrac{\sigma^{\mathrm{NCD}}_{\mathrm{expt.}}}{\sigma^{\mathrm{NCD}}_{\mathrm{theor}}} = 0.92 \pm 0.18$
	$\sigma^{\mathrm{CCD}} = 1.17 \pm 0.14 \pm 0.07$	$\dfrac{\sigma^{\mathrm{CCD}}_{\mathrm{expt.}}}{\sigma^{\mathrm{CCD}}_{\mathrm{theor}}} = 1.08 \pm 0.19$
	$\dfrac{\sigma^{\mathrm{CCD}}_{\mathrm{expt.}}}{\sigma^{\mathrm{NCD}}_{\mathrm{expt.}}} = 0.43 \pm 0.10$	$\dfrac{\sigma^{\mathrm{CCD}}_{\mathrm{theor}}}{\sigma^{\mathrm{NCD}}_{\mathrm{theor}}} = 0.37 \pm 0.08$
Bugey [4] σ, $\times 10^{-44}$ cm^2/fission event	$\sigma^{\mathrm{NCD}} = 3.29 \pm 0.42$	$\dfrac{\sigma^{\mathrm{NCD}}_{\mathrm{expt.}}}{\sigma^{\mathrm{NCD}}_{\mathrm{theor}}} = 1.01 \pm 0.13$
	$\sigma^{\mathrm{CCD}} = 1.10 \pm 0.23$	$\dfrac{\sigma^{\mathrm{CCD}}_{\mathrm{expt.}}}{\sigma^{\mathrm{CCD}}_{\mathrm{theor}}} = 0.97 \pm 0.20$
	$\dfrac{\sigma^{\mathrm{CCD}}_{\mathrm{expt.}}}{\sigma^{\mathrm{NCD}}_{\mathrm{expt.}}} = 0.33 \pm 0.08$	$\dfrac{\sigma^{\mathrm{CCD}}_{\mathrm{theor}}}{\sigma^{\mathrm{NCD}}_{\mathrm{theor}}} = 0.348 \pm 004$

ground from the stainless-steel wall, and the Teflon layer is covered with a 2-μm pure-copper layer to keep the counter able to work. The counter is filled with a mixture of 4 kPa ^{3}He and 4 kPa ^{40}Ar gases.

3. CHARACTERISTICS OF THE DETECTOR AND MONTE CARLO SIMULATIONS

The reaction n(He, T)p is used to detect neutrons. The amplitude spectrum is shown in Fig. 2. The losses of part of energy in the counter wall (wall effect) have been measured and are shown in Fig. 3. The efficiency of the detector was calculated by the Monte Carlo method both for the inverse-beta-decay reaction and for the antineutrino–deuteron reaction. Also, calculations were performed for the 252 Cf source, and this result was checked experimentally. The difference (less than 1%) between the calculated and experimental data shows good reliability of the Monte Carlo calculations. The neutron efficiency and the neutron lifetime are quoted in Table 2.

Special attention was given to the correlated background for the NCD channel associated with the antineutrino–proton interaction (we mean here the protons of H_2 atoms), because the cross section for this process is relatively large. The design of the detector

Table 2

Target Parameters	H_2O	D_2O
Efficiency of one neutron detection by tank counters alone	2.7 ± 0.3%	56.0 ± 0.7%
Efficiency of double-neutron detection by all counters	9.9 ± 0.1%	41.6 ± 0.4%
Neutron lifetime	138 ± 2 μs	203 ± 2 μs

Table 3

Set	Reactor power		Effect
	ON	OFF	
I	403.5 ± 4.5	201.4 ± 7.5	202.1 ± 8.0
II	395.5 ± 3.6	204.9 ± 7.5	190.7 ± 7.7
III	381.4 ± 3.9	187.9 ± 7.5	196.2 ± 6.9
IV	379.0 ± 4.6	169.6 ± 5.6	209.4 ± 3.8
Σ			205.1 ± 3.8

allowed us to reduce the efficiency of the detection of neutrons from boron polyethylene down to 0.002%. As a result, we estimated the correlated background at 0.6 event/d owing to the fact that the concentration of ordinary water in heavy water was 0.15%.

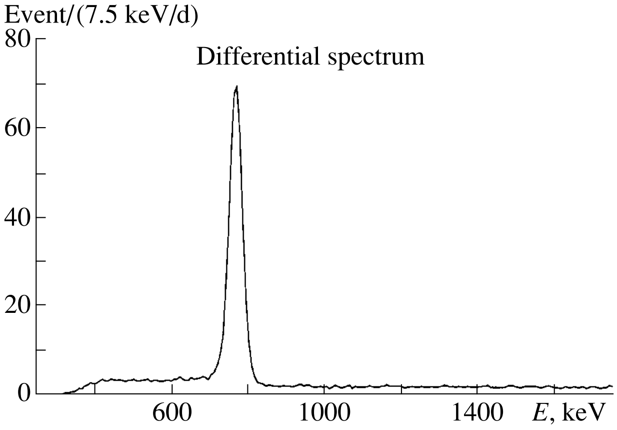

Fig. 2. Amplitude spectrum.

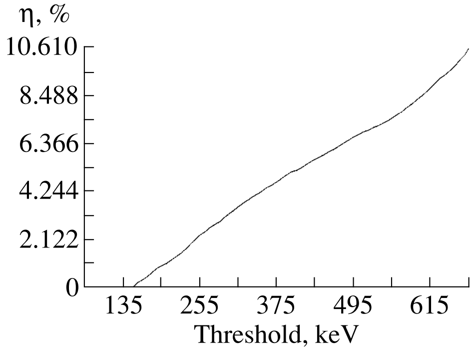

Fig. 3. Dependence of “wall” effect from threshold.

4. DESCRIPTION OF EXPERIMENT

4.1. Data Acqusition

The experiment was monitored on-line with CAMAC. A physical event is a detection of a neutron in the detector. Total information about an event includes the amplitude of any neutron, the astronomic time, the zone of neutron detection (detector was divided into 32 groups of counters), the multiplicity (the number of neutrons in a 800-μs detection window after the first neutron in the event), the condition of the event (no veto comes in the 800-μs interval before and after any neutron), and the time between neutrons in the same event.

4.2. H_2O Target

The reaction of inverse beta decay on a proton,

$$\bar{\nu}_e + p \longrightarrow n + e^+,$$

was used to check and improve some parameters of the detector. The exposure time was about 133 d. Four sets of measurements under different background conditions were performed. The results are presented in Table 3. The results were obtained when only tank events were analyzed and when the amplitude region of the detection of neutrons with energies from 644 to 884 keV was taken into account. The CCP cross section was found to be

$$\sigma_{\text{expt}}^{\text{CCP}} = (6.39 \times 10^{-43}$$

$$\pm 3.0\%)\ \text{cm}^2/(^{235}\text{U fission event}).$$

This result is in good agreement with the theoretical estimate of the cross section in the standard *V–A* theory. The ratio is (at a 68% C.L.)

$$R = \frac{\sigma_{\text{expt}}^{\text{CCP}}}{\sigma_{V-A}}(^{235}\text{U}) = 1.00 \pm 0.04.$$

4.3. D_2O Target

From the beginning of 1997 and up to now, the antineutrino–deuteron experiment has been in progress. Data have been collected for 360 d during the reactor operating period and for 120 d during the reactor shutdown period. There were eight sets of measurements. The results are shown in Table 4. The following extra cuts were used:

(i) For the CCD channel, events were selected with the energy of the first neutron in the interval from 644 to 844 keV and the energy of the second neutron in the interval from 190 to 884 keV and with the time between two neutrons from 5 to 800 μs.

(ii) For the NCD reaction, events were selected that were detected by the tank of the detector.

To be sure that the electronic and background conditions are quite stable, we analyzed events where the

Table 4

Set	T measured, 10^5 s		Effect per 10^5 s	
	Reactor ON	Reactor OFF	NCD (only tank)	CCD
I	27.96	13.77	23.25 ± 5.97	3.37 ± 1.46
II	34.94	10.16	21.14 ± 6.38	3.93 ± 1.55
III	26.82	5.94	11.79 ± 8.19	4.16 ± 1.87
IV	45.04	20.44	28.38 ± 5.72	4.27 ± 1.15
V	59.43	8.75	22.67 ± 7.76	4.14 ± 1.53
VI	62.10	24.10	28.15 ± 5.10	4.91 ± 1.00
VII	28.26	18.96	17.33 ± 6.37	5.03 ± 1.20
VIII	43.34	9.90	26.15 ± 7.17	4.75 ± 1.37
Σ	327.89	112.00	24.39 ± 2.24	4.44 ± 0.47

neutron multiplicity was not less than three. The results are shown in Table 5.

4.4. Preliminary Results

Considering the "wall" effect, the time rejection for double-neutron events, and the amplitude selection, we found that the neutron detection efficiencies are

$$\varepsilon_1^{\mathrm{NCD}}\ (\text{whole detector}) = 0.584,$$

$$\varepsilon_1^{\mathrm{CCD}}\ (\text{whole detector}) = 0.584\ (\text{first neutron detection}),$$

$$\varepsilon_2^{\mathrm{CCDd}}\ (\text{whole detector}) = 0.619\ (\text{second neutron detection}),$$

$$\varepsilon_1^{\mathrm{NCD}}\ (\text{tank}) = 0.507.$$

With the correction for the correlated background and for the possible detection in the NCD channel of some events that correspond to the CCD channel, one arrives at the following result (for tank only)

$$N^{\mathrm{NCD}} = 18.30 \pm 1.71 \text{ event}.$$

With

$$N^{\mathrm{NCD}} = P_{\mathrm{reactor}} \times \varepsilon_1^{\mathrm{ncd}} \times N_d \times \sigma_{\mathrm{expt}}^{\mathrm{ncd}},$$

$$N^{\mathrm{CCD}} = P_{\mathrm{reactor}} \times \varepsilon_1^{\mathrm{ccd}} \times N_d \times \sigma_{\mathrm{expt}}^{\mathrm{ccd}},$$

$$N^{\mathrm{CCP}} = P_{\mathrm{reactor}} \times \varepsilon_1^{\mathrm{ccp}} \times N_p \times \sigma_{\mathrm{expt}}^{\mathrm{ccd}},$$

one can obtain

Table 5

Multiplicity	ON	OFF	ON–OFF
3	3.108 ± 0.097	3.115 ± 0.169	–0.007 ± 0.19
More then 2	4.70 ± 1.12	4.68 ± 0.21	0.02 ± 0.24

Table 6

	σ, ×10^{-44} cm^2/(^{235}U fission event)	
	NCD	CCD
Experiment	3.09 ± 0.30	1.05 ± 0.12
Theory (Schreckenbach spectrum)	3.18 ± 0.17	1.07 ± 0.07
Ratio (experiment/theory)	0.97 ± 0.11	0.99 ± 0.13

$$\sigma_{\mathrm{expt}}^{\mathrm{NCD}} = (3.09 \pm 0.30) \times 10^{-44}\ \mathrm{cm}^2/(^{235}\mathrm{U}\ \text{fission event}),$$

$$\sigma_{\mathrm{expt}}^{\mathrm{CCD}} = 1.05 \pm 0.12 \times 10^{-44}\ \mathrm{cm}^2/(^{235}\mathrm{U}\ \text{fission event}).$$

These results are in good agreement with theory (Table 6).

In the future, we plan to continue the experiment till 2000; therefore, data will be taken for about 500 and 170 d during the reactor operating and shutdown periods, respectively. This will reduce the error down to 8% for the NCD and the CCD channel. To reduce the statistical error for the CCD channel, we plan to reject events using the geometry of the events involving detected neutrons.

ACKNOWLEDGMENTS

We would like to thank the staff of the Krasnoyarsk reactor for permanent support and Academician S.T. Belyaev and Dr. Yu.V. Gaponov for stimulating discussions.

This work is supported by the Russian Foundation for Basic Research (project nos. 99-15-96640 and 98-02-16313).

REFERENCES

1. E. Pasierb *et al.*, Phys. Rev. Lett. **43**, 96 (1979).
2. Yu. Kozlov *et al.*, Pis'ma Zh. Éksp. Teor. Fiz. **51**, 245 (1990) [JETP Lett. **51**, 279 (1990)].
3. Yu. Vershinsky *et al.*, Pis'ma Zh. Éksp. Teor. Fiz. **53**, 489 (1991) [JETP Lett. **53**, 513 (1991)].
4. M. Skorokhvatov, Study of Interaction of Electron Antineutrino with Protons and Deuterons (in press).

Physics of Atomic Nuclei, Vol. 63, No. 6, 2000, pp. 1020–1028. From Yadernaya Fizika, Vol. 63, No. 6, 2000, pp. 1095–1103.
Original English Text Copyright © 2000 by Khlopov.

ASTROPARTICLE PHYSICS AND COSMOLOGY

Physically Self-Consistent Basis for Modern Cosmology*

M. Yu. Khlopov**

Center for Cosmion Cosmoparticle Physics, Moscow, 125047 Russia

Abstract—Cosmoparticle physics appeared as a natural result of internal development of cosmology seeking physical grounds for inflation, baryosynthesis, and nonbaryonic dark matter and of particle physics going outside the Standard Model of particle interactions. Its aim is to study the foundations of particle physics and cosmology and their fundamental relationship in the combination of respective indirect cosmological, astrophysical, and physical effects. The ideas on new particles and fields predicted by particle theory and on their cosmological impact are discussed, as well as the methods of cosmoparticle physics to probe these ideas, are considered with special analysis of physical mechanisms for inflation, baryosynthesis, and nonbaryonic dark matter. These mechanisms are shown to reflect the main principle of modern cosmology, putting, instead of formal parameters of cosmological models, physical processes governing the evolution of the big-bang universe. Their realization on the basis of particle theory induces additional model-dependent predictions, accessible to various methods of nonaccelerator particle physics. Probes for such predictions, with the use of astrophysical data, are the aim of cosmoarcheology studying astrophysical effects of new physics. The possibility of finding quantitatively definite relationships between cosmological and laboratory effects on the basis of cosmoparticle approach, as well as of obtaining a unique solution to the problem of physical candidates for inflation, mechanisms of baryogenesis, and multicomponent dark matter, is exemplified in terms of gauge model with broken family symmetry, underlying horizontal unification and possessing quantitatively definite physical grounds for inflation, baryosynthesis, and effectively multicomponent dark-matter scenarios. *© 2000 MAIK “Nauka/Interperiodica”.*

1. INTRODUCTION

The Standard Model of particle interactions, which is based on the $SU(2) \times U(1)$ local gauge symmetry of electroweak interaction and on the $SU(3)_c$ symmetry of quantum chromodynamics (QCD, gauge theory of strong interactions), does not find at present any direct contradiction with experimental data. But the internal theoretical inconsistencies and aesthetic challenges to unify all the fundamental forces of nature make the theory go beyond the Standard Model, losing, along this path, the possibilities of direct experimental proofs.

The practical theoretical need for extending the Standard Model follows from internal problems of the Standard Model such as a quadratic divergence of loop radiative corrections to the mass of the Higgs field or strong *CP* violation in QCD. A solution to the former problem implies supersymmetry—symmetry between bosons and fermions—giving rise to cancellation of boson and fermion loop contributions to the Higgs mass due to the difference between Bose–Einstein and Fermi–Dirac statistics. Supersymmetry should be broken, since we do not observe it in the fermion and boson mass spectra, and the search for supersymmetric partners to known particles is one of the strongest challenges for the next generation of particle accelerators. But there is no hope to detect gravitino (a supersymmetric partner to the graviton), predicted in local supersymmetric models, even with far-future accelerators, because of its very weak, semigravitational coupling to other particles. A solution to the problem of strong *CP* violation in QCD implies the existence of the invisible axion, a pseudo-Goldstone boson, the “smaller brother” of π^0, with superweak interaction, being practically elusive in the direct search at accelerators.

The aesthetic motivation to extend the Standard Model is the attractive idea of unifying fundamental forces. Similarity in the description of electromagnetic, weak, and strong interactions achieved in the Standard Model finds deeper grounds in Grand Unified Theories (GUT), extending the fundamental gauge symmetry and putting $SU(2) \times U(1) \times SU(3)_c$ group of symmetry of the Standard Model into the unique group *G*. Arranging the set of known particles into the representation of the group *G*, one finds “white spots” to be occupied to make the representation complete. The larger *G*, the vaster the amount of new particles and fields that must be introduced to complement the basic particle and field content to the set corresponding to the full symmetry. Such particles and fields correspond to the “hidden sector” of respective theory, since they are hidden from the direct experimental probes either because of their large mass or because of very weak interaction with known particles. In either case, one needs some indirect means to test the respective predictions. The same is true for the parts of hidden sector, such as the “invisible axion” and gravitino, invoked in order to render the Standard Model self-consistent.

---

* This article was submitted by the author in English.

** e-mail: mkhlopov@orc.ru

There are a very few indirect effects of superheavy and superweakly interacting particles and fields accessible to laboratory probes. These are the neutrino mass, *CP* violation, and lepton- and baryon-number nonconservation (reflected in neutrino oscillations, neutrinoless double-beta decay, flavor-changing neutral currents, proton decay, and neutron–antineutron and hydrogen–antihydrogen oscillations). However rare, these effects may be discriminated owing to a manifest violation of conservation laws held in the Standard Model. The relatively small amount of such effects appeals for additional probes of the hidden sector of particle theory.

The problem of proper choice for an extensive hidden sector becomes more important in the models of the Theory of Everything (TOE), putting, into a unique theoretical framework, the foundations for all four fundamental natural forces, including gravity. Such a framework may follow from successive extensions of gauge symmetry—say, from the combination of local gauge models and supersymmetry, as this occurs in supergravity. Here, unification follows from the extension of internal symmetries to the symmetries of spacetime. An alternative approach is based on the extension of geometry of spacetime to include the description of particle interactions. A geometric approach ascribes fundamental forces to the effects of additional compactified dimensions and extends symmetries of spacetime to include symmetries of elementary particles. Both trends are accumulated by superstring theories on the basis of radically new fundamental concepts of string theories. In heterotic string theory, one combines $d = 10$ heterotic string theory with $E_8 \times E'_8$ gauge symmetry. Thus, its hidden sector should contain, in principle, all the zoo of particles, fields, and new phenomena arising in various extensions of the Standard Model, but direct experimental searches for these are either very hard or impossible.

For this reason, the Universe as a possible source of information about elementary particles has long since drawn the most serious attention of particle physicists. Ya. Zeldovich called the Universe the “poor man’s accelerator,” but, as A. Linde followed, even the richest man cannot build an accelerator reaching GUT or TOE physics to be naturally released at the earliest stages of cosmological evolution. Thus, the internal development of particle physics has led its theory to the big-bang Universe, probing its fundamental ideas.

Modern cosmology is based on two observational facts—namely, that the Universe expands and that the Universe contains electromagnetic blackbody background radiation. Putting them together, one comes to the ideas of the big-bang Universe. One inevitably arrives at the conclusion that, at earlier stages of cosmological expansion, the physical conditions in the Universe should have been much different from what we observe now. Extrapolating, or more precisely interpolating, the law of cosmological expansion to the past, one finds that, at much earlier stages of cosmological expansion, the energy density of radiation exceeded the matter density, so that the radiation-dominated stage should have occurred. One can easily check that matter and radiation were in equilibrium and that there were no galaxies and stars, but that matter was in the form of nearly homogeneous plasma. The old big-bang scenario was a self-consistent combination of general relativity, thermodynamics, and laws of atomic and nuclear physics that are well proven in laboratories and which are successively applied to the evolution of the Universe as a whole, under the assumption that only baryonic matter and electromagnetic radiation (and neutrinos) maintain its content [1]. According to this scenario, nuclear reactions should have occurred at the first three minutes, leading to the primordial chemical composition. This picture found qualitative confirmation in a comparison of the predictions of big-bang nucleosynthesis with the observed abundances of light elements. It gave a qualitative explanation to the observed structure of inhomogeneities as a result of gravitational instability in nearly homogeneous matter. However, quantitative disagreements that have become more and more profound render the whole picture controversial, unless some additional fundamental elements are added to the basis of the entire construction.

Namely, the level of initial fluctuations that were needed in the old big-bang scenario to provide the formation of the observed large-scale structure of the Universe proved to correspond to the expected effect in the anisotropy of thermal electromagnetic background inconsistent with the observed level of its isotropy. On the other hand, the low baryonic density that is needed to reproduce the observed abundance of light elements as a result of big-bang nucleosynthesis [2] was inconsistent with a much higher density needed to provide the formation of the large-scale structure as a result of development of gravitational instability during the matter-dominated stage.

Either problem seemed to find its laboratory-based solution within the old big-bang scenario when it was claimed in 1980 that the electron neutrino has the mass of about 30 eV. The neutrino thermal background as abundant as the photon thermal background was one of stable predictions of the old big-bang scenario. Multiplying this abundance by the neutrino mass claimed to be measured in the ITEP experiment, one found that the modern density of massive neutrinos should exceed the baryon-matter density by one to two orders of magnitude. One came to the scenario of the neutrino-dominated Universe, where massive neutrinos, weakly interacting with matter and radiation, has driven the formation of the cosmological large-scale structure with thermal-background-radiation anisotropy consistent with observational data and dominate the modern cosmological density. But successive experimental studies did not confirm the indication of the electron-neutrino mass as large as was claimed, and cosmological analysis, which proved the need for dark matter, dominating the Universe in the period of the formation of the large-scale structure, found serious problems in the scenario of the neutrino-dominated Universe. This leads the physics of dark matter outside the experimentally proven Standard Model of elementary particles. This made it necessary to modify the old big-bang scenario by an additional fundamental element—dark matter—by finding physical grounds for it in the hidden sector of particle theory. The problem of the true physical nature of the cosmological dark matter is accomplished by the fact that, however different from the cosmological viewpoint the models of large-scale-structure formation by hot, cold, unstable dark matter, or more sophisticated models, implying cosmic strings plus hot dark matter, late phase transitions, etc., are, they are not alternatives from the viewpoint of particle physics, having grounds in different and in general complementary parts of the hidden sector of particle theory. Therefore, the mixture of all of them should in principle be considered as a general case. Another important initial condition for the formation of the large-scale structure is the spectrum of initial fluctuations. It could be checked easily that statistical fluctuations alone cannot grow to form the structure of inhomogeneities in the expanding Universe. One has to assume the existence of small initial inhomogeneities originating from the very early stages of cosmological evolution. The old big-bang scenario had no physical mechanism for their origin. Moreover, the important questions of why the Universe expands, why its initial conditions were so close to those of the flat Universe, why they were so similar in causally disconnected regions, and why it contains matter and no antimatter had no fundamental relevance in the old cosmological paradigm.

The first three questions were solved in principle in inflationary cosmological models [3] under the assumption that there existed the stage of superluminous (in the simplest case, exponential) expansion in the very early Universe. This stage cannot be provided by matter, radiation, or relativistic-plasma dominance, but it can be realized under some conditions as a cosmological consequence of particle theory—for example, in a strong first-order phase transition or by slow evolution of a scalar field to its true vacuum state. Simultaneously, inflationary models found the physical mechanisms for the generation of the spectrum of initial fluctuations. The majority of these effects are related to experimentally inaccessible parts of particle theory—in particular, to the mechanisms of symmetry breaking at superhigh energy scales. One can also find that different inflationary models follow from different theoretical grounds and, in general, may coexist in the complete cosmological scenario. Sakharov [4] and then Kuzmin [5] were the first who related the observed baryon asymmetry of the Universe to the generation of baryon excess owing to out-of-equilibrium *CP*-violating effects in hypothetical baryon-nonconserving processes at very early stages of the initially baryon-symmetric Universe. Grand unified models provided a physical basis for these original ideas of baryogenesis, having the existence of baryon-nonconserving interactions among their predictions. The mechanisms of baryosynthesis found then some other grounds in supersymmetric models, where primordial condensate of scalar quarks is possible, resulting in a baryon excess after scalar-quark decay into ordinary quarks, and even in the Standard Model leading to baryon nonconservation at very high temperatures, provided that it is extended by considering the case of a larger Higgs sector or by including lepton-number-violating processes associated with the mechanism of the generation of the Majorana neutrino mass.

Thus, the modern cosmological paradigm reflects a fundamental change in our understanding of what big-bang cosmology is. From the old big-bang scenario, which is self-consistent, but which is basically controversial and incomplete, we arrive at the picture of inflationary cosmology with baryosynthesis and (multicomponent?) nonbaryonic dark matter. Thus, old big-bang theory is supplemented in the modern standard big-bang Universe, directly or indirectly, with at least three necessary elements (inflation, baryosynthesis, and nonbaryonic dark matter). These elements are based on the physical laws and are predicted by particle theory, but they have no experimental proofs. There are a wide variety of physical mechanisms for inflation and baryosynthesis and of candidates for the role of dark-matter particles; since neither the early Universe at the stage when inflation and baryosynthesis must have occurred nor dark matter could be observed directly by astronomical means, one should elaborate a system of indirect means to make the proper choice between these versions corresponding to various cosmological scenarios and particle models underlying them.

The problem is that the space of cosmological and physical parameters is, in general, multidimensional, since physical grounds for different mechanisms of inflation and baryosynthesis and for different candidates for dark matter follow from different physical motivations and are complementary rather than alternative. On the other hand, cosmological tests for particle models should generally take into account both the particular realization of inflation, baryosynthesis, and dark matter and the additional modifications to cosmological scenarios corresponding to the chosen realization.

Cosmoarcheology, which seeks, in astrophysical data, the footprints of new physical phenomena in the Universe, may be viewed as an already existing branch of Cosmoparticle physics proper [6, 7], where all its components are mixed in a nontrivial manner. As a result, there arises a set of astrophysical probes for the existence and the possible properties of hypothetical particles, fields, objects, and phenomena predicted as cosmological implications of particle theory. Cosmoarcheology treats the Universe as a unique natural accelerator laboratory, so that astrophysical data play here the role of a specific experimental sample in Gedanken

Experiments that cosmoarcheology undertakes. As in any experiment, it is necessary to have precise understanding of the experimental device used and to develop methods for data sampling and analysis in order to obtain meaningful results. The problem is that, in the Universal particle laboratory, both the source and detectors are out of control. Astrophysical processes cannot be directly reproduced in laboratories, but, however complicated the combination of effects is, theoretical astrophysics usually uses, in its analysis, natural laws proven experimentally. The trouble is that, in theoretical treatment of the Universe and its evolution, basic physical laws are not known. This renders a self-consistent formulation of cosmoarcheological approach model-dependent in general. One should account for the relationship between the hypothetical particle or field probed by the astrophysical data and the physics underlying inflation, baryosynthesis, and nonbaryonic dark matter. Since the latter is model-dependent, one should consider cosmological consequences of the hypothesis in question referred to the picture of cosmological evolution, based on the chosen particle model, underlying these necessary elements of modern cosmology. This means that the cosmological trace of a hypothetical particle or field may be multistep, following the nontrivial cosmological path that the model implies. On the other hand, one should expect, provided that inflationary baryon-asymmetric cosmology with nonbaryonic dark matter is indeed a proper basis of the Universe, the real picture of its evolution to be much more complicated than Gamow's original big-bang Universe scenario and generally more sophisticated than simple addition of inflation, baryosynthesis, and nonbaryonic-dark-matter dominance to the big-bang scenario. The reason is that any physically reasonable theoretical framework, giving rise to the necessary elements of cosmology, is generally much more extensive, supplementing these elements with a number of additional cosmologically relevant details. Testing these details, cosmoarcheology extends the might of observational cosmology, relating the true theory of the Universe to observations. Assuming that inflationary baryon-asymmetric cosmology with nonbaryonic dark matter is closer to reality than Gamow's original big-bang scenario, one should face the problem of observational evidence, specifying the choice for inflation model, mechanism of baryosynthesis, and the proper form of nonbaryonic dark matter. In cosmoarcheology, it is the problem of specifying the Universe as a natural accelerator.

2. INFLATION

One considers inflation as a necessary element of the cosmological picture. Inflation models explain why the Universe expands. They provide a solution to horizon, flatness, magnetic monopole, and some other problems ([3]; for an overview, see [7]). The solution is based on superluminous expansion, which occurs for the equation of state $p < -(1/3)\epsilon$. Neither matter nor radiation dominance can provide such an equation of state. One needs some hypothetical phenomena to occur in the very early Universe, inducing unstable negative-pressure stage of cosmological evolution. Such hypothetical processes may be related to R^2 effects in gravity, to strong first-order phase transitions, or to slow evolution of effective potential to the true vacuum state. To make the proper choice between these possibilities or, at least, to restrict their wide variety, additional traces of inflation mechanism should be considered.

(i) Fluctuations at the stage of inflation induce the spectrum of initial density fluctuations, giving rise to galaxy and large-scale-structure formation on respective scales. The amplitude of these fluctuations is constrained by the observed isotropy of the thermal electromagnetic background. It rules out all the inflation models with a high amplitude of predicted fluctuations and the majority of the GUT-induced phase-transition scenarios, in particular. In the simplest models featuring a quasi-De Sitter equation of state close to $p = -\epsilon$ at the stage of inflation, the flat Harrison–Zeldovich form of the spectrum is predicted. Then, the estimated amplitude of initial fluctuations at the modern LSS scale provides some information about the possible inflationary properties—for example, about the form and the parameters of the scalar-field potential.

(ii) For more complicated inflation models (multicomponent inflation), the form of the predicted spectrum of fluctuations may differ from the simple flat one. Phase transitions at the stage of inflation lead to specific peaks or plateaus in the spectrum, with the position and amplitude determined by the parameters of the model. One should also take into account phase transitions after the stage of global inflation which are capable of modifying the initial spectrum.

(iii) Both in the R^2 and in the scalar-field-driven (chaotic) inflation scenarios, a long dustlike postinflation stage appears, induced by coherent inflation-field oscillations. The duration of such stages determines the maximal temperature of the Universe after reheating, when the radiation-dominated stage starts. It also determines the specific entropy of the Universe after reheating.

(iv) The initial density fluctuations grow during the postinflation dustlike stage, following the general law of development of gravitational instability at the matter-dominated stage in the expanding Universe ($\delta\rho/\rho \sim t^{2/3}$). If the ratio of the cosmological time scales corresponding to the end (t_1) and the beginning (t_0) of the dustlike stage exceeds $\delta^{-3/2}$, where δ is the amplitude of the fluctuations, in the respective scale, an inhomogeneity is formed. Evolution of such inhomogeneities may lead to the formation of primordial black holes (PBH). The spectrum of PBHs reflects the scales at which inhomogeneities are formed, as well as the mechanism of PBH formation. The minimal probability W_{PBH} of PBH formation is proportional to $\sim\delta^{13/2}$, estimated for a direct formation of PBHs in contraction of a very small fraction of configurations evolved from specifically isotropic and homogeneous fluctuations. The amount of expected PBHs increases strongly upon taking into account PBH formation as the result of evolution of the bulk of inhomogeneities.

(v) Peaks in the spectrum of density fluctuations produced at the stage of inflation may also induce PBH formation even at the radiation-dominated stage with the probability $W_{\text{PBH}} \sim \exp(-\delta^2/18)$.

3. BARYOSYNTHESIS

The generally accepted motivation for the baryon-asymmetric Universe is the observed absence of antimatter at macroscopic scales up to the scales of galaxy clusters. In the baryon-asymmetric Universe, the observed baryonic matter, which originated from the initial baryon excess, survives local nucleon–antinucleon annihilation occurring within the first millisecond of cosmological evolution. The baryon excess is assumed to be generated in the process of baryogenesis [4, 5, 7], resulting in the baryon asymmetry of the initially baryon-symmetric Universe. Under some conditions, almost all the existing mechanisms of baryogenesis may lead to inhomogeneous baryosynthesis and even to the generation of antibaryon excess in some places. Thus, inhomogeneities of the baryon-excess distribution and even domains of antimatter in the baryon-asymmetric Universe may provide a probe for the mechanism of baryogenesis. In the original scenario of baryosynthesis due to Sakharov, with *CP*-violating effects in out-of-equilibrium *B*-nonconserving processes—for instance, the decays of some particles *X* generated in the charge-symmetric Universe with equal amounts of *X* and the corresponding antiparticles—the baryon excess is proportional to n_X and $\text{Im}\Phi$, Φ being the *CP*-violating phase. If the sign and the magnitude of $\Phi(x)$ varies in space, the same out-of-equilibrium *B*-nonconserving processes that lead to baryon asymmetry result in $B(x)$ and $B(x) < 0$ in the regions where $\text{Im}\Phi(x) < 0$. A spatial dependence of Φ is predicted in the model of spontaneous *CP* violation or in models where *CP*-violating phase is associated with the amplitude of the invisible-axion field. The size and amount of antimatter in domains generated in this case is related to the parameters of *CP*-violation models or of the invisible axion [7–10].

The baryon-asymmetry mechanisms motivated by SUSY GUT imply the flatness of the superpotential relative to the existence of squark condensate. Such a condensate, formed with $B > 0$, induces baryon asymmetry, after squark decays into quarks and gluinos. However, the mechanism does not fix the value and sign of *B* in the condensate, opening the possibilities for a nonuniform baryon-charge distribution and antibaryon domains [7, 9, 10].

A new approach to baryosynthesis that is based on electroweak-baryon-charge nonconservation at high temperatures also implies the possibility of antimatter domains—for example, owing to spontaneous *CP* violation [11]. Thus, antimatter domains may appear in the baryon-asymmetric Universe and may be associated with almost all the mechanisms of baryosynthesis, with the mechanisms of *CP* violation, and the possible mechanisms of primordial baryon-charge inhomogeneity. The size of these domains depends on the details of the respective phase transitions and on the initial distributions of variable (in space) *CP*-violating phase; in view of inflation, it may be as large as the modern horizon, which is so in the "island Universe" models [12] with inhomogeneities of the baryon-charge distribution of very large scale. The general parameters of the averaged effect of the domain structure are the relative amount of antimatter, $\Omega_a = \rho_a/\rho_{\text{crit}}$, where ρ_a is the cosmological antimatter density averaged over large scales and $\rho_{\text{crit}} = 3H^2/(8\pi G)$ is the critical density, and the mean size of domains, *l* (the characteristic scale in their distribution with respect to sizes), or, for small domains, t_{an}, the time scale of their annihilation with surrounding matter. Dense antimatter domains with the size exceeding the survival scale can form antimatter globular clusters in our Galaxy. It was shown in [13, 14] that the minimal mass of such a cluster is determined by the survival scale and that the maximal total mass of antimatter stars in our Galaxy is constrained by the galactic gamma-ray background. Such a cluster should be a galactic source of the antinuclear component of cosmic rays, which is accessible in the entire allowed range to search for antimatter in AMS experiment on the Alpha station [15].

4. NONBARYONIC DARK MATTER

The main arguments favoring nonbaryonic nature of dark matter in the Universe are big-bang nucleosynthesis (BBN) in inflation cosmology and the formation of the large-scale structure of the Universe at the observed isotropy of relic radiation. The first line of arguments accounts for the reasonable fits of BBN predictions to the observed abundances of light element at $\Omega_b < 0.15$–0.20 and at $\Omega_{\text{tot}} = 1$ predicted by inflation cosmology, ascribing the difference to nonbaryonic dark matter. The second type of arguments is that one can not accommodate both the formation of the large scale structure and the observed isotropy of thermal electromagnetic background without some weakly interacting form of matter triggering structure formation with minor effect in relic radiation angular distribution [7]. There are several scenarios of structure formation by hot dark matter (HDM), cold dark matter (CDM), unstable dark matter (UDM), mixed hot + cold dark matter [(H + C)DM], hierarchical decaying dark matter (HDS), etc. Physically, these scenarios differ by the ways and succession in which the elements of structure are formed, as well as by the number of model parameters. Bearing in mind the general independence of the motivations for each type of dark-matter candidates, one finds, however, from a particle-physics viewpoint that HDM, CDM, UDM, etc., are supplementary options to be taken together (accounting for the whole set of reasonable physical arguments) rather than alternatives. Indeed, one considers the would-be eV (10-eV) neutrino mass as a physical motivation for HDM scenario. But massive neutralinos predicted in supersymmetric models or invisible axions following from the Peccei–Quinn solution to the problem of strong *CP* violation in QCD—these particle species are CDM candidates—are based on physical grounds, which are in no case an alternative to the physics of neutrino mass. Thus, the mixed (H + C)DM scenarios seem physically more reasonable than the simple one-parameter HDM or CDM models. However, all these motivations do not correlate with the problem of quark–lepton families and the problem of the existence of three types of neutrinos. Physical mechanisms of family-symmetry breaking lead to new interactions causing massive-neutrino instability relative to decays into lighter neutrinos and a light Goldstone boson, a familon, or a singlet Majoron. Neutrino instability, intimately related to family-symmetry breaking, provides physical grounds for the UDM scenarios [7]. At the expense of an additional parameter (unstable-particle lifetime), the UDM models remove the contradiction between data on the total density within the inhomogeneities, $\Omega_{\text{inhom}} < 1$, and the prediction of inflationary cosmology, $\Omega = 1$, ascribing the difference in Ω to a homogeneous background of the products of unstable-particle decays. The UDM models also recover the disadvantages of the HDM scenarios that are associated with too rapid an evolution of the structure after its formation. Owing to neutrino instability, the large-scale structure formed at redshifts corresponding to observed distant objects survives the decay of the major part of dark matter that formed the structure. The actual multicomponent content of dark matter may be much richer if one takes into account the hypothesis of shadow matter, which follows from the need to recover the equivalence of left- and right-hand coordinate systems in Kaluza–Klein and superstring models. One runs into the problem of taking into account the whole set of matter fields and interactions arising from the E'_8 sector of the $E_8 \times E'_8$ heterotic string model. Even the above list of options, which is far from being complete, poses the serious problem of properly choosing the true combination of various dark-matter candidates in physically motivated multicomponent-dark-matter scenarios.

Since physical grounds for all nonbaryonic dark-matter candidates are outside the Standard Model and lose the proper experimentally proven basis, we either have to take into account all possible ways to extend the Standard Model, treating all the candidates as independent ones, or find a quantitatively definite way to estimate their relative contribution.

Cosmologically relevant consequences of both aesthetically and pragmatically motivated extensions of the Standard Model are generally related to stable or sufficiently metastable particles or objects predicted in them. Since (meta)stability is based in particle theory on some (approximate) conservation law reflecting respective fundamental symmetry or the mechanism of symmetry breaking, cosmoarcheology probes the most fundamental new laws of nature that are assumed by the respective extension of the Standard Model. Indeed, new symmetries extending the symmetry of the Standard Model imply new charges conserved exactly or approximately, and the lightest particle possessing respective charge should be either stable or metastable. The new charges may be related to local or global symmetry, a continuous or a discrete one. They may be topological, induced by the topology of the respective symmetry group. In the majority of cases, the mass of hypothetical particles and objects reflects the scale at which the assumed symmetry is broken. From the above, we can draw the following conclusions (see [7, 16] for details):

(i) In all GUT models unifying electromagnetism with other forces within a compact group of symmetry, magnetic-monopole solutions appear as a topological point object bearing the Dirac magnetic charge $g = hc/e$ and having a mass of order Λ/e, where Λ is the scale at which $U(1)$ symmetry that corresponds to electromagnetism decouples from the rest of the interactions.

(ii) Some specific GUT models imply a topology of the symmetry group that leads to the existence of a domain wall (spontaneously broken discrete symmetry), a cosmic string [spontaneously broken $U(1)$ symmetry], wall-surrounded-by-strings topological solutions, etc. The respective unit-surface (unit-length) energy density is on the order of the respective power of the scale Λ of symmetry breaking—that is, Λ^2 for walls and Λ for strings.

(iii) In supersymmetric models, *R* symmetry (exact or approximate) protects (meta)stability of the lightest supersymmetric particle (LSP). Its mass is generally related to the scale of supersymmetry breaking. In local supersymmetric models, this scale also defines the mass of the gravitino—a supersymmetric partner to the graviton—which has a semigravitational coupling to other particles, inversely proportional to the Planck scale m_{Pl}.

(iv) The seesaw mechanism of neutrino-mass generation implies a heavy right-handed neutrino with the Majorana mass M_R related to the scale of lepton-number nonconservation, the Majorana mass of the ordinary left-handed neutrino being m_{D}^2/M_R, where m_{D} is the Dirac fermion mass (typically related to the mass of the respective charged lepton). The lifetime of the heavy right-handed neutrino, which is determined by its mixing with the left-handed one ($\sim m_{\text{D}}/M_R$), proves to be inversely proportional to the mass of the light left-handed neutrino.

(v) A spontaneous breakdown of Peccei–Quinn symmetry, which is used to remove the problem of strong *CP* violation in QCD, results in the existence of the (pseudo)Goldstone boson, the axion with a mass $m_a \sim m_\pi f_\pi/F$, where F is the scale at which Peccei–Quinn symmetry is broken. The axion couplings to fermions are inversely proportional to F, and its lifetime with respect to decay into 2γ is of order $64\pi F^2/m_a^3 \sim F^5$.

(vi) Equivalence of right- and left-hand coordinate frames implies the existence of mirror partners to ordinary particles. Mirror particles should not have ordinary gauge interactions, and their own mirror interactions should be symmetric relative to the respective interactions of respective ordinary partners. Then, the mirror particles, which have the same mass spectrum and the same internal mirror couplings as their ordinary partners, are coupled to ordinary matter only by gravity.

(vii) The inclusion of mirror particles, together with ordinary particles, into the unifying GUT leads, after the symmetry of the GUT is broken and the ordinary and mirror sectors, which retain the discrete symmetry between them, are decoupled, to the existence of Alice strings, cosmic strings changing the relative minority of objects along closed paths around them.

(viii) In superstring models, initial mirror symmetry is broken owing to the concerted effect of compactification and gauge-symmetry breaking, so that shadow matter appears, losing discrete symmetry with ordinary partners. In the heterotic string model, the initial $E_8 \times E'_8$ gauge symmetry, which assumes exact symmetry between the ordinary (E_8) and the mirror (E'_8) world in the string model of ten spacetime dimensions is reduced, after compactification and gauge-symmetry breaking, to (broken) $E_6 \times$ (broken?) E'_8 four-dimensional effective field model with ordinary matter embraced by (broken) E_6 symmetry and the enormously extensive world of shadow particles and their interactions corresponding to the (broken?) E'_8 gauge group.

(ix) The mechanism of gauge-symmetry breaking in compactification onto Calabi–Yau manifolds or orbifolds, which is used in superstring models, implies homotopically stable solutions with a mass of $\sim r_c/\alpha'$, where r_c is the radius of compactification and α' is the string tension. These objects are sterile relative to gauge interactions and may act on ordinary matter only through gravity.

These and many other examples of the particle zoo induced by the extensions of the Standard Model of electroweak and strong interactions are related to the new phenomena whose direct experimental searches are either very hard or impossible in principle.

Thus, their cosmological effects are important or even unique sources of information about their possible existence.

One may reduce the effect of new particles and fields in the Universe to the two principal possibilities: (1) general dynamical influence on the cosmological expansion and (2) specific influence on particular astrophysical processes. In the first case, the very presence of hypothetical particles and fields in the Universe, irrespective of their specific properties, causes some observable effects. In the second case, some properties of the considered particles and fields should be specified in order to estimate the expected result. In the Universe viewed as a particle laboratory, these two types of effects may be compared with integral and differential detectors used in particle experiments. One can refer to the two widely known cosmological probes of new particles—(i) the age of the Universe (the modern total density is restricted by the observational lower bounds on the age of the Universe) and (ii) the primordial abundance of ^{4}He (the total density of the Universe in the period of big-bang nucleosynthesis is restricted by the observational upper limit on the primordial abundance of He or, in more refined approaches, by the set of constraints on the primordial abundances of light element)—as to the integral detectors probing the contribution to the cosmological density of any form of matter, irrespective of its particular properties.

In either case, the only thing that we assume on the hypothetical forms of matter is their existence in our spacetime, resulting in their contribution to the total density of the Universe. The same is true for the condition of sufficient growth of density fluctuations, which follows from the existence of the observed large-scale structure of the Universe and from the observed isotropy of the thermal-radiation background. This condition leads to the existence of a dustlike stage of (dark) matter dominance sufficiently long to ensure the formation of large-scale structure from the initial density fluctuations, which is small enough to satisfy the observed level of isotropy of relic radiation. It excludes the range of parameters of unstable particles (or objects) that lead to the dominance of their relativistic decay products in the period of large-scale-structure formation.

In the latter case, the properties or decay modes of unstable matter are not specified either. All these methods, being universal, have rather crude sensitivity to the parameters of hypothetical matter. Only the amount of such matter comparative with or dominant in the total cosmological density may be definitively excluded by the integral detectors. More refined and sensitive tools are available as soon as specific tracers of hypothetical matter are specified.

For stable charge-symmetric species that are present in the halo of Galaxy, their weak annihilation, which results in neutrino–antineutrino, gamma-ray, electron–positron, or proton–antiproton production, provides the possibility of excluding the range of respective parameters from (a) the observed nonthermal electromagnetic backgrounds or observational upper limits on them; (b) the observed gamma-ray background; (c) the observed electron–positron background; (d) data on the cosmic ray fluxes; and (e) the restrictions on high-energy neutrino cosmic backgrounds, which may be viewed as the "experimental" data from various detectors for the hypothetical processes.

For unstable species with a lifetime smaller than the age of the Universe, the same types of data trace the respective decay modes if the Universe is transparent to decay products. For each type of decay product, one may fix the redshift value from which the Universe is opaque to respective fluxes. Then, the data on the distortions of the thermal-background spectrum and on the abundances of light elements from nonequilibrium cosmological nucleosynthesis provide indirect information about the effects of interaction of the fluxes with plasma and radiation in the early Universe. The spectrum of relic radiation may be viewed as "electromagnetic calorimeter" of the early Universe, since any electromagnetic energy release from 10^5 s distorts the Planck form of the spectrum of thermal microwave-radiation background. The abundances of light elements provide an even more sensitive probe for nonequilibrium processes at the radiation-dominated stage owing to a strong possible change in the concentration of less abundant light elements (D, ^{3}He, Li, Be, B, …) in nuclear reactions induced by energetic-particle fluxes from hypothetical sources with comparatively small electromagnetic-energy release.

Almost all the aforementioned differential detectors may probe the products of PBH evaporation, so that the restrictions on the sources of respective particle fluxes or effects may be rescaled in terms of the constraints on the concentration of PBHs with masses 10^9–10^{15} g, which have been evaporated from the first second to the present time. Taking into account the possible mechanisms of PBH formation, one may use the data sensitive to the effects of PBH evaporation to probe hypothetical processes in the very early Universe.

The relative sensitivities of the integral and differential detectors, discussed above, to the hypothetical particles with relative abundance $\nu = n/n_\gamma$ (n is the concentration of the particles, while n_γ is the concentration of relic photons) and a mass m that cause the respective effects in the period τ is quoted in the review article [8] (see also [7, 16]), which presents a more detailed discussion of various detectors of the Universe and extensive bibliography.

To compare the immediate cosmological impact of particle theory with the set of restrictions following from astrophysical data, one generally has to evolve a multistep logical chain linking the hypothetical processes in the early Universe with the effects accessible to astrophysical observations.

In the old big-bang scenario, which assumed the simple picture of relativistic dominance from Planck times followed by the modern stage of matter dominance, such a link was established by analyzing the freezing-out or the decoupling of respective hypothetical species on the basis of Boatsman equations and by tracing the successive evolution of the frozen-out or decoupled species against the "smooth" cosmological background up to the period of their decay or to the modern Universe. The picture assumed that, at all stages, the physical conditions are well known, so that the only laboratory-unproved element was related to the hypothetical species studied.

The new big-bang paradigm of inflationary cosmology with baryosynthesis and nonbaryonic dark matter renders the linking much more complicated, since the initial or some successive stages of cosmological evolution of hypothetical species may generally differ strongly from the "smooth" thermodynamic picture of the hot Universe; moreover, the complete story of new standard cosmology is not well defined. One may use two ways to resolve this puzzle. A self-consistent approach is to consider physical grounds for inflation, baryosynthesis, and dark matter within the same class of particle models that features the phenomenon being considered. If, for example, we study some hypothetical cosmological implications of supersymmetric models, we should use a SUSY-based cosmological scenario, etc. At the expense of self-consistency, we may alternatively treat inflation, baryosynthesis, and dark matter phenomenologically, not specifying their physical relevance, and apply the approaches used within the old big-bang scenario. Provided that the abundances of light elements (especially of primordial ^{4}He) and the Planck form of the spectrum of relic radiation render the true cosmological evolution at the radiation-dominated stage after the first second effectively very close to the old big-bang scenario, such an approach may not cause considerable errors in many cases of interest.

To combine methods of cosmoparticle physics, one can consider an approach that tries to incorporate the main properties of elementary particles and the cosmologically relevant parameters corresponding to the physical mechanisms of inflation, baryosynthesis, and dark matter into a unique quantitatively definite theoretical framework.

Such an approach may be illustrated by the model of horizontal unification (see [17] and references therein). It was shown in those studies that not only does the extension of the standard $SU(2) \times U(1) \times SU(3)_c$ model of electroweak and strong (QCD) interactions of elementary particles to the gauge symmetry $SU(3)_H$ of quark and lepton families provide a reasonable theoretical description of the established existence of three families of quarks and leptons (ν_e, e, u, d), (ν_μ, μ, c, s), and (ν_τ, τ, t, b), but it proves to be, in its realization, a theoretical framework that incorporates, in a unique scheme, physical grounds for inflation, baryosynthesis, and dark matter. Even at the present level of "minimal" horizontal unification, the quantitatively definite choice of the parameters of the model as the result of a combined analysis of its physical, astrophysical, and cosmological predictions has led to reasonable dark matter models for the formation of cosmological large-scale structure, as well as to quantitatively definite scenario of cosmological evolution from Planck times to the period of galaxy formation and to a set of predictions open to experimental and observational tests.

This model, offering an alternative (horizontal) way to unification, is in no case an alternative to the more popular GUT or supersymmetric extensions of the Standard Model. The internal problems of minimal horizontal unification imply its further supersymmetric and GUT extensions, which are expected to provide better consistency with observations for its astrophysical and cosmological predictions. But even in the present form, the model reflects the main cosmoparticle principles. On the basis of a local gauge model with spontaneous symmetry breaking, it provides the phenomenology of world system, putting together almost all of the known basic particle properties and the main necessary cosmological parameters related to the hidden sector of particle theory. It offers the quantitatively definite correspondence between fundamental cosmological parameters (form of the inflation potential; lepton-number violation; mass, spectrum, and lifetime of dark-matter particles and fields), astrophysical effects (rate of stellar archion emission contributing significantly to stellar energy losses and to the dynamics of stellar collapse), and particle properties (seesaw mechanism of mass generation, hierarchy of the masses and mixings of quark and lepton families, Majorana mass ratio of neutrinos, rates of archion decays, neutrinoless double-beta decays). Finally, the number of free parameters of the model proves to be much less than the number of its signatures in particle processes, astrophysics, and cosmology, thus providing its definite test and exhibiting its completeness.

Thus, the model illustrates the might of the cosmoparticle approach. Its fundamental scale of horizontal-symmetry breaking is a priori unknown and corresponds to the hidden sector of particle theory, but an involved analysis of the set of its physical, astrophysical, and cosmological predictions makes it possible to fix the value of this scale in two rather narrow windows (around 10^6 and around 10^{10} GeV). The second solution, corresponding to the higher energy scale, seems to reproduce all basic features of the cosmological scenario with inflation, baryosynthesis, and cold (axionic) dark matter, which is widely assumed to be a standard one. The practical realization of this scenario, which in no case reflects a complete physical basis, shows that even the simplest reduced cosmological scenario does contain some additional elements (for example, the postinflation dustlike stage, during which PBH formation is possible with subsequent PBH evaporation at the radiation-dominated stage after primordial nucleosynthesis, formation of the primordial percolation structure of archioles, etc.). This example favors the conclusion that in no case are new cosmological elements based on the hypothetical effects of particle physics reduced to inflation, baryosynthesis, and dark matter. It also resembles the system of nontrivial cross-disciplinary links that should be used to probe the true world system with the aid of the methods of cosmoparticle physics, including nonaccelerator probes for new physics.

ACKNOWLEDGMENTS

The work was performed in the framework of the section “Cosmoparticle Physics” of the State Scientific–Technological Program “Astronomy: Fundamental Space Research” and of Astrodamus International Project with the support of Cosmion–ETHZ and AMS–Epicos collaborations.

REFERENCES

1. Ya. B. Zeldovich and I. D. Novikov, *Structure and Evolution of the Universe* (Nauka, Moscow, 1975).
2. D. N. Schramm and C. Copi, in *Proceedings of Cosmion-94*, Ed. by M. Yu. Khlopov *et al.* (Editions Frontieres, 1996).
3. A. Guth, Phys. Rev. D **23**, 347 (1981); in *Inflationary Universe*, Ed. by L. F. Abbott and S.-Y. Pi (World Scientific, Singapore, 1986).
4. A. D. Sakharov, Pis’ma Zh. Éksp. Teor. Fiz. **5**, 17 (1967) [JETP Lett. **5**, 12 (1967)].
5. V. A. Kuzmin, Pis’ma Zh. Éksp. Teor. Fiz. **12**, 335 (1970) [JETP Lett. **12**, 228 (1970)].
6. A. D. Sakharov, Vestn. Akad. Nauk SSSR **4**, 39 (1989); M. Yu. Khlopov, in *Cosmoparticle Physics: Ser. Physics* (Znanie, Moscow, 1989); M. Yu. Khlopov, in *Proceedings of Cosmion-94*, Ed. by M. Yu. Khlopov *et al.* (Editions Frontieres, 1996), p. 1.
7. M. Yu. Khlopov, *Cosmoparticle Physics* (World Sci., Singapore, 1999).
8. M. Yu. Khlopov and V. M. Chechetkin, Fiz. Élem. Chastits At. Yadra **18**, 627 (1987) [Sov. J. Part. Nucl. **18**, 267 (1987)].
9. V. M. Chechetkin, M. Yu. Khlopov, and M. G. Sapozhnikov, Riv. Nuovo Cimento **5–10**, 1 (1982).
10. M. Yu. Khlopov, *Astronuclear Experiment ASTROBELIX: Ser. Physics* (Znanie, Moscow, 1990); M. Yu. Khlopov, Sov. J. Nucl. Phys. **55**, 765 (1992).
11. D. Comelli, M. Pietroni, and A. Riotto, Nucl. Phys. B **412**, 441 (1994).
12. A. D. Dolgov, A. F. Illarionov, N. S. Kardashev, and I. D. Novikov, Zh. Éksp. Teor. Fiz. **93**, 1 (1987).
13. M. Yu. Khlopov, Gravitation and Cosmology **4**, 69 (1998).
14. K. M. Belotsky *et al.*, Gravitation and Cosmology (Suppl.): Cosmoparticle Physics **5**, 47 (1999).
15. R. Battiston, Gravitation and Cosmology (Suppl.): Cosmoparticle Physics **5**, 54 (1999).
16. M. Yu. Khlopov, in *Proceedings of Cosmion-94*, Ed. by M. Yu. Khlopov *et al.* (Editions Frontieres, 1996), p. 67.
17. M. Yu. Khlopov and A. S. Sakharov, in *Proceedings of Cosmion-94*, Ed. by M. Yu. Khlopov *et al.* (Editions Frontieres, 1996), p. 273.

Physics of Atomic Nuclei, Vol. 63, No. 6, 2000, pp. 1029–1036. From Yadernaya Fizika, Vol. 63, No. 6, 2000, pp. 1104–1111.
Original English Text Copyright © 2000 by Nath.

ASTROPARTICLE PHYSICS AND COSMOLOGY

Some Recent Developments in SUSY Dark Matter Analyses*

P. Nath**

Northeastern University, Boston, USA

Abstract—A brief summary of some of the recent developments in the analyses of supersymmetric dark matter is given. © *2000 MAIK "Nauka/Interperiodica".*

1. INTRODUCTION

In supersymmetric theories with *R* parity invariance, the least massive supersymmetric particle is absolutely stable [1]. In supergravity theories with spontaneous breaking of the electroweak symmetry generated by radiative corrections, the LSP turns out to be the light-est neutralino [2]. Under the constraints of *R* parity invariance, the LSP thus becomes a candidate for cold dark matter, and there have been numerous analyses for both the direct [3–6] and the indirect [7–9] detection for such dark matter. In this paper, we give a brief review of some of the recent developments. In Section 2, we discuss the neutralino relic density and the constraints on it in supergravity unified models. In Section 3, we discuss the direct detection of dark matter. We also discuss the effects of the uncertainties in the neutralino matter density and the effects of uncertainties in the rms WIMP velocity on event rates. Effects of naturalness assumptions on event rates are also discussed. In Section 4, we discuss the recent claims of the observation of an annual modulation signal by the DAMA experiment in the underground laboratory at Gran Sasso. In Section 5, we discuss indirect detection from the annihilation of neutralinos in the core of the Sun and the Earth and discuss the relative merits of the outgoing muon flux measurements from the Sun and the Earth as a function of the fine tuning parameter. We show that flux measurements from both the Earth and the Sun are necessary in order to map the parameter space of supergravity models. A comparison of the indirect vs. the direct measurements is also given. In Section 6, we discuss the effect of *CP*-violating phases on event rates in the direct detection of dark matter. *CP*-violating phases arise naturally in softly broken supersymmetric theories, and such phases can be large, i.e., *O*(1). These phases, however, are stringently constrained by the experimental EDM constraints on the electron and on the neutron EDMs. It is shown that, while the event rates are generally very sharply dependent on the *CP* phases, their effects are significantly reduced when the EDM constraints are included. Conclusions are given in Section 7.

2. RELIC DENSITY OF NEUTRALINO DARK MATTER

As discussed in the introduction, under *R* parity invariance the lowest mass supersymmetric particle (LSP) is absolutely stable. Further, in supergravity unified models the lowest mass neutralino turns out to be the LSP over most of the parameter space of the model. Thus, the lowest mass neutralino becomes a candidate for cold dark matter (CDM). The analysis of neutralino relic density follows the usual pattern. The neutralinos are copiously produced at Big Bang and subsequently annihilate by collisions through processes of the type $\chi + \chi \longrightarrow a + b$, where a and b are standard model particles. The number density of the relic neutralinos follows the Boltmann equation [1]

$$\frac{dn}{dt} = -3Hn - \langle\sigma v\rangle(n^2 - n_0^2), \qquad (1)$$

where n is the number/volume of χ's at time t, n_0 is n at thermal equilibrium, H is the Hubble parameter, σ is the annihilation cross section, v is the relative velocity of the neutralinos, and $\langle\sigma v\rangle$ represents the thermal average

$$\langle\sigma v\rangle = \int_0^\infty dv\, v^2(\sigma v)e^{-v^2/4x} \Big/ \int_0^\infty dv\, v^2 e^{-v^2/4x}. \qquad (2)$$

Here, $x = kT/m_{\chi_1}$, and T is the temperature. From this equation, one finds that the neutralinos decouple from the background when the annihilation rate becomes smaller than the expansion rate. The temperature at which this occurs is the freeze-out temperature T_f. Integrating the Boltzmann equation from the current temperature T_0 to the freeze-out temperature T_f, one finds the relic density $\Omega_{\tilde\chi_1^0} = \rho_{\tilde\chi_1^0}/\rho_c$ (where $\rho_{\tilde\chi_1^0}$ is the neutralino mass density and ρ_c is the critical mass density) at the current temperature

$$\Omega_{\tilde\chi_1^0}h^2 \cong 2.48\times10^{-11}\left(\frac{T_{\tilde\chi_1^0}}{T_\gamma}\right)^3\left(\frac{T_\gamma}{2.73}\right)^3\frac{N_f^{1/2}}{J(x_f)}, \qquad (3)$$

---

* This article was submitted by the author in English.

** e-mail: nath@albert.physics.neu.edu

1063-7788/00/6306-1029$20.00 © 2000 MAIK "Nauka/Interperiodica"

where $x_f = \frac{kT_f}{m_{\tilde\chi_1}}$, h is the Hubble parameter in units of 100 km/s Mpc, N_f is the number of degrees of freedom at freeze-out, $(T_{\tilde\chi_1^0}/T_\gamma)^3$ is the reheating factor, T_γ is the current microwave background temperature and $J(x_f)$ is given by

$$J(x_f) = \int_0^{x_f} dx\langle\sigma v\rangle(x) \ \ (\mathrm{GeV}^{-2}). \tag{4}$$

In the computation of the thermal average, one should use the accurate method [10, 11] to take account of the Z and Higgs poles. In supergravity models, the relic density is computed at each point of the parameter space which is allowed by the radiative breaking of the electroweak symmetry, accelerator constraints, and by the experimental constraints on the FCNC process $b \longrightarrow s + \gamma$. There is a considerable range for $\Omega_{\tilde\chi_1^0}h^2$ that is used in theoretical analyses. Various analyses have taken a range from 0.01 to 0.3. The effects of coannihilation may be important in certain regions of the parameter space, and a recent analysis is given in [12].

3. DIRECT DETECTION OF DARK MATTER

One of the most promising techniques for the detection of dark matter is that of scattering of neutralinos from nuclei. For processes without CP violation, this scattering is governed by the basic microscopic interaction [3–6]

$$\begin{aligned} L_{\mathrm{eff}} &= (\bar{\tilde\chi}_1\gamma^\mu\gamma_5\tilde\chi_1)[\bar q\gamma_\mu(A_LP_L + A_RP_R)q] \\ &\quad + (\bar{\tilde\chi}_1\tilde\chi_1)(\bar q C m_q q). \end{aligned} \tag{5}$$

The above interaction consists of a spin dependent part governed by the A_L and the A_R terms and a spin independent part governed by the C term. The event rates are given by [3–6]

$$\begin{aligned} R &= [R_{\mathrm{SI}} + R_{\mathrm{SD}}] \\ &\times\left[\frac{\rho_{\tilde\chi_1}}{0.3\ \mathrm{GeV\ cm}^{-3}}\right]\left[\frac{v_{\tilde\chi_1}}{320\ \mathrm{km/s}}\right]\left(\frac{\mathrm{events}}{\mathrm{kg\ d}}\right). \end{aligned} \tag{6}$$

Here R_{SI} is the spin independent part, R_{SD} is the spin dependent part, $v_{\tilde\chi_1}$ is the velocity of relic neutralinos in our galaxy impinging on the target, and $\rho_{\tilde\chi_1}$ is the local density of the relic neutralinos. R_{SI} is given by

$$R_{\mathrm{SI}} = \frac{16m_{\tilde\chi_1}M_N^3M_Z^4}{[M_N + m_{\tilde\chi_1}]^2}|A_{\mathrm{SI}}|^2, \tag{7}$$

where A_{SI} is the spin independent amplitude. R_{SD} is given by

$$R_{\mathrm{SD}} = \frac{16m_{\tilde\chi_1}M_N}{[M_N + m_{\tilde\chi_1}]^2}\lambda^2J(J+1)|A_{\mathrm{SD}}|^2, \tag{8}$$

where M_N is the mass and J is the spin of the target nucleus, λ is defined so that $\langle N|\Sigma\mathbf{S}_i|N\rangle = \lambda\langle N|\mathbf{J}|N\rangle$, and A_{SD} is the spin dependent amplitude. For heavy targets, one has $R_{\mathrm{SI}} \sim M_N$ and $R_{\mathrm{SD}} \sim 1/M_N$. Thus, one expects that the scalar interaction will dominate over the spin dependent interaction for heavy targets.

3.1. Uncertainties of Input Data

In the analysis, one must take account of the uncertainties of the input data. These consist of the uncertainties in the local WIMP density of [13] (0.2-0.7) GeV cm^{-3}. Defining

$$\xi = \rho_{\tilde\chi_1^0}/\rho_0, \quad \rho_0 = 0.3\ \mathrm{GeV\ cm}^{-3}, \tag{9}$$

one finds that ξ lies in the range

$$0.7 \le \xi \le 2.3. \tag{10}$$

Effects of variations in local WIMP density have been investigated by many authors. Recently, there have also been investigations of the effects of variations in the rms WIMP velocity. One generally assumes a Maxwellian velocity distribution for the WIMPs. Estimates of the rms WIMP velocity range give [14] $v = 270 \pm 50$ km/s. The effects of variations of the rms WIMP velocity have been investigated for direct detection in [15, 16] and for indirect detection in [9]. There could also be effects due to the rotation of the galaxy. However, an analysis of these effect on the direct detection rates is found to be only ~10% [17].

3.2. Fine Tuning

An interesting question concerns the effect of naturalness assumption on dark matter. A simple criterion that is often used for naturalness is that the SUSY mass spectrum lies in the TeV mass range, i.e., m_0, $m_{\tilde g}$ = $O(1)$ TeV [18]. However, one can quantify this criterion further via radiative breaking of the EW symmetry where one needs to fine tune the SUSY parameters to get the Z boson mass. Thus, in radiative breaking, one defines $(1/2)M_Z^2 = \lambda^2 - \mu^2$, where λ depends on the parameters m_0, $m_{1/2}$, A_0, and $\tan\beta$. These are the parameters of the minimal supergravity unified models [19, 20]. Here, m_0 is the universal scalar mass, $m_{1/2}$ is the universal gaugino mass, A_0 is the universal trilinear coupling, and $\tan\beta = \langle H_2\rangle/\langle H_1\rangle$, where $\langle H_2\rangle$ gives mass to the up quarks and $\langle H_1\rangle$ gives mass to the down quarks and the leptons. Fine tuning can be quantified by [21]

$$\Phi = \frac{1}{4} + \frac{\mu^2}{M_Z^2}. \tag{11}$$

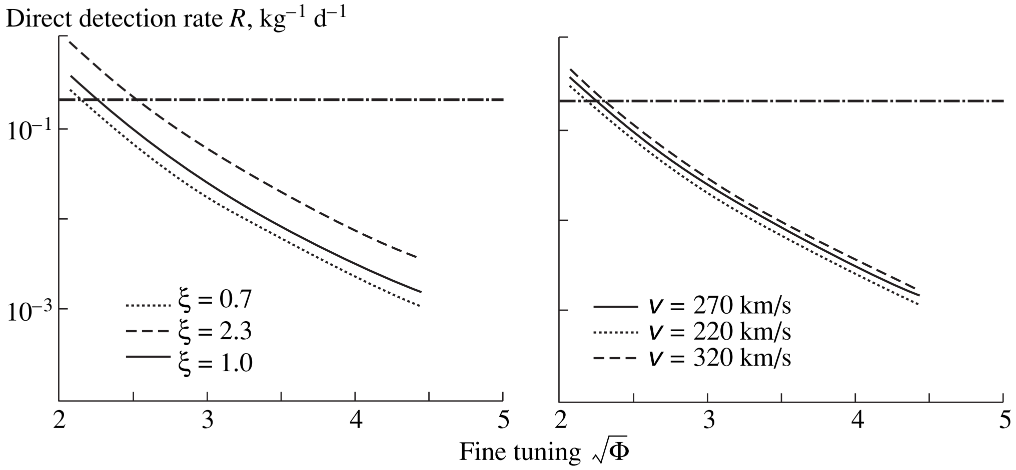

Fig. 1. Plot of the event rate R for Ge as a function of the fine tuning parameter $\Phi^{1/2}$. The effects of uncertainties in the input data on the relic density and on the rms WIMP velocity are also exhibited. The horizontal dot-dashed line corresponds to the current experimental limit [24] (from [9]).

Using Φ the EW symmetry breaking condition is

$$C_1 m_0^2 + C_3 m_{1/2}'^2 + C_2' A_0^2 + \Delta\mu_{\mathrm{loop}}^2 \simeq M_Z^2 \Phi, \qquad (12)$$

where $C_1 > 0$, $C_2' > 0$, and $C_3 > 0$ at the scale $Q = M_Z$. The loop corrections are typically small for small $\tan\beta$ ($\tan\beta \le 5$), and the EWSB equation here takes on an ellipsoidal form [21]

$$\frac{m_{1/2}^2}{a} + \frac{m_0^2}{b} + \frac{A_0^2}{c} \simeq 1 \qquad (13)$$

with $a > 0$, $b > 0$, and $c > 0$; i.e., the soft parameters lie on the surface of an ellipsoid whose radii are fixed by the value chosen for the fine tuning Φ, and thus m_0, $m_{1/2} \sim \sqrt{\Phi} \sim |\mu/M_Z|$. Thus, $\sqrt{\Phi}$ controls how large the SUSY breaking scale can get. There are, however, regions of the parameter space where large SUSY masses can result even for small values of fine tuning [22, 23]. Fine tuning affects analyses of dark matter. In Fig. 1, we plot the event rate for Ge as a function of the fine tuning parameter. One finds that larger fine tunings imply smaller event rates. Thus, as the SUSY spectrum gets heavier, the fine tuning parameter becomes larger and the event rates decrease.

4. CONSTRAINTS FROM DAMA

DAMA has examined the possibility of the direct detection of Milky Way WIMPS using the annual modulation signal which arises due to the motion of the Earth around the Sun. Thus, v_{E}, the velocity of the Earth relative to the Galaxy, is given by

$$v_{\mathrm{E}} = v_{\mathrm{S}} + v_0 \cos\gamma \cos\omega(t - t_0), \qquad (14)$$

where v_{S} is the Sun's velocity relative to the Galaxy ($v_{\mathrm{S}} = 232$ km/s), v_0 is the Earth's orbital velocity around the Sun ($v_0 = 30$ km/s), and γ is the angle of inclination of the plane of the Earth's orbit relative to the galactic plane ($\gamma \cong 60°$). One has $\omega = 2\pi/T$ ($T = 1$ yr), and the maximum velocity occurs at t_0 = June 2. The change in the Earth's velocity relative to the incident WIMPs leads to a yearly modulation of the scattering event rates of about 7%. Using ~100 kg of radiopure NaI at Gran Sasso, DAMA has collected a total of 19511 kgd of data and has examined the possibility of the direct detection of Milky Way WIMPS using the annual modulation signal which arises due to the motion of the Earth around the Sun. The first DAMA analysis [25] gave a WIMP mass and proton cross section of $M_{\mathrm{WIMP}} = 59^{+17}_{-14}$ GeV and $\xi\sigma_{\mathrm{W}-p} = (7.0^{+0.4}_{-1.2}) \times 10^{-6}$ pb, where $\xi = \rho_{\mathrm{W}}/\rho_0$ and ρ_{W} is the local Milky Way WIMP mass density and $\rho_0 = 0.3$ GeV cm^{-3} and $\rho_{\chi_1^0}$ may vary from about (0.2-0.7) GeV cm^{-3}, i.e., $0.7 \lesssim \xi \lesssim 2.3$ as given by (10). A revised analysis by DAMA taking into account uncertainties in the WIMP velocity gives $30 \le m_\chi \le 130$ GeV [15]. It appears possible to accommodate the DAMA signal within the framework of the supergravity unified models [26, 27].

5. INDIRECT DETECTION

There are several different possibilities for the indirect detection of neutralino dark matter such as the annihilation of neutralinos in the galactic halo and their annihilation in the centers of the Sun and the Earth. Here we discuss the latter possibility, i.e., their annihilation in the center of the Sun and the Earth. The basic idea here is that the Milky Way neutralinos are trapped by scattering and gravitational pull by the Earth and the Sun and accumulate in their cores, where they eventu-

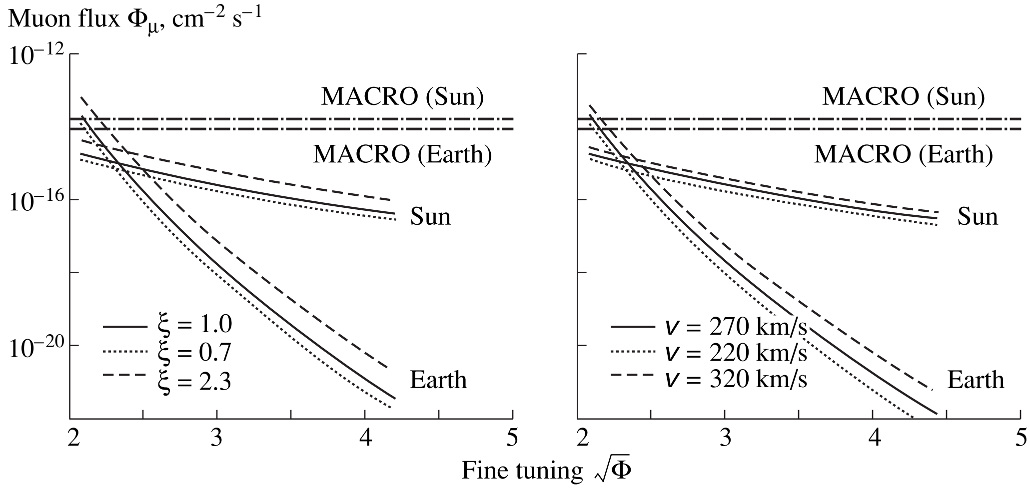

Fig. 2. The figure gives the average out going muon flux for the Earth and the Sun as a function of the fine tuning parameter Φ. Effects of neutralino relic density and of the rms WIMP velocity are also exhibited. The lower limits from MACRO [29] are also plotted as horizontal dot-dashed lines (from [9]).

ally annihilate. The number density n_χ of χ_1^0 in the center of the Sun or the Earth obeys the relation $\dot{n}_\chi = C - C_A n_\chi^2$, where the first term governs the capture and the second term governs the annihilation, and thus C and C_A control the equilibrium between capture and annihilation. The neutrino flux from the χ_1–χ_1 annihilation remnants is given [7, 8]

$$\frac{d\phi}{dE} = \frac{\Gamma_A}{4\pi R^2}\sum_F \mathrm{Br}_{Fi}\left(\frac{dN}{dE}\right)_{Fi}, \tag{15}$$

where R is the distance from the source; F stands for the final states into which χ_1 annihilate; Br_{Fi} are the branching ratios into τ's, heavy quarks, and gluons; and $\left(\frac{dN}{dE}\right)_{Fi}$ is the ν_i energy spectrum from the injected particle F in the core of the Sun or the Earth. The annihilation rate Γ_A is given by [28]

$$\Gamma_A = \frac{C}{2}\tanh^2(t/\tau), \tag{16}$$

where $\tau = (CC_A)^{-1/2}$ and t is age of the Sun or Earth (4.5 Gyr), and C_A depends on the WIMP annihilation cross section. In the limit $t \gg \tau$, $\Gamma_A \sim C/2$; i.e., an equilibrium is reached between annihilation and capture. Equilibrium depends on the particulars of the SUSY parameter space. For the Sun, the equilibrium is realized over essentially all of the parameter space. For the case of the Earth, this condition depends sharply on the parameter space. The energetic neutrinos arising from the χ_1 annihilation in the core of Sun or Earth will produce muons in the rock surrounding the detector. The out going muon flux is given by

$$\Gamma_{\mathrm{detect}} = 1.27\times 10^{-29} C m_{\chi_1}^2 \sum_i a_i b_i \sum_F \mathrm{Br}_F \langle Nz^2\rangle_{Fi} m^{-2} \quad (\mathrm{yr}^{-1}), \tag{17}$$

where $m_{\chi_1}^2\langle Nz^2\rangle_{Fi}$ are the second moments defined by $\langle Nz^2\rangle_{Fi} = \frac{1}{m_{\chi_1}^2}\int\left(\frac{dN}{dE}\right)_{Fi}E^2dE$. The out going muon flux is sensitive to the characteristics of the SUGRA models. The size of the fine tuning parameter also has significant implications for the indirect detection of dark matter [9]. In Fig. 2, we plot the average out going muon flux from the Earth and the Sun as a function of the fine tuning parameter Φ, and we also show the current experimental limits [29]. First one finds that the outgoing muon flux falls sharply with increasing value of fine tuning as expected. More interestingly one finds that while the outgoing muon flux from the Earth is larger than the outgoing muon flux from the Sun for the case when the fine tuning parameter is relatively small, i.e., $\Phi < 2.5$, the reverse situation occurs for the case for relatively larger values of Φ. Here, it is the outgoing muon flux from the Sun that is significantly larger than the outgoing muon flux from the Earth. A similar situation occurs when the outgoing flux from the Earth and the Sun is plotted as a function of the direct detection rate for Ge. This is done in Fig. 3 [9]. Thus, from Fig. 3, one arrives at the conclusion that the observation of the outgoing muon flux from both the Earth and the Sun is necessary in mapping the parameter space of supergravity models. For relatively small values of fine tuning, it is the Earth which gives the larger sensitivity for

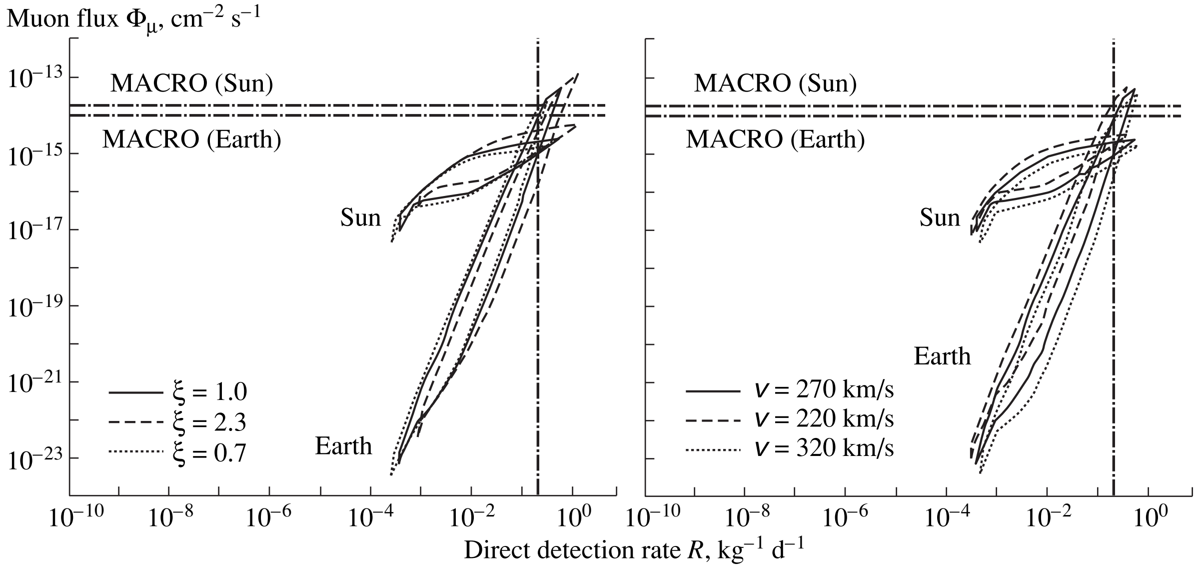

Fig. 3. Plot of the maximum and the minimum flux rates from the Earth and the Sun plotted as a function of the direct detection rate for Ge. Effects of uncertainties in the relic density and in the rms velocity of WIMPs are also exhibited. The horizontal dot-dashed lines correspond to the current experiment on the outgoing muon flux from Macro [29], and the vertical dot-dashed line is the current limit on the direct detection from [24] (from [9]).

detection of dark matter, while for larger values of fine tuning it is the Sun which gives the larger flux and hence the larger sensitivity for dark matter detection.

6. *CP* VIOLATION AND DARK MATTER

In general, the soft SUSY breaking parameters that arise from spontaneously broken supersymmetry can be complex and such complex parameters generate *CP* violation. The *CP*-violating phases enter in low-energy physics, e.g., in the susy particle spectrum, in dark matter analyses, and in other low-energy phenomena. The *CP* phases are sharply constrained by the electric dipole moments constraints on the electron and on the neutron. For the electron, the current experimental limit is [30] $|d_e| < 4.3 \times 10^{-27}$ e cm, and for the neutron the limit is [31] $|d_n| < 6.5 \times 10^{-26}$ e cm. Normally SUSY theories with *CP*-violating phases $O(1)$ lead to the electron and the neutron EDMs which are far in excess of the current experiment. One approach to resolve this problem is to assume that the phases are very small [32], i.e., $O(10^{-(2-3)})$. However, it is difficult to understand how such small phases will arise naturally in a theory, and thus small phases are generally viewed as constituting a fine tuning. A second possibility is that the phases are not small, but that the SUSY spectrum is heavy in the several TeV region, which would also lead to a suppression of the EDMs [33]. However, a heavy spectrum also can be construed as fine tuning except in certain limited regions of the parameter space [22, 23]. Further, a heavy SUSY spectrum would be disappointing in that it would put the SUSY spectrum even beyond the reach of the Large Hadron Collider (LHC). Recently, a third possibility was proposed [34], i.e., that of internal cancellations among the various contributions to the EDMs reducing the supersymmetric contributions to a level below the current experiment even for phases $O(1)$ for a SUSY spectrum that is not too heavy. Such a possibility opens up a new region of the SUSY parameter space not investigated so far [34–42]. In this region, the *CP*-violating phases play an important role affecting low-energy phenomena including analyses of dark matter. We note that the EDM constraints apply to all models including those where one has a TeV scale unification. Before proceeding further, we describe briefly the cancellation mechanism [34]. For the electron EDM, the cancellation mechanism implies that for specific choices of the *CP* phases and other soft SUSY parameters one has destructive interference between the chargino and the neutralino contributions to the electric dipole moment operator. For the case of the neutron EDM, there are contributions arising from the electric dipole operator, the chromoelectric dipole operator, and the purely gluonic dimension six operator. The electric dipole operator receives contributions from the chargino, the neutralino, and from the gluino exchange contributions, and cancellations can arise among these contributions. Similarly, there can be cancellations among the chargino, the neutralino, and the gluino exchanges in the chromoelectric dipole operator. Further, cancellations can arise among the electric dipole, the chromoelectric dipole, and the purely gluonic dimension six operator contributions to the EDM of the neutron. Detailed analyses show that there exist large regions of the parameter space where such cancellations can arise. With the cancellation mechanism, one can have large *CP*-violating phases consistent with the experimental EDM constraints.

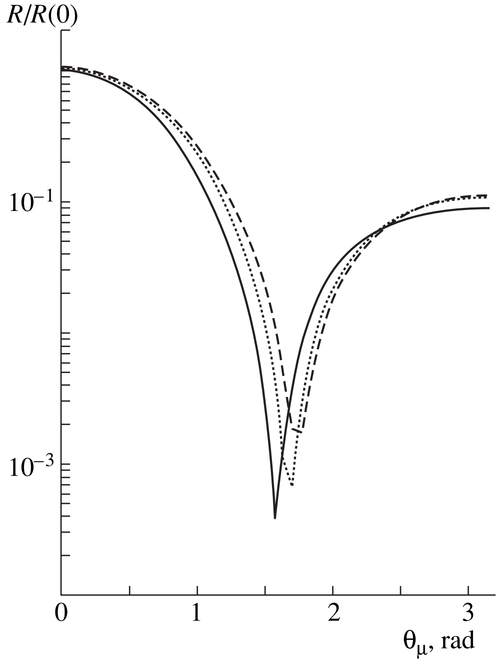

Fig. 4. Event rates from Ge as a function of the *CP*-violating phase θ_μ without the imposition of the EDM constraints (from [44]).

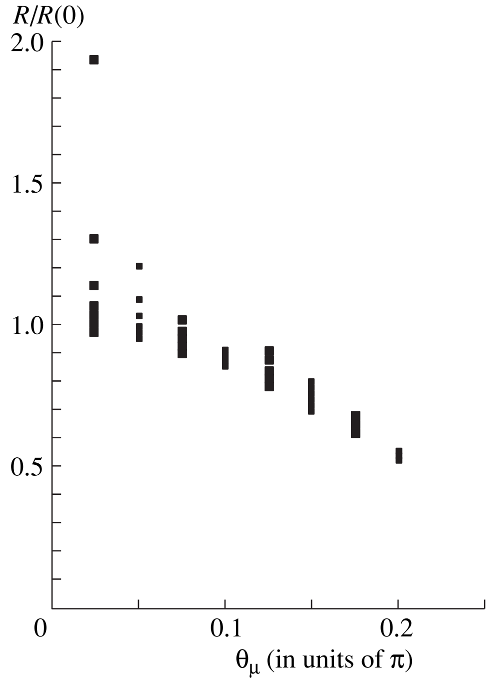

Fig. 5. Scatter plot of event rates from Ge as a function of the *CP*-violating phase θ_μ with the imposition of the EDM constraints (from [44]).

We discuss now the effect of *CP*-violating phases on the direct detection of dark matter [43–48]. In the presence of *CP*-violation phases, the effective Lagrangian governing neutralino-quark scattering is modified from its form given by (5) in the absence of *CP* violation to the form given by [44]

$$\mathcal{L}_{\text{eff}} = \bar{\chi}\gamma_\mu\gamma_5\chi\bar{q}\gamma^\mu(AP_L + BP_R)q + C\bar{\chi}\chi m_q\bar{q}q + D\bar{\chi}\gamma_5\chi m_q\bar{q}\gamma_5 q + E\bar{\chi}i\gamma_5\chi m_q\bar{q}q + F\bar{\chi}\chi m_q\bar{q}i\gamma_5 q,$$

where the functions *A*–*F* depend on *CP* phases and further *E* and *F* arise only when there is *CP* violation [44]. Without the EDM constraints the *CP*-violating phases can generate very large variations in the event rates. An analysis of the event rates for Ge as a function of the *CP*-violating phase θ_μ is given in Fig. 4. One finds that the event rates can vary by 2–3 orders of magnitude. However, inclusion of the EDM constraints reduces the effects of the *CP* phases considerably. The analysis of event rates as a function of the *CP*-violating phase θ_μ with inclusion of the EDM constraints is given in Fig. 5. One finds here that with the inclusion of the EDM constraints events rates are affected by not more than a factor of 2 and most often the effects are significantly smaller [44].

7. CONCLUSION

In this paper, we have given a brief review of some of the recent developments in the analyses of supersymmetric dark matter. We have discussed the effects of the uncertainties of the neutralino matter density and of the uncertainty of the rms WIMP velocity on the direct and on the indirect detection of dark matter. We discussed the recent claims by the DAMA experiment for the observation of an annual modulation signal in the direct detection of dark matter due to the motion of the Earth around the Sun. Such a signal is compatible with predictions of neutralino–proton scattering cross sections in supergravity unified models. We also discussed indirect detection of dark matter from the annihilation of neutralinos in the center of the Earth and the Sun and showed that the outgoing muon flux predictions in supergravity for the case of the Sun and the Earth are very sensitive to the fine tuning parameter. We found that the measurements from the Earth and the Sun are complementary in mapping the parameter space of supergravity models. Further, we compared the indirect detection vs. the direct detection techniques since such comparisons shed light on the relative merits of each technique in different parts of the parameter space. Finally, we discussed the effects of *CP* violation on the analyses of supersymmetric dark matter. We showed that *CP*-violating phases can have large effects on the event rates in the direct detection of dark matter when the EDM constraints are not included. However, inclusions of the EDM constraints from the experimental limits on the electron and on the neutron EDM reduce the *CP*-violating effects by a significant amount.

ACKNOWLEDGMENTS

This research was supported in part by NSF grant PHY-9901057.

REFERENCES

1. G. Jungman, M. Kamionkowski, and K. Griest, Phys. Rep. **267**, 195 (1996).
2. P. Nath and R. Arnowitt, in *Dark Matter in Astro- And Particle Physics* (World Sci., Singapore, 1997), p. 333; hep-ph/9610460.
3. M. W. Goodman and E. Witten, Phys. Rev. D **31**, 3059 (1985); I. Wasserman, Phys. Rev. D **33**, 2071 (1986); K. Freese, J. Frieman, and A. Gould, Phys. Rev. D **37**, 3388 (1988); K. Griest, Phys. Rev. D **37**, 2703 (1988); M. Srednicki and R. Watkins, Phys. Lett. B **225**, 140 (1989); M. Kamionkowski, Phys. Rev. D **44**, 3021 (1991).
4. G. Gelmini, P. Gondolo, and E. Roulet, Nucl. Phys. B **351**, 623 (1991); J. Engel, S. Pittel, and P. Vogel, Int. J. Mod. Phys. E **1**, 1 (1992); T. Ressel *et al*., Phys. Rev. D **48**, 5519 (1993); J. Ellis and R. Flores, Phys. Lett. B **300**, 175 (1993); M. Drees and M. Nojiri, Phys. Rev. D **48**, 3483 (1993); V. Bednyakov, H. V. Klapdor-Kleingrothaus, and S. Kovalenko, Phys. Rev. D **50**, 7128 (1994); A. Bottino *et al*., Astropart. Phys. **2**, 77 (1994).
5. P. Nath and R. Arnowitt, Phys. Rev. Lett. **74**, 4592 (1995); Phys. Rev. D **56**, 2820 (1997); **54**, 2374 (1996); E. Diehl, G. Kane, C. Kolda, and J. Wells, Phys. Rev. D **52**, 4223 (1995); L. Bergstrom and P. Gondolo, Astropart. Phys. **5**, 263 (1996); H. Baer and M. Brhlik, Phys. Rev. D **57**, 567 (1998).
6. V. A. Bednyakov, H. V. Klapdor-Kleingrothaus, and S. G. Kovalenko, Phys. Rev. D **55**, 503 (1997); V. A. Bednyakov and H. V. Klapdor-Kleingrothaus, hep-ph/9908427.
7. J. Silk, K. Olive, and M. Srednicki, Phys. Rev. Lett. **55**, 257 (1985); T. Gaisser, G. Steigman, and S. Tilav, Phys. Rev. D **34**, 2206 (1986); K. Freese, Phys. Lett. B **167**, 295 (1986); L. Krauss, M. Srednicki, and F. Wilczek, Phys. Rev. D **33**, 2079 (1986); K. Greist and S. Seckel, Nucl. Phys. B **279**, 804 (1987); G. F. Giudice and E. Roulet, Nucl. Phys. B **316**, 429 (1989); G. B. Gelmini, P. Gondolo, and E. Roulet, Nucl. Phys. B **351**, 623 (1991).
8. M. Kamionkowski, Phys. Rev. D **44**, 3021 (1991); F. Halzen, T. Stelzer, and M. Kamionkowski, Phys. Rev. D **45**, 4439 (1992); M. Drees, G. Jungman, M. Kamionkowski, and M. M. Nojiri, Phys. Rev. D **49**, 636 (1994); R. Gandhi *et al*., Phys. Rev. D **49**, 3691 (1994); K. Freese and M. Kamionkowski, Phys. Rev. D **55**, 1771 (1997); L. Bergström, J. Edsjö, and P. Gondolo, Phys. Rev. D **55**, 1765 (1997); Phys. Rev. D **58**, 103519 (1998); L. Bergström, J. Edsjö, and M. Kamionkowski, Astropart. Phys. **7**, 147 (1997); E. Diehl, G. Kane, C. Kolda, and J. Wells, Phys. Rev. D **52**, 4223 (1995); A. Bottino *et al*., Astropart. Phys. **3**, 65 (1995); V. Berezinsky *et al*., Astropart. Phys. **5**, 333 (1996); A. Bottino *et al*., Astropart. Phys. **10**, 3 (1999).
9. A. Corsetti and P. Nath, hep-ph/9904497.
10. K. Greist and D. Seckel, Phys. Rev. D **43**, 3191 (1991); P. Gondolo and G. Gelmini, Nucl. Phys. B **360**, 145 (1991).
11. R. Arnowitt and P. Nath, Phys. Lett. B **299**, 58 (1993); erratum: **303**, 403 (1993); P. Nath and R. Arnowitt, Phys. Rev. Lett. **70**, 3696 (1993); H. Baer and M. Brhlick, Phys. Rev. D **53**, 597 (1996).
12. J. Ellis, T. Falk, K. Olive, and M. Srednicki, hep-ph/9905481.
13. E. Gates, G. Gyuk, and M. S. Turner, Phys. Rev. D **53**, 4138 (1996); Astrophys. J. Lett. **449**, L123 (1995).
14. G. R. Knapp, S. D. Tremaine, and J. E. Gunn, Astron. J. **83**, 1585 (1978); F. J. Kerr and D. Lynden-Bell, Mon. Not. R. Astron. Soc. **221**, 1023 (1986); J. A. R. Caldwell and J. M. Coulsen, Astron. J. **93**, 1090 (1987).
15. P. Belli *et al*., hep-ph/9903501.
16. M. Brhlik and L. Roskowski, hep-ph/9903468.
17. M. Kamionkowski and A. Kinkhabwala, Phys. Rev. D **57**, 3256 (1998).
18. R. Arnowitt and P. Nath, hep-ph/9309277.
19. A. Chamseddine, R. Arnowitt, and P. Nath, Phys. Rev. Lett. **49**, 970 (1982).
20. P. Nath, R. Arnowitt, and A. H. Chamseddine, *Applied N = 1 Supergravity, Trieste Lectures* (World Sci., Singapore, 1983); H. P. Nilles, Phys. Rep. **110**, 1 (1984); H. E. Haber and G. L. Kane, Phys. Rep. **117**, 195 (1985).
21. K. L. Chan, U. Chattopadhyay, and P. Nath, Phys. Rev. D **58**, 096004 (1998); R. Barbieri and G. F. Giudice, Nucl. Phys. B **306**, 63 (1988); S. Dimopoulos and G. F. Giudice, Phys. Lett. B **357**, 573 (1995); G. W. Anderson, D. J. Castano, and A. Riotto, Phys. Rev. D **55**, 2950 (1997); P. H. Chankowski, J. Ellis, M. Olechowski, and S. Pokorski, Nucl. Phys. B **544**, 39 (1999); G. L. Kane and S. F. King, Phys. Lett. B **451**, 113 (1999).
22. See K. L. Chan *et al*. in [21].
23. J. L. Feng, K. T. Matchev, and T. Moroi, hep-ph/9908309; hep-ph/9909334.
24. Heidelberg-Moscow Collab. (M. Beck), Nucl. Phys. B (Proc. Suppl.) **35**, 150 (1994).
25. R. Bernabei *et al*., Phys. Lett. B **424**, 195 (1998); INFN/AE-98/34 (1998).
26. A. Bottino *et al*., Phys. Rev. D **59**, 095004 (1999); Astropart. Phys. **10**, 203 (1999).
27. R. Arnowitt and P. Nath, Phys. Rev. D **60**, 044002 (1999).
28. K. Greist and D. Seckel, Nucl. Phys. B **283**, 681 (1987).
29. M. Ambrosio *et al*., Phys. Rev. D **60**, 082002 (1999); V. A. Balkanov *et al*., astro-ph/9903341; M. M. Boliev *et al*., Nucl. Phys. B (Proc. Suppl.) **48**, 83 (1996); M. Mori *et al*., Phys. Rev. D **48**, 5505 (1993); Y. Fukuda *et al*., Phys. Rev. Lett. **82**, 2644 (1999).
30. E. Commins *et al*., Phys. Rev. A **50**, 2960 (1994); K. Abdullah *et al*., Phys. Rev. Lett. **65**, 2347 (1990).
31. P. G. Harris *et al*., Phys. Rev. Lett. **82**, 904 (1999); S. K. Lamoreaux and R. Golub, hep-ph/9907282.
32. S. M. Barr and W. J. Marciano, in *CP Violation*, Ed. by C. Jarlskog (World Sci., Singapore, 1989), p. 455; W. Bernreuther and M. Suzuki, Rev. Mod. Phys. **63**, 313 (1991).

33. P. Nath, Phys. Rev. Lett. **66**, 2565 (1991); Y. Kizukuri and N. Oshimo, Phys. Rev. D **46**, 3025 (1992); **45**, 1806 (1992).
34. T. Ibrahim and P. Nath, Phys. Lett. B **418**, 98 (1998); Phys. Rev. D **57**, 478 (1998); erratum: **58**, 019901 (1998); Phys. Rev. D **58**, 111301 (1998).
35. T. Falk and K. Olive, Phys. Lett. B **439**, 71 (1998).
36. M. Brhlik, J. L. Good, and G. L. Kane, Phys. Rev. D **59**, 115004 (1999).
37. A. Bartl *et al.*, Phys. Rev. D **60**, 073003 (1999).
38. S. Pokorski, J. Rosiek, and C. A. Savoy, hep-ph/9906206.
39. A. Pilaftsis, Phys. Rev. D **58**, 096010 (1998); A. Pilaftsis, Phys. Lett. B **435**, 88 (1998).
40. D. Demir, Phys. Rev. D **60**, 055006 (1999).
41. M. Brhlik, L. Everett, G. Kane, and J. Lykken, hep-ph/9905215; hep-ph/9908326.
42. E. Accomando, R. Arnowitt, and B. Datta, hep-ph/9907446; hep-ph/9909333.
43. T. Falk, A. Ferstl, and K. Olive, Phys. Rev. D **59**, 055009 (1999).
44. U. Chattopadhyay, T. Ibrahim, and P. Nath, Phys. Rev. D **60**, 063505 (1999).
45. S. Khalil and Q. Shafi, hep-ph/9904448.
46. T. Falk, A. Ferstl, and K. Olive, hep-ph/9908311.
47. P. Gondolo and K. Freese, hep-ph/9908390.
48. S. Y. Choi, hep-ph/9908391.

Physics of Atomic Nuclei, Vol. 63, No. 6, 2000, pp. 1037–1041. From Yadernaya Fizika, Vol. 63, No. 6, 2000, pp. 1112–1117.
Original English Text Copyright © 2000 by Drobyshevski.

In Searches for Daemons*

E. M. Drobyshevski**

Ioffe Institute for Physics and Technology, Russian Academy of Sciences,
Politekhnicheskaya ul. 26, St. Petersburg, 194021 Russia

Abstract—A possibility is considered of detecting Planckian particles carrying an electric charge $Z \approx 10$ and supposedly forming the dark matter of the Galactic disk, whence they are captured by combined action of the Sun and the Earth into strongly elongated Earth-crossing orbits. The flux of such dark electric matter objects, daemons, at the Earth's orbit may reach $f_\oplus \approx 3 \times 10^{-7}$ cm^{-2} s^{-1} at a velocity about 52 km/s. Negatively charged daemons are capable of catalyzing the fusion of light ($Z_n < 10$) nuclei. The rate of capture (and fusion) of nuclei should be particularly high in a metallic phase. A detection system is described that consists of beryllium plates 45 mm thick and 1200 cm^2 in area coated with a ZnS(Ag) scintillator. It is assumed that the products of the fusion reaction $2^9\mathrm{Be} \longrightarrow {}^{18}\mathrm{O}$ that are ejected in amounts of up to about 10^4 from the points of daemon entrance and exit would give rise to scintillations with a delay of about 1 μs. An exposure of the system for 300 h revealed no event. The reason for the negative result can be (1) too optimistic an estimate of the flux (the inclusion of some factors could lower it by 1.5–3 orders of magnitude) and (2) the poisoning of the catalyst by capture of nuclei with $Z_n \geq 10$. The time required for the recovery of the daemon catalytic properties is estimated from the analysis of the energy release in the Sun at no less than 3×10^{-7} s. The analysis of the total available data suggests that the daemon flux at the Earth is about 3×10^{-8} cm^{-2} s^{-1}. The experiments will be continued. *© 2000 MAIK “Nauka/Interperiodica”.*

1. INTRODUCTION

The birth of the Universe occurred at the Planckian scale, and the hypothesis of dark matter (DM) consisting of relic Planckian particles—that is, elementary black holes (EBH), with a mass of $M \sim (\pi\hbar c/4G)^{1/2} \approx 2 \times 10^{-5}$ g—appears to be the only natural hypothesis. Since the temperature of EBHs is equal to their mass, they probably do not evaporate completely, so that they could even represent the final product of more massive, evaporating black holes [1]. The possible existence of additional dimensions suggests that EBHs can also carry a stable electric charge $Ze \leq G^{1/2}M \approx 10e$ [2] corresponding to their mass.

Such stable, negatively charged dark electric matter objects, daemons, can catalyze the fusion of light nuclei. This hypothesis suggests new ways for solving the problem of deficiency of solar neutrinos and of the solar energetics as a whole [3], understanding the reasons for the lack of reproducibility among experiments devoted to low-level cold fusion in the deuterides of transition metals [4], etc.

A remarkable property of daemons is the possibility of their buildup in strongly elongated Earth-crossing orbits with perihelia not less than $R_\odot$. The accumulation in such orbits is effected by perturbation by the Earth of daemons making up the DM of the Galactic disk, which become partially slowed down when traversing the Sun. An optimistic estimate [4] suggests that the resultant flux of the accumulated daemons moving toward and from the Sun may reach, at the Earth, a level of $f_\oplus \approx 3 \times 10^{-7}$ cm^{-2} s^{-1}, which exceeds their primary flux from the Galactic disk by a factor of about 10^5. Their velocity with respect to an observer on the Earth is $V_r \approx (3GM_\odot/r_{\odot-\oplus})^{1/2} \approx 52$ km/s. Our work was aimed at searches for objects of this population.

2. METHODS FOR DAEMON DETECTION

Markov pointed out the difficulties associated with detection of charged EBHs (he called them “maximons”), which result from their extremely high penetrating ability (about 10^7 km in condensed matter) and inability to ionize atoms at the conventional astronomic velocities of about 10^6–10^7 km/s [5]. An additional pessimistic note was struck by his estimate of a possible flux of such particles, $f_\oplus \leq R_\oplus H/3Mc^2 \sim 10^{-14}$ cm^{-2} s^{-1}, based on the heat flux emitted by the Earth, under the assumption of their capture by the Earth and their conversion to conventional matter entailing an energy release of about $\sim Mc^2$. Here, $H \cong 1.7 \times 10^5$ eV/cm^3 is the Earth-averaged volume energy release [6].

We pointed out the possibility of the nuclear and subnuclear interaction of daemons with matter [4, 7], as well as of their interaction with coherent structures of the type of magnetic domains [4].

The simplest of such interactions is the catalysis of the fusion of light nuclei by negatively charged daemons. This catalysis could probably account for a sizable part of solar energetics, excluding the electron-

---

* This article was submitted by the author in English.

** e-mail: emdrob@pop.ioffe.rssi.ru

1063-7788/00/6306-1037$20.00 © 2000 MAIK “Nauka/Interperiodica”

capture branches and the corresponding neutrinos. Note also that the large daemon charge could make possible the fusion of fairly heavy nuclei, probably up to fluorine and neon, as well as collective fusion modes, where several (up to about 10) protons could participate in one fusion event to produce, say, two alpha particles, etc. An important feature of the daemon-assisted catalysis is multiparticle, rather than pairwise, interaction in the vicinity of a supermassive multiply charged object. Therefore, due to internal conversion, one can envisage the realization of primarily those reactions that are unlikely to occur in a conventional collision of two nuclei. As a result, the excess energy of an excited compound nucleus is transformed, as a rule, into its kinetic energy rather than expended in nucleon evaporation, etc. [3, 4].

We also pointed out the advantages of a metallic phase for a more efficient capture of nuclei by a daemon moving through such a material. The point is that the conduction electrons of a metal are repelled from a daemon by its electric field. The ions left in the electron-free void start to fall onto the daemon. Their collisions increase the probability of their capture into near-daemon levels. In covalent substances, the nuclei are captured in direct collisions with daemons because of the excitation of the inner levels of these nuclei.

As a consequence, nuclei produced in the fusion of metal nuclei become ejected away from the daemon trajectory as a daemon traverses a light metal (for instance, metallized deuterium in PdD_x for $x \leq 0.6$, lithium, beryllium, carbon). They slow down rapidly and heat the material surrounding the trajectory. As a rule, neutrons and other radiations are not emitted because of internal conversion.

Straightforward estimates show that a daemon traversing a light metal with a velocity of about 50 km/s initiates up to $\dot{N} \sim 10^7$ fusion events per centimeter of its trajectory, which corresponds to an energy release of $\sim 10^3$ erg/cm [4]. There naturally arises the question of how one could detect this process.

3. ATTEMPT AT ACOUSTIC DETECTION

The rapid heating of a material along the daemon path by the slowing-down nuclei produced in the fusion event results in the expansion of the material and in the generation of an acoustic wave propagating away from the daemon trajectory.

For a material, we chose two triangular lithium plates 20 cm on a side and 12 mm thick, spaced by d = 5 cm. Piezoelectric sensors were attached to plate corners. Knowing the sound velocity (in lithium, our measurement yielded c_{Li} = 6.1 km/s,), one derives the particle trajectory from the difference between the sound arrivals to the sensors on the plates [8].

The range in Li of a carbon nucleus produced in the reaction $2^7\mathrm{Li} \longrightarrow {}^{14}\mathrm{C}$ (plus about 25 MeV) is $r \sim 60$ μm, which corresponds to the frequency of the excited acoustic wave about 25 MHz. A calibration performed by generating a cylindrical wave by a magnetic-pressure impact showed that a heat release greater than 20 erg/cm produces a reliably measurable acoustic pulse in the metal (Al) [8]. We were unable, however, to detect such a calibration signal in Li. The reason for this is an extremely high sound damping at frequencies above 10 MHz; the characteristic damping length was found to be only 1 to 2 cm (in Al, it is about 10^2 cm).

A continuation of the work on the acoustic detection of a daemon propagation hardly makes sense now [8]. Therefore, we turned our attention to Be, where the sound velocity is c_{Be} = 12.6 km/s. The range of ^{18}O nuclei with an energy of about 20 MeV is $r \approx 5$ μm, so that the characteristic frequency of the excited sonic wave is as high as approximately 600 MHz. Acoustic measurements at such frequencies are far from routine and require additional investigations. In particular, the Be plates at our disposal were prepared by powder metallurgy from grains about 50 μm in size, which is comparable with the wavelength of interest ($\lambda \approx 20$ μm). Therefore, one could expect a strong damping of the acoustic signal in this case as well. All this forced us to look for simpler methods of daemon detection.

4. SCINTILLATION METHOD OF DETECTION

The possibility of using the scintillation method when the fusion reactions occur in the bulk of the metal yielding primarily heavy nuclei with a range r on the order of ten micrometers is far from being obvious. Nevertheless, we decided to make use of the fact that the number of reactions per unit path length may be as large as $\dot{N} \sim 10^7$ cm^{-1}. Therefore, as the daemon enters or exits a piece of a light metal (Li, Be), jets of reaction products would be ejected from the latter from a depth $\leq r$. In the case of Be, these will be ^{18}O nuclei in amounts of about $\sim r\dot{N}/2 \approx 2 \times 10^3$. These jets should be observable by standard techniques, for instance, by the scintillation method. The above estimate suggests that this method should permit detection of the daemon even if the number of the reactions catalyzed by it is only $\dot{N} \sim 10^4$ cm^{-1} = 1 μm^{-1}. It would exceed in sensitivity the acoustic method by a factor of about 10^2.

Description of a Scintillation Experiment

The sensors of our system were two Be plates of dimensions 300 × 200 × 45 mm^3 each. Their largest faces were coated with a ZnS(Ag) scintillator-powder layer 6 mg/cm^2 thick (grain size about 2 μm). These faces were viewed by four FEU-167 photomultiplier tubes (PMT) with photocathodes of diameter 100 mm. The plates were mounted in the same plane, so that the total observation area was 1200 cm^2. The system could be rotated about the vertical and horizontal axes to direct it at any point on the celestial sphere. In the search for daemons captured by the Earth's perturbing action into strongly elongated heliocentric orbits and moving away from the Sun (their flux is $f_\oplus/2$), we directed the system at the point leading the Sun, and its angular coordinates were determined by taking into account the gravitational attraction of daemons by the Earth. The signals from the PMT pair viewing the front and rear sides of each plate were fed into two-channel digital storage oscilloscopes interfaced to a computer. The latter recorded the signals if they were produced by both PMTs within ±50 μs. The signals were discriminated both in amplitude and in shape. The coincident signals supplied from the two PMTs and due primarily to relativistic-electron showers generated by cosmic rays produce scintillations with fast leading edges (≤ 0.1 μs) in ZnS(Ag), whereas those originating from heavy nonrelativistic particles exhibit 2.3-μs-long leading edges (the calibration was carried out with a ^{238}Po alpha-particle source). Signals from each PMT caused by a scintillation from a single heavy background particle occur once every two or three minutes, so that a spurious appearance of such signals on two oscillograms with a sweep 100 μs long may happen once in $\sim 10^8$ s ≈ 3 yr.

For 45-mm-thick Be plates oriented perpendicular to the daemon flux moving with $V_r \approx 52$ km/s, the signal shift should be about 0.9 μs. An accidental coincidence of two background signals within 1 μs can happen once in approximately 300 yr.

A two-month exposure for five hours a day (300 h altogether) did not reveal a single event where scintillation signals characteristic of heavy nonrelativistic particles would be shifted within 0.5–1.5 μs and where the signal amplitude would be close to or in excess of that due to a single scintillation. At the same time, for a flux of $f_\oplus/2 \approx 1.5 \times 10^{-7}$ cm^{-2} s^{-1}, a daemon should strike the area of 1200 cm^2 once every ~1.5 h.

5. ANALYSIS OF THE RESULTS OBTAINED

How could one explain this disagreement? Staying within the hypothesis of the existence of daemons and of their circumsolar population, one can assume that (1) the daemon flux was overestimated or (2) the daemon as a catalyst was poisoned on the way to the sensors of our detection system.

5.1. On the Daemon-Flux Intensity at the Earth

Our original estimate of $f_\oplus$ is apparently too optimistic [4]. This is indeed so for the following reasons:

(a) It was assumed that all daemons carry a negative electric charge; actually, the population of negative daemons may be substantially smaller—for instance, about 1/3 of their total number.

(b) We accepted the upper DM limit in the Galactic disk from [9, 10]; the lower limit quoted in those papers (about 0.07 $M_\odot$/pc^3) is 2.3 times smaller.

(c) The primary flux of daemons incident on the Sun from the Galactic disk was assumed to be isotropic and have a velocity of $V_\infty \leq 20$–30 km/s at infinity; it is not clear to what extent this is true.

(d) We disregarded the secular variation of the Earth's orbit inclination (±3°) with a characteristic time of a few Myr [11] relative to a fixed plane of the planetary system, which reduces the average volume density of daemons captured by the Sun into Earth-crossing orbits by half an order of magnitude.

(e) The time for the daemon population in Earth-crossing orbits to build up, $\Delta t_{\max}$ (about 10^9 yr), was determined only from the condition of the slowing-down of daemons required for their trapping in the bulk of the Earth after multiple (about 10^2) crossings of the material of the latter; in actual fact, however, within 10^9 yr, the majority of the daemons would forget, as it were, their previous passages through the Earth or even leave the zone of possible interaction with it as a result of building up purely gravitational perturbations by the Earth and other planets.

The weakening in time of the stepwise mass extinctions of the Earth's biota caused by an impact with one large (~1–10 km) meteoroid could serve as a reference here. Such an impact results in ejection of rock fragments up to ~0.1–1 km in size into space. They move in heliocentric orbits close to that of the Earth. On gaining additional energy through gravitational perturbations by the Earth and other planets, some of them would fall back on the Earth with a velocity considerably in excess of that of their ejection, and this is what accounts for the observed extra steps in mass extinction originating from the initial impact [12]. As a result, the extinction slows down on the scale of about 3 Myr, which is substantially less than $\Delta t_{\max} \sim 10^9$ yr. It is possible that these 3 Myr reflect primarily the (independent) change in orbital inclinations of both the Earth and the Earth-crossing asteroids pointed out in item (d). In the case of bodies in strongly elongated orbits, which are, in particular, the daemons captured by the Sun, the intensity of their interaction with the Earth is appreciably weakened in relation to that of near-Earth asteroids. One may therefore expect the characteristic time in which the daemons are swept out of the Earth-crossing orbits to increase from about 3 to about 30 Myr, which is still one and a half orders of magnitude short of our initial estimate of $\Delta t_{\max}$.

All this reduces the original estimate of $f_\oplus$ at the very least by one and a half to two, or even three orders of magnitude, i.e., down to $f_\oplus \sim 10^{-8}$–3×10^{-10} cm^{-2} s^{-1}, which is still two to three orders of magnitude larger than the direct flux of Galactic-disk daemons near the Earth's orbit. Note that the values presented here are in accord with the so-called Jones level of 10^{-23}–10^{-24} fusion events per pair of deuterons per second for cold-fusion yield in transition-metal deuterides if this process is assumed to be associated with daemon-assisted catalysis [4].

Range of a free daemon ($Ze = 10e$, $V_r = 52$ km/s) between physical collisions with nuclei of various substances without (λ_0) and with (λ_n) allowance for their displacement due to Coulomb interaction [see equations (1) and (2)] (nuclear excitation is not considered)

	Z_n	A	ρ, g cm^{-3}	λ_0, cm	λ_n, cm
Be	4	9	1.8	42	2.3×10^{-4}
N	7	14	1.0×10^{-3}	9.1×10^{4}	0.51
O	8	16	0.3×10^{-3}	3.1×10^{5}	1.8
Al	13	27	2.7	41	3.0×10^{-4}
Si	14	28	2.4	47	3.3×10^{-4}
S	16	32	2.1	56	4.2×10^{-4}
Ar	18	40	1.7×10^{-5}	7.5×10^{6}	67
Fe	26	56	7.9	18	1.7×10^{-4}
Zn	30	65	7.1	21	2.1×10^{-4}
Pd	46	106	12.2	14	1.8×10^{-4}

5.2. “Poisoning” of Daemon Catalytic Properties

An additional reason for the absence of a signal in our experiments may be the temporary “poisoning” of the daemon as a catalyst as the result of its capturing nuclei with $Z_n \geq 10$.

We started our experiment under the assumption that, as a daemon passes close to a heavy nucleus, the latter remains fixed, so that the cross section for their interaction (and capture) is

$$\sigma_0 = \pi R_0^2 A^{2/3}, \tag{1}$$

where $R_0 \approx 1.2 \times 10^{-13}$ cm and A is the atomic weight of the nucleus. The daemon range λ_0 between collisions with nuclei in condensed matter then constitutes tens of centimeters (see table). Therefore, daemon interaction with the metal of the PMT casing or argon in air was neglected. It was assumed that the captured nitrogen or oxygen nuclei ($Z_n < 10$) of the air fuse catalytically in the vicinity of the daemon, and heavier nuclei formed in the process are ejected in the recoil. The possible capture of Si, Al, and other nuclei present in the room walls restricted the time of observation from the window to five hours each day.

A subsequent analysis showed that, as a daemon travels with a supposedly slow velocity past a nucleus, the displacement of the latter cannot be neglected. If the excitation of the nucleus is disregarded, the geometric cross section for the interaction with the daemon can be written as

$$\sigma = \sigma_0 \left(\frac{V_{\text{esc}}}{V_r}\right)^2 = \sigma_0 \frac{2}{m_n V_r^2} \frac{Z Z_n e^2}{R_0 A^{1/3}}, \tag{2}$$

which exceeds σ_0 by five orders of magnitude, thus yielding a few microns for the mean free path (λ_n) to nuclear capture in a condensed medium (m_n is the nuclear mass) (see table).

We showed earlier [7] that the time τ_{ex} taken by the daemon catalyst to recover after the capture of a heavy nucleus is in any case short on the cosmological scale. But it still remains unclear how long it is in actual fact.

As follows from the estimate $\tau_{\text{ex}} \sim 3 \times 10^{-7}$ s presented in the Appendix, our original apprehension of the poisoning of the catalytic activity of daemons in their passage through air, walls, etc., was apparently exaggerated.

The same applies to beryllium of which our sensors were prepared by powder metallurgy. It contains heavy elements ($Z_n > 10$) in amounts of about 0.1 at. %. The mean free path passed by daemons between collisions with these heavy nuclei is $\lambda_n \sim 0.5$ cm. Within the time $\tau_{\text{ex}} \sim 3 \times 10^{-7}$ s, they need to recover their catalytic activity; they pass a length of $l_{\text{ex}} \leq 1.5$ cm, which is comparable with the thickness of the Be plates used. For this reason, the flux measured with our setup will be less than the true one by approximately a factor $(l_{\text{ex}} + \lambda_n)/\lambda_n$.

The first (external) layer of the ZnS(Ag) scintillator may provide a more substantial reason for underestimation in our measurements. Its average thickness is approximately 12–15 μm, which exceeds by far the daemon free path before the capture of a Zn or a S nucleus (about 2 μm; see table). Thus, it would seem that a daemon enters Be already poisoned, and one could not expect that it would be capable of catalyzing the fusion of Be nuclei in the surface layer with the resultant ejection of a jet of oxygen nuclei from a depth of up to about 5 μm.

It follows from photomicrographs (e.g., [13, 14]) that, actually, ZnS(Ag) powder layers are fairly nonuniform—the scintillator grains and their aggregates are distributed in them in an arbitrary way, so that a layer has numerous pores. Microscopic observations showed that the pores make up about 0.1 of all coated surface area in our case. Therefore, approximately 10% of the total daemon flux reaches unimpeded the Be surface, and one may expect that the jet of oxygen nuclei ejected hemispherically from the point of daemon penetration should nevertheless excite the closely lying scintillator grains.

6. CONCLUSION

Thus, despite a still negative result of the search and a number of complicating circumstances, the outlook for the detection of a circumsolar population of negatively charged daemons, if they do exist, appears to be optimistic. Based on the measurements already made and taking into account the poisoning of daemons discussed at the end of Section 5, we may presently estimate their flux at the Earth as $f_{\oplus} \leq 3 \times 10^{-8}$ cm^{-2} s^{-1}. This large value exceeds the possible lower limit of about 3×10^{-10} cm^{-2} s^{-1} (Section 5.1) by about two orders of magnitude. Therefore, one should continue the observations while improving, on the way, the detection system.

ACKNOWLEDGMENTS

I am greatly indebted to the NANP-99 organizers for financial support.

APPENDIX

Estimation of the Recovery Time of Daemon Catalytic Activity

One can roughly estimate the time $\tau_{\rm ex}$ required for the daemon catalyst to recover, assuming that solar energetics is indeed dominated by the daemon-assisted catalysis of proton fusion [3].

We use a simplified balance of the number of daemons in the Sun, assuming that, in addition to free daemons, there are N_a active ones that captured ten protons, as well as daemons poisoned by heavy nuclei, primarily by iron (with a concentration $N_{\rm Fe}$). Because the number of particles in each state is proportional to the probability of capture into this state and the time the particle spends in it, one can write

$$\frac{N_a}{N_{\rm Fe}} = \frac{\tau_{pp}}{\tau_{\rm ex}}\frac{\tau_{c\rm Fe}}{\tau_{cp}}, \qquad (A.1)$$

where τ_{cp} and $\tau_{c\rm Fe}$ are the times taken by a daemon to capture ten protons and an iron nucleus, respectively; $\tau_{pp} \approx 0.3 \times 10^{-8}$ s is the average time from the capture of ten protons to a flare-up of their fusion reactions in the near-daemon shell estimated in [3], and $\tau_{\rm ex}$ is the recovery time of the daemon catalytic properties. One may expect that the recovery occurs as the result of an explosion or absorption of a daemon-containing nucleon in a heavy nucleus, or even of the whole nucleus, accompanied by the corresponding release of energy (about m_pc^2 or m_nc^2). The first possibility appears to be more realistic.

From equation (2), it follows that

$$\frac{\tau_{c\rm Fe}}{\tau_{cp}} = \frac{n_p\sigma_p}{29n_{\rm Fe}\sigma_{\rm Fe}} = \frac{n_p}{29n_{\rm Fe}}\frac{A^{2/3}}{Z_{\rm Fe}} \approx 10^2. \qquad (A.2)$$

The heavy-nucleus-to-proton concentration ratio is taken to be $n_{\rm Fe}/n_p = 2 \times 10^{-4}$. The factor of 29 in the denominator of equation (A.2) takes into account, to a certain extent, a decrease in the daemon charge as it is capturing ten protons. One should also take into account the decrease in $\tau_{c\rm Fe}$ because of the possibility of excitation of the heavy nucleus in the course of its capture and some finer details.

Based on some optimistic assumptions of the amount of negatively charged daemons in the Galactic disk for $\tau_{pp} = 10^{-8}$ s, we came earlier [3] to the conclusion that the number of daemons N_0 captured by the Sun is capable of providing its luminosity with a $\kappa \approx N_0/N_a \approx 5$ excess. Assuming that $\tau_{pp} = 0.3 \times 10^{-8}$ s, we obtain the daemon excess of $\kappa \approx 15$. In view of items (a)–(c) from Section 5.1, κ could be possibly an order of magnitude smaller. For the sake of definiteness, we set $\kappa \approx 2$. With $N_0 - N_a$ being the number of daemons excluded from the catalysis of *pp* fusion because of being poisoned during the time $\tau_{\rm ex}$, equations (A.1) and (A.2) yield the following estimate for $\tau_{\rm ex}$:

$$\begin{aligned}\tau_{\rm ex} &= \frac{N_{\rm Fe}}{N_a}\frac{\tau_{c\rm Fe}}{\tau_{cp}}\tau_{pp} \\ &\approx (\kappa-1)\frac{\tau_{c\rm Fe}}{\tau_{cp}}\tau_{pp} \approx 0.3\times 10^{-6}\ \text{s}.\end{aligned} \qquad (A.3)$$

Note that, if one accepts the $\tau_{\rm ex}$ value obtained in this way, the energy release in the Sun due to the daemon-assisted nucleon explosions in heavy nuclei alone constitutes only a few percent of $L_\odot$. Nevertheless, the disintegration of heavy elements in this process may prove to be of importance for a further evolution of stars of later spectral classes. It may be conjectured that, at later stages of their evolution, the balance between the daemon-assisted catalysis of nuclei lighter than S–Si and the disintegration of the iron-peak nuclei will raise the concentration of nuclei in the $Z_n \sim 10$–16 region.

The result obtained here is also important because it provides a certain reference for future quantum-gravity theories of the fundamental interactions of daemons with matter at the subnuclear level.

REFERENCES

1. J. D. Bekenstein, Phys. Rev. D **49**, 1912 (1994).
2. K. C. K. Chan, J. H. Home, and R. B. Mann, Nucl. Phys. B **447**, 441 (1995).
3. E. M. Drobyshevski, Mon. Not. R. Astron. Soc. **282**, 211 (1996).
4. E. M. Drobyshevski, in *Dark Matter in Astro- and Particle Physics* (World Sci., Singapore, 1997), p. 417.
5. M. A. Markov, Prog. Theor. Phys. (Suppl., Extra Numb.), 1965 p. 85.
6. C. W. Allen, *Astrophysical Quantities*, 3rd ed. (Univ. of London: Athlone Press, London, 1973).
7. E. M. Drobyshevski, Preprint No. PhTI-1663, (Ioffe Institute for Physics and Technology, Russian Academy of Sciences, St. Petersburg, 1996).
8. E. M. Drobyshevski, in *Proceedings of 2nd International Workshop on Identification of Dark Matter, Buxton, 1998* (in press).
9. J. H. Bahcall, Astropart. Phys. **276**, 169 (1984).
10. J. H. Bahcall, C. Flynn, and A. Gould, Astropart. Phys. **389**, 234 (1992).
11. D. Brouwer and G. M. Clemence, in *Planets and Satellites* (Univ. of Chicago Press, Chicago, 1961), p. 31.
12. E. M. Drobyshevski, Earth, Moon, Planets **72**, 251 (1996).
13. I. Broser, Ann. Phys. (Leipzig) **5**, 401 (1950).
14. B. Chinaglia, F. Demichelis, and R. A. Ricci, Nuovo Cimento **4** (1), 134 (1956).

Physics of Atomic Nuclei, Vol. 63, No. 6, 2000, pp. 1042–1045. From Yadernaya Fizika, Vol. 63, No. 6, 2000, pp. 1118–1121.
Original English Text Copyright © 2000 by Zakharov.

ASTROPARTICLE PHYSICS
AND COSMOLOGY

Possible Evidence for the Observation of Noncompact (Nonbaryonic) Gravitational Microlenses ("Neutralino Stars")*

A. F. Zakharov**

Institute of Theoretical and Experimental Physics, Bol'shaya Cheremuskinskaya ul. 25, Moscow, 117259 Russia

Abstract—The microlensing of distant stars by noncompact objects such as neutralino stars is considered. Recently, Gurevich and Zybin considered the objects as microlenses. Using a nonsingular density distribution, we analyze microlensing by noncompact objects. We obtain analytic solutions to the gravitational-lens equation and an analytic expression for the amplification factor of the gravitational lens. We show that, on the basis of a model of microlensing by noncompact objects, it is possible to interpret microlensing-event candidates having two typical maxima of light curves which are usually interpreted as binary microlenses. © *2000 MAIK "Nauka/Interperiodica".*

The first results on the observation of microlensing, which were presented in [1–3], have discovered a phenomenon predicted in [4, 5]. The fundamentals of microlensing theory and observational data are discussed in [6–10]. The material of gravitational microlenses is unknown till now, although the most widespread hypothesis assumes that they are compact dark objects like brown dwarfs. Nevertheless, they could be represented by other objects. In particular, the existence of dark objects consisting of supersymmetric weakly interacting particles (neutralinos) was discussed in [11, 12]. The authors showed that the stars could be formed at the early stages of Universe evolution and be stable on the cosmological time scale. Microlensing by noncompact lenses was analyzed in [13–17] by using a singular model distribution. Geometric optics is used in our model, so that effects that are associated with diffraction and mutual interference of images and which are analyzed in [18–20] are neglected here.

We approximate the distribution of the mass density in a neutralino star as

$$\rho_{\mathrm{NeS}}(r) = 2\rho_0\frac{r_c^2}{r^2+r_c^2}, \tag{1}$$

where r is the current distance from the stellar center, ρ_0 is the mass density of the neutralino star for the boundary of the core (or for the distance r_c from the center), and r_c is the radius of the core. Thus, we use the nonsingular isothermal-sphere model (or the model of an isothermal sphere with a core). The dependence in question is an approximation of the dependence that was used in [8], where the authors considered the model of a noncompact object with a core. It is clear that the singular (degenerate) dependence is the limit of the dependence in (1) for $r_c \longrightarrow 0$.

Thus, it is not difficult to obtain the surface mass density according to expression (1):

$$\Sigma(\boldsymbol{\xi}) = 4\rho_0 r_c^2 \int\limits_0^{\sqrt{R_x^2-\xi^2}} \frac{a_0^2}{\xi^2+h^2+r_c^2}dh$$

$$= 4\rho_0\frac{r_c^2}{\sqrt{\xi^2+r_c^2}}\arctan\frac{\sqrt{R_x^2-\xi^2}}{\sqrt{\xi^2+r_c^2}}.$$

If $R_0 \gg \xi$, then $\Sigma(\boldsymbol{\xi}) \longrightarrow 2\pi\rho_0\frac{r_c^2}{\sqrt{\xi^2+r_c^2}}$. In this case, the lens equation has the form

$$\boldsymbol{\eta} = \frac{D_s}{D_d}\boldsymbol{\xi} - D_{ds}\hat{\boldsymbol{\alpha}}_{\mathrm{NeS}}(\boldsymbol{\xi}), \tag{2}$$

where D_s is the distance from the source to the observer; D_d is the distance from the gravitational lens to the observer; D_{ds} is the distance from the source to the gravitational lens; the vectors $\boldsymbol{\eta}$ and $\boldsymbol{\xi}$ determine the deflection in the plane of the source and the lens, respectively; and

$$\hat{\boldsymbol{\alpha}}_{\mathrm{NeS}}(\boldsymbol{\xi}) = \int\limits_{R^2} d^2\xi'\frac{4G\Sigma(\boldsymbol{\xi}')}{c^2}\frac{\boldsymbol{\xi}-\boldsymbol{\xi}'}{|\boldsymbol{\xi}-\boldsymbol{\xi}'|^2}. \tag{3}$$

We calculate the microlens mass:

$$\begin{aligned} M_x &= 8\pi\rho_0 r_c^2\int\limits_0^{R_x}\frac{r^2dr}{r^2+r_c^2} \\ &= 8\pi\rho_0 r_c^2\left(R_x - r_c\arctan\frac{R_x}{r_c}\right) \approx 8\pi\rho_0 r_c^2 R_x. \end{aligned} \tag{4}$$

---

* This article was submitted by the author in English.

** e-mail: zakharov@vitep5.itep.ru

1063-7788/00/6306-1042$20.00 © 2000 MAIK "Nauka/Interperiodica"

We use the characteristic value of the radius r_c corresponding to the microlens mass $M_x = 8\pi\rho_0 r_c^2 R_x$. Thus, we obtain the lens equation in the dimensionless form. We introduce the dimensionless variables in the following way:

$$\mathbf{x} = \frac{\boldsymbol{\xi}}{r_c}, \quad \mathbf{y} = \frac{\boldsymbol{\eta}}{\eta_0}, \quad \eta_0 = r_c\frac{D_s}{D_d},$$

$$\Sigma_{\rm cr} = \frac{c^2 D_s}{4\pi G D_d D_{ds}}, \quad k(\mathbf{x}) = \frac{\Sigma(a_0\mathbf{x})}{\Sigma_{\rm cr}}, \tag{5}$$

$$\hat{\boldsymbol{\alpha}}(\mathbf{x}) = \frac{1}{\pi}\int\limits_{R^2} d^2x' k(\mathbf{x}')\frac{\mathbf{x}-\mathbf{x}'}{|\mathbf{x}-\mathbf{x}'|^2}.$$

Since we assumed that the surface density is an axisymmetric function, the equation of the gravitational lens can be written in the scalar form [10, 21]

$$y = x - \alpha(x) = x - \frac{m(x)}{x},$$

$$m(x) = 2\int\limits_0^x x'dx'k(x').$$

Recall that, for the function $k(x)$, we have

$$k(x) = \frac{k_0}{\sqrt{1+x^2}},$$

$$k_0 = \frac{2\pi\rho_0 r_0}{\Sigma_{\rm cr}} = \frac{2\pi M_x}{r_c R_x}\frac{G}{c^2}\frac{D_d D_{ds}}{D_s}$$

$$= \frac{\pi}{4r_c R_x}\frac{4GM_x}{c^2}\frac{D_d D_{ds}}{D_s} = \frac{\pi}{4}\frac{R_E^2}{r_c R_x}.$$

Hence, the lens equation has the form [10]

$$y = x - D\frac{\sqrt{x^2+1}-1}{x}, \tag{6}$$

where $D = 2k_0$.

We will show that the gravitational-lens equation has only one solution if $D < 2$ and three solutions if $D > 2$ and $y > y_{\rm cr}$ (we consider the gravitational-lens equation for $y > 0$), where $y_{\rm cr}$ is the local maximal value of the right-hand side of equation (6). It is possible to show that we determine the value $x_{\rm cr}$ that corresponds to $y_{\rm cr}$ by using the expression

$$x_{\rm cr}^2 = \frac{2D-1-\sqrt{4D+1}}{2}. \tag{7}$$

It is easy to see that, according to (7), $x_{\rm cr}^2 > 0$ if—and only if—$D > 2$ and

$$y_{\rm cr} = x_{\rm cr} - D\frac{\sqrt{1+x_{\rm cr}^2}-1}{x_{\rm cr}}. \tag{8}$$

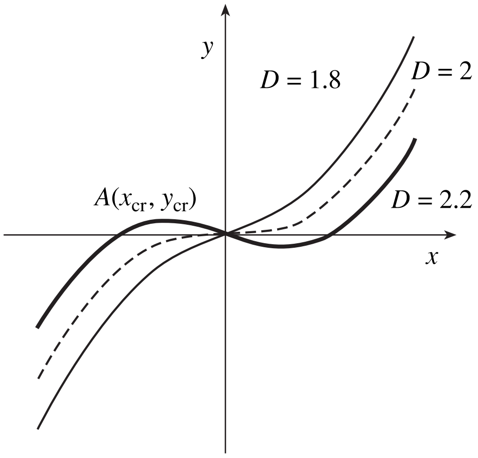

Fig. 1. Right-hand side of the gravitational-lens equation for $D = 1.8$, 2, and 2.2.

If we choose $x_{\rm cr} < 0$, then $y_{\rm cr} > 0$. If $D \le 2$, then the gravitational-lens equation has only one solution for $y > 0$; for $D > 2$, the gravitational-lens equation has one solution if $y > y_{\rm cr}$, three distinct solutions if $y < y_{\rm cr}$, and one single solution and one double solution if $y = y_{\rm cr}$. The right-hand side of the gravitational-lens equation is shown in Fig. 1.

It is possible to show that the gravitational-lens equation is equivalent to the equation

$$x^3 - 2yx^2 - (D^2 - y^2 - 2D)x - 2yD = 0, \tag{9}$$

jointly with the inequality

$$x^2 - yx + D > 0. \tag{10}$$

Thus, it is possible to obtain analytic solutions to the gravitational-lens equation by a well-known method. With $z = x - 2y/3$, we obtain an incomplete equation of third degree,

$$z^3 + pz + q = 0, \tag{11}$$

where $p = 2D - D^2 - \frac{y^2}{3}$ and $q = \frac{2y}{3}\left(\frac{y^2}{9} - D(D+1)\right)$, so that the discriminant is given by

$$Q = \left(\frac{p}{3}\right)^2 + \left(\frac{q}{2}\right)^2$$
$$= \frac{D^2}{27}[-y^4 + y^2(2D^2 + 10D - 1) + D(2-D)^3]. \tag{12}$$

If $Q \ge 0$, then (11) has a unique real solution; therefore, the gravitational-lens equation (6) has a unique real solution. We use the Cardano expression for the solution:

$$x = \sqrt[3]{-q/2 + \sqrt{Q}} + \sqrt[3]{-q/2 - \sqrt{Q}} + 2y/3. \tag{13}$$

We assume that $D > 2$. If $y > y_{\rm cr}$, then the gravitational-lens equation has a unique solution. If $Q \ge 0$, then we

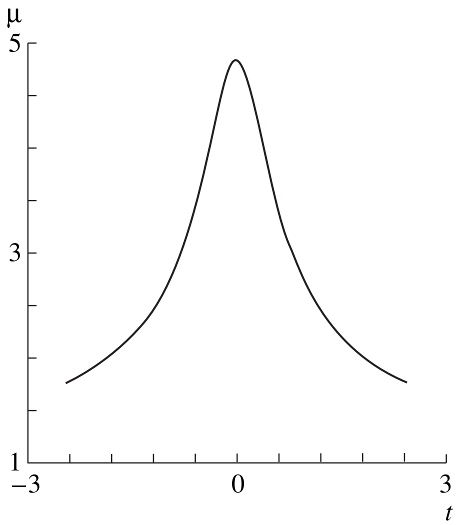

Fig. 2. Light curve (light magnification μ versus dimensionless time t) corresponding to microlensing by a noncompact object (a neutralino star) for $D = 1.9$. The light curve resembles the standard light curve for microlensing by a compact object.

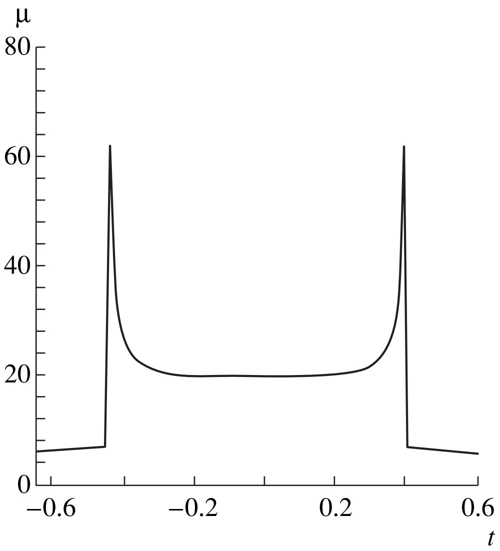

Fig. 3. Light curve corresponding to microlensing by a noncompact object for $D = 4$. The light curve resembles the light curve for OGLE # 7 event.

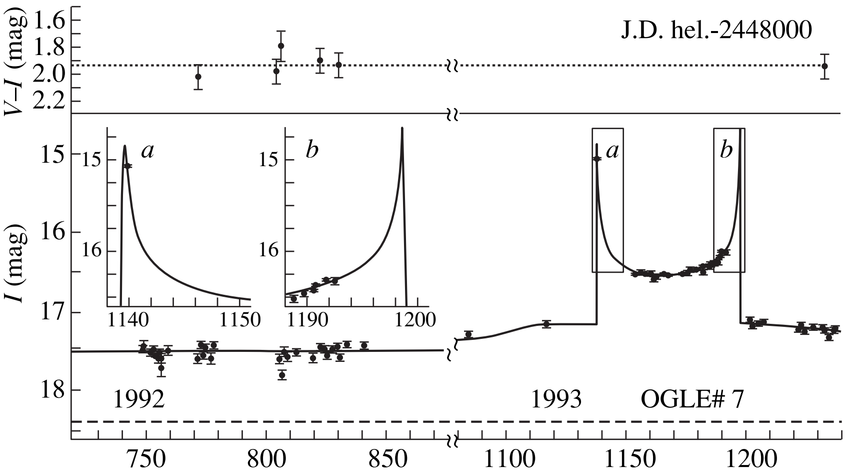

Fig. 4. Light curve for the possible sample of microlensing. The event OGLE # 7 is usually interpreted in terms of the binary compact microlens model. The regions of caustic crossing (a and b) are shown on a large scale in two insets. Time is shown in Julian days. Stellar magnitudes are shown in the I band and in the $V–I$ band.

use expression (13) for the solution. If $Q < 0$, then we have the expression

$$x = 2\sqrt{-\frac{p}{3}}\cos\frac{\alpha + 2k\pi}{3} + 2y/3 \quad (k = 0, 1, 2), \quad (14)$$

where

$$\cos\alpha = -\frac{q}{2\sqrt{-(p/3)^3}}, \quad (15)$$

and we choose only one solution that corresponds to inequality (10), which corresponds to $k = 0$ in (14), because, if the gravitational-lens equation has only one solution, then we have a positive solution x for a positive value of the impact parameter y; therefore, there is the inequality $x > y$, which can easily be derived from (8). It is possible to check that the maximal solution to (9) corresponds to $k = 0$; therefore, this solution is a solution to (8).

If $y < y_{\mathrm{cr}}$, then the gravitational-lens equation has three distinct solutions, and we use (14) and (15) to obtain the solutions.

We now consider the case of $D < 2$. We know that the gravitational-lens equation has a unique solution for this case. If $Q \geq 0$, then we use expression (13) for the solution. If $Q < 0$, then we have expressions (14) and (15) and select only one solution that corresponds to inequality (10), which also corresponds to $k = 0$ as in the preceding case.

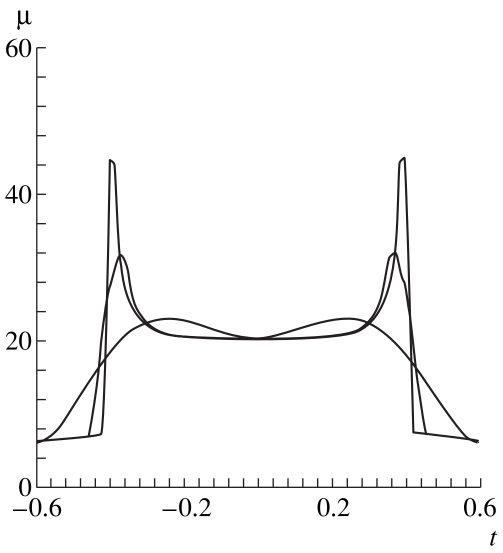

Fig. 5. Light curves corresponding to microlensing by a noncompact object for $D = 4$ and various sizes of a nonpoint source. The maximal values of the light curves decrease with increasing source radius, which is equal to $R_s = 0.01$, 0.03, and 0.1.

It is known that the magnification for the gravitational-lens solution x_k is determined by the expression

$$\mu_k = \left|\left(1 - \frac{D(\sqrt{1+x^2}-1)}{x}\right)\right.$$
$$\left.\times\left(1 + D\frac{\sqrt{1+x^2}-1}{x^2} - \frac{D}{\sqrt{1+x^2}}\right)\right|, \tag{16}$$

so that the total magnification is

$$A_{\text{tot}}(y) = \sum \mu_k, \tag{17}$$

where summation is taken over all solutions of the gravitational-lens equation for a fixed value of y.

The light curve corresponding to a noncompact microlens is shown in Fig. 2 (for $D = 1.9$). The light curve resembles the light curves that are usually interpreted in terms of the simple Schwarzschild microlens model [9, 10]. The light curve corresponding to the noncompact microlens is shown in Fig. 3 (for $D = 4$). The finite maximal value of the amplification in Fig. 3 is associated with the calculation of amplification for a finite set of times, and, if we consider the amplification in the entire interval, the maximal value of the amplification must be infinite. It is easy to see that the light curves resemble the light curve for the OGLE # 7 candidate event (Fig. 4), which is usually interpreted in terms of the binary-lens model [22].

The light curves for a finite-size source (nonpoint sources) are demonstrated in Fig. 5. We recall that the appearance of two types of light curves for a toy density-distribution model for a noncompact object was discussed by Ossipov and Kurian [23]. A more detailed analysis of the nonsingular model and its consequences are presented in [24, 25]. Polarization during microlensing is analyzed by using the singular and nonsingular models, and degenerate properties of the singular model are discussed in [9].

ACKNOWLEDGMENTS

I am grateful to M.V. Sazhin for stimulating discussions. It is a pleasure to thank the members of the Organizing Committee of NANP-99 conference for their hospitality in Dubna.

REFERENCES

1. C. Alcock *et al.*, Nature **365**, 621 (1993).
2. E. Aubourg *et al.*, Nature **365**, 623 (1993).
3. A. Udalski *et al.*, Astrophys. J. Lett. **426**, 69 (1994).
4. A. V. Byalko, Astron. Zh. **46**, 998 (1969) [Sov. Astron. **13**, 784 (1969)].
5. B. Paczynski, Astrophys. J. **304**, 1 (1986).
6. B. Paczynski, astro-ph/9604011.
7. E. Rouiet and S. Mollerach, astro-ph/9603119.
8. A. V. Gurevich, K. P. Zybin, and V. A. Sirota, Usp. Fiz. Nauk **167**, 913 (1997) [Phys. Usp. **40**, 869 (1997)].
9. A. F. Zakharov and M. V. Sazhin, Usp. Fiz. Nauk **168**, 1041 (1998) [Phys. Usp. **41**, 945 (1998)].
10. A. F. Zakharov, *Gravitational Lenses and Microlenses* (Yanus, Moscow, 1997).
11. A. V. Gurevich and K. P. Zybin, Phys. Lett. A **208**, 276 (1995).
12. A. V. Gurevich, K. P. Zybin, and V. A. Sirota, Phys. Lett. A **214**, 232 (1996).
13. A. F. Zakharov and M. V. Sazhin, Zh. Éksp. Teor. Fiz. **110**, 1921 (1996) [JETP **83**, 1057 (1996)].
14. A. F. Zakharov and M. V. Sazhin, Pis'ma Zh. Éksp. Teor. Fiz. **63**, 894 (1996) [JETP Lett. **63**, 937 (1996)].
15. A. F. Zakharov and M. V. Sazhin, Pis'ma Astron. Zh. **23**, 403 (1997) [Astron. Lett. **23**, 349 (1997)].
16. A. F. Zakharov and M. V. Sazhin, Yad. Fiz. **61**, 1220 (1998) [Phys. At. Nucl. **61**, 1120 (1998)].
17. A. F. Zakharov and M. V. Sazhin, Yad. Fiz. **61**, 1226 (1998) [Phys. At. Nucl. **61**, 1126 (1998)].
18. A. F. Zakharov, Astron. Astrophys. Trans. **5**, 85 (1994).
19. A. F. Zakharov, Pis'ma Astron. Zh. **20**, 359 (1994) [Astron. Lett. **20**, 300 (1994)].
20. A. F. Zakharov and A. V. Mandzhos, Zh. Éksp. Teor. Fiz. **104**, 3249 (1993) [JETP **77**, 529 (1993)].
21. P. Schneider, J. Ehlers, and E. E. Falco, *Gravitational Lenses*, Ed. by R. Kayser, T. Schramm, and L. Nieser (Spinger-Verlag, Heidelberg, 1992).
22. A. Udalski *et al.*, Astrophys. J. Lett. **436**, L103 (1994).
23. D. L. Ossipov and V. E. Kurian, Phys. Lett. A **223**, 157 (1996).
24. A. F. Zakharov, Astron. Zh. **76**, 423 (1999) [Astron. Rep. **43**, 325 (1999)].
25. A. F. Zakharov, Phys. Lett. A **250**, 67 (1998).

Physics of Atomic Nuclei, Vol. 63, No. 6, 2000, pp. 1046–1049. From Yadernaya Fizika, Vol. 63, No. 6, 2000, pp. 1122–1125.
Original English Text Copyright © 2000 by Mikheev, Parkhomenko, Vassilevskaya.

ASTROPARTICLE PHYSICS AND COSMOLOGY

Magnetic-Field Influence on Radiative Axion Decay into Photons of the Same Polarization*

N. V. Mikheev, A. Ya. Parkhomenko, and L. A. Vassilevskaya**
Yaroslavl State University, Sovetskaya ul. 14, Yaroslavl, 150000 Russia

Abstract—The decays of a pseudoscalar particle, the axion, into two photons of the same polarization are studied in the model involving direct axion–electron coupling. These processes, which are forbidden in a vacuum because of a pseudoscalar nature of the axion, become possible in a magnetic field. It is shown that the kinematics of ultrarelativistic-axion decay substantially depends on photon polarizations. The probability of radiative axion decay in the limit of a strong magnetic field substantially exceeds the corresponding probability in a vacuum. *© 2000 MAIK “Nauka/Interperiodica”.*

1. INTRODUCTION

At present, attractiveness of the axion [1, 2], the pseudo-Goldstone boson of global Peccei–Quinn symmetry, is associated with its role as one of the main cold-dark-matter candidates [3]. Being a very light particle, with a mass in the range [4]

$$10^{-5} \lesssim m_a \lesssim 10^{-2}\ \text{eV}, \qquad (1)$$

the axion is a very long-lived particle, with the lifetime [3]

$$\tau_0 \sim 6.3 \times 10^{42}\ \text{s}\left(\frac{10^{-2}\ \text{eV}}{m_a}\right)^6 \left(\frac{E_a}{1\ \text{MeV}}\right). \qquad (2)$$

This lifetime is determined by the radiative decay $a \longrightarrow \gamma\gamma$. An electromagnetic field can significantly change the properties of particles—in particular, it can catalyze quantum processes [5], open novel “forbidden-in-vacuum” channels [6, 7], etc. Two “forbidden-in-vacuum” axion decay modes, $a \longrightarrow \gamma^{(1)} + \gamma^{(1)}$ and $a \longrightarrow \gamma^{(2)} + \gamma^{(2)}$, become possible in an external field in addition to the allowed decay $a \longrightarrow \gamma^{(1)} + \gamma^{(2)}$, where $\gamma^{(1)}$ and $\gamma^{(2)}$ are photons whose polarizations are, respectively,

$$\varepsilon^{(1)}_\mu = \frac{(Fq)_\mu}{(qFFq)}, \quad \varepsilon^{(2)}_\mu = \frac{(\tilde{F}q)_\mu}{(q\tilde{F}\tilde{F}q)}, \qquad (3)$$

where q_μ is the photon 4-momentum, while $F_{\mu\nu}$ and $\tilde{F}_{\mu\nu}$ are, respectively, the tensor and the dual tensor of an external electromagnetic field. An analysis of ultrarelativistic-axion decay in a crossed external field shows [5] that the probability of $a \longrightarrow \gamma^{(1)} + \gamma^{(2)}$ is substantially catalyzed, but that the probabilities of $a \longrightarrow \gamma^{(1)} + \gamma^{(1)}$ and $a \longrightarrow \gamma^{(2)} + \gamma^{(2)}$ are strongly suppressed because of collinearity of the particle 4-momenta.

In this paper, we investigate the magnetic-field influence on the axion-decay modes $a \longrightarrow \gamma^{(1)} + \gamma^{(1)}$ and $a \longrightarrow \gamma^{(2)} + \gamma^{(2)}$ in the Dine–Fischler–Srednicki–Zhitnitskiĭ (DFSZ) model of an “invisible” axion [8] with a direct axion–electron coupling.

2. DECAY AMPLITUDES

The amplitude of the axion decay $a \longrightarrow \gamma\gamma$ in an external magnetic field is described by the triangle diagrams in Fig. 1, where double lines represent the field influence in the electron propagators. The fact that the axion and the photon are neutral particles allows us to use the usual definition of the invariant matrix element $M^{(ij)}$; that is,

$$S(a \longrightarrow \gamma^{(i)} + \gamma^{(j)}) = \frac{i(2\pi)^4 \delta^{(4)}(k - q_1 - q_2)}{\sqrt{2E_a V \cdot 2\omega_1 V \cdot 2\omega_2 V}} M^{(ij)}, \qquad (4)$$

where the indices i and j imply the photon polarizations (3), $k_\mu = (E_a, \mathbf{k})$ is the axion 4-momentum, $q_{1\mu} = (\omega_1, \mathbf{q}_1)$ and $q_{2\mu} = (\omega_2, \mathbf{q}_2)$ are the final-photon 4-momenta, and V is the normalized phase-space volume. The invariant amplitudes $M^{(11)}$, $M^{(12)}$, and $M^{(22)}$ describe the decays $a \longrightarrow \gamma^{(1)} + \gamma^{(1)}$, $a \longrightarrow \gamma^{(1)} + \gamma^{(2)}$, and $a \longrightarrow \gamma^{(2)} + \gamma^{(2)}$, respectively. Below, we investigate the magnetic-field influence on axion decays into photons of the same

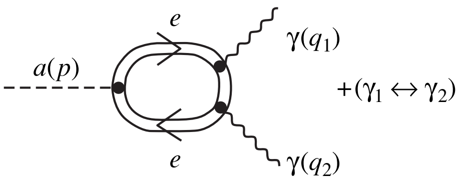

Fig. 1. Triangle loop diagram describing effective axion interaction with two photons.

---

* This article was submitted by the authors in English.
** e-mail: parkh@uniyar.ac.ru

polarizations. The relevant amplitudes $M^{(11)}$ and $M^{(22)}$ are given by

$$\begin{aligned} M^{(11)} \; &= \; \frac{2g_{ae}\alpha\beta m_e}{\pi}\frac{(q_1\tilde{\varphi}q_2)}{\sqrt{q_{1\perp}^2 q_{2\perp}^2}}\int\limits_0^\infty\frac{ds\,dt\,dv}{z\sin(\beta z)} \\ &\times \exp\{-im_e^2 z + i\Delta\Phi\}[(q_1\varphi q_2)\cos(\beta(z-2v)) \\ &\times \cos\delta\Phi + i(q_1q_2)_\perp\sin(\beta(z-2v))\sin\delta\Phi], \end{aligned} \tag{5}$$

$$\begin{aligned} M^{(22)} \; &= \; \frac{g_{ae}\alpha\beta m_e}{\pi}\frac{(q_1\tilde{\varphi}q_2)}{\sqrt{q_{1\parallel}^2 q_{2\parallel}^2}}\int\limits_0^\infty\frac{ds\,dt\,dv}{z\sin(\beta z)} \\ &\times \exp\{-im_e^2 z + i\Delta\Phi\}\Bigg[\Bigg\{(q_1\varphi q_2)[\sin(\beta(2s-z)) \\ &+ \sin(\beta(2t-z)) + \sin(\beta(2v-z)] \\ &\times [\sin(2\beta s) + \sin(2\beta t) + \sin(2\beta v)] \\ &- 2\sin^3(\beta z)\frac{\partial\delta\Phi}{\partial z}\Bigg\}\cos\delta\Phi \\ &- i\sin\delta\Phi\Bigg\{-2\sin^3(\beta z)\left[\frac{(tq_1-sq_2)_\parallel^2}{z^2} + \frac{\partial\Delta\Phi}{\partial z}\right] \\ &- 2i\sin(\beta z)[\sin(2\beta s) + \sin(2\beta t) + \sin(2\beta v)] \\ &+ [q_{1\perp}^2 + q_{2\perp}^2 + k_\perp^2][\sin(\beta(2z-s)) + \sin(\beta(2t-z)) \\ &+ \sin(\beta(2v-z)] + q_{1\perp}^2\cos(2\beta s) + q_{2\perp}^2\cos(2\beta t) \\ &+ k_\perp^2\cos(2\beta v) + (q_1k)_\perp\sin(\beta(2t-z)) \\ &\times [\cos(2\beta s) - \cos(2\beta t) + \cos(2\beta v) - 1] \\ &+ (q_2k)_\perp\sin(\beta(2s-z))[\cos(2\beta t) - \cos(2\beta s) \\ &+ \cos(2\beta v) - 1] - (q_1q_2)_\perp\sin(\beta(2v-z)) \\ &\times [\cos(2\beta s) + \cos(2\beta t) - \cos(2\beta v) - 1]\Bigg\}\Bigg], \end{aligned} \tag{6}$$

where g_{ae} is the axion–electron coupling constant; α is the fine-structure constant; $\beta = eB$ is the field parameter; $\mathbf{B}$ is the magnetic-field strength; e and m_e are the electron charge and mass, respectively; $\varphi_{\mu\nu} = F_{\mu\nu}/B$ and $\tilde{\varphi}_{\mu\nu} = \tilde{F}_{\mu\nu}/B$ are the dimensionless tensor of the external magnetic field and its dual tensor; $(v_1v_2)_\perp = (v_1\varphi\varphi v_2) = v_{1\mu}\varphi^{\mu\nu}\varphi_{\nu\rho}v_2^\rho$, $(v_1v_2)_\parallel = (v_1\tilde{\varphi}\tilde{\varphi}v_2) = v_{1\mu}\tilde{\varphi}^{\mu\nu}\tilde{\varphi}_{\nu\rho}v_2^\rho$, $v_{1\mu}$, and $v_{2\mu}$ are arbitrary 4-vectors; s, t, and v are the Schwinger proper-time variables, $z = s + t + v$; and, finally,

$$\begin{aligned} \Delta\Phi = \frac{stv}{z}\left[\frac{q_{1\parallel}^2}{s} + \frac{q_{2\parallel}^2}{t} + \frac{k_\parallel^2}{v}\right] \\ - \frac{\sin(\beta s)\sin(\beta t)\sin(\beta v)}{\beta\sin(\beta z)} \\ \times\left[\frac{q_{1\perp}^2}{\tan(\beta s)} + \frac{q_{2\perp}^2}{\tan(\beta t)} + \frac{k_\perp^2}{\tan(\beta v)}\right], \end{aligned} \tag{7}$$

$$\delta\Phi \; = \; 2\frac{\sin(\beta s)\sin(\beta t)\sin(\beta v)}{\beta\sin(\beta z)}(q_1\varphi q_2). \tag{8}$$

In this paper, we study the interesting case of large values of the field parameter β ($\beta \gg m_e^2, E_a^2$), which corresponds to the limit of a strong magnetic field. After integration with respect to the proper-time variables, amplitudes (5) and (6) can be simplified to become

$$\begin{aligned} M^{(11)} \simeq -\frac{4ig_{ae}\alpha m_e}{\pi}\frac{(q_1\varphi q_2)(q_1\tilde{\varphi}q_2)}{\sqrt{q_{1\perp}^2 q_{2\perp}^2 k_\parallel^2}} \\ \times\Bigg[\frac{\Theta(4m_e^2 - k_\parallel^2)}{\sqrt{4m_e^2 - k_\parallel^2}}\arctan\sqrt{\frac{k_\parallel^2}{4m_e^2 - k_\parallel^2}} + \frac{\Theta(k_\parallel^2 - 4m_e^2)}{\sqrt{k_\parallel^2 - 4m_e^2}} \\ \times\left(\ln\left|\frac{2m_e}{\sqrt{k_\parallel^2} + \sqrt{k_\parallel^2 - 4m_e^2}}\right| - \frac{i\pi}{2}\right)\Bigg], \end{aligned} \tag{9}$$

$$M^{(22)} \simeq \frac{ig_{ae}\alpha}{2\pi m_e}\frac{(q_1\varphi q_2)(q_1\tilde{\varphi}q_2)}{\sqrt{q_{1\parallel}^2 q_{2\parallel}^2}}\left[1 + \frac{m_e^2}{4\beta}\ln\frac{4\beta}{m_e^2}\right], \tag{10}$$

where $\Theta(x)$ is a unit step function. One can see that the amplitude $M^{(11)}$ has a square-root singularity at $k_\parallel^2 \longrightarrow 4m_e^2$, while $M^{(22)}$ is regular.

3. PHOTON DISPERSION IN A STRONG MAGNETIC FIELD

To obtain the decay probability, one has to analyze photon dispersion in a field. The dispersion relations for photons in a magnetic field were investigated in detail by Shabad [9]. The dashed line in Fig. 2 corresponds to the vacuum dispersion relation $q^2 = q_\parallel^2 - q_\perp^2 = 0$. The curve describing the dispersion of the first photon polarization [polarization vector $\varepsilon_\mu^{(1)}$ (3)] has a small deviation from the vacuum dispersion curve and, hence, the small field-induced "effective mass" squared, which is defined as the difference between the vacuum dispersion line and the curve labeled with $\varepsilon^{(1)}$. The dispersion curve corresponding to the photon of second polarization, $\varepsilon_\mu^{(2)}$ (3), has a discontinuity in the region $q_\parallel^2 \longrightarrow 4m_e^2$. We note that the photon of second

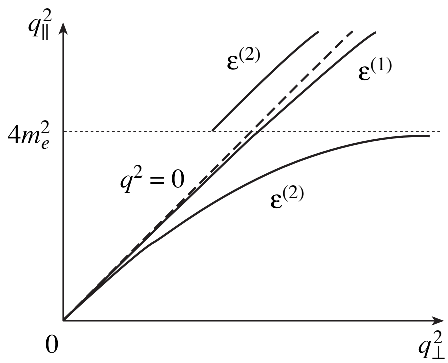

Fig. 2. Dispersion curves for photons in a strong external magnetic field. The dashed line corresponds to photon dispersion in a vacuum. The lines labeled with $\varepsilon^{(1)}$ and $\varepsilon^{(2)}$ represent the dispersion relations for the photon modes of first and second polarization, respectively.

polarization is stable only when its dispersion is described by the lower branch with $q_\parallel^2 < 4m_e^2$. The upper branch, $q_\parallel^2 > 4m_e^2$, corresponds to an unstable photon, which can decay into an electron–positron pair. In the following, we will consider the axion decay $a \longrightarrow \gamma^{(2)} + \gamma^{(2)}$ only into stable photons. We emphasize that both photon modes considered have negative "effective masses" squared, so that the decay is possible even for a massless pseudoscalar particle—for example, the arion [10].

The smallness of the field-induced "effective mass" squared of the first-polarization photon allows one to use the condition of collinear kinematics in the ultrarelativistic axion decay, $k_\mu \sim q_{1\mu} \sim q_{2\mu}$, in which case the $a \longrightarrow \gamma^{(1)} + \gamma^{(1)}$ amplitude is suppressed: $M^{(11)} \simeq 0$. A similar suppression is observed for the amplitude $M^{(22)}$ under the condition $q_{1\parallel}^2, q_{2\parallel}^2 \ll 4m_e^2$, since the deviation of the dispersion curve for the second-polarization photon from the vacuum line is rather small in this region (Fig. 2). In the resonance region $q_\parallel^2 \longrightarrow 4m_e^2$, the photon acquires a large negative "effective mass" squared owing to a singular behavior of the photon polarization operator [9]. In this case, the amplitude $M^{(22)}$ is not suppressed because the kinematics of axion decay differs significantly from collinear kinematics.

A large value of the photon polarization operator near the resonance requires that large radiative corrections be taken into account. This amounts to renormalizing the photon wave function as

$$\varepsilon_\mu^{(2)} \longrightarrow \sqrt{Z}\varepsilon_\mu^{(2)}, \tag{11}$$

where Z is the renormalization factor. In general, the expression for the factor Z is rather complicated. In the resonance region, its asymptotic behavior is [9]

$$Z(q)\big|_{q_\parallel^2 \to 4m_e^2} \simeq \frac{(4m_e^2 - q_\parallel^2)^{3/2}}{\alpha\beta m_e}. \tag{12}$$

4. DECAY PROBABILITY

With allowance for large radiative corrections, the probability of axion decay into two photons of second polarization has the form

$$\begin{aligned} E_a W = {} & \frac{1}{64\pi^2}\int Z(q_1)Z(q_2) \\ & \times |M^{(22)}|^2 \delta^{(4)}(k - q_1 - q_2)\frac{d\mathbf{q}_1 d\mathbf{q}_2}{\omega_1\omega_2}. \end{aligned} \tag{13}$$

The probability of the axion decay $a \longrightarrow \gamma^{(2)} + \gamma^{(2)}$ can be represented as the sum of two nonvanishing contributions:

$$W = W_{\text{SRC}} + W_{\text{DRC}}. \tag{14}$$

Here, W_{SRC} is the single-resonance contribution (SRC) when the photon momenta satisfy the conditions $q_{1\parallel}^2 \ll 4m_e^2$ and $q_{2\parallel}^2 \simeq 4m_e^2$ or $q_{1\parallel}^2 \simeq 4m_e^2$ and $q_{2\parallel}^2 \ll 4m_e^2$. We have

$$\begin{aligned} & E_a W_{\text{SRC}} \\ & \simeq \frac{g_{ae}^2\alpha^4\beta^2}{2^9\pi^3 m_e^2}\left[1 + \frac{m_e^2}{4\beta}\ln\frac{4\beta}{m_e^2}\right]^2\left[\ln\frac{E_a^2\sin^2\theta}{m_e^2} - \frac{3}{2}\right], \end{aligned} \tag{15}$$

where θ is the angle between the axion momentum $\mathbf{k}$ and the magnetic-field strength $\mathbf{B}$. Next, W_{DRC} is the double-resonance contribution (DRC) when the momenta of both photons are in the resonance region ($q_{1\parallel}^2, q_{2\parallel}^2 \simeq 4m_e^2$):

$$\begin{aligned} E_a W_{\text{DRC}} \simeq {} & \frac{g_{ae}^2\alpha^6\beta^4}{2^{10}\pi^3 m_e^4 E_a^2\sin^2\theta}\left[1 + \frac{m_e^2}{4\beta}\ln\frac{4\beta}{m_e^2}\right]^2 \\ & \times\left[1 + \frac{12m_e^2}{E_a^2\sin^2\theta}\ln\frac{E_a^2\sin^2\theta}{4m_e^2}\right]. \end{aligned} \tag{16}$$

Note that (15) and (16) are valid under the conditions $E_a \gg m_e$ and $\alpha \ll E_a^2/\beta \ll 1$. It is interesting to compare the contributions in (15) and (16):

$$\frac{W_{\text{DRC}}}{W_{\text{SRC}}} \simeq \frac{E_a^2\sin^2\theta}{2m_e^2}\left(\frac{\alpha\beta}{E_a^2\sin^2\theta}\right)^2\left[\ln\frac{E_a^2\sin^2\theta}{m_e^2} - \frac{3}{2}\right]^{-1}. \tag{17}$$

This ratio contains both enhancing and suppressing factors (E_a^2/m_e^2 and $\alpha\beta/E_a^2$, respectively.) Therefore, the relative importance of each contribution to the decay probability depends strongly on the initial conditions. Below, we present the numerical evaluations of (15) and (16) for the decaying-axion energy of $E_a \sim 5$ MeV in the field of strength $B \sim 10^{16}$ G:

$$W_{\mathrm{SRC}} \simeq 2.2 \times 10^{-14}\ \mathrm{s}^{-1}\left(\frac{g_{ae}}{10^{-13}}\right)^2\left(\frac{B}{10^{16}\ \mathrm{G}}\right)^2 \times\left(\frac{5\ \mathrm{MeV}}{E_a}\right)\left[1+\frac{2}{3}\ln\left(\frac{E_a}{5\ \mathrm{MeV}}\right)\right], \qquad (18)$$

$$W_{\mathrm{DRC}} \simeq 3.7 \times 10^{-15}\ \mathrm{s}^{-1}\left(\frac{g_{ae}}{10^{-13}}\right)^2\left(\frac{B}{10^{16}\ \mathrm{G}}\right)^4 \times\left(\frac{5\ \mathrm{MeV}}{E_a}\right)^3\left[1+\frac{3}{5}\ln\left(\frac{E_a}{5\ \mathrm{MeV}}\right)+\frac{13}{5}\left(\frac{E_a}{5\ \mathrm{MeV}}\right)^2\right]. \qquad (19)$$

It can be seen that both contributions are comparable for the parameters considered. A comparison of the decay probability $W \sim 10^{-14}$ s^{-1} with the decay probability in a vacuum, $W_0 \sim 10^{-50}$ s^{-1}, shows that the forbidden-in-vacuum channel $a \longrightarrow \gamma^{(2)} + \gamma^{(2)}$ becomes substantial in a strong magnetic field.

ACKNOWLEDGMENTS

This work was supported in part by INTAS (grant no. 96-0659) and by the Russian Foundation for Basic Research (project no. 98-02-16694). L. Vassilevskaya thanks DESY for the hospitality during the time over which this work was done.

REFERENCES

1. R. D. Peccei and H. R. Quinn, Phys. Rev. Lett. **38**, 1440 (1977); Phys. Rev. D **16**, 1791 (1977).
2. S. Weinberg, Phys. Rev. Lett. **40**, 223 (1978); F. Wilczek, Phys. Rev. Lett. **40**, 279 (1978).
3. G. G. Raffelt, *Stars as Laboratories for Fundamental Physics* (Univ. of Chicago Press, Chicago, 1996).
4. G. G. Raffelt, Nucl. Phys. B (Proc. Suppl.) **72**, 43 (1999).
5. N. V. Mikheev and L. A. Vassilevskaya, Phys. Lett. B **410**, 207 (1997); L. A. Vassilevskaya, N. V. Mikheev, and A. Ya. Parkhomenko, Yad. Fiz. **60**, 2224 (1997) [Phys. At. Nucl. **60**, 2041 (1997)]; N. V. Mikheev, A. Ya. Parkhomenko, and L. A. Vassilevskaya, Phys. Rev. D **60**, 035001 (1999).
6. A. V. Borisov and V. Yu. Grishina, Zh. Éksp. Teor. Fiz. **106**, 1553 (1994) [JETP **79**, 837 (1994)]; M. Kachelriess, C. Wilke, and G. Wunner, Phys. Rev. D **56**, 1313 (1997); N. V. Mikheev, G. G. Raffelt, and L. A. Vassilevskaya, Phys. Rev. D **58**, 055008 (1998).
7. N. V. Mikheev and L. A. Vassilevskaya, Phys. Lett. B **410**, 203 (1997).
8. M. Dine, W. Fischer, and M. Srednicki, Phys. Lett. B **104**, 199 (1981); A. R. Zhitnitskiĭ, Yad. Fiz. **31**, 497 (1980) [Sov. J. Nucl. Phys. **31**, 260 (1980)].
9. A. E. Shabad, Ann. Phys. (N.Y.) **90**, 166 (1975); Tr. Fiz. Inst. im. P.N. Lebedeva, Akad. Nauk SSSR **192**, 5 (1988).
10. A. A. Anselm and N. G. Uraltsev, Phys. Lett. B **114**, 39 (1982).

Physics of Atomic Nuclei, Vol. 63, No. 6, 2000, pp. 1050–1052. From Yadernaya Fizika, Vol. 63, No. 6, 2000, pp. 1126–1128.
Original English Text Copyright © 2000 by Volkova, Zatsepin.

ASTROPARTICLE PHYSICS AND COSMOLOGY

On Charm Production at High Energies*

L. V. Volkova and G. T. Zatsepin
Institute for Nuclear Research, Russian Academy of Sciences, pr. Shestidesyatiletiya Oktyabrya 7a, Moscow, 117312 Russia

Abstract—A number of new huge neutrino telescopes have been built, are being built, and are planned to be built all over the world. With these setups, cosmic neutrinos of high energies can be studied experimentally. Atmospheric neutrinos represent the main backgrounds to such experiments—namely, the atmospheric neutrinos determine how large a setup should be to measure diffuse cosmic neutrino fluxes or what angular resolution of a setup should be in order that searches for pointlike neutrino sources in the sky be successful. The atmospheric-neutrino fluxes are calculated in the present study. At high energies, the atmospheric-neutrino fluxes consist mostly of neutrinos produced in the atmosphere through charmed-particle decays. Three sources of information about charm production are used: (1) data obtained in accelerator experiments, (2) data on cosmic-ray muons, and (3) predictions of the NLO and QGSM QCD models for the charm-production at energies not available at modern accelerators. The uncertainties in the calculated fluxes of atmospheric neutrinos from charmed-particle decays are estimated to be at a level of 3–5 orders of magnitude. *© 2000 MAIK “Nauka/Interperiodica”.*

1. INTRODUCTION

In a number of studies (see, for example, [1–4]), cosmic-ray-muon and atmospheric-neutrino fluxes produced in the atmosphere through decays of charmed particles were calculated. The results of these calculations show as great a scatter as two orders of magnitude at energies of about 100 TeV because different spectra of charmed particles produced in the interactions of primary nucleons with air nuclei were used. These spectra were calculated within different theoretical models based on QCD. At accelerator energies, all these spectra are in agreement with one another and with data obtained in accelerator experiments. But at higher energies, they differ greatly.

In this study, the aforementioned fluxes are calculated for the spectra of charmed particles produced at accelerators. We assume that these spectra have almost a scaling behavior in the fragmentation region and do not change significantly with nucleon energy in a wide energy interval. This assumption is supported by data on cosmic-ray muons [5] and by the predictions of the QGSM [6–9] and NLO [10–13] models of QCD for the behavior of the charm-production process at high energies. In fact, $ud\sigma/du$ varies with nucleon energy, but the variation of its form is very small (even less than in pion production). Here, $d\sigma/du$ is the differential cross section for the production of a charmed particle η with a fraction $u = E_\eta/E_N$ of the nucleon energy E_N.

In what follows, the “neutrino flux” is considered to mean the “neutrino plus antineutrino flux.”

2. NEUTRINOS FROM CHARMED-PARTICLE DECAYS

If the differential energy spectrum of primary nucleons is a power-law spectrum of the nucleon energy E_N with a power-law exponent γ,

$$P_N(E_N)dE_N = A \times E_N^{-(\gamma+1)}dE_N, \qquad (1)$$

where $A = 1.9$ and $\gamma = 1.7$ for $E_N \leq 3 \times 10^6$ GeV and $A = 228$ and $\gamma = 2$ for $E_N \geq 3 \times 10^6$ GeV, and if the spectra of charmed particles η produced in nucleon interactions are assumed to be proportional to $(1 - u)^\delta$ ($u = E_\eta/E_N$), then the number of neutrinos produced in the atmosphere in the energy interval between E_ν and $(E_\nu + dE_\nu)$ through charmed-particle decays (prompt neutrinos) per nuclear interaction of a primary nucleon can be represented as

$$\alpha^{\text{charm}}_{\nu_{\mu,e}}(E_\nu, \theta) = \sum_i W^\eta_{\text{sl}} \int\limits_{w_{\min}}^{w_{\max}} \int\limits_0^1 b\varphi^\eta(u)(1-u)^\delta \times \frac{\sigma_{NA}^{D\bar{D},\,\Lambda_c\bar{D}}(E_\nu/u/w)}{\sigma_{\text{in}}^{NA}(E_\nu/u/w)} \frac{w^\gamma f(w)}{(1 + E_\nu/w/E_\eta^{\text{cr}}(\theta))} du dw, \qquad (2)$$

where i runs over all kinds of charmed particles; W^η_{sl} is the probability of the decay of a charmed particle η with neutrino production; $b = 1.08$ and $\delta = 5$ for D mesons and $b = 1.4$ and $\delta = 0.4$ for Λ_c baryons; $w = E_\nu/E_\eta$; $w_{\max}$, $w_{\min}$, and $f(w)$ are associated with the kinematics of a three-body decay of the charmed particle; $\varphi^\eta(u) = u^{\gamma-1}$ for D mesons and $\varphi^\eta(u) = u^\gamma$ for Λ_c baryons; and $E^{\text{cr}}_\eta(\theta)$ is the critical energy of the charmed particle. This critical energy is defined as the energy of

---

* This article was submitted by the authors in English.

1063-7788/00/6306-1050$20.00 © 2000 MAIK “Nauka/Interperiodica”

a particle when the probability for the particle to decay over the length of nuclear interaction is equal to that of the nuclear interaction. This energy is proportional to $m_0^{\text{charm}}/(\tau_0^{\text{charm}} c\zeta(\theta))$ (m_0^{charm} is the rest mass of the charmed particle; τ_0^{charm} is its lifetime at rest; c is the speed of light; and $\rho(\theta, x) = \zeta(\theta)x$, where $\rho(\theta, x)$ is the air density at a level x g/cm^2 in the atmosphere in the direction θ to the vertical). In (2), we have also denoted by $\sigma_{NA}^{D\bar{D}, \Lambda_c\bar{D}}$ and σ_{in}^{NA} the cross section for the production of a charmed-particle pair ($D\bar{D}$ or $\Lambda_c\bar{D}$ pair) in the interactions of nucleons with air nuclei and the cross section for inelastic interactions of nucleons with air nuclei, respectively.

The charm-production cross sections for proton–proton interactions as functions of the proton energy are given in Fig. 1, where circles represent data from accelerators, the curve illustrates a version of calculations performed on the basis of the NLO model (the data were taken from [13]), and stars correspond to the QGSM calculations from [10]. One can see that all results are in good agreement with each other, although the accuracies of the experimental data are not sufficiently high. In our calculations, we have used an approximation of charm-production cross sections obtained on the basis of the QGSM data [14]:

$$\sigma_{NA}^{\bar{C}C}(E_N) = 0.48 \times (\log E_p - 3.075) \quad \text{for } E_p \geq 2 \times 10^3 \text{ GeV}. \tag{3}$$

The spectra of product charmed particles were taken in accordance with data from accelerators: $\sim(1-u)^5/u$ for D mesons and $\sim(1-u)^{0.4}$ for Λ_c baryons. Our main assumption is that these spectra have almost scaling behavior in the fragmentation region ($u \sim 0.1$–0.2), where the contribution of charmed particles to particle fluxes considered is dominant due to the nature of the primary-nucleon spectrum in cosmic rays. There are some reasons for the assumption. First of all, an analysis of the cosmic-ray-muon data shows [5] that the spectra of particles produced in nucleon interactions do not change significantly in the fragmentation region when the nucleon energy varies from a few TeV to a few thousand TeV. Next, the predictions of these spectra in the NLO and in the QGSM support this assumption too. In Fig. 2, $u^\gamma d\sigma(u, E_N)/du$ are given in arbitrary units and are normalized to each other at $u = 0.2$. Curves *2* and *2*' were calculated in [9] on the basis of the QGSM. It can be seen that the forms of the curves do not change significantly when the nucleon energy is varied in a wide energy interval (curve *1* was calculated for the D-meson spectrum obtained from accelerator experiments; curves *2* and *2*' are the NLO predictions for the center-of-mass energies of 123.2 GeV and 16 TeV, respectively; and curve *3* represents the QGSM prediction for the energy of 27.4 GeV).

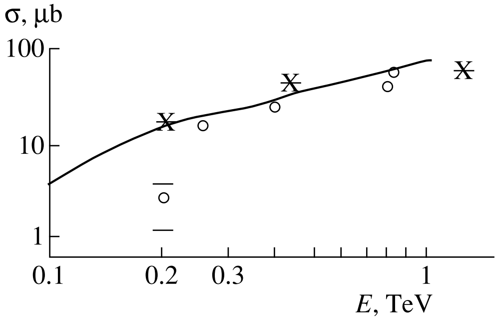

Fig. 1. Charm-production cross sections: (circles) data from accelerator experiments, (stars) results of the calculations within the QGSM, and (curve) version of the calculations within the NLO.

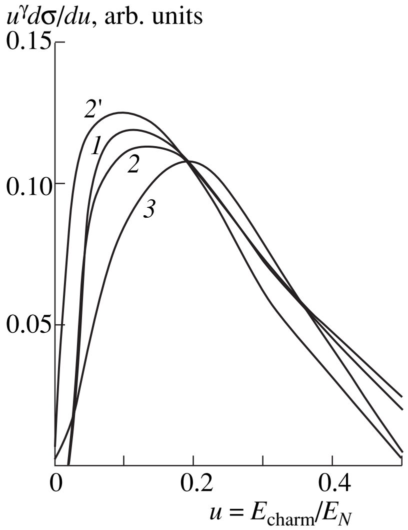

Fig. 2. $u^\gamma d\sigma/du$ in arbitrary units ($d\sigma/du$ is the differential cross section for the production of a charmed particle with a fraction u of the nucleon energy) for (curve *1*) the D-meson spectrum [$\sim(1-u)^5$] measured in accelerator experiments. Curves *2* and *2*' represent the QGSM predictions at the c.m. energies of 123.2 GeV and 16 TeV, respectively, while curve *3* corresponds to the NLO predictions at the c.m. energy of 27.4 GeV.

The calculated differential energy spectra of electron and muon atmospheric neutrinos and antineutrinos are shown in Figs. 3*a* and 3*b*. The curves labeled as charmed particles correspond to neutrinos from the decays of charmed particles. The curves labeled as conventional correspond to neutrinos produced in decays of pions and kaons (these spectra were taken from [15] and were rescaled to $\gamma = 1.7$). The spectra are given for neutrinos coming to sea level in the vertical (0°) and horizontal (90°) directions.

The energy at which the contribution of charmed particles to atmospheric-neutrino fluxes becomes equal to that of pions and kaons is about 1 TeV for electron neutrinos and about 10 TeV for muon neutrinos (vertical direction). At higher energies, the contribution of

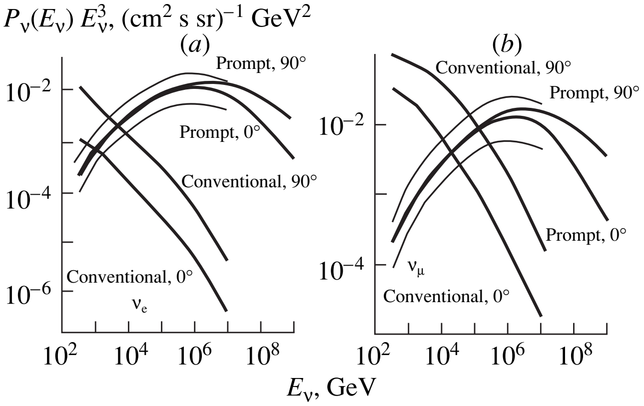

Fig. 3. (*a*) Differential energy spectra of atmospheric neutrinos multiplied by the neutrino energy cubed for electron (ν_e) and (*b*) muon (ν_μ) neutrinos (curves labeled with 0° and 90° correspond to neutrinos coming to sea level in, respectively, the vertical and the horizontal direction): (conventional) results for neutrinos from pion and kaon decays and (prompt) results for neutrinos from charmed-particle decays. To illustrate the uncertainties in the calculations of the prompt-neutrino fluxes, thin curves are given for the prompt-neutrino fluxes at the charm-pair-production cross section twice as large or small as that in (3).

charmed particles becomes dominant; at still higher energies, almost all fluxes of atmospheric neutrinos consist of neutrinos from charmed-particle decays.

3. CONCLUSION

The main assumption of the present study is that the spectra of charmed-particle production have almost scaling behavior in the fragmentation region for a wide energy interval. This is supported by data on cosmic-ray muons and by the predictions of the QGSM and NLO QCD models.

Uncertainties in the calculated fluxes of prompt atmospheric neutrinos have been estimated at 3–5 orders of magnitude if all uncertainties in the parameters and functions used in the calculations have been taken into account.

The contribution from charmed particles to the atmospheric-neutrino fluxes becomes equal to that from pions and kaons at an energy of about 1 TeV for electron neutrinos and about 10 TeV for muon neutrinos (vertical direction).

Neutrinos from charmed particles significantly increase the background to experiments with cosmic neutrinos at high energies. Therefore, some features of these fluxes differ from those of cosmic neutrinos. For example, atmospheric neutrinos have different angular distributions and different ratios of neutrinos of different flavors and conjugations.

REFERENCES

1. E. Zas, F. Halzen, and R. A. Vázquez, Astropart. Phys. **1**, 297 (1993).
2. M. Thunman, G. Indelman, and P. Gondolo, Astropart. Phys. **5**, 309 (1996).
3. V. A. Naumov, T. S. Sinegovskaya, and G. T. Zatsepin, Nuovo Cimento A **111**, 129 (1998).
4. V. I. Gurentsov, L. V. Volkova, and G. T. Zatsepin (submitted for publication in Astropart. Phys.).
5. L. V. Volkova, G. T. Zatsepin, and L. A. Kuzmichev, Yad. Fiz. **29**, 1252 (1979) [Sov. J. Nucl. Phys. **29**, 645 (1979)].
6. A. B. Kaĭdalov and K. A. Ter-Martirosyan, Yad. Fiz. **39**, 1545 (1984) [Sov. J. Nucl. Phys. **39**, 979 (1984)].
7. A. B. Kaĭdalov and O. I. Piskounova, Yad. Fiz. **43**, 1545 (1986) [Sov. J. Nucl. Phys. **43**, 994 (1986)].
8. A. B. Kaĭdalov, Yad. Fiz. **45**, 1452 (1987) [Sov. J. Nucl. Phys. **45**, 902 (1987)].
9. A. De Rujula, E. Fernandez, and J. J. Gomez-Canenas, Nucl. Phys. B **405**, 80 (1993).
10. G. Altarelli *et al.*, Nucl. Phys. B **308**, 724 (1988).
11. P. Nason, S. Dawson, and R. K. Ellis, Nucl. Phys. B **327**, 49 (1989).
12. W. Beenakker, W. L. van Neerve, R. Meng, *et al.*, Nucl. Phys. B **351**, 507 (1991).
13. Yu. M. Shabelski, Talk Given at HERA Monte Carlo Workshop, DESY, Hamburg, April 1998.
14. A. B. Kaidalov and O. I. Piskunova, Preprint No. ITEP-157, ITÉF (Institute of Theoretical and Experimental Physics, Moscow, 1985).
15. L. V. Volkova, Yad. Fiz. **31**, 1510 (1980) [Sov. J. Nucl. Phys. **31**, 784 (1980)].

Physics of Atomic Nuclei, Vol. 63, No. 6, 2000, pp. 1053–1057. From Yadernaya Fizika, Vol. 63, No. 6, 2000, pp. 1129–1132.
Original English Text Copyright © 2000 by Novosel'tsev.

ASTROPARTICLE PHYSICS AND COSMOLOGY

About the Character of the "Knee" at $E \simeq 3 \times 10^{15}$ eV in the Energy Spectrum and the Mass Composition of Primary Cosmic Rays in the Energy Range 10^{15}–10^{17} eV*

Yu. F. Novosel'tsev**

Baksan Neutrino Observatory, Institute for Nuclear Research, Russian Academy of Sciences, Kabardino-Balkariya, Russia

Abstract—The method of rescaling from the muon-multiplicity spectrum to the extensive-air-shower spectrum as a function of the total muon number n_μ is presented. The method allows a direct comparison of data obtained in different experiments with muon groups. A direct comparison of data at $n_\mu > 1800$ and $n_\mu = 75$–660 has been performed. The data in the region $n_\mu = 75$–3500 agree better with the assumption that the slope change in the energy spectrum of primary cosmic rays occurs approximately at the same energy per nucleus, $E_c \simeq 3 \times 10^{15}$ eV, and the mass composition in the energy range 10^{15}–10^{17} eV is close to that observed at 10^{14} eV. © *2000 MAIK "Nauka/Interperiodica".*

1. INTRODUCTION

In [1–3], we presented a method for detecting muon groups with multiplicities $n_\mu(E \geq 220$ GeV$) \geq 1800$ (E is the muon energy) and data obtained at the Baksan Underground Scintillation Telescope (BUST). Events with $n_\mu > 1800$ furnish information about fluxes of primary nuclei with energies in excess of 3×10^{16} eV. The efficiency of detection of events with $n_\mu \geq 1800$ is 100%, and the error in the n_μ determination in an individual event is not greater than 15%.

Unfortunately, this method cannot be used for $n_\mu <$ 1800 because the error in the n_μ determination increases, the compact spots of hit logarithmic channels disappear [1–3], and an accurate determination of the axis of an extensive air shower (EAS) becomes impossible.

In order obtain information about the energy spectrum and the mass composition of primary cosmic rays before and after the "knee" in the region around 3×10^{15} eV, it is necessary to compare our data for $n_\mu >$ 1800 with the results of other experiments at smaller values of n_μ and, first of all, with data from [4], which were also obtained with the Baksan scintillation telescope [5]. However, the hindrance for such a comparison is the fact that, in [4] and in all other papers, the multiplicity spectrum is presented (i.e., the number m of muons hitting the facility at an unknown position of the EAS axis), whereas, in our experiment [1–3], the total number of muons in the EASs was determined. It is known that the multiplicity spectrum depends on the geometry of a facility and on the conditions of event selection. Therefore, multiplicity spectra obtained in different experiments cannot be compared with one another. It would be better to present experimental data on some invariant variable in order that the data not be dependent on experimental conditions. For such a variable, we have chosen the total number of muons in an EAS, n_μ.

In the present study, we propose a method for rescaling the muon-multiplicity spectrum to the EAS spectrum versus n_μ, which allows us to perform a direct comparison of data obtained in different experiments with muon groups. The formulation of the problem is the following. Let $I(m)$ be the integrated multiplicity spectrum obtained at a certain facility. Let us define the parameter

$$\Delta(m) = \bar{m}_1/n_\mu, \qquad (1)$$

which represents the average fraction of muons hitting the facility when the latter is crossed by $m_1 > m$ muons. Assuming that $n_\mu = m/\Delta(m)$, we obtain the integrated spectrum of an EAS as a function of the total number of muons, $F(n_\mu)$.

Below, we briefly describe the procedure for rescaling $I(m)$ to $F(n_\mu)$. This was performed for the data from [4], where the muon-multiplicity spectrum for $20 \leq m <$ 300 was obtained. The data from [4] were used to increase the range of measurement and to obtain the experimental information before "the knee." Further, we demonstrate a comparison of muon-group data at $n_\mu(E \geq 220$ GeV$) \geq 1800$ from [2, 3] and those in the region $n_\mu = 75$–660 obtained by rescaling the multiplicity spectrum from [4]. We conclude with some discussion on the combined Baksan results.

2. DESCRIPTION OF THE METHOD

To calculate $\Delta(m)$, we used a Monte Carlo simulation and the approximation of spatial and energy distri-

---

* This article was submitted by author in English.

** e-mail: novoseltsev@neutr.novoch.ru

Table 1. Values of $\Delta(m)$ and $G(m)$ for composition II (the accuracy in the calculation of $\Delta(m)$ and $G(m)$ is 3%—see main body of the text)

m	$\Delta(m)$	$G(m)$, m^2 sr	n_μ
21.9	0.280	60.5	78.2
32.9	0.289	57.9	113.9
44.5	0.295	56.6	150.8
56.5	0.299	54.8	188.6
82.1	0.306	53.2	268.2
124.9	0.313	51.6	399.3
211.6	0.319	50.4	663.8

bution function (SDF) of muons in an EAS, obtained in [6], which was used in [1–3]:

$$f(r, \geq E, E_0) = C\exp[-(r/r_0)^d], \tag{2}$$

$$r_0 = \frac{0.95}{(1+12.5E)^{0.92}} + \frac{0.42}{E^{1.23}E_0^{0.9}},$$

$$d = 0.43 + \frac{0.2}{0.2 + E_0}.$$

Here, E_0 (in TeV) is the energy per nucleon (r is measured in meters), and C is a normalization factor. The quantity $\Delta(m)$ was determined for the event selection used in [4]. Recall that, in [4], the multiplicity spectrum $I(m)$ in the region $20 \leq m < 300$ was obtained. The muon groups were selected in which the zenith angle θ of the EAS axis was not greater than 20°. In the case of this selection, the threshold muon energy is equal to 240 GeV.

For a fixed number of nucleons in the nucleus, A, and a fixed energy per nucleon, E_0, we determine the average number $m_1(R)$ of muons hitting the facility when the EAS axis is located at a distance R from the facility center (it must be $m_1 \geq m$). In this way, we determine the quantity

$$\Delta_1(m, R, E_0, A) = \frac{m_1(R, E_0, A)}{n_\mu(E_0, A)}. \tag{3}$$

The quantity $\Delta_1(m)$ was determined by means of a Monte Carlo simulation: muons dropped and hit (or did not hit) the detectors according to the SDF (2) of muons in the EAS. The propagation of muons through the rock above the facility was taken into account by the code PROPMU (P. Lipari and T. Stanev) kindly presented to us by the MACRO collaboration.

To obtain $\Delta(m)$, it is necessary to perform averaging over R, E_0, and A in (3). Details of the calculation are described elsewhere [7]. Here, we present the final results.

Table 1 quotes the numerical values of $\Delta(m)$ and $G(m)$ for the mass composition of version II [$G(m)$ is the effective acceptance of the facility]. The error in the calculation of $\Delta(m)$ and $G(m)$ does not exceed 2 to 3%. Noninteger values of m are obtained because of corrections in reconstructing the trajectories [4].

To study the dependence of $\Delta(m)$ and $G(m)$ on the mass composition of cosmic rays, we performed averaging over nuclear types for two versions of the composition at $E_N = 10^{14}$ eV ($E_N = AE_0$):

	p	He	CNO	Ne–S	Fe
I, %	39	24	13	13	11
II, %	25	31	19	12	13

Here, version I is the standard composition observed at low energies ($E_0 \sim 10$ GeV), while version II is the Swordy composition [8], where the fraction of protons was increased (at the expense of the fraction of He nuclei) in accordance with the JACEE data [9]. We assume that the energy spectra of the nuclei have the form

$$J_A(E_0)dE_0 = K_A E_0^{-2.7}\left(1 + \frac{E_0}{E_c}\right)^{-0.4} dE_0, \tag{4}$$

where E_c is the energy of the change in the slope, which can depend on the charge of the nucleus. The total flux of cosmic rays at 10^{14} eV was chosen to be [8, 10]

$$F_{\mathrm{tot}}(10^{14}\ \mathrm{eV}) = 12 \times 10^{-10} (\mathrm{m}^2\ \mathrm{sr\ s\ GeV})^{-1}. \tag{5}$$

For composition I, $\Delta(m)$ will be 0.7–0.1% greater and $G(m)$ will be 0.6% smaller than for composition II. It is worth noting that the results obtained for $G(m)$ (60–50 m^2 sr) mean that, in the experiment from [4] at $m \geq 20$, the EAS axis is almost always within the facility area. Thus,

$$F(n_\mu) = \frac{1}{G(m)} I(m) \tag{6}$$

is the flux of the EAS with the number of muons not less than $n_\mu = m/\Delta(m)$.

3. EXPERIMENTAL DATA

Figure 1 displays our data for $F(n_\mu)$ at $n_\mu \geq 1800$. There are 28 recorded events with $n_\mu(\geq 220\ \mathrm{GeV}) \geq 1800$; of these, 15 have $n_\mu \geq 2500$ and 7 have $n_\mu \geq 3500$. The "lifetime" of detection is 69220 h. (Here, we present statistics that are twice those from [1, 2].) The crosses in Fig. 1 represent the integrated multiplicity spectrum $I(m)$ [divided by $G(m)$] as obtained in [4] (in the region $m = 21.9 - 211.6$). Applying transformation (6) to $I(m)$, we obtained the EAS spectrum versus n_μ in the region $n_\mu = 75$–660 (closed boxes). In Fig. 1, we also show the calculated EAS fluxes in the region $50 \leq n_\mu \leq 10^4$,

$$F(n_\mu) = \sum_{i \geq n_\mu} \sum_A \int_{E_0^{\mathrm{th}}}^{\infty} B(i, \bar{l}, k) J_A(E_0) dE_0, \tag{7}$$

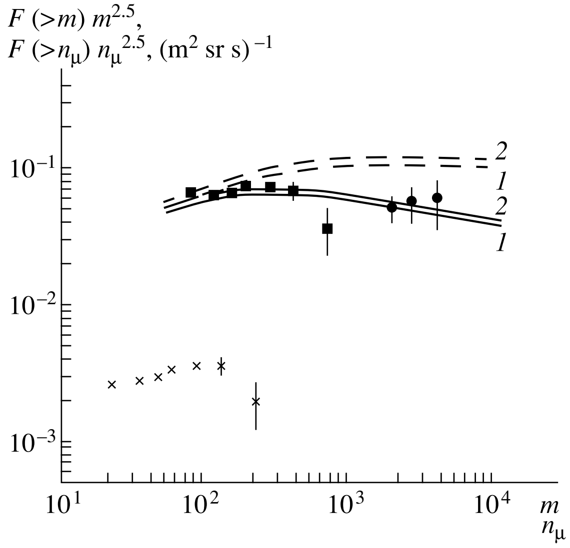

Fig. 1. Integrated multiplicity spectra: (●) present study, (×) muon multiplicity spectrum obtained in [4], and (■) data from [4] rescaled to $F(n_\mu)$. The solid (dashed) curves represent the expected fluxes at $E_c = 3 \times 10^{15}$ eV/nucleus ($E_c = 3Z \times 10^{15}$ eV). The numbers on the curves indicate the composition versions.

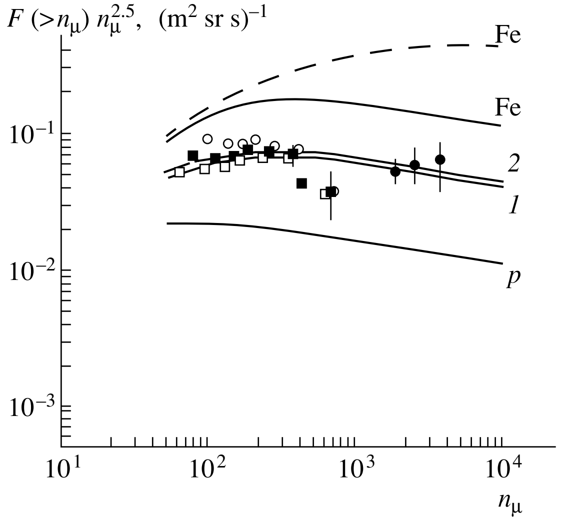

Fig. 2. Rescaling to $F(n_\mu)$ of the data from [4] for the (○) pure iron and (□) pure proton compositions along with the calculated spectra. The rest of the notation is identical to that in Fig. 1.

where E_0^{th} depends on A; $B(i, \bar{l}, k)$ represents the muon-multiplicity fluctuations according to the negative binomial distribution; and $\bar{l}$ is the average number of muons (with $E \geq 220$ GeV) produced by a nucleus with energy $E_N = AE_0$. For $\bar{l}$, we used the expression [6]

$$\bar{l}(A, E_0, \geq E, \theta) = \frac{0.0187 Y(\theta) A}{E^a}\left(\frac{E_0}{E}\right)^{0.78}\left(\frac{E_0}{E_0 + E}\right)^b, \quad (8)$$

where E_0 and E are measured in TeV and where

$$a = 0.9 + 0.1\log(E), \quad b = E + \frac{11.3}{\log(10 + 0.5E_0)},$$

$$Y(\theta) = \frac{1 + 0.36\ln(\cos\theta)}{\cos\theta}.$$

The solid curves in Fig. 1 show the expected fluxes when the slope change in the primary energy spectrum occurs at the same energy per nucleus, $E_c = 3 \times 10^{15}$ eV, while the dashed curves correspond to the case of $E_c = 3Z \times 10^{15}$ eV (Z is the charge of the nucleus). We obtained amazing agreement of the data in the region $n_\mu = 75$–3500 with the expected flux for the case of $E_c = 3 \times 10^{15}$ eV. As the main criterion for assessing the agreement, we used the slope of the curves, because, at present, the absolute values of $F(n_\mu)$ at $E_0 \geq 10^{15}$ eV cannot be calculated reliably (see, for example, [11]). Nevertheless, one can derive additional conclusions from the agreement of absolute values. We emphasize that the boxes show the data for the muon threshold energy of $E_{\text{thr}} = 240$ GeV, whereas the points and the curves correspond to $E_{\text{thr}} = 220$ GeV. This means that the boxes are shifted upward by 15–20% for $E_{\text{thr}} = 220$ GeV. This only increases the discrepancy between the case of $E_c = 3Z \times 10^{15}$ eV and our data.

4. DISCUSSION

Let us examine how the data for $F(n_\mu)$ from [4] are changed if we use the mass composition which is very different from versions I or II of rescaling $I(m)$. Figure 2 shows the results of rescaling to $F(n_\mu)$ for the pure iron composition (open circles) and pure proton composition (open boxes), along with the calculated spectra labeled with Fe and p. As follows from Fig. 2, there is a large difference between the data and the calculated curves. It decreases as we go over from the pure iron composition to version II and begins to increase again as we go over from composition I to a lighter one.

Thus, the combined BUST data obtained at $n_\mu \geq 1800$ [2, 3] and $n_\mu = 75$–660 [4] lead to the conclusion that the slope change in the primary energy spectrum occurs approximately at the same energy per nucleus, $E_c \simeq 3 \times 10^{15}$ eV. This means that the mass composition in the range around “the knee” does not change or

Table 2. Average number of muons with $E > 200$ GeV produced by a nucleus with energy E_N

$A = 1$				$A = 56$		
E_N, eV	[6]	[14]	[17]	E_N, eV	[6]	[14]
10^{15}	55	55	255/4	10^{15}	132	120
10^{16}	329	350	1540/4	10^{16}	798	750
10^{17}	1982			10^{17}	4808	

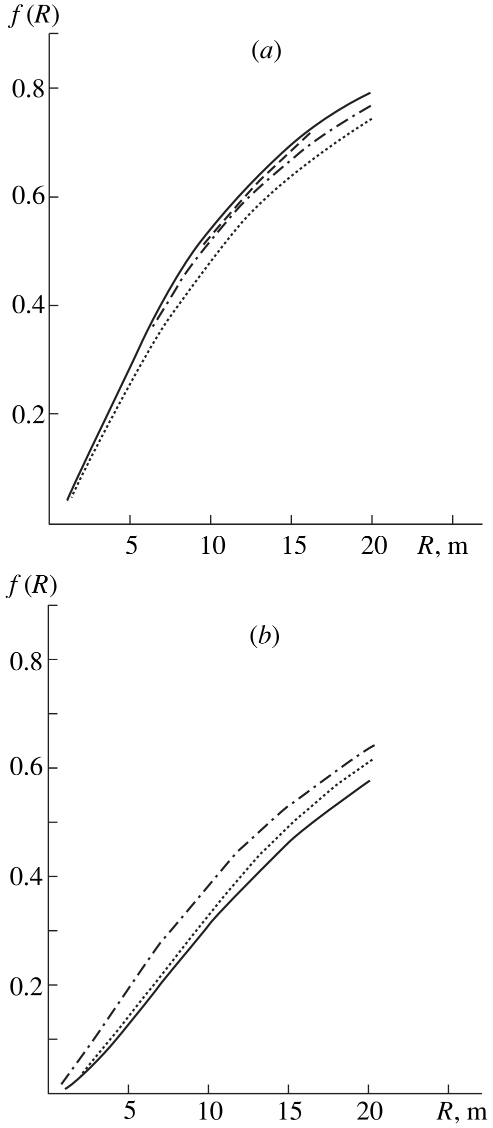

Fig. 3. Fraction of muons (with energies $E > 200$ GeV) produced by a primary nucleus with energy 10^{15} eV into the circle with radius R around the EAS axis: (*a*) primary proton and (*b*) iron nucleus. The dash-dotted curves represent data from [6]. The remaining curves were obtained on the basis of [14]: (solid curves) CORSIKA (DPM), (dashed curve) CORSIKA (VENUS), and (dotted curves) JNC (in figure 3*b*) (VENUS and JNC curves coincide).

changes slightly. The region $75 \le n_\mu \le 3500$ corresponds to the energies of primary nuclei between 2×10^{15} and 2.8×10^{17} eV for protons and between 8×10^{14} and 8×10^{16} eV for iron nuclei. Hence, the data presented in Fig. 1 indicate that the mass composition of cosmic rays in the energy range 10^{15}–10^{17} eV is close to that observed at 10^{14} eV.

In rescaling, we have used expression (8) for the average number $\bar{l}$ of muons and the SDF of muons in an EAS according to (2). The SDF was calculated in a number of studies (for example, [6, 12–14]). In [12, 13], the validity of Feynman scaling was assumed. In [6, 14], a simulation of EAS evolution was performed within the dual parton model (DPM) [15] or the model of quark–gluon strings [16].

Table 2 shows the average number of muons (with $E \geq 200$ GeV) produced by a primary nucleus with energy E_N obtained on the basis of the results from [6, 14, 17]. The fourth column of Table 2 shows the data from [17]. The number of nucleons in the primary nucleus is unknown in the experiment; therefore, one should associate the data from [17] with some "mean" nucleus. If we choose helium as a "mean" nucleus, the results from [17] must be divided by $A = 4$. From Table 2, one can see fairly good agreement of the results of the different studies, although the accuracy of the predictions of n_μ in such models (at $E_0 > 10^{15}$ eV) is 20–30%.

In Fig. 3, several SDFs obtained in different models are compared at the primary energy of $E_N = 10^{15}$ eV. The function $f(R)$ is the fraction of muons (with energy $E \geq 200$ GeV) within the circle of radius R around the EAS axis. From Fig. 3, one can see fairly good agreement of the results of the different models (with exception of JNC) for the proton. For iron nuclei, $f(R)$ from [6] is 15–20% greater than the other ones. It should be noted that, in the proton (Fig. 3*a*) $f(R)$ from [6] is wider than that in the DPM, whereas, for the iron nuclei (Fig. 3*b*), the situation is opposite. This allows us to expect that, in the case of mixed composition, the uncertainty associated with the choice of the SDF will affect our data in the region $n_\mu = 75$–660 only slightly.

We hope that the proposed method of comparison is universal and that it will allow one to carry out a direct comparison of data obtained at different facilities.

REFERENCES

1. V. N. Bakatanov, V. N. Novosel'tsev, and R. V. Novosel'tseva, Izv. Ross. Akad. Nauk, Ser. Fiz. **61**, 562 (1997).
2. V. N. Bakatanov, Yu. F. Novosel'tsev, and R. V. Novosel'tseva, Astropart. Phys. **8**, 59 (1997).
3. V. N. Bakatanov, Yu. F. Novosel'tsev, and R. V. Novosel'tseva, Yad. Fiz. **61**, 1618 (1998) [Phys. At. Nucl. **61**, 1507 (1998)].
4. V. A. Voevodsky *et al*., Izv. Ross. Akad. Nauk, Ser. Fiz. **58**, 127 (1994).
5. E. N. Alexeyev *et al.*, in *Proceedings of 16th International Cosmic Ray Conference, Kyoto, 1979*, Vol. 10, p. 276.
6. S. N. Boziev, A. V. Voevodsky, and A. E. Chudakov, Preprint No. P-0630, IYaI RAN (Institute for Nuclear Research, Russian Academy of Sciences, Moscow, 1989).
7. V. N. Bakatanov, Yu. F. Novosel'tsev, and R. V. Novosel'tseva, Astropart. Phys. (in press).
8. S. P. Swordy, in *Proceedings of 23rd International Cosmic Ray Conference, Calgary, 1993*, Ed. by D. A. Leahy,

R. B. Hicks, and D. Venkatesan (World Sci., 1993), p. 243 and references therein.

9. K. Asakimori *et al.*, in *Proceedings of 24th International Cosmic Ray Conference, Rome, 1995,* Vol. 2, p. 728.
10. M. Amenomori *et al.*, in *Proceedings of 24th International Cosmic Ray Conference, Rome, 1995,* Vol. 2, p. 736.
11. J. Knapp, D. Heck, and G. Schatz, Preprint No. FZKA 5828 (Kernforschungszentrum Karlsruhe, Karlsruhe, 1996).
12. J. Elbert and P. Sommers, Preprint No. UUHEP-83/20 (Univ. of Utah, Utah, 1983).
13. T. Gaisser and T. Stanev, Nucl. Instrum. Methods Phys. Res. A **235**, 183 (1985).
14. R. Attallah *et al.*, Preprint No. ISSN 1232-5309 (Soltan Inst. for Nuclear Studies, Soltan, 1995); in *Proceedings of 24th International Cosmic Ray Conference, Rome, 1995*, Vol. 1, p. 573.
15. A. Capella *et al.*, Phys. Lett. B **81**, 68 (1979); Z. Phys. C **10**, 249 (1981).
16. A. B. Kaĭdalov and K. A. Ter-Martirosyan, Yad. Fiz. **39**, 1545 (1984) [Sov. J. Nucl. Phys. **39**, 979 (1984)].
17. V. V. Vashkevich *et al.*, Yad. Fiz. **47**, 1054 (1988) [Sov. J. Nucl. Phys. **47**, 672 (1988)].

Physics of Atomic Nuclei, Vol. 63, No. 6, 2000, pp. 1058–1077. From Yadernaya Fizika, Vol. 63, No. 6, 2000, pp. 1133–1152.
Original English Text Copyright © 2000 by Pati.

PHYSICS BEYOND THE STANDARD MODEL

The Link between Neutrino Masses and Proton Decay in Supersymmetric Unification*

J. C. Pati**

Physics Department, University of Maryland, USA

Abstract—Following recent joint works with K. Babu and F. Wilczek, I stress here that supersymmetric unification, based on symmetries like $SO(10)$ or a string-derived $G(224) = SU(2)_L \times SU(2)_R \times SU(4)^C$ possesses some crucial features that are intimately linked to each other. They are (a) gauge-coupling unification; (b) the masses and mixings of all fermions, including especially the neutrinos; and last but not least (c) proton decay. In this context, it is noted that the value of $m_{\nu_L^\tau} \sim 1/20$ eV, suggested by the Super-Kamiokande result, goes extremely well with the unification-hypothesis, based on the ideas of (i) $SU(4)$-color, (ii) left-right symmetry, and (iii) supersymmetry. A concrete proposal is presented within an economical $SO(10)$-framework that makes five successful predictions for the masses and mixings of the quarks and the charged leptons. The same framework explains why the ν_μ–ν_τ oscillation angle is so large ($\sin^2 2\theta^{\text{osc}}_{\nu_\mu\nu_\tau} \approx 0.82$–$0.96$) and yet V_{bc} is so small (≈ 0.04), both in accord with observation. The influence of the masses of the neutrinos and of the charged fermions on proton decay is discussed concretely, within this framework. The $\bar{\nu} K^+$ mode is expected to be dominant for SUSY $SO(10)$ as well as $SU(5)$. A distinctive feature of the $SO(10)$ model, however, is the likely prominence of the μ^+K^0 mode, which, for $SU(5)$, is highly suppressed. Our study shows that while current limits on the rate of proton decaying into $\bar{\nu} K^+$ are compatible with theoretical expectations, improvements in these limits by a factor of 5–10 should either turn up events, or else the $SO(10)$-framework described here, which is otherwise so successful, will be in jeopardy. Prominence of the μ^+K^0 mode, if observed, will be most significant in that it will reveal the intriguing link that exists between neutrino masses and proton decay in the context of supersymmetric unification.

1. INTRODUCTION

The Super-Kamiokande (SK) result, convincingly showing the oscillation of ν_μ to ν_τ (or ν_X) with a value of $\delta m^2 \approx 10^{-2}$–$10^{-3}$ eV^2 and an almost maximal oscillation angle $\sin^2 2\theta > 0.83$ [1], clearly seems to require new physics beyond that of the Standard Mode (SM) [2].[1]

This and the other relatively firm result of solar neutrino deficit [4] serve as important clues to physics at a deeper level. Understanding these neutrino anomalies as well as the bizarre pattern of masses and mixings of the quarks and the charged leptons is a major challenge that ought to be met within a fundamental unified theory.

It is of course known that the ideas of grand unification [5–8], as well as those of superstrings [9], call for gauge coupling unification at a high scale and for nucleon instability. Furthermore, both of these features are known to acquire a new perspective [10, 11] in the context of supersymmetry [12]. For recent reviews on this topic and relevant references see, e.g., [13] and [14]. While proton decay is yet to show, the clearest empirical support in favor of grand unification and supersymmetry has so far come from the dramatic meeting of the three gauge couplings of the SM, which is found to occur at a scale of $M_X \approx 2 \times 10^{16}$ GeV, when these couplings are extrapolated from their measured values at LEP to high energies, in the context of supersymmetry [10].

One major goal of this talk will be to stress that supersymmetric unification based on symmetries like $SO(10)$ [15], or (for most purposes) a string-derived $G(224) = SU(2)_L \times SU(2)_R \times SU(4)^C$ [6, 16], has implications not only for (i) gauge coupling unification and (ii) proton decay, but also for (iii) the masses and mixings of the charged fermions, as well as for (iv) those of the neutrinos. In fact, within a unified theory, all four features (i)–(iv) get intimately linked to each other, much more so than commonly thought. Each of these, including even charged fermion and neutrino masses,

---

* This article was submitted by the author in English.

** e-mail: pati@physics.umd.edu

[1] This is because the SM, having ν_L (but no ν_R) and a Higgs doublet ϕ_H, in the presence of quantum gravity, can possibly lead to an effective Majorana mass-term violating $B - L$ for ν_L of the form: $\nu_L \nu_L \langle\phi_H\rangle^2/M_{\text{Pl}}$ [3], yielding $m_{\nu_L} \sim (250\ \text{GeV})^2/(2 \times 10^{18}\ \text{GeV}) \sim 3 \times 10^{-5}$ eV. This is, however, too small to account for the SK result. See, e.g., [2] for discussion of this point and estimate of m_{ν_τ} in the context of left–right symmetric unified theories.

provides some essential clue to the nature of higher unification. As regards the link between the four features, even neutrino masses turn out to have direct influence on proton decay. This is because the latter receives important contributions through a new set of $d = 5$ operators that depend directly on the Majorana masses of the right-handed neutrinos [17]. These new $d = 5$ operators, which were missed in the literature, contribute significantly to proton decay amplitudes, in addition of course to the "standard" $d = 5$ operators [11], which arise through the exchange of the color-triplet Higgsinos related to the electroweak doublets. The standard and the new $d = 5$ operators, related to the charged fermion as well as the neutrino-masses, together raise our expectation that proton decay should be observed in the near future [18].

I elucidate these remarks in the next four sections, covering the following topics:

1. In Section 2, I first recall briefly the motivations for left–right symmetric unified theories, utilizing neutrino masses, suggested by the SK result, as a guide. The support for supersymmetric unification in the light of the LEP data is noted. Further, the origin of such a unification in the context of superstrings, as well as the potential problem of rapid proton decay that arises within supersymmetric theories, is briefly reviewed. These discussions provide the background needed to cover the materials in the remaining sections.

2. I then present arguments [2] to show that the SK result, especially the observed δm^2, interpreted as $m^2_{\nu_\tau}$, receives a simple and natural explanation within the ideas of higher unification based on the symmetry group *G*(224) [6], and thus *SO*(10) or E_6. Such an explanation would not be possible within *SU*(5).

3. In Section 4, I present the first part of a recent work by Babu, Wilczek, and myself [18], in which we attempt to understand, in the context of supersymmetric *SO*(10), the masses and mixings of the neutrinos, suggested by the atmospheric and the solar neutrino anomalies, in conjunction with those of the quarks and the charged leptons. Adopting familiar ideas of generating hierarchical eigenvalues through off-diagonal mixings, and correspondingly Cabibbo-like mixing angles, we find that the bizarre pattern of masses and mixings observed in the charged fermion sector, remarkably enough, can be adequately described (with ~10% accuracy) within an economical and thus predictive *SO*(10) framework. A concrete proposal is presented involving a minimal Higgs system that provides five successful predictions for the masses and mixings of the quarks and the charged leptons in the three families. The same description goes extremely well with a value of $m_{\nu_\tau} \sim 1/20$ eV as well as with a large ν_μ–ν_τ oscillation-angle ($\sin^2 2\theta^{\mathrm{osc}}_{\nu_\mu\nu_\tau} \approx 0.82$–$0.96$), despite highly nondegenerate masses of the light neutrinos. Both these features are in good agreement with the SK result. Furthermore, this framework generically seems to support the small-angle MSW-explanation for the solar neutrino deficit [19].

4. I next present the second part of the work by Babu, Wilczek, and myself [18] in which we link the rather successful supersymmetric *SO*(10) framework describing fermion masses (noted above), with expectations for proton decay. We find that, given the SK result that suggests $m_{\nu_\tau} \sim 1/20$ eV and a large oscillation angle, the contribution from the new $d = 5$ operators mentioned above and to some extent that from the standard operators as well are significantly enhanced. As a result, in spite of generous allowance for uncertainties in the matrix elements and the SUSY spectrum, the inverse decay rate for the dominant $\bar{\nu} K^+$ mode is found to be bounded from above by about 7×10^{33} yr. Typically, the lifetime should of course be lower than this bound. Furthermore, the $\mu^+ K^0$ mode is found to be prominent, with a branching ratio typically in the range of 10–50%, entirely because of contribution from the new operators. For comparison, minimal SUSY *SU*(5), which has only the standard operators, typically leads to branching ratios $\leq 10^{-3}$ for this mode. Thus, our study of proton decay, correlated with fermion masses, strongly suggests that at least candidate events for proton decay should be observed in the very near future, already at SK. The $\mu^+ K^0$ mode, if observed, would be specially important in exhibiting the link between neutrino masses and proton decay that exists within the *G*(224)/*SO*(10) route to supersymmetric unification [18].

2. LEARNING FROM NEUTRINO MASSES ABOUT HIGHER UNIFICATION

2.1. Motivations for SU(4)-Color Left–Right Symmetric Theories

If one assumes a hierarchical pattern of masses for the light neutrinos (with $m_{\nu_e} \ll m_{\nu_\mu} \ll m_{\nu_\tau}$), which goes well within a quark–lepton unified theory, the SK result interpreted as ν_μ–ν_τ oscillation suggests a value for the ν_τ-mass: $m_{\nu_\tau} \approx 1/20$ eV (1/2 to 2). One can argue, as shown later in this section (see also [2] and footnote 1), that a ν_τ mass of this order can be understood simply within supersymmetric unified theories which are forced to introduce the existence of right-handed (RH) neutrino, accompanying the observed left-handed ones. Postponing an estimate of the ν_τ mass for a moment if one asks the question: what symmetry, on one hand, dictates the existence of the RH neutrinos and, on the other hand, also ensures quantization of electric charge, together with quark-lepton unification, one is led to two very beautiful conclusions: (i) quarks and leptons must be unified minimally within the symmetry *SU*(4)-color, and (ii) deep down, the fundamental theory should possess a left–right symmetric gauge structure: $SU(2)_L \times SU(2)_R$. In short, the SM symmetry must be extended minimally to the gauge symmetry [5, 6]

$$G(224) = SU(2)_L \times SU(2)_R \times SU(4)^C. \qquad (1)$$

With respect to $G(224)$, all members of the electron-family fall into the neat pattern

$$F^e_{L,R} = \begin{bmatrix} u_r & u_y & u_b & \nu_e \\ d_r & d_y & d_b & e^- \end{bmatrix}_{L,R}. \qquad (2)$$

The left–right-conjugate multiplets F^e_L and F^e_R transform as (2, 1, 4) and (1, 2, 4), respectively, with respect to $G(224)$; likewise for the μ and the τ families.

Viewed against the background of the SM, the symmetry structure $G(224)$ brought some attractive features to particle physics which include

(i) Organization of all members of a family ($8_L + 8_R$) within one left–right self-conjugate multiplet, with their peculiar hypercharges fully explained.

(ii) Quantization of electric charge, explaining why $Q_{\text{electron}} = -Q_{\text{proton}}$.

(iii) Quark-lepton unification through $SU(4)$-color.

(iv) Left–Right (i.e. parity) and particle–antiparticle symmetries in the fundamental laws which are violated only spontaneously [6, 20]. Thus, within the symmetry-structure $G(224)$, quark–lepton distinction and parity violation may be viewed as low-energy phenomena which should disappear at sufficiently high energies.

(v) Existence of right-handed neutrinos: within $G(224)$, there must exist a RH neutrino (ν_R), accompanying the left-handed one (ν_L), for each family, because ν_R is the fourth color-partner of the corresponding RH up-quarks. It is also the $SU(2)_R$-doublet partner of the associated RH charged lepton (see (2)). The RH neutrinos seem to be essential now (see later discussions) for understanding the nonvanishing light masses of the neutrinos, as suggested by the recent observations of neutrino-oscillations.

(vi) $B - L$ as a local gauge symmetry: $SU(4)$ color introduced $B - L$ as a local gauge symmetry. Thus, following the limits from Eötvos experiments, one can argue that $B - L$ must be violated spontaneously. It has been realized, in the light of recent works, that to implement baryogenesis in spite of electroweak sphaleron effects, such spontaneous violation of $B - L$ at high temperatures may well be needed [21].

2.2. Route to Higher Unification: SU(5) Versus G(224)/SO(10)

To realize the idea of a single gauge coupling governing the three forces [5, 6], one must embed the SM symmetry, or $G(224)$, into a simple (or effectively simple, like $SU(N) \times SU(N)$) gauge group. The smallest such group is $SU(5)$ [7], which contains the SM symmetry, but not $G(224)$. As a result, $SU(5)$ does not possess some of the main advantages of $G(224)$ listed above. In particular, $SU(5)$ splits members of a family into two multiplets: $\bar{5} + 10$, where as $G(224)$, subject to left-right symmetry, groups them into just one multiplet. $SU(5)$ violates parity explicitly. It does not possess $SU(4)$ color and therefore does not gauge $B - L$ as a local symmetry. Further, $SU(5)$ does not contain the RH neutrinos as an integral feature. As I will discuss below, these distinctions between $SU(5)$ versus $G(224)$, or its extensions, turn out to be especially relevant to considerations of neutrino as well as charged fermion masses, and thereby to those of proton decay.

Since $G(224)$ is isomorphic to $SO(4) \times SO(6)$, the smallest simple group to which it can be embedded is $SO(10)$ [15]. Historically, by the time $SO(10)$ was proposed, all the advantages of $G(224)$ ((i) to (vi), listed above) and the ideas of higher unification were in place. Since $SO(10)$ contains $G(224)$, the features (i) to (vi) are of course retained to $SO(10)$. In addition, the 16-fold left–right conjugate set ($F^e_L + \bar{F}^e_R$) of $G(224)$ corresponds to the spinorial 16 of $SO(10)$. Thus, $SO(10)$ preserves even the 16-plet family-structure of $G(224)$, without a need for any extension. If one extends $G(224)$ to the still higher symmetry E_6 [22], the advantages (i) to (vi) are retained, as in $SO(10)$, but in this case, one must extend the family-structure from a 16 to a 27-plet.

Comparing $G(224)$ with $SO(10)$, as mentioned above, $SO(10)$ possesses all the features (i) to (vi) of $G(224)$; in addition it offers gauge coupling unification. I should, however, mention at this point that the perspective on coupling unification and proton decay has changed considerably in the context of supersymmetry and superstrings. In balance, a string-derived $G(224)$ offers some advantages over a string-derived $SO(10)$, while the reverse is true as well. Thus, it seems that a definite choice of one over the other, as an effective theory below the string scale, is hard to make at this point. I will return to this point shortly.

2.3. Gauge Coupling Unification: Need for Supersymmetry

It has been known for some time that the precision measurements of the SM coupling constants (in particular $\sin^2\theta_W$) at LEP put severe constraints on the idea of grand unification. Owing to these constraints, the non-supersymmetric minimal $SU(5)$ and, for similar reasons, the one-step breaking minimal non-supersymmetric $SO(10)$-model as well are now excluded [23].

But the situation changes radically if one assumes that the Standard Model is replaced by the Minimal Supersymmetric Standard Model (MSSM) above a threshold of about 1 TeV. In this case, the three gauge couplings are found to meet [10], at least approximately, provided $\alpha_3(m_Z)$ is not too low (see figures in, e.g., [13, 23]). Their scale of meeting is given by

$$M_X \approx 2 \times 10^{16}\ \text{GeV} \quad (\text{MSSM or SUSY } SU(5)). \quad (3)$$

M_X may be interpreted as the scale where a supersymmetric Grand Unification Theory (GUT) symmetry (like minimal SUSY $SU(5)$ or $SO(10)$) breaks spontaneously into the supersymmetric standard model symmetry $SU(2)_L \times U(1) \times SU(3)^C$.

The dramatic meeting of the three gauge couplings thus provides a strong support for both grand unification and supersymmetry.

2.4. Compatibility between MSSM and String-Unifications

The superstring theory [9] and now the M-theory [24] provide the only known framework that seems capable of providing a good quantum theory of gravity as well as a unity of all forces, including gravity. It thus becomes imperative that the meeting of the gauge couplings of the three nongravitational forces, which occur by the extrapolation of the LEP data in the context of MSSM, be compatible with string unification.

Now, string theory does provide gauge coupling unification for the effective gauge symmetry, below the compactification scale. The new feature is that even if the effective symmetry is not simple, like $SU(5)$ or $SO(10)$, but instead is of the form $G(213)$ or $G(224)$ (say), the gauge couplings of $G(213)$ or $G(224)$ should still exhibit familiar unification at the string-scale, for compactification involving appropriate Kac–Moody levels (i.e., $k_2 = k_3 = 1$, $k_Y = 5/3$ for $G(213)$), barring of course string-threshold corrections [25]. And even more, the gauge couplings unify with the gravitational coupling $(8\pi G_N)/\alpha'$ at the string scale, where G_N is Newton’s constant and α' is the Regge slope.

Thus, one can realize coupling unification without having a GUT-like symmetry below the compactification scale. This is the new perspective brought forth by string theory. There is, however, an issue to be resolved. Whereas the MSSM-unification scale, obtained by extrapolation of low-energy data, is given by $M_X \approx 2 \times 10^{16}$ GeV, the expected one-loop level string-unification scale [25] of $M_{\text{st}} \approx g_{\text{st}}(5.2 \times 10^{17}\ \text{GeV}) \approx 3.6 \times 10^{17}$ GeV is about twenty times higher. Here, one has used $\alpha_{\text{st}} \approx \alpha_{\text{GUT(MSSM)}} \approx 0.04$.

Possible resolutions of this mismatch between M_X and M_{st} by about a factor of 20 have been proposed (for a comprehensive review, see, e.g., [13] and [14]). These include (i) utilizing the idea of string-duality that allows a lowering of M_{st} [26] compared to the value suggested by [25]; alternatively (ii) the idea of a semi-perturbative unification that assumes the existence of two vectorlike families at the TeV-scale, $(16 + \overline{16})$ which raise α_{GUT} to about 0.25–0.3, and thereby also M_X to a few $\times 10^{17}$ GeV [27]; or (iii) the alternative of a string-GUT solution, which would arise if superstrings yield an intact grand unification symmetry like $SU(5)$ of $SO(10)$, together with supersymmetry and the right spectrum (i.e., three chiral families and a suitable Higgs system) at M_{st}, and if the symmetry would break spontaneously at $M_X \sim (1/20)M_{\text{st}}$ to the SM symmetry. In this last case, the gauge couplings would run together between M_X and M_{st}, and thus the question of a mismatch between the two scales would not even arise. However, as yet, there does not seem to be even a semi-realistic string-derived GUT model [28]. Further, to date, no string-GUT solution exists with a resolution of the well-known doublet-splitting problem, without which one would face the problem of rapid proton decay through the $d = 5$ operators [11] (see discussions below). This does not necessarily mean that a realistic GUT solution exhibiting doublet-triplet splitting cannot ultimately emerge from the string or the M-theory.

While each of the solutions mentioned above possesses a certain degree of plausibility (see [13] for some additional possibilities), it is not clear, which, if any, is utilized by the true string vacuum. This is related to the fact that, as yet, there is unfortunately no insight as to how the true vacuum is selected in the string or in the M-theory.

2.5. A GUT or a Non-GUT String-Solution?

Comparing string-derived GUT solutions with non-GUT solutions, where the former yield symmetries like $SU(5)$ or $SO(10)$, while the later lead to symmetries like $G(2113)$ or $G(224)$ at the string scale, we see from the discussions above that each class has a certain advantage and possible disadvantages as well, compared to the other. In particular, a string-GUT solution has the positive feature, explained above, that the issue of a mismatch between M_{st} and M_X does not arise for such a solution. For a non-GUT solution, however, although plausible mechanisms of the type mentioned above could remove the mismatch, a priori it is not clear whether any such mechanism is realized.

On the other hand, for a string-derived GUT solution [28], achieving doublet-triplet splitting so as to avoid rapid proton decay, is still a major burden. In this regard, the non-GUT solutions possess a distinct advantage, because the dangerous color triplets are often naturally projected out [29, 30]. Furthermore, these solutions invariably possess new “flavor” gauge symmetries, which are not available in GUTs. The flavor symmetries turn out to be immensely helpful in (a) providing the desired protection against gravity-induced rapid proton decay [31], (b) resolving certain naturalness problems of supersymmetry such as those pertaining to the issues of squark degeneracy, neutrino-Higgsino mixing and CP violation (see e.g. [32–34]), and (c) explaining qualitatively the observed fermion mass-hierarchy [29].

Weighing the advantages and possible disadvantages of both, it seems hard at present to make a clear choice between a GUT versus a non-GUT string solution. We will therefore keep our options open and look for other means, for example, certain features of proton decay and neutrino masses, to provide a distinction. We will thus proceed by assuming that for a GUT solution, string theory will somehow provide a resolution of the problem of the doublet-triplet splitting, while, for a non-GUT string solution, we will assume that one of the mechanisms mentioned above (for instance, that based on string-duality [26]) does materialize, removing the mismatch between M_X and $M_{\rm st}$. In general, a combination of the two mechanisms [26, 27] may also play a role.

It turns out that there are many similarities between the predictions of $SO(10)$ and of a string-derived $G(224)$, especially as regards neutrino and charged fermion masses, primarily because both contain $SU(4)$-color.

With these discussions on higher unification, including the ideas of supersymmetry and superstrings, to serve as a background I proceed to discuss more concretely, in the next three sections, the masses and mixings of all fermions (in Sections 3 and 4) and finally their link to proton decay (in Section 5). First, an estimate of m_{ν_τ} is presented in the next section.

3. MASS OF ν_τ: AN EVIDENCE IN FAVOR OF THE $G(224)$ ROUTE

One can now obtain an estimate for the mass of ν_L^τ in the context of $G(224)$ or $SO(10)$ by using the following three steps [2]:

(i) First, assume that $B - L$ and I_{3R}, contained in a string-derived $G(224)$ or $SO(10)$, break near the unification-scale,

$$M_X \sim 2\times 10^{16}\ \text{GeV}, \tag{4}$$

through VEVs of Higgs multiplets of the type suggested by string solutions [35], i.e., $\langle(1, 2, 4)_H\rangle$ for $G(224)$ or $\langle\overline{16}_H\rangle$ for $SO(10)$, as opposed to 126_H. In the process, the RH neutrinos (ν_R^i), which are singlets of the SM, can and generically will acquire superheavy Majorana masses of the type $M_R^{ij}\nu_R^{iT}C^{-1}\nu_R^j$, by utilizing the VEV of $\langle\overline{16}_H\rangle$ and effective couplings of the form

$$\mathcal{L}_{\rm M}(SO(10)) \;=\; f_R^{ij}16_i\times 16_j\overline{16}_H\times\overline{16}_H/M + \text{h.c.} \tag{5}$$

A similar expression holds for $G(224)$. Here $i, j = 1, 2, 3$ correspond respectively to e, μ, and τ families. Such gauge-invariant nonrenormalizable couplings might be expected to be induced by Planck-scale physics, involving quantum gravity of stringy effects and/or tree-level exchange of superheavy states, such as those in the string tower. With f_{ij} (at least the largest among them) being of order unity, we would thus expect M to lie between $M_{\rm Pl} \approx 2\times 10^{18}$ GeV and $M_{\rm st} \approx 4\times 10^7$ GeV. Ignoring for the present off-diagonal mixings (for simplicity), one thus obtains2)

$$M_{3R} \approx \frac{f_{33}\langle\overline{16}_H\rangle^2}{M} \approx f_{33}(2\times 10^{14}\ \text{GeV})\eta^2(M_{\rm Pl}/M). \tag{6}$$

This is the Majorana mass of the RH tau neutrino. Guided by the value of M_X, we have substituted $\langle\overline{16}_H\rangle = (2\times 10^{16}\ \text{GeV})\eta$, where $\eta \approx 1/2$ to 2, for this estimate.

(ii) Second, assume that the effective gauge symmetry below the string-scale contains $SU(4)$ color. Now, using $SU(4)$ color and the Higgs multiplet $(2, 2, 1)_H$ of $G(224)$ or equivalently 10_H of $SO(10)$, one obtains the relation $m_\tau(M_X) = m_b(M_X)$, which is known to be successful. Thus, there is a good reason to believe that the third family gets its masses primarily from the 10_H or equivalently $(2, 2, 1)_H$. In turn, this implies

$$m_{\nu_\tau}^{\rm Dirac} \approx m_t(M_X) \approx 100\text{–}120\ \text{GeV}. \tag{7}$$

Note that this relationship between the Dirac mass of the tau neutrino and the top mass is special to $SU(4)$ color. It does not emerge in $SU(5)$.

(iii) Given the superheavy Majorana masses of the RH neutrinos as well as the Dirac masses, as above, the seesaw mechanism [36] yields naturally light masses for the left-handed neutrinos. For ν_L^τ (ignoring mixing), one thus obtains, using (6) and (7),

$$m_{\nu_L^\tau} \approx \frac{(m_{\nu_\tau}^{\rm Dirac})^2}{M_{3R}} \approx \left[\frac{1}{20}\ \text{eV}\times(1\text{–}1.44)/f_{33}\eta^2\right]\frac{M}{M_{\rm Pl}}. \tag{8}$$

Considering that on the basis of the seesaw mechanism, we naturally expect that $m_{\nu_L^e} \ll m_{\nu_L^\mu} \ll m_{\nu_L^\tau}$, and assuming that the SK observation represents ν_L^μ–ν_L^τ (rather than ν_L^μ–ν_X) oscillation, so that the observed $\delta m^2 \approx (10^{-2}\text{–}10^{-3})/2\ \text{eV}^2$ corresponds to $m_{\nu_L^\tau}^{\rm obs} \approx 1/15\text{–}1/40$ eV, it seems truly remarkable that the expected magnitude of $m_{\nu_L^\tau}$, given by (8), is just about what is observed if $f_{33}\eta^2(M_{\rm Pl}/M) \approx 1.3\text{–}1/2$. Such a range for the value of $f_{33}\eta^2(M_{\rm Pl}/M)$ seems most plausible and natural (see discussion in [2]). It should be stressed that the estimate (8) utilizes the ideas of both supersymmetric unification, which yields the scale of M_{3R} (6), and of $SU(4)$ color that yields $m_{\nu_\tau}^{\rm Dirac}$ (7). The agreement between the

---

2) The effects of neutrino mixing and of possible choice of $M = M_{\rm st} \approx 4\times 10^{17}$ GeV (instead of $M = M_{\rm Pl}$) on M_{3R} are considered in [18] (Sections 5 and 6) and here, briefly, in Section 4.

expected and the SK result thus suggests that, at a deeper level, near the string of the coupling unification scale M_X, the symmetry group $G(224)$ and thus the ideas of $SU(4)$ color and left–right symmetry are likely to be relevant to nature.

By providing clear support for $G(224)$, the SK result selects out $SO(10)$ or E_6 as the underlying grand unification symmetry, rather than $SU(5)$. Either $SO(10)$ or E_6 or both of these symmetries ought to be relevant at some scale, and in the string context, as discussed in Section 2, that may well be in higher dimensions, above the compactification-scale, below which there need be no more than just the $G(224)$ symmetry. If, on the other hand, $SU(5)$ were regarded as a fundamental symmetry, first, there would be no compelling reason, based on symmetry alone, to introduce a ν_R, because in is a singlet of $SU(5)$. Second, even if one did introduce ν_R^i by hand, their Dirac masses, arising from the coupling $h^i\bar{5}_i\langle 5_H\rangle\nu_R^i$, would be unrelated to the up-flavor masses and thus rather arbitrary (contrast with (7)). So also would be the Majorana masses of the ν_R^i's, which are $SU(5)$ invariant and thus can even be of order Planck scale (contrast with (6)). This would give $m_{\nu_L^\tau}$ in gross conflict with the observed value. In this sense, the SK result appears to disfavor $SU(5)$ as a fundamental symmetry, with or without supersymmetry.

4. FERMION MASSES AND NEUTRINO OSCILLATIONS IN *SO*(10)

4.1. Preliminaries

I now discuss the masses and mixings of the quarks and charged leptons in conjunction with those of the neutrinos, to see first of all how well they can be understood together within the ideas of higher unification.

The most striking regularity in the masses of the fermions belonging to the three families (at least of the charged ones) is their interfamily hierarchy. This is reflected by the uniform pattern: $m_t \gg m_c \gg m_u$, $m_b \gg m_s \gg m_d$, and $m_\tau \gg m_\mu \gg m_e$. Apart from this gross feature, however, if one examines the pattern in more detail, it looks rather bizarre, especially when one compares intrafamily mass splittings of the three families. For instance, while $m_t^0/m_b^0 \sim 60$, one finds that $m_c^0/m_s^0 \sim 10$ and $m_u^0/m_d^0 \sim 1/2$. Here, the superscript zero denotes that the respective mass is evaluated at the unification scale. Note that the ratio of the up- and down-flavor masses within a family varies widely in going from the third to the second to the first family. Further, comparing quark versus lepton masses of the down-flavor within a family in contrast to $m_b^0 \approx m_\tau^0$, which suggests b–τ unification for the third family, one finds $m_s^0 \sim m_\mu^0/3$ and $m_d^0 \sim 3m_e^0$ [37]. In short, there does not seem to be any obvious regularity in the intrafamily mass splittings. The question is: do these apparent irregularities may still have a simple origin?

The pattern seems to be equally bizarre when one examines the mixing angles. While the parameter $V_{us} = \theta_C$, representing the mixing between the electron and the muon families in the quark sector, is moderately large (≈ 0.21), the parameter V_{cb}, representing μ–τ family mixing, also in the quark sector, is small (≈ 0.04). This feature seems even more strange, when one compares V_{cb} with the ν_μ–ν_τ oscillation angle, which also represents μ–τ family mixing, although in the leptonic sector. This angle seems to be almost maximal: $\sin^2 2\theta^{\text{osc}}_{\nu_\mu\nu_\tau} > 0.83$ (Section 3). One might have been tempted to associate such a large mixing angle with near degeneracy of ν_μ and ν_τ, as has been attempted by several authors. But, then, such degeneracy does not go well with the seesaw formula, especially within a unified scheme in which the Dirac masses of the neutrinos are related to those of the quarks, which exhibit a large interfamily hierarchy. Thus one major puzzle is: Why V_{bc} is so small and yet $\theta^{\text{osc}}_{\nu_\mu\nu_\tau}$ so large? Could the smallness of one imply the largeness of the other within a quark–lepton unified theory? Further, are these peculiarities of the mixing angles related to the irregularities in the intrafamily mass splittings mentioned above.

From a theoretical viewpoint, the goal is to resolve some of these puzzles within a unified predictive theory, in particular, to understand the masses and mixings of the neutrinos in conjunction with those of the quarks and the charged leptons, rather than in isolation. It is, however, known that there is no obvious way to address any of these puzzles in the context of the SM, because, a priori, the SM allows for all the masses and mixings to be arbitrary parameters. Even ignoring *CP* violation for the present discussion, there are 12 such observables: m_t, m_b, m_τ, m_c, m_s, m_μ, m_u, m_d, m_e, V_{us}, V_{cb}, and V_{ub}. The 3×3 mass matrices of the 3 sectors (up, down, and charged lepton) would in general have as many as $9 \times 3 = 27$ real parameters, which represent, however, only 12 observables. The parameters would even increase if one introduces RH neutrinos and considers both the Dirac and the Majorana mass matrices of the three neutrinos.

To reduce the number of parameters, it thus seems that one may have to appeal to symmetries of two kinds: first like those in $G(224)$ or $SO(10)$, which relate quark versus lepton as well as up-versus-down Yukawa couplings, and second "flavor" symmetries which distinguish between the three families (e, μ, and τ) and could account for interfamily mass hierarchy. Interestingly enough, these latter symmetries do seem to arise in string solutions (see e.g. [29, 30]), though not in GUTs.

To proceed further, we will use the following guidelines.

1. Hierarchy Through Off-Diagonal Mixings: Recall earlier attempts [38] that attribute hierarchy in the quark mass matrices of the first two families to matrices of the type

$$M = \begin{pmatrix} 0 & \epsilon \\ \epsilon & 1 \end{pmatrix} m_s^0, \tag{9}$$

for the (d, s) quarks, and likewise for the (u, c) quarks. Here $\epsilon \sim 1/10$. Note the symmetric form of (9) ($M_{12} = M_{21}$) and especially the hierarchical pattern: $(1, 1) \ll (1, 2) \ll (2, 2)$, where $(1, 1) \le O(\epsilon^3)$. The symmetric nature of (9) is guaranteed by group theory if the relevant Higgs field is a 10 of $SO(10)$. The hierarchical entries in (9) can be ensured by imposing a suitable flavor symmetry that distinguishes between the two families. The origin of such symmetries must ultimately be attributed to, for example, string theory. The pattern (9) has the virtues that (a) it generates a hierarchy larger than the input parameter ϵ: $|m_d/m_s| \approx \epsilon^2 \ll \epsilon$, and (b) it leads to the rather successful expression for the Cabibbo angle:

$$\theta_C \simeq \left|\sqrt{\frac{m_d}{m_s}} - e^{i\phi}\sqrt{\frac{m_u}{m_c}}\right|. \tag{10}$$

Using $\sqrt{m_d/m_s} \simeq 0.22$ and $\sqrt{m_u/m_c} \simeq 0.06$, we see that (10) works within 30% for any value of the phase ϕ and perfectly for a value of the phase parameter ϕ around $\pi/2$.

A generalization of the pattern (9) to the case of three families would suggest that the first and the second families (the e and the μ families) receive their masses primarily through their mixings with the third family (τ); the (3, 3) element in this case is then the leading one in each sector. One must also rely on flavor symmetries that distinguish between the e, μ and τ-families, so as to ensure that the (1, 3) and (1, 2) mixing elements are smaller than the (2, 3) element. We will follow this guideline, except, however, for the modification noted below.

2. The Need for an Antisymmetric Component: Although the symmetric hierarchical mass matrix (9) works well for the first two families, a matrix of the same form fails altogether to reproduce V_{cb}, for which it would yield

$$|V_{cb}| \simeq \left|\sqrt{\frac{m_c}{m_t}} - e^{i\chi}\sqrt{\frac{m_s}{m_b}}\right|. \tag{11}$$

Given that $\sqrt{m_s/m_b} \simeq 0.17$ and $\sqrt{m_c/m_t} \simeq 0.06$, we see that (11) would yield $|V_{cb}|$ varying between 0.11 and 0.23, depending upon the value of the phase χ. This is however, too big, compared to the observed value of $V_{cb} \approx 0.04 \pm 0.003$, by at least a factor of 3. We thus see that the simple square root formula for the mixing angle in each sector ($\sin\theta_{ij} \approx \tan\theta_{ij} = \sqrt{m_i/m_j}$, see (10) or (11)), arising from a symmetric matrix of the form (9), fails for V_{cb}. We would interpret this failure as a clue to the presence of antisymmetric contribution to off-diagonal mixing in the mass matrix together with a symmetric one (thus $m_{ij} \ne m_{ji}$), which would modify the square-root formula for the mixing angle to $\sqrt{m_i/m_j}\sqrt{m_{ij}/m_{ji}}$, where m_i and m_j denote the respective eigenvalues. We will note below a simple group theoretical origin of such an antisymmetric component in $SO(10)$, even for a minimal Higgs system, and point out its crucial role in resolving some of the puzzles alluded to above. The resolution would depend, however, on an additional feature, noted below.

3. The Need for a Contribution Proportional to $B - L$: The success of the relations $m_b^0 \approx m_t^0$ and also $m_\tau^0 \approx (m_{\nu_\tau}^{\text{Dirac}})^0$ (Section 3) suggests that members of the third family receive their masses primarily from the VEV of a Higgs field, which is a singlet of $SU(4)$ color and thus independent of $B - L$. That is in fact the case for the Higgs transforming as (2, 2, 1) of $G(2, 2, 4)$ or 10 of $SO(10)$. However, the empirical observations of $m_s^0 \sim m_\mu^0/3$ and $m_d^0 \sim 3m_e^0$, as well as the suppression of V_{bc} (noted above) together with the enhancement of $\theta^{\text{osc}}_{\nu_\mu\nu_\tau}$ (SK result), clearly call for a contribution proportional to $B - L$ as well. This would be the case for contributions from the VEV of a Higgs transforming as 15 of $SU(4)$ color. We note below how such a contribution can arise simply for a minimal Higgs system in $SO(10)$. The amusing thing is that such a contribution, while it is proportional to $B - L$, turns out to be antisymmetric as well, in the family space, fulfilling the need 2.

I now present, following [18], a simple and predictive mass matrix, based on $SO(10)$, which is constructed by using the guidelines 1–3. For simplicity, I first consider only the μ and the τ families. The discussion is extended later to include the electron family.

4.2. The Minimal Higgs System for SO(10)-Breaking and Fermion Masses

The minimal Higgs system capable of breaking $SO(10)$ at the unification scale M_X into the SM symmetry $G(213)$ consists of a 45_H, a 16_H, and (for supersymmetry) a $\overline{16}_H$. Of these, $\langle 45_H\rangle \sim M_X$ breaks $SO(10)$ into $G(2213) = SU(2)_L \times SU(2)_R \times U(1)_{B-L} \times SU(3)^C$, while $\langle 16_H\rangle = \langle \overline{16}_H\rangle \sim M_X$ breaks $SU(2)_R$ and $B - L$ and thus $G(2213)$ into $G(213)$. To break $G(213)$ into $U(1)_{\text{em}} \times SU(3)^C$ at the electroweak scale, one minimally needs in addition the VEV of a 10_H. Thus, the minimal Higgs system that is needed for appropriate $SO(10)$ breaking consists of the set

$$H_{\text{min}} = \{45_H, 16_H, \overline{16}_H, 10_H\}. \tag{12}$$

Of these, only 10_H can have Yukawa coupling with the fermions at the cubic level of the form $h_{ij}16_i16_j10_H$, which could be the dominant source of masses, especially for fermions belonging to the third family. But the first two families must have additional sources for their masses, because a $\langle 10_H\rangle$, by itself, would lead to three undesirable results: (a) $V_{\text{CKM}} = 1$, (b) purely symmetric mass matrices, and (c) $(B - L)$-independent masses. We have, on the other hand, argued above that antisymmetric and $(B - L)$-dependent contributions to mass matrices are needed.

Now, there exist large-dimensional tensorial multiplets of $SO(10)$, that is, 126_H and 120_H, which can have cubic-level Yukawa couplings with the fermions and can give $(B - L)$-dependent contributions. Further, $\langle 120_H\rangle$ gives purely family-antisymmetric contributions, as needed. There are, however, two a priori reasons why we prefer not to use these large-dimensional multiplets: (a) they seem to be hard, if not impossible, to emerge from string solutions [35], and (b) generically, such large-dimensional multiplets tend to give large threshold corrections (typically exceeding 20%) to $\alpha_3(m_Z)$, thereby rendering observed coupling unification fortuitous. By contrast, the multiplets in the minimal set can arise in string solutions leading to $SO(10)$ ((45_H) arises at Kac-Moody level ≥2, while 16_H, $\overline{16}_H$, and 10_H arise at level 1), and their threshold corrections have been computed. They were found not only to be smaller in magnitude, but also to have the right sign to go well with observed coupling unification [18].

Given these advantages of the minimal Higgs system (compared to those containing large multiplets like 126_H and/or 120_H) for $SO(10)$ breaking, the question arises: Can this minimal system meet the requirements arising from fermion masses and mixings—that is (a) $V_{\text{CKM}} \neq 1$, (b) presence of antisymmetric, and (c) that of $(B - L)$-dependent contributions? It was noted in [18] that the minimal Higgs system can indeed meet all three requirements quite simply, if one allows for not just cubic but also (seemingly) nonrenormalizable effective quartic couplings of this minimal set with the 16-plets of fermions. Such quartic couplings could well arise through exchanges of superheavy particles (for example, those in the string tower) involving renormalizable couplings and/or through quantum gravity.

Allowing for such cubic and quartic couplings of the minimal Higgs system and adopting the guideline (1) of family hierarchical couplings, we are led to suggest the following effective Lagrangian for generating masses and mixings of the μ and the τ families [18]:

$$\begin{aligned}\mathcal{L}_{\text{Yukawa}} = {} & h_{33}16_316_310_H + \frac{a_{23}}{M}16_216_310_H45_H \\ & + \frac{g_{23}}{M}16_216_316_H16_H + h_{23}16_216_310_H.\end{aligned} \tag{13}$$

The same consideration is extended later to include the electron family. (For a related but different pattern, see [39].) Note that a mass matrix of the type shown in (9) (barring its symmetric form) results if the first term $h_{33}\langle 10_H\rangle$ is dominant. This ensures $m_b^0 \approx m_\tau^0$ and $m_t^0 \approx (m_{\nu_\tau}^{\text{Dirac}})^0$. The smallness of the remaining terms responsible for off-diagonal mixings, by about an order of magnitude compared to the h_{33}-term, may come about as follows. First, as mentioned before, the smallness of the $SO(10)$-invariant coupling $h_{22}16_216_210_H$ (not shown) compared to the h_{23} coupling and that of h_{23} compared to h_{33} (i.e. $h_{22} \ll h_{23} \ll h_{33}$) may well have its origin in a flavor symmetry (or symmetries), which assigns different charges to the three different families, and also to the Higgs-like fields. In this case, assuming that the h_{33} term is allowed by the flavor symmetries and that the second and the third families have different flavor charges, the h_{23} term will not be allowed as a genuine cubic coupling. It can still arise effectively by utilizing an effective nonrenormalizable coupling $\hat{h}_{23}\,16_216_310_H\langle S\rangle/M$, where S is an $SO(10)$ singlet carrying appropriate flavor charge(s) and acquires a VEV ~ M_{U}. In this case, $h_{23}(= \hat{h}_{23}\,S/M)$ can naturally be $O(1/10)h_{33}$, if $\hat{h}_{23} \sim h_{33}$ and $\langle S\rangle/M \sim M_{\text{U}}/M_{\text{st}} \sim 1/10$. The h_{22} term would then be suppressed by $(\langle S\rangle/M)^2 \sim 10^{-2}$, compared to h_{33}, as desired.[3] Now, as regards the effective nonrenormalizable terms in (13), assuming that they are generated by quantum gravity or stringy effects and/or by tree-level exchanges of superheavy states (see, e.g., those in the string tower), the scale M is naturally expected to be of order $M_{\text{st}} \sim \text{few} \times 10^{17}$ GeV, while $\langle 45_H\rangle \sim \langle 16_H\rangle \sim M_{\text{U}} \sim \text{few} \times 10^{16}$ GeV. Thus, effectively, $a_{23}\langle 45_H\rangle/M$ and $g_{23}\langle 16_H\rangle/M$ could quite plausibly be of order $h_{33}/10$.

It is interesting to observe the symmetry properties of the a_{23} and g_{23} terms. Although $10_H \times 45_H = 10 + 120 + 320$, given that $\langle 45_H\rangle$ is along $B - L$, which is needed to implement doublet-triplet splitting (Section 5), only 120 in the decomposition contributes to the mass matrices. This contribution is, however, antisymmetric in the family index and, at the same time, proportional to $B - L$. Thus, the a_{23} term fulfills the requirements of both (2) and (3) simultaneously. With only h_{ij} and a_{ij} terms, however, the up and down quark mass matrices will be proportional to each other, which would yield $V_{\text{CKM}} = 1$. This is remedied by the g_{ij} coupling as follows. While the 16_H has a VEV, primarily along its SM singlet component (transforming as $\bar{\nu}_R$), which is of order M_{U}, it

---

[3] Although no explicit string solution with the hierarchy in h_{ij} mentioned above, together with the a_{23} and g_{23} couplings of (13), exists as yet, flavor symmetries of the type alluded to, as well as SM singlets carrying flavor-charge and acquiring VEVs of order M_{U}, do emerge generically in string solutions. And there exist solutions with the top Yukawa coupling being leading [29, 16].

also has an electroweak down-type Higgs doublet (but not up-type)—call it 16_d—which can acquire a VEV of the electroweak scale by its mixing with the corresponding doublet—call it 10_d in the 10_H. The MSSM doublet H_d, which is light, is then a mixture of 10_d and 16_d, while the orthogonal combination is superheavy. This feature is discussed in more detail in conjunction with the mechanism for doublet-triplet splitting in [18] and also briefly in the following section. With $\langle 16_d \rangle$ contributing only to the down-flavor mass matrices, but not to the up-flavor, the g_{23} coupling generates nontrivial CKM mixing. We thus see that the minimal Higgs system satisfies a priori all the qualitative requirements 1–3 and also the condition $V_{\rm CKM} \neq 1$. I now discuss that this system works well even quantitatively.

With these four effective Yukawa couplings, the Dirac mass matrices of quarks and leptons of the second and the third families at the unification scale take the form

$$U = \begin{pmatrix} 0 & \epsilon + \sigma \\ -\epsilon + \sigma & 1 \end{pmatrix} m_U, \quad D = \begin{pmatrix} 0 & \epsilon + \eta \\ -\epsilon + \eta & 1 \end{pmatrix} m_D,$$

$$N = \begin{pmatrix} 0 & -3\epsilon + \sigma \\ 3\epsilon + \sigma & 1 \end{pmatrix} m_U, \tag{14}$$

$$L = \begin{pmatrix} 0 & -3\epsilon + \eta \\ 3\epsilon + \eta & 1 \end{pmatrix} m_D.$$

Here, the matrices are multiplied by left-handed fermion fields from the left and by antifermion fields from the right. (U, D) stand for the mass matrices of up and down quarks, while (N, L) are the Dirac mass-matrices of the neutrinos and the charged leptons.

The entries ($1, \epsilon, \sigma$) arise respectively from the h_{33}, a_{23}, and h_{23} terms in (13), while η entering into D and L receives contributions from both g_{23} and h_{23}; thus, $\eta \neq \sigma$. Note the quark–lepton correlations between (U, N) as well as (D, L), and the up–down correlation between (U, D) as well as (N, L). These correlations arise because of the symmetry structure of $G(224)$. The relative factor of –3 between quarks and leptons involving the ϵ entry reflects the fact that $\langle 45_H \rangle \propto (B - L)$, while the antisymmetry in this entry arises from the $SO(10)$ structure as explained above.

Assuming $\epsilon, \eta, \sigma \ll 1$, we obtain at the unification scale

$$\left|\frac{m_c}{m_t}\right| \simeq |\epsilon^2 - \sigma^2|, \quad \left|\frac{m_s}{m_b}\right| \simeq |\epsilon^2 - \eta^2|,$$
$$\left|\frac{m_\mu}{m_\tau}\right| \simeq |9\epsilon^2 - \eta^2|, \quad |m_b| \simeq |m_\tau||1 - 8\epsilon^2|, \tag{15}$$

$$|V_{cb}| \simeq |\sigma - \eta|$$
$$\approx \left| \sqrt{\frac{m_s}{m_b}} \left(\frac{\eta + \epsilon}{\eta - \epsilon}\right)^{1/2} - \sqrt{\frac{m_c}{m_t}} \left(\frac{\sigma + \epsilon}{\sigma - \epsilon}\right)^{1/2} \right|, \tag{16}$$

$$\theta^\ell_{\mu\tau} \approx -3\epsilon + \eta \approx \sqrt{m_\mu / m_\tau} \left(\frac{-3\epsilon + \eta}{3\epsilon + \eta}\right)^{1/2}. \tag{17}$$

The relations in (15) and (16) lead to two sum rules:

$$\left|\frac{m_b}{m_\tau}\right| \simeq \left| 1 - 8\left\{ \left|\frac{m_\mu}{m_\tau}\right| - \left|\frac{m_s}{m_b}\right| \right\} \right|,$$
$$\frac{m_s}{m_b} \simeq \frac{m_c}{m_t} - \frac{5}{4} V_{cb}^2 \pm V_{cb} \left[\frac{9}{16} V_{cb}^2 + \frac{1}{2}\frac{m_\mu}{m_\tau} - \frac{9}{2}\frac{m_c}{m_t} \right]^{1/2}. \tag{18}$$

The superscript zero, meaning unification-scale values, is not exhibited, but should be understood in all the relations in (15)–(18).

The mass matrices in (14) contain five parameters[4]: ϵ, σ, η, $m_D = h_{33}\langle 10_d \rangle$, and $m_U = h_{33}\langle 10_U \rangle$. These may be determined by using, for example, the following input values: $m_t^{\rm phys}$ = 174 GeV, $m_c(m_c)$ = 1.37 GeV, m_s(1 GeV) = 110–116 MeV, and the observed masses of μ and τ. While the input value of m_s is somewhat lower than that advocated in [40], it is in good agreement with recent lattice calculations [41]. With these input values, the parameters are found to be

$$\sigma \simeq -0.110\eta_{cb}, \quad \eta \simeq -0.151\eta_{cb},$$
$$\epsilon \simeq 0.095\eta_\epsilon,$$
$$m_U \simeq m_t(M_{\rm U}) \simeq 100\text{–}120\ \text{GeV}, \tag{19}$$
$$m_D \simeq m_b(M_{\rm U}) \simeq 1.5\ \text{GeV}.$$

Here η_ϵ and η_{cb} denote the phases of ϵ and V_{cb}, respectively (i.e., $\epsilon = \eta_\epsilon|\epsilon|$, etc.). We assume for simplicity that they are real (barring phase angles of ±10°). Thus, $\eta_\epsilon = \pm 1$ and $\eta_{cb} = \pm 1$. The relative signs of σ, η, and ϵ get fixed by ensuring that the results are optimized as regards their agreement with observation. This yields $\eta_{cb} = \eta_\epsilon$. Note that, in accord with our general expectations discussed above, each of these parameters are found to be of order 1/10, as opposed to being[5] $O(1)$ or $O(10^{-2})$, compared to the leading (3, 3) element. Having determined these parameters, one can now obtain the following predictions:

$$m_b(m_b) \simeq 4.6\text{–}4.9\ \text{GeV}, \quad V_{cb} \simeq 0.045,$$
$$m_{\nu_\tau}^{\rm Dirac}(M_{\rm U}) \simeq m_t(M_{\rm U}) \simeq 100\text{–}120\ \text{GeV}, \tag{20}$$

---

[4] Of these, $m_U^0 \approx m_t^0$ can in fact be estimated to within 20% accuracy by either using the argument of radiative electroweak symmetry breaking or in the context of a class of string solutions [29].

[5] This is one characteristic difference between our work and that of [38], where the (2, 3) element is even bigger than the (3, 3).

$$m_{\nu_\mu}^{\mathrm{Dirac}}(M_{\mathrm{U}}) \simeq (9\epsilon^2 - \sigma^2)m_U \simeq 8\ \mathrm{GeV},$$

$$\theta_{\mu\tau}^{\ell} \simeq -3\epsilon + \eta \simeq -0.437\eta_\epsilon\ (\text{for } \eta_{cb}/\eta_\epsilon = +1). \quad (21)$$

In quoting the numbers in (20), we have extrapolated the GUT scale, values down to low energies using the beta functions of MSSM, assuming $\alpha_s(M_Z) = 0.118$, an effective SUSY threshold of 500 GeV, and $\tan\beta = 5$. Our results depend only weakly on these input choices, so long as $\tan\beta$ is neither too large (≥ 30) nor too small (≤ 2). The first two of the predictions listed in (20) correspond to directly observed entities. The last three from (21) cannot be observed directly, but they are important because they need to be combined with the Majorana masses of the RH neutrinos to yield observable entities.

Given the bizarre pattern of quark and lepton masses and mixings, it seems remarkable that the simple pattern of fermion mass matrices, motivated by the group theory of $G(224)/SO(10)$, gives an overall fit to all of them which is good to within 10%. This includes the two successful predictions on m_b and V_{cb} (20). It is worth noting that, in supersymmetric unified theories, the "observed" value of $m_b(m_b)$ and renormalization-group studies suggest that, for a wide range of the parameter $\tan\beta$, m_b^0 should in fact be about 10–20% lower than m_τ^0 [42]. This is neatly explained by the relation $m_b^0 \approx m_\tau^0(1 - 8\epsilon^2)$ (15), where exact equality holds in the limit $\epsilon \longrightarrow 0$ (due to $SU(4)$ color), while the decrease by $8\epsilon^2 \sim 10\%$ is precisely because the off-diagonal ϵ entry is proportional to $B - L$ (see (14)).

Specially intriguing is the result on $V_{cb} \approx 0.045$, which compares well with the observed value of $\simeq 0.04$. The suppression of V_{cb}, compared to the value of 0.17 ± 0.06 obtained from (6), is now possible because the mass matrices (14) contain an antisymmetric component $\propto\epsilon$. Such a component corrects the square-root mixing angle formula $\theta_{sb} = \sqrt{m_s/m_b}$ (appropriate for symmetric matrices of the type given by (9)) by the asymmetry factor $[(\eta + \epsilon)/(\eta - \epsilon)]^{1/2}$ (15), and similarly for the angle θ_{ct}. This factor suppresses V_{cb} if η and ϵ have opposite sings. The interesting point is that the same feature necessarily enhances the corresponding mixing angle $\theta_{\mu\tau}^{\ell}$ in the leptonic sector, since the asymmetry factor in this case is given by $[(-3\epsilon + \eta)/(3\epsilon + \eta)]^{1/2}$ (15). This enhancement of $\theta_{\mu\tau}^{\ell}$ also seems to be borne out by observation in the sense that is a key factor in accounting for the nearly maximal oscillation angle observed at SK (see discussion below). Note that this intriguing correlation between the mixing angles in the quark versus leptonic sectors—that is suppression of one implying enhancement of the other—has become possible because the ϵ contribution is simultaneously antisymmetric and is proportional to $B - L$. As a result, it changes sign as one goes from the quarks to the leptons.

Taking stock, we see an overwhelming set of evidences in favor of $B - L$ and in fact for the full $SU(4)$ color symmetry. These include (i) the suppression of V_{cb}, together with the enhancement of $\theta_{\mu\tau}^{\ell}$; (ii) the successful relation $m_b^0 \approx m_\tau^0(1 - 8\epsilon^2)$, where the near equality follows from $SU(4)$ color, while the decrease of m_b^0 relative to m_τ^0 by $8\epsilon^2 \sim 10\%$ is a consequence of the $(B - L)$-dependence of the off-diagonal ϵ-entry; (iii) the usefulness again of the $SU(4)$ color relation $(m_{\nu_\tau}^{\mathrm{Dirac}})^0 \approx m_t^0$ in accounting for $m_{\nu_L^\tau}$, as discussed in Section 3; and (iv) the agreement of the relation $|m_s^0/m_\mu^0| = |(\epsilon^2 - \eta^2)/(9\epsilon^2 - \eta^2)|$ with the data, in that the ratio is naturally less than 1 if $\eta \sim \epsilon$. The presence of $9\epsilon^2$ in the denominator as opposed to ϵ^2 in the numerator is again a consequence of the off-diagonal entry being proportional to $B - L$. Finally, as mentioned in Section 2, a spontaneously broken $(B - L)$ local symmetry may well be needed to ensure preservation of baryon excess in the presence of electroweak sphaleron effects [21].

Although all the entries for the Dirac mass matrix are now fixed, to obtain the parameters for the light neutrinos one needs to specify the Majorana mass-matrix of the RH neutrinos (ν_R^μ and ν_R^τ). For concreteness, we assume that this too has the hierarchical form of (9):

$$M_\nu^R = \begin{pmatrix} 0 & y \\ y & 1 \end{pmatrix} M_R. \quad (22)$$

In the spirit of our discussion that flavor symmetries are the origin of hierarchical masses, we will assume that $10^{-2} \ll |y| \leq 1/10$ as opposed to, for example, $|y| \geq 0.3$. A priori, $y = \eta_y|y|$ can have either sign, i.e., $\eta_y = \pm 1$. Note that Majorana mass matrices are constrained to be symmetric by Lorentz invariance. The seesaw mass-matrix $(-N(M_\nu^R)^{-1}N^T)$ for the light (ν_μ–ν_τ) system is then

$$M_\nu^{\mathrm{light}} = \begin{pmatrix} 0 & A \\ A & B \end{pmatrix} \frac{m_U^2}{M_R}, \quad (23)$$

where $A \simeq (\sigma^2 - 9\epsilon^2)/y$ and $B \simeq -(\sigma + 3\epsilon)(\sigma + 3\epsilon - 2y)/y^2$. With $A \ll B$, this yields

$$m_{\nu_3} \simeq B\frac{m_U^2}{M_R}, \quad \frac{m_{\nu_2}}{m_{\nu_3}} \simeq -\frac{A^2}{B^2}, \quad \tan\theta_{\mu\tau}^{\nu} = \sqrt{\frac{m_{\nu_2}}{m_{\nu_3}}}. \quad (24)$$

For a given choice of the sign of y relative to that of ϵ, and for a given mass ratio m_{ν_2}/m_{ν_3}, we can now determine y using (23) and (24), and the values of ϵ and σ

obtained in (19). Taking m_{ν_2}/m_{ν_3} = 1/10, 1/15, 1/20, 1/25, 1/30[6], the requirement of hierarchy mentioned above—$10^{-2} \ll |y| \leq 0.2$—can be satisfied only provided y is positive relative to ϵ, i.e., $\eta_y = \eta_\epsilon$; the corresponding values for y are $y = (0.0543; 0.0500, 0.0468, 0.0444, 0.0424)\eta_\epsilon$. With $\eta_y = \eta_\epsilon = \pm 1$, we obtain for the neutrino oscillation angle

$$\theta^{\mathrm{osc}}_{\nu_\mu\nu_\tau} \simeq \theta^{\ell}_{\mu\tau} - \theta^{\nu}_{\mu\tau} \simeq \left(0.437 + \sqrt{\frac{m_{\nu_2}}{m_{\nu_3}}}\right)(-\eta_\epsilon), \tag{25}$$

$$\begin{gathered} \sin^2 2\theta^{\mathrm{osc}}_{\nu_\mu\nu_\tau} = 0.96, 0.91, 0.86, 0.83, 0.81 \\ \text{for } m_{\nu_2}/m_{\nu_3} = 1/10, 1/15, 1/20, 1/25, 1/30. \end{gathered} \tag{26}$$

Note the interesting point that just the requirement that $|y|$ should have a natural hierarchical value leads to $\eta_y = \eta_\epsilon$ and that in turn implies that the two contributions in (25) must add rather than subtract, leading to an almost maximal oscillation angle. The other factor contributing to the enhancement of $\theta^{\mathrm{osc}}_{\nu_\mu\nu_\tau}$ is, of course, also the asymmetry ratio which increased $|\theta^{\ell}_{\mu\tau}|$ from 0.25 to 0.437 (see (17) and (21)). We see that one can derive rather plausibly a large ν_μ–ν_τ oscillation angle $\sin^2 2\theta^{\mathrm{osc}}_{\nu_\mu\nu_\tau} \geq 0.8$, together with an understanding of hierarchical masses and mixings of the quarks and the charged leptons, while maintaining a large hierarchy in the seesaw derived masses (m_{ν_2}/m_{ν_3} = 1/10–1/30) of ν_μ and ν_τ, all within a unified framework including both quarks and leptons. In the example exhibited here, the mixing angles for the mass eigenstates of neither the neutrinos nor the charged leptons are really large, $\theta^{\ell}_{\mu\tau} \simeq 0.437 \simeq 23°$ and $\theta^{\nu}_{\mu\tau} \simeq 0.18$–$0.31 \approx (10$–$18)°$, yet the oscillation angle obtained by combining the two is near-maximal. This contrasts with most previous work, in which a large oscillation angle is obtained either entirely from the neutrino sector (with nearly degenerate neutrinos) of almost entirely from the charged lepton sector.

It is worth noting that the interplay due to the mixing in the Dirac and the Majorana mass matrices via the seesaw mechanism has the net effect of enhancing $M_R \approx B(m_{\nu_2}/m_{\nu_3})$, for a given m_{ν_3}, precisely by a factor of $|B| \approx 5$ (23), compared to what it would be without mixing. Using $m_U \sim 100$ GeV (see (7) or (19)), $m_{\nu_3} \approx$ 1/10–1/30 eV (SK result) and $|B| \approx 5$, one gets

$$M_R \approx (5\text{–}15) \times 10^{14}\ \text{GeV}; \tag{27}$$

compare this with its counterpart, estimated in (6), which yields $M_{3R} \approx$ few $\times\, 10^{14}$ GeV for $f_{33}\eta^2 = 1$ if $M \approx M_{\mathrm{Pl}}$. It is interesting that the larger value of $M_R \approx 10^{15}$ GeV goes well with the theoretical estimate of (6) if the characteristic mass M is chosen (perhaps more appropriately) to be $M_{\mathrm{st}} \approx 4 \times 10^{17}$ GeV rather than M_{Pl}. Further, this larger value of M_R also goes well with the observed m_{ν_3}, once one includes the effect of mixing (which was dropped in Section 3).

4.3. Inclusion of the First Family

The first family may now be included following the spirit of the hierarchical structure shown in (9) and (14). As mentioned before, this may have its origin in flavor symmetries of a deeper theory. In the absence of such a deeper understanding, however, the theoretical uncertainties in dealing with the masses and mixings of the first family are much greater than for the heavier families, simply because the masses of the first family are so small that relatively small perturbations can significantly affect their values.

Assuming that flavor symmetries and $SO(10)$ permit the (3, 3) coupling at a genuine cubic level, but the (2, 3) couplings only at the quartic level, which are thus effectively suppressed by about an order of magnitude compared to the (3, 3) element (see discussion following (13)),we would naturally expect that the (1, 2) and (1, 3) couplings (e.g., a_{12} and g_{12}, see below) would be suppressed compared to the corresponding (2, 3) couplings. This in turn would account for the observed interfamily mass hierarchy.

Following this as a guide, and in the interest of economy, we add only two effective quartic couplings to (13), to include the first family: $a_{12}16_1 16_2 45_H 10_H/M$ and $g_{12}16_1 16_2 16_H 16_H/M$. The first coupling introduces an ϵ' term in the (1, 2)-entry, which is antisymmetric and proportional to $B - L$ (analog of ϵ); the second introduces an η' term in the (1, 2) entry of only D and L, which is symmetric. The resulting 3×3 Dirac mass-matrices are

$$\begin{gathered} U = \begin{pmatrix} 0 & \epsilon' & 0 \\ -\epsilon' & 0 & \epsilon + \sigma \\ 0 & -\epsilon + \sigma & 1 \end{pmatrix} m_U, \\ D = \begin{pmatrix} 0 & \epsilon' + \eta' & 0 \\ -\epsilon' + \eta' & 0 & \epsilon + \eta \\ 0 & -\epsilon + \eta & 1 \end{pmatrix} m_D, \\ N = \begin{pmatrix} 0 & -3\epsilon' & 0 \\ 3\epsilon' & 0 & -3\epsilon + \sigma \\ 0 & 3\epsilon + \sigma & 1 \end{pmatrix} m_U, \end{gathered} \tag{28}$$

---

[6] With $m_{\nu_3} \sim$ 1/10–1/40 eV (Section 3), these values of the ratio m_{ν_2}/m_{ν_3} are suggested by the MSW solution for the solar neutrino puzzle. A posteriori, they also go well with a hierarchical value of y, i.e., $10^{-2} \ll |y| \leq 1/10$.

$$L = \begin{pmatrix} 0 & -3\epsilon' + \eta' & 0 \\ 3\epsilon' + \eta' & 0 & -3\epsilon + \eta \\ 0 & 3\epsilon + \eta & 1 \end{pmatrix} m_D.$$

With ϵ, σ, η, m_U, and m_D determined essentially by considerations of the second and the third families (19), we now have just two new parameters in (28)—ϵ' and η'—which describe five new observables in the quark and charged lepton sector: m_u, m_d, m_e, θ_C, and V_{ub}. Thus, with $m_u \approx 1.5$ MeV (at M_U) and m_e/m_μ taken as inputs one obtains $\epsilon' \simeq \sqrt{m_u/m_c}\,(m_c/m_t) \approx 2 \times 10^{-4}$ and $|\eta'| \simeq \sqrt{m_e/m_\mu}\,(m_\mu/m_\tau) \simeq 4.4 \times 10^{-3}$. We can now calculate m_d, θ_C, and V_{ub}. Combining the two predictions for the second and the third families, obtained before in (19), we are thus led to a total of five predictions for the observable parameters of the quarks and charged leptons belonging to the three families:

$$m_b(m_b) \simeq 4.6\text{–}4.9 \text{ GeV}, \quad V_{cb} \simeq 0.045,$$

$$m_d(1 \text{ GeV}) \simeq 8 \text{ MeV}, \quad \theta_C \simeq \left|\sqrt{m_d/m_s} - e^{i\phi}\sqrt{m_u/m_c}\right|,$$

$$|V_{ub}/V_{cb}| \simeq \sqrt{m_u/m_c} \simeq 0.07.$$

Further, the Dirac masses and mixings of the neutrinos and the mixings of the charged leptons also get determined. Including those for the μ–τ families listed in (21) we obtain

$$m_{\nu_\tau}^{\text{Dirac}}(M_U) \simeq 100\text{–}120 \text{ GeV}, \quad m_{\nu_\mu}^{\text{Dirac}}(M_U) \simeq 8 \text{ GeV},$$

$$\theta_{\mu\tau}^{\ell} \simeq -0.437\eta_\epsilon, \quad m_{\nu_e}^{\text{Dirac}} \simeq \frac{9\epsilon'^2}{9\epsilon^2 - \sigma^2} m_U \simeq 0.4 \text{ MeV},$$

$$\theta_{e\mu}^{\ell} \simeq \left[\frac{\eta' - 3\epsilon'}{\eta' + 3\epsilon'}\right]^{1/2} \sqrt{m_e/m_\mu} \tag{29}$$

$$\simeq 0.85\sqrt{m_e/m_\mu} \simeq 0.06,$$

$$\theta_{e\tau}^{\ell} \simeq \frac{1}{0.85}\sqrt{m_e/m_\tau}(m_\mu/m_\tau) \simeq 0.0012.$$

In evaluating $\theta_{e\mu}^{\ell}$, we have assumed ϵ' and η' to be relatively positive.

Note that the first five predictions in (29) pertaining to observed parameters in the quark system are fairly successful. Considering the bizarre pattern of the masses and mixings of the fermions in the three families (recall comments on V_{cb}, m_b/m_τ, m_s/m_μ, and m_d/m_e), we feel that the success of the mass pattern exhibited by (28) is rather remarkable. This is one reason for taking patterns like (28) seriously as a guide for considerations on proton decay. A particularly interesting variant is obtained in the limit $\epsilon' \longrightarrow 0$, as I will mention at the end of this section.

To obtain some guidelines for the neutrino system involving ν_e, we need to extend the Majorana mass-matrix of (22) by including entries for ν_R^e. Guided by economy and the assumption of hierarchy, as in (9), we consider the following pattern:

$$M_\nu^R = \begin{pmatrix} x & 0 & z \\ 0 & 0 & y \\ z & y & 1 \end{pmatrix} M_R. \tag{30}$$

Equation (30) introduces four effective parameters: x, y, z, and M_R. The magnitude of $M_R \approx (5\text{–}15) \times 10^{14}$ GeV can quite plausibly be justified in the context of supersymmetric unification (see estimate give in (6) and discussion following (27)). And, to the same extent, the magnitude of $m_{\nu_\tau} \approx 1/10\text{–}1/30$ eV, which is consistent with the SK value, can also be anticipated. Since all the Dirac parameters are determined, there are, effectively, three new parameters: x, y, and z. However, there are six observables in the light three neutrino system: the three masses and the three oscillation angles. Thus, one can expect three predictions for the light neutrinos. These may be taken to be $\theta_{\nu_\mu\nu_\tau}^{\text{osc}}$ (25), m_{ν_τ} (see (8) and (24)), and, for example, $\theta_{\nu_e\nu_\mu}^{\text{osc}}$.

Recall that the parameter y was determined above by assuming that the MSW (small or large angle) solution for the solar neutrino deficit corresponds to ν_e–ν_μ oscillation, with $(\delta m^2)_{\text{MSW}} \approx m_{\nu_\mu}^2 \sim 10^{-5}$ eV^2. This gave a value of $|y| \approx 1/20$, in full accord with our general expectation of a hierarchy of order 1/10 for the (2, 3) entry compared to the (3, 3). We do not, however, have much experimental information at present to determine the other two parameters x and y reliably, because very little is known about the observable parameters involving ν_e. To have a feel, consistent with out presumption that the interfamily hierarchical masses arise through successively smaller off-diagonal mixing elements, we will assume that $y \approx 1/20$ (as above), $z \leq y/10$, and $x \sim z^2$. Thus, in addition to $M_R \approx (5\text{–}15) \times 10^{14}$ GeV and $y \approx 1/20$, which are better determined, we take as a guide $z \sim (1\text{–}5) \times 10^{-3}$ and $x \sim (1\text{–few})(10^{-6}\text{–}10^{-5})$. Including the three predictions mentioned above, the mass eigenvalues and the oscillation angles are

$$m_{\nu_\tau} \approx 1/10\text{–}1/30 \text{ eV}, \quad m_{\nu_\mu} \simeq (1\text{–}5) \times 10^{-3} \text{ eV},$$

$$m_{\nu_e} \simeq 10^{-5}\text{–}(1\text{–few}) \times 10^{-4} \text{ eV},$$

$$\theta_{\mu\tau}^{\text{osc}} \simeq 0.437 + \sqrt{m_{\nu_2}/m_{\nu_3}}, \tag{31}$$

$$\theta_{e\mu}^{\text{osc}} \simeq \theta_{e\mu}^{\ell} - \theta_{e\mu}^{\nu} \simeq 0.06 \pm 0.015,$$

$$\theta_{e\tau}^{\text{osc}} \simeq \theta_{e\tau}^{\ell} - \theta_{e\tau}^{\nu} \simeq 10^{-3} \pm 0.03.$$

We see that the masses of ν_e and ν_μ and the oscillation angle $\theta_{e\mu}^{\mathrm{osc}}$ goes well with the small angle MSW explanation of the solar neutrino deficit.[7)]

Although, the superheavy Majorana masses of the RH neutrinos can not be observed directly, they can be of cosmological significance. The pattern given above and the arguments given in Section 3 and in this section suggests that $M(\nu_R^\tau) \approx (5\text{–}15) \times 10^{14}$ GeV, $M(\nu_R^\mu) \approx (1\text{–}4) \times 10^{12}$ GeV (for $y \approx 1/20$), and $M(\nu_R^e) \sim (1/2\text{–}10) \times 10^9$ GeV (for $x \sim (1/2\text{–}10) \times 10^{-6} > z^2$). A mass of $\nu_R^e \sim 10^9$ GeV is of the right magnitude for producing ν_R^e following reheating and inducing lepton asymmetry in ν_R^e decay into $H^0 + \nu_L^i$, which is subsequently converted into baryon asymmetry by the electroweak sphalerons [21].

We have demonstrated that a rather simple pattern for the four Dirac mass matrices, motivated and constrained by the group structure of $SO(10)$, is consistent within 10% with the observed masses and mixing of all the quarks and the charged leptons. This fit is significantly overconstrained, leading to five predictions, which are successful. The same pattern, supplemented with a similar structure for the Majorana mass matrix, quite plausibly accounts for the SK result with the large ν_μ–ν_τ oscillation angle required for the atmospheric neutrinos and accommodates a small ν_e–ν_μ oscillation angle relevant for theories of the solar neutrino deficit.

Before turning to proton decay, it is worth noting that much of our discussion of fermion masses and mixings, including those of the neutrinos, is essentially unaltered if we go to the limit $\epsilon' \longrightarrow 0$ of (28). This limit clearly involves

$$\begin{aligned} m_u &= 0, \quad \theta_{\mathrm{C}} \simeq \sqrt{m_d/m_s} \\ |V_{ub}| &\simeq \sqrt{\frac{\eta - \epsilon}{\eta + \epsilon}}\sqrt{m_d/m_b}(m_s/m_b) \\ &\simeq (2.1)(0.039)(0.023) \simeq 0.0019, \\ m_{\nu_e} &= 0, \quad \theta_{e\mu}^\nu = \theta_{e\tau}^\nu = 0. \end{aligned} \tag{32}$$

All other predictions will remain unaltered. Now, among the observed quantities in the list above, $\theta_{\mathrm{C}} \simeq \sqrt{m_d/m_s}$ is indeed a good result. Considering that $m_u/m_t \approx 10^{-5}$, $m_u = 0$ is also a pretty good result. There are, of course, plausible small corrections arising from higher dimensional operators (for example) involving Planck scale physics which could induce a small value for m_u through the (1, 1) entry $\delta \approx 10^{-5}$. For considerations of proton decay, it is worth distinguishing between these two variants, which we will refer to as cases I and II respectively:

$$\begin{aligned} &\text{Case I: } \epsilon' \approx 2 \times 10^{-4}, \quad \delta = 0; \\ &\text{Case II: } \delta \approx 10^{-5}, \quad \epsilon' = 0. \end{aligned} \tag{33}$$

5. LINK BETWEEN FERMION MASSES AND PROTON DECAY IN SUPERSYMMETRIC *SO*(10)

5.1. Preliminaries

Following paper [18], I present now the results of a recent study of proton decay in SUSY $SO(10)$, which was carried out by paying attention specially to the link that exists in SUSY $SO(10)$ between proton decay and the masses and mixings of all fermions, including especially the neutrinos.

It is well known that in supersymmetric unified theories (GUTs), with $M_X \sim 2 \times 10^{16}$ GeV, the gauge-boson-mediated $d = 6$ proton decay operators, for which $e^+\pi^0$ would have been the dominant mode, are strongly suppressed. The dominant mechanism for proton decay in these theories is given by effective $d = 5$ operators of the form $Q_iQ_jQ_kL_l/M$ in the superpotential, which arise through the exchange of color triplet Higgsinos that are the GUT partners of the standard Higgs doublets, such as those in $5_H + \bar{5}_H$ of $SU(5)$ or the 10_H of $SO(10)$. Subject to a doublet-triplet splitting mechanism which makes these color triplets acquire heavy GUT-scale masses, while the doublets remain light, these standard $d = 5$ operators, suppressed by just one power of the heavy mass and the small Yukawa couplings, lead to proton decay, with a lifetime $\tau_p \sim 10^{30}\text{–}10^{34}$ yr [43–46]. Note that these standard $d = 5$ operators are proportional to the product of two Yukawa couplings, which are related to the masses and mixings of the charged fermions. Further, for these operators to induce proton decay, they must be dressed by wino or gluino exchange so as to convert a pair of squarks to quarks. Owing to (a) Bose symmetry of the superfields in $QQQL/M$, (b) color antisymmetry, and especially (c) the hierarchical Yukawa couplings of the standard Higgs doublets, it turns out that these operators exhibit a strong preference for the decay of a proton into channels involving $\bar{\nu}$ rather than e^+ or (even) μ^+ and those involving an $\bar{s}$ rather than a $\bar{d}$. Thus, the standard operators lead to dominant $\bar{\nu}K^+$ and comparable $\bar{\nu}K^+$ modes, but in all cases to highly suppressed $e^+\pi^0$, e^+K^0, and even μ^+K^0 modes. For instance, for SUSY $SU(5)$, one obtains (for $\tan\beta \le 15$) $[\Gamma(\mu^+K^0)/\Gamma(\bar{\nu}_\mu K^+)]_{\mathrm{std}} \sim [m_u/m_c \sin^2\theta_{\mathrm{C}}]^2 R \approx 10^{-3}$, where $R_{\mu k} \approx 0.1$ is the ratio of the products of the relevant $|\text{matrixelement}|^2 \times$ (phase space) for the two modes.

Now, it was recently realized that in left–right symmetric unified theories possessing supersymmetry,

---

[7)] Although the small angle MSW solution appears to be more generic within the approach outlined above [18], the large angle solution can still plausibly emerge within this approach, in some limited region of the parameter space. This will be analyzed.

such as those based on $G(224)$ or $SO(10)$, there is very likely a new source of $d = 5$ proton decay operators, which are related to the Majorana masses of the right-handed neutrinos [17]. For instance, in the context of the minimal set of Higgs multiplets[8] $\{45_H, 16_H, \overline{16}_H$, and $10_H\}$, which have been utilized in Sections 3 and 4 to break $SO(10)$ and generate fermion masses, these new $d = 5$ operators arise by combining three effective couplings: (a) the couplings $f_{ij}16_i16_j\overline{16}_H\,\overline{16}_H/M$ (5) which are essential to assign Majorana masses to the RH neutrinos, (b) the couplings $g_{ij}16_i16_j16_H16_H/M$, which are needed to generate nontrivial CKM mixing, and (c) the mass-term $M_{16}16_H\overline{16}_H$. In the presence of these three (unavoidable) effective couplings and the VEVs $\langle 16_H\rangle = \langle\overline{16}_H\rangle \sim M_X$ (Sections 3 and 4), the color triplet Higgsinos in 16_H and $\overline{16}_H$ of mass M_{16} can be exchanged between $\tilde{q}_i q_j$ and $\tilde{q}_k l_l$-pairs. This exchange gives rise to a new set of effective $d = 5$ couplings of the form

$$\mathcal{L}^{d=5}_{\text{new}} = [f_{ij}g_{kl}(16_i16_j)(16_k16_l)/M_{16}]\frac{\langle\overline{16}_H\rangle\langle 16_H\rangle}{M^2}, \tag{34}$$

which induce proton decay, just as the standard operators do. Note that these new $d = 5$ operators depend, through the couplings f_{ij} and g_{kl}, both on the Majorana and on the Dirac masses of the respective fermions. This is why, within SUSY $G(224)$ or $SO(10)$, proton decay gets intimately linked to the masses and mixings of all fermions, including neutrinos.

Specifically, it is found that the SK result on atmospheric neutrinos, which suggests $m_{\nu_L^\tau} \sim 1/20$ eV and a large ν_μ–ν_τ oscillation angle, leads to a significant enhancement especially in the new $d = 5$ operators, compared to previous estimates, which were based on guesses of much larger values of $m_{\nu_L^\tau} \sim 2$–4 eV [17]. Curiously enough, the net effect of including the enhancement of f_{33} (due to a lowering of $m_{\nu_L^\tau}$) and the suppression of the relevant CKM mixings is such that the strength of the new $d = 5$ operators is found to be comparable to that of the standard ones [18]. The flavor structure of the new operators are, however, very different from those of the standard ones, in part because the former depend on the Majorana masses of the RH neutrinos, and the latter do not. As a result, the new operators lead to some characteristic differences in the proton decay pattern (that is, branching ratios of different decay modes) compared to the standard ones (see below).

5.2. Framework for Calculating Proton Decay Rate

To establish notations, consider the case of minimal SUSY $SU(5)$ and, as an example, the process $\tilde{c}\tilde{d} \longrightarrow \bar{s}\bar{\nu}_\mu$, which induces $p \longrightarrow \bar{\nu}_\mu K^+$. Let the strength of the corresponding $d = 5$ operator, multiplied by the product of the CKM mixing elements entering into wino-exchange vertices (which in this case is $\sin\theta_C\cos\theta_C$), be denoted by $\hat{A}$. Thus (putting $\cos\theta_C = 1$), one obtains

$$\begin{aligned}\hat{A}_{\tilde{c}\tilde{d}}(SU(5)) &= \frac{h^u_{22}h^d_{12}}{M_{H_C}}\sin\theta_C \\ &\simeq (m_c m_s \sin^2\theta_C/v_u^2)(\tan\beta/M_{H_C}) \\ &\simeq (1.9\times10^{-8})(\tan\beta/M_{H_C}),\end{aligned} \tag{35}$$

where $\tan\beta \equiv v_u/v_d$, and we have put $v_u = 174$ GeV and the fermion masses extrapolated to the unification scale, i.e., $m_c \simeq 300$ MeV and $m_s \simeq 40$ MeV. The amplitude for the associated four-fermion process $dus \longrightarrow \bar{\nu}_\mu$ is given by

$$A_5(dus \longrightarrow \bar{\nu}_\mu) = (\hat{A}_{\tilde{c}\tilde{d}}) \times (2f), \tag{36}$$

where f is the loop-factor associated with wino dressing. Assuming $m_{\tilde{w}} \ll m_{\tilde{q}} \sim m_{\tilde{\ell}}$ one gets $f \simeq (m_{\tilde{w}}/m^2_{\tilde{q}})(\alpha_2/4\pi)$. Using the amplitude for $(du)(s\nu_\ell)$ ($\ell = \mu$ or τ), one then obtains [18, 44–46]

$$\begin{aligned}\Gamma^{-1}(p \longrightarrow \bar{\nu}_\tau K^+) &\approx 2.2\times10^{31}\ \text{yr} \times\left(\frac{0.67}{A_S}\right)^2 \\ &\times\left[\frac{0.006\ \text{GeV}^3}{\beta_H}\right]^2\left[\frac{1/6}{m_{\tilde{w}}/m_{\tilde{q}}}\right]^2 \\ &\times\left[\frac{m_{\tilde{q}}}{1\ \text{TeV}}\right]^2\left[\frac{2\times10^{-24}\ \text{GeV}^{-1}}{\hat{A}(\bar{\nu})}\right]^2.\end{aligned} \tag{37}$$

Here, β_H denotes the hadronic matrix element defined by $\beta_H u_L(\mathbf{k}) \equiv \epsilon_{\alpha\beta\gamma}\langle 0|(d^\alpha_L u^\beta_L)u^\gamma_L|p, \mathbf{k}\rangle$. While the range $\beta_H = 0.003$–0.03 GeV^3 has been used in the past [45], given that one-lattice calculations yield $\beta_H = (5.6 \pm 0.5) \times 10^{-3}$ GeV^3 [47], we will take as a plausible range $\beta_H = 0.006$ GeV$^3 \times (1/2$–$2)$. $A_S \approx 0.67$ stands for the short distance renormalization factor of the $d = 5$ operator. Note that the familiar factors that appear in the expression for proton lifetime—M_{H_C}, $(1 + y_{tK})$ representing the interference between the $\tilde{t}$ and $\tilde{c}$ contributions and $\tan\beta$—are all effectively contained in $\hat{A}(\bar{\nu})$.

---

[8] The origin of these new $d = 5$ operators in the context of other Higgs multiplets, in particular, in the cases where 126_H and $\overline{126}_H$ are used to break $B - L$, has been discussed in [17].

Allowing for plausible and rather generous uncertainties in the matrix element and the spectrum we take

$$\begin{aligned}\beta_H &= 0.006\ \text{GeV}^3 \times (1/2\text{–}2),\\ \frac{m_{\tilde{w}}}{m_{\tilde{q}}} &= \frac{1/2\text{–}2}{6}\end{aligned} \tag{38}$$

and

$$m_{\tilde{q}} \approx m_{\tilde{\ell}} \approx 1\ \text{TeV} \times (1/\sqrt{2}\text{–}\sqrt{2}).$$

Using (37) and (38), we get

$$\begin{aligned}\frac{1}{\Gamma(p \longrightarrow \bar{\nu}_\tau K^+)} &\approx 2.2 \times 10^{31}\ \text{yr}\\ &\times \left(\frac{2.2 \times 10^{-24}\ \text{GeV}^{-1}}{\hat{A}(\bar{\nu}_\ell)}\right)^2 \left[32\text{–}\frac{1}{32}\right].\end{aligned} \tag{39}$$

This relation is general, depending only on $\hat{A}(\bar{\nu}_\ell)$ and on the range of parameters given in (38). It can thus be used for both $SU(5)$ and $SO(10)$. The experimental lower limit on the inverse rate for the $\bar{\nu} K^+$ modes is given by [48]

$$\left[\sum_\ell \Gamma(p \longrightarrow \bar{\nu}_\ell K^+)\right]^{-1}_{\text{exp}} > 7 \times 10^{32}\ \text{yr}. \tag{40}$$

Allowing for all the uncertainties to stretch in the same direction (in this case, the square bracket = 32) and assuming that just one neutrino flavor (e.g., ν_μ for $SU(5)$) dominates, the observed limit (40) provides an upper bound on the amplitude,[9]

$$\hat{A}(\bar{\nu}_\ell) \le 2 \times 10^{-24}\ \text{GeV}^{-1}, \tag{41}$$

which holds for both $SU(5)$ and $SO(10)$. For minimal $SU(5)$, using (35) and $\tan\beta \ge 2$ (which is suggested on several grounds), one obtains a lower limit on M_{H_C} given by

$$M_{H_C} \ge 2 \times 10^{16}\ \text{GeV}\ (SU(5)). \tag{42}$$

At the same time, higher values of $M_{H_C} > 3 \times 10^{16}$ GeV do not go very well with gauge coupling unification [49]. Thus, keeping $M_{H_C} \le 3 \times 10^{16}$ GeV and $\tan\beta \ge 2$, we find from (35) that $\hat{A}\,(SU(5)) \ge (4/3) \times 10^{-24}\ \text{GeV}^{-1}$. Using (39), this in turn implies that

$$\Gamma^{-1}(p \longrightarrow \bar{\nu} K^+) \le 1.5 \times 10^{33}\ \text{yr}\ (SU(5)). \tag{43}$$

This a conservative upper limit. In practice, it is unlikely that all the uncertainties, including that in M_{H_C}, would stretch in the same direction to nearly extreme values so as to prolong proton lifetime. A more reasonable upper limit, for minimal $SU(5)$, thus seems to be $\Gamma^{-1}(p \longrightarrow \bar{\nu} K^+)(SU(5)) \le 0.7 \times 10^{33}$ yr. Given the experimental lower limit (40), we see that minimal SUSY $SU(5)$ is almost on the verge of being excluded by proton decay searches. We have of course noted in Section 3 that SUSY $SU(5)$ does not go well with the neutrino oscillations observed at SK.

Now, to discuss proton decay in the context of supersymmetric $SO(10)$, it is necessary to discuss first the mechanism for doublet-triplet (DT) splitting. Details of this discussion may be found in [18]. Here, I present only a synopsis.

5.3. A Natural Doublet-Triplet Splitting Mechanism in SO(10)

In supersymmetric $SO(10)$, a natural DT splitting can be achieved by coupling the adjoint Higgs 45_H to a 10_H and a $10'_H$, with 45_H acquiring a unification-scale VEV in the $B - L$ direction [50]: $\langle 45_H \rangle = (a, a, a, 0, 0) \times \tau_2$ with $a \sim M_{\text{U}}$. As discussed in Section 2, to generate CKM mixing for fermions we require $\langle 16_H \rangle_d$ to acquire an electroweak scale vacuum expectation value. To insure accurate gauge coupling unification, the effective low energy theory should not contain split multiplets beyond those of MSSM. Thus, the MSSM Higgs doublets must be linear combinations of the $SU(2)_L$ doublets in 10_H and 16_H. A simple set of superpotential terms that ensures this and incorporates DT splitting is

$$\begin{aligned}W_H &= \lambda 10_H 45_H 10'_H + M_{10} 10'^2_H\\ &+ \lambda' \overline{16}_H \overline{16}_H 10_H + M_{16} 16_H \overline{16}_H.\end{aligned} \tag{44}$$

A complete superpotential for 45_H, 16_H, $\overline{16}_H$, 10_H, $10'_H$, and possibly other fields, which ensure that 45_H, 16_H, and $\overline{16}_H$ acquire unification scale VEVs with $\langle 45_H \rangle$ being along the $B - L$ direction; that exactly two Higgs doublets (H_u, H_d) remain light, with H_d being a linear combination of $(10_H)_d$ and $(16_H)_d$; and that there are no unwanted pseudo-Goldstone bosons, can be constructed. With the vacuum expectation value $\langle 45_H \rangle$ in the $B - L$ direction; it does not contribute to the doublet matrix, so one pair of Higgs doublet remains light, while all triplets acquire unification scale masses. The light MSSM Higgs doublets are

$$H_u = 10_u, \quad H_d = \cos\gamma 10_d + \sin\gamma 16_d, \tag{45}$$

with $\tan\gamma \equiv \lambda' \langle \overline{16}_H \rangle / M_{16}$. Consequently, $\langle 10 \rangle_d = \cos\gamma v_d$, $\langle 16_d \rangle = \sin\gamma v_d$, with $\langle H_d \rangle = v_d$ and $\langle 16_d \rangle$ and $\langle 10_d \rangle$ denoting the electroweak VEVs of those multiplets. Note that the H_u is purely in 10_H and that $\langle 10_d \rangle^2 + \langle 16_d \rangle^2 = v_d^2$.

---

[9] If there are subdominant $\bar{\nu}_\ell K^+$ modes with branching ratio R, the right side of (41) should be divided by $\sqrt{1 + R}$.

This mechanism of DT splitting is rather unique for the minimal Higgs systems in that it meets the requirements of both DT splitting and CKM mixing. In turn, it has three important consequences:

(i) It modifies the familiar $SO(10)$ relation $\tan\beta \equiv v_u/v_d = m_t/m_b \approx 60$ to

$$\tan\beta / \cos\gamma \approx m_t / m_b \approx 60. \tag{46}$$

As a result, even low to moderate values of $\tan\beta \approx 3$–10 are perfectly allowed in $SO(10)$ (corresponding to $\cos\gamma \approx 1/20$–$1/6$).

(ii) In contrast to $SU(5)$, for which the strengths of the standard $d = 5$ operators are proportional to $(M_{H_C})^{-1}$, where $M_{H_C} \sim M_{\mathrm{U}} \sim$ few $\times\, 10^{16}$ GeV (see (35)), for the $SO(10)$ model, with DT splitting given as above, they become proportional to M_{eff}^{-1}, where $M_{\mathrm{eff}} = (\lambda a)^2/M_{10'} \sim M_{\mathrm{U}}^2/M_{10'}$. $M_{10'}$ can be naturally smaller than M_{U} and thus M_{eff} correspondingly larger (than M_{U}) by one to two orders of magnitude [18]. Now, the proton decay amplitudes for $SO(10)$ in fact possess an intrinsic enhancement compared to those for $SU(5)$, owing primarily due to differences in their Yukawa couplings for the up sector (see Appendix C in [18]). As a result, these larger values of $M_{\mathrm{eff}} \sim 10^{18}$ GeV are found to lead to expected proton decay lifetimes that are, on one hand, compatible with observed limits but, on the other hand, allow optimism as regards future observation of proton decay.

(iii) M_{eff} gets bounded above by considerations of coupling unification and GUT-scale threshold effects. Owing to mixing between 10_d and 16_d (45), the correction to $\alpha_3(m_Z)$ due to DT splitting becomes proportional to $\ln(M_{\mathrm{eff}}/\cos\gamma)$. Inclusion of this correction and those due to splittings within the gauge and the Higgs multiplets (i.e., 45_H, 16_H, and $\overline{16}_H$)[10)], together with the observed degree of coupling unification, allows us to obtain a conservative upper limit on $M_{\mathrm{eff}} \leq 3 \times 10^{18}$ GeV [18]. Thus in turn helps provide an upper limit on the expected proton decay lifetime.

The calculation of the amplitudes $\hat{A}_{\mathrm{std}}$ and $\hat{A}_{\mathrm{new}}$ for the standard and the new operators for the $SO(10)$ model are given in detail in [18]. Here, I will present only the results. It is found that the four amplitudes $\hat{A}_{\mathrm{std}}(\bar{\nu}_\tau K^+)$, $\hat{A}_{\mathrm{std}}(\bar{\nu}_\mu K^+)$, $\hat{A}_{\mathrm{new}}(\bar{\nu}_\tau K^+)$, and $\hat{A}_{\mathrm{new}}(\bar{\nu}_\nu K^+)$ are in fact very comparable to each other, within about a factor of two, either way. Since there is no reason to expect a near cancellation between the standard and the new operators, especially for both $\bar{\nu}_\tau K^+$ and $\bar{\nu}_\mu K^+$ modes, we expect the net amplitude (standard + new) to be in the range exhibited by either one. Following [18], I therefore present the contributions from the standard and the new operators separately. Using the upper limit on $M_{\mathrm{eff}} \geq 3 \times 10^{18}$ GeV, we obtain a lower limit for the standard proton decay amplitude given by

$$\hat{A}(\bar{\nu}_\tau K^+)_{\mathrm{std}} \geq \begin{bmatrix} (7 \times 10^{-24}\ \mathrm{GeV}^{-1})(1/6\text{–}1/4) \\ (3 \times 10^{-24}\ \mathrm{GeV}^{-1})(1/6\text{–}1/2) \end{bmatrix}. \tag{47}$$

Substituting into (39) and adding the contribution from the second competing mode $\bar{\nu}_\mu K^+$ with a typical branching ratio $R \approx 0.3$, we obtain

$$\Gamma^{-1}(\bar{\nu} K^+)_{\mathrm{std}} \leq \begin{bmatrix} (3 \times 10^{31}\ \mathrm{yr})(1.6\text{–}0.7) \\ (6.8 \times 10^{31}\ \mathrm{yr})(4(\text{–}0.44)) \end{bmatrix} (32\text{–}1/32). \tag{48}$$

The upper and lower entries in (47) and (48) and henceforth correspond to the cases I and II of the fermion mass matrix (33) ($\epsilon' \neq 0$ and $\epsilon' = 0$, respectively). The uncertainty shown inside the square brackets corresponds to that in the relative phases of the different contributions. The uncertainty (32–1/32) corresponds to the uncertainty in β_H, $(m_{\tilde{w}}/m_{\tilde{q}})$ and $m_{\tilde{q}}$ by factors of 2, 2, and $\sqrt{2}$, respectively, either way, around the "central" values reflected in (38). Thus, we find that, for MSSM embedded in $SO(10)$, the inverse partial proton decay rate should satisfy

$$\begin{aligned} \frac{1}{\Gamma(p \longrightarrow \bar{\nu} K^+)_{\mathrm{std}}} &\leq \begin{bmatrix} 3.0 \times 10^{31 \pm 1.7}\ \mathrm{yr} \\ 6.8 \times 10^{31^{+2.1}_{-1.5}}\ \mathrm{yr} \end{bmatrix} \\ &\leq \begin{bmatrix} 1.5 \times 10^{33}\ \mathrm{yr} \\ 7.0 \times 10^{33}\ \mathrm{yr} \end{bmatrix} (SO(10)). \end{aligned} \tag{49}$$

The central value of the upper limit in (49) essentially reflects the upper limit on M_{eff}, while the remaining uncertainties of matrix elements and spectrum are reflected in the exponents.

Evaluating similarly the contribution from the new operator, we obtain

$$\hat{A}(\bar{\nu}_\mu K^+)_{\mathrm{new}} \approx (1.5 \times 10^{-24}\ \mathrm{GeV}^{-1})(1/4\text{–}1.3), \tag{50}$$

$$\Gamma^{-1}(\bar{\nu} K^+)_{\mathrm{new}} \approx (3 \times 10^{31}\ \mathrm{yr})(16\text{–}1/1.7)(32\text{–}1/32). \tag{51}$$

In this estimate, we have included the contribution of the $\bar{\nu}_\tau K^+$ mode with a typical branching ratio $R \approx 0.4$. Here the second factor, inside the square bracket, reflects the uncertainties in the amplitude, while the last factor corresponds to varying β_H, $(m_{\tilde{w}}/m_{\tilde{q}})$ and $m_{\tilde{q}}$ around the central values reflected in (38). With a net factor of even 20 to 100 arising jointly from the square and the curly brackets, i.e., without going to extreme ends of all parameters, the new operators related to neu-

---

[10)] The correction to $\alpha_3(m_Z)$ due to Planck scale physics through the effective operator $F_{\mu\nu}F^{\nu\mu}45_H/M$ vanishes due to antisymmetry in the $SO(10)$ contraction.

trino masses lead by themselves to proton decay lifetimes

$$\Gamma^{-1}(\bar{\nu}K^+)^{\text{expect}}_{\text{new}} \approx (0.6\text{–}3)\times 10^{33}\ \text{yr}\ (SO(10)). \quad (52)$$

5.4. The Charged Lepton Decay Mode ($p \longrightarrow \mu^+K^0$)

I now discuss a special feature of the $SO(10)$ model pertaining to the possible prominence of the charged lepton decay mode $p \longrightarrow \mu^+K^0$, which is not permissible in SUSY $SU(5)$. Allowing for uncertainties in the way the standard and the new operators can combine with each other for the three leading modes, i.e., $\bar{\nu}_\tau K^+$, $\bar{\nu}_\mu K^+$ and μ^+K^0, we obtain (see [18] for details)

$$B(\mu^+K^0)_{\text{std + new}} \approx [1\div(50\text{–}60)\%]\rho\ (SO(10)), \quad (53)$$

where ρ denotes the ratio of the squares of relevant matrix elements for the μ^+K and $\bar{\nu}K^+$ modes.

In the absence—presumably temporary—of a reliable lattice calculation, which is presently missing for the $\bar{\nu}K^+$ mode [47], one should remain open to the possibility of $\rho \approx 1/2$ to 1. Using (53), we find that, for a large range of parameters, the branching ratio $B(\mu^+K^0)$ can lie in the range of 20 to 30% (if $\rho \approx 1$). Thus, we see that the μ^+K^0 mode is likely to be prominent in the $SO(10)$ model presented here, and if $\rho \approx 1$, it can even become a dominant mode. This contrasts sharply with the minimal $SU(5)$ model, in which the μ^+K^0 is expected to have a branching ratio of only about 10^{-3}. In the $SO(10)$ model, the standard operator by itself gives a branching ratio for this mode of (1–10)%, while the potential prominence of the μ^+K^0 mode arises only through the new operator related to neutrino masses.

6. SOME CRUCIAL OBSERVATIONS PERTAINING TO UNIFICATION: A SUMMARY

The discussion in the preceding sections can be best summarized by listing the implications of some crucial findings which bear on unification.

A. The family multiplet structure: The observed multiplet structure in each family consisting of either sixteen members (including the ν_R) or fifteen members (without ν_R) is the first empirical hint in favor of an underlying gauge symmetry like $G(224)$, $SO(10)$, or $SU(5)$. As mentioned in Section 2, while the SM organizes the 15 members of a family into five multiplets, $SU(5)$ groups them into two, and $G(224)$ with left–right discrete symmetry, as well as $SO(10)$, place all sixteen members within just one multiplet. Further, each of these higher symmetries ($G(224)$, $SO(10)$, or $SU(5)$) explain precisely the $SU(3)^C \times SU(2)_L$ representations and the weak hypercharge Y_W quantum numbers of all the members in a family. This feature and the need to explain observed quantization of electric charge, have been two of the primary motivations for proposing the idea of grand unification [5–7].

B. Meeting of the gauge couplings: The meeting of the gauge couplings, which is found to occur when their measured values at LEP are extrapolated to higher energies, in the context of supersymmetry, clearly supports the ideas of

an underlying unity of forces, as well as of supersymmetry;

the relevance of effective gauge symmetries like $SU(5)$, or $SO(10)$, or a string-derived $G(224)$, or $[SU(3)]^3$ at the underlying level; and

unification at a scale $M_X \sim 2\times 10^{16}$ GeV (assuming MSSM spectrum below M_X).

C. Neutrino masses, especially $m_{\nu_\tau} \sim 1/20$ eV: This single piece of information, suggested by the SK result, brings to light the existence of the RH neutrinos, accompanying the left-handed ones, and reinforces the ideas of (Sections 2 and 3):

$SU(4)$ color,
left–right symmetry,
supersymmetric unification, and
seesaw mechanism.

In short, the SK result, suggesting $m_{\nu_\tau} \sim 1/20$ eV, selects out the route to higher unification based on a string-derived $G(224)$ or $SO(10)$, as opposed to $SU(5)$. Further, it suggests that $B - L$ breaking occurs at the unification scale, $M_{B-L} \sim M_X \sim 2\times 10^{16}$ GeV rather than at an intermediate scale.

D. Masses and mixings of all fermions (*q*, *l*, ν): Adopting familiar ideas of generating lighter eigenvalues through off-diagonal mixings and using the group-theory of $SO(10)$ for the effective Yukawa couplings of the minimal Higgs system, it was found in [18] that, remarkably enough, the bizarre pattern of the masses and mixings of the charged fermions as well as of the neutrinos can be adequately described (with ~10% accuracy) within an economical and predictive $SO(10)$ framework. In particular, the framework provides five successful predictions for the masses and mixings of the quarks and the charged leptons. The same description goes extremely well with a value of $m_{\nu_\tau} \sim 1/20$ eV as well as with a large ν_μ–ν_τ oscillation angle ($\sin^2 2\theta_{\nu_\mu\nu_\tau} \approx 0.82\text{–}0.96$), despite highly nondegenerate masses for the light neutrinos. Both these features are in good agreement with the SK results on atmospheric neutrinos. The same framework also typically leads to the small angle MSW solution for the solar neutrino puzzle, with $m_{\nu_e} \sim 3\times 10^{-3}$ eV $\gg m_{\nu_e}$. These results are listed in Section 4.

One intriguing feature of the $SO(10)$ framework, presented in Section 4, is that the largeness of the ν_μ–ν_τ oscillation angle emerges naturally together with the smallness of the analogous mixing parameter in the quark-sector: $V_{bc} \approx 0.04$. This remarkable correlation between the leptonic versus the quark mixing angles clearly points to the presence of a contribution to the mass matrices, which is proportional to $B - L$, and is antisymmetric in the family space. The minimal Higgs system together with the group theory of $SO(10)$ precisely yields such a contribution.

E. Proton decay: the hallmark of quark–lepton unification: Proton decay, if seen, would directly verify the idea of quark-lepton unification. Note that this crucial aspect of grand unification is not probed directly by the other three observations listed above: B, C, and D.

We have argued that three different sets of observations, (a) the observed meeting of the three gauge couplings, (b) the SK result on atmospheric neutrino oscillations, and (c) fermion masses and mixings, go extremely well with the idea of supersymmetric unification, based on symmetry structures such as $SO(10)$. Badu, Wilczek, and I have studied proton decay in this context, paying attention to its correlation with fermion masses and mixings [18]. We found that the proton decay amplitudes receive a major contribution from a set of new $d = 5$ operators which are directly related to the Majorana masses of the RH neutrinos and to the CKM mixings [17, 18]. This is in addition to the contribution from the standard $d = 5$ operators, which are related to the Dirac masses of the charged fermions. The study shows that the mass of $m_{\nu_\tau} \sim 1/20$ eV (as opposed to previously considered values of a few eV) and the large oscillation angle, suggested by the SK result, in fact imply a net enhancement in the rates of proton decay into the $\bar{\nu} K^+$ and especially the $\mu^+ K^0$ modes [18], relative to previous estimates.

There are of course uncertainties in the prediction for proton decay rates owing to those in the SUSY spectrum, the hadronic matrix elements, and the relative phases of the different contributions. Allowing for rather generous uncertainties in this regard (Section 5), we expects proton to decay dominantly into the $\bar{\nu} K^+$ and very likely to the $\mu^+ K^0$ mode as well, with a lifetime

$$\tau_p \le 7 \times 10^{33} \text{ yr } (SO(10)). \tag{54}$$

This is a conservative upper limit which is obtained only if all the uncertainties are stretched in the same direction to nearly their extreme values, so as to extend proton longevity. Since the likelihood of this happening is small, we expect that within either a string-derived $G(224)$ or the $SO(10)$ model, of the sort presented here, proton should decay with a lifetime shorter than the limit shown above. With the current experimental lower limit already at 7×10^{32} yr, we conclude that improvement in the present limit for $p \longrightarrow \bar{\nu} K^+$ and $p \longrightarrow \mu^+ K^0$ modes by a factor of 2 to at most 10 should either turn up events, or else the remarkably successful $SO(10)$-framework described here will be called into question seriously. On the basis of our study, we expect that the SK detector should in fact see a few proton decay events in the $\bar{\nu} K^+$ and quite possibly in the $\mu^+ K^0$ channel, in the near future. To establish the reality of this important process firmly and also to study efficiently the branching ratios of some crucial modes, like the $\mu^+ K^0$, next-generation detectors with sensitivity of at least 5×10^{34} and perhaps 10^{35} yr are essential.

We have stressed that observation of proton decay into $\mu^+ K^0$ with a branching ratio exceeding, for example, 20% would provide a clear signature in favor of (a) supersymmetric unification based on symmetry structures such as a string-derived $G(224)$ or $SO(10)$, as well as (b) the mechanism described here of generating the masses and mixings of all fermions including especially the neutrinos [18].

To conclude, proton decay has been anticipated for quite some time as a hallmark of grand unification. With coupling unification and neutrino masses revealed, proton decay is the missing link. While its discovery, with dominance of the $\bar{\nu} K^+$ mode, would confirm supersymmetric unification, prominence of the $\mu^+ K^0$ mode would establish the beautiful link that exists between the neutrino masses and proton decay within the $G(224)/SO(10)$ route to unification.

ACKNOWLEDGMENTS

I would like to thank specially Kaladi S. Babu and Frank Wilczek for a most enjoyable collaboration on the research described here. I would also like to thank the organizers of the NANP' 99 conference, especially Professor S. Kovalenko, for the kind hospitality extended to me during the conference. The research presented here is supported in part by DOE grant no. DE-FGO2-96ER-41015.

REFERENCES

1. Super-Kamiokande Collab. (Y. Fukuda *et al.*), Phys. Rev. Lett. **81**, 1562 (1998).
2. J. C. Pati, Nucl. Phys. B (Proc. Suppl.) **77**, 299 (1999); hep-ph/9807315.
3. S. Weinberg, Phys. Rev. Lett. **43**, 1566 (1979); E. Akhmedov, Z. Berezhiani, and G. Senjanovic, Phys. Rev. Lett. **69**, 3013 (1992).
4. For a recent update see J. N. Bachall, P. Krastev, and A. Yu. Smirnov, Phys. Rev. D **58**, 096016 (1998).
5. J. C. Pati and A. Salam, in *Proceedings of 15th High Energy Physics Conference (reported by J. D. Bjorken), Batavia, 1972*, Vol. 2, p. 301; Phys. Rev. D **8**, 1240 (1973).
6. J. C. Pati and A. Salam, Phys. Rev. Lett. **31**, 661 (1973); Phys. Rev. D **10**, 275 (1974).
7. H. Georgi and S. L. Glashow, Phys. Rev. Lett. **32**, 438 (1974).
8. H. Georgi, H. Quinn, and S. Weinberg, Phys. Rev. Lett. **33**, 451 (1974).

9. M. Green and J. H. Schwarz, Phys. Lett. B **149**, 117 (1984); D. J. Gross, J. A. Harvey, E. Martinec, and R. Rohm, Phys. Rev. Lett. **54**, 502 (1985); P. Candelas, G. T. Horowitz, A. Strominger, and E. Witten, Nucl. Phys. B **258**, 46 (1985); for introductions and reviews see M. B. Green, J. H. Schwarz, and E. Witten, *Superstring Theory* (Cambridge Univ. Press, Cambridge, 1988), Vols. 1 and 2; *String Theory in Four Dimensions*, Ed. by M. Dine (North-Holland, Amsterdam, 1988); J. Polchinski, *What is String Theory?* (Les Houches Lectures, 1994); hep-th/9411028.
10. P. Langacker and M. Luo, Phys. Rev. D **44**, 817 (1991); U. Amaldi, W. de Boer, and H. Furstenau, Phys. Lett. B **260**, 111 (1991); J. Ellis, S. Kelley, and D. V. Nanopoulos, Phys. Lett. B **260**, 131 (1991); F. Anselmo, L. Cifarelli, A. Peterman, and A. Zichichi, Nuovo Cimento A **104**, 1817 (1991); the essential features pertaining to coupling unification in SUSY GUTs were noted earlier by S. Dimopoulos, S. Raby, and F. Wilczek, Phys. Rev. D **24**, 1681 (1981); W. Marciano and G. Senjanovic, Phys. Rev. D **25**, 3092 (1982); M. Einhorn and D. R. T. Jones, Nucl. Phys. B **196**, 475 (1982).
11. S. Weinberg, Phys. Rev. D **26**, 287 (1982); N. Sakai and T. Yanagida, Nucl. Phys. B **197**, 533 (1982).
12. Y. A. Gelfand and E. S. Likhtman, Pis'ma Zh. Éksp. Teor. Fiz. **13**, 452 (1971) [JETP Lett. **13**, 323 (1971)]; J. Wess and B. Zumino, Nucl. Phys. B **70**, 139 (1974); D. Volkov and V. P. Akulov, Pis'ma Zh. Éksp. Teor. Fiz. **16**, 621 (1972) [JETP Lett. **16**, 438 (1972)].
13. For a recent discussion see K. Dienes, Phys. Rep. **287**, 447 (1997); hep-th/9602045 and references therein.
14. J. C. Pati, in *Proceedings of Salam Memorial Meeting, 1998* (World Sci., Singapore, 1998), p. 98; hep-ph/9811442.
15. H. Georgi, in *Particles and Fields*, Ed. by C. Carlson (AIP, New York, 1975), p. 575; H. Fritzsch and P. Minkowski, Ann. Phys. (N.Y.) **93**, 193 (1975).
16. I. Antoniadis, G. Leontaris, and J. Rizos, Phys. Lett. B **245**, 161 (1990); G. Leontaris, Phys. Lett. B **372**, 212 (1996).
17. K. S. Babu, J. C. Pati, and F. Wilczek, Phys. Lett. B **423**, 337 (1998).
18. K. S. Babu, J. C. Pati, and F. Wilczek, *Fermion Masses, Neutrino Oscillations and Proton Decay in the Light of the Super-Kamiokande*, hep-ph/9812538V3; Nucl. Phys. B (in press).
19. S. Mikheyev and A. Smirnov, Nuovo Cimento C **9**, 17 (1986); L. Wolfenstein, Phys. Rev. D **17**, 2369 (1978).
20. J. C. Pati and A. Salam, Phys. Rev. D **10**, 275 (1974); R. N. Mohapatra and J. C. Pati, Phys. Rev. D **11**, 566 (1975); **11**, 2558 (1975); G. Senjanovic and R. N. Mohapatra, Phys. Rev. D **12**, 1502 (1975).
21. V. Kuzmin, Va. Rubakov, and M. Shaposhnikov, Phys. Lett. B **155**, 36 (1985); M. Fukugita and T. Yanagida, Phys. Lett. B **174**, 45 (1986); M. A. Luty, Phys. Rev. D **45**, 455 (1992); W. Buchmuller and M. Plumacher, hep-ph/9608308.
22. F. Gürsey, P. Ramond, and P. Sikivie, Phys. Lett. B **60**, 177 (1976).
23. For recent reviews see, e.g., P. Langacker and N. Polonsky, Phys. Rev. D **47**, 4028 (1993) and references therein.
24. The literature on string-dualities and M-theory is large. A few pioneering papers relevant to gauge-coupling unification are E. Witten, Nucl. Phys. B **443**, 85 (1995); P. Horava and E. Witten, Nucl. Phys. B **460**, 506 (1996); for reviews see, e.g., J. Polchinski, hep-th/9511157; A. Sen, hep-th/9802051 and references therein; for a Layman's guide, see M. Duff, hep-ph/9805177V3.
25. P. Ginsparg, Phys. Lett. B **197**, 139 (1987); V. S. Kaplunovsky, Nucl. Phys. B **307**, 145 (1988); **382**, 436(E) (1992).
26. E. Witten, hep-th/9602070.
27. J. C. Pati and K. S. Babu, Phys. Lett. B **384**, 140 (1996); hep-ph/9606215.
28. See, e.g., D. Lewellen, Nucl. Phys. B **337**, 61 (1990); A. Font, L. Ibanez, and F. Quevedo, Nucl. Phys. B **345**, 389 (1990); S. Chaudhari, G. Hockney, and J. Lykken, Nucl. Phys. B **456**, 89 (1995); hep-th/9510241; G. Aldazabal, A. Font, L. Ibáñez, and A. Uranga, Nucl. Phys. B **452**, 3 (1995); **465**, 34 (1996); D. Finnell, Phys. Rev. D **53**, 5781 (1996); A. A. Maslikov, I. I. Naumov, and G. G. Volkov, Int. J. Mod. Phys. A **11**, 1117 (1996); J. Erler, hep-th/9602032; G. Cleaver, hep-th/9604183; Z. Kakushadze and S. H. Tye, hep-th/9605221; hep-th/9609027; Z. Kakushadze *et al.*, hep-ph/9705202.
29. A. Faraggi, Phys. Lett. B **278**, 131 (1992); **274**, 47 (1992); Nucl. Phys. B **403**, 101 (1993); A. Faraggi and E. Halyo, Nucl. Phys. B **416**, 63 (1994).
30. See, e.g., [16].
31. J. C. Pati, Phys. Lett. B **388**, 532 (1996); hep-ph/967446.
32. A. Faraggi and J. C. Pati, hep-ph/9712516V3; Nucl. Phys. B (in press).
33. A. Faraggi and J. C. Pati, Phys. Lett. B **400**, 314 (1997).
34. K. S. Babu and J. C. Pati, *Towards A Resolution of the Supersymmetric CP Problem Through Flavor and Left-Right Symmetries* (in press).
35. See, e.g., K. R. Dienes and J. March-Russell, hep-th/9604112; K. R. Dines, hep-ph/9606467.
36. M. Gell-Mann, P. Ramond, and R. Slansky, in *Supergravity*, Ed. by F. van Nieuwenhuizen and D. Freedman (North-Holland, Amsterdam, 1979), p. 315; T. Yanagida, in *Proceedings of Workshop on the Unified Theory and Baryon Number in the Universe*, Ed. by O. Sawada and A. Sugamoto (KEK, Tsukuba, 1979), p. 95; R. N. Mohapatra and G. Senjanovic, Phys. Rev. Lett. **44**, 912 (1980).
37. H. Georgi and C. Jarlskog, Phys. Lett. B **86**, 297 (1979).
38. S. Weinberg, at I. I. Rabi Festschrift (1977); F. Wilczek and A. Zee, Phys. Lett. B **70**, 418 (1977); H. Fritzsch, Phys. Lett. B **70**, 436 (1977).
39. For a related but different *SO*(10) model see C. Albright, K. S. Babu, and S. M. Barr, Phys. Rev. Lett. **81**, 1167 (1998).
40. J. Gasser and H. Leutwyler, Phys. Rep. **87**, 77 (1982).
41. See, e.g., R. Gupta and T. Bhattacharya, Nucl. Phys. B (Proc. Suppl.) **53**, 292 (1997); **63**, 45 (1998).
42. See e.g., V. Barger, M. Berger, and P. Ohmann, Phys. Rev. D **47**, 1093 (1993); M. Carena, S. Pokorski, and C. Wagner, Nucl. Phys. B **406**, 59 (1993); P. Langacker and N. Polonsky, Phys. Rev. D **49**, 1454 (1994); D. M. Pierce, J. A. Bagger, K. Matchev, and R. Zhang, Nucl. Phys. B **491**, 3 (1997); K. S. Babu and C. Kolda, hep-ph/9811308.

43. S. Dimopoulos, S. Raby, and F. Wilczek, Phys. Lett. B **112**, 133 (1982); J. Ellis, D. V. Nanopoulos, and S. Rudaz, Nucl. Phys. B **202**, 43 (1982).
44. P. Nath, A. N. Chemseddine, and R. Arnowitt, Phys. Rev. D **32**, 2348 (1985); P. Nath and R. Arnowitt, hep-ph/9708469.
45. J. Hisano, H. Murayama, and T. Yanagida, Nucl. Phys. B **402**, 46 (1993).
46. K. S. Babu and S. M. Barr, Phys. Rev. D **50**, 3529 (1994); **51**, 2463 (1995).
47. For a recent work, comparing the results of lattice and chiral Lagrangian calculations for the $p \longrightarrow \pi^0$, $p \longrightarrow \pi^+$ and $p \longrightarrow K^0$ modes, see JLQCD Collab. (N. Tatsui *et al.*), hep-lat/9809151.
48. Super-Kamiokande Collab. (Y. Hayato), Talk Given at the International Conference High Energy Physics, Vancouver, 1998.
49. See, e.g., [45].
50. S. Dimopoulos and F. Wilczek, in *Proceedings of the 19th Course of the International School on Subnuclear Physics, Erice, Italy*, Ed. by A. Zichichi (Plenum Press, New York, 1981); K. S. Babu and S. M. Barr, Phys. Rev. D **48**, 5354 (1993).

Physics of Atomic Nuclei, Vol. 63, No. 6, 2000, pp. 1078–1082. From Yadernaya Fizika, Vol. 63, No. 6, 2000, pp. 1153–1157.
Original English Text Copyright © 2000 by Haug, Vergados, Faessler, Kovalenko.

PHYSICS BEYOND THE STANDARD MODEL

Neutrino Masses Originating from SUSY *R*-Parity-Violating Terms with *U*(1) Flavor Symmetry*

O. Haug, J. D. Vergados, A. Faessler, and S. G. Kovalenko*****
Institut für Theoretische Physik, Universität Tübingen, Germany

Abstract—We discuss results on neutrino mixing in a three family scenario. We use the $\not R_p$ MSSM for the theoretical description of the neutrino masses. We show that one has to include the tree-level and the $q\tilde{q}$ one-loop as well as the $l\tilde{l}$ one-loop contribution to the neutrino mass matrix to get three massive neutrinos. By introducing an additional $U(1)$ flavor symmetry which has been successful in explaining the mass hierarchy of quarks and leptons, we are able to correlate many parameters of our model. Confronting the experimental and theoretical results for the neutrino mass matrices, we find a unique scenario for the neutrino masses and the couplings relevant for the neutrino mixing. *© 2000 MAIK “Nauka/Interperiodica”.*

1. INTRODUCTION

Neutrino oscillations are a key signature for the existence of physics beyond the Standard Model (SM). The recent SuperKamiokande result strongly supports the existence of neutrino oscillations [1] by the observation of the zenith-angle dependence of the high energy atmospheric ν_μ events. Other hints for the existence of neutrino oscillations are observations of solar neutrinos [2, 3] and accelerator neutrino experiments [4–7]. There exists a controversy whether a three neutrino family scenario will be able to describe all the existing neutrino data or an additional fourth light sterile neutrino must exist in nature. Recently some analyses of all neutrino data [8–10] have been published that claim to get a reasonable fit in a three family scenario. On the other hand, the LSND result [6, 7], which seems not to fit in a three family scenario, still waits for confirmation. Therefore we will restrict ourselves in the following to the three family model.

To understand now the physics that describe three massive neutrinos, one has to extend the successful SM. A natural way for this are supersymmetric (SUSY) models. A popular version of SUSY models is the minimal supersymmetric standard model (MSSM) without *R*-parity conservation ($\not R_p$). It is the minimal extension of the SM introducing as few particles as possible, without isosinglet Majorana neutrinos [11]. In this model one has three neutrinos which acquire a mass already at tree level [12] and by one -loop corrections. We will use the constraints imposed by the three generation neutrino oscillation phenomenology. We will see that these data cannot uniquely determine the Majorana neutrino mass matrix. The problem will be tackled by imposing on the *R*-parity-violating superpotential a $U(1)$ flavor symmetry analogous to that imposed on the fermion Higgs Yukawa couplings. This symmetry has been very successful in describing the mass matrix of the charged fermions [13, 14].

We will first describe the entries of the mass matrix in terms of the oscillation data. Then, we will discuss the different contributions to the neutrino mass matrix in the $\not R_p$-MSSM. After this, we discuss how we apply a $U(1)$ flavor symmetry on some of our coupling constants and finally confront theory with experiment.

2. CONSEQUENCES OF NEUTRINO OSCILLATIONS

As we discussed in the previous section, neutrino oscillations seem to be realized in nature. A first consequence of this is that the weak eigenstates $|\nu_\alpha\rangle$, $\alpha = e, \mu, \tau$, do not coincide with the mass eigenstates $|\nu_i\rangle$, $i = 1, 2, 3$. They are connected by the unitary matrix U, which can be parameterized by three angles, θ_{12}, θ_{13}, and θ_{23} and *CP* phases, by $|\nu_\alpha\rangle = \sum_{i=1}^{3} U_{\alpha i}|\nu_i\rangle$. In the case where *CP* -violation phases are small, it can be written as

$$U = \begin{pmatrix} c_{12}c_{13} & s_{12}c_{13} & s_{13} \\ -s_{12}c_{23} - c_{12}s_{23}s_{13} & c_{12}c_{23} - s_{12}s_{23}s_{13} & s_{23}c_{13} \\ s_{12}s_{23} - c_{12}c_{23}s_{13} & -c_{12}s_{23} - s_{12}c_{23}s_{13} & c_{23}c_{13} \end{pmatrix}, \quad (1)$$

where s_{ij} and c_{ij} stand for $\sin(\theta_{ij})$ and $\cos(\theta_{ij})$ respectively. The second consequence of the existence of neutrino oscillations is that neutrinos have different, nonvanishing masses. If these two conditions are fulfilled,

---

* This article was submitted by the authors in English.

** Theoretical Physics Division, Ioannina University, Ioannina, Greece.

*** Joint Institute for Nuclear Research, Dubna, Russia.

1063-7788/00/6306-1078$20.00 © 2000 MAIK “Nauka/Interperiodica”

a neutrino which is produced in the weak eigenstate $|\nu_\alpha\rangle$ will change its flavor content when propagating in space. The probability to find the neutrino that was produced in the flavor state α at a given distance L from the production point with the energy E in the flavor state β is then given as

$$P(\alpha \longrightarrow \beta) = \delta_{\alpha,\beta} - 4\sum_{i<j=1}^{3} U_{\alpha i}U_{\beta i}U_{\alpha j}U_{\beta j}\sin^2\left[\frac{\Delta m_{ij}^2 L}{4E}\right]. \tag{2}$$

Here, $\Delta m_{ij}^2 \equiv |m_i^2 - m_j^2|$ is the difference of the squared masses of the mass eigenstates i and j, and $U_{\alpha i}$ are the elements αi of the mixing matrix U. The phenomenological mass matrix $\mathcal{M}_{\mathcal{P}}$ in flavor space is then connected with the mixing matrix by

$$\mathcal{M}_{\mathcal{P}} = U\mathrm{diag}(m_1, m_2, m_3)U^T. \tag{3}$$

From oscillation experiments by using (2), one can extract the mixing angles θ_{ij} and the differences of the squared masses Δm_{ij}^2. $\mathcal{M}_{\mathcal{P}}$ can therefore never be determined totally by using oscillation experiments. The mass scale still is undetermined. So are the *CP* eigenvalues of the neutrino mass eigenstates (+1 or –1 in our model). With data from other experiments, one can extract upper limits for the masses. The neutrino masses, however, seem to be small, and the sensitivity of experiments measuring the neutrino masses directly is not as good as the one of oscillation experiments. The upper limits for the masses derived form direct experiments like the ^{3}H beta decay or the neutrinoless double-beta decay are presently quite weak.

3. NEUTRINO MASSES IN THE $R\!\!\!/_p$-MSSM

To describe massive neutrinos, we have to extend the SM. One natural way to do this are SUSY models. In the following, we will use the MSSM with explicitly broken *R*-parity to describe massive neutrinos. The MSSM is the minimal supersymmetric extension of the SM. By inclusion of additional terms in the superpotential which break the multiplicative Z_2 symmetry $R_P = (-1)^{3B+L+2S}$, where B, L, and S are the baryon and the lepton numbers and the spin of the particle, one can have the following additional terms in the superpotential:

$$W_{R\!\!\!/_p} = \lambda_{ijk}L_iL_jE_k^c + \lambda'_{ijk}L_iQ_jD_k^c + \mu_jL_jH_2 + \lambda''_{ijk}U_i^cD_j^cD_k^c. \tag{4}$$

Other additional contributions that break *R*-parity arise from the terms of the softly SUSY-breaking scalar potential

$$V_R^{\mathrm{soft}} = \Lambda_{ijk}\tilde{L}_i\tilde{L}_j\tilde{E}_k^c + \Lambda'_{ilk}\tilde{L}_i\tilde{Q}_j\tilde{D}_k^c + \Lambda''_{ijk}\tilde{U}_i^c\tilde{D}_j^c\tilde{D}_k^c + \tilde{\mu}_{2j}^2\tilde{L}_jH_2 + \tilde{\mu}_{1j}^2\tilde{L}_jH_1^\dagger + \mathrm{h.c.}, \tag{5}$$

where summation over the generations is implied. Here, L and Q stand for the lepton and quark doublet left-handed superfields, while E^c, U^c, and D^c stand for the lepton and up- and down-quark singlet superfields; H_1 and H_2 are the Higgs doublet superfield with hypercharge $Y = -1, +1$, respectively. The terms in (4) and (5) break lepton and baryon number conservation. To prevent fast proton decay, one assumes $\lambda'' = \Lambda'' = 0$. In the framework of this model, one has three different contributions to neutrino masses at lowest order.

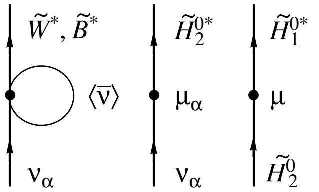

Fig. 1. Mixing of neutralinos and neutrinos.

1. Tree-level contribution. The bilinear terms in (4) and (5) lead to linear sneutrino field terms in the scalar potential and thereby to a nonvanishing vacuum expectation value for this fields. This leads to a mass term for the neutrinos by mixing with the SUSY fields $\tilde{B}^0$ and $\tilde{W}^3$. The term $\mu_iL_iH_2$ in (4) gives an additional mass term from the mixing of neutrinos with the neutral Higgsino fields $\tilde{H}_1^0$, $\tilde{H}_2^0$. The diagrams that describe these terms are shown in Fig. 1. The generated nontrivial 7 × 7 mass matrix in the basis (ν_e, ν_μ, ν_τ, $-i\lambda$, $-i\lambda_3$, $\tilde{H}_1^0$, $\tilde{H}_2^0$) can be brought into a block diagonal form [15], and an effective neutrino mass matrix at tree level can be extracted. It has at lowest order the form

$$M_{\alpha\beta}^{\mathrm{tree}} = \mathcal{X}_1\Lambda_\alpha\Lambda_\beta,$$

$$\Lambda_\alpha = \mu\langle\bar{\nu}_\alpha\rangle - \langle H_1\rangle\mu_\alpha, \tag{6}$$

$$\mathcal{X}_1 = g_2^2\left|\frac{M_1 + \tan^2\theta_W M_2}{4(\sin(2\beta)M_W^2\mu(M_1 + \tan^2\theta_W M_2) - M_1M_2\mu^2)}\right|.$$

2. $q\tilde{q}$-loop contributions. Another contribution to the neutrino masses arises due to quark–squark loops, coming from the term $\lambda'_{ijk}L_iQ_jD_k^c$ in the *R*-parity-violating superpotential given in (4). The relevant diagram is shown in Fig. 2, and its contribution to the neutrino

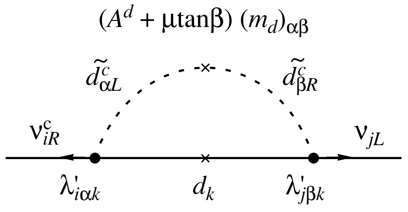

Fig. 2. Quark–squark one-loop contribution to neutrino masses.

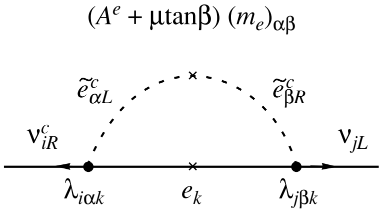

Fig. 3. Lepton–slepton one-loop contribution to neutrino masses.

mass matrix in a perturbative calculation is given as

$$M_{ij}^{q\tilde q} \simeq \sum_{k,\,l,\,m} \frac{3\lambda'_{ikl}\lambda'_{jkm}}{8\pi^2}\frac{m_k^d m_{ml}^d (A_{ml}^d + \mu\tan\beta)}{\tilde m_q^2}$$

$$\sim \frac{3\lambda'_{i33}\lambda'_{j33}}{8\pi^2}\frac{m_b^2(A_b^d + \mu\tan\beta)}{\tilde m_b^2} = \mathcal{L}_2\lambda'_{i33}\lambda'_{j33}. \qquad (7)$$

Here, m_{lm}^d is the charged-lepton mass matrix, and m_k^d are the current masses of the *d*, *s*, and *b* quarks. The angle β is defined as usually by $\tan\beta = \langle H_2^0\rangle/\langle H_1^0\rangle$. The factor 3 arises due to the color of the quarks. The last step is valid if there is no hierarchy in the sense that the trilinear couplings grow strongly for smaller indices and due to the fact that the *b* quark is heavier than the *d* and *s* quark. It is also a common practice to assume that the trilinear couplings are real.

3. $l\tilde l$-loop contributions. The lepton–slepton loop has the same structure as the $q\tilde q$ loop (Fig. 3). Its contribution to the neutrino mass matrix is given as

$$M_{ij}^{l\tilde l} \simeq \sum_{k,\,l,\,m} \frac{\lambda_{ikl}\lambda_{jkm}}{8\pi^2}\frac{m_k^e m_{ml}^e (A_{ml}^e + \mu\tan\beta)}{\tilde m_e^2}$$

$$\sim \frac{\lambda_{i33}\lambda_{j33}}{8\pi^2}\frac{m_\tau^2(A_\tau^e + \mu\tan\beta)}{\tilde m_\tau^2} = \mathcal{L}_3\lambda_{i33}\lambda_{j33}. \qquad (8)$$

In the last step, we used the same assumptions as for the $q\tilde q$ loop.

The theoretical neutrino mass matrix $\mathcal{M}_T$ in the $R\!\!\!/_p$ MSSM in our framework is

$$\mathcal{M}_T = M^{\mathrm{tree}} + M^{q\tilde q} + M^{l\tilde l}. \qquad (9)$$

With the form of (6)–(8), one has to include all three of them to get all three neutrino masses nonzero.[1] If we use now the existing upper bounds for the coupling constants (see, e.g., [16]) of our model, we can reproduce all phenomenological allowed scenarios. In this sense, the model has no predictive power and needs additional constraints from other sources to reduce the "free" number of parameters in our model. This we try to do in the following section by the introduction of an additional symmetry.

4. MASS HIERARCHIES AND TRILINEAR *R*-PARITY-VIOLATING COUPLINGS

Our model will be supplemented by imposing on the *R*-parity-violating superpotential a $U(1)$ flavor symmetry which is known to predict the hierarchical structure of the charged fermion sector and to yield results in agreement with phenomenology [13, 14]. After all, the superpotential (4) is similar to the corresponding Yukawa fermion–Higgs interactions. Following [17, 18], we can write

$$\lambda_{ijk} \sim \epsilon^{\tilde l_i - \tilde l_0}\lambda_{jk}^E, \qquad (10)$$

$$\lambda'_{ijk} \sim \epsilon^{\tilde l_i - \tilde l_0}\lambda_{jk}^D. \qquad (11)$$

The parameter ϵ is the same as that appearing in the charged-lepton and quark mass matrices and takes the value $\epsilon = 0.23$. The lepton charges $\tilde l_i$ are similarly obtained. There remains an ambiguity of the flavor independent quantity $\tilde l_0$ which will not affect our result (it can be absorbed when we take ratios). Equation (10) must be properly antisymmetrized with respect to the indices *i* and *j*. We write

$$\lambda_{ijk} \sim \frac{1}{2}(\epsilon^{\tilde l_i - \tilde l_0}\lambda_{jk}^E - \epsilon^{\tilde l_j - \tilde l_0}\lambda_{ik}^E). \qquad (12)$$

The ratio of the λ_{ijk} and λ'_{ijk} is then given as

$$\frac{\lambda_{ijk}}{\lambda'_{ijk}} = \frac{1}{2}\left(\frac{\lambda_{jk}^E}{\lambda_{jk}^D} - \epsilon^{\tilde l_j - \tilde l_i}\frac{\lambda_{ik}^E}{\lambda_{jk}^D}\right). \qquad (13)$$

Approximating now the ratio $\lambda_{ik}^E/\lambda_{jk}^D \sim -2$ (see [18])

---

[1] $M_{ij} = \sum_{k=1,2} a_i^k a_j^k$ has an eigenvector $\mathbf{x} = \sum_{ijk}^3 \varepsilon_{ijk} a_i^1 a_j^2 \hat{\mathbf{e}}_k$ with eigenvalue zero.

and assigning the $U(1)$ charges found by [13], we get

$$\boldsymbol{\lambda}' = \lambda'_{333}\begin{pmatrix} \epsilon^4 \\ \epsilon \\ 1 \end{pmatrix}, \tag{14}$$

$$\boldsymbol{\lambda} = \lambda_0\begin{pmatrix} (\epsilon^4-1)\epsilon^4 \\ (\epsilon-1)\epsilon \\ 0 \end{pmatrix}, \quad \lambda_0 \simeq \lambda'_{333}. \tag{15}$$

Since the parameter ϵ is determined, we have only one unspecified parameter λ'_{333}. We may of course relax the assumption $\lambda_0 \simeq \lambda'_{333}$. By using the $U(1)$ symmetry, which seems to be a good tool to describe the quark and lepton mass matrices, we have now been able to reduce the free parameters in the neutrino mass matrix in our framework. There is only the trilinear coupling λ'_{333} and the three Λ_α left. All other quantities are in principle calculable, e.g. using RGE [19, 20], and are treated here as known values.

5. THEORY CONFRONTS EXPERIMENT

In this section, we discussed the phenomenological scenario which one finds if neutrinos exist only in three different flavors. This is supported by recent analyses of all existing neutrino data [8–10]. By using only the experimental data, one was able to fix the entries of the neutrino mass matrix up to the mass scale and the ambiguities associated with the sign combination resulting when one has to solve nonlinear equations. On the other side, we discussed the neutrino masses that can arise in the $\not{R}_p$-MSSM, and by using an additional $U(1)$ symmetry, we were able to reduce the free parameters for the neutrino masses to four effective parameters. When we confront now the phenomenological neutrino mass matrix with the theoretical mass matrix

$$\mathcal{M}^P \overset{!}{=} \mathcal{M}^T, \tag{16}$$

we get a system of six linear independent equations. By simultaneously solving this system of equations, one can uniquely determine the mass scale on the phenomenological side and in addition the absolute values of the theoretical couplings. The results for the neutrino masses are shown for different phenomenological analysis in Table 1. The values for the couplings are given in Table 2. For all examined oscillation analysis, we find a hierarchical mass scenario. For the couplings, we find agreement with expectations for the tree-level contributions, and the values for trilinear couplings are also not in conflict with any existing constraint. The coupling constants not displayed are given by using (14) and (15).

The averaged neutrino Majorana mass, which plays an important role in the search for the $0\nu\beta\beta$ decay, is in our model $|\langle m_\nu\rangle| = \left|\sum_i \zeta_i U_{ei}^2 m_i\right| \sim 0.01$–$0.05$ eV, taking the results from Table 1. Here, we also show the averaged neutrino Majorana masses for the different analyses which we used as input. The value we found is more than one order of magnitude below the existing limit of $|\langle m_\nu\rangle| < 0.62$ eV recently extracted from $0\nu\beta\beta$ decay experiments by [22].

Table 1. Neutrino masses obtained from conditions (16) utilizing as input the cited phenomenological analyses. $\lambda_{CP}(i)$, $i = 1, 2$, are the *CP* phases of the masses. All masses are given in eV

m_1, eV	m_2, eV	m_3, eV	$\lambda_{CP}(1)$	$\lambda_{CP}(2)$	$\lvert\langle m_\nu\rangle\rvert$	
0.004	0.032	0.549	+	+	0.041	[8]
0.018	0.036	0.549	–	+	0.045	[8]
0.002	0.002	0.030	+	+	0.010	[21]
0.000	0.0224	0.633	–	+	0.028	[9]
0.019	0.026	1.054	–	+	0.009	[10]

Note: This scenario arises if the term $(A + \mu\tan\beta)$ is positive, which is in agreement with most RGE analyses. Also given is the averaged Majorana neutrino mass, which is defined as $|\langle m_\nu\rangle| = |\Sigma_i \lambda_{CP}(i)\, U_{ei}^2\, m_i|$ and which can in principle be measured in the neutrinoless double-beta decay.

Table 2. The same as Table 1 for the coupling constants of our model for the tree-level and one-loop contribution

$\lvert\Lambda_1\rvert$, GeV^2	$\lvert\Lambda_2\rvert$, GeV^2	$\lvert\Lambda_3\rvert$, GeV^2	$\lvert\lambda'_{333}/10^{-4}\rvert$	
0.008	0.012	0.019	2.1	[8]
0.008	0.014	0.016	2.4	[8]
0.004	0.004	0.002	0.7	[21]
0.006	0.013	0.021	2.1	[9]
0.004	0.022	0.022	3.0	[10]

Note: For this calculation of the coupling constants, we assumed all SUSY masses and soft breaking parameters to be ~100 GeV, $\tan\beta$ was taken to be 1. Here, the effective tree-level couplings Λ_i are in units GeV^2, and the trilinear coupling constant λ_{333} is dimensionless.

6. SUMMARY

We examined the theoretical description of neutrino masses. We did this in the $\not{R}_p$-MSSM and showed that all three neutrinos acquire Majorana masses in this model. To reduce the number of parameters of our model, an additional $U(1)$ flavor symmetry that was found to be relevant in the description of quark and charged lepton mass matrices [13, 14] was applied as in [17, 18] on the $\not{R}_p$ superpotential. By using the $U(1)$ flavor charges of [13], we were able to correlate the trilinear coupling constants and by doing so reduced the number of free parameters of our model. Confronting now theory with experiment, we found a unique scenario for a given set of oscillation parameters. All the trilinear coupling constants fulfill existing limits. It is interesting to note that the averaged Majorana mass $\langle m_\nu \rangle$ is about ~0.01–0.05 eV. This is a region which is one order of magnitude below the existing upper bound recently found by [22] of $|m_\nu| < 0.62$ eV. But the next generation of $0\nu\beta\beta$ experiments, e.g., the GENIUS experiment [23], claim to be able to explore this small values of averaged Majorana neutrino masses. We therefore can hope to test the validity of the $\not{R}_p$-MSSM with an additional $U(1)$ flavor symmetry in the near future.

ACKNOWLEDGMENTS

O.H. wishes to thank Th. Gutsche for enlightening discussion about physical problems.

J.V. is grateful for an award from the Humboldt Foundation. O.H. was supported by the Graduiertenkolleg under contract DFG GRK 132/2.

REFERENCES

1. Y. Fukuda *et al.*, Phys. Rev. Lett. **81**, 1562 (1998).
2. B. T. Cleveland *et al.*, Astrophys. J. **496**, 505 (1998).
3. J. N. Abdurashitov *et al.*, Phys. Rev. C **59**, 2246 (1999).
4. W. C. Louis, Prog. Part. Nucl. Phys. **40**, 151 (1998).
5. B. Zeitnitz *et al.*, Prog. Part. Nucl. Phys. **40**, 169 (1998).
6. C. Athanassopoulos *et al.*, Evidence for Muon-Neutrino–Electron-Neutrino Oscillations from Pion Decay in Flight Neutrinos, 1997.
7. C. Athanassopoulos *et al.*, Phys. Rev. Lett. **81**, 1774 (1998).
8. G. Berenboim and F. Scheck, Phys. Lett. B **440**, 322 (1998).
9. R. P. Thun and S. McKee, Phys. Lett. B **439**, 123 (1998).
10. T. Ohlsson and H. Snellman, hep-ph/9903252 (1999).
11. H. P. Nilles, Phys. Rep. **110**, 1 (1984).
12. V. Bednyakov, A. Faessler, and S. Kovalenko, Phys. Lett. B **442**, 203 (1998).
13. L. Ibáñez and G. G. Ross, Phys. Lett. B **332**, 100 (1994).
14. S. Lola and J. D. Vergados, Prog. Part. Nucl. Phys. **40**, 71 (1998).
15. M. Nowakowski and A. Pilaftsis, Nucl. Phys. B **461**, 19 (1996).
16. S. Rakshit, G. Bhattacharyya, and A. Raychaudhuri, Phys. Rev. D **59**, 091701 (1999).
17. R. Barbier *et al.*, hep-ph/9810232 (1998).
18. P. Binétruy, E. Dudas, S. Lavignac, and C. A. Savoy, Phys. Lett. B **442**, 171 (1998).
19. G. L. Kane *et al.*, Phys. Rev. D **49**, 6173 (1994).
20. D. J. Castaño *et al.*, Phys. Rev. D **49**, 4882 (1994).
21. G. Fogli, E. Lisi, A. Marrone, and G. Scioscia, Phys. Rev. D **59**, 033001 (1999).
22. F. Simkovic, A. Faessler, G. Pantis, and J. D. Vergados, Additional Nucleon Current Contributions to Neutrinoless Double Beta Decay, Phys. Rev. C (1999) (in press).
23. L. Baudis *et al.*, Phys. Rep. **307**, 301 (1998).

Physics of Atomic Nuclei, Vol. 63, No. 6, 2000, pp. 1083–1087. From Yadernaya Fizika, Vol. 63, No. 6, 2000, pp. 1158–1162.
Original English Text Copyright © 2000 by Kong.

PHYSICS BEYOND THE STANDARD MODEL

Neutrino Oscillations from Supersymmetry without *R*-Parity—Its Implications on the Flavor Structure of the Theory*

O. C. W. Kong
University of Rochester, USA

Abstract—We discuss here some flavor structure aspects of the complete theory of supersymmetry without *R*-parity addressed from the perspective of fitting neutrino oscillation data based on the recent Super-Kamiokande result. The single-VEV parameterization of supersymmetry without *R*-parity is first reviewed, illustrating some important features not generally appreciated. For the flavor structure discussions, a naive, flavor-model-independent, analysis is presented, from which a few interesting things can be learned. © *2000 MAIK "Nauka/Interperiodica".*

1. INTRODUCTION AND OUTLINE

We discuss here a simple and specific issue—some flavor structure aspects of the complete theory of supersymmetry without *R*-parity addressed from the perspective of fitting neutrino oscillation data. We will first review our formulation of supersymmetry without *R*-parity and its application to study of neutrino masses. The formulation has been reported in [1]. It is based on a specific choice of flavor bases that allows the maximal simplification of the tree level fermion mass matrices, as well as a comprehensive treatment of all the *R*-parity-violating (RPV) couplings together without any assumption. We will go on then to discuss a simple scenario of three neutrino masses and mixings inspired by the recent SuperKamiokande (SuperK) result [2], incorporating it into our framework of supersymmetry without *R*-parity. Our concentration here is at its implication on the flavor structure of the theory. We will discuss a naive, flavor-model-independent, analysis from which a few interesting things can be learned. The discussion is mainly based in results presented in [3].

2. OBTAINING THE SUPERSYMMETRIZED STANDARD MODEL

Let us start from the beginning and look carefully at the supersymmetrization of the Standard Model. In the matter field sector, all fermions and scalars have to be promoted to chiral superfields containing both parts. It is straightforward for the quark doublets and singlets, and also for the leptonic singlet. The leptonic doublets, however, has the same quantum number as the Higgs doublet that couples to the down-sector quarks. Nevertheless, one cannot simply get the Higgs, H_d, from the scalar partners of the leptonic doublets, *L*'s. Holomorphicity of the superpotential requires a separate superfield to contribute the Higgs coupling to the up-sector quarks. This $\hat{H}_u$ superfield then contributes a fermionic doublet, the Higgsino, with nontrivial gauge anomaly. To cancel the latter, an extra fermionic doublet with the quantum number of H_d or L is needed. So, the result is that we need four superfields with that quantum number. As they are a priori indistinguishable, we label them by $\hat{L}_\alpha$ with the Greek subscript being an (extended) flavor index going from 0 to 3.

The most general renormalizable superpotential for the supersymmetric Standard Model (without *R*-parity) can be written then as

$$\begin{aligned} W \;=\; \varepsilon_{ab}[\mu_\alpha \hat{L}^a_\alpha \hat{H}^b_u + h^u_{ik} \hat{Q}^a_i \hat{H}^b_u \hat{U}^c_k + \lambda'_{i\alpha k} \hat{Q}^a_i \hat{L}^b_\alpha \hat{D}^c_k \\ + \lambda_{\alpha\beta k} \hat{L}^a_\alpha \hat{L}^b_\beta \hat{E}^c_k] + \lambda''_{ijk} \hat{D}^c_i \hat{D}^c_j \hat{U}^c_k, \end{aligned} \tag{1}$$

where (*a*, *b*) are *SU*(2) indices; (*i*, *j*, *k*) are the usual family (flavor) indices; λ and λ'' are antisymmetric in the first two indices as required by *SU*(2) and *SU*(3) product rules respectively, though only the former is shown explicitly here; $\varepsilon = \begin{pmatrix} 0 & -1 \\ 1 & 0 \end{pmatrix}$, while the *SU*(3) indices are suppressed.

At the limit where λ_{ijk}, λ'_{ijk}, λ''_{ijk}, and μ_i all vanish, one recovers the expression for the *R*-parity-preserving model, with $\hat{L}_0$ identified as $\hat{H}_d$. *R*-parity is exactly an ad hoc symmetry put in to make $\hat{H}_d$ stand out from the other $\hat{L}_i$'s. It is defined in terms of baryon number, lepton number, and spin as, explicitly, $\mathcal{R} = (-1)^{3B + L + 2S}$. The consequence is that the accidental symmetries of baryon number and lepton number in the Standard Model are preserved, at the expense of making particles and superparticles having a categorically different quantum number, *R*-parity. The latter is actually the most restrictive but not the most effective discrete symmetry to control superparticle-mediated proton decay [4].

---

* This article was submitted by the author in English.

1063-7788/00/6306-1083$20.00 © 2000 MAIK "Nauka/Interperiodica"

3. THE SINGLE-VEV PARAMETERIZATION

With the above discussion, it is clear that in the phenomenology of low energy supersymmetry, one approach worth studying is to take the complete version of a supersymmetrized Standard Model without extra assumption and check the phenomenological constraints on the various RPV couplings. The large number of couplings make the task sound formidable. For instance, the (color-singlet) charged fermion mass matrix is then given by

$$\mathcal{M}_c = \begin{pmatrix} M_2 & \frac{g_2 v_u}{\sqrt{2}} & 0 & 0 & 0 \\ \frac{g_2 v_d}{\sqrt{2}} & \mu_0 & -h^e_{i1}\frac{v_i}{\sqrt{2}} & -h^e_{i2}\frac{v_i}{\sqrt{2}} & -h^e_{i3}\frac{v_i}{\sqrt{2}} \\ \frac{g_2 v_1}{\sqrt{2}} & \mu_1 & h^e_{11}\frac{v_0}{\sqrt{2}} + 2\lambda_{1i1}\frac{v_i}{\sqrt{2}} & h^e_{12}\frac{v_0}{\sqrt{2}} + 2\lambda_{1i2}\frac{v_i}{\sqrt{2}} & h^e_{13}\frac{v_0}{\sqrt{2}} + 2\lambda_{1i3}\frac{v_i}{\sqrt{2}} \\ \frac{g_2 v_2}{\sqrt{2}} & \mu_2 & h^e_{21}\frac{v_0}{\sqrt{2}} + 2\lambda_{2i1}\frac{v_i}{\sqrt{2}} & h^e_{22}\frac{v_0}{\sqrt{2}} + 2\lambda_{2i2}\frac{v_i}{\sqrt{2}} & h^e_{23}\frac{v_0}{\sqrt{2}} + 2\lambda_{2i3}\frac{v_i}{\sqrt{2}} \\ \frac{g_2 v_3}{\sqrt{2}} & \mu_3 & h^e_{31}\frac{v_0}{\sqrt{2}} + 2\lambda_{3i1}\frac{v_i}{\sqrt{2}} & h^e_{32}\frac{v_0}{\sqrt{2}} + 2\lambda_{3i2}\frac{v_i}{\sqrt{2}} & h^e_{33}\frac{v_0}{\sqrt{2}} + 2\lambda_{3i3}\frac{v_i}{\sqrt{2}} \end{pmatrix}, \tag{2}$$

from which the only definite experimental data are the three physical lepton masses as the light eigenvalues, and the overall magnitude of the electroweak symmetry breaking VEV. We must emphasize here that the easier analysis of a model with only some small number of RPV couplings admitted is, in general, lack of any theoretical motivation and of very limited experimental relevance. Even the case of having only trilinear RPV couplings in the superpotential is very difficult to motivate. Moreover, most studies of the type in the literature have extra assumptions about the scalar potential or soft supersymmetry-breaking terms which are usually not explicitly addressed. This has led to quite some confusion and misleading statements in the literature on the subject.

It has been pointed out in [1] that the single-VEV parameterization renders the task of studying the complete theory of supersymmetry without R-parity quite manageable. The parameterization is nothing but an optimal choice of flavor bases. In fact, doing phenomenological studies without specifying a choice of flavor bases is ambiguous. Recall that in quark physics of the Standard Model, there are only 10 physical parameters from the 36 real parameters of the two quark mass matrices written in a generic set of flavor bases. To Standard Model physics, the 26 extra parameters are absolutely meaningless. Here for supersymmetry without R-parity, the choice of an optimal parameterization mainly concerns the four $\hat{L}_\alpha$ flavors. In the single-VEV parameterization, flavor bases are chosen such that (i) among $\hat{L}_\alpha$'s, only $\hat{L}_0$, bears a VEV; (ii) $h^e_{ik}\,(\equiv 2\lambda_{i0k} = -2\lambda_{0ik}) = \frac{\sqrt{2}}{v_d}\,\mathrm{diag}\{m_1,\ m_2,\ m_3\}$; (iii) $h^d_{ik}\,(\equiv \lambda'_{i0k}) = \frac{\sqrt{2}}{v_d}\,\mathrm{diag}\{m_d, m_s, m_b\}$; and (iv) $h^u_{ik} = \frac{-\sqrt{2}}{v_u}V^\dagger_{\mathrm{CKM}}\,\mathrm{diag}\{m_u, m_c, m_t\}$. Under the parameterization, the (tree-level) mass matrices for all the fermions do not involve any of the trilinear RPV couplings, though the approach makes no assumption on any RPV coupling including even those from soft supersymmetry breaking; and all the parameters used are uniquely defined. In fact, the above mass matrix is reduced to the simple form

$$\mathcal{M}_c = \begin{pmatrix} M_2 & \frac{g_2 v_u}{\sqrt{2}} & 0 & 0 & 0 \\ \frac{g_2 v_d}{\sqrt{2}} & \mu_0 & 0 & 0 & 0 \\ 0 & \mu_1 & m_1 & 0 & 0 \\ 0 & \mu_2 & 0 & m_2 & 0 \\ 0 & \mu_3 & 0 & 0 & m_3 \end{pmatrix}. \tag{3}$$

Each μ_i parameter here characterizes directly the RPV effect on the corresponding charged lepton ($l_i = e$, μ, and τ). For any set of other parameter inputs, the m_i's can then be determined, through a numerical procedure, to guarantee that the correct mass eigenvalues of m_e, m_μ, and m_τ are obtained—an issue first addressed and solved in [1].

4. NEUTRINO MASSES FROM THE FRAMEWORK

Under the single-VEV parameterization, the tree-level neutral-fermion (neutralino–neutrino) mass matrix has also RPV contributions from the three μ_i 's only. For the discussion below, we write the mass matrix here as

$$\mathcal{M}_N = \begin{pmatrix} M_1 & 0 & \frac{g_1 v_u}{2} & -\frac{g_1 v_d}{2} & 0 & 0 & 0 \\ 0 & M_2 & -\frac{g_2 v_u}{2} & \frac{g_2 v_d}{2} & 0 & 0 & 0 \\ \frac{g_1 v_u}{2} & -\frac{g_2 v_u}{2} & 0 & -\mu_0 & -\mu_1 & -\mu_2 & -\mu_3 \\ -\frac{g_1 v_d}{2} & \frac{g_2 v_d}{2} & -\mu_0 & W & 0 & Y & Z \\ 0 & 0 & -\mu_1 & 0 & 0 & 0 & 0 \\ 0 & 0 & -\mu_2 & Y & 0 & A & C \\ 0 & 0 & -\mu_3 & Z & 0 & C & B \end{pmatrix}, \quad (4)$$

with parameters A, B, and C, and W, Y, and Z being two groups of relevant one-loop contributions to be addressed. Setting all these to zero retrieves the tree-level result where an admixture of the three neutral fermionic states from the $\hat{L}_i$'s gets a nonzero mass from mixing with the gauginos and higgsinos. Note that, in the limit of small μ_i 's, the neutral states correspond to ν_e, ν_μ, and ν_τ.

An important question is whether the μ_i 's are large or small. A careful analysis of an exhaustive list of constraints from tree-level leptonic phenomenology illustrates that while μ_1 has to be small, μ_2 and, especially, μ_3 do not have to [5]. In fact, MeV scale neutrino mass is easily admitted, with interesting implications on lepton-number-violating processes. Fitting neutrino oscillation data will then call for extensions of the model. We are interested here in the complementary scenario of sub-eV neutrino mass(es). In that case, the one-loop contributions could also be significant. Explicitly, we assume a three neutrino scenario motivated by the recent zenith angle dependence measurement by the Super-K experiment [2]. There have been a lot of studies on the topic, details on which we are not going into here [6]. The scenario is summarized by

$$\Delta m^2_{\text{atm}} \simeq (0.5\text{–}6) \times 10^{-3} \text{ eV}^2,$$

$$\sin^2 2\theta_{\text{atm}} \simeq 0.825\text{–}1,$$

$$\Delta m^2_{\text{sol}} \simeq (4\text{–}10) \times 10^{-6} \text{ eV}^2,$$

$$\sin^2 2\theta_{\text{sol}} \simeq (0.12\text{–}1.2) \times 10^{-2}$$

with ν_μ–ν_τ to be responsible for the SuperK atmospheric result and MSW oscillations of ν_e for the solar neutrino problem. The most natural setting then would be for the two neutrino mass eigenvalues of the ν_μ–ν_τ system to have $m^2 \simeq \Delta m^2_{\text{sol}}$ and Δm^2_{atm}. We will concentrate on this particular scenario below. Our concern will be focused on the compatibility of the required maximal mixing between ν_μ and ν_τ, with the general hierarchical flavor structure of the quarks and charged leptons.

Consider $\mathcal{M}_N$ of (4) in the 3 + 4 block form $\begin{pmatrix} \mathcal{M} & \xi^T \\ \xi & m_\nu^0 \end{pmatrix}$. For small μ_i 's, it has a "seesaw"-type structure, with the effective neutrino mass matrix given by

$$m_\nu = -\xi \mathcal{M}^{-1} \xi^T + m_\nu^0. \quad (5)$$

In the case that the μ_i contributions dominate, the first term of the equation gives

$$m_\nu = -\frac{1}{2} \frac{v^2 \cos^2\beta (x g_2^2 + g_1^2)}{\mu_0 [2 x M_2 \mu_0 - (x g_2^2 + g_1^2) v^2 \sin\beta \cos\beta]} \times \begin{pmatrix} \mu_2^2 & \mu_2 \mu_3 \\ \mu_2 \mu_3 & \mu_3^2 \end{pmatrix}, \quad (6)$$

where we have neglected contribution involving the ν_e state and hence shrinked the matrix to 2 × 2. Dropping the prefactor, the matrix is diagonalized by a rotation of $\tan\theta = \mu_2/\mu_3$, giving eigenvalues 0 and $\mu_2^2 + \mu_3^2$. For this to fit in our neutrino-oscillation scenario, it requires $\sqrt{\mu_2^2 + \mu_3^2} \cos\beta \sim 10^{-4}$ GeV and $\mu_2/\mu_3 \gtrsim 0.6358$. It is interesting to note that the structure of matrix in the form $\begin{pmatrix} a^2 & ab \\ ab & b^2 \end{pmatrix}$ naturally admits maximal mixing with a hierarchy in mass eigenvalues.

There are two types of one-loop contributions to (4) or m_ν^0 of (5)—the quark–squark and lepton–lepton loops. The former is given by

$$(m^{LL})^q_{\alpha\beta} = \frac{3}{16\pi^2} \lambda'_{i\alpha j} \lambda'_{j\beta i} \left(\frac{A^d_j m^d_i}{\tilde{m}^2_{q_j}} + \frac{A^d_i m^d_j}{\tilde{m}^2_{q_i}} \right), \quad (7)$$

where m^{LL} corresponds to the lower 4 × 4 block of (4), and the soft supersymmetry breaking trilinear terms A^d

are assumed to be dominately diagonal, as generally expected. We get the dominating contribution to m_ν^0 as

$$(m_\nu^0)^q \simeq \frac{3}{8\pi^2}\frac{m_b^2}{M_{\mathrm{SUSY}}}\begin{pmatrix} \lambda'^2_{323} & \lambda'_{323}\lambda'_{333} \\ \lambda'_{323}\lambda'_{333} & \lambda'^2_{333} \end{pmatrix}. \quad (8)$$

If this contribution dominates, we have a mass matrix with the same general structure as the μ_i dominating case above, hence again natural maximal mixing with a hierarchy in mass eigenvalues. It requires $\lambda' \sim 10^{-4}$ and $\lambda'_{323}/\lambda'_{333} \gtrsim 0.6358$. However, it is important to note that the natural structure would be spoiled if the μ_i contribution and the present one are at about the same level. Finally, we note also that the 4 × 4 form of (7) allows one to check that the contributions to the W, Y, and Z entries of (4) are really negligible.

The lepton–slepton loop contributions have a different structure. We have, similar to the previous case,

$$(m^{LL})^l_{\alpha\beta} = \frac{1}{16\pi^2}\lambda_{i\alpha j}\lambda_{j\beta i}\left(\frac{A^l_j m^l_i}{\tilde{m}^2_{l_j}} + \frac{A^l_i m^l_j}{\tilde{m}^2_{l_i}}\right). \quad (9)$$

In this case, however, the antisymmetry in $\lambda\hat{L}\hat{L}\hat{E}^c$ couplings between the two $\hat{L}$'s gives the dominating contribution as

$$(m_\nu^0)^l \simeq \frac{1}{8\pi^2 M_{\mathrm{SUSY}}} \times \begin{pmatrix} m_\tau^2\lambda^2_{323} & -m_\mu m_\tau\lambda_{322}\lambda_{323} \\ -m_\mu m_\tau\lambda_{322}\lambda_{323} & m_\mu^2\lambda^2_{322} \end{pmatrix}, \quad (10)$$

which is in general incompatible with large mixing. To fit in the neutrino oscillation scenario, we would hence like the lepton–slepton loops to play a secondary role, which requires λ's of order 10^{-4} or less.

5. FLAVOR STRUCTURE AMONG THE $\hat{L}_\alpha$'s

After the above discussion of the various sources of neutrino masses, let us look at the flavor structure more carefully. We will adopt a flavor-model-independent approach along the idea of the approximate flavor symmetry [7]. The idea is to attach a suppression factor to each choral multiplet. For example, the down-quark mass matrix would look like

$$\mathcal{M}_d = \begin{pmatrix} \varepsilon_{Q_1}\varepsilon_{D_1^c} & \varepsilon_{Q_1}\varepsilon_{D_2^c} & \varepsilon_{Q_1}\varepsilon_{D_3^c} \\ \varepsilon_{Q_2}\varepsilon_{D_1^c} & \varepsilon_{Q_2}\varepsilon_{D_2^c} & \varepsilon_{Q_2}\varepsilon_{D_3^c} \\ \varepsilon_{Q_3}\varepsilon_{D_1^c} & \varepsilon_{Q_3}\varepsilon_{D_2^c} & \varepsilon_{Q_3}\varepsilon_{D_3^c} \end{pmatrix}$$

with the flavor hierarchy $\varepsilon_{Q_1} \ll \varepsilon_{Q_2} \ll \varepsilon_{Q_3}$ and $\varepsilon_{D_1^c} \ll \varepsilon_{D_2^c} \ll \varepsilon_{D_3^c}$. Diagonalization gives $m_d : m_s : m_b = \varepsilon_{Q_1}\varepsilon_{D_1^c} : \varepsilon_{Q_2}\varepsilon_{D_2^c} : \varepsilon_{Q_3}\varepsilon_{D_3^c}$ with mixings given by factors of the form $\varepsilon_{Q_i}/\varepsilon_{Q_j}$. We adopt the approach here for two major reasons. First of all, while an explicit flavor model may be designed to contain very specific features needed to reconcile with experimental number, the approach emphasizes on generic flavor structure features which would fit in easily any natural flavor model. If the approach can easily accommodate the required “smallness” of various RPV couplings, it builds a strong case for the latter couplings to be considered on the same footing as the R-parity-conserving ones. Second, it is clear, from the above discussions, that we are dealing with a large number of parameters but a small amount of data. In such a situation, detailed model construction is very unlikely to be fruitful. We would rather take a humble approach and discuss issues that will not be easily washed away when more data becomes available.

In the small μ_i case considered, the $\hat{L}_i$ basis under the single-VEV parameterization gives excellent alignment with the charged lepton mass eigenstate basis. However, going into the approximate flavor symmetry perspective, we have to start with generic, nondiagonal, flavor bases. The misalignment between the two is a major problem hindering a complete discussion of the flavor structure here. This is tied up with the question of the natural values of our μ_i's. Careful analysis of the scalar potential and vacuum solution is needed to settle the issue. We will leave that to future studies while trying to learn something from a naive analysis.

It is easy to see that our neutrino oscillation scenario, together with the known charged lepton masses, suggests

$$\varepsilon_{L_1} \ll \varepsilon_{L_2} \sim \varepsilon_{L_3} \ll \varepsilon_{L_0}$$

and

$$\varepsilon_{E_1^c} \ll \varepsilon_{E_2^c} \ll \varepsilon_{E_3^c}.$$

With $\varepsilon_{L_2} \sim \varepsilon_{L_3}$, however, the factors that go with L_2 and L_3 (after a diagonalizing rotation is taken into consideration) would be $\sin 2\theta_{23}\sqrt{\varepsilon^2_{L_2} + \varepsilon^2_{L_3}}$ and $\cos 2\theta_{23}\sqrt{\varepsilon^2_{L_2} + \varepsilon^2_{L_3}}$. These are, of course, still of the same order of magnitude as ε_{L_2} and ε_{L_3}. If we take $\varepsilon_{E_3^c} \sim 1$, as we do with other third family factors such as ε_{Q_3}, we would use

$$\cos 2\theta_{23}\sqrt{\varepsilon^2_{L_2} + \varepsilon^2_{L_3}} \sim \frac{m_\tau}{m_t}$$

to fix the τ mass. That is the maximal suppression in the L_3 flavor factor we can have. If we further take

$$\varepsilon_{D_3^c} \sim \frac{m_b}{m_t},$$

we would have naturally, at $M_{\rm SUSY} = 100$ GeV [cf. (8) and (10)], $\lambda'_{333} \sim \lambda'_{323} \sim 5 \times 10^{-4}$, $\lambda_{323} \sim 10^{-4}$, and $\lambda_{322} \sim 10^{-5}$. Hence, amazing enough, a bit larger value of $M_{\rm SUSY}$ (squark and slepton masses) would give the quark–squark-loop-dominating scenario naturally.

To fit our neutrino oscillation scenario with μ_i's being the dominating neutrino mass contribution will require a higher $M_{\rm SUSY}$ and $\mu_1 \ll \mu_2 \sim \mu_3 \ll \mu_0$ with $\mu_3/\mu_0 < 10^{-6}$. Feasibility of this case we cannot judge, as mentioned above, until the complicated analysis of the scalar potential has been performed.

6. SUMMARY

In summary, from our brief analysis here, we have illustrated a few interesting issues in the flavor structure of supersymmetry without R parity. The question of the natural suppression of the μ_i's is important. It is, however, a subtle issue which has to be analyzed from a careful study of the full five-doublet $(4\hat{L}_\alpha + \hat{H}_u)$ scalar potential with the most generic terms softly breaking supersymmetry. Assuming that can be explained, we illustrate above that the suppressed values of the RPV couplings, required for fitting the limiting scenario of neutrino oscillations motivated by the recent Super-K result, fit very well into an approximate flavor symmetry perspective. Success of the latter is a strong indication that the R-parity-violating (or lepton number-violating) couplings are "naturally" small, as the light fermion masses are, and their explanation most probably lies under a common theory of flavor structure.

ACKNOWLEDGMENTS

A. Mitov is to be thanked for reading the manuscript. This work was supported in part by the U.S. Department of Energy, under grant DE-FG02-91ER40685.

REFERENCES

1. M. Bisset, O. C. W. Kong, C. Macesanu, and L. H. Orr, Phys. Lett. B **430**, 274 (1998).
2. Super-Kamiokande Collab. (Y. Fukuda *et al.*), hep-ex/9803006; hep-ex/9805006; hep-ex/9807003; Talk by T. Kajita *et al.*, Neutrino-98, Takayama, Japan, June 1998.
3. O. C. W. Kong, Mod. Phys. Lett. A **14**, 903 (1999).
4. L. E. Ibáñez and G. G. Ross, Nucl. Phys. B **368**, 3 (1992).
5. M. Bisset, O. C. W. Kong, C. Macesanu, and L. H. Orr, hep-ph/9811498.
6. See, for example, various contributions to the NANP-99 Conference.
7. A. Antaramian, L. J. Hall, and A. Rašin, Phys. Rev. Lett. **69**, 1871 (1992); see also T. P. Cheng and M. Sher, Phys. Rev. D **35**, 3484 (1987).

Physics of Atomic Nuclei, Vol. 63, No. 6, 2000, pp. 1088–1096. From Yadernaya Fizika, Vol. 63, No. 6, 2000, pp. 1163–1171.
Original English Text Copyright © 2000 by Nanopoulos.

PHYSICS
BEYOND THE STANDARD MODEL

Search for Quantum Spacetime Foam*

D. V. Nanopoulos**
Center for Theoretical Physics, Texas A&M University, USA

Abstract—The possibility that quantum fluctuations in the structure of spacetime at the Planck scale might be subject to experimental probes in discussed. The effects of spacetime foam in an approach inspired by string theory, in which solitonic *D*-brane excitations are taken into account when considering the ground state, are studied. The properties of this medium are described by analyzing the recoil of a *D* particle which is induced by the scattering of a closed-string state. This recoil causes an energy-dependent perturbation of the background metric, which in turn induces an energy-dependent refractive index in vacuo, and stochastic fluctuations of the light cone. Distant astrophysical sources such as Gamma-Ray Bursters (GRBs) may be used to test this possibility, and an illustrative analysis of GRBs whose redshifts have been measured is presented. The propagation of massive particles through such a quantum spacetime foam is also discussed. © *2000 MAIK "Nauka/Interperiodica".*

1. INTRODUCTION

The concept of spacetime foam is an old one, first suggested by Wheeler [1], which has subsequently reappeared in various forms [2–8]. The basic intuition is that quantum-gravitational fluctuations in the fabric of spacetime cause the vacuum to behave like a stochastic medium. Most physicists who have studied the problem would surely agree that quantum-gravitational interactions must alter dramatically our classical perception of the spacetime continuum when one attains Planckian energy scales $E \sim M_P \simeq 10^{19}$ GeV or Planckian distance scales $\ell \sim \ell_P \simeq 10^{-33}$ cm, which are the scales where gravitational interactions are expected to become strong. At issue are the following questions: how may classical spacetime be altered at these scales? and is there any way of testing these possibilities?

At first sight, in might seem impossible to test such a suggestion within the foreseeable future, given the restrictions on the energies attainable with particle accelerators and their corresponding limitations as microscopes. However, there are many instances in which new physics has revealed itself as a novel phenomenon far below its intrinsic mass scale M, a prime example being the weak interaction. In general, new physics are suppressed by some inverse power of the heavy mass scale M, e.g., weak-interaction amplitudes are suppressed by $1/M_W^2$, However, some new-physics effects may be suppressed by just one power of the heavy mass scale, e.g., proton-decay amplitudes in some supersymmetric GUTs are $\propto 1/M_{\mathrm{GUT}}$. Although gravitational amplitudes are generally suppressed by $1/M_P^2$, one should be open to the possibility that some quantum-gravitational effects might be suppressed simply by $1/M_P$. Moreover, there are many suggestions nowadays that M_P might not be a fundamental mass scale, and the quantum-gravitational effects might appear at some much lower scale related to the size(s) of one or more extra dimensions [9]. It has sometimes been suggested that Lorentz invariance might require quantum-gravitational effects to be suppressed by at least $O[(E/M_P)^2]$, where E is a typical low-energy scale. However, Lorentz invariance is a casualty of many approaches to quantum gravity, and it is not clear how the very concept of spacetime foam could be formulated in a Lorentz invariant way. For example, many approaches to the physics of very small distances suggest that the classical spacetime continuum may no longer exist, but might instead be replaced by a cellular structure.

String theory, plausibly in its current formulation as M theory, is at present the best (only?) candidate for a true quantum theory of gravity, so it is natural to ask what guidance it may offer us into the possible observability of quantum-gravitational effects. A first tool for this task was provided by two-dimensional string models [4, 10], but a much more powerful tool has now been provided by D (dirichlet) branes [11]. In this talk, I review one particular D-brane approach to the modeling of spacetime foam [12, 13]. A characteristic feature of this approach is a treatment of D-brane recoil effects, in an attempt to incorporate the back-reaction of propagating particles on the ambient metric. This leads to the sacrifice of Lorentz invariance at the Planck scale and suggests that spacetime-foam effects arise already at the order $O(E/M_P)$, in which case they might well be observable.

We have argued in the past that such minimally suppressed quantum-gravitational effects could be probed

---

* This article was submitted by the author in English.

** Astro Particle Physics Group, Houston Advanced Research Center (HARC), The Mitchell Campus, Woodlands, USA; Academy of Athens, Chair of Theoretical Physics, Division of Natural Sciences, Athens, Greece; e-mail: dimitri@soda.physics.tamu.edu

1063-7788/00/6306-1088$20.00 © 2000 MAIK "Nauka/Interperiodica"

Observational sensitivities and limits on M

Source	Distance, Mpc	E	Δt, S	Sensitivity to M, GeV
GRB 920229 [5, 15]	3000 (?)	200 keV	10^{-2}	0.6×10^{16} (?)
GRB 980425	40	1.8 MeV	10^{-3} (?)	0.7×10^{16} (?)
GRB 920925c	40 (?)	200 TeV (?)	200	0.4×10^{19} (?)
Mrk 421 [16]	100	2 TeV	280	$>7 \times 10^{16}$
Crab pulsar [17]	2.2×10^{-3}	2 GeV	0.35×10^{-3}	$>1.3 \times 10^{15}$
GRB 990123	5000	4 MeV	1 (?)	2×10^{15} (?)

Note: The mass-scale parameter M is defined by $\delta c/c = E/M$. The question marks indicate uncertain observational inputs. Hard limits are indicated by inequality signs.

in the neutral-kaon system [3], which is well known to be a sensitive laboratory for testing quantum mechanics and fundamental symmetries. In this talk, I focus more on the possibility that the propagation of other particles such as photons or neutrinos might be affected in a way that could be testable in the foreseeable future, for instance, through astrophysical observations of pulsed sources such as γ-ray bursters (GRBs), active galactic nuclei (AGNs), or pulsars [5]. Our basic suggestion is that spacetime foam may act as a nontrivial optical medium with, e.g., an energy- or frequency-dependent refractive index, through which the propagation of energetic particles might be slowed down so that they travel at less than the speed of light c: $\delta c/c \sim -E/M_{\mathrm{P}}$. A secondary effect might be a stochastic spread in the velocities of particles with identical energies.

The primary tool for measuring small variations δc in the velocity of light c is the variation in arrival time [5, 14] $\delta t \simeq -(L/c)(\delta c/c)$ observed for a photon traveling a distance L. This clearly places a premium on observing sources whose emissions exhibit structure on short time scales $\Delta t \lesssim \delta t$ located at large distances. Some typical numbers for some astrophysical sources are shown in the table. The relevant photon property that could be correlated with velocity variations δc is its frequency ν, or equivalently its energy E, for which characteristic values are also listed in the table. As I discuss in more detail later, any such effect could be expected to increase with E, and the simplest possibility, for which there is some theoretical support, is that $\delta c \propto E/M$, where M is some high energy scale. In this case, the relevant figure of merit for observational test is the combination

$$\frac{LE}{c\delta t} \tag{1}$$

which measures directly the experimental sensitivity to such a high energy scale M. This sensitivity is also listed in the table, where we see that our favored astrophysical sources are potentially sensitive to M approaching $M_{\mathrm{P}} \simeq 10^{19}$ GeV, the mass scale at which gravity becomes strong. Therefore, these astrophysical sources may begin to challenge any theory of quantum gravity that predicts such a linear dependence of δc on E.

Alternatively, it could be that $\delta c/c \simeq (E/\tilde{M})^2$, in which case the appropriate figure of merit is $E\sqrt{L/c\delta t}$. In this case, astrophysical observations may be sensitive to $\tilde{M} \sim 10^{11}$ TeV.

2. SPACETIME FOAM FROM *D*-PARTICLE RECOIL

The string-inspired prototype model of spacetime foam is based on one particular treatment of D branes [12, 13]. This model involves naturally the breaking of Lorentz covariance, as a sort of spontaneous breaking. The basic idea may be summarized as follows. In the modern view of string theory, D particles must be included in the consistent formulation of the ground-state vacuum configuration [11]. Consider a closed-string state propagating in a $(D + 1)$-dimensional spacetime, which impacts a very massive D(irichlet) particle embedded in this spacetime. We argue that the scattering of the closed-string state on the D particle induces recoil of the latter, which distorts the surrounding spacetime in a stochastic manner. From the point of view of the closed-string particle and any low-energy spectators, this is a nonequilibrium process, in which information is "lost" during the recoil, being carried by recoiling D-brane degrees of freedom that are inaccessible to a low-energy observer. Thus, although the entire process is consistent with quantum-mechanical unitarity, the low-energy effective theory is characterized by information loss and entropy production. From a string-theory point of view, the loss of information is encoded in a deviation from conformal invariance of the relevant world-sheet σ model that describes the recoil, that is compensated by the introduction of a Liouville field [18], which in turn is identified with the target time in the approach [10] adopted here.

In the case of a D-brane string soliton, its recoil after interaction with a closed-string state [19] is characterized by a pair of logarithmic operators [20]

$$C_\epsilon \sim \epsilon\Theta_\epsilon(t), \quad D_\epsilon \sim t\Theta_\epsilon(t) \tag{2}$$

defined on the boundary $\partial\Sigma$ of the string world sheet. The operators (2) act as deformations of the conformal field theory of the world sheet: $u_i\int_{\partial\Sigma}\partial_n X^i D_\epsilon$ describes the shift of the D brane induced by the scattering, where u_i is its recoil velocity, and $y_i\int_{\partial\Sigma}\partial_n X^i C_\epsilon$ describes quantum fluctuations in the initial position y_i of the D particle. It has been shown [21] that energy–momentum is conserved during the recoil process:

$$u_i = k_1 - k_2, \tag{3}$$

where $k_1(k_2)$ is the momentum of the propagating closed-string state before (after) the recoil, as a result of the summation over world-sheet genera. Thus, the result (3) is in exact result, as far a s world-sheet perturbation theory is concerned. I also note that $u_i = g_s P_i$, where P_i is the momentum and g_s is the string coupling, which is assumed here to be weak enough to ensure that D branes are very massive, with mass $M_D = 1/(\ell_s g_s)$, where ℓ_s is the string length.

The correct specification of the logarithmic pair (2) entails a regulating parameter $\epsilon \longrightarrow 0^+$, which appears inside the $\Theta_\epsilon(t)$ operator: $\Theta_\epsilon(t) = \int\frac{d\omega}{2\pi}\frac{1}{\omega - i\epsilon}e^{i\omega t}$. In order to realize the logarithmic algebra between the operators C and D, one takes [19]:

$$\epsilon^{-2} \sim \mathrm{Log}\Lambda/a \equiv \alpha, \tag{4}$$

where $\Lambda(a)$ are infrared (ultraviolet) world-sheet cutoffs. The pertinent two-point functions then have the following form [19]:

$$\begin{gathered}\langle C_\epsilon(z)C_\epsilon(0)\rangle \sim 0 + O[\epsilon^2],\\ \langle C_\epsilon(z)D_\epsilon(0)\rangle \sim 1,\\ \langle D_\epsilon(z)D_\epsilon(0)\rangle \sim \frac{1}{\epsilon^2} - 2\eta\log|z/L|^2\end{gathered} \tag{5}$$

up to an overall normalization factor, which is the logarithmic algebra [20] in the limit $\epsilon \longrightarrow 0^+$, modulo the leading divergence in the $\langle D_\epsilon D_\epsilon\rangle$ recoil correlator. This leading divergent term will be important for our subsequent analysis.

The recoil deformations of the D_0 brane (2) are relevant deformations, in the sense of conformal field theory, with anomalous dimension $-\epsilon^2/2$. However [21], the velocity operator D_ϵ (2) becomes exactly marginal, in a world-sheet renormalization-group sense, when it is divided by ϵ, in which case the recoil velocity is renormalized [21]

$$u_i \longrightarrow \bar{u}_i \equiv u_i/\epsilon, \tag{6}$$

and becomes exactly marginal, playing the role of the physical velocity of the recoiling D particle.

Although such a renormalization is compatible with global world-sheet scaling, local world-sheet scale (conformal) symmetry is broken by the nonmarginal character of the deformations (2), and restoration of conformal invariance requires Liouville dressing [18]. To determine the effect of such dressing on the spacetime geometry, it is essential to write [12, 13] the boundary recoil deformation as a bulk world-sheet deformation

$$\begin{aligned}&\int_{\partial\Sigma} d\tau \bar{u}_i X^0\Theta_\epsilon(X^0)\partial_n X^i\\ &= \int_{\Sigma} d^2\sigma\partial_\alpha([\bar{u}_i X^0]\Theta_\epsilon(X^0)\partial_\alpha X^i),\end{aligned} \tag{7}$$

where the $\bar{u}_i$ denote the renormalized recoil couplings (6), in the sense discussed in [21]. As I have already mentioned, the couplings (7) are marginal in a flat world sheet and become marginal on a curved world sheet if one dresses [18] the bulk integrand with a factor $e^{\alpha_i\phi}$, where ϕ is the Liouville field and α_i is the gravitational conformal dimension. This is related to the flat-world-sheet anomalous dimension $-\epsilon^2/2$ of the recoil operator, viewed as a bulk world-sheet deformation, as follows [18]:

$$\alpha_i = -\frac{Q_b}{2} + \sqrt{\frac{Q_b^2}{4} + \frac{\epsilon^2}{2}}, \tag{8}$$

where Q_b is the central-charge deficit of the bulk world-sheet theory. In the recoil problem at hand, as discussed in [22], $Q_b^2 \sim \epsilon^4/g_s^2$ for weak deformations. This yields $\alpha_i \sim -\epsilon$ to leading order in perturbation theory in ϵ, to which I restrict myself here.

I next remark that, as the analysis of [12] indicates, the X^0-dependent operator $\Theta_\epsilon(X^0)$ scales as follows with ϵ for $X^0 > 0$: $\Theta_\epsilon(X^0) \sim e^{-\epsilon X^0}\Theta(X^0)$, where $\Theta(X^0)$ is a Heaviside step function without any field content, evaluated in the limit $\epsilon \longrightarrow 0^+$. The bulk deformations, therefore, yield the following σ-model terms:

$$\frac{1}{4\pi\ell_s^2}\epsilon\sum_{I=m+1}^{D-1} g_{Ii}X^I e^{\epsilon(\phi_{(0)} - X^I_{(0)})}\Theta(X^I_{(0)})\int_\Sigma \partial^\alpha X^I\partial^\alpha y_i, \tag{9}$$

where the subscripts (0) denote world-sheet zero modes.

When we interpret the Liouville zero mode $\phi_{(0)}$ as target time, $\phi_{(0)} \equiv X^0 = t$, the deformations (9) yield spacetime metric deformations in a σ-model sense, which were interpreted in [12] as expressing the distortion of the spacetime surrounding the recoiling D-brane soliton. For clarity, we now drop the subscripts (0) for the rest of this paper. The resulting spacetime distortion is then described by the metric elements:

$$\begin{gathered}G_{ij} = \delta_{ij}, \quad G_{00} = -1, \quad G_{0i} = \epsilon(\epsilon y_i + \epsilon\bar{u}_i t)\Theta_\epsilon(t),\\ i = 1, \ldots D-1,\end{gathered} \tag{10}$$

where the suffix 0 denotes temporal (Liouville) components.

The transformation laws for the couplings y_i and u_i, which are conjugate to D_ϵ and C_ϵ, are

$$u_i \longrightarrow u_i, \quad y_i \longrightarrow y_i + u_i t. \tag{11}$$

These are consistent with the interpretations of u_i as the velocity after the scattering process and y_i as the spatial collective coordinates of the brane if and only if the parameter ϵ^{-2} is identified with the target Minkowski time t for $t \gg 0$ after the collision:

$$\epsilon^{-2} \simeq t. \tag{12}$$

I have assumed in this analysis that the velocity u_i is small, as is appropriate in the weak-coupling regime studied here. The D-brane σ-model formalism is completely relativistic, and I anticipate that a complete treatment beyond the one-loop order discussed here will incorporate correctly all relativistic effects, including Lorentz factors wherever appropriate.

In view of (12), one observes that for $t \gg 0$ the metric (10) becomes to leading order

$$G_{ij} = \delta_{ij}, \quad G_{00} = -1, \quad G_{0i} \sim \bar{u}_i, \quad i = 1, \ldots, D-1, \tag{13}$$

which is constant in spacetime. However, the effective metric depends on the energy content of the low-energy particle that scattered on the D particle, because of momentum conservation during the recoil process (3). This energy dependence is the primary deviation from Lorentz invariance induced by the D-particle recoil.

3. REFRACTIVE INDEX IN VACUO

I now proceed to discuss possible phenomenological consequences of the above phenomena, starting with the propagation of photons and relativistic particles. The above discussion of recoil suggests that the spacetime background should be regarded as nontrivial. Light propagating through media with nontrivial optical properties may exhibit a frequency-dependent refractive index, namely, a variation in the light velocity with photon energy. Another possibility is a difference between the velocities of light with different polarizations, namely, birefringence, and a third is a diffusive spread in the apparent velocity of light for light of fixed energy (frequency). Within the framework described in the previous section, the first [5] and third [13] effects have been derived via a formal approach based on a Born–Infeld Lagrangian using D-brane technology. The possibility of birefringence has been raised [23] within a canonical approach to quantum gravity, but I do not pursue such a possibility here. A different approach to light propagation has been taken in [24], where quantum-gravitational fluctuations in the light-cone have been calculated. Here, I use this formalism together with the microscopic model background obtained in the previous section to derive a nontrivial refractive index and a diffusive spread in the arrival times of photons of given frequency.

As I commented earlier, one may expect Lorentz invariance to be broken in a generic theory of quantum gravity and specifically in the recoil context discussed in the previous section. In the context of string theory, violations of Lorentz invariance entail the exploration of noncritical string backgrounds, since Lorentz invariance is related to the conformal symmetry that is a property of critical strings. As I discussed in the previous section, a general approach to the formulation of noncritical string theory involves introducing a Liouville field [18] as a conformal factor on the string world sheet, which has nontrivial dynamics and compensates the nonconformal behavior of the string background, and I showed in the specific case of D branes that their recoil after interaction with a closed-string state produces a local distortion of the surrounding spacetime (10).

Viewed as a perturbation about a flat target spacetime, the metric (10) implies that the only nonzero components of $h_{\mu\nu}$ are:

$$h_{0i} = \epsilon^2 \bar{u}_i t \Theta_\epsilon(t) \tag{14}$$

in the case of D-brane recoil. I now consider light propagation along the x direction in the presence of a metric fluctuation h_{0x} (14) in flat space, along a null geodesic given by $(dt)^2 = (dx)^2 + 2h_{0x}dtdx$. For large times $t \sim \log\Lambda/a \sim \epsilon^{-2}$ [22], $h_{0x} \sim \bar{u}$, and thus I obtain

$$\frac{cdt}{dx} = \bar{u} + \sqrt{1+\bar{u}^2} \sim 1 + \bar{u} + O(\bar{u}^2), \tag{15}$$

where the recoil velocity $\bar{u}$ is in the direction of the incoming light ray. Taking into account energy-momentum conservation in the recoil process, which has been derived in this formalism as mentioned previously, one has a typical order of magnitude $\bar{u}/c = O(E/M_D c^2)$, where $M_D = g_s^{-1} M_s$ is the D-brane mass scale, with $M_s \equiv \ell_s^{-1}$. Hence, (15) implies a subluminal energy-dependent velocity of light,

$$c(E)/c = 1 - O(E/M_D c^2), \tag{16}$$

which corresponds to a classical refractive index. This appears because the metric perturbation (14) is energy-dependent, through its dependence on $\bar{u}$.

The subluminal velocity (16) induces a delay in the arrival of a photon of energy E propagating over a distance L of order

$$(\Delta t)_r = \frac{L}{c} O\left(\frac{E}{M_D c^2}\right). \tag{17}$$

This effect can be understood physically from the fact that the curvature of spacetime induced by the recoil is $\bar{u}$—and hence energy-dependent. This affects the paths of photons in such a way that more energetic photons see more curvature and thus are delayed with respect to low-energy ones.

As recalled above, the absence of superluminal light propagation was found previously via the formalism of the Born–Infeld Lagrangian dynamics of D branes [21, 13]. Furthermore, the result (17) is in agreement with the analysis of [14, 5], which was based on a more abstract analysis of Liouville strings. It is encouraging that this result appears also in this more conventional general-relativity approach [24], in which the underlying physics is quite transparent.

Also, a diffusive spread in the apparent velocity of light for light of fixed energy frequency is expected to lead to a diffusive spread in the arrival times of the photons. I find a contribution

$$|(\Delta t)_{\text{obs}}| \simeq O\left(\bar{g}_s \frac{E}{M_D c^2}\right)\frac{L}{c} \tag{18}$$

to the RMS fluctuation in arrival times. As expected, the quantum effect (18) is suppressed by a power of the string coupling constant, when compared with the classical refractive index effect (17). The result (18) was derived in [13] using the techniques of Liouville string theory, via the Born–Infeld Lagrangian for the propagation of photons in the D-brane foam. It should be noted that the recoil-induced effect (18) is larger than the effects discussed in [24], which are related to metric perturbations associated with the squeezed coherent states relevant to particle creation in conventional local field theories.

4. MAXWELL'S EQUATIONS REVISITED

I now consider [25] the effects of the recoil-induced spacetime (13), viewed as a "mean field solution" of the D-brane-inspired quantum-gravity model, on the propagation of electromagnetic waves. Maxwell's equations in the background metric (13) in empty space can be written as [26]

$$\begin{aligned} &\nabla \cdot \mathbf{B} = 0, \quad \nabla \times \mathbf{H} - \frac{1}{c}\frac{\partial}{\partial t}\mathbf{D} = 0, \\ &\nabla \cdot \mathbf{D} = 0, \quad \nabla \times \mathbf{E} + \frac{1}{c}\frac{\partial}{\partial t}\mathbf{B} = 0, \end{aligned} \tag{19}$$

where

$$\mathbf{D} = \frac{\mathbf{E}}{\sqrt{h}} + \mathbf{H} \times \mathcal{G}, \quad \mathbf{B} = \frac{\mathbf{H}}{\sqrt{h}} + \mathcal{G} \times \mathbf{E}. \tag{20}$$

Thus, there is a direct analogy with Maxwell's equations in a medium with $1/\sqrt{h}$ playing the role of the electric and magnetic permeability. In our case [12], $h = 1$, so one has the same permeability as the classical vacuum. In the case of the constant metric perturbation (13), after some elementary vector algebra and appropriate use of the modified Maxwell's equations, the equations (19) read

$$\begin{aligned} &\nabla \cdot \mathbf{E} + \bar{\mathbf{u}} \cdot \frac{1}{c}\frac{\partial}{\partial t}\mathbf{E} = 0, \\ &\nabla \times \mathbf{B} - (1 - \bar{u}^2)\frac{1}{c}\frac{\partial}{\partial t}\mathbf{E} + \bar{\mathbf{u}} \times \frac{1}{c}\frac{\partial}{\partial t}\mathbf{B} + (\bar{\mathbf{u}} \cdot \nabla)\mathbf{E} = 0, \\ &\nabla \cdot \mathbf{B} = 0, \\ &\nabla \times \mathbf{E} + \frac{1}{c}\frac{\partial}{\partial t}\mathbf{B} = 0. \end{aligned} \tag{21}$$

Dropping nonleading terms of order $\bar{u}^2$ from these equations, one obtains after some straightforward algebra the following modified wave equations for E and B:

$$\begin{aligned} &\frac{1}{c^2}\frac{\partial^2}{\partial^2 t}B - \nabla^2 B - 2(\bar{\mathbf{u}} \cdot \nabla)\frac{1}{c}\frac{\partial}{\partial t}B = 0, \\ &\frac{1}{c^2}\frac{\partial^2}{\partial^2 t}E - \nabla^2 E - 2(\bar{\mathbf{u}} \cdot \nabla)\frac{1}{c}\frac{\partial}{\partial t}E = 0. \end{aligned} \tag{22}$$

If we consider one-dimensional motion along the x direction, we see that these equations admit wave solutions of the form

$$\begin{aligned} &E_x = E_z = 0, \quad E_y(x, t) = E_0 e^{i(kx - \omega t)}, \\ &B_x = B_y = 0, \quad B_z(x, t) = B_0 e^{i(kx - \omega t)}, \end{aligned} \tag{23}$$

with the modified dispersion relation

$$k^2 - \omega^2 - 2\bar{u}k\omega = 0. \tag{24}$$

Since the sign of $\bar{u}$ is that of the momentum vector k along the x direction, the dispersion relation (24) corresponds to subluminal propagation with a refractive index:

$$c(E) = c(1 - \bar{u}) + \mathcal{O}(\bar{u}^2), \tag{25}$$

where we estimate that

$$\bar{u} = O\left(\frac{E}{M_D c^2}\right) \tag{26}$$

with M_D the D-particle mass scale. This is in turn given by $M_D = g_s^{-1} M_s$ in string model, where g_s is the string coupling and M_s is the string scale [13]. The relation (26) between $\bar{u}$ and the photon energy has been shown [21] to follow from a rigorous world-sheet analysis of modular divergences in string theory, but the details need not concern us here. It merely expresses elementary energy–momentum conservation, as discussed earlier.

The refractive index effect (25) is a mean-field effect, which implies a delay in the arrival times of photons relative to that of an idealized low-energy photon,

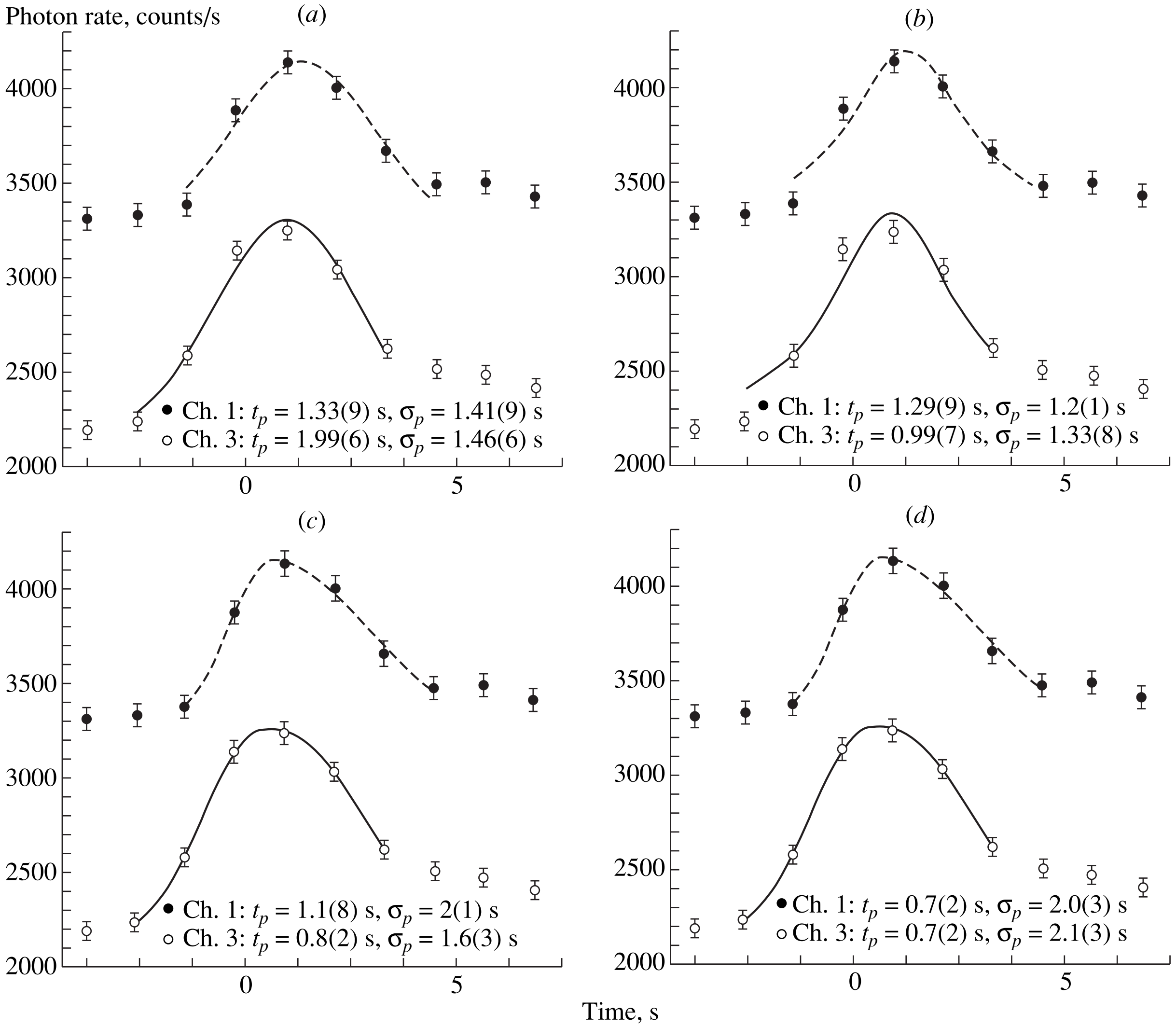

Fig. 1. Time distribution of the number of photons observed by BATSE in channels 1 and 3 for GRB 970508, compared with the following fitting functions [25]: (*a*) Gaussian, (*b*) Lorentzian, (*c*) "tail" function, and (*d*) "pulse" function. We list below each panel the positions t_p and widths σ_p (with statistical errors) found for each peak in each fit. I recall that the BATSE data are binned in periods of 1.024 s.

for which quantum-gravity effects can be ignored, of order

$$\Delta t \sim \frac{L}{c}|\bar{u}| = \mathbb{O}\left(\frac{EL}{M_D c^3}\right). \tag{27}$$

As I have discussed above (see also [13]), one would also expect quantum fluctuations about the mean-field solution (27), corresponding in field theory to quantum fluctuations in the light cone that could be induced by higher genus effects in a string approach. Such effects would result in stochastic fluctuations in the velocity of light which are of order

$$\delta c \sim 8 g_s E / M_D c^2, \tag{28}$$

where g_s is the string coupling, which varies between $\mathbb{O}(1)$ and $\ll 1$ in different string models. Such an effect would motivate the following parametrization of any possible stochastic spread in photon arrival times:

$$(\delta\Delta t) = \frac{LE}{c\Lambda}, \tag{29}$$

where the string approach suggests $\Lambda \sim M_D c^2/8g_s$. I emphasize that, in contrast to the variation (25) in the refractive index—which refers to photons of different energy—the fluctuation (29) characterizes the statistical spread in the velocities of photons of the same energy. I recall that the stochastic effect (29) is suppressed, as compared to the refractive index mean field effect (26), by an extra power of g_s.

We presented in [25] a detailed analysis of the astrophysical data for a sample of Gamma Ray Bursters (GRB) whose redshifts z are known (see Fig. 1 for the data of a typical burst: GRB 970508). We looked (with-

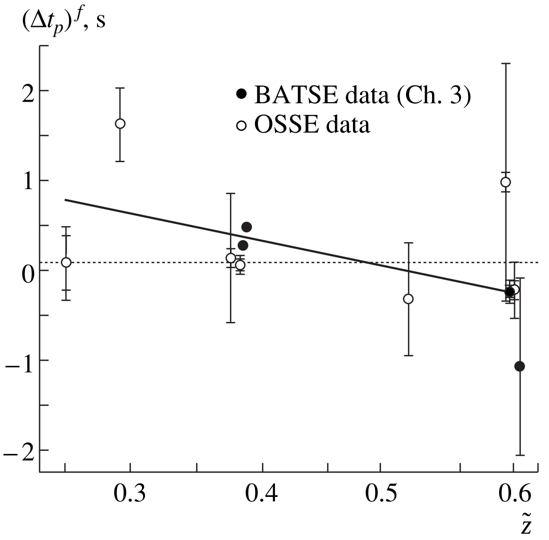

Fig. 2. Values of the shifts $(\Delta t_p)^f$ in timing of the peaks fitted for each GRB studied using BATSE and OSSE data [25], plotted versus $\tilde{z} = 1 - (1 + z)^{-1/2}$, where z is the redshift. Indicated errors are the statistical errors in the in the "pulse" fit provided by the fitting routine, combined with systematic error estimates obtained by comparing the results obtained using the "tail" fitting function. The values obtained by comparing OSSE with BATSE Channel 3 data have been rescaled by the factor $\left(E_{\text{min}}^{\text{BATSE Ch. 3}} - E_{\text{max}}^{\text{BATSE Ch. 1}}\right)/\left(E_{\text{min}}^{\text{OSSE}} - E_{\text{max}}^{\text{BATSE Ch. 3}}\right)$, so as to make them directly comparable with the comparisons of BATSE Channels 1 and 3. The solid line is the best linear fit.

out success) for a correlation with the redshift, calculating a regression measure (see Fig. 2) for the effect (27) and its stochastic counterpart (29). Specifically, we looked for linear dependences of the "observed" $\Delta t/\Delta E_0$ and the spread $\Delta\sigma/E$ on $\tilde{z} \equiv 2[1 - (1/(1 + z))^{1/2}] \simeq z - (3/4)z^2 + \ldots$. We determined limits on the quantum gravity scales M and Λ by constraining the possible magnitudes of the slopes in linear-regression analyses of the differences between the arrival times and widths of pulses in different energy ranges from five GRBs with measured redshifts, as functions of $\tilde{z}$. Using the current value for the Hubble expansion parameter, $H_0 = 100h_0$ km/(s Mpc), where $0.6 < h_0 < 0.8$, we obtained the limits [25]

$$M \gtrsim 10^{15}\ \text{GeV}, \quad \Lambda \gtrsim 2 \times 10^{15}\ \text{GeV} \tag{30}$$

on the possible quantum-gravity effects.

5. MASSIVE RELATIVISTIC PARTICLES REVISITED

So far, I have concentrated my attention on massless particles, namely, photons, because of the very interesting experimental (observational) possibilities they provide. It should, however, be clear that the metric perturbation (13) produced by our D-brane recoil model, which implies a breakdown of Lorentz invariance, alters the Einstein dispersion relation for massive particles too. One expects, on general grounds, that the photon dispersion relation (24),

$$\omega^2 - k^2 + 2\bar{u}k\omega = 0,$$

will become in the case of massive particles

$$\omega^2 - k^2 + 2\bar{u}k\omega - m_0^2 = 0, \tag{31}$$

leading to the modified Einstein relation,

$$\omega^2 \approx (k^2 + m_0^2)\left[1 - \frac{k^2}{\sqrt{k^2 + m_0^2}}\frac{1}{M}\right]^2 \tag{32}$$

to leading order in $O\left(\frac{k}{M}\right)$. It is useful to recast (32) in the more familiar notation

$$E^2 = (p^2 + m_0^2)\left[1 - \left(\frac{1}{\sqrt{1 + m_0^2/p^2}}\right)\frac{p}{M}\right]^2, \tag{33}$$

which in the nonrelativistic limit yields

$$E = m_0 + \frac{p^2}{2m_0} - \frac{p^2}{M} + \ldots O\left(\left(\frac{p}{M}\right)^2\right). \tag{34}$$

Thus, an effective rest mass

$$(m_{\text{eff}})_0 \approx m_0\left(1 + \frac{2m_0}{M}\right) \tag{35}$$

appears in the nonrelativistic kinetic energy: $E_{\text{kin}} = \frac{p^2}{2m_{\text{eff}}}$. Alternatively, one may use (33) to recast the T-shirt formula $E = mc^2$ in the form

$$E \approx mc^2\left[1 - \frac{m}{M}\left(\frac{\bar{u}^2}{c^2}\right)\right], \tag{36}$$

where $m \equiv \frac{m_0}{\sqrt{1 - \bar{u}^2/c^2}}$, as usual.

We see again that, although quantum gravitational fluctuations in spacetime, as modeled by D-brane quantum recoil, may lead to a spontaneous breakdown of Lorentz symmetry, the resulting corrections to the standard Einstein relations are very small, so that conventional special relativity is still a good approximation to the world.

I recall that another possible probe of quantum-gravitational effects on massive particles is offered by tests of quantum mechanics in the neutral kaon system. A parametrization of possible deviations from the

Schrödinger equation has been given [3], assuming energy and probability conservation, in terms of quantities α, β, γ that must obey the conditions

$$\alpha, \gamma > 0, \quad \alpha\gamma > \beta^2 \tag{37}$$

stemming from the positivity of the density matrix ρ. These parameters induce quantum decoherence and violate CPT [27]. Experimental data in neutral kaon decays so far agree perfectly with conventional quantum mechanics, imposing only the following upper limits [28]:

$$\begin{gathered}\alpha < 4.0 \times 10^{-17}\ \text{GeV}, \quad \beta < 2.3 \times 10^{-19}\ \text{GeV}, \\ \gamma < 3.7 \times 10^{-21}\ \text{GeV}.\end{gathered} \tag{38}$$

I cannot help being impressed that these bounds are in the ballpark of m_K^2/M_{P}, which is the maximum magnitude that I could expect any such effect to have.

This and the example of photon propagation give hope that experiments may be able to probe physics close to the Planck scale, if its effects are suppressed by only one power of $M_{\mathrm{P}} \simeq 10^{19}$ GeV. One should not exclude the possibility of being able to test some of the speculative ideas about quantum gravity reviewed in this article. Indeed, if the analysis of photon propagation can be extended to energetic neutrinos, and if GRBs emit ~10 s ν pulses, one could be sensitive to mass scales as large as 10^{28} GeV!

6. CONCLUSIONS

I have discussed here some possible low-energy of quantum gravity, concentrating on the possibility that the velocity of light might depend on its frequency, i.e., the corresponding photon energy. This idea is very speculative, and the model calculations that I have reviewed require justification and refinement. However, I feel that the suggestion is well motivated by the basic fact that gravity abhors rigid bodies and the related intuition that the vacuum should exhibit back-reaction effects and act as a nontrivial medium. I recall that these features have appeared in several approaches to quantum gravity, including the canonical approach and ideas based on extra dimensions. Therefore, I consider the motivation from fundamental physics for a frequency-dependent velocity of light, and the potential significance of any possible observation, to be sufficient to examine this possibility from a phenomenological point of view.

As could be expected, we have found no significant effect in the data available on GRBs [25], either in the possible delay times of photons of higher energies or in the possible stochastic spreads of velocities of photons with the same energy. However, it has been established that such probes may be sensitive to scales approaching the Planck mass if these effects are linear in the photon energy. We expect that the redshifts of many more GRBs will become known in the near future, as alerts and follow-up observations become more effective, for example, after the launch of the HETE II satellite [29, 30]. Observations of higher energy photons from GRBs would be very valuable, since they would provide a longer level arm in the search for energy-dependent effects on photon propagation. Such higher energy observations could be provided by future space experiments such as AMS [31] and GLAST [32].

This is not the only way in which quantum gravity might be probed: an example that we have advertised previously is provided by test of quantum mechanics in the neutral-kaon system [3, 27, 28]. Forthcoming data from the DAΦNE accelerator may provide new opportunities for this quest. An alternative possibility might be provided by inteferrometric devices intended to detect gravity waves [8]. We also regard the emerging astrophysical suggestion on nonvanishing cosmological vacuum energy as a great opportunity for theoretical physics. If confirmed, this would provide a number to calculate in a complete quantum theory of gravity. The possibility that this vacuum energy might not be constant, but might actually be relaxing towards zero [33, 34], is a possibility that may be tested by forthcoming cosmological observations. I therefore believe that the phrase "experimental quantum gravity" may not be an oxymoron.

ACKNOWLEDGMENTS

This work is supported in part by D.O.E. grant DE-F-G03.95.ER-40917.

REFERENCES

1. J. A. Wheeler, Ann. Phys. (N.Y.) **2**, 605 (1958); J. A. Wheeler, *Relativity, Groups and Topology* (Gordon and Breach, New York, 1963).
2. S. W. Hawking, Nucl. Phys. B **144**, 349 (1978); S. W. Hawking, D. N. Page, and C. N. Pope, Phys. Lett. B **86**, 175 (1979).
3. J. Ellis, J. Hagelin, D. Nanopoulos, and M. Srednicki, Nucl. Phys. B **241**, 381 (1984).
4. J. Ellis, N. E. Mavromatos, and D. V. Nanopoulos, Phys. Lett. B **293**, 37 (1992).
5. G. Amelino-Camelia *et al.*, Nature **393**, 763 (1998).
6. L. J. Garay, Phys. Rev. D **58**, 124015 (1998).
7. A. Ashtekar, gr-qc/9901023.
8. G. Amelino-Camelia, Nature **398**, 216 (1999); gr-qc/9903080.
9. I. Antoniadis, hep-th/9909212.
10. J. Ellis, N. E. Mavromatos, and D. V. Nanopoulos, in *Lectures Presented at the Erice Summer School, 31st Course: From Supersymmetry to the Origin of Space-Time* (World Sci., Singapore, 1994), p. 1; hep-th/9403133.
11. J. Dai, R. G. Leigh, and J. Polchinski, Mod. Phys. Lett. A **4**, 2073 (1989); J. Polchinski, Phys. Rev. Lett. **75**, 184 (1995); hep-th/9611050.

12. J. Ellis, N. E. Mavromatos, and D. V. Nanopoulos, Int. J. Mod. Phys. A **12**, 2639 (1997); **13**, 1059 (1998).
13. J. Ellis, N. E. Mavromatos, and D. V. Nanopoulos, gr-qc/9904068: gr-qc/9906029: *General Relativity and Gravitation* (in press).
14. G. Amelino-Camelia, J. Ellis, N. E. Mavromatos, and D. V. Nanopoulos, Int. J. Mod. Phys. A **12**, 607 (1997).
15. B. E. Schaefer, Phys. Rev. Lett. **82**, 4964 (1999).
16. S. D. Biller *et al*., Phys. Rev. Lett. **83**, 2108 (1999).
17. P. Kaaret, Astron. Astrophys. **345**, L3 (1999).
18. I. Antoniadis, C. Bachas, J. Ellis, and D. V. Nanopoulos, Phys. Lett. B **211**, 393 (1988); Nucl. Phys. B **328**, 117 (1989).
19. I. I. Kogan, N. E. Mavromatos, and J. F. Wheater, Phys. Lett. B **387**, 483 (1996).
20. V. Gurarie, Nucl. Phys. B **410**, 535 (1993); J. S. Caux, I. I. Kogan, and A. V. Tsvelik, Nucl. Phys. B **466**, 444 (1996); M. A. I. Flohr, Int. J. Mod. Phys. A **11**, 4147 (1996); M. R. Gaberdiel and H. G. Kausch, Nucl. Phys. B **489**, 293 (1996); I. I. Kogan and N. E. Mavromatos, Phys. Lett. B **375**, 111 (1996); M. R. Rahimi-Tabar, A. Aghamohammadi, and M. Khorrami, Nucl. Phys. B **497**, 555 (1997); I. I. Kogan, A. Lewis, and O. A. Soloviev, Int. J. Mod. Phys. A **13**, 1345 (1998).
21. N. E. Mavromatos and R. Szabo, Phys. Rev. D **59**, 104018 (1999).
22. J. Ellis *et al*., Mod. Phys. Lett. A **13**, 303 (1998).
23. R. Gambini and J. Pullin, Phys. Rev. D **59**, 124021 (1999).
24. L. Ford, Phys. Rev. D **51**, 1692 (1995); H. Yu and L. Ford, gr-qc/9904082; gr-qc/9907037.
25. J. Ellis *et al*., astro-ph/9907340.
26. L. D. Landau and E. M. Lifshitz, in *Classical Theory of Fields* (Nauka, Moscow, 1973; Pergamon Press, London, 1975), Vol. 2, p. 257.
27. J. Ellis, N. E. Mavromatos, and D. V. Nanopoulos, Phys. Lett. B **293**, 142 (1992); J. Ellis, J. Lopez, N. E. Mavromatos, and D. V. Nanopoulos, Phys. Rev. D **53**, 3846 (1996).
28. R. Adler *et al*., Phys. Lett. B **364**, 239 (1995).
29. G. Ricker, in *Proceedings of Conference on Gamma-Ray Bursts in the Afterglow Era, Rome, November 1998*; Astron. Astrophys., Suppl. Ser. (in press).
30. K. Hurley, astro-ph/9812393.
31. AMS Collab. (S. Ahlen *et al*.), Nucl. Instrum. Methods Phys. Res. A **350**, 351 (1994).
32. E. D. Bloom *et al*. (GLAST Team), in *Proceedings of International Heidelberg Workshop on TeV Gamma-Ray Astrophysics*, Ed. by H. J. Volk and F. A. Aharonian (Kluwer, 1996), p. 109.
33. J. Lopez and D. V. Nanopoulos, Mod. Phys. Lett. A **9**, 2755 (1994); **11**, 1 (1996).
34. J. Ellis, N. E. Mavromatos, and D. V. Nanopoulos, gr-qc/9810086.

Physics of Atomic Nuclei, Vol. 63, No. 6, 2000, pp. 1097–1102. From Yadernaya Fizika, Vol. 63, No. 6, 2000, pp. 1172–1177.
Original English Text Copyright © 2000 by Colladay.

PHYSICS BEYOND THE STANDARD MODEL

Possible Spontaneous Breaking of Lorentz and *CPT* Symmetry*

D. Colladay
The College of Wooster, USA

Abstract—One possible ramification of unified theories of nature such as string theory that may underlie the conventional standard model is the possible spontaneous breakdown of Lorentz and *CPT* symmetry. In this talk, the formalism for inclusion of such effects into a low-energy effective field theory is presented. An extension of the standard model that includes Lorentz- and *CPT*-breaking terms is developed. The restriction of the standard model extension to the QED sector is then discussed. © *2000 MAIK “Nauka/Interperiodica”.*

1. INTRODUCTION AND MOTIVATION

Virtually all modern particle physics theories are constructed using Lorentz invariance as a basic axiom. Local point-particle field theories coupled with this assumed Lorentz invariance along with some mild technical assumptions leads one to conclude that *CPT* must also be preserved [1]. The standard model, its supersymmetric extensions, and grand unified models are all of this type.

However, if the fundamental theory underlying the standard model is constructed using nonlocal objects such as strings, Lorentz symmetry may be spontaneously broken in the low-energy limit of the full theory. An explicit mechanism of this type has been proposed in the context of string theory [2, 3]. The Lorentz- and *CPT*-violating terms are generated when tensor fields gain vacuum expectation values through spontaneous symmetry breaking.

The approach adopted here is to use the mechanism of spontaneous symmetry breaking to generate a list of possible Lorentz violating interactions between standard model fields. The standard model extension is then constructed by selecting those terms satisfying $SU(3) \times SU(2) \times U(1)$ gauge invariance and power-counting renormalizability [4]. By only using the property of spontaneous symmetry breaking and not referring to explicit details of the underlying theory, we are able to construct a general model of Lorentz breaking in the context of the conventional standard model.

Many experimental tests of Lorentz and *CPT* invariance have been performed, so it is useful to have a general theory with explicit parameters that can be used to relate the various experiments as well as motivate new ones. For example, high precision measurements involving atomic systems [5, 6], clock comparisons [7], and neutral meson oscillations [8, 9] provide stringent tests of Lorentz and *CPT* symmetry. The implications of *CPT*-violating terms on baryogenesis have also been investigated [10].

To describe spontaneous Lorentz and *CPT* breaking, it is convenient to first review the Higgs mechanism in the standard model. Conventional spontaneous symmetry breaking occurs in the Higgs sector of the standard model where the Higgs field obtains an expectation value, thereby partially breaking $SU(2) \times U(1)$ gauge invariance. This happens because an assumed potential for the Higgs field is minimized at some nonzero value of the field.

As an example, consider a simple Lagrangian describing a single fermion field ψ and a single scalar field ϕ of the form

$$\mathcal{L} = \mathcal{L}_0 - \mathcal{L}',$$

where

$$\mathcal{L}' \supset \lambda\phi\bar{\psi}\psi + \text{h.c.} - (\phi^\dagger\phi - a^2)^2. \qquad (1)$$

A nonzero vacuum expectation value $\langle\phi\rangle$ for the scalar field will minimize the energy, hence generating a mass for the fermion of $m_f = \lambda\langle\phi\rangle$. This expectation value to the scalar field breaks $SU(2) \times U(1)$ gauge invariance because $\langle\phi\rangle$ no longer transforms in a nontrivial way under this gauge group. Lorentz symmetry is maintained in this case because $\langle\phi\rangle$ and ϕ are both scalars under the action of the Lorentz group.

Suppose instead that a tensor T gains a nonzero vacuum expectation value, $\langle T\rangle$. Lorentz invariance is spontaneously broken in this case. To see how this form of symmetry breaking might occur, consider a Lagrangian describing a fermion ψ and a tensor T of the form

$$\mathcal{L} = \mathcal{L}_0 - \mathcal{L}',$$

where

$$\mathcal{L}' \supset \frac{\lambda}{M^k} T\bar{\psi}\Gamma(i\partial)^k\psi + \text{h.c.} + V(T). \qquad (2)$$

In this expression, λ is a dimensionless coupling, M is a heavy mass scale of the underlying theory, Γ denotes a general gamma matrix structure in the Dirac algebra, and $V(T)$ is a potential for the tensor field (indices are suppressed for notational simplicity). Terms contribut-

---

* This article was submitted by the author in English.

ing to $V(T)$ are precluded from conventional renormalizable four-dimensional field theories, but may arise in the low-energy limit of a more general theory such as string theory [2].

If the potential $V(T)$ is such that it has a nontrivial minimum, a vacuum expectation value $\langle T\rangle$ will be generated for the tensor field. There will then be a term of the form

$$\mathcal{L}' \supset \frac{\lambda}{M^k}\langle T\rangle\bar{\psi}\Gamma(i\partial)^k\psi + \text{h.c.} \tag{3}$$

present in the Lagrangian after spontaneous symmetry breaking occurs. These terms can break Lorentz invariance and various discrete symmetries *C*, *P*, *T*, *CP*, and *CPT*.

2. RELATIVISTIC QUANTUM MECHANICS AND FIELD THEORY

To develop theoretical techniques for treating generic terms of the type given in (3), we first study a specific example. The example presented here involves a Lagrangian for a single fermion field containing Lorentz-violating terms with no derivative couplings ($k = 0$) that also violate *CPT*.

We proceed by listing the possible gamma-matrix structures that could arise within such a term:

$$\Gamma \sim \{1, \gamma^\mu, \gamma^5\gamma^\mu, \sigma^{\mu\nu}, \gamma^5\}. \tag{4}$$

The condition that a fermion bilinear with no derivative couplings violates *CPT* is equivalent to the requirement that Γ be chosen such that $\{\Gamma, \gamma^5\} = 0$. Half the matrices in (4) satisfy this condition: $\Gamma \sim \gamma^\mu$ and $\Gamma \sim \gamma^5\gamma^\mu$. The contribution to the Lagrangian from these terms can be written as

$$\mathcal{L}'_a \equiv a_\mu\bar{\psi}\gamma^\mu\psi, \quad \mathcal{L}'_b \equiv b_\mu\bar{\psi}\gamma_5\gamma^\mu\psi, \tag{5}$$

where a_μ and b_μ are constant coupling that parametrize the tensor expectation values and relevant coupling constants arising in (3). These parameters are assumed suppressed with respect to other physically relevant energy scales in the low-energy effective theory in order to be in agreement with current experimental bounds.

Including these contributions from the spontaneous symmetry breaking mechanism into a theory containing a free Dirac fermion yields a model Lagrangian of

$$\mathcal{L} = \frac{i}{2}\bar{\psi}\gamma^\mu\overset{\leftrightarrow}{\partial}_\mu\psi - a_\mu\bar{\psi}\gamma^\mu\psi - b_\mu\bar{\psi}\gamma_5\gamma^\mu\psi - m\bar{\psi}\psi. \tag{6}$$

Several features of this modified theory are immediately apparent upon inspection. The first feature is that the Lagrangian is Hermitian, thereby leading to a theory obeying conventional quantum mechanics, conservation of probability, and unitarity. The second feature is that translational invariance implies the existence of a conserved energy and momentum. This conserved four-momentum is explicitly constructed as

$$P_\mu = \int d^3x\Theta^0_\mu = \int d^3x\frac{1}{2}i\bar{\psi}\gamma^0\overset{\leftrightarrow}{\partial}_\mu\psi, \tag{7}$$

just as in the conventional case. The third feature is that the Dirac equation resulting from fermion field allows an exact solution to the free theory. Finally, a global $U(1)$ invariance of the model Lagrangian implies the existence of a conserved current $j_\mu = \bar{\psi}\gamma^\mu\psi$.

The Dirac equation obtained by variation of (6) with respect to the fermion field is

$$(i\gamma^\mu\partial_\mu - a_\mu\gamma^\mu - b_\mu\gamma_5\gamma^\mu - m)\psi = 0. \tag{8}$$

Due to the linearity of the equation, plane-wave solutions

$$\psi(x) = e^{\pm ip_\mu x^\mu}w(\mathbf{p}), \tag{9}$$

are used to solve the equation exactly. Substitution of the planewave solution into the modified Dirac equation yields

$$\begin{aligned}(\pm p_\mu\gamma^\mu - a_\mu\gamma^\mu - b_\mu\gamma_5\gamma^\mu - m)w(\mathbf{p})\\ \equiv M_\pm w(\mathbf{p}) = 0.\end{aligned} \tag{10}$$

A nontrivial solution exists only if et $M_\pm = 0$. This imposes a condition on $p^0(\mathbf{p}) \equiv E(\mathbf{p})$, hence generating a dispersion relation for the fermion.

The general solution involves finding the roots of a fourth-order polynomial equation. The solutions can be found algorithmically, but the resulting solution is complex and not very illuminating. For simplicity, we consider only the special case of $\mathbf{b} = 0$ here. The exact dispersion relations for this case are

$$E_+(\mathbf{p}) = [m^2 + (|\mathbf{p} - \mathbf{a}| \pm b_0)^2]^{1/2} + a_0, \tag{11}$$

$$E_-(\mathbf{p}) = [m^2 + (|\mathbf{p} + \mathbf{a}| \mp b_0)^2]^{1/2} - a_0. \tag{12}$$

Examination of the above energies reveals several qualitative effects of the *CPT*-violating terms. The usual four-fold energy degeneracy of spin-1/2 particles and antiparticles is removed by the a_μ and b_0 terms. The particle–antiparticle energy degeneracy is broken by a_μ, and the helicity degeneracy is split by b_0. The corresponding spinor solutions $w(\mathbf{p})$ have been explicitly calculated, forming an orthogonal basis of states as expected.

An interesting feature of these solutions is the unconventional relationship that exists between momentum and velocity. A wave packet of positive helicity particles with four momentum $p^\mu = (E, \mathbf{p})$ has an expectation value of the velocity operator $\mathbf{v} = i[H, \mathbf{x}] = \gamma^0\boldsymbol{\gamma}$ of

$$\langle\mathbf{v}\rangle = \left\langle\frac{(|\mathbf{p} - \mathbf{a}| - b_0)}{(E - a_0)}\frac{(\mathbf{p} - \mathbf{a})}{|\mathbf{p} - \mathbf{a}|}\right\rangle. \tag{13}$$

Examination of the above velocity using a general dispersion relation reveals that $|v_j| < 1$ for arbitrary b_μ and that the limiting velocity as $\mathbf{p} \longrightarrow \infty$ is 1. This implies that the effects of the *CPT*-violating terms are mild enough to preserve causality in the theory. This will be verified independently using the perspective of field theory that will now be developed.

To quantize the theory, the general expansion for ψ in terms of its spinor components given by

$$\psi(x) = \int \frac{d^3p}{(2\pi)^3} \sum_{\alpha=1}^{2} \left[\frac{m}{E_u^{(\alpha)}} b_{(\alpha)}(\mathbf{p}) e^{-ip_u^{(\alpha)}x} u^{(\alpha)}(\mathbf{p}) + \frac{m}{E_v^{(\alpha)}} d^*_{(\alpha)}(\mathbf{p}) e^{ip_v^{(\alpha)}x} v^{(\alpha)}(\mathbf{p}) \right] \tag{14}$$

is promoted to an operator acting on a Hilbert space of basis states. The energy is calculated from (7) using conventional normal ordering. The result is a positive definite quantity (for $|a_0| < m$) provided the following nonvanishing anticommutation relations are imposed on the creation and annihilation operators:

$$\begin{aligned} \{b_{(\alpha)}(\mathbf{p}), b^\dagger_{(\alpha')}(\mathbf{p}')\} &= (2\pi)^3 \frac{E_u^{(\alpha)}}{m} \delta_{\alpha\alpha'} \delta^3(\mathbf{p} - \mathbf{p}'), \\ \{d_{(\alpha)}(\mathbf{p}), d^\dagger_{(\alpha')}(\mathbf{p}')\} &= (2\pi)^3 \frac{E_v^{(\alpha)}}{m} \delta_{\alpha\alpha'} \delta^3(\mathbf{p} - \mathbf{p}'). \end{aligned} \tag{15}$$

The resulting equal-time anticommutators for the fields are

$$\begin{aligned} \{\psi_\alpha(t, \mathbf{x}), \psi^\dagger_\beta(t, \mathbf{x}')\} &= \delta_{\alpha\beta} \delta^3(\mathbf{x} - \mathbf{x}'), \\ \{\psi_\alpha(t, \mathbf{x}), \psi_\beta(t, \mathbf{x}')\} &= 0, \\ \{\psi^\dagger_\alpha(t, \mathbf{x}), \psi^\dagger_\beta(t, \mathbf{x}')\} &= 0. \end{aligned} \tag{16}$$

These relations show that conventional Fermi statistics remain unaltered in the presence of Lorentz- and *CPT*-violating terms.

The conserved charge Q and four-momentum P^μ are computed as

$$Q = \int \frac{d^3p}{(2\pi)^3} \sum_{\alpha=1}^{2} \left[\frac{m}{E_u^{(\alpha)}} b^\dagger_{(\alpha)}(\mathbf{p}) b_{(\alpha)}(\mathbf{p}) - \frac{m}{E_v^{(\alpha)}} d^\dagger_{(\alpha)}(\mathbf{p}) d_{(\alpha)}(\mathbf{p}) \right], \tag{17}$$

$$P_\mu = \int \frac{d^3p}{(2\pi)^3} \sum_{\alpha=1}^{2} \left[\frac{m}{E_u^{(\alpha)}} p^{(\alpha)}_{u\mu} b^\dagger_{(\alpha)}(\mathbf{p}) b_{(\alpha)}(\mathbf{p}) + \frac{m}{E_v^{(\alpha)}} p^{(\alpha)}_{v\mu} d^\dagger_{(\alpha)}(\mathbf{p}) d_{(\alpha)}(\mathbf{p}) \right]. \tag{18}$$

From these expressions, we see that the charge of the fermion is unperturbed and the energy and momentum satisfy the same relations that are found using relativistic quantum mechanics.

Causality is governed by the anticommutation relations of the fermion fields at unequal times. Explicit integration in the special case $\mathbf{b} = 0$ proves that

$$\{\psi_\alpha(x), \bar{\psi}_\beta(x')\} = 0, \tag{19}$$

for spacelike separations $(x - x')^2 < 0$. The above result shows that physical observables separated by spacelike intervals will in fact commute (for case $\mathbf{b} = 0$). This agrees with our previous results obtained by examination of the velocity using relativistic quantum mechanics.

Next, the problem of extending the free field theory to interacting theory is addressed. Much of the conventional formalism developed for perturbative calculations in the interacting theory carries over directly to the present case. The main reason that these techniques work is that the Lorentz-violating modifications which are introduced are linear in the fermion fields. The main result is that the usual Feynman rules apply provided the Feynman propagator is modified to

$$S_F(p) = \frac{i}{p_\mu\gamma^\mu - a_\mu\gamma^\mu - b_\mu\gamma_5\gamma^\mu - m}, \tag{20}$$

and the exact spinor solutions of the modified free fermion theory are used on the external legs of the diagrams.

3. EXTENSION OF THE STANDARD MODEL

In this section, the question of how to apply spontaneous symmetry breaking to generate Lorentz-violating terms using standard model fields is addressed. Our approach involves consideration of all possible terms that can arise from spontaneous symmetry breaking that satisfy power-counting renormalizability and preserve the $SU(3) \times SU(2) \times U(1)$ gauge invariance of the standard model [4]. Even with these constraints, terms are found to contribute to all sectors of the standard model. In listing the terms here, the Lorentz violating terms are classified according to their properties under the *CPT* transformation.

In the lepton sector, the left- and right-handed multiplets are defined as

$$L_A = \begin{pmatrix} \nu_A \\ l_A \end{pmatrix}_L, \quad R_A = (l_A)_R, \tag{21}$$

where $A = 1, 2, 3$ labels the flavor:

$$l_A \equiv (e, \mu, \tau), \quad \nu_A \equiv (\nu_e, \nu_\mu, \nu_\tau). \tag{22}$$

The Lorentz-violating terms that satisfy the required properties are

$$\mathcal{L}^{CPT\text{-even}}_{\text{lepton}} = \frac{1}{2}i(c_L)_{\mu\nu AB}\bar{L}_A\gamma^\mu \overleftrightarrow{D}^\nu L_B + \frac{1}{2}i(c_R)_{\mu\nu AB}\bar{R}_A\gamma^\mu \overleftrightarrow{D}^\nu R_B, \tag{23}$$

$$\mathcal{L}^{CPT\text{-odd}}_{\text{lepton}} = -(a_L)_{\mu AB}\bar{L}_A\gamma^\mu L_B - (a_R)_{\mu AB}\bar{R}_A\gamma^\mu R_B. \tag{24}$$

In the above expression $c_{\mu\nu}$ and a_μ are constant coupling coefficients related to the background expectation values of the relevant tensor fields, and D^μ is the conventional covariant derivative.

The final form of the standard model terms is different because the $SU(2) \times U(1)$ symmetry is broken by the Higgs mechanism. Once this breaking occurs, the fields in (24) are rewritten in terms of the physical Dirac spinors corresponding to the observed leptons and neutrinos. As an example, the *CPT*-odd lepton terms become

$$\mathcal{L}^{CPT\text{-odd}}_{\text{lepton}} = -(a_\nu)_{\mu AB}\bar{\nu}_A\frac{1}{2}(1+\gamma_5)\gamma^\mu\nu_B - (a_l)_{\mu AB}\bar{l}_A\gamma^\mu l_B - (b_l)_{\mu AB}\bar{l}_A\gamma_5\gamma^\mu l_B. \tag{25}$$

Note that b_μ coupling coefficients arise in the process of combining the right- and left-handed fields into Dirac spinors.

If we now examine the first generation electron contribution corresponding to $A = B = 1$, we find the terms

$$\mathcal{L}^{CPT\text{-odd}}_{\text{lepton}} \supset -(a_l)_{\mu 11}\bar{e}\gamma^\mu e - (b_l)_{\mu 11}\bar{e}\gamma_5\gamma^\mu e. \tag{26}$$

These terms are exactly the form as the contributions to the model Lagrangian of (6) that were analyzed in the previous section. The relativistic quantum mechanics and field theoretic techniques that were developed to handle these terms are therefore directly applicable to electrons. Terms in (25) of the form $A \neq B$ contribute small lepton flavor-changing amplitudes.

The construction of the standard model extension in the quark sector is similar to that in the lepton sector. The main difference is that corresponding right-handed quark fields are present for each left-handed field unlike the case in the lepton sector. The left- and right-handed quark multiplets are denoted by

$$Q_A = \begin{pmatrix} u_A \\ d_A \end{pmatrix}_L, \quad U_A = (u_A)_R, \quad D_A = (d_A)_R, \tag{27}$$

where $A = 1, 2, 3$ labels quark flavor

$$u_A \equiv (u, c, t), \quad d_A \equiv (d, s, b). \tag{28}$$

The Lorentz-violating terms in the quark sector are of the same form as in the lepton sector. The diagonal $A = B$ terms are again of the same form as (5). The quark a_μ terms are particularly interesting because they can lead to observable *CPT*-violating effects in neutral meson systems [11].

In the Higgs sector, there are contributions involving two Higgs fields and generalized Yukawa coupling terms involving a single Higgs and two fermion fields. The Lorentz-violating terms that are quadratic in the Higgs fields are

$$\mathcal{L}^{CPT\text{-even}}_{\text{Higgs}} = \frac{1}{2}(k_{\phi\phi})^{\mu\nu}(D_\mu\phi)^\dagger D_\nu\phi + \text{h.c.} - \frac{1}{2}(k_{\phi B})^{\mu\nu}\phi^\dagger\phi B_{\mu\nu} - \frac{1}{2}(k_{\phi W})^{\mu\nu}\phi^\dagger W_{\mu\nu}\phi, \tag{29}$$

$$\mathcal{L}^{CPT\text{-odd}}_{\text{Higgs}} = i(k_\phi)^\mu\phi^\dagger D_\mu\phi + \text{h.c.}, \tag{30}$$

where $W_{\mu\nu}$ and $B_{\mu\nu}$ are the field strengths for the $SU(2)$ and $U(1)$ gauge fields and the various k parameters are coupling constants related to tensor expectation values.

The Yukawa type terms involving one Higgs field are

$$\mathcal{L}^{CPT\text{-even}}_{\text{Yukawa}} = -\frac{1}{2}[(H_L)_{\mu\nu AB}\bar{L}_A\phi\sigma^{\mu\nu}R_B + (H_U)_{\mu\nu AB}\bar{Q}_A\phi^c\sigma^{\mu\nu}U_B + (H_D)_{\mu\nu AB}\bar{Q}_A\phi\sigma^{\mu\nu}D_B] + \text{h.c.}, \tag{31}$$

where the H parameters are related to tensor expectation values.

One interesting result of including these terms into the standard model is a modification of the conventional $SU(2) \times U(1)$ breaking. When the full static potential is minimized, the Z^0 boson gains an expectation value of

$$\langle Z^0_\mu \rangle = \frac{1}{q}\sin 2\theta_W(\text{Re}\hat{k}_{\phi\phi})^{-1}_{\mu\nu}k^\nu_\phi, \tag{32}$$

where $\hat{k}^{\mu\nu}_{\phi\phi} = \eta^{\mu\nu} + k^{\mu\nu}_{\phi\phi}$, q is the electric charge, and θ_W is the weak mixing angle. If the *CPT*-odd term k_ϕ vanishes, then $\langle Z^0_\mu \rangle = 0$. This is reasonable since a nonzero value of $\langle Z^0_\mu \rangle$ violates *CPT* symmetry.

The gauge sector is the final sector to be examined. The various Lorentz-breaking terms satisfying the relevant criteria are

$$\mathcal{L}^{CPT\text{-even}}_{\text{gauge}} = -\frac{1}{2}(k_G)_{\kappa\lambda\mu\nu}\text{Tr}(G^{\kappa\lambda}G^{\mu\nu}) - \frac{1}{2}(k_W)_{\kappa\lambda\mu\nu}\text{Tr}(W^{\kappa\lambda}W^{\mu\nu}) - \frac{1}{4}(k_B)_{\kappa\lambda\mu\nu}B^{\kappa\lambda}B^{\mu\nu}, \tag{33}$$

$$\mathcal{L}^{CPT\text{-odd}}_{\text{gauge}} = k_{3\kappa}\epsilon^{\kappa\lambda\mu\nu}\text{Tr}\left(G_\lambda G_{\mu\nu} + \frac{2i}{3}G_\lambda G_\mu G_\nu\right) + k_{2\kappa}\epsilon^{\kappa\lambda\mu\nu}\text{Tr}\left(W_\lambda W_{\mu\nu} + \frac{2i}{3}W_\lambda W_\mu W_\nu\right) + k_{1\kappa}\epsilon^{\kappa\lambda\mu\nu}B_\lambda B_{\mu\nu}. \tag{34}$$

In these expressions, the k terms are constant coupling constants and the $G^{\mu\nu}$, $W^{\mu\nu}$, and $B^{\mu\nu}$ are the field strengths for the $SU(3)$, $SU(2)$, and $U(1)$ gauge fields respectively.

The *CPT*-odd terms can generate negative contributions to the conserved energy [12], hence creating an instability in the theory. It is therefore desirable to set these coefficients to zero, provided they remain zero at the quantum level. This procedure has been carried out to the one-loop level by utilizing an anomaly cancellation mechanism that must be inherited from any consistent theory underlying the standard model [4]. This point is discussed further in the following section.

4. QED RESTRICTION

We now restrict our attention to the theory of electrons and photons that results from the above extension of the standard model. The conventional QED Lagrangian is

$$\mathcal{L}^{\mathrm{QED}}_{\mathrm{electron}} = \frac{1}{2}i\bar{\psi}\gamma^{\mu}\overleftrightarrow{D}_{\mu}\psi - m_e\bar{\psi}\psi - \frac{1}{4}F_{\mu\nu}F^{\mu\nu}, \qquad (35)$$

where ψ is the electron field, m_e is its mass, and $F^{\mu\nu}$ is the photon field strength tensor.

The *CPT*-even electron terms that violate Lorentz symmetry in the full standard model extension are

$$\begin{aligned}\mathcal{L}^{CPT\text{-even}}_{\mathrm{electron}} = & -\frac{1}{2}H_{\mu\nu}\bar{\psi}\sigma^{\mu\nu}\psi + \frac{1}{2}ic_{\mu\nu}\bar{\psi}\gamma^{\mu}\overleftrightarrow{D}^{\nu}\psi \\ & + \frac{1}{2}id_{\mu\nu}\bar{\psi}\gamma_5\gamma^{\mu}\overleftrightarrow{D}^{\nu}\psi,\end{aligned} \qquad (36)$$

where H, c, and d are constant coupling coefficients. The *CPT*-odd electron terms are

$$\mathcal{L}^{CPT\text{-odd}}_{\mathrm{electron}} = -a_{\mu}\bar{\psi}\gamma^{\mu}\psi - b_{\mu}\bar{\psi}\gamma_5\gamma^{\mu}\psi, \qquad (37)$$

where a and b are parameters analogous to those in (5) applied to electrons.

Experiments involving conventional QED tests can be used to place stringent bounds on the above violation parameters. For example, Penning traps may be used to compare energy levels of e^- and e^+ or p and $\bar{p}$ orbits to constrain various combinations of parameters to a few parts in 10^{20} [6]. In addition, tests involving comparison of hydrogen and antihydrogen $1S$–$2S$ and hyperfine transitions can place comparable bounds on other combinations of parameters [13].

The corrections to the photon from the gauge sector are given by

$$\mathcal{L}^{CPT\text{-even}}_{\mathrm{photon}} = -\frac{1}{4}(k_F)_{\kappa\lambda\mu\nu}F^{\kappa\lambda}F^{\mu\nu} \qquad (38)$$

and

$$\mathcal{L}^{CPT\text{-odd}}_{\mathrm{photon}} = +\frac{1}{2}(k_{AF})^{\kappa}\epsilon_{\kappa\lambda\mu\nu}A^{\lambda}F^{\mu\nu}, \qquad (39)$$

where the parameters k_F and k_{AF} are the appropriate linear combinations of parameters in (33) and (34) that result when the photon is defined as the unbroken $U(1)$ electric force mediator.

A stringent limit of $(k_{AF})^{\mu} < 10^{-42}$ GeV has been placed on the *CPT*-odd term using cosmological birefringence tests [12]. Coupled with the theoretical difficulties involving negative contributions to the energy, this experimental bound indicates that this coefficient should be set identically to zero in the theory. At first sight, radiative corrections appear to induce a nonzero term at the quantum level. However, such corrections must cancel provided the underlying theory is anomaly free.

The only QED correction term with matching C, P, and T symmetry properties that contributes to $(k_{AF})^{\mu}$ is b^{μ}. The one-loop diagram produces an ambiguous, finite, and regularization dependent correction of $(k_{AF})^{\mu} = \zeta b^{\mu}$, where ζ is an arbitrary constant [4]. When this correction is summed over all fermion species, the contributions must cancel provided there is no anomaly in the full underlying theory. A zero result to lowest order in b^{μ} has also been argued as a consistent choice using arguments based on the gauge invariance of the Lagrangian [14]. Several other recent works have shown similar results in various regularization schemes [15].

More recently, a calculation to all orders in b^{μ} using the exact modified propagator has been carried out [16]. Remarkably, the full result is the same as the correction generated by the linear term. This means that the anomaly cancellation mechanism applies to all orders in b^{μ} and the coefficient $(k_{AF})^{\mu}$ remains zero at the quantum level.

The *CPT*-even terms are more interesting for several reasons. First, the total canonical energy is positive provided the couplings are reasonably suppressed. Secondly, the contribution to cosmological birefringence is suppressed relative to the *CPT*-odd term. Constraints of a few parts in 10^{23} have been obtained on the rotationally invariant term using cosmic-ray tests [14]. More general terms can be bounded to $k_F \le 10^{-28}$ using cosmological birefringence measurements [4].

5. SUMMARY

A framework has been presented that incorporates Lorentz- and *CPT*-violating effects into the context of conventional quantum field theory. Using a generic spontaneous symmetry-breaking mechanism as the source for these terms, an extension of the standard model that includes Lorentz and *CPT* breaking was developed. This extension preserves power-counting renormalizability and $SU(3) \times SU(2) \times U(1)$ gauge invariance. The parameters that have been introduced can be used to establish quantitative bounds on *CPT*- and Lorentz-breaking effects in nature. Implications for electron and photon propagation in the QED sector were discussed.

This work was supported in part by the United-States Department of Energy under grant number DE-FGO2-91ER40661.

REFERENCES

1. See, for example, J. Schwinger, Phys. Rev. **82**, 914 (1951).
2. V. A. Kostelecký and S. Samuel, Phys. Rev. D **39**, 683 (1989); Phys. Rev. Lett. **63**, 224 (1989); Phys. Rev. D **40**, 1886 (1989).
3. V. A. Kostelecký and R. Potting, Nucl. Phys. B **359**, 545 (1991); Phys. Lett. B **381**, 389 (1996).
4. D. Colladay and V. A. Kostelecký, Phys. Rev. D **55**, 6760 (1997); Phys. Rev. D **58**, 116002 (1998).
5. See, for example, R. S. van Dyck, Jr., P. B. Schwinberg, and H. G. Dehmelt, Phys. Rev. Lett. **59**, 26 (1987); G. Gabrielse *et al.*, Phys. Rev. Lett. **74**, 3544 (1995).
6. R. Bluhm, V. A. Kostelecký, and N. Russel, Phys. Rev. Lett. **79**, 1432 (1997); Phys. Rev. D **57**, 3932 (1998).
7. See, for example, J. D. Prestage *et al.*, Phys. Rev. Lett. **54**, 2387 (1985); S. K. Lamoreaux *et al.*, Phys. Rev. Lett. **57**, 3125 (1986); T. E. Chupp *et al.*, Phys. Rev. Lett. **63**, 1541 (1989).
8. B. Schwingenheuer *et al.*, Phys. Rev. Lett. **74**, 4376 (1995); L. K. Gibbons *et al.*, Phys. Rev. D **55**, 6625 (1997); R. Carosi *et al.*, Phys. Lett. B **237**, 303 (1990).
9. OPAL Collab. (R. Ackerstaff *et al.*), Z. Phys. C **76**, 401 (1997); DELPHI Collab. (M. Feindt *et al.*), Preprint No. 97-98, DELPHI (Geneva, 1997).
10. O. Bertolami *et al.*, Phys. Lett. B **395**, 178 (1997).
11. See, for example, V. A. Kostelecký, Phys. Rev. Lett. **80**, 1818 (1998).
12. S. M. Carroll, G. B. Field, and R. Jackiw, Phys. Rev. D **41**, 1231 (1990).
13. R. Bluhm, V. A. Kosteleský, and N. Russell, Phys. Rev. Lett. **82**, 2254 (1999).
14. S. Coleman and S. Glashow, Phys. Rev. D **59**, 116008 (1999).
15. R. Jackiw and V. A. Kostelecký, Phys. Rev. Lett. **82**, 3572 (1999); J.-M. Chung and P. Oh, hep-th/9812132; W. F. Chen, hep-th/9903258.
16. M. Perez-Victoria, hep-th/9905061; J.-M. Chung, hep-th/9905095.

Physics of Atomic Nuclei, Vol. 63, No. 6, 2000, pp. 1103–1109. From Yadernaya Fizika, Vol. 63, No. 6, 2000, pp. 1178–1184.
Original English Text Copyright © 2000 by Gugluelmi.

NEUTRINO PHYSICS AT ACCELERATORS

Perspectives for Neutrino Physics at CERN*

A. Guglielmi**

Istituto Nazionale di Fisica Nucleare and Department of Physics "G. Galilei", Padova, Italy

Abstract—The experimental status of neutrino oscillation searches at accelerators is presented, and the future medium and long baseline projects at CERN are discussed, including the knowledge on the neutrino beam production. Perspectives on future neutrino factories based on muon storage rings are also presented. *© 2000 MAIK "Nauka/Interperiodica".*

1. INTRODUCTION

Neutrino oscillation studies offer an exciting scenario from the observed anomalies in neutrino fluxes from the Sun [1] and cosmic-ray interactions in the Earth's atmosphere [2, 3]. The measured solar ν_e fluxes are significantly lower than expected, and the observed atmospheric neutrino fluxes have shown a ν_μ to ν_e ratio which is approximately half of the expected one with, in addition, an anomaly in the up-going/down-going μ produced by ν_μ interactions [3]. The probability of oscillations $\nu_\alpha \longrightarrow \nu_\beta$ between neutrinos of different flavor,

$$P = \sin^2 2\theta_{ij} \sin^2\left(1.27\frac{L(\mathrm{km})}{E(\mathrm{GeV})}\Delta m_{ij}^2(\mathrm{eV}^2)\right), \qquad (1)$$

where θ_{ij} is the mixing angle between ν_i and ν_j mass eigenstates which differ by $\Delta m_{ij}^2 = m_i^2 - m_j^2$ and E is the energy of neutrinos traveling over a distance L, could account for those anomalies with $\Delta m^2 \le 10^{-5}$ eV^2 and $\Delta m^2 \sim 10^{-2}$–10^{-3} eV^2, respectively. The Super-Kamiokande results on atmospheric neutrinos exclude $\nu_\mu \longrightarrow \nu_e$ oscillations down to the level of 10^{-3} eV^2 and explain the observed data in terms of $\nu_\mu \longrightarrow \nu_\tau$ [3]. Moreover the conjectured dark matter in the Universe needed to explain the rotational velocity of galaxies could be constituted of neutrinos with masses of the order of eV.

Neutrino oscillation searches have been carried out in the last 20 yr at nuclear reactors and accelerators with negative results. Recently, the LSND experiment [4] observed a $\bar{\nu}_\mu \longrightarrow \bar{\nu}_e$ oscillation signal in a $\bar{\nu}_\mu$ beam with $\Delta m^2 \ge 10^{-1}$ eV^2. The advantage of experiments at accelerators derives from the possibility to generate intense fluxes of neutrinos with good control of their energy spectra and composition. Different regions of the $(\sin^2 2\theta, \Delta m^2)$ plane are at present explored depending on the neutrino energy E and distance L between neutrino source and detector (Table 1).

The short-baseline experiments CHORUS [5] and NOMAD [6] are exploring the Δm^2 region of cosmological interest looking for ν_τ appearance in the WANF ν_μ beam of SPS-CERN (Table 1), where the ν_τ contamination is negligible, using two complementary methods. CHORUS based its search on the detection of the kink due to the short lived τ^- decay, while NOMAD uses the measured kinematic characteristics of the events reconstructing the missing transverse momentum due to the undetected neutrino(s) produced in τ decays. No evidence for $\nu_\mu \longrightarrow \nu_\tau$ oscillations was found in a large fraction of the collected data by both experiments during the years 1994–1998 to provide new limits for $\nu_\mu \longrightarrow \nu_\tau$ oscillations (Fig. 1). Detailed studies including also recent results are described elsewhere [7].

LSND [4] and KARMEN [8] medium-baseline experiments were performed at the Los Alamos Meson Physics Facility and at the Neutron Spallation Facility of the Rutherford Appleton Laboratory, respectively (Table 1). Both use a 800-MeV/*c* proton beam hitting a target located next to a beam dump where most of the produced π^+ come to rest, giving rise to the decay chain

Table 1. Present neutrino oscillation experiments at accelerators. (E_ν's are given for π^+ and μ^+ decays at rest for LSND and KARMEN. The average E_ν value is quoted for NOMAD, CHORUS and K2K. *D* is the proton target to detector distance.)

Experiment	Accelerator	Beam	E_ν, GeV	*D*, km
NOMAD	SPS-CERN	ν_μ	24	0.84
CHORUS	SPS-CERN	ν_μ	26	0.82
LSND	Los Alamos	$\bar{\nu}_\mu$ (ν_μ)	0–0.052(0.03)	0.03
KARMEN	Appl. Ruth.	$\bar{\nu}_\mu$ (ν_μ)	0–0.052(0.03)	0.018
K2K	PS-KEK	ν_μ	1.5	250

---

* This article was submitted by the author in English.

** e-mail: guglielmi@pd.infn.it

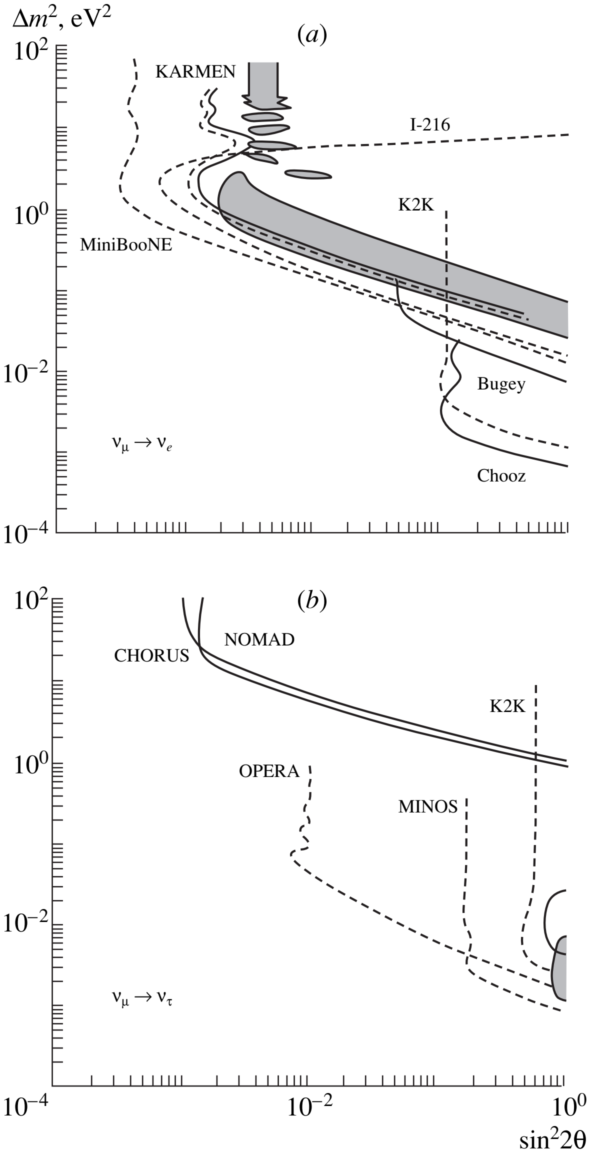

Fig. 1. (*a*) $\nu_\mu \longrightarrow \nu_e$: LSND (gray, 99% C.L.) allowed region and the KARMEN, Bugey, Chooz (90% C.L., full line) excluded regions compared to the expected sensitivity from K2K, KARMEN, I-216 and MiniBooNE (dashed line) experiments. (*b*) $\nu_\mu \longrightarrow \nu_\tau$: Kamiokande, Super-Kamiokande (gray) 90% allowed region and CHORUS, NOMAD excluded regions compared to the expected sensitivity at 4σ of K2K, OPERA, and MINOS.

$\pi^+ \longrightarrow \mu^+\nu_\mu$, $\mu^+ \longrightarrow \bar{\nu}_\mu e^+ \nu_e$, while π^- are absorbed. Neutrinos are detected in liquid scintillator (167 t LSND, 56 t KARMEN) instrumented with photomultipliers. The signature for $\bar{\nu}_\mu \longrightarrow \bar{\nu}_e$ oscillations via the reactions

$$\bar{\nu}_e p \longrightarrow e^+ n,\ np \longrightarrow d\gamma,\ E_{e^+} \le 52.8\ \text{MeV}, \qquad (2)$$

requires a spatially correlated and delayed coincidence of an e^+ with the γ emitted in *n* capture process (the $\bar{\nu}_e/\bar{\nu}_\mu$ contamination is totally negligible). LSND measured in the 1993–1998 data sample an excess of 39.5 ± 8.8 *e*, γ events, which corresponds to a $\bar{\nu}_\mu \longrightarrow \bar{\nu}_e$ oscillation probability

$$P(\bar{\nu}_\mu \longrightarrow \bar{\nu}_e) = (3.1 \pm 0.9(\text{stat.}) \pm 0.5(\text{syst.})) \times 10^{-3}, \qquad (3)$$

while KARMEN did not observe any $\bar{\nu}_e$ excess, resulting in a limit $P(\bar{\nu}_\mu \longrightarrow \bar{\nu}_e) \le 3.8 \times 10^{-3}$ at 90% C.L. (Fig. 1). The experiment will run until 2001, but the expected sensitivity $P(\bar{\nu}_\mu \longrightarrow \bar{\nu}_e) \le 2.6 \times 10^{-3}$ at 90% C.L. is not enough to fully verify the LSND result.

The first long-baseline neutrino oscillation experiment K2K [9] just started in Japan. It sends a wideband ν_μ beam with $E_\nu \sim 1.5$ GeV from KEK to the Super-Kamiokande detector 250 km away. A near detector, 1-kt water Cherenkov plus a fine grained detector, 300 m from the proton beam target, is used as a reference for the neutrino spectrum. Globally, ~380 ν_μ events are expected in Super-Kamiokande for a 10^{20} proton on target (p.o.t.) exposure. The $\nu_\mu \longrightarrow \nu_e$ ($\nu_\mu \longrightarrow \nu_\tau$) sensitivity using the appearance (disappearance) method, which, however, only partially covers the Δm^2 region of the atmospheric anomaly, is shown in Fig. 1.

2. PERSPECTIVES FOR NEUTRINO PHYSICS AT CERN

The typical values of LSND, $L/E \sim 30$ m/30 MeV, can be perfectly matched by experiments using a ν_μ beam with $E_\nu \sim 1$ GeV which can be produced at CERN PS and propagated over 1 km of distance.

Moreover, the SuperKamiokande results on the atmospheric ν's gave an additional boost to the world interest in accelerator long-baseline oscillation experiments. In Europe, the focus is on ν_τ appearance experiments using the high energy CNGS ν_μ beam from CERN SPS directed toward the Gran Sasso laboratory in Italy, 732 km from CERN.

2.1. Medium-Baseline Neutrino Beam at CERN: the I-216 $\nu_\mu \longrightarrow \nu_e$ Experiment

An intense ν_μ beam of 1.5 GeV of average energy with ν_e to ν_μ contamination of ~0.4% will be produced by the CERN PS, where π, *K* from 19.2 GeV/*c* protons interacting in a Be target will be focused by a pulsed magnetic horn into a 50-m long decay tunnel. The main characteristics of the proposed I-216 $\nu_\mu \longrightarrow \nu_e$ experiment are [10]

the high statistics of the collected data, 2.5×10^{20} p.o.t. for two years, a factor 10 more than all previous experiments at the PS;

the use of the close–far detector technique in order to compare the ratio of ν_e to ν_μ events in the close and in the far stations, largely canceling the systematics in the background subtraction;

the use of the quasi-elastic reactions only, $\nu_\mu n \longrightarrow \mu^- p$ (normalization) and $\nu_e n \longrightarrow e^- p$ (signal).

The apparatus would consist of three identical detector modules of 150 t each with a fine grain to detect e, μ, and π^0's; one will be positioned at 130 m (close detector) and two at 880 m (far detector) from the proton target. In two years, I-216 would collect 0.9×10^5 ν_μ events and 309 ν_e-like events in the far detector (248 from the ν_e contamination in the beam and only 61 from wrongly identified π^0's). The expected oscillation signal, for $\sin^2 2\theta = 0.006$ and $\Delta m^2 = 2$ eV^2, would add 295 ν_eCC events so that the difference between the ratio of ν_eCC-like to ν_μCC events in the far and in the near detector would be $\Delta = (3.1 \pm 0.29 \pm 0.10) \times 10^{-3}$, ten standard deviations from zero.

A similar project, MiniBooNe [11] at FNAL, will use a intense ν_μ beam with $E_\nu \sim 0.8$ GeV produced from the Booster (Table 2). The detector, 465 fiducial volume of pure mineral oil surrounded by 1220 phototubes, will be located 500 m from the proton target. Similarly to I-216, this experiment will try to identify the reactions $\nu_\mu \mathrm{C} \longrightarrow \mu^- N$, $\nu_e \mathrm{C} \longrightarrow e^- N$ rejecting $\nu_\mu \mathrm{C} \longrightarrow \nu_\mu \pi^0 X$, which constitutes the largest background to the electron signal. In one year of data taking, (5×10^{20} p.o.t.) ~ 5.9×10^5 ν_μ events will be collected with 3000 ν_e-like interactions plus 1200 ν_e extra events for $\sin^2 2\theta = 0.002$ and $\Delta m^2 = 0.4$ eV^2. The larger statistics of MiniBooNE is balanced in I-216 by a more direct control of the background obtained by the close–far detector technique. Both experiments will be able to confirm the LSND result or disprove it if no signal will be found.

2.2. *Long-Baseline Neutrino Beam at CERN: the CNGS Facility*

Similarly to its predecessor, the WANF, the CNGS ν_μ beam will be produced by the 400-GeV/c proton beam from CERN SPS hitting a new specially designed segmented graphite target [12]. The WANF experience allowed the choice for the focusing elements (horn and reflector); the decay tunnel will be 1 km long. The SPS will deliver ~4.5×10^{19} p.o.t./yr in "shared running" conditions, while an intensity of 7.6×10^{19} p.o.t./yr could be achieved in "dedicated running" conditions. The CNGS beam-line was optimized for the $\nu_\mu \longrightarrow \nu_\tau$ oscillation appearance (the ν_τ contamination is totally negligible). The expected ν_τCC event rate at the Gran Sasso is

$$R_\tau = N_\mathrm{A} M_d \int \phi_\mu(E) \sigma_\tau(E) P_\mathrm{osc}(E) dE, \qquad (4)$$

Table 2. Comparison of I-216 at PS-CERN with MiniBooNe at Booster-FNAL

	I-216	MiniBooNE
Proton momentum (GeV/c)	19.4	8
$\langle E_{\nu_\mu} \rangle$ (GeV)	1.5	0.8
ν_e/ν_μ (%)	0.4	0.3
Close detector:		
distance D (km)	0.13	–
ν_μ events	1.6×10^6	–
ν_e-like events	6813	–
ν_e signal events	680	–
Far detector:		
distance D (km)	0.88	0.50
ν_μ events	0.9×10^5	5.9×10^5
ν_e-like events	309	3000
ν_e signal events	295	1200

Table 3. Comparison of CNGS ν_μ beam with NuMI ν_μ beam at the detector site

	CNGS	NuMI		
Proton momentum (GeV/c)	400	120		
P. o. t./yr, 10^{19}	4.5	36		
Distance D (km)	732	730		
		Low E	Medium E	High E
$\langle E_{\nu_\mu} \rangle$ (GeV)	17	4	8	16
ν_μCC/(10^{19} p. o. t. kt)	540	13	39	87
ν_μCC/(kt yr)	2400	460	1400	3100

where ϕ_μ is the ν_μ flux at the detector site, P_osc is the $\nu_\mu \longrightarrow \nu_\tau$ oscillation probability, σ_τ is the ν_τCC interaction cross section, N_A is the Avogadro number, and M_d is the detector mass. Since σ_τ increases with the energy of ν_τ, the CNGS neutrino beam was designed maximizing $\int \phi(E) \sigma_\tau(E) P_\mathrm{osc}(E) dE$; i.e., the ϕ_μ fluence must match the quantity $\sigma_\tau P_\mathrm{osc}$ (Fig. 2 and Table 3).

Different experiments have been proposed for the oscillation search at the Gran Sasso using the SNGS beam.

The ICARUS detector [13], a modular 2.4 t liquid Argon TPC, will offer excellent imaging capability and calorimetry, good particle identification through dE/dx measurements, and an efficient e/π^0 separation. Because of the expected high resolution in measuring kinematic quantities, the $\nu_\mu \longrightarrow \nu_\tau$ appearance search will be performed by using methods analogous to those of the NOMAD experiment. The expected signal and

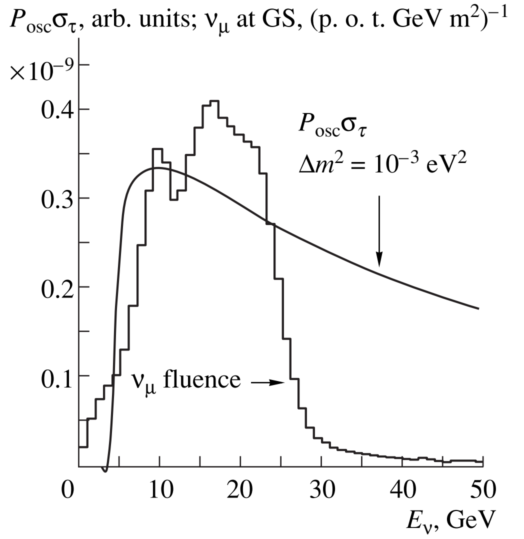

Fig. 2. Expected CNGS neutrino beam fluence at the Gran Sasso laboratory.

background rates for different Δm^2 values are quoted in Table 4 for 1.8×10^{20} p.o.t. A larger evolution of the project up to 30-kt module, SUPER-I, is also envisaged for a higher sensitivity to $\nu_\mu \longrightarrow \nu_\tau$ searches down to $\Delta m^2 \leq 10^{-3}$ eV^2 in the appearance mode and to study the $\nu_\mu \longrightarrow \nu_e$ transitions covering the LSND parameter region. With this apparatus, it will be also possible to explore the same Δm^2 region by using atmospheric neutrinos.

A complementary approach to $\nu_\mu \longrightarrow \nu_\tau$ searches is proposed by OPERA [14], 750-t lead/emulsion target modules subdivided in bricks of 8 kg mass. Each brick will consist of a sequence of 30 sandwiches. Each sandwich is composed of a 1-mm-thick lead plate followed by two 50-μm Emulsion Sheets (ES) spaced by 100 μm, a 3-mm gap, and two additional ES. The τ^-'s produced by CC reaction in the lead will decay within a few millimeters, hopefully in the 3-mm gap. In this case, the τ^- can be detected by measuring the angle between the charged daughter and the τ^- direction (kink). This requires the reconstruction of the track directions by means of the emulsion sheets downstream of the lead plate where the primary vertex occurred. Electronic detectors behind each target module will be used to identify the brick where the neutrino interaction took place and to guide the scanning. The apparatus will be completed by an instrumented toroid magnet, $B = 1.5$ T, for the μ^- identification and measurement of the hadronic showers tail. The expected sensitivity (Fig. 1, Table 4) is quite similar to ICARUS.

Table 4. Estimates of background and τCC events for different Δm^2 values by ICARUS, SUPER-I, and OPERA long-baseline experiments at the CNGS beam

Experiment	Backgr.	τCC events		
		Δm^2(eV^2): 2.5×10^{-3}	3.5×10^{-3}	5.0×10^{-3}
ICARUS	3.2	14	27	54
SUPER-I	4.8	71	139	278
OPERA	0.5	13	27	53

A parallel and complementary long-baseline neutrino oscillation program is in preparation at FNAL, where the NuMI ν_μ beam produced by 120 GeV/c protons of the Main Injector will be sent to the MINOS detector (3.3 kt of fiducial mass) at the Soudan mine [15]. Three different neutrino beams, low, medium, and high energy, have been designed (Table 3). Motivated by a first disappearance experiment, the MINOS project will use at first the low energy neutrino beam with a 100-t fiducial mass near detector (Fig. 1, 10 kt yr exposure). Despite the higher rate of p.o.t./yr, the expected ν_μCC/(kt yr) rate with the NuMI high energy beam is equivalent to CNGS beam due to the more favorable ν_μCC/(p.o.t./kt) of 400 GeV/c protons at CERN.

3. A CAVEAT: THE KNOWLEDGE OF NEUTRINO BEAM

High energy accelerators provide neutrino beams through the decay of π, K produced by high energy protons on light targets. It follows that a good knowledge of π and K production is required to predict the neutrino beam spectra and composition in oscillation experiments at accelerators. In particular, the accurate determination of the $K^\pm$ flux relative to the $\pi^\pm$ flux ($K^\pm/\pi^\pm$) is essential to predict the fraction of the ν_e content in the ν_μ beam and to improve the sensitivity of the oscillation searches. Monte Carlo generators of hadronic interactions based on different models are available to simulate the proton target interactions: GEANT-FLUKA [16] and GEANT-GHEISHA [17] as implemented in the GEANT 3.21 package [18], and the FLUKA standalone code [19], which has undergone a continuous development in the last years. The comparison between the predictions for π, K production obtained using these generators for proton interactions in Be at 450 GeV/c and the experimental measurements performed by Atherton *et al.* [20] and recently by the SPY Collaboration [21] is of particular interest for the neutrino beam simulations.

Large discrepancies between the π, K spectra generated with GEANT-FLUKA and the measured data were observed for momenta above 50 GeV/c, especially for negative particles [22] (Figs. 3, 4). A better agreement was found generating π and K with FLUKA, which reproduces the measured K^+/π^+(K^-/π^-) ratio to better than 10% (20%) in the momentum region 30–100 GeV/c, which mainly contribute to the neutrino flux at WANF of CERN SPS. The GEANT-GHEISHA package

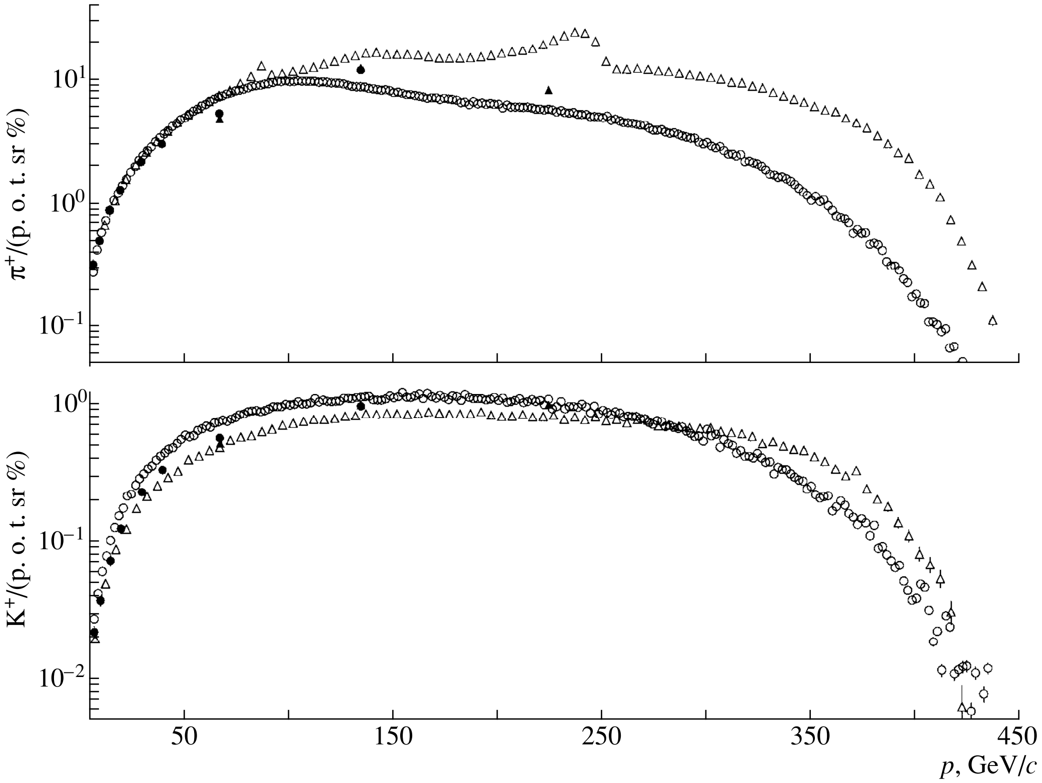

Fig. 3. The forward direction π^+ and K^+ yields from 100-mm Be target as measured by SPY ($p \leq 135$ GeV/c, ●) and Atherton *et al.* ($p \geq 67.5$ GeV/c, ▲)) compared with the FLUKA (○) and the GEANT-FLUKA (△) predictions. The Atherton *et al.* points have been rescaled accounting for the different primary proton momentum, $p = 400$ GeV/c.

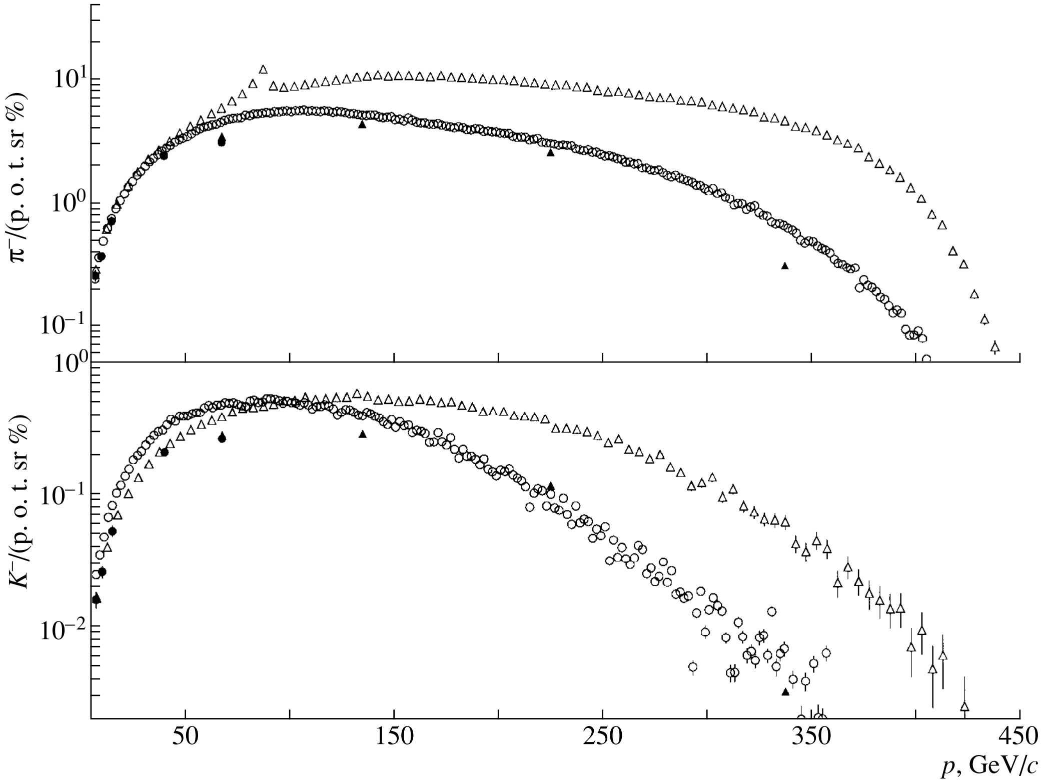

Fig. 4. The momentum dependence of the forward π^- and K^- yields (see Fig. 3 for the symbols).

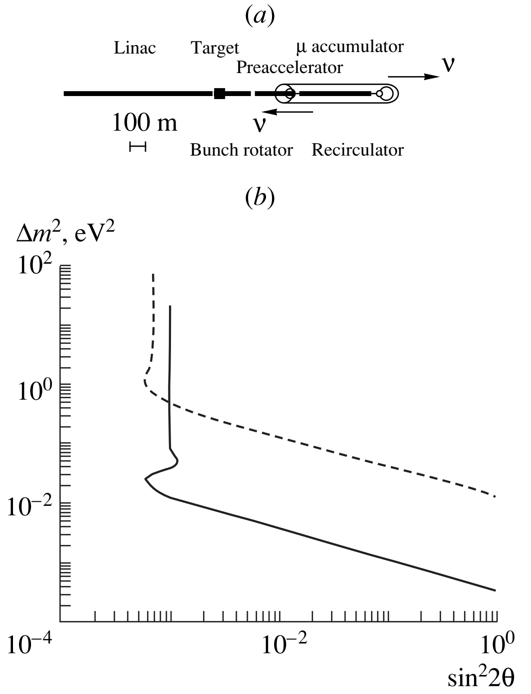

Fig. 5. (*a*) A possible layout for the neutrino factory (*b*) and the expected sensitivity at 90% C.L. for $\nu_\mu \longrightarrow \nu_e$ medium baseline (dashed line) and $\nu_\mu \longrightarrow \nu_\tau$ long-baseline (full line).

proved to be unsuitable for precise studies of neutrino beams [22].

Both GEANT-FLUKA and FLUKA generators were used to simulate the WANF neutrino beam at CERN SPS. Globally π^+, K^+, (π^-, K^-) fluxes from the 2-m-long Be target, inside the angular acceptance of the WANF beam line, had to be reduced by more than 10% (18%) by using FLUKA instead of GEANT-FLUKA, with large discrepancies on the spectrum shapes. As a consequence a 12% reduction of ν_μCC/p.o.t. with a 26% decrease of $\bar{\nu}_\mu$CC contamination at the NOMAD detector was predicted with the FLUKA generator with respect to GEANT-FLUKA. Preliminary comparisons of the measured and predicted ν_μ and $\bar{\nu}_\mu/\nu_\mu$ interactions in NOMAD using FLUKA for the ν-beam simulation instead of GEANT-FLUKA showed a better agreement. However, further corrections to the meson production based on the residual differences between the predicted and measured yields in beryllium should be done in order to reach a better accuracy for the neutrino beam description. The NOMAD and CHORUS neutrino interaction data will provide an important benchmark for neutrino beam studies.

4. A POSSIBLE NEUTRINO OSCILLATION SOLUTION

Neutrino experiments at accelerators suffer from beam knowledge coming mainly from the uncertainties on the hadronic processes involved at generation. As an alternative approach to overcome this difficulty, neutrino beam production by muon decay from a pure muon beam is being considered, since this is a perfectly well-known weak process.

The basic concepts for a muon collide were introduced by Budker in 1969 and Skrinsky in 1971 [23] and then developed inside the Muon Collider Collaboration in the United States. The μ lifetime at rest is 2.2 μs, and its decay length ($c\tau$) 660 m. It may nevertheless be possible to have high-energy muon beams: for an average acceleration of 1 MeV/m, the muon acceleration from 250 MeV/*c* up to 2.5 TeV/*c* takes 8 ms over 2500 km, and 25% of the muon beam survives, the losses being the most severe at the beginning of the acceleration. Recently a prospective study at CERN proposed a scenario with three successive steps [24]:

1. Neutrino factory.
2. Higgs factory.
3. Muon collider for the high energy frontiers.

A tentative layout for a neutrino factory is given in Fig. 5. Protons are accelerated up to 2 GeV/*c* by a Linac to produce π's in a light target. Muons originating from π decay are conveyed and accelerated up to 20 GeV/*c* in the recirculator, which is composed of a 500-m-long (10 MeV/m) Linac and a "petal arc" transport system ($B \sim 1.2$ T) at both ends. Then muons will be injected in the μ accumulator, which will deliver, through the processes $\mu^+ \longrightarrow e^+\nu_e\bar{\nu}_\mu$ ($\mu^- \longrightarrow e^-\bar{\nu}_e\nu_\mu$), a pure beam of an equal number of $\bar{\nu}_\mu$, ν_e(ν_μ, $\bar{\nu}_e$), two neutrinos per μ decay, with a perfectly calculable 1–10 GeV energy spectra. The intensity is estimated to be more than 100 times the corresponding from the π, *K* decay in classical beams.

The neutrino factory lends itself naturally to the exploration of neutrino oscillations between all neutrino flavors with high sensitivity to small mixing amplitude, $\sin^2 2\theta_{ij}$, and small mass differences, Δm^2_{ij} (see Table 5). In particular $\nu_\mu \longrightarrow \nu_e$ oscillations can be studied in appearance mode with neutrino beams where the neutrino type which is searched for is totally absent. The combination of the different oscillation transitions will allow complementary information on the ν_e, ν_μ, ν_τ mixing for the matrix elements. Potentially, a *CP* violation test is envisaged by comparing $\nu_e \longrightarrow \nu_\mu$ and $\bar{\nu}_\mu \longrightarrow \bar{\nu}_e$ oscillation rate at the same time with the same detector.

Expected sensitivities using such a neutrino factory for a $\nu_\mu \longrightarrow \nu_e$ medium-baseline experiment at CERN and a $\nu_\mu \longrightarrow \nu_\tau$ long-baseline experiment from CERN to Gran Sasso laboratory is shown in Fig. 5. The former was determined by assuming the use of the CERN PS as a proton source and muons accelerated to 7 GeV/*c*. The NOMAD detector (2.7 t of target) located at 3.5 km from the ν source will be sufficient to fully investigate

Table 5. Oscillation channel accessible at a muon factory

Oscillation channel	Experimental signature
$\nu_e \longrightarrow \nu_\mu$	Appearance mode: detection of wrong-sing muons, μ^-
$\bar{\nu}_\mu \longrightarrow \bar{\nu}_e$	Appearance mode: detection of wrong-sing electrons, μ^+
$\nu_e \longrightarrow \nu_x$	Disappearance mode: energy spectrum and NC/CC
$\bar{\nu}_\mu \longrightarrow \bar{\nu}_x$	Disappearance mode: energy spectrum and NC/CC
$\nu_e \longrightarrow \nu_\tau$	Appearance mode: detection of τ^- events
$\bar{\nu}_\mu \longrightarrow \bar{\nu}_\tau$	Appearance mode: detection of τ^+ events

the LSND result with just 4×10^{19} μ^- decays. The $\nu_\mu \longrightarrow \nu_\tau$ calculation refers to a 20 GeV/c muon beam, 3×10^{21} μ^- decays, 1-kt detector, and 25% τ^- detection efficiency.

Due to the expected high luminosity of a muon storage ring, a very long-baseline experiment, $L \sim 5000$ km, $E_\nu \sim 10$ GeV, will be also possible in order to explore $\nu_\mu \longrightarrow \nu_\tau$ with $\Delta m^2 < 10^{-3}$ eV^2 and to look for matter effects inside the Earth which could lead to observable effects in $\nu_\mu \longrightarrow \nu_e$ transitions.

ACKNOWLEDGMENTS

It's a real pleasure to thank V. Brudanin, S. Kovalenko, and V. Kovalenko and the Organizing Committee of NAN 99 for setting up such a very inspiring meeting and for the kind hospitality.

REFERENCES

1. T. A. Kirsten, in *Proceedings of VIII International Workshop on Neutrino Telescopes, Venezia, 1999*, Ed. by M. Baldo Ceolin, p. 63 and references therein.
2. K. S. Hirata *et al.*, Phys. Lett. B **280**, 146 (1992).
3. Y. Fukuda *et al.*, Phys. Rev. Lett. **81**, 1562 (1998); W. Gajewski, Yad. Fiz. **63** (2000) [Phys. At. Nucl. **63** (2000)].
4. C. Athanassopoulos *et al.*, Phys. Rev. C **54**, 2685 (1996); Phys. Rev. Lett. **77**, 3082 (1996); G. Mills, in *Proceedings of XXXIV Rencontres de Morion on Electrow. Int. and Unified Theories, Les Arcs, 1999* (in press).
5. E. Eskut *et al.*, Nucl. Instrum. Methods Phys. Res. A **401**, 7 (1997); Phys. Lett. B **434**, 205 (1998).
6. J. Altegoer *et al.*, Nucl. Instrum. Methods Phys. Res. A **404**, 96 (1998); P. Astier *et al.*, Phys. Lett. B **453**, 169 (1999).
7. M. Doucet, Yad. Fiz. **63** (2000) [Phys. At. Nucl. **63** (2000)]; B. Popov, Yad. Fiz. **63** (2000) [Phys. At. Nucl. **63** (2000)].
8. T. Jannakos, in *Proceedings of XXXIV Rencontres de Morion on Electrow. Int. and Unified Theories, Les Arcs, 1999* (in press).
9. K. Nishikawa *et al.*, E362KWK-PS proposal (1995); H. Sobel, in *Proceedings of VIII International Workshop on Neutrino Telescopes, Venezia, 1999*, Ed. by M. Baldo Ceolin, p. 351.
10. N. Armenise *et al.*, Preprint No. CERN-SPSC/97-21, SPSC/I216, CERN (Geneva, 1997).
11. E. Church *et al.*, Fermilab Proposal P-0898 (1997).
12. G. Aquistapace *et al.*, Report No. 98-08, INFN/AE-98/05, CERN (Geneva, 1998); addendum CERN-SL/99-034(DI), INFN/AE-99/05.
13. ICARUS Collab, Preprint No. CERN-SPSC/98-33, SPSC/M620, CERN (Geneva, 1998); A. Rubbia, in *Proceedings of International Workshop on Particles in Astrophysics and Cosmology: From Theory to Observation, Valencia 1999* (in press).
14. K. Kodama *et al.*, Preprint No. CERN-SPSC/98-05, SPSC/M612, CERN (Geneva, 1998).
15. The Fermilab NuMI Group, Report No. NUMI-346, Fermilab (Batavia, 1998); E. Ables *et al.*, Fermilab Proposal P-875 (1995); NuMI-L-337 (1998); NuMI-L-375 (1998); D. Petyt, Yad. Fiz. **63** (2000) [Phys. At. Nucl. **63** (2000)].
16. A. Fassó *et al.*, in *Proceedings of "Simulating Accelerator Radiation Environment," 1994*, (World Sci., Singapore, 1994), p. 88.
17. H. Fesenfeldt, *GHEISHA; The Simulation of Hadronic Showers—Physics and Applications*, Report PITHA 85/02 (1985).
18. R. Brun *et al.*, GEANT: Detector Description and Simulation Tool, CERN Program Library Long Writeup W5013.
19. A. Ferrari and P. R. Sala, in *Proceedings of Conference on "Nuclear Data for Science and Technology," ICTP, Miramare-Trieste, 1997*, SIF Attie Conference, Vol. 1, p. 247 (1998).
20. H. W. Atherton *et al.*, Report No. 80-07, CERN (Geneva, 1980).
21. G. Ambrosini *et al.*, Phys. Lett. B **420**, 225 (1998); **425**, 208 (1998); Preprint No. CERN-EP/99-19, CERN (Geneva, 1999), submitted to Eur. Phys. J. C.
22. G. Collazuol *et al.*, Preprint No. CERN-OPEN-98-32, CERN (Geneva, 1998), submitted to Nucl. Instrum. Methods Phys. Res.
23. G. I. Budker, in *Proceedings of 7th International Conference on High Energy Accelerators, Yerevan, 1969*, p. 33; extract: AIP Conf. Proc. **352**, 4 (1996); A. N. Skrinsky, in *Proceedings of Prospects of High Energy Physics, Morges, 1971*; extract: AIP Conf. Proc. **372**, 133 (1996).
24. B. Autin, Report No. 99-2, EFCA 99-197, CERN, Ed. by A. Blondel and J. Ellis (Geneva, 1999).

Physics of Atomic Nuclei, Vol. 63, No. 6, 2000, pp. 921–933. From Yadernaya Fizika, Vol. 63, No. 6, 2000, pp. 997–1009.
Original English Text Copyright © 2000 by Valle.

Neutrino Physics at the Turn of the Millennium*

J. W. F. Valle**

Instituto de Física Corpuscular, CSIC, Departamento de Física Teórica, Universidad de Valencia,
Edificio Institutos de Paterna, Valencia, Spain

Abstract—I discuss the implications of the latest data on solar and atmospheric neutrinos which strongly indicate the need for physics beyond the Standard Model. I review the theoretical options for reconciling these data in terms of three-neutrino oscillations. Even though not implied by the data, bimaximal models of neutrino mixing emerge as an attractive possibility. Supersymmetry with broken R-parity provides a predictive way to incorporate it, opening the possibility of testing neutrino anomalies at high-energy collider experiments such as the LHC or at the upcoming long-baseline or neutrino factory experiments. Reconciling, in addition, the hint provided by the LSND experiment requires a fourth, light sterile, neutrino. The simplest theoretical scenarios are the most symmetric ones, in which two of the four neutrinos are maximally mixed and lie at the LSND scale, while the others are at the solar mass scale. The lightness of the sterile neutrino, the nearly maximal atmospheric neutrino mixing, and the generation of $\Delta m^2_\odot$ & $\Delta m^2_{\rm atm}$ all follow naturally from the assumed lepton-number symmetry and its breaking. These two basic schemes can be distinguished at neutral-current-sensitive solar & atmospheric neutrino experiments such as the Sudbury Neutrino Observatory. However, underground experiments have not yet proven neutrino masses, since there is a variety of alternative mechanisms. For example, flavor changing interactions can play an important role in the explanation of solar and of contained atmospheric data and could be tested through effects such as $\mu \longrightarrow e + \gamma$, μ–e conversion in nuclei, unaccompanied by neutrino-less double beta decay. Conversely, the room is still open for heavy unstable neutrinos. A short-lived ν_μ might play a role in the explanation of the atmospheric data. Finally, in the presence of a sterile neutrino ν_s, a long-lived ν_τ in the MeV range could delay the time at which the matter and radiation contributions to the energy density of the Universe become equal, reducing the density fluctuations on the smaller scales and rescuing the standard cold-dark-matter scenario for structure formation. In this case, the light ν_e, ν_μ, and ν_s would account for the solar and atmospheric data. © *2000 MAIK “Nauka/Interperiodica”.*

1. INTRODUCTION

Undoubtedly the solar [1-4] and atmospheric [5, 6] neutrino problems provide the two most important milestones in the search for physics beyond the Standard Model (SM). Of particular importance has been the recent confirmation by the SuperKamiokande Collaboration [6] of the zenith-angle-dependent deficit of atmospheric neutrinos. Altogether solar and atmospheric data give a strong evidence for ν_e and ν_μ conversions, respectively. Neutrino conversions are a natural consequence of theories beyond the SM [7]. The first example is oscillations of small-mass neutrinos. The simplest way to account for the lightness of neutrinos is in the context of Majorana neutrinos: their mass violates lepton number. Its most obvious consequences would be processes such as neutrinoless double-beta decay [8] or CP violation properties of neutrinos [9], so far unobserved. Neutrino masses could be hierarchical, with the light ν_τ much heavier than the ν_μ and ν_e. While solar neutrino rates favor the Small Mixing Angle (SMA) MSW solution, present data on the recoil-electron spectrum prefer the Large Mixing MSW [10] (LMA) solution [11]. When interpreted in terms of neutrino oscillations, the observed atmospheric neutrino zenith-angle-dependent deficit clearly indicates that the mixing involved is maximal. In short we have the intriguing possibility that, unlike the case of quarks, neutrino mixing is bimaximal. Supersymmetry with broken R-parity provides an attractive origin for bimaximal neutrino oscillations, which can be tested not only at the upcoming long-baseline or neutrino factory experiments but also at high-energy collider experiments such as the LHC.

One should however bear in mind that there is a variety of alternative solutions to the neutrino anomalies. Just as an example let me stress the case for lepton-flavor-violating neutrino transitions, which can arise without neutrino masses [12–14]. They may still fit present solar [15] and contained atmospheric [16] data pretty well. They may arise in models with extra heavy leptons [17–20] and in supergravity theories [21]. A possible signature of theories leading to FC interactions would be the existence of sizeable flavor nonconservation effects, such as $\mu \longrightarrow e + \gamma$, μ–e conversion in nuclei, unaccompanied by neutrino-less double beta decay if neutrinos are massless. In contrast to the intimate relationship between the latter and the nonzero Majorana mass of neutrinos due to the Black Box theorem [8], there is no fundamental link between lepton

---

* This article was submitted by the author in English.
** http://neutrinos.uv.es

1063-7788/00/6306-0921$20.00 © 2000 MAIK “Nauka/Interperiodica”

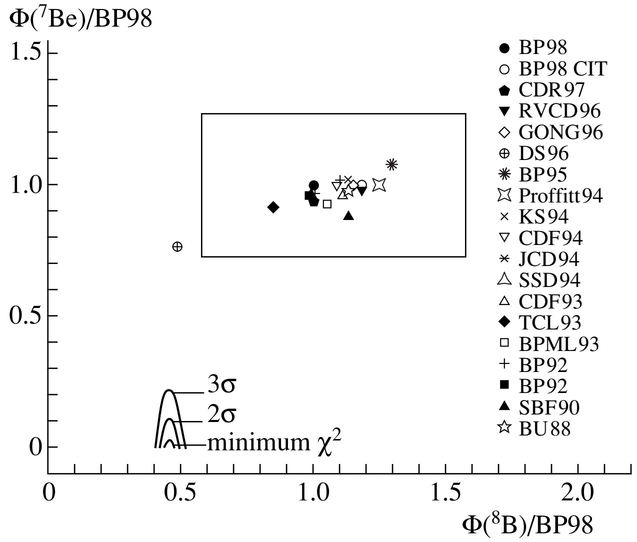

Fig. 1. SSM predictions, from [33].

flavor violation and neutrino mass. Other possibilities involve neutrino decays [22] and transition magnetic moments [23] coupled to either to regular [24, 25] or to random magnetic fields [26].

In addition to the solar- and atmospheric-neutrino data from underground experiments, there is also some indication for neutrino oscillations from the LSND experiment [27, 28]. Barring exotic neutrino-conversion mechanisms, one requires three mass scales in order to reconcile all of these hints, hence the need for a light sterile neutrino [29–31]. Out of the four neutrinos, two of them lie at the solar neutrino scale and the other two maximally mixed neutrinos are at the HDM/LSND scale. The prototype models proposed in [29, 30] enlarge the $SU(2) \otimes U(1)$ Higgs sector in such a way that neutrinos acquire mass radiatively, without unification nor seesaw. The LSND scale arises at one-loop, while the solar and atmospheric scales come in at the two-loop level, thus accounting for the hierarchy. The lightness of the sterile neutrino, the nearly maximal atmospheric neutrino mixing, and the generation of the solar and atmospheric neutrino scales all result naturally from the assumed lepton-number symmetry and its breaking. Either ν_e–ν_τ conversions explain the solar data with ν_μ–ν_s oscillations accounting for the atmospheric deficit [29], or else the roles of ν_τ and ν_s are reversed [30]. These two basic schemes have distinct implications at future solar & atmospheric neutrino experiments with good sensitivity to neutral current neutrino interactions. Cosmology can also place restrictions on these four-neutrino schemes [32].

2. INDICATIONS FOR NEW PHYSICS

The most solid hints in favor of new physics in the neutrino sector come from underground experiments on solar [1–4] and atmospheric [5, 6] neutrinos. The most recent data correspond to 825-day solar [4] and 52 kt yr atmospheric data samples, respectively [6].

2.1. Solar Neutrinos

The solar neutrino event rates recorded at the radiochemical Homestake, Gallex, and Sage experiments are summarized as 2.56 ± 0.22 SNU (Chlorine) and 72.3 ± 5.6 SNU (Gallex and Sage) [1, 2]. Note that only the gallium experiments are sensitive to the solar *pp* neutrinos. On the other hand, the ^{8}B flux from SuperKamiokande water Cherenkov experiment is $(2.4 \pm 0.08) \times 10^6$ cm^{-2} s^{-1} [4]. In Fig. 1, one can see the predictions of various Standard Solar Models (SSM) in the plane defined by the ^{7}Be and ^{8}B neutrino fluxes, normalized to the predictions of the BP98 solar model [34]. Abbreviations such as BP95 identify different solar models, as given in [35]. The rectangular error box gives the 3σ error range of the BP98 fluxes. On the other hand, the values of these fluxes indicated by present data on neutrino event rates are shown by the contours in the lower-left part of the figure. The best-fit ^{7}Be neutrino flux is negative! The theoretical predictions clearly lie well away from the 3σ contour, strongly suggesting the need for new particle physics in order to account for the data [36]. Since possible nonstandard astrophysical solutions are rather constrained by helioseismology studies [33, 37], one is led to assume the existence of neutrino conversions, such as those induced by very small neutrino masses. Possibilities include the MSW effect [10], vacuum neutrino oscillations [38, 39] and, possibly, flavor changing neutrino interactions [15]. Moreover, if neutrinos have transition magnetic moments, then one may have, in addition, the possibility of Majorana neutrino spin-flavor precessions [23]. Based upon these, there emerge two new solutions to the solar neutrino problem: the resonant [24, 25] and the aperiodic spin-flavor precession mechanisms [26], based on regular and random magnetic fields, respectively.

The recent 825-day data sample [4] presents no major surprises, except that the recoil energy spectrum produced by solar neutrino interactions shows more events in the highest bins. Barring the possibly of poorly understood energy resolution effects, it has been noted [40] that if the flux for neutrinos coming from the $^3He + p \longrightarrow {}^4He + e^+ + \nu_e$, the so-called *hep* reaction, is well above the (uncertain) SSM predictions, then this could significantly influence the electron energy spectrum produced by solar neutrino interactions in the high recoil region, with hardly any effect at lower energies. Fig. 2 shows the expected normalized recoil electron energy spectrum compared with the most recent experimental data [4]. The solid line represents the prediction for the best-fit SMA solution with free ^{8}B and *hep* normalizations (0.69 and 12, respectively), while the dotted line gives the corresponding prediction for the best-fit LMA solution (1.15 and 34 respectively). Finally, the dashed line represents the prediction for the best no-oscillation scheme with free ^{8}B and *hep* normalizations (0.44 and 14, respectively). Clearly the spectra with enhanced *hep* neutrinos provide better fits to the data. However, Fiorentini *et al*. [41] have argued that the required *hep* amount is too large to accept on theoretical grounds. We look forward to the improvement of the situation. The increasing role played by rate-independent observables such as the spectrum, as well as seasonal and day–night asymmetries, will eventually select amongst different solutions of the solar neutrino problem.

The required solar neutrino parameters are determined through a χ^2 fit of the experimental data. In Fig. 3, we show the allowed regions in Δm^2 and $\sin^2 2\theta$ from the measurements of the total event rates at the Chlorine, Gallium, and SuperKamiokande (825-day data sample) experiments, combined with the zenith angle distribution, the recoil energy spectrum, and the seasonal dependence of the event rates, observed in SuperKamiokande. Panels (*a*) and (*b*) correspond to active–active and active–sterile oscillations, respectively. The best-fit points in each case are indicated by a star [11], while the local best-fit points are indicated by a dot. An analysis with free ^{8}B and *hep* normalizations has also been given in [11] and does not change significantly the allowed regions.

One notices from the analysis that rate-independent observables, such as the electron recoil energy spectrum and the day–night asymmetry (zenith angle distribution), are playing an increasing role in the determination of solar neutrino parameters [11]. An observable which has been neglected in most analyzes of the MSW effect and which could be sizeable in the large mixing angle regions (LMA and LOW) is the seasonal dependence in the solar neutrino flux which would result from the regeneration effect at the Earth and which has been discussed in [42]. This should play a more significant role in future investigations.

A theoretical issue which has raised some interest recently is the study of the possible effect of random fluctuations in the solar matter density [43-45]. The possible existence of such noise fluctuations at a few percent level is not excluded by present helioseismology studies. In Fig. 4 we show averaged solar neutrino survival probability as a function of $E/\Delta m^2$ for $\sin^2 2\theta$ = 0.01. This figure was obtained via a numerical integration of the MSW evolution equation in the presence of noise, using the density profile in the Sun from BP95 in [35] and assuming that the correlation length L_0 (which corresponds to the scale of the fluctuation) is L_0 = $0.1\lambda_m$, where λ_m is the neutrino oscillation length in matter. An important assumption in the analysis is that $l_{\text{free}} \ll L_0 \ll \lambda_m$, where $l_{\text{free}} \sim 10$ cm is the mean free path of the electrons in the solar medium. The fluctuations may strongly affect the ^{7}Be neutrino component of the solar neutrino spectrum, so that the Borexino experiment should provide an ideal test, if sufficiently small errors can be achieved. The potential of Borexino in probing the level of solar matter density fluctuations provides an additional motivation for the experiment [46].

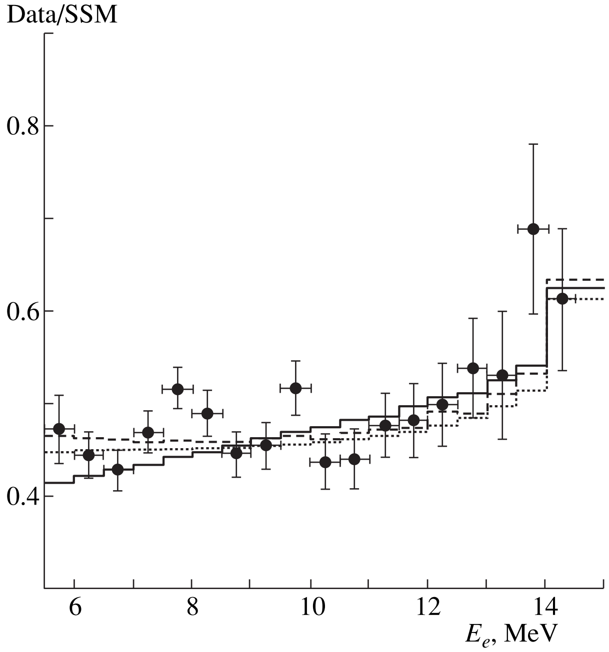

Fig. 2. Expected normalized recoil-electron energy spectra versus 825-day SuperKamiokande data from [11].

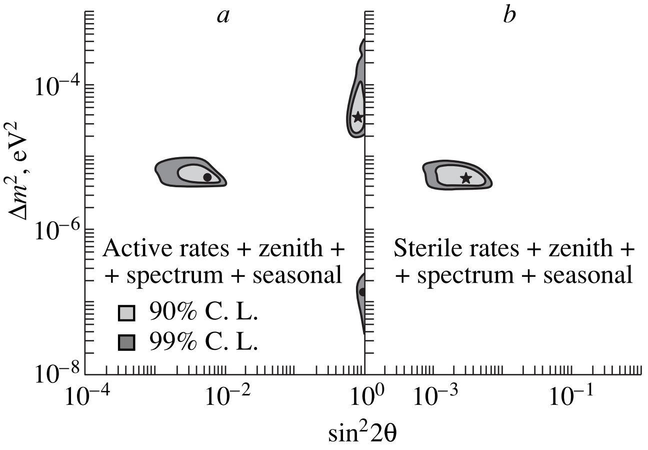

Fig. 3. Solar neutrino parameters at 90 and 99% C.L. for 2-flavor MSW neutrin conversions with 825-day SuperKamiokande data sample in the BP98 model, from [11].

The most popular alternative solution to the solar neutrino problem is the vacuum oscillation solution [38], which clearly requires large neutrino mixing and the adjustment of the oscillation length so as to coincide roughly with the Earth–Sun distance. Figure 5 shows the regions of just-so oscillation parameters at the 95% C.L. obtained in a recent fit of the data, including the rates, the recoil energy spectrum, and seasonal effects, which are expected in this scenario [48] and could potentially help in discriminating it from sce-

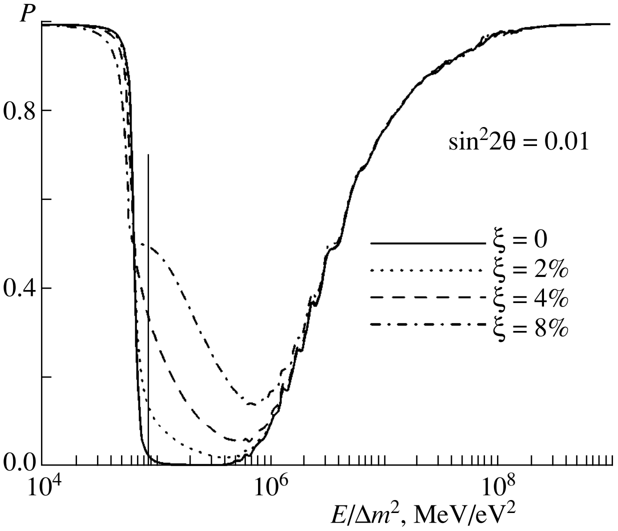

Fig. 4. Solar neutrino survival probability in a noisy Sun, from [44].

nario [48] and could potentially help in discriminating it from the MSW scenario.

2.2 Atmospheric Neutrinos

Neutrinos produced as decay products in hadronic showers from cosmic ray collisions with nuclei in the upper atmosphere have been observed in several experiments [49–55]. There has been a long-standing discrepancy between the predicted and measured μ/e ratio of the muon ($\nu_\mu + \bar{\nu}_\mu$) over the electron atmospheric neutrino flux ($\nu_e + \bar{\nu}_e$) [56]. The anomaly has been found in water Cherenkov experiments (Kamiokande, SuperKamiokande, and IMB) as well as in the iron calorimeter Soudan 2 experiment. Negative experiments, such as Frejus and Nusex, have much larger errors. Although individual ν_μ or ν_e fluxes are only known to within 30% accuracy, their ratio is predicted to within 5% over energies varying from 0.1 to 100 GeV [57]. The most important feature of the atmospheric neutrino data sample [6] is that it exhibits a zenith-angle-dependent deficit of muon neutrinos. Experimental biases and uncertainties in the prediction of neutrino fluxes and cross sections are unable to explain the data.

The most popular way to account for this anomaly is in terms of neutrino oscillations. It has already been noted [58] that the Chooz reactor data [59] excludes the $\nu_\mu \longrightarrow \nu_e$ channel, when all experiments are combined. So I concentrate here on the other possible oscillation channels.

The results of the most recent χ^2 fit of the SuperKamiokande atmospheric neutrino data in the framework of the neutrino oscillation hypothesis can be seen in Fig. 6, taken from [60]. This analysis updates previous studies in [58] and [61] and includes the upgoing muon event samples. This figure shows the allowed regions of oscillation parameters at 90 and 99% C.L. Notice that matter effects lead to differences between the allowed regions for the various channels. For $\nu_\mu \longrightarrow \nu_s$ with

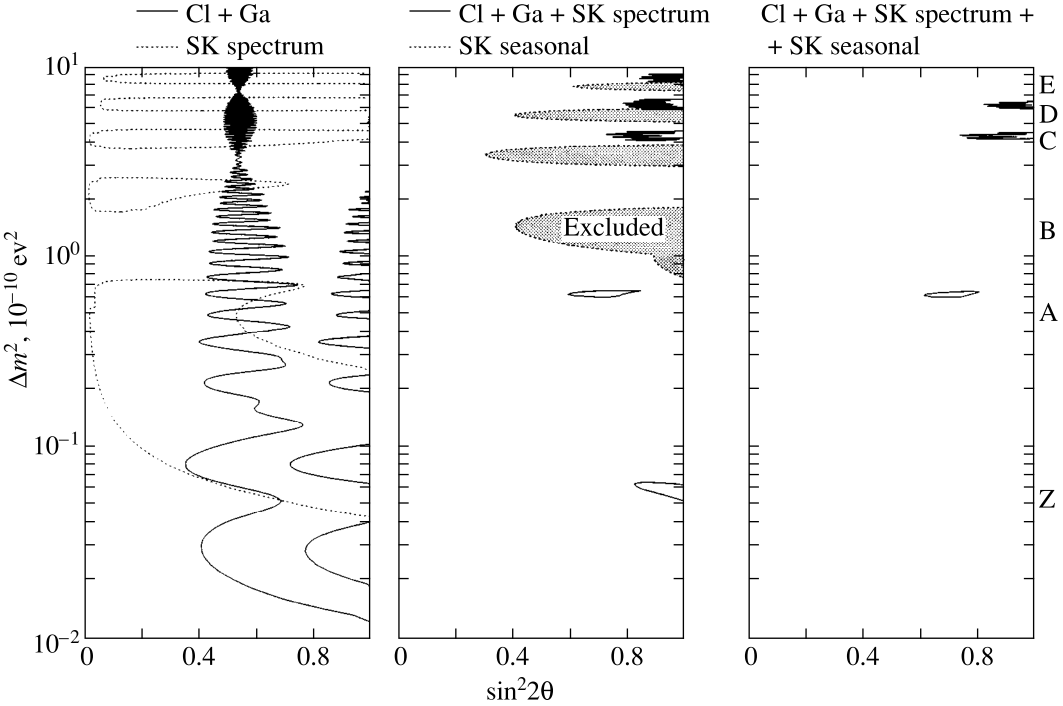

Fig. 5. Vacuum oscillation parameters, from [47].

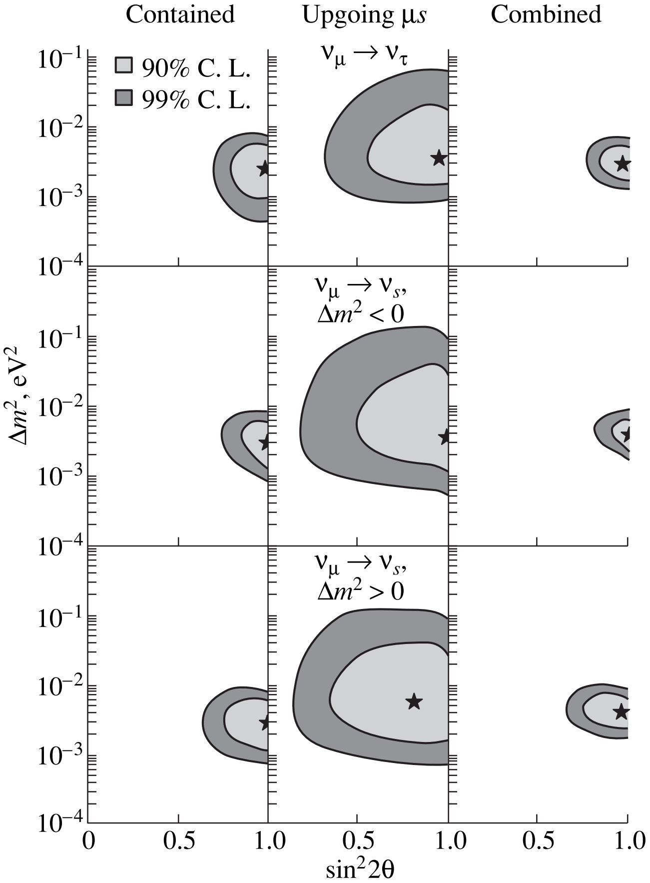

Fig. 6. Allowed regions of the oscillation parameters at 90 and 99% C.L. for various SuperKamiokande data samples and oscillation channels, as labeled in the figure. Best-fit points are denoted by a star in each case.

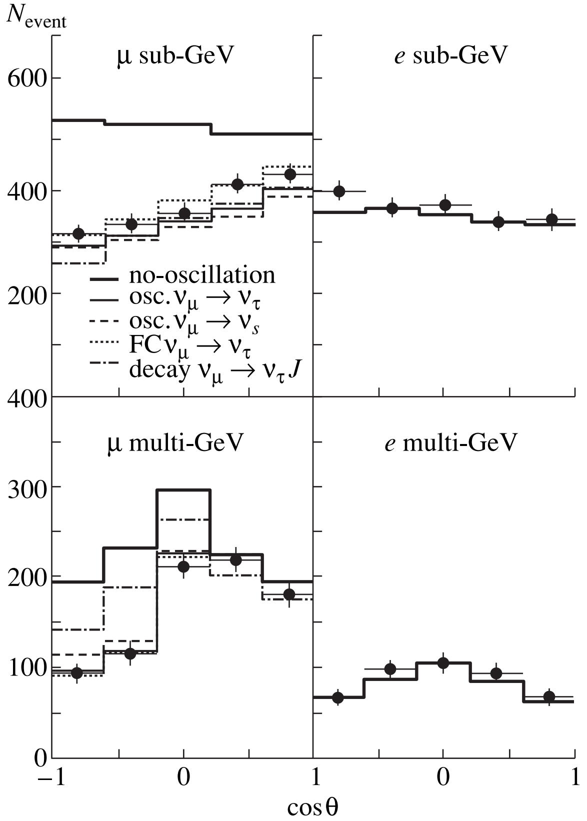

Fig. 7. Angular distributions for contained SuperKamiokande events, together with the SM prediction (no-oscillation) and the predictions for the best-fit points to the contained event data in various conversion mechanisms labeled in the figure. The error in the experimental points is only statistical.

$\Delta m^2 > 0$, matter effects enhance the oscillations for neutrinos, and therefore smaller values of the vacuum mixing angle would lead to larger conversion probabilities, so that the regions are larger than compared to the $\nu_\mu \longrightarrow \nu_\tau$ case. For $\nu_\mu \longrightarrow \nu_s$ with $\Delta m^2 < 0$, the matter enhancement occurs only for anti-neutrinos, suppressing the conversion in ν_μ's. Since the yield of atmospheric neutrinos is larger than that of antineutrinos, clearly the matter effect suppresses the overall conversion probability. Therefore, one needs in this case a larger value of the vacuum mixing angle. This trend can indeed be seen by comparing the regions in different columns of Fig. 6.

Notice that in all channels where matter effects play a role, the range of acceptable Δm^2 is slightly shifted towards larger values, as compared with the $\nu_\mu \longrightarrow \nu_\tau$ case. This follows from the relation between mixing in vacuo and in matter. In fact, away from the resonance region, independently of the sign of the matter potential, there is a suppression of the mixing inside the Earth. As a result, the lower allowed Δm^2 value is higher than for the $\nu_\mu \longrightarrow \nu_\tau$ channel.

Concerning the quality of the fits, we note that the best-fit to the full sample is obtained for the $\nu_\mu \longrightarrow \nu_\tau$ channel, although from the global analysis oscillations into sterile neutrinos cannot be ruled out. There is also an improvement in the quality of the fits to the contained events as compared to previous analysis performed with lower statistics [58]. These features can be easily understood by looking at the predicted zenith angle distribution of the different event types for the various oscillation channels shown in Fig. 7 and 8. From Fig. 7, one can see the excellent agreement between the observed distributions of *e*-like events and the SM predictions. This has led to an improvement of the quality of the fit for any conversion mechanism that only involves muons. From Fig. 8, one can also see that due to matter effects the distributions for upgoing muons in the case of $\nu_\mu \longrightarrow \nu_s$ are flatter than for $\nu_\mu \longrightarrow \nu_\tau$ [62]. The data show a somewhat steeper angular dependence, which is better described by $\nu_\mu \longrightarrow \nu_\tau$ oscillations. In order to exploit this feature, the SuperKamiokande Collaboration has presented a preliminary partial analysis of the angular dependence of the through-going muon data in combination with

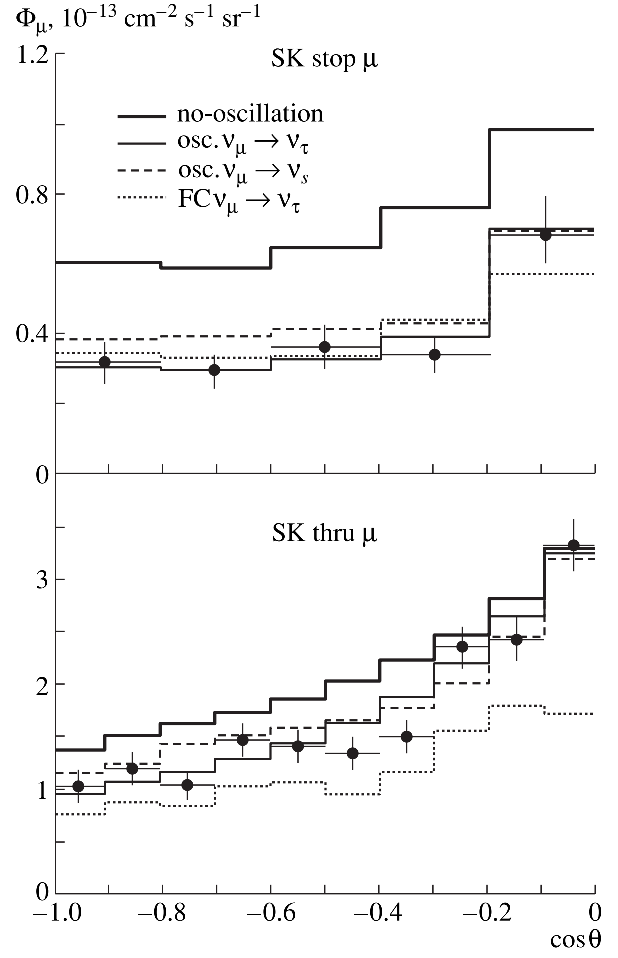

Fig. 8. Angular distribution for SuperKamiokande upgoing muon data together with the SM prediction (no-oscillation) as well as the prediction for the best-fit point to the full data sample for the different conversion mechanisms labeled in the figure.

the up–down asymmetry of partially contained events, which seems indeed to disfavor $\nu_\mu \longrightarrow \nu_s$ oscillations at the 2σ level [50]. For a comparison of the oscillation parameters as determined from the atmospheric data with the sensitivity of the present accelerator and reactor experiments, as well as the expectations of upcoming long-baseline experiments, see [58].

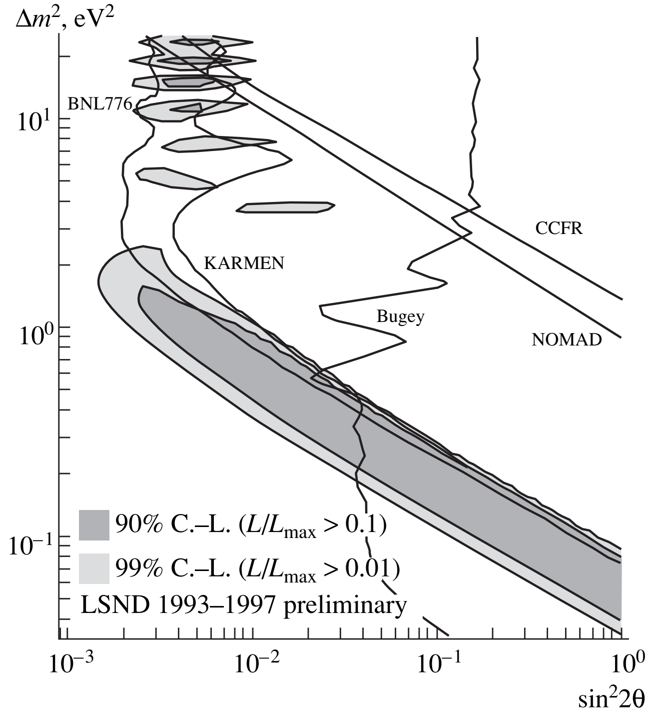

Fig. 9. Allowed LSND oscillation parameters versus competing experiments [63].

2.3. LSND

The Los Alamos Meson Physics Facility looked for $\bar{\nu}_\mu \longrightarrow \bar{\nu}_e$ oscillations using $\bar{\nu}_\mu$ from μ^+ decay at rest [27]. The $\bar{\nu}_s$'s are detected via the reaction $\bar{\nu}_e p \longrightarrow e^+ n$, correlated with a γ from $np \longrightarrow d\gamma$ (2.2 MeV). The results indicate $\bar{\nu}_\mu \longrightarrow \bar{\nu}_e$ oscillations, with an oscillation probability of $(0.31^{+0.11}_{-0.10} \pm 0.05)\%$, leading to the oscillation parameters shown in Fig. 9. The shaded regions are the favored likelihood regions given in [27]. The curves show the 90 and 99% likelihood allowed ranges from LSND and the limits from BNL776, KARMEN, Bugey, CCFR, and NOMAD. A search for $\nu_\mu \longrightarrow \nu_e$ oscillations has also been conducted by the LSND Collaboration. Using ν_μ from π^+ decay in flight, the ν_e appearance is detected via the charged-current reaction $C(\nu_e, e^-)X$. Two independent analyzes are consistent with the above signature, after taking into account the events expected from the ν_e contamination in the beam and the beam-off background. If interpreted as an oscillation signal, the observed oscillation probability is $(2.6 \pm 1.0 \pm 0.5) \times 10^{-3}$, consistent with the evidence for oscillation in the $\bar{\nu}_\mu \longrightarrow \bar{\nu}_e$ channel described above. Figure 10 compares the LSND region with the expected sensitivity from MiniBooNE, which was recently approved to run at Fermilab [28, 63]. A possible confirmation of the LSND anomaly would be a discovery of far-reaching implications.

2.4. Dark Matter

Galaxies, as well as the large scale structure in the Universe, should arise from the gravitational collapse of fluctuations in the expanding universe. They are sensitive to the nature of the cosmological dark matter. The data on cosmic background temperature anisotropies on large scales performed by the COBE satellite [64] combined with cluster-cluster correlation data, e.g., from IRAS [65], can not be reconciled with the simplest

COBE-normalized $\Omega_m = 1$ Cold Dark Matter (CDM) model, since it leads to too much power on small scales. Adding to CDM neutrinos with mass of a few eV (a scale similar to the one indicated by the LSND experiment [27]), corresponding to $\Omega_\nu \approx 0.2$, results in an improved fit to data on the nearby galaxy and cluster distribution [66]. The resulting Cold + Hot Dark Matter (CHDM) cosmological model is the most successful $\Omega_m = 1$ model for structure formation, preferred by inflation. However, other recent data have begun to indicate a lower value for Ω_m, thus weakening the cosmological evidence favoring neutrino mass of a few eV in flat models with cosmological constant $\Omega_\Lambda = 1 - \Omega_m$ [66]. Future sky maps of the Cosmic Microwave Background Radiation (CMBR) with high precision at the MAP and PLANCK missions should bring more light into the nature of the dark matter and the possible role of neutrinos [32]. Another possibility is to consider unstable dark matter scenarios [67]. For example, an MeV range tau neutrino may provide a viable unstable dark matter scenario [68] if the ν_τ decays before the matter dominance epoch. Its decay products would add energy to the radiation, thereby delaying the time at which the matter and radiation contributions to the energy density of the universe become equal. Such delay would allow one to reduce the density fluctuations on the smaller scales purely within the standard cold dark matter scenario. Upcoming MAP and PLANCK missions may place limits on neutrino stability [69] and rule out such schemes.

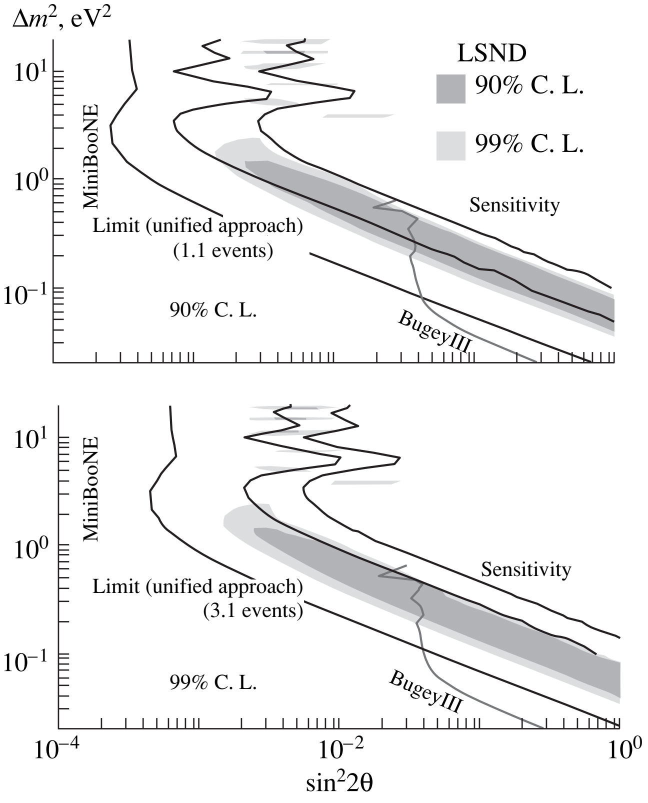

Fig. 10. Expected sensitivity of the proposed MiniBooNE experiment [63].

2.5. Pulsar Velocities

One of the most challenging problems in modern astrophysics is to find a consistent explanation for the high velocity of pulsars. Observations [70] show that these velocities range from zero up to 900 km/s with a mean value of 450 ± 50 km/s. An attractive possibility is that pulsar motion arises from an asymmetric neutrino emission during the supernova explosion. In fact, neutrinos carry more than 99% of the new-born protoneutron star's gravitational binding energy, so that even a 1% asymmetry in the neutrino emission could generate the observed pulsar velocities. This could in principle arise from the interplay between the parity violation present in weak interactions with the strong magnetic fields which are expected during a SN explosion [71, 72]. However, it has recently been noted [73] that no asymmetry in neutrino emission can be generated in thermal equilibrium, even in the presence of parity violation. This suggests that an alternative mechanism is at work. Several neutrino conversion mechanisms in matter have been invoked as a possible engine for powering pulsar motion. They all rely on the polarization [74] of the SN medium induced by the strong magnetic fields 10^{15} Gs present during a SN explosion. This would affect neutrino propagation properties, giving rise to an angular dependence of the matter-induced neutrino potentials. This would lead in turn to a deformation of the "neutrino-sphere" for, say, tau neutrinos and thus to an anisotropic neutrino emission. As a consequence, in the presence of nonvanishing ν_τ mass and mixing, the resonance sphere for the ν_e–ν_τ conversions is distorted. If the resonance surface lies between the ν_τ and ν_e neutrino spheres, such a distortion would induce a temperature anisotropy in the flux of the escaping tau neutrinos produced by the conversions, hence a recoil kick of the proto–neutron star. This mechanism was realized in [75] invoking MSW conversions [10] with $m_{\nu_\tau} \gtrsim$ 100 eV or so, assuming a negligible ν_e mass. This is necessary in order for the resonance surface to be located between the two neutrinospheres. It should be noted, however, that such requirement is at odds with cosmological bounds on neutrinos masses unless the τ neutrino is unstable. On the other hand, in [76] a realization was proposed in the resonant spin-flavor precession scheme (RSFP) [24]. The magnetic field would not only affect the medium properties, but would also induce the spin-flavor precession through its coupling to the neutrino transition magnetic moment [23].

Perhaps the simplest and probably most elegant suggestion was proposed in [77], where the required pulsar velocities would arise from anisotropic neutrino emission induced by resonant conversions of massless neutrinos (hence no magnetic moment). Raffelt and Janka

[78] have subsequently argued that the asymmetric neutrino emission effect was overestimated in [75–77], since the temperature variation over the deformed neutrinosphere is not an adequate measure for the anisotropy of the neutrino emission. This would invalidate all neutrino conversion mechanisms, leaving the pulsar velocity problem without any viable solution. However, Kusenko and Segrè still maintain that sizeable pulsar kicks can arise from neutrino conversions [79]. In any case, invoking conversions into sterile neutrinos could be an interesting possibility, since the conversions could take place deeper in the star [80].

3. MAKING SENSE OF ALL THAT

Physics beyond the SM is required in order to explain solar and atmospheric neutrino data. While neutrino oscillations provide an excellent fit and a powerful way to determine neutrino mass and mixing, there is a plethora of alternative mechanisms, some of which quite attractive, which could play an important role in the interpretation of the data. These include flavor-changing neutrino interactions in both solar [15] and atmospheric [16, 81] neutrino problems; resonant [24, 25] and the aperiodic spin-flavor precession mechanisms [26] for solar neutrinos, which use the transition magnetic moments of Majorana neutrinos [23]; and the possibility of fast neutrino decays [22] which could play a role in the atmospheric neutrino problem [82]. Moreover, I note that more exotic explanations of the underground neutrino data based upon violations of equivalence principle, Lorentz invariance, and *CPT* have been proposed [83]. Nevertheless, in what follows, I will assume the standard neutrino oscillation interpretation of the data.

3.1. Solar Plus Atmospheric

These data can be accounted for with the three known neutrinos. They fix the two mass splittings $\Delta m^2_\odot$ & Δm^2_{atm} and two of the three neutrino mixing angles, the third being small on account of the Chooz reactor results [59]. Such scenario can easily be accommodated in seesaw theories of neutrino mass since, in general, the mixing angles involved are not predicted; in particular, the maximal mixing indicated by the atmospheric data and possibly also by the solar data can be accommodated by hand. In contrast, it is not easy to reconcile maximal or bimaximal mixing of neutrinos [39] with a predictive quark–lepton unification seesaw scheme that relates lepton and quark mixing angles, since the latter are known to be small. For attempts to reconcile solar and atmospheric data in unified models with specific texture ansatz, see [84, 85].

An alternative way to predict a hierarchical pattern of neutrino mass and mixing, which naturally accommodates the possibility of maximal mixing, is to appeal to supersymmetry. In [86], it was shown that the simplest unified extension of the Minimal Supersymmetric Standard Model with bilinear *R*-parity violation provides a predictive scheme for neutrino masses which can account for the observed atmospheric and solar neutrino anomalies in terms of bimaximal neutrino mixing. The maximality of the atmospheric mixing angle arises dynamically, by minimizing the scalar potential of the theory, while the solar neutrino problem can be accounted for either by large or by small mixing oscillations. The spectrum is naturally hierarchical, since only the tau neutrino picks up mass at the tree level (though this may be itself calculable from renormalization-group evolution from unification down to weak-scale), by mixing with neutralinos, while the masslessness of the other two neutrinos is lifted only by calculable loop corrections. Despite the smallness of neutrino masses, *R*-parity violation can be observable at present and future high-energy colliders, providing an unambiguous cross-check of the model and the possibility of probing the neutrino anomalies at accelerators.

Bimaximal models may also be tested at the upcoming long-baseline experiments or at a possible neutrino factory experiment [87] through the *CP*-violating phases, which could lead to nonnegligible *CP* asymmetries in neutrino oscillation [88]. Unfortunately, the effects of the *CP* violation intrinsic to the Majorana neutrino system [89] is helicity-suppressed [9], though a potential test of the *CP* properties and Majorana nature of neutrinos has been suggested in [90].

3.2. Solar and Atmospheric Plus Dark Matter

The story gets more complicated if one wishes to account also for the hot dark matter. The only possibility to fit the solar, atmospheric, and HDM scales in a world with just the three known neutrinos is if all of them have nearly the same mass [31] of about ~1.5 eV or so in order to provide the right amount of HDM [66] (all three active neutrinos contribute to HDM). This can be arranged in a unified *SO*(10) seesaw model, where, to a first approximation, all neutrinos lie at the above HDM mass scale (~1.5 eV), due to a suitable horizontal symmetry, the splittings $\Delta m^2_\odot$ & Δm^2_{atm} appearing as symmetry-breaking effects. An interesting fact is that the ratio $\Delta m^2_\odot/\Delta m^2_{\text{atm}}$ is related to m_c^2/m_t^2 [91]. There is no room in this case to accommodate the LSND anomaly. To what extent this solution is theoretically natural has been discussed recently in [92]. One finds that the degeneracy is stable in the phenomenologically relevant case where neutrinos have opposite *CP* parities, leading to a suppression in the neutrino-less double-beta-decay rate [93].

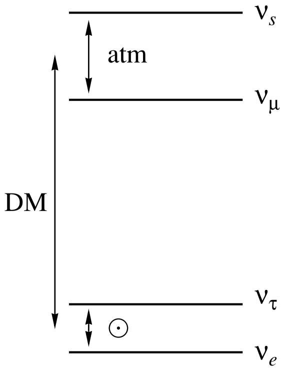

Fig. 11. $(e\tau)(\mu s)$ scheme: ν_e–ν_τ conversions explain the solar neutrino data, and ν_μ–ν_s oscillations account for the atmospheric deficit [29].

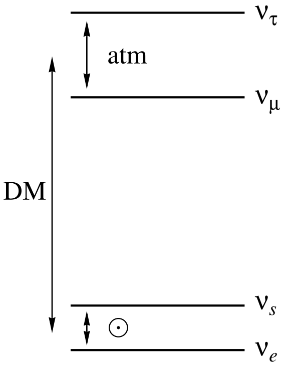

Fig. 12. $(es)(\mu\tau)$ scheme: ν_e–ν_s conversions explain the solar neutrino data, and ν_μ–ν_τ oscillations account for the atmospheric deficit [30].

3.3. Solar & Atmospheric with Dark Matter & LSND: Four-Neutrino Models

An alternative way to include hot dark matter scale is to invoke a fourth light sterile neutrino [29–31]. As a bonus, we can accommodate the LSND hint. The sterile neutrino ν_s must also be light enough in order to participate in the oscillations together with the three active neutrinos. Since it is an $SU(2) \otimes U(1)$ singlet, it does not affect the invisible Z decay width, well measured at LEP. The theoretical requirements are

to understand what keeps the sterile neutrino light, since the $SU(2) \otimes U(1)$ gauge symmetry would allow it to have a large bare mass,

to account for the maximal neutrino mixing indicated by the atmospheric data and possibly by the solar data,

to account from first principles for the scales $\Delta m^2_\odot$, Δm^2_{atm}, and $\Delta m_{\text{LSND/HDM}}$.

With this in mind, we have formulated the simplest maximally symmetric schemes, denoted as $(e\tau)(\mu s)$ [29] and $(es)(\mu\tau)$ [30], respectively. One should realize that a given scheme (mainly the structure of the leptonic charged current) may be realized in more than one theoretical model. For example, an alternative to the model in [30] was suggested in [31]. Higher dimensional theories contain light sterile neutrinos which can arise from the bulk sector and reproduce the basic features of these models [94]. For a recent discussion of the experimental constraints of four-neutrino mixing, see [95]. For alternative theoretical and phenomenological scenarios, see [96, 97].

Although many of the phenomenological features also arise in other models, here I concentrate the discussion mainly on the theories developed in [29, 30]. These are characterized by a very symmetric mass spectrum in which there are two ultralight neutrinos at the solar neutrino scale and two maximally mixed almost degenerate eV-mass neutrinos (the LSND/HDM scale [98]), split by the atmospheric neutrino scale [29, 30]. Before the global $U(1)$ lepton symmetry breaks, the heaviest neutrinos are exactly degenerate, while the other two are massless [99]. After the $U(1)$ breaks down, the heavier neutrinos split and the lighter ones get mass. The scale $\Delta m^2_{\text{LSND/HDM}}$ is generated radiatively at one-loop due to the additional Higgs bosons, while the splittings Δm^2_{atm} and $\Delta m^2_\odot$ are two-loop effects. The models are based only on weak-scale physics: no large mass scale is introduced. They explain the lightness of the sterile neutrino,[1] the large mixing required by the atmospheric neutrino data, as well as the generation of the mass splittings responsible for solar and atmospheric neutrino conversions as natural consequences of the underlying lepton-number symmetry and its breaking. They are minimal in the sense that they add a single $SU(2) \otimes U(1)$ singlet lepton to the SM. The models differ according to whether the ν_s lies at the dark matter scale or at the solar neutrino scale. In the $(e\tau)(\mu s)$ scheme, the ν_s lies at the LSND/HDM scale, as illustrated in Fig. 11, while, in the alternative $(es)(\mu\tau)$ model, ν_s is at the solar neutrino scale as shown in Fig. 12 [30]. In the $(e\tau)(\mu s)$ case, the atmospheric neutrino puzzle is explained by ν_μ to ν_s oscillations, while in $(es)(\mu\tau)$ it is due to ν_μ to ν_τ oscillations. Correspondingly, the deficit of solar neutrinos is explained in the first case by ν_e to ν_τ conversions, while in the second the relevant channel is ν_e to ν_s. In both models [29, 30], one predicts close-to-maximal mixing in the atmospheric neutrino sector, a feature which emerges as the global best-fit points in the analyses discussed above.

The presence of additional weakly interacting light particles, such as our light sterile neutrino, is constrained by BBN since the ν_s would enter into equilibrium with the active neutrinos in the early Universe

---

1) In higher dimensional theories, such sterile neutrinos may arise from bulk matter and be light without need for a protecting symmetry (see [94]).

(and therefore would contribute to $N_\nu^{\max}$) via neutrino oscillations [100] unless $\Delta m^2 \sin^4 2\theta \lesssim 3 \times 10^{-6}$ eV^2. Here, Δm^2 denotes a typical mass-square difference of the active and sterile species, and θ is the vacuum mixing angle. However, systematic uncertainties in the BBN bounds still caution us not to take them too literally. For example, it has been argued that present observations of primordial helium and deuterium abundances may allow up to $N_\nu = 4.5$ neutrino species if the baryon to photon ratio is small [101]. Adopting this as a limit, clearly both models described above are consistent. Should the BBN constraints get tighter [102], e.g., $N_\nu^{\max} < 3.5$, they could rule out the $(e\tau)(\mu s)$ model and leave out only the competing scheme as a viable alternative. However, the possible role of a primordial lepton asymmetry might invalidate this conclusion; for recent work on this, see [103].

It is well known that the neutral-to-charged current ratios are important observables in neutrino oscillation phenomenology, especially sensitive to the existence of singlet neutrinos, light or heavy [89]. On this basis, the two models above would be distinguishable at future neutral-current-sensitive solar and atmospheric neutrino experiments. For example, they may be tested in the SNO experiment [104] once they measure the solar neutrino flux (Φ_ν^{NC}) in their neutral current data and compare it with the corresponding CC value (Φ_ν^{CC}). If the solar neutrinos convert to active neutrinos, as in the $(e\tau)(\mu s)$ model, then one expects $\Phi_\nu^{\mathrm{CC}}/\Phi_\nu^{\mathrm{NC}}$ around 0.5, whereas in the $(es)(\mu\tau)$ scheme (ν_e conversion to ν_s), the above ratio would be nearly $\simeq 1$. Looking at pion production via the neutral current reaction $\nu_\tau + N \longrightarrow \nu_\tau + \pi^0 + N$ in the atmospheric data might also help in distinguishing between these two possibilities [105], since this reaction is absent in the case of sterile neutrinos, but would exist in the $(es)(\mu\tau)$ scheme.

If light sterile neutrinos indeed exist, one can show that they might contribute to a cosmic hot dark matter component and to an increased radiation content at the epoch of matter-radiation equality. These effects leave their imprint in sky maps of the cosmic microwave background radiation (CMBR) and may thus be detectable with the very high precision measurements expected at the upcoming MAP and PLANCK missions as noted in [32].

3.4. Heavy Tau Neutrino

Finally, the door is not closed to heavy neutrinos. Indeed, an alternative to the inclusion of hot dark matter is to simulate its effects through the late decay of an MeV tau neutrino [68], in the presence of a light sterile neutrino. Indeed, such a model was presented [106] where an unstable MeV Majorana tau neutrino naturally reconciles the cosmological observations of large- and small-scale density fluctuations with the cold dark matter picture. The model assumes the spontaneous violation of a global lepton number symmetry at the weak scale. The breaking of this symmetry generates the cosmologically required decay of the ν_τ with lifetime $\tau_{\nu_\tau} \sim 10^2$–$10^4$ s, as well as the masses and oscillations of the three light neutrinos ν_e, ν_μ, and ν_s which may account for the present solar and atmospheric data, though a dedicated three-neutrino fit in which one of the neutrinos is sterile would be desirable.

4. CONCLUSION

The angle-dependent atmospheric neutrino deficit provides, together with the solar neutrino data, strong evidence for physics beyond the Standard Model. Small neutrino masses provide the simplest, but not unique, explanation of the data. Allowing for alternative explanations of the underground experiments involving nonstandard neutrinos opens new possibilities involving either massless or even very heavy cosmologically unstable neutrinos, which naturally arise in many models. From this point of view, it is still too early to infer with great certainty neutrino masses and angles from underground experiments alone. Keeping within the framework of the standard neutrino oscillation interpretation of the data, one has an interesting possibility of bi-maximal neutrino mixing and of testing the neutrino anomalies not only at the upcoming long-baseline or neutrino factory experiments, but also at high-energy accelerators. On the other hand if the LSND result stands the test of time, this would be a strong indication for the existence of a light sterile neutrino. The two most attractive ways to reconcile underground observations with LSND invoke either ν_e–ν_τ conversions to explain the solar data, with ν_μ–ν_s oscillations accounting for the atmospheric deficit, or the opposite. At the moment, the latter is favored by the atmospheric data. These two basic schemes have distinct implications at future neutral-current-sensitive solar & atmospheric neutrino experiments, such as SNO and SuperKamiokande. To end in a philosophical mood, I would say that it is important to search for manifestations of massive and/or nonstandard neutrinos at the laboratory in an unbiased way. Though most of the recent excitement now comes from underground experiments, one should bear in mind that models of neutrino mass may lead to a plethora of new signatures which may be accessible also at high-energy accelerators, thus illustrating the complementarity between the two approaches.

ACKNOWLEDGMENTS

I am grateful to the organizers for their kind hospitality and to all my collaborators, especially Concha González-García and her student Carlos Peña, for the reanalysis of solar neutrino data. This work was supported by DGICYT, grant PB95-1077, and by the TMR, contract ERBFMRX-CT96-0090.

REFERENCES

1. B. T. Cleveland *et al.*, Astrophys. J. **496**, 505 (1998).
2. CALLEX Collab. (W. Hampel *et al.*), Phys. Lett. B **447**, 127 (1999); T. Kirsten, Talk Given at VI International Workshop on Topics in Astroparticle and Underground Physics (TAUP 99), Paris, September 1999; SAGE Collab. (J. N. Abdurashitov *et al.*), Phys. Rev. C **59**, 2246 (1999); astro-ph/9907113.
3. Super-Kamiokande Collab. (Y. Fukuda *et al.*), Phys. Rev. Lett. **82**, 1810 (1999); **82**, 2430 (1999); hep-ex/9812009.
4. Y. Suzuki, Talk Given at XIX International Symposium on Lepton and Photon Interactions at High Energies, Stanford University, August 9–14, 1999.
5. NUSEX Collab. (M. Aglietta *et al.*), Europhys. Lett. **8**, 611 (1989); Fréjus Collab. (Ch. Berger *et al.*), Phys. Lett. B **227**, 489 (1989); IMB Collab. (D. Casper *et al.*), Phys. Rev. Lett. **66**, 2561 (1991); R. Becker-Szendy *et al.*, Phys. Rev. D **46**, 3720 (1992); Kamiokande Collab. (H. S. Hirata *et al.*), Phys. Lett. B **205**, 416 (1988); **280**, 146 (1992); Kamiokande Collab. (Y. Fukuda *et al.*), Phys. Lett. B **335**, 237 (1994); Soudan Collab. (W. W. M. Allison *et al.*), Phys. Lett. B **391**, 491 (1997).
6. Super-Kamiokande Collab. (Y. Fukuda *et al.*), Phys. Rev. Lett. **81**, 1562 (1998); hep-ex/9807003; Y. Fukuda *et al.*, Phys. Rev. Lett. **82**, 2644 (1999); hep-ex/9812014; hep-ex/9908049; the most recent 52 kt yr data were presented by A. Mann in *Proceedings of the XIX Lepton Photon Symposium at Stanford University, August 1999.*
7. For review see J. W. F. Valle, Prog. Part. Nucl. Phys. **26**, 91 (1991).
8. J. Schechter and J. W. F. Valle, Phys. Rev. D **25**, 2951 (1982); for review see A. Morales, hep-ph/9809540.
9. J. Schechter and J. W. F. Valle, Phys. Rev. D **23**, 1666 (1981).
10. A. Yu. Smirnov and S. P. Mikheev, in *Proceedings of Neutrino Oscillations in Matter With Varying Density, '86 Massive Neutrinos, Tignes, 1986,* p. 355; L. Wolfenstein, Phys. Rev. D **20**, 2634 (1979).
11. M. C. González-García, P. C. De Holanda, C. Peña-Garay, and J. W. F. Valle, hep-ph/9906469; Nucl. Phys. B (in press).
12. J. W. F. Valle, Phys. Lett. B **199**, 432 (1987).
13. M. M. Guzzo and S. T. Petcov, Phys. Lett. B **271**, 172 (1991).
14. H. Nunokawa, Y. Z. Qian, A. Rossi, and J. W. F. Valle, Phys. Rev. D **54**, 4356 (1996); hep-ph/9605301.
15. P. I. Krastev and J. N. Bahcall, hep-ph/9703267.
16. M. C. González-García *et al.*, Phys. Rev. Lett. **82**, 3202 (1999); hep-ph/9809531.
17. D. Wyler and L. Wolfenstein, Nucl. Phys. B **218**, 205 (1983).
18. R. Mohapatra and J. W. F. Valle, Phys. Rev. D **34**, 1642 (1986); J. W. F. Valle, Nucl. Phys. B (Proc. Suppl.) **11**, 118 (1989).
19. J. Bernabeu *et al.*, Phys. Lett. B **187**, 303 (1987); J. G. Korner, A. Pilaftsis, and K. Schilcher, Phys. Lett. B **300**, 381 (1993).
20. M. C. González-García and J. W. F. Valle, Mod. Phys. Lett. A **7**, 477 (1992); erratum: **9**, 2569 (1994); A. Ilakovac and A. Pilaftsis, Nucl. Phys. B **437**, 491 (1995); A. Pilaftsis, Mod. Phys. Lett. A **9**, 3595 (1994).
21. L. J. Hall, V. A. Kostelecky, and S. Raby, Nucl. Phys. B **267**, 415 (1986).
22. J. W. F. Valle, Phys. Lett. B **131**, 87 (1983); G. Gelmini and J. W. F. Valle, Phys. Lett. B **142**, 181 (1984); J. W. F. Valle, Phys. Lett. B **159**, 49 (1985); A. Joshipura and S. Rindani, Phys. Rev. D **46**, 3000 (1992).
23. J. Schechter and J. W. F. Valle, Phys. Rev. D **24**, 1883 (1981); erratum: **25**, 283 (1982).
24. E. Kh. Akhmedov, Phys. Lett. B **213**, 64 (1988); C. S. Lim and W. Marciano, Phys. Rev. D **37**, 1368 (1988).
25. E. Kh. Akhmedov, hep-ph/9705451.
26. V. B. Semikoz *et al.*, hep-ph/9808274.
27. LSND Collab. (C. Athanassopoulos *et al.*), Phys. Rev. Lett. **75**, 2650 (1995); **77**, 3082 (1996); C. Athanassopoulos *et al.*, Phys. Rev. Lett. **81**, 1774 (1998).
28. LSND Collab. (W. C. Louis), Prog. Part. Nucl. Phys. **40**, 151 (1998).
29. J. T. Peltoniemi, D. Tommasini, and J. W. F. Valle, Phys. Lett. B **298**, 383 (1993).
30. J. T. Peltoniemi and J. W. F. Valle, Nucl. Phys. B **406**, 409 (1993).
31. D. O. Caldwell and R. N. Mohapatra, Phys. Rev. D **48**, 3259 (1993).
32. S. Hannestad and G. Raffelt, Phys. Rev. D **59**, 043001 (1999); astro-ph/9805223.
33. J. N. Bahcall, astro-ph/9808162.
34. J. N. Bahcall, S. Basu, and M. H. Pinsonneault, Phys. Lett. B **433**, 1 (1998).
35. GONG Collab. (J. Christensen-Dalsgaard *et al.*), Science **272**, 1286 (1996); J. N. Bahcall and M. H. Pinsonneault, Rev. Mod. Phys. **67**, 781 (1995); A. Kovetz and G. Shaviv, Astrophys. J. **426**, 787 (1994); V. Castellani *et al.*, Phys. Lett. B **324**, 425 (1994); J. Christensen-Dalsgaard, Europhys. News **25**, 71 (1994); X. Shi, D. N. Schramm, and D. S. P. Dearborn, Phys. Rev. D **50**, 2414 (1994); A. Dar and G. Shaviv, Astrophys. J. **468**, 933 (1996); V. Castellani, S. Degl'Innocenti, and G. Fiorentini, Astron. Astrophys. **271**, 601 (1993); S. Turck-Chièze and I. Lopes, Astrophys. J. **408**, 347 (1993); G. Berthomieu, J. Provost, P. Morel, and Y. Lebreton, Astron. Astrophys. **268**, 775 (1993); J. N. Bahcall and M. H. Pinsonneault, Rev. Mod. Phys. **64**, 885 (1992); I.-J. Sackman, A. I. Boothroyd, and W. A. Fowler, Astrophys. J. **360**, 727 (1990); J. N. Bahcall and R. K. Ulrich, Rev. Mod. Phys. **60**, 297 (1988); O. Richard, S. Vauclair, C. Charbonnel, and W. A. Dziembowski, Astron. Astrophys. **312**, 1000 (1996); F. Ciacio, S. Degl'Innocenti, and B. Ricci, Astron. Astrophys., Suppl. Ser. **123**, 449 (1997); astro-ph/9605157.
36. J. N. Bahcall, Phys. Lett. B **338**, 276 (1994); V. Castellani *et al.*, Phys. Lett. B **324**, 245 (1994); N. Hata, S. Bludman, and P. Langacker, Phys. Rev. D **49**, 3622 (1994); V. Berezinsky, Comments Nucl. Part. Phys. **21**, 249 (1994).

37. J. N. Bahcall *et al*., Phys. Rev. Lett. **78**, 171 (1997).
38. V. Barger, K. Whisnant, and R. J. Phillips, Phys. Rev. D **24**, 538 (1981); S. L. Glashow and L. M. Krauss, Phys. Lett. B **190**, 199 (1987); S. L. Glashow, P. J. Kernan, and L. M. Krauss, Phys. Lett. B **445**, 412 (1999).
39. V. Barger *et al*., Phys. Lett. B **437**, 107 (1998); hep-ph/9806387; E. Torrente-Lujan, Phys. Lett. B **389**, 557 (1996); S. Davidson and S. F. King, Phys. Lett. B **445**, 191 (1998).
40. J. N. Bahcall and P. I. Krastev, Phys. Lett. B **436**, 243 (1998); R. Escribano *et al*., Phys. Lett. B **444**, 39 (1998).
41. G. Fiorentini *et al*., Phys. Lett. B **444**, 387 (1998); astro-ph/9810083.
42. P. C. De Holanda *et al*., Phys. Rev. D **60**, 093010 (1999); hep-ph/9903473; see also J. N. Bahcall, P. I. Krastev, and A. Yu. Smirnov, hep-ph/9905220.
43. A. B. Balantekin, J. M. Fetter, and F. N. Loreti, Phys. Rev. D **54**, 3941 (1996); F. N. Loreti and A. B. Balantekin, Phys. Rev. D **50**, 4762 (1994); F. N. Loreti *et al*., Phys. Rev. D **52**, 6664 (1995).
44. H. Nunokawa, A. Rossi, V. Semikoz, and J. W. F. Valle, Nucl. Phys. B **472**, 495 (1996); hep-ph/9610526.
45. P. Bamert, C. P. Burgess, and D. Michaud, Nucl. Phys. B **513**, 319 (1998); C. P. Burgess, hep-ph/9711425; C. P. Burgess and D. Michaud, Ann. Phys. (N.Y.) **256**, 1 (1997); hep-ph/9611368.
46. C. Arpesella *et al*., Proposal of the Borexino Experiment (1991).
47. V. Barger and K. Whisnant, hep-ph/9903262; S. Goswami, D. Majumdar, and A. Raychaudhuri, hep-ph/9909453.
48. S. P. Mikheyev and A. Yu. Smirnov, Phys. Lett. B **429**, 343 (1998); B. Faid, G. L. Fogli, E. Lisi, and D. Montanino, hep-ph/9805293.
49. Y. Fukuda *et al*., Phys. Lett. B **433**, 9 (1998); **436**, 33 (1998).
50. M. Nakahata, Talk Given at VI International Workshop on Topics in Astroparticle and Underground Physics (TAUP 99), Paris, September 1999.
51. K. Daum *et al*., Z. Phys. C **66**, 417 (1995).
52. NUSEX Collab. (M. Aglietta *et al*.), see [5].
53. H. S. Hirata *et al*., Phys. Lett. B **280**, 146 (1992); Y. Fukuda *et al*., Phys. Lett. B **335**, 237 (1994).
54. R. Becker-Szendy *et al*., Phys. Rev. D **46**, 3720 (1992).
55. W. W. M. Allison *et al*., Phys. Lett. B **449**, 137 (1999).
56. T. K. Gaisser, F. Halzen, and T. Stanev, Phys. Rep. **258**, 174 (1995).
57. T. K. Gaisser and T. Stanev, Phys. Rev. D **57**, 1977 (1998); G. Barr, T. K. Gaisser, and T. Stanev, Phys. Rev. D **39**, 3532 (1989); **38**, 85 (1988); V. Agrawal *et al*., Phys. Rev. D **53**, 1314 (1996); L. V. Volkova, Sov. J. Nucl. Phys. **31**, 784 (1980); M. Honda, T. Kajita, S. Midorikawa, and K. Kasahara, Phys. Rev. D **52**, 4985 (1995).
58. M. C. González-García *et al*., Phys. Rev. D **58**, 033004 (1998); hep-ph/9801368; for the 535 days data sample update and the comparison of active and sterile channels see M. C. González-García, H. Nunokawa, O. L. Peres, and J. W. F. Valle, Nucl. Phys. B **543**, 3 (1999); hep-ph/9807305.
59. M. Appollonio *et al*., Phys. Lett. B **420**, 397 (1998); hep-ex/9711002.
60. M. C. González-García, Talk Given at International Workshop on Particles in Astrophysics and Cosmology: From Theory to Observation, Valencia, Spain, May 3–8, 1999, Ed. by V. Berezinsky, G. Raffelt, and J. W. F. Valle, Nucl. Phys. B (Proc. Suppl.) (in press).
61. R. Foot, R. R. Volkas, and O. Yasuda, TMUP-HEL-9801; O. Yasuda, Phys. Rev. D **58**, 091301 (1998); G. L. Fogli, E. Lisi, A. Marrone, and G. Scioscia, Phys. Rev. D **59**, 033001 (1999); hep-ph/9808205; E. Kh. Akhmedov, A. Dighe, P. Lipari, and A. Yu. Smirnov, hep-ph/9808270.
62. P. Lipari and M. Lusignoli, Phys. Rev. D **60**, 013003 (1999); **58**, 073005 (1998).
63. W. Louis, http://www.neutrino.lanl.gov/LSND/
64. G. F. Smoot *et al*., Astrophys. J. Lett. **396**, L1 (1992); E. L. Wright *et al*., Astrophys. J. Lett. **396**, L13 (1992).
65. R. Rowan-Robinson, *Cosmological Dark Matter* (World Sci., Singapore, 1994), p. 7.
66. J. R. Primack and M. A. Gross, astro-ph/9810204; E. Gawiser and J. Silk, astro-ph/9806197; Science **280**, 1405 (1998) and references therein.
67. G. Gelmini, D. N. Schramm, and J. W. F. Valle, Phys. Lett. B **146**, 311 (1984).
68. J. Bond, Phys. Lett. B **265**, 245 (1991); M. Davis *et al*., Nature **356**, 489 (1992); S. Dodelson, G. Gyuk, and M. Turner, Phys. Rev. Lett. **72**, 3754 (1994); H. Kikuchi and E. Ma, Phys. Rev. D **51**, R296 (1995); H. B. Kim and J. E. Kim, Nucl. Phys. B **433**, 421 (1995); M. White, G. Gelmini, and J. Silk, Phys. Rev. D **51**, 2669 (1995); A. Masiero, D. Montanino, and V. Peloso, hep-ph/9902380.
69. S. Hannestad, Phys. Rev. D **59**, 125020 (1999); astro-ph/9903475.
70. A. G. Lyne and D. R. Lorimer, Nature **369**, 127 (1994).
71. N. N. Chugai, Pis'ma Astron. Zh. **10**, 210 (1984) [Sov. Astron. Lett. **10**, 87 (1984)].
72. A. Vilenkin, Astrophys. J. **451**, 700 (1995); Dong Lai and Y.-Z. Qian, astro-ph/9712043.
73. A. Kusenko, G. Segrè, and A. Vilenkin, Phys. Lett. B **437**, 359 (1998); astro-ph/9806205.
74. H. Nunokawa, V. B. Semikoz, A. Yu. Smirnov, and J. W. F. Valle, Nucl. Phys. B **501**, 17 (1997).
75. A. Kusenko and G. Segrè, Phys. Rev. Lett. **77**, 4872 (1996); **79**, 2751 (1997); Y.-Z. Qian, Phys. Rev. Lett. **79**, 2750 (1997).
76. E. Kh. Akhmedov, A. Lanza, and D. W. Sciama, Phys. Rev. D **56**, 6117 (1997).
77. D. Grasso, H. Nunokawa, and J. W. F. Valle, Phys. Rev. Lett. **81**, 2412 (1998); astro-ph/9803002.
78. H. T. Janka and G. G. Raffelt, Phys. Rev. D **59**, 023005 (1999); astro-ph/9808099.
79. A. Kusenko and G. Segrè, Phys. Rev. D **59**, 061302 (1999); astro-ph/9811144.
80. D. Grasso *et al*. (in preparation).
81. N. Fornengo, M. C. González-García, and J. W. F. Valle, hep-ph/9906539.
82. V. Barger *et al*., Phys. Rev. Lett. **82**, 2640 (1999); hep-ph/9907421.

83. M. Gasperini, Phys. Rev. D **38**, 2635 (1988); J. Pantaleone, A. Halprin, and C. N. Leung, Phys. Rev. D **47**, R4199 (1993); A. Halprin, C. N. Leung, and J. Pantaleone, Phys. Rev. D **53**, 5365 (1996); S. Coleman and S. L. Glashow, Phys. Lett. B **405**, 249 (1997); S. L. Glashow *et al*., Phys. Rev. D **56**, 2433 (1997); S. Coleman and S. L. Glashow, Phys. Rev. D **59**, 116008 (1999); A. M. Gago, H. Nunokawa, and R. Zukanovich-Funchal, hep-ph/9909250.
84. S. Lola and J. D. Vergados, Prog. Part. Nucl. Phys. **40**, 71 (1998); G. Altarelli and F. Feruglio, Phys. Lett. B **439**, 112 (1998); hep-ph/9807353.
85. G. Altarelli and F. Feruglio, Phys. Lett. B **451**, 388 (1999); hep-ph/9812475; S. Lola and G. G. Ross, hep-ph/9902283; R. Barbieri, L. J. Hall, and A. Strumia, Phys. Lett. B **445**, 407 (1999); hep-ph/9808333; M. E. Gómez, G. K. Leontaris, S. Lola, and J. D. Vergados, Phys. Rev. D **59**, 116009 (1999); hep-ph/9810291; G. K. Leontaris, S. Lola, C. Scheich, and J. D. Vergados, Phys. Rev. D **53**, 6381 (1996).
86. J. C. Romao *et al*., hep-ph/9907499.
87. C. Quigg, hep-ph/9908357.
88. J. Sato, hep-ph/9910442; O. Yasuda, hep-ph/9910428; H. Minakata and H. Nunokawa, Phys. Rev. D **57**, 4403 (1998); hep-ph/9705208; A. Romanino, hep-ph/9909425.
89. J. Schechter and J. W. F. Valle, Phys. Rev. D **22**, 2227 (1980).
90. S. Pastor, J. Segura, V. B. Semikoz, and J. W. F. Valle, hep-ph/9905405; Nucl. Phys. B (in press).
91. A. Ioannissyan and J. W. F. Valle, Phys. Lett. B **332**, 93 (1994); B. Bamert and C. P. Burgess, Phys. Lett. B **329**, 289 (1994); D. Caldwell and R. N. Mohapatra, Phys. Rev. D **50**, 3477 (1994); D. G. Lee and R. N. Mohapatra, Phys. Lett. B **329**, 463 (1994); A. S. Joshipura, Z. Phys. C **64**, 31 (1994).
92. J. A. Cases *et al*., hep-ph/9905381; J. Ellis and S. Lola, hep-ph/9904279; N. Haba, Y. Matsui, N. Okamura, and M. Sugiura, hep-ph/9908429.
93. E. Ma, hep-ph/9907503.
94. R. N. Mohapatra and A. Pérez-Lorenzana, hep-ph/9910474; A. Ioannissyan and J. W. F. Valle (in preparation).
95. C. Guinti, hep-ph/9909465.
96. Qu. Y. Liu and A. Yu. Smirnov, Nucl. Phys. B **524**, 505 (1998); V. Barger, K. Whisnant, and T. Weiler, Phys. Lett. B **427**, 97 (1998); S. Gibbons, R. N. Mohapatra, S. Nandi, and A. Raichoudhuri, Phys. Lett. B **430**, 296 (1998); Nucl. Phys. B **524**, 505 (1998); S. Bilenky, C. Giunti, and W. Grimus, Eur. Phys. J. C **1**, 247 (1998); S. Goswami, Phys. Rev. D **55**, 2931 (1997); N. Okada and O. Yasuda, Int. J. Mod. Phys. A **12**, 3669 (1997).
97. E. J. Chun, A. Joshipura, and A. Smirnov, *Elementary Particle Physics: Present and Future* (World Sci., Singapore, 1996); P. Langacker, Phys. Rev. D **58**, 093017 (1998); M. Bando and K. Yoshioka, Prog. Theor. Phys. **100**, 1239 (1998).
98. J. R. Primack *et al*., Phys. Rev. Lett. **74**, 2160 (1995).
99. J. Schechter and J. W. F. Valle, Phys. Rev. D **21**, 309 (1980).
100. R. Barbieri and A. Dolgov, Phys. Lett. B **237**, 440 (1990); K. Enqvist, K. Kainulainen, and J. Maalampi, Phys. Lett. B **249**, 531 (1990); D. P. Kirilova and M. Chizov, hep-ph/9707282.
101. S. Sarkar, Rep. Prog. Phys. **59**, 1493 (1996); P. J. Kernan and S. Sarkar, Phys. Rev. D **54**, R3681 (1996).
102. G. Fiorentini, E. Lisi, S. Sarkar, and F. L. Villante, Phys. Rev. D **58**, 063506 (1998); E. Lisi, S. Sarkar, and F. L.Villante, Phys. Rev. D **59**, 123520 (1999).
103. R. Foot and R. R. Volkas, Phys. Rev. D **55**, 5147 (1997); A. D. Dolgov, S. H. Hansen, S. Pastor, and D. V. Semikoz, hep-ph/9910444.
104. SNO Collab. (E. Norman *et al*.), in *Proceedings of the Fermilab Conference: DPF'92, 1992* (World Sci., Singapore, 1992), p. 1450.
105. A. Smirnov and F. Vissani, Phys. Lett. B **432**, 376 (1998); J. G. Learned, S. Pakvasa, and J. Stone, hep-ph/9805343; H. Murayama and L. Hall, hep-ph/9806218.
106. A. Joshipura and J. W. F. Valle, Nucl. Phys. B **440**, 647 (1995).

Physics of Atomic Nuclei, Vol. 63, No. 6, 2000, pp. 934–942. From Yadernaya Fizika, Vol. 63, No. 6, 2000, pp. 1010–1018.
Original English Text Copyright © 2000 by Gajewski.

Update of Results from the SuperKamiokande Detector (June 1999)*

W. Gajewski
(for the SuperKamiokande Collaboration)
University of California, Irvine, USA

Abstract—The data collected in the SuperKamiokande detector as of June 1999 are presented. This review covers the complete spectrum of neutrino interactions from solar neutrinos, through the entire spectrum of atmospheric neutrinos, and ending with the neutrino beam produced at KEK for a long-baseline experiment. Different interpretations of these data as demonstrations of neutrino oscillations are discussed. The results of a search for nucleon decay are also summarized. *© 2000 MAIK “Nauka/Interperiodica”.*

1. INTRODUCTION

This paper roughly summarizes the data collected in the SuperKamiokande detector as of July 1999 and outlines some results of their analysis. Minimal explanations are provided. For more in depth descriptions, the reader is advised to consult the papers referred to.

SuperKamiokande is a large, 50 kt water-Cherenkov detector situated inside Mt. Ikeno near Toyama, Japan. It consists of two optically separated volumes. The 32 kt inner volume is viewed by 11146 50-cm diameter photomultiplier tubes (PMT); 22.5 kt of the inner detector is used as the fiducial volume. The outer 18 kt, confined within reflective walls, is viewed by 1885 20-cm diameter PMTs and serves as an active shield/veto for the inner detector. The pattern of light recorded by the PMTs permits reconstruction of event geometry and identification of particles inducing electromagnetic cascades (showers). The total amount of light provides a measure of the energy released in the event. The methodologies of reconstruction and calibration are discussed elsewhere [1]. The detector has been collecting data since April 1, 1996, with a data taking efficiency of about 90% (the rest is used for frequent calibration runs). At the time of this update, from about 850 live-days have been analyzed. The next update is foreseen in the middle of 2000.

The material discussed here is concerned with the following subjects:

(1) Interactions of neutrinos produced inside the sun. These involve neutrino elastic scattering on electrons with recoiling electrons greater than 5 MeV. That means that, out of all the neutrinos produced in the Sun, the detector is sensitive only to those produced in decays of ^{8}B.

(2) Interactions of neutrinos produced by cosmic rays in the Earth’s atmosphere. These are classified according to their energy and topology as

low energy events totally contained in the inner detector volume (sub-GeV sample),

higher energy events totally contained in the inner detector volume (multi-GeV sample),

events originating in the inner detector but having exiting tracks (Partially contained (PC) sample),

events with a track originating outside of the inner detector, but stopping inside (stopping-mu),

events with a track originating outside and passing through the inner detector (thru-mu).

(3) Interactions of neutrinos produced by the 12-GeV proton synchrotron at KEK (in Tsukuba near Tokyo). In this case, the SuperKamiokande detector serves as the far detector for a long-baseline neutrino-oscillation experiment.

(4) Search for a signal of spontaneous nucleon decay.

In the next sections of this report, we review the most recent results in each of these fields.

2. SOLAR NEUTRINOS

The current update covers 825 d of lifetime for the data with recoil energy larger than 6.5 MeV and 524 d of data for recoils in the energy interval of 5.5–6.5 MeV (their collection began with almost a year’s delay). The first sample consists of 11236 events contained in the 22.5 kt fiducial volume. From this number of events, one can estimate the flux of neutrinos to be

$$(2.45^{+0.04}_{-0.04}(\text{stat.})^{+0.07}_{-0.07}(\text{syst.}) \times 10^6)/(\text{cm}^2\ \text{s}),$$

which constitutes only a

$$0.475^{+0.008}_{-0.007}(\text{stat.})^{+0.013}_{-0.013}(\text{syst.})$$

part of the expected flux according to the PB98 model [2]. This result, dominated by systematic uncertainties, is similar to the one published in previous reviews. It

---

* This article was submitted by the author in English.

led to the speculations that the smaller than expected fluxes measured by various solar neutrino experiments indicate neutrino oscillations. Considering the fact that each experiment is sensitive to a different part of the solar neutrino energy spectrum, one can derive three distinct regions of squared mass difference (δm^2) and the mixing of the neutrino mass eigenstates which explains the experimental data (see [3]):

very low $\delta m^2 \sim 10^{-10}$ eV^2 and large mixing, thus oscillations taking place in the vacuum on the way from the Sun to the Earth (so called "just so" region),

larger δm^2 close to 10^{-5} eV^2, thus oscillations being due to electron-neutrino interactions with the matter of the Sun (MSW effect),

either with large mixing ($\sin^2 2\theta \sim 1$) (LMA region),

or small mixing ($\sin^2 2\theta \sim 10^{-2}$) (SMA region).

In addition to measurements of the total flux of solar neutrinos, SuperKamiokande is able to detect new neutrino physics in a model independent way. If, for instance, a significant difference between neutrino fluxes at night (neutrinos passing through the earth) and during the day were observed, it would indicate a matter-oscillation effect. The results of the day–night variation of the neutrino flux are shown in Fig. 1. These fluxes are

day (403.2 d)

$$\text{flux} = (2.37^{+0.05}_{-0.05}(\text{stat.})^{+0.07}_{-0.06}(\text{syst.}) \times 10^6)/(\text{cm}^2\ \text{s}),$$

night (421.5 d)

$$\text{flux} = (2.51^{+0.06}_{-0.05}(\text{stat.})^{+0.07}_{-0.07}(\text{syst.}) \times 10^6)/(\text{cm}^2\ \text{s}).$$

The difference between day and night fluxes is equal to

$$\frac{D-N}{D+N} = -0.065 \pm 0.031(\text{stat.}) \pm 0.013(\text{syst.}),$$

which is only a 1.9σ effect.

Similarly, a seasonal variation of the flux, different from that resulting merely from the eccentricity of the Earth's orbit, would indicate an effect of vacuum oscillations. The result of the measured seasonal variation is shown in Fig. 2 together with the predicted variation due to the Earth's orbit. Again, there is no significant effect; both measured and predicted fluxes agree.

Finally, both matter and vacuum oscillations could cause distortions of the energy spectrum of recoiling electrons. The ratio of the measured spectrum to that predicted by the solar model is shown in Fig. 3. They agree with each other again on the level of 1.6σ. The only slight disagreement might exist at the higher energy part of the spectrum. Here, in addition to neutrinos from decays of ^{8}B, some contribution from the so called Hep reaction ($^3\text{He} + p \longrightarrow {}^4\text{He} + e^+ + \nu_e$) is expected. The cross section of this reaction is estimated to be in the range of 0.5 to 7 times that used in the standard solar model [4]. Leaving that cross section as a

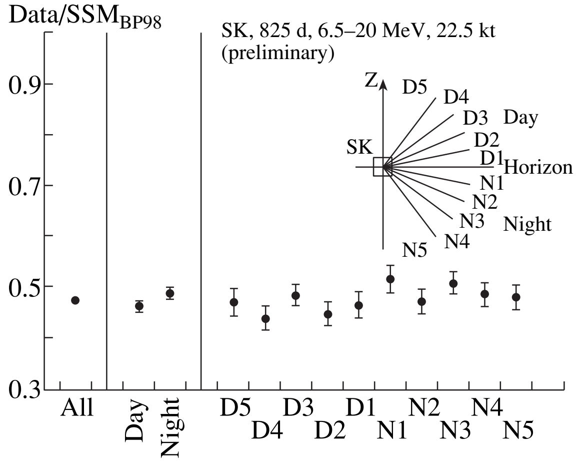

Fig. 1. Day–night variation of the solar neutrino flux.

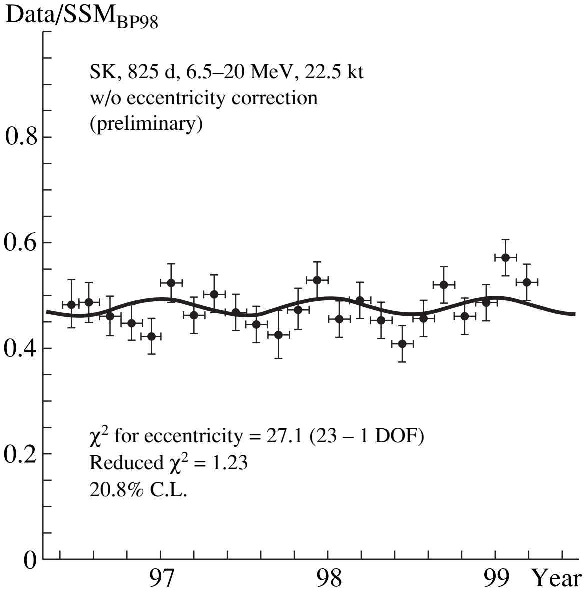

Fig. 2. Seasonal variation of the solar-neutrino flux.

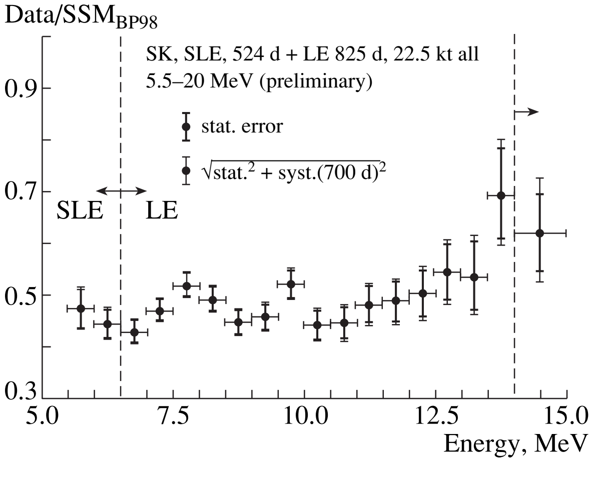

Fig. 3. Spectrum of the recoil electrons from solar-neutrino interactions.

Table 1. Summary of atmospheric neutrino interactions in the SuperKamiokande detector as June 1999

Sample	Data	MC-Honda	MC-Bartol
Sub-GeV (848 d)			
1-ring	3678	4371.6	4268.1
e-like	1826	1754.0	1729.5
μ-like	1852	2617.6	2538.6
$R = \left(\frac{\mu}{e}\right)^{\text{data}} / \left(\frac{\mu}{e}\right)^{\text{MC-H}}$	$0.680^{+0.023}_{-0.022}$ (stat.) $\pm 0.005 \pm 0.053$		
$R = \left(\frac{\mu}{e}\right)^{\text{data}} / \left(\frac{\mu}{e}\right)^{\text{MC-B}}$	$0.691^{+0.023}_{-0.022}$ (stat.) $\pm 0.005 \pm 0.054$		
2-ring	1156	1389.1	1369.0
≥3-ring	300	481.7	480.8
Multi-GeV (848 d)			
1-ring	790	901.3	917.6
e-like	439	414.3	430.8
μ-like	351	487.0	486.8
$R = \left(\frac{\mu}{e}\right)^{\text{data}} / \left(\frac{\mu}{e}\right)^{\text{MC-H}}$	$0.680^{+0.050}_{-0.047}$ (stat.) $\pm 0.011 \pm 0.099$		
$R = \left(\frac{\mu}{e}\right)^{\text{data}} / \left(\frac{\mu}{e}\right)^{\text{MC-B}}$	$0.708^{+0.052}_{-0.049}$ (stat.) $\pm 0.011 \pm 0.103$		
2-ring	451	575.7	592.2
≥3-ring	416	503.8	525.8
PC (848 d)	451	656.4	695.7
Multi-GeV + PC			
$R = \left(\frac{\mu}{e}\right)^{\text{data}} / \left(\frac{\mu}{e}\right)^{\text{MC-H}}$	$0.662^{+0.041}_{-0.038}$ (stat.) $\pm 0.009 \pm 0.078$		
$R = \left(\frac{\mu}{e}\right)^{\text{data}} / \left(\frac{\mu}{e}\right)^{\text{MC-B}}$	$0.668^{+0.041}_{-0.038}$ (stat.) $\pm 0.009 \pm 0.078$		
Thru-μ (923 d)	1028		
Flux $\times 10^{13}$	$1.70 \pm 0.05 \pm 0.02$	1.84 ± 0.41	1.97 ± 0.44
Stopping-μ (902 d)	245		
Flux $\times 10^{13}$	$0.40 \pm 0.03 \pm 0.02$	0.68 ± 0.15	0.73 ± 0.16
$R = \Phi_s/\Phi_t$	$0.235 \pm 0.018^{+0.013}_{-0.011}$	$0.368^{+0.049}_{-0.044}$	$0.372^{+0.049}_{-0.044}$

free parameter, the fit to the measured spectrum yields a He*p* cross section 9–16 times larger, and the measured and predicted spectra are in agreement within 1σ.

One must notice that, although the disagreement of any of these measurements with its prediction would indicate neutrino oscillations, agreement does not exclude oscillations. As a matter of fact, it has been shown [5] that each of these measurements separately and all of them together do not significantly exclude any of the δm^2-mixing regions derived from the flux measurements, with the exception of the vacuum oscillation region. These measurements predict a new allowed region just above the excluded vacuum oscillation region. However, it requires a flux 25% smaller than that predicted by the Standard Model.

3. ATMOSPHERIC NEUTRINOS

From the time of the announcement in 1998 by the SuperKamiokande Collaboration of the discovery of neutrino oscillation, the sample of atmospheric neutrino interactions collected in the detector has been increased almost twofold. However, all the major features of the sample which led to this revolutionary conclusion have remained unchanged, and their significance has been enhanced by the smaller statistical errors.

A summary of the currently available experimental sample is given in Table 1. These data conclusively confirm the deficit of muon neutrino interactions previously reported by Kamiokande, IMB, Soudan 2, and MACRO, while the number of electron-neutrino interactions remains close to that expected.

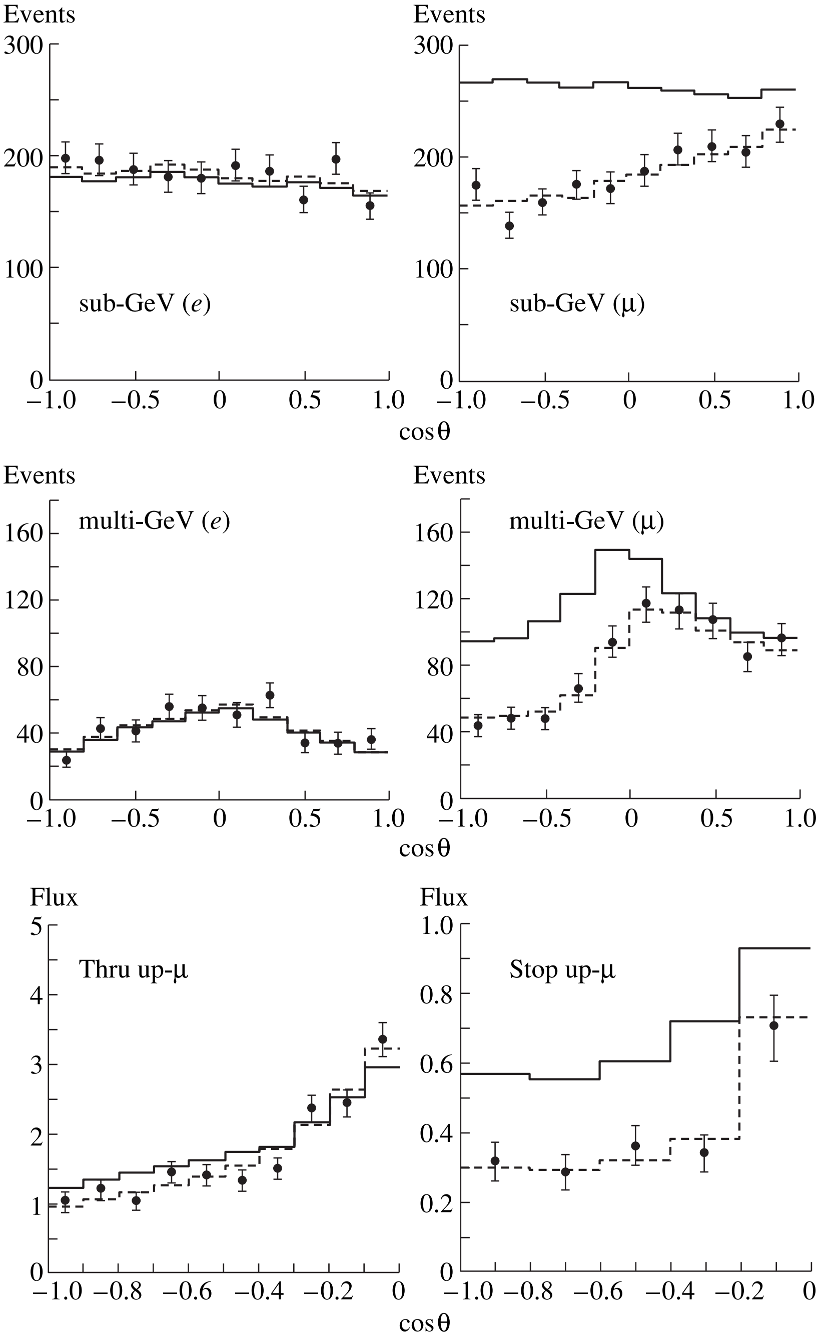

Fig. 4. Zenith-angle distributions of various samples of neutrino interactions observed in the SuperKamiokande detector. Starting from the left top and going down by rows: sub-GeV electrons and muons, multi-GeV electrons and muons, thru up-muons and up-muon stoppers. Solid lines are MC predictions, while broken lines show best fit predictions for ν_x–ν_τ oscillations.

Zenith-angle distributions, related to the path length of neutrinos between their production point and the detector, reveal the reason for this deficit. These distributions for all the available samples of neutrino interactions are shown in Fig. 4. It is the first time that, due to the extraordinary size of the SuperKamiokande detector, these distributions can be observed so clearly. While the electron neutrino interactions have zenith-angle distributions similar to the ones expected, the muon neutrinos seem to disappear when passing about 13000 km through the Earth. Those arriving from above are almost undisturbed. These global features of zenith-angle distributions remain unchanged with the increasing statistics of the experimental samples. So far, the only explanation of this effect is that muon neutrinos disappear due to oscillations $\nu_\mu \longrightarrow \nu_x$, where the most probable candidate for ν_x is ν_τ.

Table 2. Results of the fits of two-component oscillation to the atmospheric neutrino interactions in the SuperKamiokande detector

	$\nu_\mu \longrightarrow \nu_\tau$	$\nu_\mu \longrightarrow \nu_s$	$\nu_\mu \longrightarrow \nu_e$	Global $\nu_\mu \longrightarrow \nu_\tau$
χ^2	55.4	55.6	101.7	67.5
DOF	67	67	67	77
$\delta m^2 \times 10^3$, eV^2	3.1	3.2	5.6	3.5
$\sin^2 2\theta$	0.995	0.985	0.993	1.0
α	0.049	0.054	–0.170	0.055
β_L	0.013	0.005	0.130	0.026
β_H	–0.078	–0.130	–0.015	–0.070
β_{PC}	–0.030	–0.044	–0.048	–0.025
UT/FC				0.090
US/FC				–0.060

The simplest approach to the analysis of the oscillation effect is based on the assumption of two-component mixing. The fits were made to the contained event samples considering ν_μ oscillations to ν_e, ν_τ, and ν_s following the procedure described in detail in [6]. The results of these fits are provided in Table 2, where in addition to the oscillation parameters δm^2 and $\sin^2 2\theta$ we also list the global normalization of the data to the Monte Carlo α, and the relative normalizations β of the electron neutrino sample $(1 + \beta/2)$ and the muon neutrino sample $(1 – \beta/2)$. The hypothesis of no oscillations leads to a χ^2 of 177/67 DOF, which is far too high to accept the observed effect as merely a statistical fluctuation. The results in the table show that, while one cannot judge between ν_τ and ν_s, the oscillations to ν_e are much less favored. For the acceptable fits, the δm^2 values are close to 3×10^{-3} eV^2, and the mixing is close to maximal.

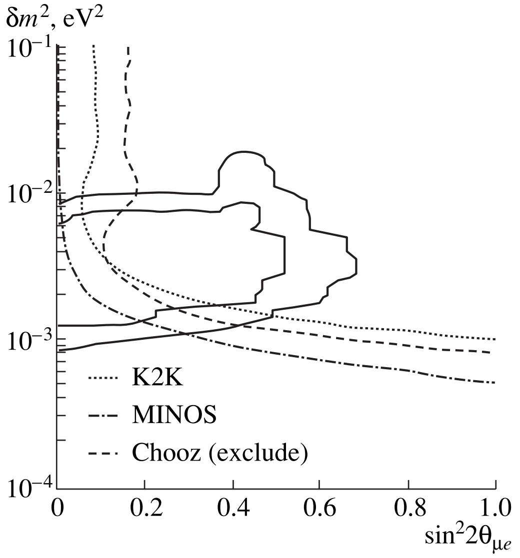

Fig. 5. The region of $(\delta m^2, \sin^2 2\theta_{\mu e})$ allowed by three component oscillation analysis.

An attempt was also made [7] to fit to the data a three-component neutrino-oscillation model. The flavor neutrino states $|\nu_\alpha\rangle$ $(\alpha = e, \mu, \tau)$ are a linear superposition of mass eigenstates $|\nu_i\rangle$ $(i = 1, 2, 3)$

$$|\nu_\alpha\rangle = \sum U_{\alpha i} |\nu_i\rangle.$$

To simplify the problem, it was assumed, in accordance with the solar neutrino results, that the masses of electron and muon neutrinos are almost equal and much smaller than that of the tau neutrino. In such a scheme, the oscillations can be described by only three parameters: one δm^2 and two mixing parameters $|U_{e3}|^2$ and $|U_{\mu 3}|^2$ (often respectively denoted as $\sin^2\vartheta_{13}$ and $\cos^2\vartheta_{13}\sin^2\vartheta_{23}$). Then, the transition and survival probabilities are given by

$$P(\nu_\beta \longrightarrow \nu_\alpha) = 4|U_{\alpha 3}|^2 |U_{\beta 3}|^2 \sin^2\left(\frac{\delta m^2 L}{4p}\right)$$

$$= \sin^2 2\theta_{\alpha\beta} \sin^2\left(\frac{\delta m^2 L}{4p}\right),$$

$$P(\nu_\alpha \longrightarrow \nu_\alpha) = 1 - 4|U_{\alpha 3}|^2 (1 - |U_{\alpha 3}|^2) \sin^2\left(\frac{\delta m^2 L}{4p}\right)$$

$$= 1 - \sin^2 2\theta_{\alpha\alpha} \sin^2\left(\frac{\delta m^2 L}{4p}\right).$$

The fit of this model to the contained event samples resulted in $\chi^2 = 54/66$ DOF for the parameters: $\delta m^2 = 3.2 \times 10^{-3}$ eV^2, $\sin^2\vartheta_{13} = 0.025$, and $\sin^2\vartheta_{23} = 0.425$. These mixing angles correspond to $\sin^2 2\theta_{\mu\mu} = 0.97$ in good agreement with the parameters from the two-component fit. The remaining parameter, describing ν_e survival probability, has the most probable value of $\sin^2 2\theta_{ee} = 0.1$. The allowed region of the parameters for $\nu_\mu \longrightarrow \nu_e$ oscillation is shown in Fig. 5 together with the exclusion regions set or to be set by other experiments. So far, the $\nu_\mu \longrightarrow \nu_e$ oscillations with a relatively large δm^2 and a small mixing cannot be ruled out.

The most stringent limits on the δm^2 and mixing for $\nu_\mu \longrightarrow \nu_\tau$ two-component oscillations can be set using all the data available for the atmospheric neutrinos. They include not only interactions contained in the fiducial volume but also those for the entering upgoing muons. The global fit to these data leads to the parameters listed in the last column of Table 2. As one can see, the results of this fit agree with those from the fits to the samples with only contained events. The allowed regions for the parameters resulting from the global fit are shown in Fig. 6.

Still, the previously mentioned fits are not sufficiently restrictive to resolve the question whether ν_μ oscillates to ν_τ or a sterile ν_s. To resolve this question, the following observation might be applied [8]: if the

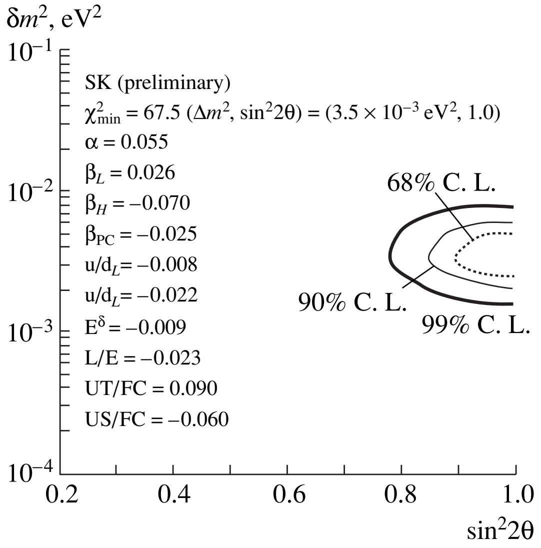

Fig. 6. The region of (δm^2, $\sin^2 2\theta$) allowed by global fit to all atmospheric-neutrino-interaction samples collected in the upper Kamiokande detector.

oscillations take place between ν_a and ν_b due to squared mass difference $\delta m^2 = m_a^2 - m_b^2$ and mixing $\sin^2 2\theta_{ab}$ over the path L, then for neutrinos traversing matter both path and the mixing undergo the following modification:

$$\sin^2 2\theta_{\text{matt}} = \frac{\sin^2 2\theta_{\text{vac}}}{(\xi - \cos 2\theta_{\text{vac}})^2 + \sin^2 2\theta_{\text{vac}}},$$

$$L_{\text{matt}} = \frac{L_{\text{vac}}}{\sqrt{(\xi - \cos 2\theta_{\text{vac}})^2 + \sin^2 2\theta_{\text{vac}}}},$$

where

$$\xi = \frac{2E_\nu V_{ab}}{\delta m^2}.$$

In this formula, V_{ab} is the difference between interaction potentials of neutrinos a and b with the matter. For ν_μ and ν_s, this difference is approximately 2×10^{-4} eV²/GeV. With this potential, the equations reveal that, for neutrino energies larger than say 20 GeV, the potential factor drives the matter oscillation parameters to zero, implying that no oscillations can occur. Contrary, for low-energy neutrinos, matter effects do not modify the oscillatory behavior. Thus, examining the samples of interactions of high energy neutrinos provides the means to distinguish $\nu_\mu \longrightarrow \nu_\tau$ from $\nu_\mu \longrightarrow \nu_s$ s oscillations. It is accomplished [9] by examining the angular distributions of events with large depositions of Cherenkov light in the detector. The rate of events coming from below, passing through the Earth, would be either close to that predicted without oscillations (for $\nu_\mu \longrightarrow \nu_s$) or somewhat depleted (for $\nu_\mu \longrightarrow \nu_\tau$). As the normalization, one can use those events which do not pass through the Earth, either arriving from above for the contained samples or horizontally for entering muons. And indeed, as shown in Figs. 7 and 8, there is more depletion of the events going through the matter in the experimental data than one would expect for the sterile neutrinos. Unfortunately, the data are still too sparse to make this statement stronger than 2σ for the whole allowed space of the oscillation parameters for sterile neutrinos.

One can come to a similar conclusion from a study of low-energy neutral-current (NC) neutrino interactions. A sample of single π^0 events was used for this purpose 84% of which, according to the Monte Carlo

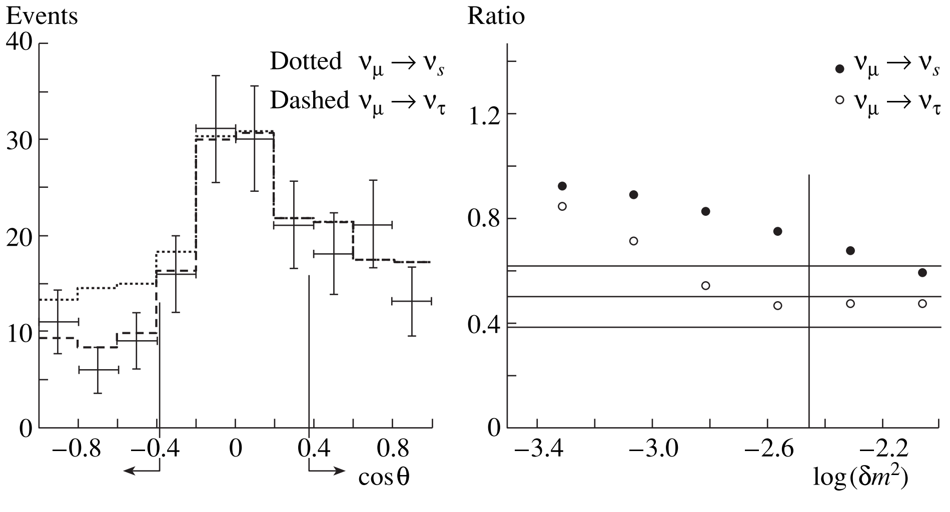

Fig. 7. Zenith-angle distribution for high energy partially contained events. On the left, the two regions which are most sensitive to the difference between oscillations to ν_τ and ν_s are indicated. Select events with total number of photoelectrons >45000 (E_ν = 25 GeV); up-going $\cos\theta < -0.4$, 26 events; down-going $\cos\theta > 0.4$, 52 events. On the right is shown how the ratio of events in these regions depends on which oscillations are taking place; ratio = 0.50 ± 0.12 ± 0.01, expected without oscillation 0.94 ± 0.04 ± 0.01.

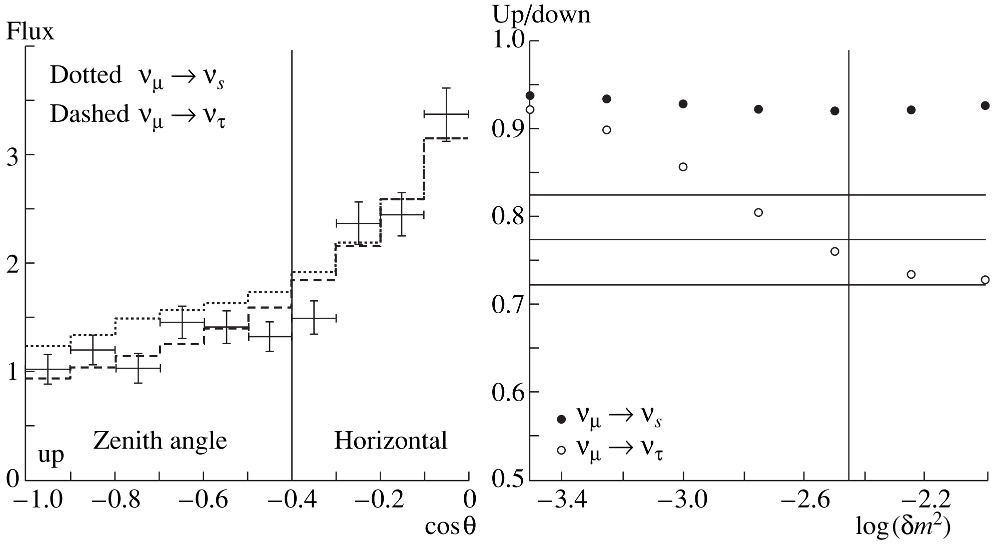

Fig. 8. Zenith-angle distribution for up-going muons. The data are divided into two parts such that the ratio of the numbers of their events is the most sensitive to the difference between oscillations to ν_τ and ν_s. Vertical-going $\cos\theta < -0.4$, flux = $(7.39 \pm 0.16) \times 10^{-13}/(\mathrm{cm}^2\ \mathrm{s\ sr})$; horizontal $\cos\theta > -0.4$, flux = $(9.58 \pm 0.12) \times 10^{-13}/(\mathrm{cm}^2\ \mathrm{s\ sr})$. On the right is shown how this ratio depends on which oscillations are taking place; up/down = 0.771 ± 0.049, expected without oscillation 0.934 ± 0.047.

studies, is produced in low energy neutrino NC interactions. If the disappearance of ν_μ is due to oscillations to ν_τ, the rate of π^0 production should be unaffected; however, it would decrease if ν_μ oscillate to ν_s. Experimentally, one can compare the ratio of the π^0 event rate to the electron neutrino interaction rate (which seems to be unaltered by oscillations) with the ratio predicted by a model. After subtraction of the background of false π^0 tracks in the data and in the Monte Carlo, the ratio is

Table 3. Summary of nucleon decay searches in the SuperKamiokande detector

Mode	Exposure, kt yr	$\epsilon \times$ BR, %	Candidates	BG	τ/BR limit, 10^{32} yr
$p \longrightarrow e\pi^0$	52	44	0	0.2	33.0
$p \longrightarrow \mu\pi^0$	52	35	0	0.1	27.0
$p \longrightarrow e\eta$	45	17	0	0.3	11.0
$p \longrightarrow \mu\eta$	45	12	0	0.0	7.8
$n \longrightarrow \nu\eta$	45	21	5	9.0	5.6
$n \longrightarrow \nu K^+$	33				7.3
$K^+ \longrightarrow \nu\mu$ (spec)		40			3.3
Prompt $\gamma + \mu$		4.4	0	0.4	2.1
$K^+ \longrightarrow \pi^+\pi^0$		6.5	0	0.7	3.1
$p \longrightarrow \mu K^0$	52				10.0
$K^0 \longrightarrow \pi^0\pi^0$		6.1	0	0.7	4.6
$K^0 \longrightarrow \pi^+\pi^-$					
2-ring		5.0	0	1.8	3.8
3-ring		3.1	0	0.4	2.4
$p \longrightarrow eK^0$	52	11	1	1.5	6.1
$n \longrightarrow \nu K^0$	52				1.8
$K^0 \longrightarrow \pi^0\pi^0$					
2-ring		3.2	9	8.0	0.6
3-ring		4.9	9	9.5	1.1
4-ring		1.7	1	3.3	0.8
$K^0 \longrightarrow \pi^+\pi^-$		4.1	4	1.6	0.9

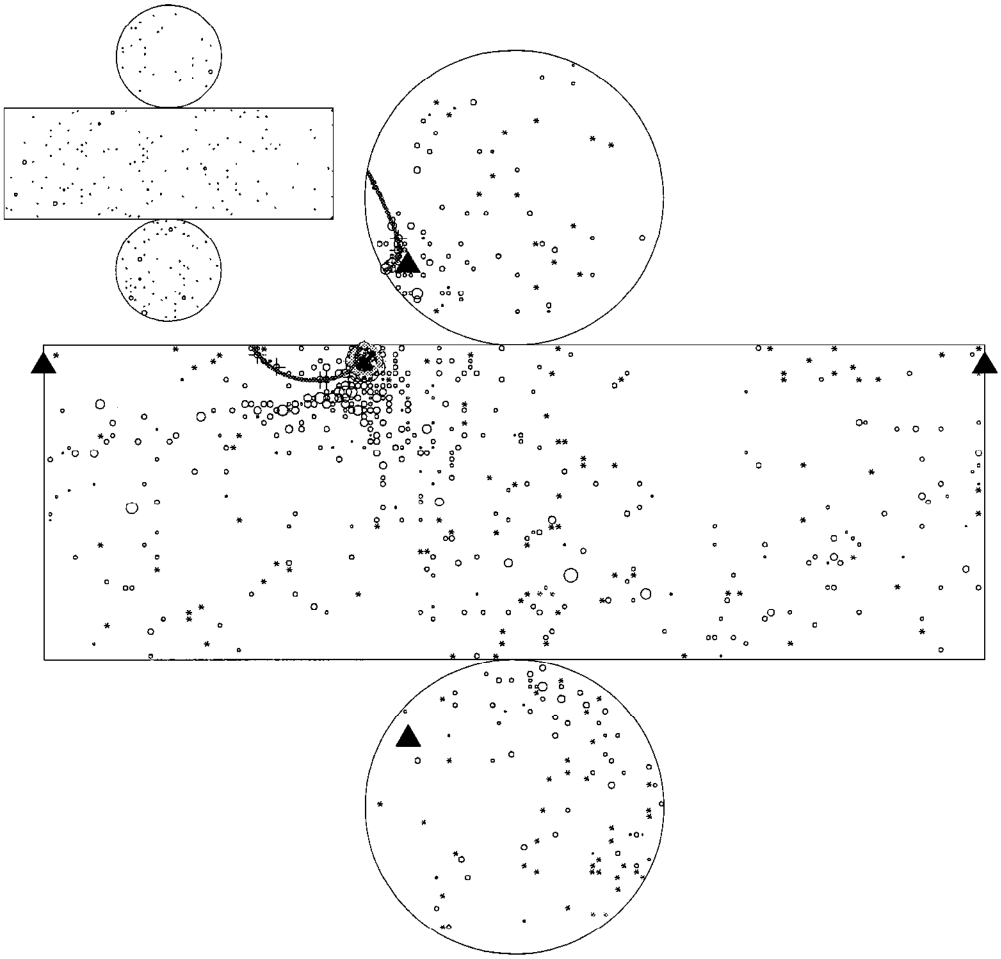

Fig. 9. The first contained event of neutrino interaction associated with the beam from the KEK 12 GeV PS.

$$\frac{(\pi^0/e)^{\mathrm{data}}}{(\pi^0/e)^{\mathrm{MC}}} = 1.11 \pm 0.06(\mathrm{stat.}) \pm 0.02 \pm 0.25(\mathrm{MC\ syst.}),$$

which would indicate oscillations of $\nu_\mu \longrightarrow \nu_\tau$. However, this result again is inconclusive. The dominating error in this measurement is due to our poor knowledge of cross sections for π^0 production in low energy NC neutrino interactions.

To summarize, with the increasing statistics of the atmospheric neutrino data, it is more and more difficult to explain the disappearance of the muon neutrinos as a statistical fluctuation or as caused by any flaws in the experimental procedure. On the other hand, it is amazing how well and how consistently all the experimental data can be described by the single hypothesis of neutrino oscillations with the parameters already pinned down with an astonishing precision.

4. SEARCH FOR NUCLEON DECAY

The results of the search for signals of spontaneous nucleon decay in the SuperKamiokande detector have been published in many papers [10]. They are summarized in the Table 3.

5. SUPERKAMIOKANDE AS A FAR DETECTOR FOR K2K EXPERIMENT

To verify the effect of $\nu_\mu \longrightarrow \nu_x$ oscillation, observed so far only in the neutrino beams produced by cosmic rays in the atmosphere, a long baseline oscillation experiment is being performed in Japan. It utilizes a pure ν_μ beam produced by the 12-GeV proton synchrotron at KEK and the SuperKamiokande detector 250 km distant as the far detector. The beam has a mean energy of 1.4 GeV, which together with the long path length makes the experiment sensitive to the δm^2 observed in the atmospheric neutrino oscillations. The duration of the accelerator spill is about 1 μs with a repetition rate of 2.2 s. The expected event rate in the

SuperKamiokande detector is roughly one event every couple of days.

To facilitate recognition of events due to the accelerator beam, a system of GPS clocks of an accuracy of 100 ns is applied at both sites. At KEK, the time of every accelerator spill is recorded, and files with such data are periodically transmitted via Internet to the detector site. At the SuperKamiokande site, the time of every event in the detector is measured and compared off-line with the file of the spill times. So far, four events in the expected 1-μs-wide time window have been found. One of them is contained in the fiducial volume. These are the first observed interactions of an artificially made neutrino beam transported so far away to a detector. A picture of the first contained event is shown in Fig. 9.

ACKNOWLEDGMENTS

The SuperKamiokande experiment is supported by the Japanese Ministry of Education, Science, Sports and Culture and the United States Department of Energy.

REFERENCES

1. M. Nakahata *et al*., Nucl. Instrum. Methods Phys. Res. A **421**, 113 (1999); Y. Fukuda *et al*., Phys. Lett. B **433**, 9 (1998); **436**, 33 (1998); Phys. Rev. Lett. **82**, 2644 (1999); submitted to Phys. Lett. B.
2. J. N. Bahcall *et al*., Phys. Lett. B **433**, 1 (1998).
3. J. N. Bahcall, P. I. Krastev, and A. Yu. Smirnov, Phys. Rev. D **58**, 096016 (1998); hep-ph/9807216.
4. J. N. Bahcall and P. I. Krastev, Phys. Lett. B **436**, 243 (1998).
5. Y. Fukuda *et al*., Phys. Rev. Lett. **82**, 1810 (1999); Y. Koshio, private communication.
6. Y. Fukuda *et al*., Phys. Rev. Lett. **81**, 1562 (1998); T. Maryama, private communication; M. D. Messier, PhD Thesis, Boston University (1999).
7. Y. Obayashi, private communication; K. Okumura, PhD Thesis, Tokyo University (1999).
8. P. Lipari and M. Lusignoli, hep-ph/9803440 (1998).
9. K. Ishihara, private communication.
10. M. Shiozawa *et al*., Phys. Rev. Lett. **81**, 3319 (1998); Y. Hayato *et al*., Phys. Rev. Lett. **83**, 1529 (1999).

Physics of Atomic Nuclei, Vol. 63, No. 6, 2000, pp. 943–950. From Yadernaya Fizika, Vol. 63, No. 6, 2000, pp. 1019–1026.
Original English Text Copyright © 2000 by Abdurashitov, Gavrin, Girin, Gorbachev, Ibragimova, Kalikhov, Khairnasov, Knodel, Mirmov, Shikhin, Veretenkin, Vermul, Yants, Zatsepin, Bowles, Teasdale, Wark, Nico, Cherry, Cleveland, Davis, Jr., Lande, Wildenhain, Elliott, Wilkerson.

NEUTRINO PHYSICS

Solar-Neutrino Results from SAGE*

J. N. Abdurashitov, V. N. Gavrin, S. V. Girin, V. V. Gorbachev, T. V. Ibragimova, A. V. Kalikhov, N. G. Khairnasov, T. V. Knodel, I. N. Mirmov, A. A. Shikhin, E. P. Veretenkin, V. M. Vermul, V. E. Yants, G. T. Zatsepin, T. J. Bowles1), W. A. Teasdale1), D. L. Wark1), 2), J. S. Nico3), M. L. Cherry4), B. T. Cleveland5), R. Davis, Jr.5), K. Lande5), P. S. Wildenhain5), S. R. Elliott6), and J. F. Wilkerson6)
(for the SAGE Collaboration)

Institute for Nuclear Research, Russian Academy of Sciences, pr. Shestidesyatiletiya Oktyabrya 7a, Moscow, 117312 Russia

Abstract—The solar-neutrino-capture rate measured by the Russian–American Gallium Experiment on metallic gallium during the period from January 1990 to December 1997 is $(67.2^{+7.2}_{-7.0}{}^{+3.5}_{-3.0})$ SNU, where the uncertainties are statistical and systematic, respectively. This result represents a 7σ depression in the neutrino flux in relation to the predicted standard-solar-model rates. The experimental procedures used and data analysis are presented. *© 2000 MAIK “Nauka/Interperiodica”.*

µ1. INTRODUCTION

Models describing nuclear-fusion processes in the Sun have been very successful in explaining numerous solar features. Although these models have had great success, the deficit in the solar-neutrino flux relative to the predictions of the standard solar model (SSM) still remains one of the outstanding problems. For 30 years, the Homestake chlorine experiment [1] has consistently observed a flux 33% of that predicted by the SSMs. In the mid-1980s, the water Cherenkov detector (Kamiokande) began its measurement of the solar-neutrino flux that is 54% of the SSMs [2], and recent results from Super-Kamiokande are in agreement with its predecessor [3].

In the early 1990s, the Russian–American Gallium Experiment (SAGE) [4] and the Gallium Experiment (GALLEX) [5] began measuring the low-energy neutrinos from proton–proton (*pp*) fusion using Ga [6] as the target material. The reaction $^{71}\mathrm{Ga}(\nu_e, e^-)^{71}\mathrm{Ge}$ provides the only feasible means at present to measure the predominant *pp* neutrinos as well as the higher energy neutrinos produced by ^{8}B and ^{7}Be. Its 233-keV threshold for inverse beta decay is important since, exotic hypotheses aside, the rate of the *pp* reaction is directly related to the solar luminosity and is insensitive to alterations in the solar models. Calculations on the basis of the SSM show [7] that the dominant contribution to the total expected capture rate in ^{71}Ga (129^{+8}_{-6}) SNU arises from the *pp* neutrinos and is 69.6 SNU, where 1 SNU = 1 interaction/s in a target that contains 10^{36} atoms of a neutrino-absorbing isotope. Contributions from ^{7}Be and ^{8}B neutrinos are 34.4 SNU and 12.4 SNU, respectively. The insensitivity to variation in the SSM for Ga is seen in the independently calculated result of 127.2 SNU [8] for the total capture rate.

SAGE Experiment

The SAGE detector is situated in a specially built underground laboratory at the Baksan Neutrino Observatory in the Northern Caucasus Mountains. It is located 3.5 km from the entrance of a horizontal adit excavated into the side of Mount Andyrchi and has an overhead shielding of 4700 mwe. Up to 55.6 t of Ga is contained in eight chemical reactors with approximately the same amount of Ga in each of them.

The data span an eight-year period during which many improvements to the experiment were made. As a result, the data are naturally divided into three periods differentiated by experimental conditions. SAGE I refers to extractions on approximately 30 t of Ga beginning in 1989 with backgrounds becoming low enough to begin solar-neutrino extractions in 1990. In the summer of 1991, the extraction mass was increased to nearly 60 t. The majority of those data were taken without digitized wave forms, and thus electronic noise levels were such that the *L* peak was inaccessible. After SAGE I completed, the experiment was greatly improved with respect to electronic noise, and the anal-

---

* This article was submitted by the authors in English.

1) Los Alamos National Laboratory, Los Alamos, NM 87545 USA.

2) Oxford University, Department of Particle and Nuclear Physics, Keble Road, Oxford OX1 3RH, United Kingdom.

3) National Institute of Standards and Technology, Gaithersburg, MD 20899 USA.

4) Louisiana State University, Baton Rouge, LA 70803 USA.

5) University of Pennsylvania, Philadelphia, PA 19104 USA.

6) University of Washington, Seattle, WA 98195 USA.

1063-7788/00/6306-0943$20.00 © 2000 MAIK “Nauka/Interperiodica”

ysis of the *L*-peak region became tractable. The period of data taking from September 1992 to December 1994 is referred to as SAGE II. The majority of SAGE II data had waveform recording capability. Only extractions for which we have waveform data are analyzed in the *L*-peak region. Beginning in December 1994, an experiment using a ^{51}Cr source was undertaken; we refer to all data taken after January 1995 as SAGE III.

2. EXPERIMENTAL PROCEDURES

Each measurement of the solar-neutrino flux begins by adding to the gallium approximately 700 μg of stable Ge carrier (distributed equally among all of the reactors) as a Ga–Ge alloy with known Ge content. The reactor contents are stirred thoroughly to disperse the carrier throughout the Ga metal. After a typical exposure interval of 4–6 weeks, the Ge carrier and any ^{71}Ge atoms produced by solar neutrinos or background sources are chemically extracted from the Ga by using procedures described elsewhere [4]. The final step of the chemical extraction procedure is the synthesis of germane (GeH_4), which is used as a proportional-counter (PC) gas with an admixture of Xe. The total efficiency of extraction, typically 80%, was determined by measuring the germane volume.

Once the ^{71}Ge is isolated in the PC, it is placed in a well-type NaI detector within a passive shield and counted for a period ranging from 2 to 6 months. The decay is identified via electron capture to ^{71}Ga with a half-life of 11.43 d [9]. Low-energy *K*- and *L*-shell Auger electrons and x rays from electron-shell relaxation produce a nearly pointlike ionization in the counter gas, resulting in a fast rise time for the subsequent pulse. Most background events leave an extended trail of ionization, producing a slower rise time. A candidate ^{71}Ge event must not only fall within an appropriate energy region, but it must also have a rise time consistent with pointlike ionization. In addition, we remove all PC events in coincidence with the NaI detector. Since ^{71}Ge has no gamma rays associated with its decay, this veto further eliminates potential backgrounds.

The data-acquisition electronics has evolved over the course of SAGE. The first two years of data relied entirely on a hardware measure of the rise time. This amplitude-of-the-differentiated-pulse (ADP) technique suffices well in studies of the *K*-peak counter response, but it is inadequate for the *L* peak, which is more sensitive to electronic drifts and where backgrounds are higher. In 1992, we implemented an 8-channel counting system with a 1-GHz digital oscilloscope, which permits an off-line analysis of the event waveforms. The digitized pulse is fit to a functional form [10] providing a measure of the energy deposited during the event and T_N, the time duration over which the ionization arrives at the anode wire of the PC. All of the *L*-peak data and the vast majority of the *K*-peak data presented here use the waveform analysis.

Counters were calibrated with a ^{55}Fe source immediately after filling. Typically, they are again calibrated with ^{55}Fe after three days of operation and approximately every two weeks subsequently. Beginning with SAGE II, calibrations were usually made with a ^{109}Cd source whenever a ^{55}Fe calibration was done. The 88-keV Ag gamma rays from the ^{109}Cd source have sufficient energy to penetrate the counter wall and fluoresce the length of the Fe cathode, thus giving the x-ray *K* peak from Fe at 6.4 keV. Beginning with the February 1993 extraction, a ^{109}Cd + Se source was periodically used, producing peaks at 1.4 and 11.21 keV. These several calibration lines were useful for checking linearity and for determining whether a correction for polymerization of the anode wire was necessary.

The measure of energy was the integral of the pulse wave form for 800 ns after pulse onset. The peak position was based on the ^{55}Fe calibration, and the energy window was two full widths at half maximum (FWHM). If the calibration centroid was shifted between two calibrations, there was an error made in the efficiency estimate. Typical gain shifts were of the order of a few percent, and the calculated uncertainty was –3.1% in the counting efficiency.

To verify the procedures for setting rise time windows, a PC with $^{71}GeH_4$ was measured in each of the counting slots. All events inside the energy windows of the *K* and *L* peaks were selected, and the rise time of each event was calculated by using the parameter T_N from the extended pulse fit. The rise-time values were arranged in ascending order and limits were set such that 5% of the events were excluded. We thus use *K*- and *L*-peak event-selection limits on T_N of 0 to 18.4 ns and 0 to 10.0 ns, respectively. The variation from counter fill and electronics channel was approximately 1.2 ns, which resulted in an uncertainty in the efficiency of about ±1%.

3. STATISTICAL ANALYSIS

The selection criteria resulted in a group of events from each extraction that were candidate ^{71}Ge decays. These events were fitted to a maximum-likelihood function [11] assuming that they originated from an undefined but constant-rate background and the exponentially decaying rate of ^{71}Ge. The production rate was corrected for the mass of gallium exposed in each extraction. In addition, a small correction (no greater than 3%) was introduced in order to consider that the Earth–Sun distance varies because of the eccentricity of the Earth's orbit.

Two time cuts were imposed on the counting intervals to minimize the potential effects of radon and radon daughters, which can mimic pulses of ^{71}Ge. To remove these spurious ^{71}Ge events, we deleted 2.6 h of counting time in the *K* and *L* peaks after any opening of the passive shield. It is also possible that the PC may have a small admixture of ^{222}Rn that enters the counter

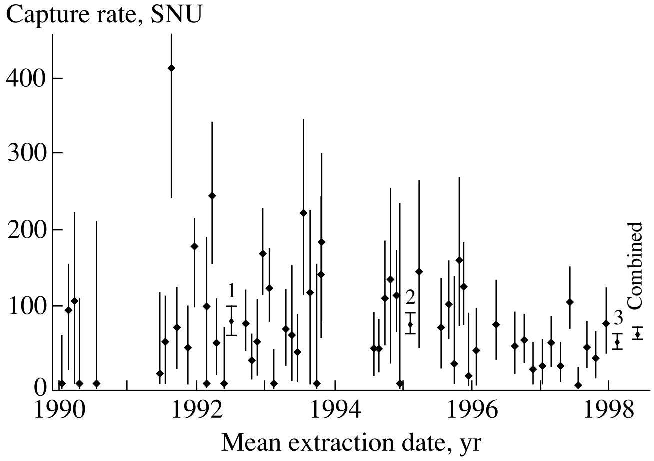

Fig. 1. Capture rate for each extraction as a function of time. All uncertainties are statistical. The symbols 1, 2, and 3 show the combined result for SAGE I, II, and III, respectively.

during filling. Most Rn decays give slow pulses at a saturated energy beyond the ^{71}Ge peaks, but approximately 8% of the pulses from Rn and its daughters make fast pulses that are indistinguishable from those of ^{71}Ge. Since the radon-decay chain takes, on average, only 50 min to reach a long-lived isotope, deleting 15 min before and 3 h after each saturated pulse removes most of these internal Rn events.

For each individual extraction, we determined the best estimate of the solar-neutrino flux by maximizing the likelihood function. The uncertainty was determined by integrating the likelihood function over the background to provide a likelihood function of signal only and then locating the minimum range in signal that includes 68% of the area under that curve. These individual results are plotted in Fig. 1. We deduced the overall result by taking the product of the likelihood expressions for all extractions, requiring that the production rate per unit mass of Ga be equivalent but

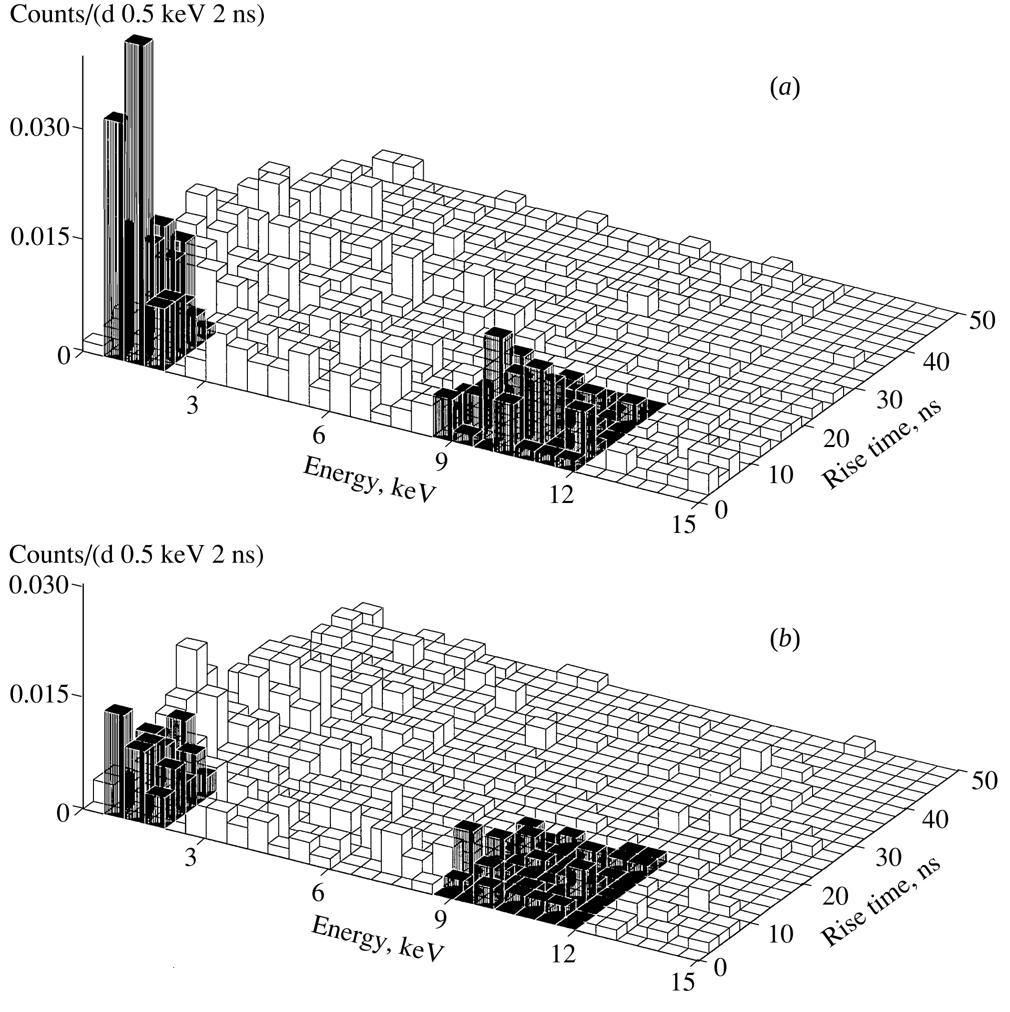

Fig. 2. (*a*) Energy-rise time histogram of all events observed over the first 30 d after extraction for all runs that could be counted in both *K* and *L* peaks (except May 96). The live time is 711.1 d. The expected location of the ^{71}Ge decays is darkened. (*b*) Same histogram for all events that occurred over an equal live time interval at the end of counting.

Table 1. Summary of systematic effects and their uncertainties in SNU (the values for extraction and counting efficiencies are based on a rate of 67.2 SNU)

Extraction efficiency	Ge carrier mass	±1.4
	Extracted Ge mass	±1.7
	Residual carrier Ge	±0.5
	Ga mass	±0.2
Counting efficiency	Counter effects	±1.9
	Gain shifts	+2.1
	Resolution	–0.3 +0.5
	Rise time limits	±0.7
	Lead and exposure times	±0.5
Backgrounds	Neutrons, U, Th, muons	–1.0
	Other Ge isotopes	–0.6
	External radon	0.0
	Internal radon	–0.2
	Total	–3.0 +3.5

allowing the background rate to fluctuate from extraction to extraction.

Upon combining the total data set over the three periods of SAGE, the statistical result of the 88 separate counting sets is $67.2^{+7.2}_{-7.0}$ SNU. If one considers the *K*-peak and *L*-peak data independently, the results are 73 ± 9 SNU and 55^{+13}_{-12} SNU, respectively. The agreement between the two peaks served as a strong check on the robustness of the event-selection criteria. Figure 2 illustrates the decay of the ^{71}Ge signal by comparing the energy-rise time histogram of all events over the first 30 d after extraction with an equal interval of time at the end of counting.

4. SYSTEMATIC EFFECTS

Table 1 summarizes systematic effects that may affect the solar-neutrino-production rate. They fall into three main categories of extraction efficiencies, counting efficiencies, and backgrounds. Several of these systematics are discussed below. In addition, we note that 2.3 t of Ga were stolen from the detector between November 1993 and June 1994. During this period, the systematic control of the experiment was clearly suspect, and we exclude those data from the quoted result.

An extensive series of measurements were performed on all the PCs used in SAGE counting to establish their efficiencies and the associated uncertainties. A series of three separate measurements using PCs filled with ^{37}Ar, ^{71}Ge, and ^{69}Ge was employed to establish the counter efficiencies. The uncertainties in the efficiencies were composed of the volume efficiency, end effects, and gas efficiency. Adding the uncertainties from each of these effects in quadrature gives a ±2.8% uncertainty due to the counters.

There exist contributions to the ^{71}Ge signal by means other than solar neutrinos. Limits on the creation of Ge isotopes through the (*n*, *p*) reaction on Ga and by cosmic-ray muons come from measurements of both the fast-neutron [12] and muon fluxes [13] in the Ga chamber. In addition, the concentrations in the Ga of U and Th have been measured independently by low-background counting in a Ge detector and by glow discharge mass spectrometry. No observable level of U or Th was found, and upper limits are given in Table 1.

In determining the total possible background rates, we have used only the ^{71}Ge production rates. The decay rate from the produced ^{68}Ge was negligible in relation to the background rate. For ^{69}Ge, with a half-life of only 1.6 d, the long exposure times (approximately 30 d) and the lead time before counting begins (approximately 1.5 d) rendered its contribution quite small. The rates contributed a total ^{71}Ge production rate of less than 0.020 d^{-1} in 60 t of Ga metal. With a SSM production rate of 2.36 d^{-1} [7] in 60 t of Ga, this corresponds to less than 1.0% of the SSM prediction. Although the Rn concentrations in the laboratory were small and several measures were taken to purge it from the counting system, systematic studies were performed to quantify the potential contamination both internal and external to the counter. A Xe-filled PC, enclosed in a cylinder into which radon could be pumped, was placed in the well of a NaI counter and studied over a period of several months. Scaling factors were obtained from the overflow events to the *K*- and *L*-peak windows that were used to determine quantitatively the remaining systematic uncertainties for Rn after the time cuts. The cut efficiencies for internal (external) radon were 90% (>98%), which, with the appropriate scaling, produce uncertainties in the assigned ^{71}Ge events of –0.2 SNU (0.0 SNU). The estimate for external Rn is conservative because it assumes all radon-induced events over this counting period to be assigned to the signal.

5. RESULTS

If we combine SAGE I with SAGE II and SAGE III, the global best fit capture rate for 88 separate counting sets is $67.2^{+7.2}_{-7.0}$ SNU, where the uncertainty is purely statistical. In the windows that define the *L* and *K* peaks, there are 1037 counts with 211.15 assigned to ^{71}Ge (the total counting live time is 28.7 yr). The total systematic uncertainty was determined by adding in quadrature all the contributions given in Table 1 and is –3.0, +3.5 SNU. Our overall result is thus $67.2^{+7.2\,+\,3.5}_{-7.0\,-\,3.0}$ SNU. If we combine the statistical and systematic uncertainties in quadrature, the result is $67.2^{+8.0}_{-7.6}$ SNU.

The validity of this result relies on the ability to extract, isolate, and count, all with well-known effi-

Table 2. Results of a global analysis of various segments of SAGE data (the uncertainty in the probability is about 4%)

Data segment	Peak	Data sets	Total events	Fit to ^{71}Ge	Best fit, SNU	68% conf., range, SNU	Nw^2	Probability, %
SAGE I	K	16	157	41.2	81	63–101	0.097	24
SAGE II	$L + K$	33	342	85.5	79	66–92	0.105	32
SAGE III	$L + K$	39	538	87.0	56	47–66	0.040	90
All	L	31	433	64.3	55	43–68	0.020	>99
All	K	57	604	143.7	73	64–82	0.110	25
All	$L + K$	88	1037	211.1	67	60–74	0.074	58

ciencies, a few atoms produced by neutrino interactions from many tons of the target material. In the case of 60 t of Ga, it is an isolation factor of about 1 part in 10^{28}. To test such a stringent requirement, we have performed several auxiliary measurements to verify that the extraction efficiency was as anticipated.

An initial test was carried out in which Ge carrier doped with a known number of ^{71}Ge atoms was added to a reactor holding 7 t of Ga. Three successive extractions were carried out, and the number of ^{71}Ge atoms in each extraction was determined by counting. The results [4] indicate that the extraction efficiency of the natural Ge carrier and ^{71}Ge track very closely.

A second experiment addressed the concern that the ^{71}Ge atom from inverse beta decay may be created in an excited or ionized state, which results in the ^{71}Ge being tied up in a chemical form that cannot be efficiently extracted. A set of measurements designed to test this question directly were carried out by observing the beta decay of radioactive Ga isotopes in liquid Ga. The results of these measurements [4] show that the expected isotopes are formed in amounts anticipated at the 10% level.

Foremost, it has been understood from the outset that a test of the entire operation of the detector (that is, its chemical-extraction efficiency, counting efficiency, and analysis technique), with a known flux of neutrinos of appropriate energy, would constitute the most rigorous check on the integrity of the experiment. Such an experiment was performed by using a 19.1 PBq (517 kCi) ^{51}Cr neutrino source. The final result, expressed as the ratio of the measured ^{71}Ge production to that expected on the basis of the source strength is 0.95 ± 0.12 [14]. This value provides strong verification that the experimental efficiencies are as claimed and validates the fundamental assumption in radiochemical experiments that the extraction efficiency of atoms produced by neutrino interactions is identical to that of the natural carrier.

5.1. Evidence for ^{71}Ge

The most direct visual evidence that we are really observing ^{71}Ge is in Fig. 2. The expected location of the ^{71}Ge L and K peaks is shown darkened in this figure. These peaks are apparent in the upper panel, but they are missing in the lower panel because the ^{71}Ge has decayed away. Events outside the two peak regions occur at about the same rate in both panels because they are mainly produced by background processes.

A quantitative indication that ^{71}Ge is being counted can be obtained by allowing the decay constant during counting to be a free variable in a maximum-likelihood fit, along with the combined production rate and all the background rates. From the best fit to all selected events in both L and K peaks, the half-life is then $(10.5^{+2.3}_{-1.9})$ d, in good agreement with the measured value [9] of 11.43 d.

5.2. Consistency of the Data with Analysis Hypotheses

5.2.1. Energy and rise-time window positions. To test whether (or not) the energy and rise-time windows are properly set, the windows can be made wider and the data reanalyzed. If the rise-time window for accepted events is increased by 30%—that is, from 0–10 to 0–13 ns in the L peak and from 0–18.4 to 0–24.0 ns in the K peak—then the overall result of all runs of SAGE II and III that were counted in system 3 is 68.3 SNU. This change is entirely consistent with a 3% increase in counting efficiency due to the increased size of the rise-time acceptance window. Similarly, if the energy window in both L and K peaks is opened from the usual 2 FWHM to 3 FWHM, then the overall result of all runs of SAGE II and III becomes 69.1 SNU. This increase from the value of 67.2 SNU in the 2 FWHM energy window is due to the occurrence of some of the ^{71}Ge decays at the ends of the counter and to the reduction of the detected energy from the full peak value. This results in an increase in the counting efficiency in the wider energy window of 2 to 3%. If this efficiency increase is included in the analysis, then the results in the two energy windows agree to better than 1%.

5.2.2. Time sequence. A major analysis hypothesis is that the time sequence of observed events for each run consists of the superposition of events from the decay of a fixed number of ^{71}Ge atoms plus background events that occur at a constant rate. The quantity Nw^2 and the goodness of fit probability inferred from it provide a quantitative measure of how well the data fit this

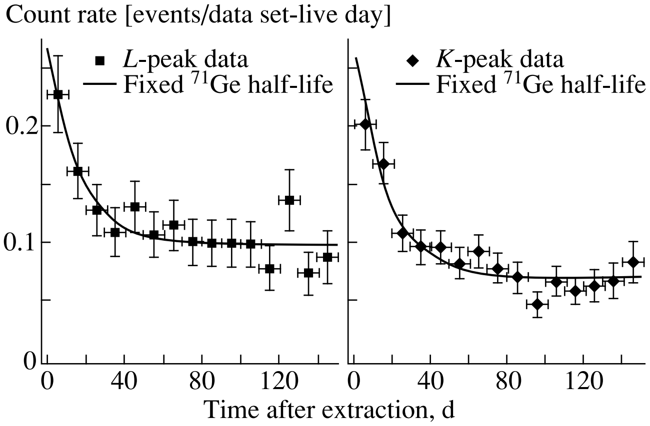

Fig. 3. Count rate for all runs in L and K peaks. The solid line is a fit to the data points with the 11.4 d half-life of ^{71}Ge plus a constant background. The vertical error bar on each point is proportional to the square root of the number of counts and is shown only to give the scale of the error. The horizontal error bar is ±5 d, equal to the 10-d bin size.

hypothesis (see [15] for the definition and interpretation of Nw^2). These numbers were evaluated for each data set. There are occasional runs with a rather low probability of occurrence, but no more of these were observed than are expected on the basis of a normal statistical variation.

This method can also be used to determine the goodness of a fit of the time sequence for any combination of runs. These numbers are given in Table 2; for the combined time sequence of all L plus K events from all runs, this test yields $Nw^2 = 0.074$, with a goodness of fit probability of (58 ± 5)%. A visual indication of the quality of this fit is provided in Fig. 3, which shows the counting rate for all events in the L and K peaks versus time after extraction. As is apparent, the observed rate fits the hypothesis quite well.

5.2.3. Production-rate sequence. Another analysis hypothesis is that the rate of ^{71}Ge production is constant in time. By examination of Fig. 1, it is apparent that, within the large statistical uncertainty for each run, there are no substantial long-term deviations from constancy.

To test quantitatively whether (or not) it is reasonable to assume that the production rate is constant, we can consider three segments of SAGE data whose results are given in Table 2. A test of the consistency of any data segment with the overall result of 67 SNU can be performed by means of a Monte Carlo simulation. For the purposes of illustration, we choose the most deviant segment, SAGE III, whose overall result is 56 SNU. We then simulate all 39 data sets of SAGE III, assuming that the true production rate is 67 SNU. To ensure that these simulations parallel the real data as closely as possible, all parameters of the simulation, such as background rates efficiencies, exposure times, and counting times, were chosen to be identical to those in live data. From the sequence of simulated event times, the combined production rate was calculated in precisely the same manner as for live data. This process was repeated 10000 times, and a histogram of the combined rate was produced. From the position of the observed rate for the live data in this histogram, we were able to calculate the probability that the live data were produced at the assumed initial production rate. We found that only 11 ± 0.3% of the 10000 simulations of SAGE III had a value that was lower than the observed value of 56 SNU. Since this probability is one-tailed (maximum of 50%), this is the most aberrant of the three sections of SAGE data; no systematic uncertainties were included in the simulations, a value of 11% was not extremely unusual, and there was thus no strong evidence for a production-rate variation. The same analysis applied to SAGE I and SAGE II yields probabilities of 35 and 38%, respectively, highly consistent with the assumption of a constant production rate.

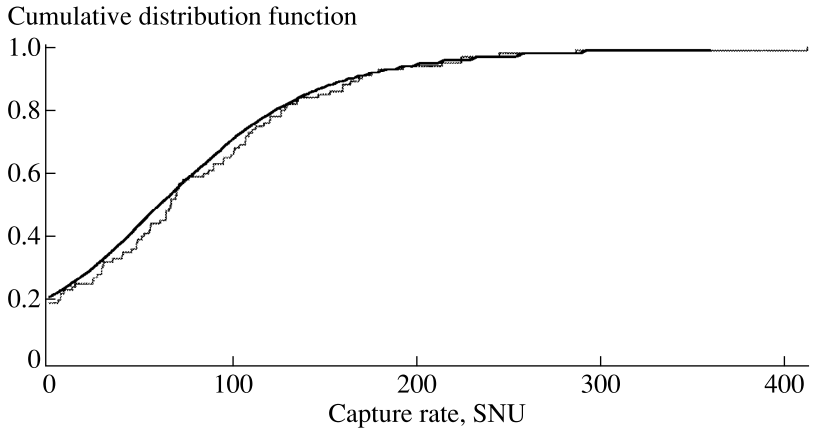

Fig. 4. Measured capture rate for all SAGE data sets (jagged curve) and expected distribution derived by 1000 Monte Carlo simulations of each set (smooth curve). The capture rate in the simulations was assumed to be 67.2 SNU.

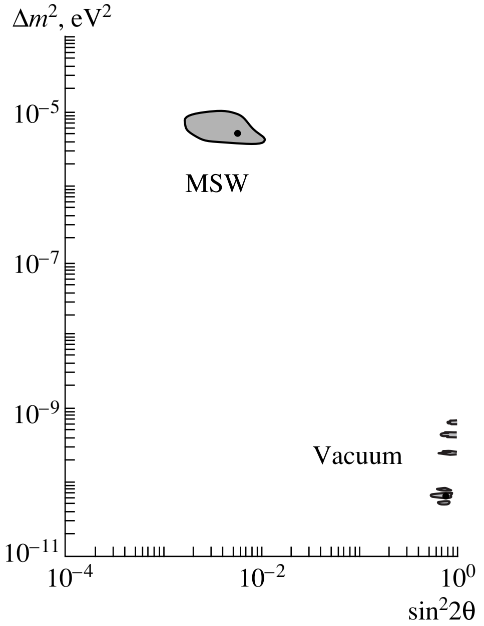

Fig. 5. Allowed regions of neutrino parameter space for two-flavor oscillations into active neutrino species. The analysis uses the results of all solar-neutrino experiments, including the constraints from the energy spectrum and zenith-angle dependence measured by Super-Kamiokande. The black circles are the best fit points, and the shading shows the allowed regions at a 99% C.L. The figure is based on calculations from [20].

Another way to consider this question is to use the cumulative distribution function for the production rate $C(p)$, defined as the fraction of data sets whose production rate is less than p. Figure 4 shows this distribution for all data sets and the expected distribution from our simulation under the assumption of a constant production rate of 67 SNU. The two spectra parallel each other closely and can be compared by calculating the Nw^2 test statistics [11]. This gives $Nw^2 = 0.343$, whose probability is 10%.

6. SUMMARY AND CONCLUSIONS

Eight years of measurement of the solar-neutrino flux give the capture-rate result of $(67.2^{+7.2}_{-7.0})$ SNU, where the uncertainty is statistical only. An analysis of all known systematic effects indicates that the total systematic uncertainty is $^{+3.5}_{-3.0}$ SNU, which is considerably smaller than the statistical uncertainty. Finally, we have examined the counting data and shown that there is good evidence that ^{71}Ge is being counted, that the counting data fit the analysis hypotheses, and that the counting data are self-consistent.

The SAGE result of 67.2 represents 52 [7] to 53% [8] of the SSM predictions. Given the extensive systematic checks and auxiliary measurements that have been performed—especially the ^{51}Cr-neutrino-source experiment [14]—this 7σ reduction in the solar-neutrino flux in relation to the SSM predictions is very strong evidence that the solar-neutrino spectrum below 2 MeV is significantly depleted, as was previously shown for the ^{8}B flux by the Cl and Kamiokande experiments. If we take into account the results of all experiments, astrophysical solutions to the solar neutrino deficit can now be nearly excluded [16–18]. This conclusion is indeed implied by the SAGE result itself, since it lies 2.5σ below the capture rate prediction of $(88.1^{+3.2}_{-2.4})$ SNU obtained by artificially setting the rate of the ^{3}He(α, γ)^{7}Be reaction to zero and 1.5σ below the minimal astrophysical capture rate of $79.5^{+2.3}_{-2.0}$ UNU [19]. The solar-neutrino problem is now a model-independent discrepancy [20, 21] that does not depend on the details of solar models or their inputs.

More credible explanations for the solar-neutrino deficit involve either matter-enhanced Mikheyev–Smirnov–Wolfenstein (MSW) neutrino oscillations, in which the solar ν_e oscillates into other flavor neutrinos or a sterile neutrino [20, 22–24], or vacuum oscillations [20, 25, 26]. For both of these possibilities, the allowed regions of $\Delta m^2 - \sin^2 2\theta$ parameter space that are determined from solar-neutrino experiments for two-flavor oscillations into active neutrino species are shown in Fig. 5. The fit quality is nearly the same in both regions. There is also a fit with similar quality for MSW oscillations into sterile neutrinos, whose allowed region approximately coincides with the region shown for MSW with active neutrinos. In addition, we have performed an analysis [27] of the constraints imposed on vacuum oscillations by the SAGE data exclusively.

There are now very strong indications that the solar-neutrino deficit has a particle-physics explanation and is a consequence of a neutrino mass. To unravel fully the solar neutrino story, however, will require more experiments, especially those with sensitivity to low-energy neutrinos or to the neutrino flavor. SAGE continues to perform regular solar-neutrino extractions every six weeks with approximately 50 t of Ga and will continue to reduce its statistical and systematic uncertainties, thus further limiting possible solutions to the solar-neutrino problem.

ACKNOWLEDGMENTS

We thank J.N. Bahcall, M. Baldo-Ceolin, P. Barnes, L.B. Bezrukov, S. Brice, L. Callis, A. E. Chudakov, A. Dar, G.T. Garvey, W. Haxton, V.N. Kornoukhov, V.A. Kuzmin, V.A. Matveev, L.B. Okun, V.A. Rubakov, R.G.H. Robertson, N. Sapporo, A.Yu. Smirnov, A.A. Smolnikov, A.N. Tavkhelidze, and many members of GALLEX for their continued interest and for fruitful and stimulating discussions.

We acknowledge the support of the Russian Academy of Sciences, the Institute for Nuclear Research (Russian Academy of Sciences), the Ministry for Science and Technology of the Russian Federation, the Russian Foundation for Basic Research (project no. 96-02-18399), the Division of Nuclear Physics of the U.S. Department of Energy, the U.S. National Science Foundation, and the U.S. Civilian Research and Development Foundation (award no. RP2-159). This work was supported in part by grant no. M7F000 from the International Science Foundation and grant no. M7F300 from the International Science Foundation and the Government of the Russian Federation.

REFERENCES

1. B. N. Cleveland *et al.*, Astrophys. J. **496**, 505 (1998).
2. Y. Fukuda *et al.*, Phys. Rev. Lett. **77**, 1683 (1996).
3. Y. Fukuda *et al.*, Phys. Rev. Lett. **81**, 1158 (1998).
4. J. N. Abdurashitov *et al.*, Phys. Lett. B **328**, 234 (1994); Phys. Rev. C (in press).
5. W. Hampel *et al.*, Phys. Lett. B **447**, 127 (1999).
6. V. A. Kuz'min, Zh. Éksp. Teor. Fiz. **49**, 1532 (1965) [Sov. Phys. JETP **22**, 1051 (1966)].
7. J. N. Bahcall, S. Basu, and M. H. Pinsonneault, Phys. Lett. B **433**, 1 (1998).
8. A. S. Brun, S. Turck-Chièze, and P. Morel, Astrophys. J. **506**, 913 (1998).
9. W. Hampel and L. Remsberg, Phys. Rev. C **31**, 666 (1985).
10. S. R. Elliott, Nucl. Instrum. Methods Phys. Res. A **290**, 158 (1990).
11. B. T. Cleveland, Nucl. Instrum. Methods **214**, 451 (1983).
12. I. R. Barabanov, V. N. Gavrin, P. P. Prokopeva, and V. Yants, Preprint No. P-0559, INR RAN (Institute for Nuclear Research, USSR Academy of Sciences, Moscow, 1987).
13. O. G. Ryazhskaya and G. T. Zatsepin, in *Proceedings of the 9th International Conference on Cosmic Rays, London, 1965* (Inst. of Physics, London, 1965), Vol. 2, p. 987.
14. J. N. Abdurashitov *et al.*, Phys. Rev. Lett. **77**, 4708 (1996); Phys. Rev. C **59**, 2246 (1999).
15. B. T. Cleveland, Nucl. Instrum. Methods Phys. Res. A **416**, 405 (1998).
16. V. Berezinsky, G. Fiorentini, and M. Lissia, Phys. Lett. B **365**, 185 (1996).
17. V. Berezinsky, in *Proceedings of the 25th International Cosmic Ray Conference, 1998* (World Sci., Singapore, 1998).
18. A. Dar and G. Shaviv, in *Proceedings of Conference on Astrophysical Plasmas: From Atomic Nuclei to Stars and Galaxies, Haifa, Israel, 1998* [Phys. Rep. (in press)].
19. J. N. Bahcall, Phys. Rev. C **56**, 3391 (1997).
20. J. N. Bahcall, P. I. Krastev, and A. Yu. Smirnov, Phys. Rev. D **58**, 096016 (1998).
21. K. M. Heeger and R. G. H. Robertson, Phys. Rev. Lett. **77**, 3720 (1996).
22. D. O. Caldwell, Int. J. Mod. Phys. A **13**, 4409 (1998).
23. S. M. Bilenky, G. Giunti, and W. Grimus, hep-ph/9812360.
24. N. Hata and P. Langacker, Phys. Rev. D **56**, 6107 (1997).
25. P. I. Krastev and S. T. Petcov, Phys. Rev. D **53**, 1665 (1996).
26. J. M. Gelb and S. P. Rosen, Phys. Rev. D (in press).
27. J. N. Abdurashitov *et al.*, submitted for publication in Phys. Rev. Lett.

Physics of Atomic Nuclei, Vol. 63, No. 6, 2000, pp. 951–961. From Yadernaya Fizika, Vol. 63, No. 6, 2000, pp. 1027–1036.
Original English Text Copyright © 2000 by Balkanov, Belolaptikov, Bezrukov, Budnev, Chensky, Danilchenko, Dzhilkibaev, Domogatsky, Doroshenko, Fialkovsky, Gaponenko, Garus, Gress, Kiss, Klimov, Klimushin, Koshechkin, Kuznetzov, Kulepov, Kuzmichev, Lovzov, Laudenskaite, Lubsandorzhiev, Milenin, Mirgazov, Moseiko, Netikov, Osipova, Panfilov, Parfenov, Pavlov, Pliskovsky, Pokhil, Popova, Rozanov, Sokalski, Spiering, Streicher, Tarashansky, Toht, Thon, Vasiliev, Wischnewski, Yashin.

NEUTRINO PHYSICS

Lake Baikal Neutrino Experiment: Selected Results*

V. A. Balkanov, I. A. Belolaptikov[1], L. B. Bezrukov, N. M. Budnev[2], A. G. Chensky[2], I. A. Danilchenko, Zh.-A. M. Dzhilkibaev, G. V. Domogatsky[1], **, A. A. Doroshenko, S. V. Fialkovsky[3], O. N. Gaponenko, A. A. Garus, T. I. Gress[2], D. Kiss[4], A. I. Klimov[5], S. I. Klimushin, A. P. Koshechkin, V. E. Kuznetzov, V. F. Kulepov[3], L. A. Kuzmichev[6], S. V. Lovzov[2], J. J. Laudenskaite[2], B. K. Lubsandorzhiev, M. B. Milenin[3], R. R. Mirgazov[2], N. I. Moseiko[6], V. A. Netikov, E. A. Osipova[6], A. I. Panfilov, Yu. V. Parfenov[2], A. A. Pavlov[2], E. N. Pliskovsky, P. G. Pokhil, E. G. Popova[6], M. I. Rozanov[7], I. A. Sokalski, Ch. Spiering[8], O. Streicher[8], B. A. Tarashansky[2], G. Toht[5], T. Thon[8], R. Vasiliev, R. Wischnewski[8], and I. V. Yashin[6]

Institute for Nuclear Research, Russian Academy of Sciences, pr. Shestidesyatiletiya Oktyabrya 7a, Moscow, 117312 Russia

Abstract—We review the present status of the Lake Baikal neutrino experiment and present selected physics results obtained during the consecutive stages of the stepwise upgrade of the detector: from NT-36 to NT-96. The results cover atmospheric muons, neutrino events, neutrinos of very high energy, searches for neutrino events from WIMP annihilation, searches for magnetic monopoles, and environmental studies. We also describe an air Cherenkov array developed for studying the angular resolution of NT-200. © *2000 MAIK “Nauka/Interperiodica”.*

1. INTRODUCTION

The Lake Baikal neutrino experiment exploits the deep water of the great Siberian lake as a detection medium for high-energy neutrinos via muons and electrons generated in high-energy neutrino interactions. High-energy neutrinos have been of particular importance for high-energy astrophysics over the last few decades to shed light on the physics of active galactic nuclei (AGN), binary star systems, gamma ray burst (GRB), etc. The lifetime of the Lake Baikal neutrino experiment spans almost two decades, from first small experiment with a few photomultiplier tubes (PMTs) to the present large-scale neutrino telescope NT-200 [1–3], which was put into a full operation on April 6, 1998. The effective area of the telescope for muons is 2000–10000 m^2, depending on the muon energy. The expected rate of muons from atmospheric neutrinos, with a muon energy thresholds of 10 GeV and after all cuts rejecting background, is about one per two days.

2. NEUTRINO TELESCOPE NT-200

2.1. Detector and Site

The neutrino telescope NT-200 is located in the southern part of Lake Baikal (51.50 N and 104.20 E) at a distance of 3.6 km from the shore and at a depth of 1 km. The absorption length $L_{\rm abs}$ of water at the site is about 20 m for wavelengths between 470 and 500 nm, and seasonal variations are less than 20%. Light scattering is subjected strongly to seasonal variations and to variations from year to year. We can say now that light scattering is rather strongly anisotropic and typical values of $L_{\rm scatt}$ are about 15 m. The NT-200 telescope (Fig. 1) consists of 192 optical modules (OMs) at eight strings arranged at an umbrella-like frame [1, 2]. Pairs of OMs are switched in coincidence with a 15 ns time window and define a channel. We pursue pairwise ide-

---

* This article was submitted by the authors in English.

[1] Joint Institute for Nuclear Research, Dubna, Moscow oblast, 141980 Russia.

[2] Irkutsk State University, ul. Lermontova 126, Irkutsk 33, 664033 Russia.

[3] Nizhni Novgorod State Technical University, Nizhni Novgorod, Russia.

[4] KFKI Research Institute for Particle and Nuclear Physics, Hungarian Academy of Sciences, PO Box 49, H-1525 Budapest, Hungary.

[5] Russian Research Centre Kurchatov Institute, pl. Kurchatova 1, Moscow, 123182 Russia.

[6] Institute of Nuclear Physics, Moscow State University, Vorob’evy gory, Moscow, 119899 Russia.

[7] St. Petersburg State Marine Technical University, St. Petersburg, Russia.

[8] DESY—Institut für Hochenenergiephysik Zeuthen, Platanenallee 6, D-15735 Zeuthen, Germany.

** e-mail: domogats@pcbai10.inr.ruhep.ru

1063-7788/00/6306-0951$20.00 © 2000 MAIK “Nauka/Interperiodica”

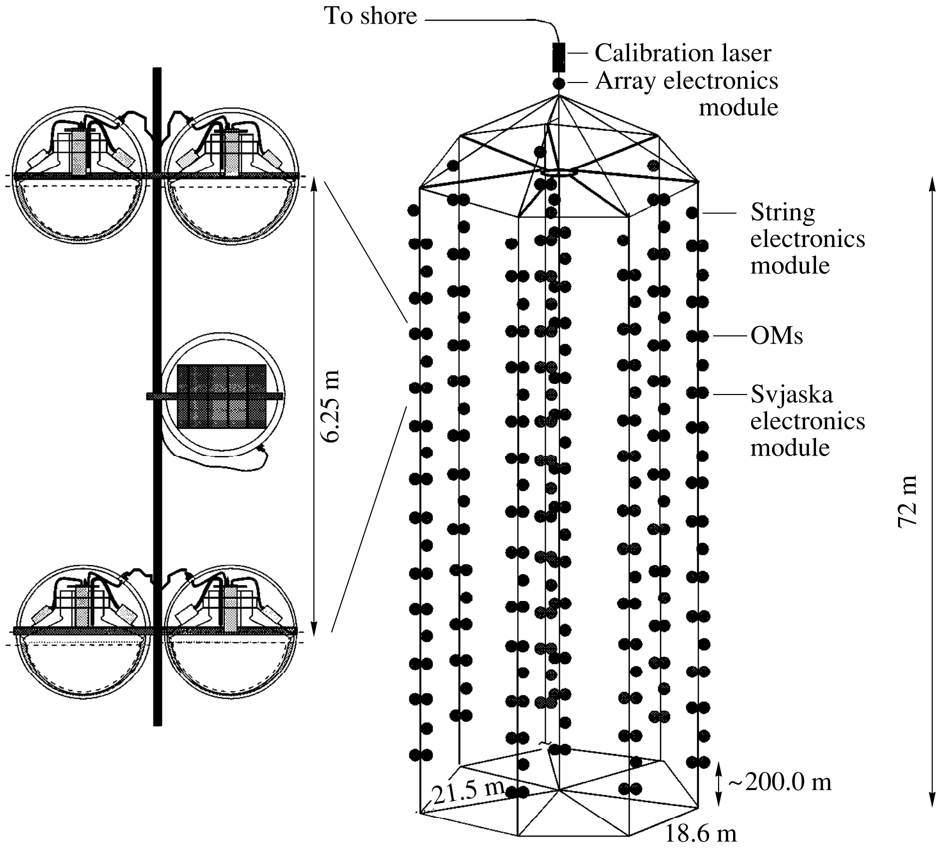

Fig. 1. Layout of the Baikal telescope NT-200. The array is time-calibrated by two nitrogen lasers. Of these, one (fiber laser) is mounted just above the array. Its light is guided via optical fibers to each OM pair. The other (water laser) is arranged 20 m below the array. Its light propagates directly through the water. The expansion on the left shows two pairs of optical modules ("svjaska") with the svjaska electronics module, which houses parts of the readout and control electronics.

ology for many reasons: to suppress individual OM background counting rates due to OM dark current and water luminescence, the level of late- and afterpulses, etc. An OM [4] consists of a QUASAR-370 phototube [5, 6] enclosed in transparent, nearly spherical pressure housing. The optical contact between the photocathode region of the phototube and the pressure sphere is ensured by liquid glycerin sealed with a layer of polyurethane. Apart from a phototube, each OM contains two HV power supplies (25 and 2 kV), a voltage divider, two preamplifiers, a calibration LED, and a vacuum probe. The QUASAR-370 phototube was developed expressly for the Lake Baikal neutrino experiment by Institute for Nuclear Research (Moscow) and the KATOD Company in Novosibirsk. The phototube is a hybrid one and has excellent time and amplitude resolutions.

The system of detector electronics [2] is hierarchical: from the lowest level to the highest one—OMs electronics; "svjaska" electronics module; string electronics module; and the detector electronics module, where the detector trigger signals are formed and all information from the string electronics module is received and sent to the shore station. The detector is controlled from the shore station. A muon trigger is formed by the requirement of $\geq N$ hits (with a hit referring to a channel) within 500 ns; here, N is typically set to the value of three or four. For such events, the amplitude and time of all actuated channels are digitized and sent to the shore. An event record includes all hits within a time window from –1000 to +800 ns with respect to the muon trigger signal. A separate monopole trigger system seeks clusters of sequential hits in individual channels, which are characteristic of the passage of slowly moving, bright objects like GUT monopoles.

There is a separate hydrological string to study permanently water parameters of the lake. This string is deployed at about 60 m from the main part of the NT-200 telescope. There are two nitrogen lasers that are intended for the time calibration of the detector and which are placed just above and below the detector. The former illuminates each individual channel via fiber optics, while the latter illuminates the detector as a whole.

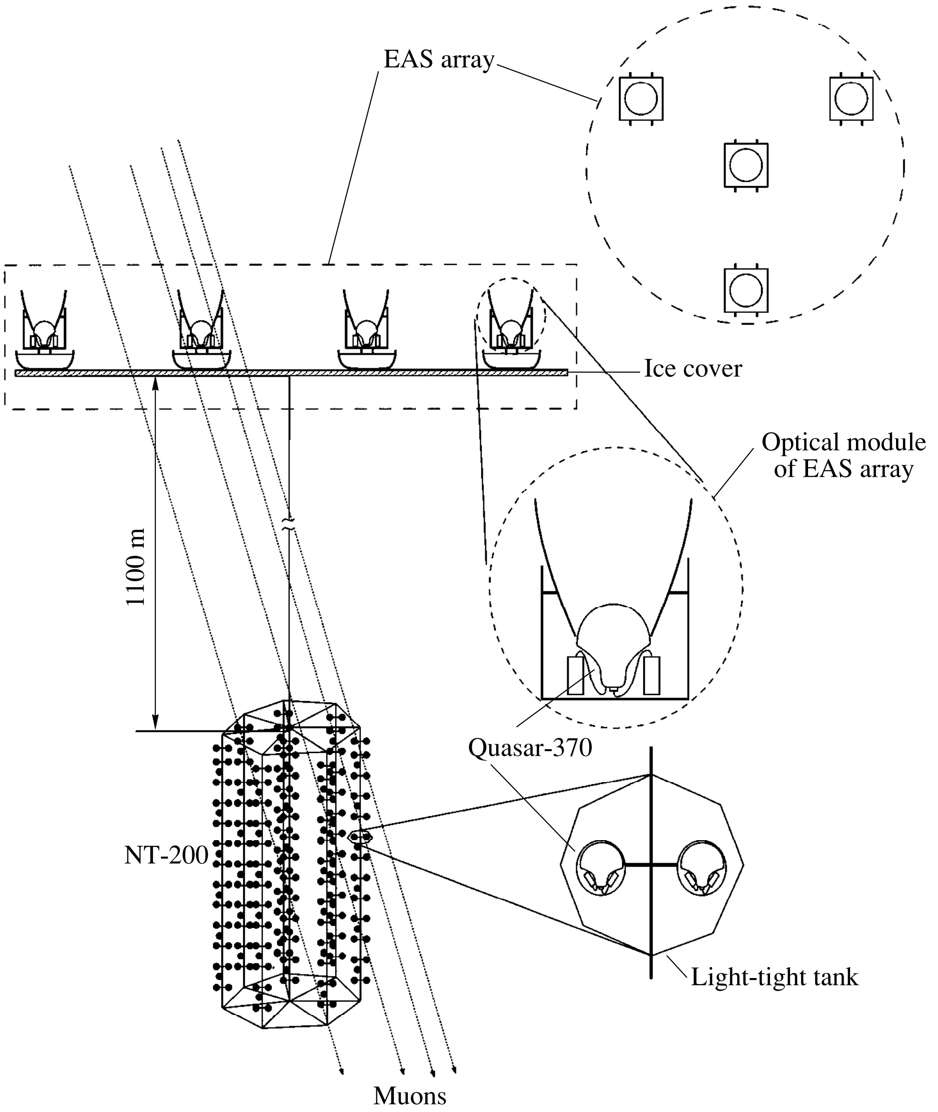

Fig. 2. Principle of joint operation of the NT-200 with an EAS Cherenkov array. Also shown (bottom right) are optical modules contained in a light-tight tank. Their signal fixes one track point as a tool for calibration.

2.2. Cherenkov EAS Array

In order to determine the angular resolution of the NT-200 telescope, a mobile wide-angle air Cherenkov array has been developed [7]. This array (Fig. 2) has been deployed for the last two expeditions on the ice just above the NT-200 telescope. It consists of four optical modules put on the sledges for a fast deployment. Three of them are fixed at the vertices of an equilateral triangle, and the remaining one, just at the center of the triangle. The length of the triangle sides is about 100 m. The analog signals from the optical modules are fed by electric coax cables to the central electronics station located near the central optical module. The data-acquisition system includes four constant-fraction discriminators, a majority coincidence unit, two TDCs with 500 and 5000 ns ranges, an ADC, an EAS event counter, counting rate scalers for each channel, and an underwater master signal counter.

Each optical module incorporates QUASAR-370G phototubes; two high-voltage power supplies of 25 and 1 kV for an electronoptical preamplifier and a small PMT, respectively; anode-pulse preamplifier; and LED for amplitude calibration. The phototube is arranged in light-tight metallic box equipped with a mechanically removable lid. To increase the sensitivity area, Winston cones are used, which provide an almost 2450 cm^2 final sensitive area; it is twofold as large as that in the 1998 array. The angular acceptance of the optical module is restricted to 30° of half-angle. The QUASAR-370G phototube is virtually identical to the phototube used in the NT-200 telescope, but the former features a small six-stage PMT developed to withstand a high mean anode current due to night-sky background (NSB). To

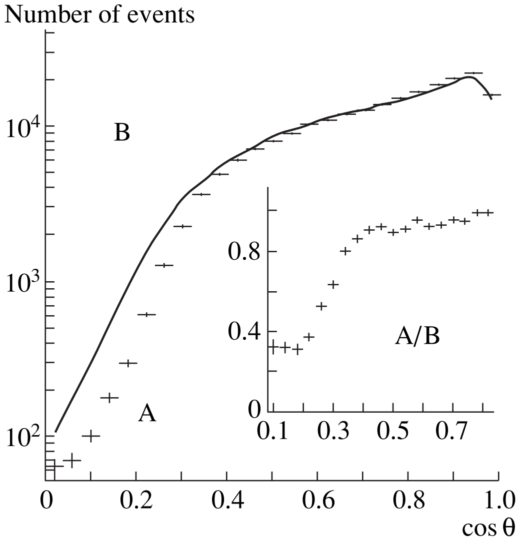

Fig. 3. Atmospheric muons (versus the zenith angle θ) as it is measured in the direction to the nearest point of the shore (A) and in the opposite direction (B), "open" water. The inset shows the ratio of A to B.

stabilize the yield of the phototubes, the high-voltage power supplies are surrounded by a thermostate.

A fourfold coincidence within a 1000-ns gate specifies the trigger of the array. The use of light concentrators permits increasing the array trigger rate by a factor of two. The trigger rate depends on the weather conditions and is on average between 0.8 and 1 Hz. The trigger signal of underwater telescope is fed via coax cable more than 1 km long to the center electronics station of the Cherenkov array and switched in coincidence with the array trigger signal. The time difference between them is measured by a wide-range TDC. The synchronization between the Cherenkov array and the underwater telescope is performed by comparing two underwater event counters in the central electronics station on the ice and detector electronic module of the underwater telescope read out from the shore station. The array energy threshold is about 100 TeV. The angular resolution of the array is about 0.5°–1°, giving a good reference point to estimate the angular resolution of the underwater telescope for muons close to the vertical direction (0°–30°) since high-energy muons retain the direction of their parent shower. In 1998, the EAS array operated in coincidence only with one string, and, in all, 450 events were recorded. An analysis of those events showed that the accuracy of zenith-angle reconstruction that takes into account only time information is close to 6°, which is in reasonable agreement with Monte Carlo calculations (5°). In 1999, we were able to establish the joint work of the EAS array and the NT-200 telescope, but, unfortunately, we collected only 150 events because of bad weather. The analysis of data is still under way, and the results will be presented elsewhere.

2.3. Shadow of the Shore in Muons

The angular distributions of muons as well as the depth dependence of the vertical flux obtained from data taken with the NT-36 telescope were presented earlier [2]. Another example that confirms the efficiency of track reconstruction uses the shore "shadow" in muons recorded with the NT-96 telescope.

As was mentioned above, the NT-200 telescope is positioned at a distance of 3.6 km from the nearest shore of the lake, the distance to the opposite shore being more than 30 km. This asymmetry allows us to study the asymmetry in the azimuth distribution of muons arriving at large zenith angles, in which case the reconstruction for the rather "thin" NT-96 telescope is the most critical.

A sharp decrease in the muon intensity at zenith angles of 70°–90° is expected. A comparison of the experimental angular distribution of muons with Monte Carlo calculations yields an estimate of the accuracy of the reconstruction error close to the horizontal direction.

Indeed, the NT-96 data show a distinct dip in the muon flux in the direction of the shore and for zenith angles larger than 70° (Fig. 3). This is in very good agreement with the calculations that take into consideration the effect of the "shadowing" shore.

3. SELECTED PHYSICS RESULTS

Here, we present some physics results based on the data collected over 70 days of effective operation of the four-string array NT-96.

3.1. Separation of Neutrino Events with a Full Track Reconstruction

The signature of neutrino-induced events is a muon crossing the detector from below. With a flux of downward muons that exceeds that of upward muons from atmospheric neutrino interactions by about six orders of magnitude, a careful reconstruction is of prime importance. The reconstruction algorithm [2] is based on the assumption that light induced by muons is emitted precisely at the Cherenkov angle (42°) relative to the muon track. For a full track reconstruction (θ, ϕ, and spatial coordinates), one needs more than five hit channels on more than three strings. In contrast to the first stages of the detector (NT-36 [8]), the NT-96 facility can be considered as a real neutrino telescope for a wide region of the zenith angle θ. After the reconstruction of all events characterized by more than nine hits on more than three strings (trigger 9/3), quality cuts were applied in order to reject spurious events. Furthermore, in order to guarantee a minimum lever arm for track fitting, events with a projection of the most distant channels onto the track (Z_{dist}) less than 35 meters were rejected. Owing to the small transverse dimensions of the NT-96 telescope, this cut excludes zenith angles close to the horizon.

The efficiency of the procedure was tested by using a sample of 1.8×10^6 atmospheric muons generated on the basis of the Monte Carlo method and upward muons associated with atmospheric neutrinos and generated by the same method. It turned out that, for this sample, the signal-to-noise ratio is in excess of unity.

The reconstructed angular distribution of 2×10^7 events that were taken with the NT-96 detector between April 1996 and September 1996 and which passed all cuts is shown in Fig. 4.

We found 12 neutrino candidates over 70 days of data taking with the NT-96 telescope. Nine of these were fully reconstructed. Three nearly upward vertical tracks (Subsection 3.2) hit only two strings and gave a clear zenith angle but ambiguities in the azimuthal angle, similar to the two events from the NT-36 telescope [2]. This is in good agreement with Monte Carlo predictions.

3.2. Searches for Nearly Vertical Upward-Moving Neutrinos

Unlike the standard analysis [2], the method presented in this section relies on the application of a series of cuts that are tailored for the response of the telescope to nearly vertically upward-moving muons [8, 9]. The cuts remove muon events far away from the opposite zenith, as well as background events, which are due largely to pair and bremsstrahlung showers below the array and to naked downward moving atmospheric muons with zenith angles close to the horizon ($\theta > 60°$). The candidates identified by the cuts are afterward fitted in order to determine the zenith angle. We included all events with no less than four hits along at least one of all hit strings. A series of six cuts is applied to this sample. First, the time differences between the hit channels along each individual string have to be compatible with a particle close to the opposite zenith. The event length should be sufficiently large, the maximum recorded amplitude should not exceed a certain value, and the center of gravity of the hit channels should not be close to the detector bottom. The latter two cuts reject efficiently bremsstrahlung showers from downward muons. Finally, the time differences between hits along different strings must also correspond to a nearly vertical muon (5), and the time difference between the top and the bottom hit in an event must be larger than a minimum value (6).

The effective area for muons moving close to opposite zenith and passing all cuts exceeds 1000 m^2.

Within 70 days of effective data taking, 8.4×10^7 events with the muon trigger $N_{\mathrm{hit}} \geq 4$ were selected.

Table 1 summarizes the number of events from all three samples of events (Monte Carlo signal, background, and experiment) surviving the subsequent cuts. After applying all cuts, four events were selected as neutrino candidates to be compared with 3.5 events expected from a Monte Carlo simulation. One of the four events has 19 hit channels on four strings; it was selected as a neutrino candidate by the standard analysis too. The zenith-angle distribution of these four neutrino candidates is shown in the inset of Fig. 3.

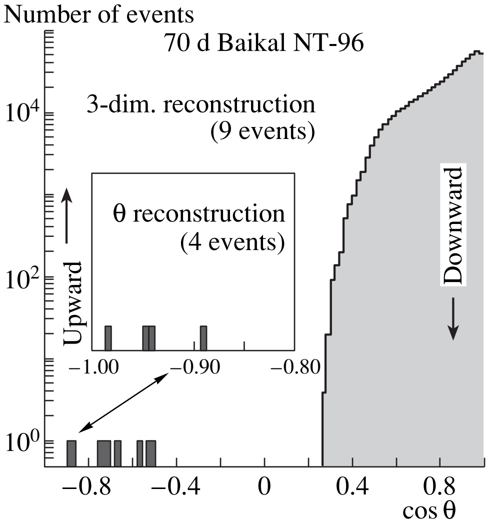

Fig. 4. Experimental angular distribution of events satisfying the 9/3 trigger, all final quality cuts, and the limit on Z_{dist} (see main body of the text). The inset shows events selected by using the method described in Subsection 3.1. The event found by both algorithms is indicated by the arrow.

Regarding the four detected events as those that are due to atmospheric neutrinos, one can derive an upper limit on the flux of muons from the center of the Earth due to annihilation of neutralinos, a favored candidate for cold dark matter.

The limits on the excess muon flux obtained with the underground experiments reported in [10–12] and with the NT-96 telescope are shown in Table 2. The limits obtained with the NT-96 telescope are 4–7 times poorer than the best underground limits since only the first 70 days of data taking with the NT-96 array have been analyzed.

This result, however, illustrates the potential of underwater experiments with respect to the search for muons due to neutralino annihilation at the center of the Earth. A Monte Carlo simulation shows that, for the NT-200 telescope, the effective area is about 2000 m^2

Table 1. Expected number of atmospheric-neutrino events and background events and observed number of events after cuts Nos. 1–6

After cut No. ⟶	1	2	3	4	5	6
Atm. ν, MC	11.2	5.5	4.9	4.1	3.8	3.5
Background, MC	7106	56	41	16	1.1	0.2
Experiment	8608	87	66	28	5	4

Table 2. 90% C.L. upper limits on the muon flux from the center of the Earth for four regions of zenith angles obtained in various experiments

Zenith angles, deg	Flux limit, 10^{-14} (cm^2 s)$^{-1}$			
	NT-96 >10 GeV	Baksan >1 GeV	MACRO >1.5 GeV	KamioKanae >3 GeV
≥150	11.0	2.1	2.67	4.0
≥155	9.3	3.2	2.14	4.8
≥160	5.9–7.7	2.4	1.72	3.4
≥165	4.8	1.6	1.44	3.3

for $E_\mu > 10$ GeV; this is twice as large as that for the NT-96 telescope. If the energy threshold for upward muons could be reduced to 5 GeV, the NT-200 would permit selecting a nonnegligible amount of contained events and estimating the energy of muons. This will allow one to study the neutrino energy spectrum for neutrinos that have traversed about 13000 km in the Earth [13]. Estimates show that the full number of contained events will be about 20 per year for $\theta > 165°$. In the case of ν_μ–ν_x oscillations, the ν_μ flux will be suppressed, and we will find only seven events for $\Delta m^2 = 10^{-3}$ eV^2.

3.3. High-Energy Neutrinos

The ultimate goal of large underwater neutrino telescopes is to identify extraterrestrial high-energy neutrinos. In this section, we present the results of a search for neutrinos with $E_\nu > 10$ TeV derived from NT-96 data. Cherenkov light is emitted by the electromagnetic and (or) hadronic particle cascades and high-energy muons produced at the neutrino-interaction vertex in a large volume around the neutrino telescope. Earlier, a similar strategy was used by the DUMAND [14] and AMANDA [15] collaborations to obtain upper limits on the diffuse flux of high-energy neutrinos.

Figure 5 illustrates the principle of detection. We select events with a high multiplicity of hit channels corresponding to bright cascades. The volume considered for generation of cascades is significantly below the geometric volume of the NT-96 (its upper plane intersects the center of the telescope). A cut is applied that accepts only time patterns corresponding to upward traveling light signals (see below). This cut rejects the majority of events from bremsstrahlung cascades along downward muons since a greater part of muons is close to the vertical; they would traverse the detector and generate a downward time pattern. Only a small number of muons with large zenith angles may escape detection and illuminate the array exclusively via bright cascades below the detector. These events then have to be rejected by a stringent multiplicity cut.

Neutrinos produce showers and high-energy muons through CC interactions

$$\nu_l(\bar{\nu}_l) + N \xrightarrow{\text{CC}} l^-(l^+) + \text{hadrons}, \tag{1}$$

through NC interactions

$$\nu_l(\bar{\nu}_l) + N \xrightarrow{\text{NC}} \nu_l(\bar{\nu}_l) + \text{hadrons}, \tag{2}$$

where $l = e$ or μ, and through the resonance-production processes [16–18]

$$\bar{\nu}_e + e^- \longrightarrow W^- \longrightarrow \text{anything}, \tag{3}$$

with the resonance neutrino energy of $E_0 = M_w^2/2m_e = 6.3 \times 10^6$ GeV and the cross section of 5.02×10^{-31} cm^2.

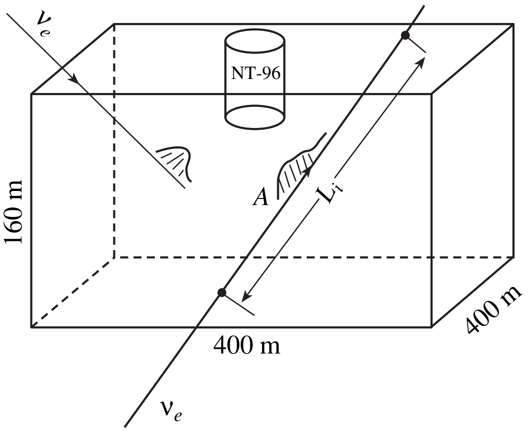

Fig. 5. Detection principle for neutrino-induced showers with the NT-96.

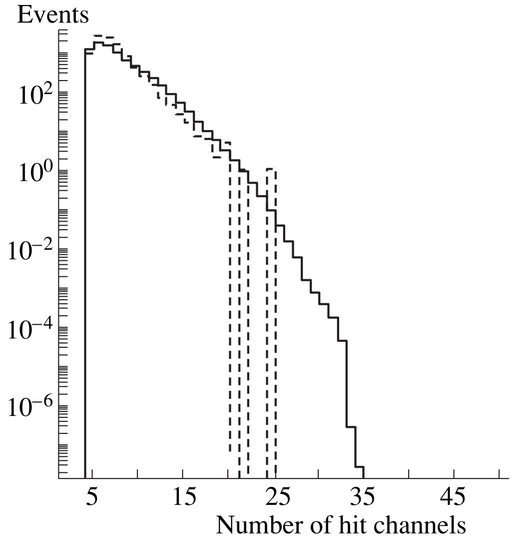

Fig. 6. Hit channel multiplicity: (solid histogram) showers produced by atmospheric muons (MC) and (dashed histogram) experiment.

Within the first 70 days of effective data taking, 8.4×10^7 events with the muon trigger $N_{\text{hit}} \geq 4$ were selected.

For this analysis, we used events featuring more than four hits along at least one of all hit strings. The time difference between any two channels deployed on the same string was required to obey the condition

$$|(t_i - t_j) - z_{ij}/c| < az_{ij} + 2\delta \quad (i < j). \tag{4}$$

Here, t_i and t_j are the times of arrival at the channels i and j, while z_{ij} is the vertical distance between these channels. At $\delta = 5$ ns taking into account the timing error, the condition $|(t_i - t_j) - z_{ij}/c| < 2\delta$ (that is, $a = 0$) would cut a signal traveling vertically upward with the speed of light c. Setting a to 1 ns/m, we slightly increase the acceptance cone around the opposite zenith. This condition was used previously for selecting almost vertically upgoing muons [3, 19].

We found that 8608 events survived the selection criterion (4). Figure 6 shows the hit-multiplicity distribution for these events (dashed histogram) along with the expected distribution for background showers produced by atmospheric muons (solid histogram). The experimental distribution is consistent with the theoretical expectation within a factor of two. This difference can be explained by the uncertainty in the atmospheric-muon flux close to the horizon at the detector depth [2] and by the uncertainties in the dead time of individual channels. The highest multiplicity of hit channels (one event) is $N_{\text{hit}} = 24$.

Since there are no events with $N_{\text{hit}} > 24$ in our data, we can derive upper limits on the flux of high-energy neutrinos producing events with the multiplicities

$$N_{\text{hit}} > 25. \tag{5}$$

The effective volume of the NT-96 for neutrino-induced events depends only slightly on the value of the threshold multiplicity in condition (5). For the stronger conditions $N_{\text{hit}} > 27$ and $N_{\text{hit}} > 29$, the effective volume decreases only by 11 and 27%, respectively.

The effective volume for neutrino-produced events that satisfy conditions (4) and (5) was calculated as a function of the neutrino energy and the zenith angle θ.

The energy dependences of the effective volumes for isotropic electron and muon neutrinos are shown in Fig. 7. Also shown are the effective volumes folded with the neutrino-absorption probability in the Earth. The absorption of neutrinos in the Earth was taken into account with the suppression factor $\exp(-l(\Omega)/l_{\text{tot}})$, where $l(\Omega)$ is the neutrino range through the Earth in the direction Ω and $l_{\text{tot}}^{-1} = N_A\rho_{\text{Earth}}(\sigma_{CC} + \sigma_{NC})$ according to [18, 20].

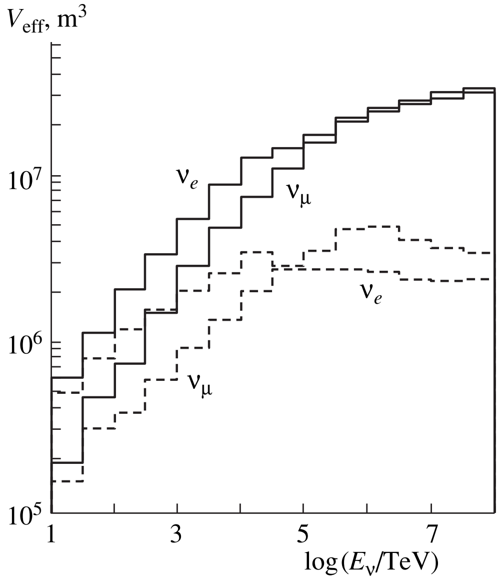

Fig. 7. Effective volumes of the NT-96 for isotropic electron and muon neutrinos (solid lines). The dashed lines represent the effective volumes folded with the neutrino-absorption probability in the Earth (see main body of the text).

3.4. Limits on the Diffuse Neutrino Flux

The number of events due to neutrino flux Φ_ν and processes (1) and (2) is given by

$$N_\nu = T\epsilon\int d\Omega\sum_\nu\int dE\,V_{\text{eff}}(\Omega, E) \times \sum_k\int dE_\nu\Phi_\nu(E_\nu)N_A\rho_{H_2O}\frac{d\sigma_{\nu k}}{dE}, \tag{6}$$

where E_ν is the neutrino energy and E is the energy transfer to a shower or to a high-energy muon; the index ν indicates summation over the neutrino types ($\nu = \nu_\mu$, $\bar{\nu}_\mu$, ν_e), and k indicates summation over CC and NC interactions; N_A is the Avogadro's number; and $\epsilon = 0.9$ is the detector efficiency. Here, we used the cross sections from [18].

The shape of the neutrino spectrum was assumed to obey the E^{-2} law, as is typically expected for Fermi acceleration. In this case, 90% of the expected events would be produced by neutrinos from the energy range 10^4–10^7 GeV with the center of gravity around 2×10^5 GeV. Comparing the calculated rates with the upper limit on the actual number of events, 2.3 at a 90% C.L., and assuming the flavor ratios $\Phi_{\nu_\mu} = \Phi_{\bar{\nu}_\mu} = \Phi_{\nu_e}$ due to photomeson production of π^+ followed by the decay $\pi^+ \longrightarrow \mu^+ + \nu_\mu \longrightarrow e^+ + \nu_e + \bar{\nu}_\mu + \nu_\mu$ for extraterrestrial sources [21, 22], we obtain the following upper limit on the diffuse neutrino flux:

$$\frac{d\Phi_\nu}{dE}E^2 < 1.43 \times 10^{-5}\ \text{cm}^{-2}\ \text{s}^{-1}\ \text{sr}^{-1}\ \text{GeV}. \tag{7}$$

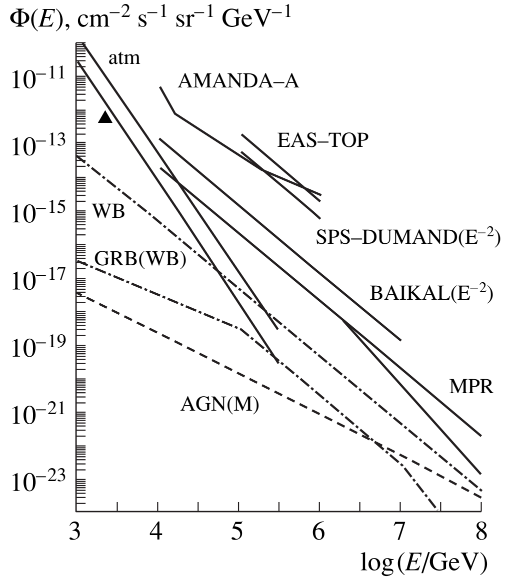

Fig. 8. Upper limits on the differential flux of high-energy neutrinos according to data from various experiments, as well as upper bounds on the neutrino fluxes from various models: [dash-dotted curves labeled with WB and GRB(WB)] upper bound and neutrino intensity from GRB estimated by Waxman and Bahcall (1997, 1999), [dashed curve labeled with AGN(M)] neutrino intensity from AGN (Mannheim model A, 1996), and (solid curves labeled with MPR) upper bounds on $\nu_\mu + \bar\nu_\mu$ in Mannheim *et al.* (1998) for pion-photoproduction neutrino sources with various optical depth τ (adapted from [13]). The triangle represents the limit obtained by the Frejus experiment for an energy of 2.6 TeV (7×10^{-13} cm^{-2} s^{-1} sr^{-1} GeV^{-1}).

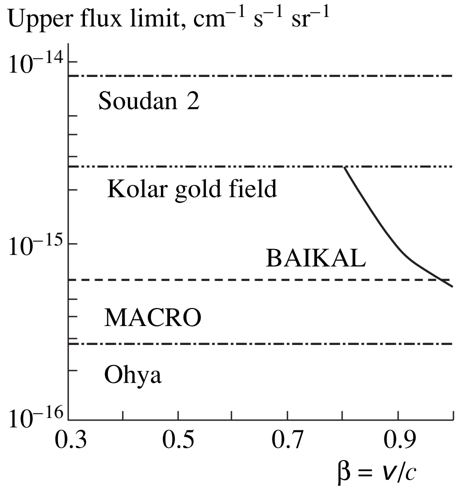

Fig. 9. 90% C.L. Baikal upper limit on the isotropic flux of bare magnetic monopoles, along with other published limits.

New theoretical upper bounds on the intensity of high-energy neutrinos from extraterrestrial sources were presented in [21, 22]. These upper bounds are shown in Fig. 8, along with our limit and the limits obtained by DUMAND [14], AMANDA [15], EAS–TOP [23], and Frejus [24] experiments. Also presented are the atmospheric neutrino fluxes [25] from horizontal and vertical directions (upper and lower curves, respectively).

For the resonance process (3), the event number is given by

$$N_{\bar\nu_e} = T\epsilon\int d\Omega\int dE V_{\mathrm{eff}}(\Omega, E)$$

$$\times \int\limits_{(M_w-2\Gamma_w)^2/2m_e}^{(M_w+2\Gamma_w)^2/2m_e} dE_\nu \Phi_{\bar\nu_e}(E_\nu)\frac{10}{18}N_{\mathrm{A}}\rho_{\mathrm{H_2O}}\frac{d\sigma_{\bar\nu_e,e}}{dE}, \qquad (8)$$

$$M_w = 80.22\ \mathrm{GeV}, \quad \Gamma_w = 2.08\ \mathrm{GeV}.$$

Our 90% C.L. limit on the W resonance energy is

$$\frac{d\Phi_{\bar\nu}}{dE_{\bar\nu}} \le 3.6 \times 10^{-18}\ \mathrm{cm}^{-2}\ \mathrm{s}^{-1}\ \mathrm{sr}^{-1}\ \mathrm{GeV}^{-1}. \qquad (9)$$

This limit lies between the limits obtained by DUMAND (1.1×10^{-18} cm^{-2} s^{-1} sr^{-1} GeV^{-1}) and EAS-TOP (7.6×10^{-18} cm^{-2} s^{-1} sr^{-1} GeV^{-1}).

The new limits (10) and (12) were obtained with the underwater detector NT-96. We hope that the analysis of data taken with the NT-200 telescope over three years [3, 19] will allow us to lower this limit substantially.

3.5. Search for Fast Monopoles ($\beta > 0.75$)

Fast bare monopoles with a magnetic Dirac charge equal to unity and velocities greater than the Cherenkov threshold in water ($\beta = v/c > 0.75$) are promising survey objects for underwater neutrino telescopes. For a given velocity β, the monopole Cherenkov radiation exceeds that of a relativistic muon by a factor of $(gn/e)^2 = 8.3 \times 10^3$ (the index of refraction, n, is 1.33 for water) [26, 27]. Therefore, fast monopoles with $\beta \ge 0.8$ can be detected up to distances 55–85 m, which corresponds to effective areas of $(1–3) \times 10^{-4}$ m^2.

The natural way for fast-monopole detection is based on the selection of events with a high multiplicity of hits. In order to reduce the background from downward atmospheric muons, we restricted ourselves to monopoles coming from the lower hemisphere.

Two independent approaches were used to select upward monopole candidates from the data taken with the NT-96 over 70 days. The first is similar to the method that was applied to upward moving muons (Subsection 3.2), but the additional cut $N_{\mathrm{hit}} > 25$ was imposed here on the hit multiplicity. The second employs a cut on the spacetime correlation followed by the cut $N_{\mathrm{hit}} > 35$ on the hit multiplicity. The upper limits on the monopole flux that were obtained within the two different methods agree within errors.

The same type of analysis was applied to the data taken with the neutrino telescope NT-36 over its lifetime period 0.42 yr [28].

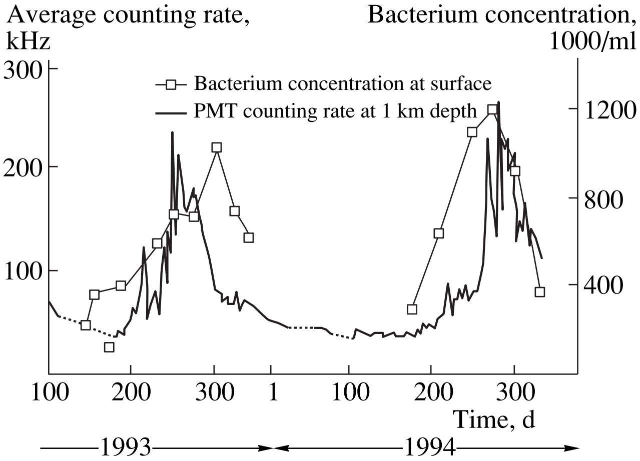

Fig. 10. Average counting rate of OMs versus time, along with bacterium concentration at the surface.

The combined 90% C.L. upper limit obtained by the Baikal experiment for an isotropic flux of bare fast magnetic monopoles is shown in Fig. 9, together with the best limits from underground experiments Soudan 2, KGF, MACRO, and Ohya [29–32].

4. LIMNOLOGY

In addition to physics goals, the NT-200 can be used as a powerful tool for monitoring water parameters. The array permanently records phototube counting rates and periodically parameters like optical transmission at various values of the wavelength, temperature, conductivity, pressure, and speed of sound. All these data, which complement traditional limnological studies, are of importance for obtaining a comprehensive understanding of processes occurring in the lake. Just for illustration, we show variations in the OM counting rate at various time scales recorded with the NT-36

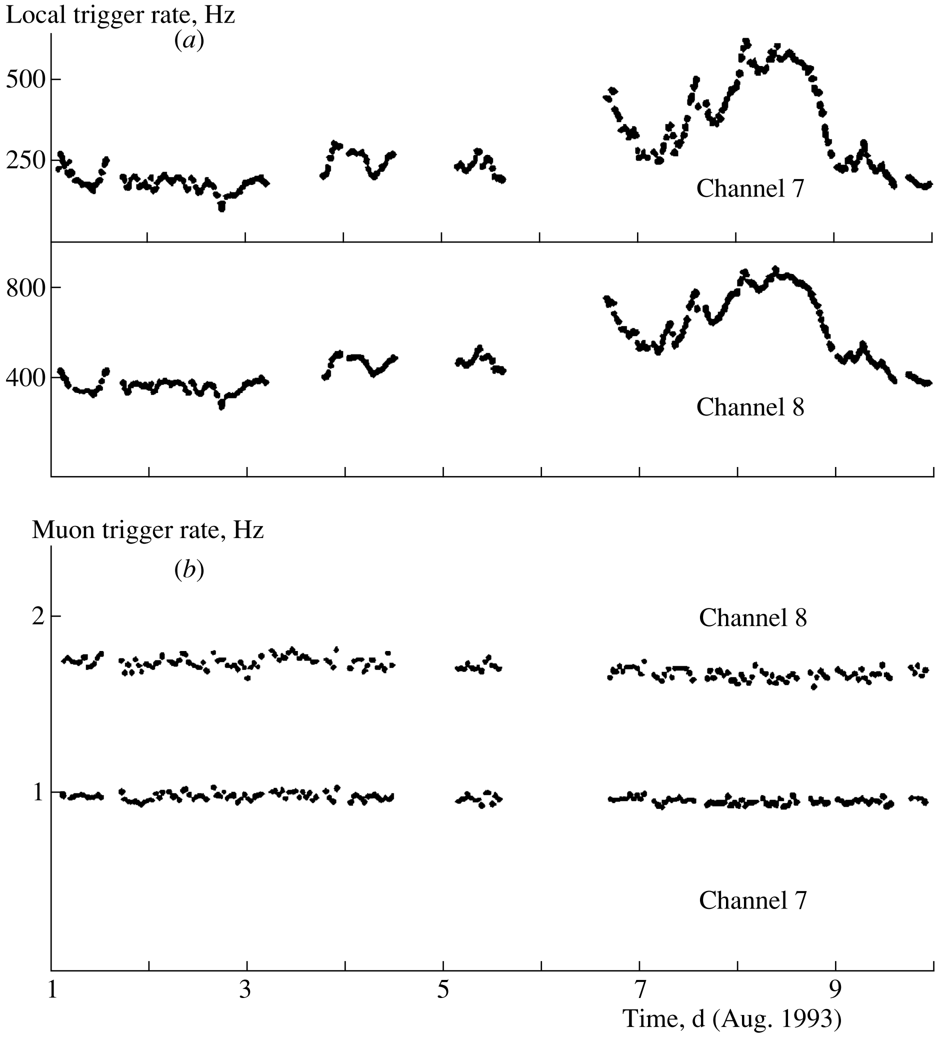

Fig. 11. (*a*) Local trigger rates for channel 7 (downward facing) and channel 8 (upward facing) for August 1–9, 1993. The counting rates are averaged over 30 min. (*b*) Muon trigger rates (condition 4/1) for channels 8 and 7. The counting rates are averaged over 50 min.

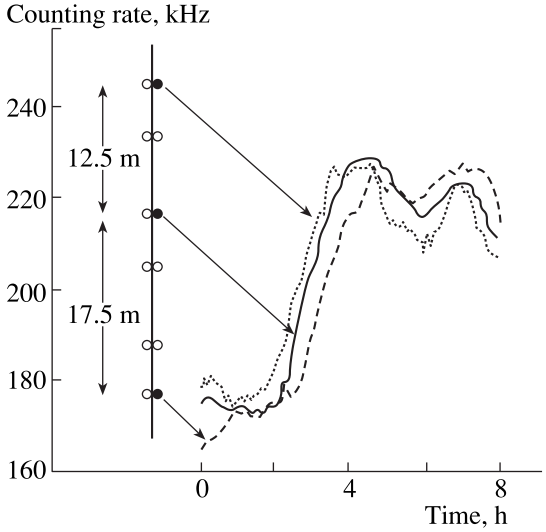

Fig. 12. Counting rate of three OMs along one string over an 8-h interval on September 24, 1993.

from 1993 to 1994. The counting rates of individual OMs, as well as of individual channels (coincidence rate of a pair of OMs), are dominated by water luminescence. Figure 10 presents the counting rate over 2 yr and compares it with the bacterium concentration measured at a distance of 50 km from the NT-200 site at a depth of 10 m below surface. From August to September, we observed an increase in the luminosity to extremely high levels. The changes in the counting rate of channels are not reflected in the muon trigger rate, since the muon trigger is dominated by atmospheric muons, with negligible contribution from random hits (water luminescence or dark-current pulses). This is demonstrated in Fig. 11 on a shorter time scale for a time interval of marked changes in the individual-channel counting rates following a severe storm on August 3, 1993, which had washed a lot of water from nearby rivers and creeks to the lake. Figure 12 shows a short period of about 8 h when the counting rates sequentially increased starting with the highest OMs and ending with the lowest ones along the string. From the time shift of the three curves, a vertical current of 2.3 cm s^{-1} was deduced. This is remarkable since the vertical velocity of water renewal, which is considered to be most intensive, is only 0.2–0.3 cm s^{-1}.

5. CONCLUSIONS AND OUTLOOK

The results obtained with intermediate detector stages show the potential of the Baikal Neutrino Telescope for seeking a wide variety of phenomena in neutrino astrophysics, cosmic-ray physics, and particle physics.

The first atmospheric neutrinos have been identified. Also, limits on the fluxes of magnetic monopoles and on the diffuse flux of very high-energy neutrinos, as well as of neutrinos from WIMP annihilation at the center of the Earth, have been derived.

In the following years, the NT-200 will operate as a neutrino telescope with an effective area between 1000 and 5000 m^2, depending on the energy, and will investigate atmospheric-neutrino spectra above 10 GeV.

The NT-200 can be used to seek neutrinos from WIMP annihilation, as well as magnetic monopoles and high-energy extraterrestrial neutrinos. It will also be a unique environmental laboratory to study water processes in Lake Baikal.

Apart from its own goals, the NT-200 is regarded as a prototype for the developing a large-scale telescope of the next generation. The basic design of such a detector is under discussion at present.

ACKNOWLEDGMENTS

This work was supported by the Russian Ministry of Research, the German Ministry of Education and Research, and the Russian Foundation for Basic Research (project nos. 99-02-18373a, 97-02-17935, 99-02-31006, 97-02-96589, and 97-05-96466).

REFERENCES

1. *The Baikal Neutrino Telescope NT-200, BAIKAL 92-03*, (1992).
2. I. A. Belolaptikov *et al.*, Astropart. Phys. **7**, 263 (1997).
3. I. A. Belolaptikov *et al.*, astro-ph/9903341; Astropart. Phys. (in press).
4. R. I. Bagduev *et al.*, Nucl. Instrum. Methods Phys. Res. A **420**, 138 (1999).
5. R. I. Bagduev *et al.*, in *Proceedings of International Conference on Trends in Astroparticle Physics, Aachen, 1994*, p. 132.
6. L. B. Bezrukov *et al.*, in *Proceedings of 3rd NESTOR Workshop, Greece, 1993*, p. 645.
7. R. A. Antonov *et al.*, in *Proceedings of 23rd International Cosmic Ray Conference, Calgary, 1993*, Vol. 2, p. 430.
8. L. B. Bezrukov *et al.*, in *Proceedings of the 2nd Workshop on the Dark Side of the Universe, Rome, 1995*, p. 221; astro-ph/9601161.
9. V. A. Balkanov *et al.*, Preprint No. 0972/98, IYaI RAN (Institute of Nuclear Research, Russian Academy of Sciences, Moscow, 1998).
10. M. M. Boliev *et al.*, Nucl. Phys. B (Proc. Suppl.) **48**, 83 (1996).
11. T. Montaruli *et al.*, in *Proceedings of 25th International Cosmic Ray Conference, Durban, 1997*, Vol. 7, p. 185.
12. M. Mori *et al.*, Phys. Rev. D **48**, 5505 (1993).
13. L. Moscoso, Oral Presentation at NOW98, 1998.
14. J. W. Bolesta *et al.*, in *Proceedings of 25th International Cosmic Ray Conference, Durban, 1997*, Vol. 7, p. 29.
15. R. Porrata *et al.*, in *Proceedings of 25th International Cosmic Ray Conference, Durban, 1997*, Vol. 7, p. 9.
16. S. L. Glashow, Phys. Rev. **118**, 316 (1960).

17. V. S. Berezinsky and A. Z. Gazizov, Pis'ma Zh. Éksp. Teor. Fiz. **25**, 276 (1977) [JETP Lett. **25**, 254 (1977)].
18. R. Gandhi *et al.*, Astropart. Phys. **5**, 81 (1996).
19. V. A. Balkanov *et al.*, Yad. Fiz. **62**, 1015 (1999) [Phys. At. Nucl. **62**, 949 (1999)].
20. V. S. Berezinsky *et al.*, Yad. Fiz. **43**, 637 (1986) [Sov. J. Nucl. Phys. **43**, 406 (1986)].
21. E. Waxman and J. Bahcall, Phys. Rev. D **59**, 023002 (1999); Phys. Rev. Lett. **78**, 2292 (1997).
22. R. J. Protheroe, astro-ph/9809144.
23. M. Aglietta *et al.*, Phys. Lett. B **333**, 555 (1994).
24. W. Rhode *et al.*, Astropart. Phys. **4**, 217 (1996).
25. P. Lipari, Astropart. Phys. **1**, 195 (1993).
26. I. M. Frank, in *Vavilov–Cherenkov Radiation* (Nauka, Moscow, 1988), p. 192.
27. D. A. Kirzhnits and V. V. Losjakov, Pis'ma Zh. Éksp. Teor. Fiz. **42**, 226 (1985) [JETP Lett. **42**, 279 (1985)].
28. V. A. Balkanov *et al.*, Preprint No. 0984, IYaI RAN (Institute of Nuclear Research, Russian Academy of Sciences, Moscow, 1998).
29. S. Orito *et al.*, Preprint No. UT-ICEPP-90-2, ICEPP (Tokyo, 1990).
30. M. Ambrosio *et al.*, MACRO Preprint No. MACRO/PUB 98/3 (1998).
31. H. Adarkar *et al.*, in *Proceedings of 21st International Cosmic Ray Conference, Adelaide, 1990*, p. 95.
32. J. L. Thorn *et al.*, Phys. Rev. D **46**, 4846 (1992).

Physics of Atomic Nuclei, Vol. 63, No. 6, 2000, pp. 962–968. From Yadernaya Fizika, Vol. 63, No. 6, 2000, pp. 1037–1043.
Original English Text Copyright © 2000 by Lobashev.

NEUTRINO PHYSICS

Direct Search for the Neutrino Mass in the Beta Decay of Tritium: Status of the "Troitsk ν-Mass" Experiment*

V. M. Lobashev**

Institute for Nuclear Research, Russian Academy of Sciences, pr. Shestidesyatiletiya Oktyabrya 7a, Moscow, 117312 Russia

Abstract—The results of the "Troitsk ν-mass" experiment on the search for the neutrino rest mass in tritium beta decay are presented. The investigation of the time dependence of the anomalous, bumplike structure at the end of the beta spectrum, reported earlier, gives an indication of the periodic shift of its position with respect to the endpoint with a period of 0.5 yr. An upper limit on the electron-antineutrino rest mass ($m_\nu < 2.5$ eV/c^2) is derived after taking the bump into account. © *2000 MAIK "Nauka/Interperiodica".*

1. INTRODUCTION

The problem of the neutrino rest mass remains one of the most important problems in elementary-particle physics and cosmology. The direct or kinematics approach to the search for the neutrino rest mass is based on the study of neutrino momentum–energy balance in weak semileptonic decays. In this case, any dependence on the leptonic or flavor quantum numbers is excluded. A maximal sensitivity to the mass effect may be attained when the neutrino energy is minimal. Such a situation can usually be obtained in a three-body or multiparticle decay. The total-energy spectrum of visible particles in the vicinity of the maximal energy is dominated by the neutrino phase-space volume, which is proportional to pE, where p is the momentum and E is the total energy of the neutrino. A deviation of this product from p^2 allows one to deduce the neutrino mass. At present, the lowest limit on the electron-neutrino mass was achieved by the study of the shape of the tritium beta spectrum near its endpoint. Now, the spectrometric facilities in Troitsk (Moscow) [1] and in Mainz [2] allowed details of the beta spectrum at about 5–15 eV below the endpoint to be observed. In addition to a significant reduction of the upper neutrino-mass limit, the experiment in Troitsk revealed the presence of an anomalous structure of the bumplike shape (for differential spectrum mode) in the tritium spectrum in the region of 5–15 eV below the endpoint with integrated intensity about 10^{-10} of the total decay rate. A very enigmatic feature of this structure turned out to be a periodic shift of its position with time. This structure, in the absence of understanding of its nature, plays the role of a systematic effect for the search for the neutrino mass, strongly increasing a possible error.

2. SEARCH FOR ELECTRON–ANTINEUTRINO REST MASS

The shape of the beta spectrum with nonzero neutrino mass is

$$W(E, Z) = AF(E, Z)Ep \times \sum W_i(E_{0i} - E)\sqrt{(E_{0i} - E)^2 - m_\nu^2 c^4}, \quad (1)$$

where E is the total energy and p is the momentum of the electron, while W_i is the probability and E_{0i} is the endpoint energy of the partial decay into the ith final state. The effect of a nonzero neutrino mass emerges as a cutoff of the spectrum at $E_{0i} - E = m_\nu c^2$ and an intensity deficiency smoothly declining to lower energy. The decay of tritium provides a unique opportunity for such experiments due to a low endpoint energy, a high spe-

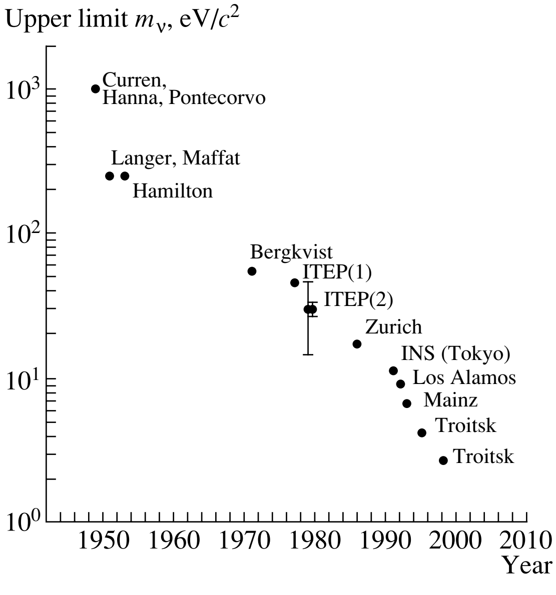

Fig. 1. Progress in upper-limit improvement in neutrino-mass measurement in tritium beta decay.

---

* This article was submitted by the author in English.
** e-mail: lobashev@al20.inr.troitsk.ru

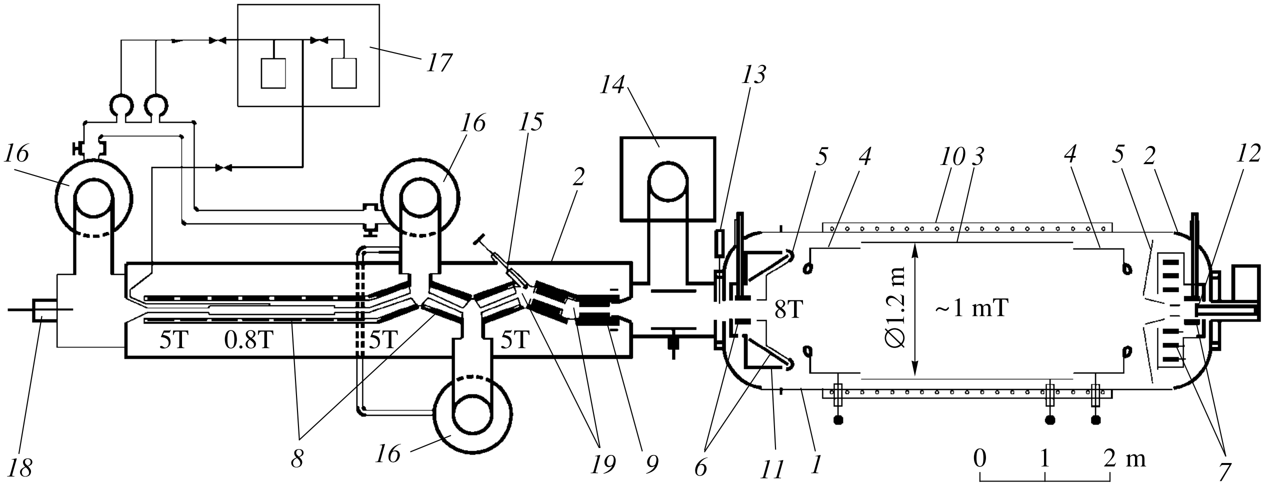

Fig. 2. Experimental setup: (*1*, *2*) vacuum tanks, (*3*, *4*) electrostatic analyzers, (*5*) grounded electrode, (*6*–*9*) superconducting coils (He system, 4.7 K), (*10*) warm coil, (*11*) LN_2 jacket, (*12*) Si(Li) detector, (*13*) fast shutter, (*14*) Ti pump, (*15*) cold valve, (*16*) Hg diffusion pump, (*17*) T_2 purification system (27 K), (*18*) electron gun, and (*19*) argon pump.

cific activity, the lowest Z, and the possibility of calculating most of the corrections for its superallowed spectrum.

The history of the search for the neutrino mass in the tritium beta decay is almost 50 years long. An illustration of the experimental progress over this time is given in Fig. 1. In 1980, a steady improvement of the upper limit on the neutrino mass was suddenly speeded up by the report of the ITEP group from Moscow on the observation of the neutrino-mass effect corresponding to the rest mass of about 30 eV/c^2 [3]. This report stimulated more than 20 experimental proposals with an intention to check this claim. After several years, the experimental groups from Zurich [4], Tokyo University [5], and Los Alamos [6] produced results that refuted the ITEP group claim, but which revealed many difficulties in measuring and analyzing the beta spectra.

Many efforts were made to develop a new tritium source. The most radical step was done by the Los Alamos group by construction of a windowless gaseous tritium source with a strong solenoidal magnetic field transporting electrons to a spectrometer of the Tretyakov type [7].

3. TROITSK ν-MASS SETUP

The development of a new approach to the spectroscopy of tritium started at the end of 1982 at the Institute for Nuclear Research (Russian Academy of Sciences, Troitsk) [8–10]. Similar ideas independently emerged at the Institute for Physics of Mainz University [11]. The main feature of this approach is an integral electrostatic spectrometer with a strong nonuniform magnetic field providing guiding and collimation of the electrons. The early version of such a spectrometer was proposed for the spectroscopy of electrons with energy below a hundred eV [12, 13]. An extension of the application area of the spectrometer to a few tens of keV proved to be possible owing to a special tailoring of magnetic and electric fields. The Troitsk setup is shown in Fig. 2. An important part of it is a chain of superconducting solenoids that produce a continuous longitudinal magnetic field through the entire setup. A cylindrical electrode in the central part of the spectrometer, with a low-strength magnetic field, is an integral electrostatic analyzer. All the magnetic and electrostatic fields are adjusted to ensure adiabaticity of the electron motion through the source and through the spectrometer along the magnetic field lines. The electron detector detects only electrons that have been produced in the magnetic-field-flux tube crossing the detector surface. The magnetic fields in the spectrometer and in the source are adjusted in just a way that this flux tube does not touch the walls.

The spectrometer resolution is a step function with an almost linear slope from 0 to 1; the total width of the slope is $\Delta E = E\dfrac{H_{\min}}{H_{\max}}$, where E is the electron energy, $H_{\max}$ is the intensity of the magnetic field at the entrance of spectrometer solenoid, and $H_{\min}$ is its intensity at the spectrometer medium plane (Fig. 2). The main advantage of this spectrometer is the energy resolution amounting to 3.5–4 eV (FW) and luminosity. The strong guiding magnetic field in the spectrometer permitted its natural coupling to the gaseous windowless tritium source, also with a strong magnetic field comprising the second important part of the Troitsk setup. The gaseous tritium source has a number of advantages in relation to the solid-state source. The most important of these are the absence of a correction for backward scattering, the weakness of interactions of tritium with other molecules, an easy control for admixture, and the absence of charging effects. Details of the setup design and of the measurement procedure can be found in [1, 14, 15].

Gaseous tritium is injected at the center of a 3-m-long tube inside the solenoids and is being pumped out by mercury diffusion pumps installed at both ends of the tube. After additional compression in the buster mercury pump and after purification, tritium returns to the injection point, thus providing continuous circulation. The tritium spectrum was measured by changing the high voltage of the spectrometer in steps. The direction of the high-voltage scanning was reversed at each cycle (between one and two hours). The measurements were made in the range of the spectrometer potential from 18000 to 18770 V. The data-acquisition system allowed one to record the amplitude and the time of each detector pulse. High-voltage stability was checked by independent measurement by three attenuators. Altogether, in the period from 1994 to 1998, the time of measurement amounted to about 200 d. An analysis of data was done by fitting the theoretical spectrum, with all the correction factors and some variable parameters, to the experimental spectrum by means of the minimum χ^2 procedure. The experimental spectrum was corrected for the dead time and pileup, for the drift of the source intensity, for the cutting-out of the part of the detector spectrum, and for events of tritium decay into the spectrometer. Those events manifest themselves as bunches of pulses with an instant counting rate corresponding to the probability less than 10^{-4}–10^{-5} in relation to the regular rate. The search for such events was possible in the area of the low counting rate from 18530 to 18770 eV. Below 18530 eV, the average of bunch counts was subtracted, which increased the statistical error because of more intense scattering of bunched particles.

The theoretical spectrum was taken in accordance with (1). Its extension to negative (unphysical) values of m_ν^2 was taken as in [1]. The spectrum was convoluted with the integral spectrum of energy losses of the electrons in the source and the final-state spectrum and corrected for the trapping effect in the source. The latter caused the intensity rise of the spectrum toward low energies reported in [1]. The final-state spectrum of the decay product (FSS) was taken from the most recent theoretical calculations [16]. Corrections for the inelastic interactions of electrons in tritium gas, as well as the FSS, strongly correlate with the neutrino mass and some other parameters of the spectrum. A special system, with an electron gun and adiabatic magnetic transportation of electrons to the rear part of the source, allowed one to measure the integral spectrum of inelastic losses of electrons in tritium as well as the density of the source. These measurements gave the total inelastic interaction cross section for electrons with molecules of tritium in good accordance with the theoretical value of 3.45×10^{-18} cm^2 at the electron energy of 18.6 keV. The spectrum of inelastic losses was found to be different from the usually accepted one. In particular, the ratio of excitation to ionization parts of it proved to be equal to 0.51/0.49, in disagreement with the usually quoted value of 0.1/0.6. As a basic set of variable parameters in the χ^2 fit procedure, we used four parameters: a normalization factor, the endpoint energy, a background, and m_ν^2. The fit was made for the spectrum interval with the low-energy boundary ($E_{\rm low}$) from 18000 eV to 18530 eV and the upper boundary of 18770 eV. A variation of $E_{\rm low}$ is very important for recognizing systematic effects.

4. ANOMALOUS STRUCTURE IN THE SPECTRUM

The fitting of the data with four basic variable parameters with all the above-mentioned corrections resulted in the value of $m_\nu^2 = -10$–20 eV^2, mostly independent of ($E_{\rm low}$). The negative values for m_ν^2 obviously indicated existence of some systematic effect not taken into account [1]. Inspection of the spectra showed that there is small enhancement near the endpoint, which resembles a small step superimposed on the regular spectrum. In the differential mode, such an addendum would be seen as a bumplike structure with a small width (about the resolution of the spectrometer). An addition of a steplike function with a variable height (size) and position ($E_{\rm step}$) to the theoretical spectrum made the theoretical and experimental spectra consistent over the entire measured part of it and brought the value of m_ν^2 to about zero, thus eliminating the negative-value problem (Figs. 3, 4).

The parameters of the step function turned out to vary from one run to another. The average variation of $\Delta N_{\rm step}$ was about 6×10^{-11} of the total decay intensity (except the last run), and $E_0 - E_{\rm step}$ varied within 5–15 eV. In the majority of the runs, where the fit program was able to give meaningful values for the six-parameter fit with the step function, the value of m_ν^2 turned out to be about zero within the fit errors. The impossibility of obtaining definite minima of χ^2 in the six-parameter fit for some run was associated with a strong correlation of $\Delta N_{\rm step}$ and m_ν^2 when the step position is too close to the endpoint. For such a run, the step parameters were obtained by setting $m_\nu^2 = 0$. Changeable positions of the step with respect to the endpoint energy from one run to another seemed to be evidence for some systematic effect. The situation became more enigmatic when the values of $E_0 - E_{\rm step}$ were plotted versus calendar time of the corresponding run. The plot is given in Fig. 5. Its very surprising feature turned out to be the possibility of describing the time dependence of the step position by a sinusoid.

The period of the fitted sinusoid proved to be equal to 0.499 ± 0.003 yr, the mean value of the position was

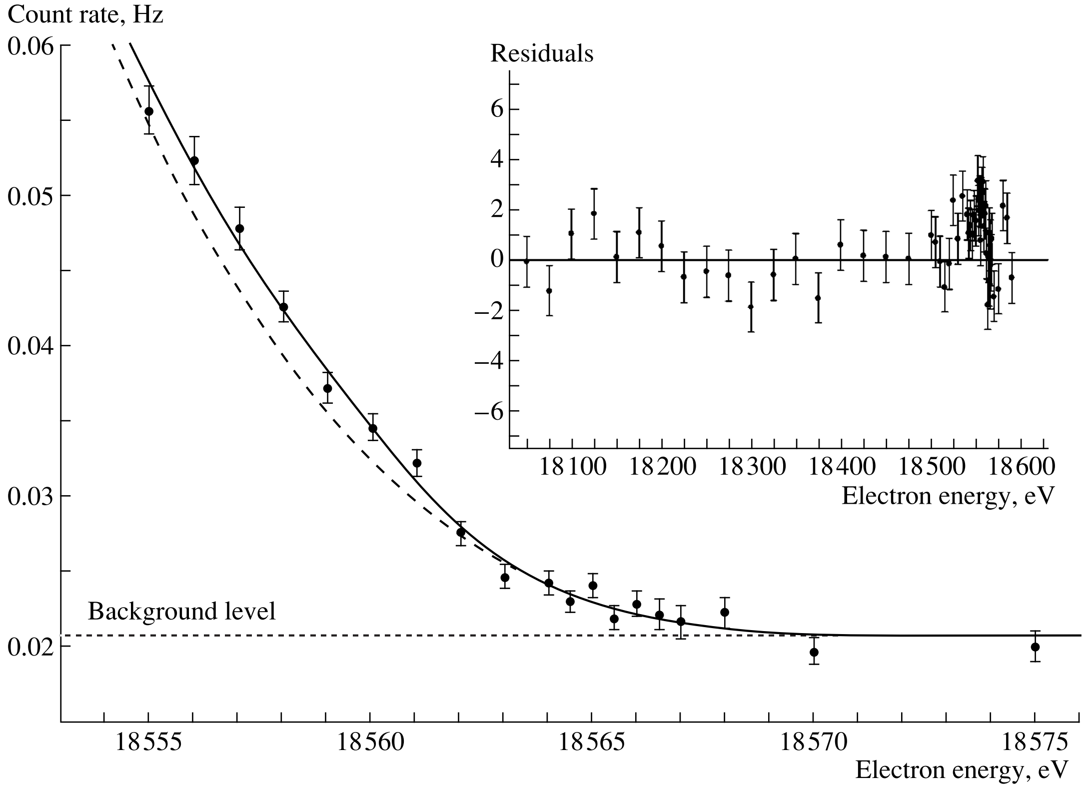

Fig. 3. Part of the experimental spectrum near the endpoint. The solid line is the fitted theoretical spectrum with a step function. The dotted line is the theoretical spectrum with a subtracted step function. The inset in the upper right corner shows the spectrum of residuals for the entire measured part of the spectrum. The residuals are $(N_{\text{exp}} - N_{\text{theor}})/\sigma$, where N_{exp} is the same as the dotted line in the previous plot, and σ is the standard deviation at each point.

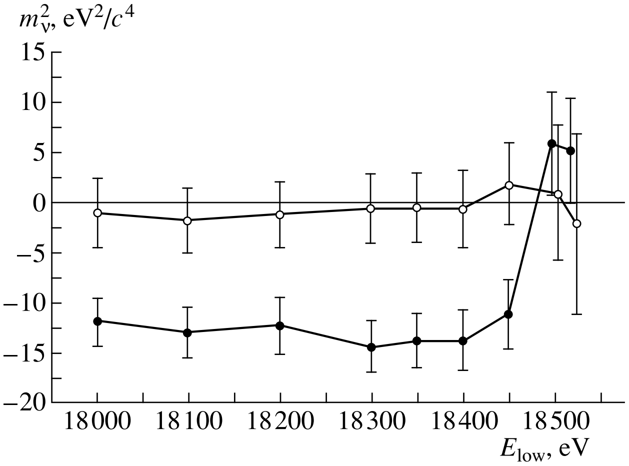

Fig. 4. m_ν^2 as a function of E_{low} for the sum of Runs 94, 96, 97.2, and 98 data. Closed circles represent the fit without the step function (four-parameter fit). Open circles represent the fit with the step function (six-parameter fit).

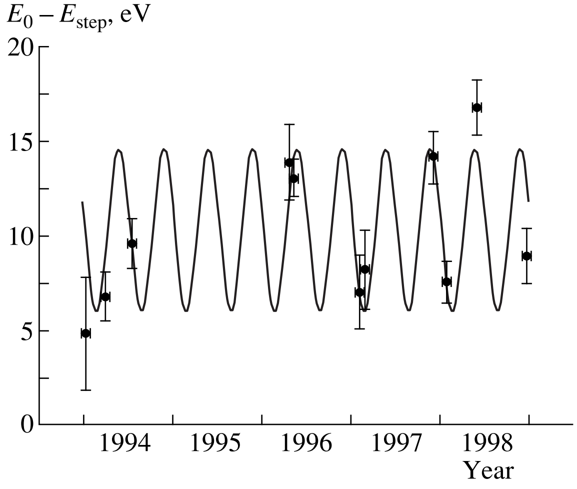

Fig. 5. Step position as a function of the calendar time of measurements. The parameters of the fitted sinusoid are as follows: the period is 0.499 ± 0.003 yr; the mean value is 10.4 ± 0.4 eV; the amplitude is 4.3 ± 0.55 eV; and the phase is 2.6 ± 0.23 rad.

10.4 eV, and the amplitude was 4.35 eV. The dependence of χ^2 on the value of the period obtained in the fit with a variable mean value, amplitude, and phase of the sinusoid is given in Fig. 6. It can be seen that a half-year period is the most probable one.

Data of all the years including points of the Mainz group reported at this conference are combined in one year plot (Fig. 7). It confirms that the variation of the step position has biseasonal character.

The plot of step-size values given in Fig. 8 proved to

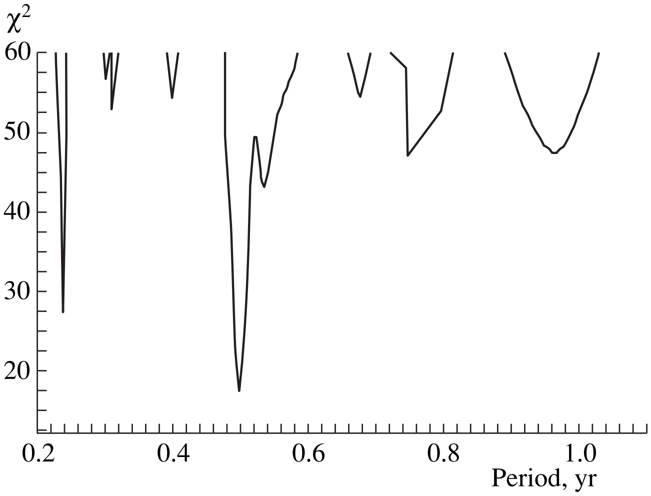

Fig. 6. χ^2 as a function of the period of the sinusoid fitted to the step position. The period value was scanned, and three other parameters were left variable.

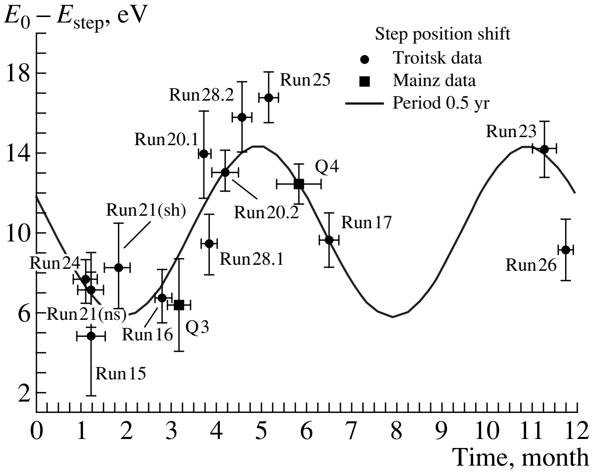

Fig. 7. Step position versus time of the year. The fitted sinusoid is the same as in Fig. 5, but with a period of 0.5 yr. Horizontal bars are the duration of the run. Indices of the points indicate the number of the run. Run 21(sh) was carried out with a potential bias (15 V) applied to the tritium source, while run 21(ns) was carried out without this bias.

be more peculiar. The data obtained before run 98.3 roughly agreed, at least for the first maximum, with the half-year period, so that a larger step size corresponds to a larger distance from the endpoint. The measurement of run 98.3, being relatively short, resulted in an almost three times larger step size and $E_0 - E_{\text{step}}$ somewhat below the sinusoid fitted to the previous data. This outburst may suggest that the step phenomenon, if it is not considered as some apparatus effect, may fluctuate in size with characteristic time less than a month, the position being close to a sinusoid. This may be confronted with the latest measurement of the Mainz group, where they did not find the step effect a few weeks earlier [17]. Unfortunately, the Troitsk setup did not run this time.

Of course, the present set of data needs to be sufficiently extended. In particular, the absence of measurement within the period from July to December and the absence of a continuous measurement over all the year make it possible to fit a more complicated periodic curve but with the half-year component as a dominant one.

At the moment, it seems impossible to propose any “customary” explanation of this phenomenon. The proximity of the oscillation period of the step (bump) to the half-period of Earth’s circulation around the Sun and its other features remind us of an old speculation about an effect produced by capture of the cosmological degenerate neutrinos by tritium atoms with the emission of almost monochromatic electrons [18]. In order to produce the bump intensity corresponding to 10^{-10} of the total decay rate, it is necessary to assume the existence of a neutrino cloud with a density as high as 0.5×10^{15} ν/cm^3, which is 10^{13} times higher than the generally accepted average density of relic massless neutrinos.

An observation of the bump below the endpoint of the beta spectrum corresponds to the capture of a neutrino with a negative energy and to the assumption that neutrinos are bound in the cloud. If the binding energy changes over the cloud, the Earth in its movement produces a periodic modulation of the binding energy and, accordingly, of the position of the step. It is interesting to point out that this hypothetical binding energy assumed to be $V = E_0 - E_{\text{step}} + E_{\text{Fermi}}$, where E_{Fermi} is calculated from the step size, being plotted as in Fig. 5, provides a somewhat better fit to a sinusoid in relation to the previous fit. In order to explain the half-year modulation period, one may suppose that the neutrino

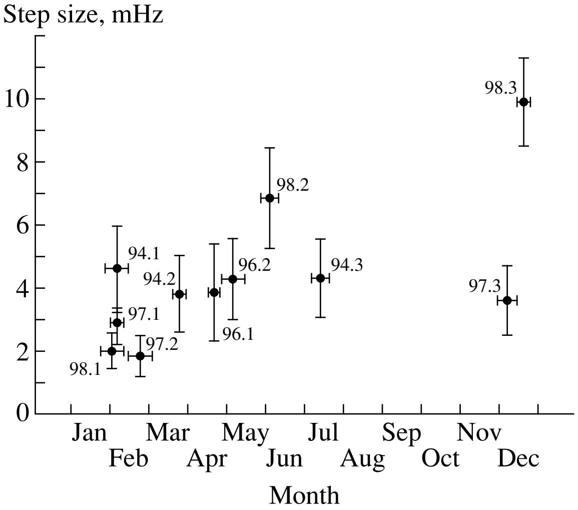

Fig. 8. Step size versus time of the year. All the size values were reduced to the same intensity of the source.

cloud has the shape of a flattered disc with the axis of symmetry inclined with respect to the normal direction to the Ecliptic plane.

The size of the neutrino cloud in this case must be comparable with the Earth's orbit, and this removes the contradiction with the average density of the relic neutrinos in the Universe. Of course, this explanation of the step phenomenon is extremely speculative and may be considered only for a stimulation of further experiments.

Up to now, the experimental data do not rule out the possibility that the shape of the endpoint region is more complicated than the one-bump structure. Nevertheless, it appears to be shown that the center of gravity of the steplike enhancement (bump) is below the endpoint of the tritium beta spectrum, and it undergoes a periodic shift with respect to the endpoint.

5. UPPER LIMIT ON THE NEUTRINO MASS

A special approach is required for deducing the neutrino mass from the data in the presence of an unexplained anomaly.

As was mentioned earlier, the procedure accepted for this purpose consisted in adding a step function with two variable parameters to the theoretical spectrum under the assumption that this addition may describe, in the first approximation, the local enhancement in the beta spectrum near the endpoint. A distortion of the beta spectrum imitating the m_ν^2 effect should also be concentrated near the endpoint; otherwise, the effect relatively fast sinks in growing statistical errors at increasing $E_0 - E$, but, unlike the local enhancement, it appears as an addition to (for negative m_ν^2) or deficiency (positive m_ν^2) of the spectrum that linearly increases with $E_0 - E$. This difference allows one to separate both effects in the fit procedure. Of course, the size and the position of the step, introduced as free parameters, correlate with m_ν^2 and increase the final error of the neutrino mass, thus acting as a kind of systematic error. This increase sufficiently compensates for the uncertainty of replacement of an a priori unknown anomaly shape by a steplike function. The possibility of distinguishing the neutrino-mass effect from the step strongly decreases with the proximity of the step position to the endpoint because of the correlation of their parameters. This correlation made it impossible to use the data of runs 97.1 and 98.1 to analyze the neutrino mass in spite of good statistics. In addition to the uncertainty caused by the step function, systematic errors come mostly from the uncertainties in the parameters of the correction factors, which are introduced in the spectrum before the fit. These factors are the trapping effect, the source density, the uncertainty in the excitation and ionization parts of the inelastic cross section, the dead time, and the effect of the highly excited FSS part. A remarkable property of the total systematic error from these factors is its reduction when E_{low} comes nearer to the endpoint E_0. To the contrary, the systematic effect associated with an a priori unknown step-function uncertainty increases when E_{low} comes closer to the endpoint, which is automatically taken into account in the fit procedure. Considering that the fit error of m_ν^2 increases with increasing E_{low}, one may select an optimal E_{low} value at which the total error, including both the fit and systematic errors, is minimal. The results for m_ν^2 for all the runs are as follows:

$$1994\quad m_\nu^2 = -2.7 \pm 10.1_{\text{fit}} \pm 4.9_{\text{syst}}\ \text{eV}^2/c^4,$$

$$1996\quad m_\nu^2 = +0.5 \pm 7.1_{\text{fit}} \pm 2.5_{\text{syst}}\ \text{eV}^2/c^4,$$

$$1997(2)\quad m_\nu^2 = -3.2 \pm 4.8_{\text{fit}} \pm 1.5_{\text{syst}}\ \text{eV}^2/c^4,$$

$$1998\quad m_\nu^2 = -0.6 \pm 8.1_{\text{fit}} \pm 2.0_{\text{syst}}\ \text{eV}^2/c^4,$$

$$1999\quad m_\nu^2 = +1.6 \pm 5.6_{\text{fit}} \pm 2.0_{\text{syst}}\ \text{eV}^2/c^4.$$

The combined value is

$$m_\nu^2 = -1.0 \pm 3.0_{\text{fit}} \pm 2.1_{\text{syst}}\ \text{eV}^2/c^4. \tag{2}$$

The combined systematic error is obtained by averaging fit errors with weights. From here, one may obtain the 95% C.L. constraint for m_ν:

$$m_\nu < 2.5\ \text{eV}/c^2. \tag{3}$$

6. FURTHER STUDY OF THE EFFECTS IN THE TRITIUM BETA SPECTRUM

A further investigation of the bumplike anomaly and the neutrino-mass search at a level of about 1 eV/c^2 require a major improvement of tritium beta spectrometry. One of the obvious ways is a few times enlargement of the existing setup. Another way could be the development of a differential spectrometer with the resolution and luminosity on a par with the integral one. The differential spectrometer allows a better study of local anomalies in continuous spectra and will serve both for the search for the kinks from heavy neutrinos and for the above-mentioned tasks. At the moment, two approaches to this problem are proposed. One is to use the integral spectrometer with pulsing of the source and the time-of-flight technique to achieve the differential regime [19]. The loss of luminosity due to the pulsing of the source is supposed to be compensated by larger dimensions of the spectrometer. The other approach is considered in [15]. It describes a new type of differential spectrometer designed by using the principles of adiabatic motion of electrons in electric and magnetic fields. The apparatus consists of an integral electrostatic spectrometer with adiabatic magnetic collimation and with the central part that is lengthened and bent by 180° or 360°. The input part of the spectrometer cuts electrons with energies below the potential of the central electrode with a relative spread less than $E_0H_{\min}/H_0$.

In the central region of the spectrometer, the electrons fly in a weak magnetic field with their momenta being aligned with the magnetic lines and the energy being $E_{\text{in}} - eV_0$, where E_{in} is the initial electron energy and V_0 is the potential of the analyzing electrode. The magnetic field in the central part, as well as the central electrode, has a toroidal shape. Electrons moving adiabatically inside the toroidal electrode are in the zero electrostatic field and drift perpendicularly to the toroidal plane owing to the well-known transverse drift. The magnitude of the drift with respect to the magnetic force lines depends on the velocity of the electron and rapidly increases with the electron energy. Although the drift is not large, a multislot collimator with slots parallel to the toroid plane, mounted inside the toroidal electrode, allows electrons with the drift more than the width of the slot to be cut off.

One can expect some increase in the background due to bombardment of the collimator ends by ions that are accelerated in the detector part of the spectrometer. To avoid this, a slot mask will be mounted on the detector, so that the adiabatic images of the end plates of the collimator are projected onto the covered regions of the detector.

Thus, only electrons with the energy not higher than a few eV inside the toroidal electrode can reach the detector. Electrons with higher or with very low energy will die on the collimator plates.

The luminosity of such a spectrometer will depend on the cross section of the central electrode and on the dimension of the tubes in the tritium source. The optimal parameters of the spectrometer should be studied in detail, but it seems quite possible to construct a device with a resolution of about 2 eV and a luminosity of 1 cm^2. This could substantially improve all the tritium spectrometry. The competition between two approaches would be very desirable in view of the complexity of the task.

REFERENCES

1. A. I. Belesev *et al.*, Phys. Lett. B **350**, 263 (1995).
2. Ch. Weinheimer *et al.*, Phys. Lett. B **300**, 210 (1993).
3. V. A. Lubimov *et al.*, Phys. Lett. B **94**, 266 (1980).
4. E. Holzschuh *et al.*, Phys. Lett. B **287**, 381 (1992).
5. H. Kawakami *et al.*, Phys. Lett. B **256**, 105 (1991).
6. G. H. Robertson *et al.*, Phys. Rev. Lett. **67**, 957 (1991).
7. E. Tret'yakov, Izv. Akad. Nauk SSSR, Ser. Fiz. **39**, 583 (1975).
8. V. M. Lobashev and P. E. Spivak, Preprint No. P-0291 IYaI RAN (Institute of Nuclear Research, Russian Academy of Sciences, Moscow, 1983).
9. V. M. Lobashev and P. E. Spivak, Nucl. Instrum. Methods Phys. Res. A **240**, 305 (1985).
10. V. M. Lobashev *et al.*, Nucl. Instrum. Methods Phys. Res. A **238**, 496 (1985).
11. A. Picard *et al.*, Nucl. Instrum. Methods Phys. Res. B **63**, 345 (1992).
12. T. Hsu and J. L. Hirshfield, Rev. Sci. Instrum. **47**, 236 (1976).
13. G. Beamson, H. G. Porter, and D. N. Turner, J. Phys. E **13**, 64 (1980).
14. V. M. Lobashev *et al.*, in *Proceedings of International Conference NEUTRINO'96, Helsinki, 1996* (World Sci., Singapore, 1996), p. 264; in *Proceedings of Weak Interaction 97, Capri, 1997.*
15. V. M. Lobashev, Prog. Part. Nucl. Phys. **40**, 337 (1998).
16. S. Jonsell and H. Monkhorst, Phys. Rev. Lett. **76**, 4476 (1996).
17. J. Bonn, in *Proceedings of Weak Interaction 99, Cape Town, 1999.*
18. G. J. Stephenson, Jr., T. Goldman, and B. H. J. McKellar, Int. J. Mod. Phys. A **13**, 2765 (1998); T. Goldman and G. J. Stephenson, Jr., hep-ph/9309308.
19. Ch. Weinheimer *et al.*, Phys. Lett. B **300**, 210 (1993).

Physics of Atomic Nuclei, Vol. 63, No. 6, 2000, pp. 969–974. From Yadernaya Fizika, Vol. 63, No. 6, 2000, pp. 1044–1049.
Original English Text Copyright © 2000 by Bonn, B. Bornschein, L. Bornschein, Fickinger, Kazachenko, Kovalik, Kraus, Otten, Ulrich, Weinheimer.

NEUTRINO PHYSICS

Newest Results from the Mainz Neutrino-Mass Experiment*

J. Bonn, B. Bornschein, L. Bornschein, L. Fickinger, O. Kazachenko[1], A. Kovalik[2], Ch. Kraus, E. W. Otten, H. Ulrich, and Ch. Weinheimer**

Institute of Physics, Joh. Gutenberg University, Mainz, Germany

Abstract—The Mainz neutrino-mass experiment investigates the endpoint region of the tritium β-decay spectrum with a MAC-E spectrometer to determine the mass of the electron antineutrino. By the recent upgrade, the former problem of dewetting T_2 films has been solved, and the signal-to-background ratio was improved by a factor of 10. The latest measurement leads to $m_\nu^2 = -3.7 \pm 5.3(\text{stat.}) \pm 2.1(\text{syst.})\ \text{eV}^2/c^4$, from which an upper limit of $m_\nu < 2.8$ eV/c^2 (95% C.L.) is derived. Some indication for the anomaly, reported by the Troitsk group, was found, but its postulated half-year period is contradicted by our data. To push the sensitivity on the neutrino mass below 1 eV/c^2, a new larger MAC-E spectrometer is proposed. Besides its integrating mode, it could run in a new nonintegration operation MAC-E-TOF mode. *© 2000 MAIK “Nauka/Interperiodica”.*

1. INTRODUCTION

The recent results from the atmospheric and solar neutrino experiments [1, 2] seem to require nonzero neutrino masses, which have strong consequences for particle physics as well as for astrophysics and cosmology. These neutrino oscillation experiments determine differences of neutrino mass squares, not absolute mass values. The latter are accessible via the kinematics of weak decays. The investigation of the tritium β spectrum near its endpoint is the most sensitive of these so-called direct methods.[3] If the differences between the different neutrino mass eigenvalues are as small as indicated by the solar and atmospheric neutrino experiments, not only hierarchical neutrino mass scales but also degenerate masses in the eV/c^2 range become interesting because of their contribution to the missing dark matter in the Universe [3].

Tritium β-decay experiments are currently running at Mainz and Troitsk [4, 5]. The Mainz experiment has been recently upgraded. The motivation was not only to improve the sensitivity to m_ν down to an ultimate limit of 2 eV/c^2 but also to check the anomalous excess in the spectrum close to the endpoint which was communicated by the Troitsk group [6]. The Troitsk group has described its anomaly as a sharp step of the count rate at a few eV below E_0 [6]. Since their spectrometer is integrating like the Mainz one, this step corresponds to a line in the primary spectrum with a relative intensity of about 10^{-10} of the total decay rate. In 1998, the Troitsk group reported that the position of this line oscillates with a frequency of 0.5 yr between 5 and 15 eV below E_0 [7]. If not considered in their analysis, the fits give significantly negative values for m_ν^2 in the range of –10 to –20 eV^2/c^4. The origin of such a monoenergetic line is not clear within standard physics. An independent experimental check is mandatory.

In this paper, the upgrade of the Mainz experiment and the results of the first four runs with the upgraded set-up in 1997 and 1998 are presented.

2. THE IMPROVED MAINZ SETUP

The principle of the Mainz spectrometer [8], Magnetic Adiabatic Collimation followed by a retarding Electrostatic Filter (MAC-E-Filter, also called Solenoid Retarding Spectrometer), combines both a very high energy resolution[4] (ΔE = 2–6 eV at 20 keV) and a large acceptance ($\Delta\Omega/2\pi$ = 0.2–0.8).

These very nice features could not been fully explored in the previous measurements [9, 10]. The main limitations of the data taking in 1991 and 1994 came from the T_2 source. The source cryostat did not allow temperatures low enough to avoid safely the dewetting of the T_2 film. Moreover, the signal-to-background ratio was limited by T_2 gas evaporating from the source into the spectrometer causing background there. These and other shortcomings were overcome by the following measures (see Fig. 1 and compare [11]):

---

* This article was submitted by the authors in English.

** e-mail: christian.weinheimer@uni-mainz.de

[1] On leave from INR, Troitsk, Russia.

[2] On leave from JINR, Dubna, Russia.

[3] The search for neutrinoless double-β decay is not fully direct, since it is only sensitive to Majorana-type neutrinos and it depends on the neutrino mixing matrix.

[4] ΔE gives the full rise of the transmission function f_{trans} from 0 to 100%. It is defined [8] for a given energy E only by the ratio of the minimum magnetic field in the analyzing plane $B_{\min}$ and the maximum magnetic field between source and analyzing plane of the spectrometer $B_{\max}$ through $\Delta E = EB_{\min}/B_{\max}$ by which it can be adjusted.

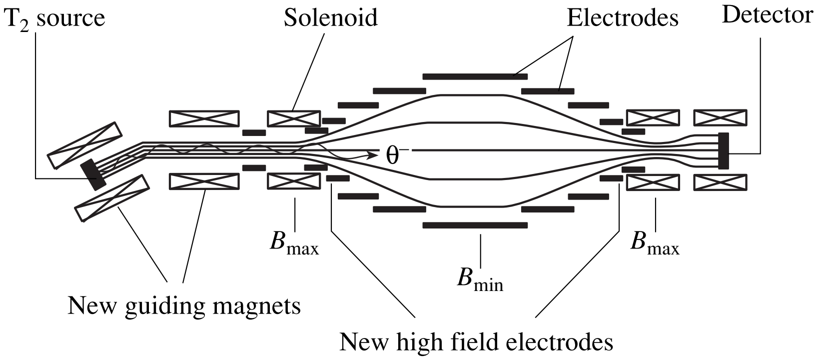

Fig. 1. The improved and enhanced Mainz setup schematically, not on a realistic scale. The outer diameter amounts to 1 m, and the distance from source to detector is 6 m.

A new source cryostat, running stably at 1.86 ± 0.03 K, suppresses effectively the dewetting of the T_2 film [11].

A pair of superconducting solenoids, tilted by 20° to each other, was installed between source and spectrometer. Consequently β particles from the source are still guided magnetically around the corner into the spectrometer without losses, whereas tritium molecules evaporating from the source are trapped on the bend of the LHe cold tube covered with graphite.

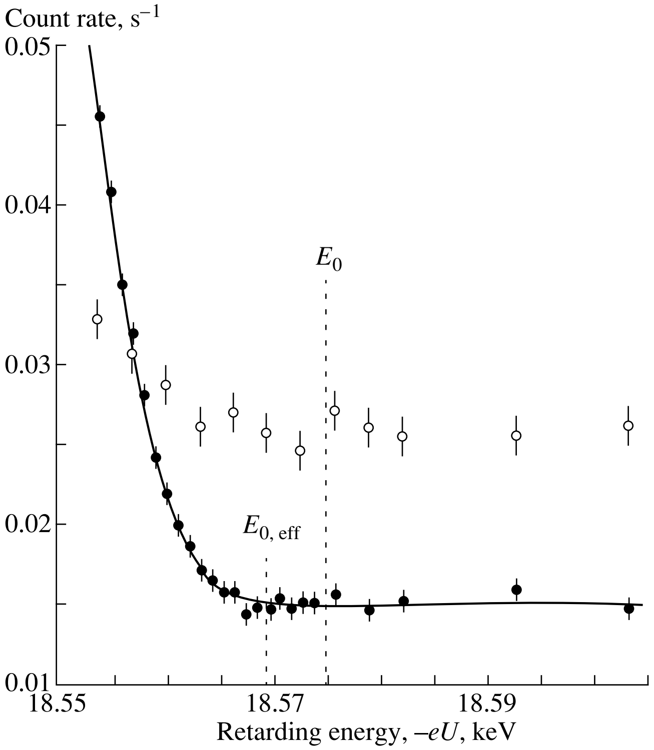

Fig. 2. Averaged count rate of runs Q3, Q4, and Q5 of 1998 (filled circles) compared with the 1994 data (open circles) near the endpoint E_0, and effective endpoint $E_{0,\,eff}$, which considers the convolution with the functions f_{trans} and f_{charge} and the mean rotational–vibrational excitation energy of the electronic ground state of the THe^+ daughter molecule. The line shows a fit to the data for $m_\nu^2 = 0$ over the interval shown.

The electrode system was slightly modified to lower the background contribution from the spectrometer itself. Due to a better alignment of the whole system, the spectrometer can operate now at a higher energy resolution of 4.4 eV compared to 6.3 eV in 1994 at same count rate.

An experiment control system combined with an alert system based on cellular phones was installed in order to run the experiment automatically. Human intervention is needed only for filling of LHe and LN_2.

3. THE FOUR RUNS OF 1997 AND 1998

With the improved setup, four runs (labeled Q2-Q5) were taken in 1997 and 1998 of 4-month measurement time in total. To increase the signal rate, we used much thicker T_2 films of 973 Å (Q2) and 490 Å (Q3-Q5), respectively, compared to 126 Å in 1994. The increase of electron scattering within the T_2 film was partly compensated by reducing the maximum path length within the film by decreasing the emission cone of accepted β particles from 78.5° (1994) to 45°. The film thickness was measured by laser ellipsometry and found to remain constant over each run. The β spectrum was scanned from 18.370 to 18.660 keV by changing the electric potential at the source in time intervals of 10 to 20 s per point and with reduced step of 1 eV around the endpoint. For each event, pulse height and time were digitized and recorded. The data were filtered for obvious hardware failures or large sparks in the high voltage system; no other filtering was applied to the data.

Figure 2 shows the event rate, averaged over the runs Q3, Q4, and Q5, which were performed under very similar conditions, as a function of the retarding energy, $-eU$. One recognizes a gain in signal-to-background-ratio by a factor of 10 and much better statistics with respect to the 1994 data.

The data were fitted by a function derived from the standard formula for an allowed β spectrum, which is summed up for all electronic final states of the daughter molecule of amplitude W_i and excitation energy V_i [12, 13]. This spectrum is then convoluted with the potential distribution within the tritium film f_{charge} [11], the functions describing the backscattering from the substrate, the inelastic processes within the T_2 film, the spectrometer transmission f_{trans}, and the energy dependence of the detection efficiency. Fitting parameters were a free amplitude A, the endpoint E_0, m_ν^2, and an energy independent background B.

Systematic uncertainties were taken into account as follows (the percentages in brackets illustrate their contribution to the total systematic uncertainty on m_ν^2 for fitting the last 70 eV of the spectrum of data set Q5):

Inelastic scattering within the tritium film (49%): In a recent investigation [14] we have measured the energy loss function $f_{\text{e. loss}}$ of 17.8 keV K-32 conversion electrons of ^{83m}Kr in D_2 films. The mean free path was found to be $\lambda_{\text{free}} = 1204 \pm 63$ Å, rescaled for an energy of 18.5 keV. This value is about 26% larger than that calculated from the total inelastic cross section in gaseous hydrogen for the density of a closely packed crystal. Also, the peak position of the excitation spectrum is shifted from 12.6 to 14.3 eV. Both effects are expected to occur as result of repulsive electrostatic interaction of the excited electrons with the neighboring ones and Pauli blocking. However, an increase of 17% in λ_{free} is due to pores within the tritium film, determined by the ellipsometry measurement of its index of refraction giving $n = 1.14$, which is about the same as for our D_2 films. For the systematics, the uncertainties of λ_{free} and of the film thickness measurement, which varies between 1 and 7%, depending on the substrate quality, were considered.

Neighbor excitation (26%): We have considered the observed peak position shift also in the energy loss caused by the sudden excitation of neighbors of the β-decaying molecule. The probability of such an event has been calculated to be 5.9% [13]. The observed increase of λ_{free} leads to an estimated reduction down to 4.6%. The two corrections were added in full amount to the systematic uncertainty for safety.

Final states (11%): Electronic repulsion and Pauli blocking effects are also expected for the excited levels of the THe^+ daughter molecule, but here the effects should be small due to the higher nuclear charge Z of the He nucleus. A rough calculation results in level shifts of the order of 1 eV for the second and higher excited levels [15]. For safety, these shifts are fully taken into account as systematic uncertainty.

Charging up of the T_2 film (14%): For the thick T_2 films used in 1997 and 1998, a charging up of the films by several volts due to the β emission was observed. By measuring the energy shift of the K-32 conversion line of ^{83m}Kr positioned in different depths of the T_2 film, we proved that the potential within the film increases linearly with the distance to the substrate at a slope of 6 mV/Å [11]. The charging effect leads to a slight decrease of the effective energy resolution. For safety, 40% of the total effect is taken into account as systematic uncertainty.

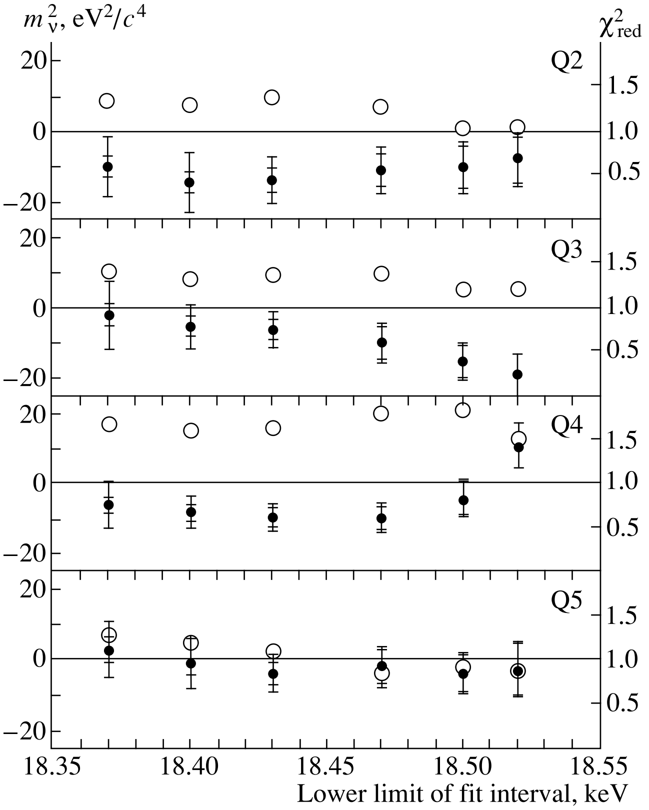

Fig. 3. Fit results on m_ν^2 (left scale, filled circles) for the four different runs with statistical uncertainties (inner bars) and total uncertainties (outer bar) in dependence on the lower limit of the fit interval. The upper limit of the fits is always 18660 keV, well above the endpoint E_0. The corresponding values of $\chi^2_{\text{red}} = \chi^2/\text{NDF}$ of the fits (open circles) can be read from the right scale.

Other contributions (<1%): We also considered uncertainties of the transmission, backscattering, and detector efficiency functions; their influence on m_ν^2 is small compared to the other effects.

Figure 3 shows the fit results on m_ν^2 with statistical and total uncertainties (statistical and systematic uncertainties added in quadrature) for the four different runs Q2 to Q5 as function of the lower energy limit of the data interval used for the analysis. The following comments apply:

(i) Systematic uncertainties shrink to a negligible level for small fit intervals, since so close to the endpoint, say above 18500 keV, only about 15% of events are subjected to any of the electronic excitation processes and their residual uncertainties.

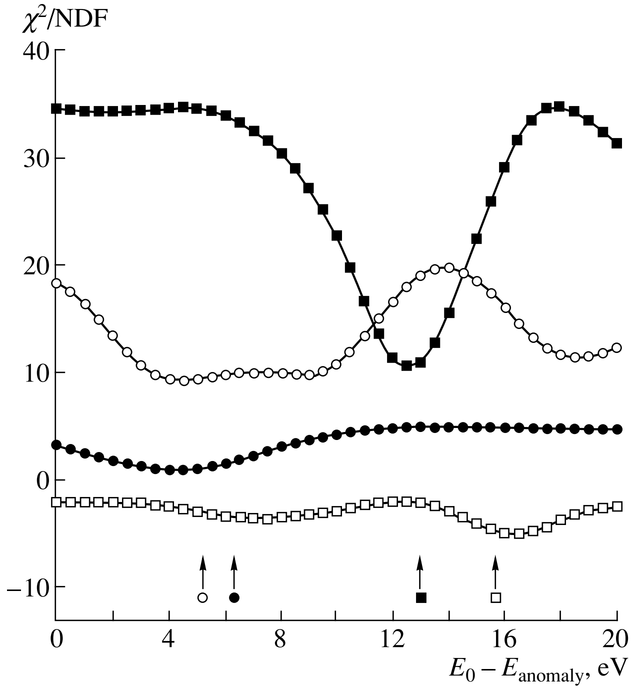

Fig. 4. χ^2 in dependence on the position E_{anomaly} of a Troitsk-like anomaly, which was fitted in addition to the β spectrum for $m_\nu^2 = 0$ fixed to the last 70 eV of the β spectrum of the Mainz data: Q2 (filled circles), Q3 (open circles), Q4 (filled squares), and Q5 (open squares), with NDF = 29 (Q2) and NDF = 39 (Q3, Q4, Q5), respectively. The arrows indicate the Troitsk predictions. Dates of the Mainz data takings: Q2: July 26–Aug. 8, 1997; Q3: Feb. 3–Mar. 16, 1998, Q4: June 7–July 13, 1998; Q5: Nov. 7–Dec. 14, 1998.

(ii) The monotonic trend towards negative values of m_ν^2 for larger fit intervals as was observed for the Mainz 1991 and 1994 data has vanished. This shows that the dewetting of the T_2 film from the graphite substrate indeed was the reason for this behavior. Now, this effect is safely suppressed at the much lower temperature of the T_2 film.

(iii) There is no indication for a nonzero neutrino mass, but, except Q5, the values of m_ν^2 are still significantly negative, and the χ^2 values are partly too large for reasonable fits. The data suffer from a small spectral anomaly which cannot be attributed anymore to a mistaken energy loss correction, as before, since such effects matter only further from the endpoint.

4. CHECK OF THE “TROITSK ANOMALY”

As a first explanation for the still partly negative values of m_ν^2 of the Mainz data, we tested whether our data could be described by a “Troitsk anomaly.” Following reference [6], we checked this possibility by adding for the fit a monoenergetic line with free amplitude and position to the β spectrum (a line results in a step after convolution with the spectrometer transmission function f_{trans}). Figure 4 shows for all four data sets the reduction of χ^2 as function of line position E_{anomaly} relative to E_0 with m_ν^2 fixed to 0. The line positions predicted by the Troitsk 0.5-yr oscillation hypothesis [7] are marked as well. The improvement of χ^2 by the free line is not significant for Q2 and Q5; it is clearly significant for Q4 and less significant for Q3. Whereas the line position in Q4 agrees with the prediction and, moreover, has a reasonable amplitude of 6 mHz, which corresponds to a fraction of 0.9×10^{-10} from all β decays, the data set Q5 clearly excludes a line with sizeable amplitude.[5] Summarizing this analysis: clear support for the “Troitsk anomaly” comes only by our data set Q4, whereas data set Q5 is at variance. Either the time structure of the anomaly is more complicated, or the effects do not arise from a common origin.

5. UPPER LIMIT ON m_ν

The faking of m_ν^2 by the local, fluctuating spectral distortion through fitting can be circumvented by the following alternative procedures (all limits are calculated by using the unified approach):

1. The combined data set of all runs of 1998, Q3, Q4 and Q5, which were taken under nearly the same conditions,[6] is fitted over the last 15 eV of the β spectrum only (see Fig. 2). Due to the thresholds for excitation of the electron shell of T_2 or the daughter THe^+, respectively, uncertainties from energy loss, final states, etc., could not affect these last 15 eV of the β spectrum. Even an anomaly with the shape of a monoenergetic line at the position compatible with our measurement Q4 does not influence the β spectrum in this energy range after having been convoluted with f_{charge} and f_{trans}. To decorrelate m_ν^2 from the endpoint position E_0 and amplitude A, the two data points at 18.470 keV and at 18.500 keV have been added for this fit to the data above 18.559 keV (last 15 eV of the β spectrum). Adding only two points to the last 15 eV of the β spectrum introduces only a small influence on m_ν^2 by systematic

---

[5] Fitting with free m_ν^2 a line at the predicted position 15.5 eV below E_0 the line amplitude becomes –2.2 ± 1.4 mHz, from which an amplitude larger than 1.1 mHz can be excluded at the 95% C.L., whereas the Troitsk prediction would indicate an amplitude about as large as the 6 mHz observed for Q4.

[6] We mention that, although we have taken data set Q5 under nearly the same conditions as Q3 and Q4 concerning T_2 film thickness, retarding voltage and magnetic field settings, we have put a voltage of ±20 V with 1 MHz frequency at one of the electrodes at the detector side of our spectrometer during the 2-s measurement pauses every 20 s to destroy the storage conditions for charged particles to reduce the rate and fluctuations of the background.

effects and Troitsk-like anomalies. This fit results in

$$m_\nu^2 = -0.1 \pm 3.8(\text{stat.}) \pm 1.8(\text{syst.})\ \text{eV}^2/c^4,$$

which corresponds to an upper limit of

$$m_\nu \le 2.9\ \text{eV}/c^2\ (95\%\ \text{C.L.}).$$

2. If we accept the "Troitsk anomaly" as phenomenon we can fit the β spectrum together with a monoenergetic line of free position and amplitude, usually done by the Troitsk group for their data. From fitting the last 70 eV of the β spectrum of data set Q4 we obtain[7)]

$$m_\nu^2 = -1.8 \pm 5.1(\text{stat.}) \pm 2.0(\text{syst.})\ \text{eV}^2/c^4,$$

which corresponds to an upper limit of

$$m_\nu \le 3.0\ \text{eV}/c^2\ (95\%\ \text{C.L.}).$$

3. If we accept as results of Section 5 that there are variations in our data, either due to unknown experimental effects or due to an anomaly varying with time like the "Troitsk anomaly," we can restrict the analysis to the data set Q5 alone, the only one which is fitted well over the entire range with a satisfying χ^2/d.o.f. ≈ 1.0 and does not show any anomaly. The fit over the last 70 eV of the β spectrum gives (see Fig. 3)

$$m_\nu^2 = -3.7 \pm 5.3(\text{stat.}) \pm 2.1(\text{syst.})\ \text{eV}^2/c^4,$$

which corresponds to an upper limit of

$$m_\nu \le 2.8\ \text{eV}/c^2\ (95\%\ \text{C.L.}).$$

6. CONCLUSION AND OUTLOOK

The improved Mainz setup enables us to carry out long term measurements with a signal-to-background-ratio enhanced by a factor of 10 compared to our measurements in 1991 and 1994. The four runs of 1997 and 1998 are competitive in sensitivity to the Troitsk measurements and capable of cross-checking them [5]. Studies on quench condensed T_2 films clarified their energy loss function, their charging up, and their dewetting as function of temperature. In particular, the suppression of the latter effect has removed the trend towards large negative values of m_ν^2 for wide data intervals from which our 1991 and 1994 suffered. But still the new Mainz data partly disagree with a pure β spectrum. Small negative values of m_ν^2 and poor values of χ^2 indicate that a small residual effect is not described by our fit function.

We tested whether this effect is compatible with the "Troitsk anomaly," which has been described by a monoenergetic line a few eV below the endpoint, whose position and amplitude seemed to vary with a 0.5-yr period. Our two best runs concerning statistics, Q4 and Q5, showed different results: Q4, taken in June/July 1998, supports the Troitsk hypothesis by a distinct anomaly, but Q5, taken half a year later in November/December 1998, does not show any anomaly at all. This means at least that a simple half-year period of the anomaly is contradicted by our data. To check whether the effects observed in Troitsk and partly in Mainz have a common origin, the groups have already started to take data synchronously in 1999. In addition, we will check by our data some other possible modifications of the β spectrum, as predicted, e.g., for tachyonic neutrinos or the admixture of right-handed weak currents. But such effects would hardly oscillate in time. Of course, one must also consider the effect possibly to be an instrumental artifact. In this case, it should originate from some critical feedback between β particles and background sources in the spectrometer. It is difficult to imagine such a coupling and how it could produce something like a step.

In spite of these problems, we can obtain upper limits on the neutrino mass by various types of analysis which gave similar results. By applying a standard analysis to our data set Q5, which is free of any anomaly, we obtain a limit of $m_\nu \le 2.8$ eV/c^2. In the case of neutrino mixing (Section 1), the limit on m_ν is valid for the following average: If the different neutrino mass eigenstates, which contribute with U_{ei} to the electron neutrino, are not resolved, the β spectrum is determined by an average electron neutrino square mass $\overline{m_\nu^2} = \sum_i |U_{ei}|^2 m_i^2$.

By collecting more data, a sensitivity on m_ν of about 2 eV/c^2 can be reached. This does not clarify the possibility of a cosmologically relevant amount of neutrino dark matter. For this task, further improvement of the sensitivity on m_ν down to less than 1 eV/c^2 is needed.

Moreover, the Troitsk anomaly must be definitely clarified and, if confirmed, precisely and repeatedly measured with short time intervals. This is mandatory in view of the very speculative but so far only explanation under discussion, namely ν_e capture from dense, variable ν_e clouds (compare [5] and references therein). Neither of these two tasks can be achieved by the present experiments. A larger spectrometer providing a higher signal rate and better energy resolution is needed. In a different paper [16], we have investigated the possibility of a spectrometer based on the same MAC-E filter principle but five times larger (in linear dimensions) than the present one. By an additional time-of-flight analysis the spectrometer transforms from an integration high-pass filter into a narrowband filter (MAC-E-Filter mode).

In a first proof of principle experiment for this new method, the K-32 conversion line of ^{83m}Kr was investigated with the present Mainz spectrometer. A periodic

---

[7)] Applying this procedure to the other three data sets Q2, Q3, and Q5 and combining the results decreases the limit further down. However, there remains the question mark that the "Troitsk anomaly" is not established yet.

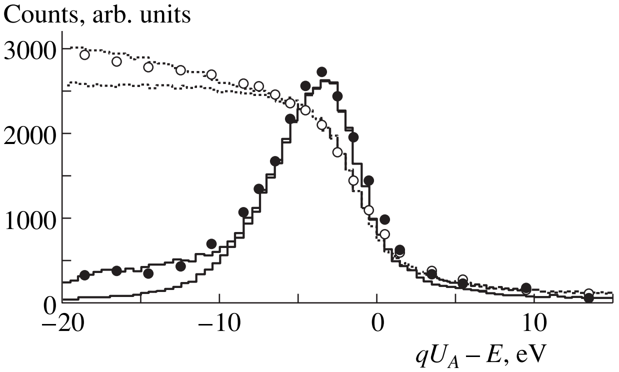

Fig. 5. Measurement of the ^{83m}Kr K-32 conversion line with the Mainz spectrometer and time-of-flight analysis: (circles) integral recording over all times, (dashed lines) corresponding simulation without N shake and including it, (full dots) narrowband recording of the spectral line with time-of-flight selection ($3.5 \leq t_{\text{arriv}} \leq 5.1$ μs), and (solid lines) corresponding simulation for the conversion line and including its N shake. Background has been subtracted. The integral data are scaled down by a factor of 4.

chopping voltage ($t_{\text{on}} = 2.5$ μs, $t_{\text{block}} = 2.5$ μs, $U_{\text{block}} = 80$ V) was applied to the conversion electron source, and the arrival time of the electrons was measured at the detector. Figure 5 shows the counts in the detector for all arrival times, which corresponds to the normal integral mode of the spectrometer. Selecting only electrons, which have a certain arrival time (which corresponds to a certain kinetic energy in the spectrometer), shows the K-32 conversion line in a narrowband mode. By this new method, a local distortion in the β spectrum will stay local and has a localized correlation to m_ν^2; thus, it becomes an ideal instrument to resolve the question of possible anomalies clearly.

ACKNOWLEDGMENTS

We like to thank A. Saenz and E. Yakushev for helpful and stimulating discussions. This work was supported by the Deutsche Forchungsgemeinschaft under contract Ot33/13. A.K. and O.K. are indebted to the Deutsche Forschungsgemeinschaft for funding theirs stays at Mainz.

REFERENCES

1. Y. Fukuda *et al*., Phys. Rev. Lett. **81**, 1562 (1998).
2. V. N. Gavrin, T. Kirsten, and Y. Suzuki, in *Proceedings of XVIII Conference on Neutrino Physics and Astrophysics, Neutrino 98, Takayama, Japan, 1998.*
3. E. Garwiser and J. Silk, Science **280**, 1405 (1998).
4. Ch. Weinheimer *et al*., Phys. Lett. B **460**, 219 (1999).
5. V. M. Lobashev *et al*., Phys. Lett. B **460**, 227 (1999).
6. A. I. Belesev *et al*., Phys. Lett. B **350**, 263 (1995).
7. V. M. Lobashev, in *Proceedings of XVIII Conference on Neutrino Physics and Astrophysics, Neutrino 98, Takayama, Japan, 1998.*
8. A. Picard *et al*., Nucl. Instrum. Methods Phys. Res. B **63**, 345 (1992).
9. Ch. Weinheimer *et al*., Phys. Lett. B **300**, 210 (1993).
10. H. Backe *et al*., in *Proceedings of XVII Conference on Neutrino Physics and Astrophysics, Neutrino 96* (World Sci., Singapore, 1996).
11. H. Barth *et al*., Prog. Part. Nucl. Phys. **40**, 353 (1998).
12. S. Jonsell and H. J. Monkhorst, Phys. Rev. Lett. **76**, 4476 (1996).
13. W. Kolos *et al*., Phys. Rev. A **37**, 2297 (1988).
14. V. N. Aseev *et al*., submitted to Eur. Phys. J. D.
15. A. Saenz, private communication.
16. J. Bonn *et al*., Nucl. Instrum. Methods Phys. Res. A **421**, 256 (1999).

Physics of Atomic Nuclei, Vol. 63, No. 6, 2000, pp. 975–978. From Yadernaya Fizika, Vol. 63, No. 6, 2000, pp. 1050–1053.
Original English Text Copyright © 2000 by Ma.

NEUTRINO PHYSICS

Nearly Mass-Degenerate Majorana Neutrinos: Double-Beta Decay and Neutrino Oscillations*

E. Ma
University of California, Riverside, USA

Abstract—Assuming equal tree-level Majorana masses for the standard-model neutrinos, either from the canonical seesaw mechanism or from a heavy scalar triplet, I discuss how their radiative splitting may be relevant to neutrinoless double-beta decay and neutrino oscillations. *© 2000 MAIK "Nauka/Interperiodica".*

1. INTRODUCTION

In this talk I will first discuss [1] two equally simple mechanisms for small Majorana neutrino masses, one famous [2] and one not so famous [3]. I will then mention briefly how they are related to neutrinoless double-beta decay and neutrino oscillations. My main focus will be on the possibility of nearly mass-degenerate neutrinos and their radiative splitting due to the different charged-lepton masses. In particular, I show [4] how a two-fold neutrino-mass degeneracy can be stable against radiative corrections. I finish with three examples: (1) a two-loop explanation [5] of vacuum $(\Delta m^2)_{\rm sol}$, (2) a one-loop connection [6] between $(\Delta m^2)_{\rm atm}$ and vacuum $(\Delta m^2)_{\rm sol}$, and (3) a one-loop explanation [7] of small-angle matter-enhanced $(\Delta m^2)_{\rm sol}$ with the prediction $0.20 < m_\nu < 0.36$ eV.

2. ORIGIN OF NEUTRINO MASSES

In the standard model, leptons are left-handed doublets $(\nu_i, l_i)_L \sim (1, 2, -1/2)$ and right-handed singlets $l_{iR} \sim (1, 1, -1)$ under the gauge group $SU(3)_c \times SU(2)_L \times U(1)_Y$. The absence of the gauge singlet $\nu_{iR} \sim (1, 1, 0)$ implies that $m_{\nu_i} = 0$. However, since the Higgs scalar doublet $\Phi = (\phi^+, \phi^0) \sim (1, 2, 1/2)$ exists, there is a unique 5-dimensional operator [8]

$$\Lambda^{-1}\phi^0\phi^0\nu_i\nu_j \tag{1}$$

for nonzero Majorana neutrino masses. The underlying theory which realizes this operator is usually assumed to be that of the seesaw mechanism [2]. In other words, the gauge-invariant operator

$$(\phi^0\nu_i - \phi^+ l_i)(\phi^0\nu_j - \phi^+ l_j) \tag{2}$$

is obtained by inserting a heavy Majorana fermion singlet N as the intermediate state, as illustrated in Fig. 1.

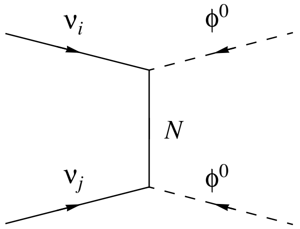

Fig. 1. Tree-level realization of the effective operator (2) with heavy fermion singlet.

The resulting neutrino-mass matrix is then given by

$$(\mathcal{M}_\nu)_{ij} = -\frac{f_i f_j v^2}{M}, \tag{3}$$

where f_i are Yukawa couplings of ν_i to N, $v = \langle\phi^0\rangle$, and M is the mass of N. On the other hand, the expression in (2) can be rewritten as [1, 3]

$$\phi^0\phi^0\nu_i\nu_j - \phi^+\phi^0(\nu_i l_j + l_i\nu_j) + \phi^+\phi^+ l_i l_j, \tag{4}$$

which allows the insertion of a scalar triplet (ξ^{++}, ξ^+, ξ^0) as the intermediate state, as illustrated in Fig. 2.

The neutrino-mass matrix is now given by

$$(\mathcal{M}_\nu)_{ij} = -\frac{2 f_{ij}\mu v^2}{M^2}, \tag{5}$$

where f_{ij} are the Yukawa couplings of ν_i to ν_j, μ is the trilinear coupling of ξ to $\Phi\Phi$, and M in the mass of ξ.

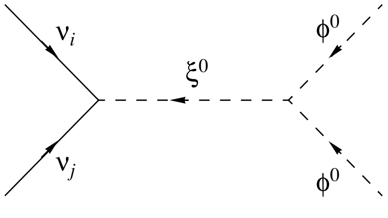

Fig. 2. Tree-level realization of the effective operator (4) with heavy scalar triplet.

---

* This article was submitted by the author in English.

1063-7788/00/6306-0975$20.00 © 2000 MAIK "Nauka/Interperiodica"

The alternative way to understand this mass is to note that ξ^0 acquires a nonzero vacuum expectation value in this model given by $u = -\mu v^2/M^2$. In other words, in the limit where M^2 is positive and large, it is natural for u to be very small. This method for generating small Majorana neutrino masses is as simple and economical as the canonical seesaw mechanism. To obtain the most general 3 × 3 neutrino-mass matrix, we need 3 N's in the latter, but only one ξ in former.

3. NEUTRINOLESS DOUBLE-BETA DECAY AND NEUTRINO OSCILLATIONS

Let the $(\nu_e, \nu_\mu, \nu_\tau)$ mass matrix $\mathcal{M}$ have eigenvalues $m_{1,2,3}$ with $\nu_e = \sum_i U_{ei}\nu_i$; then,

$$\mathcal{M}_{ee} = \sum_i U_{ei} m_i U^T_{ie} = \sum_i U^2_{ei} m_i \tag{6}$$

is what is being measured in neutrinoless double beta decay. The most recent result from the Heidelberg–Moscow experiment is [9] $\mathcal{M}_{ee} < 0.2$ eV. Note, however, that, since $U^2_{ei} m_i$ can be of either sign for each i, $\mathcal{M}_{ee}$ does not constrain $|m_i|$ without further information. For example, consider

$$\mathcal{M} = \begin{bmatrix} \cos^2\theta m_1 + \sin^2\theta m_2 & \sin\theta\cos\theta(m_2 - m_1) \\ \sin\theta\cos\theta(m_2 - m_1) & \sin^2\theta m_1 + \cos^2\theta m_2 \end{bmatrix}, \tag{7}$$

which tells us that $\nu_e = \cos\theta\nu_1 + \sin\theta\nu_2$. Now if $m_1 > 0$, $m_2 > 0$, then $m_1 < \mathcal{M}_{ee}$; but if $m_1 < 0$, $m_2 > |m_1|$, then there are no individual upper bounds on $|m_1|$ or m_2.

In neutrino oscillations, the parameters accessible to experimental determination are $\Delta m^2_{ij} = m^2_i - m^2_j$ and $U_{\alpha i}$; hence, the sign of m_i is irrelevant there. The sign of Δm^2_{ij} is important in matter-enhanced oscillations [10] because neutrino and antineutrino forward scattering amplitudes in matter have opposite sings.

4. NEARLY MASS-DEGENERATE MAJORANA NEUTRINOS AND THEIR STABILITY AGAINST RADIATIVE CORRECTIONS

Suppose neutrinos are Majorana and are equal in mass:

$$\nu_i = U^T_{ie}\nu_e + U^T_{i\mu}\nu_\mu + U^T_{i\tau}\nu_\tau, \quad i = 1, 2, 3, \tag{8}$$

and $m_1 = m_2 = m_3$. Since m_e, m_μ, and m_τ are all different, this degeneracy cannot be exact. In other words, splitting must occur, but how? This question has two answers: (i) depending on the specific mechanism by which the neutrinos become massive, there are finite radiative corrections to the mass matrix itself [4–6]; (ii) there are model-independent wave-function renormalizations which shift the values of the mass matrix from one mass scale to another [11].

The stability of neutrino mass degeneracy against radiative corrections depends [4, 12] on the symmetry of the mass matrix. Consider

$$\mathcal{M} = \begin{bmatrix} m_{ee} & m_{e\mu} \\ m_{e\mu} & m_{\mu\mu} \end{bmatrix}; \tag{9}$$

then,

$$\Delta m^2 = (m_{ee} + m_{\mu\mu})\sqrt{(m_{ee} - m_{\mu\mu})^2 + 4m^2_{e\mu}}. \tag{10}$$

Thus $\Delta m^2 = 0$ has two solutions. One is

$$\mathcal{M} = \begin{bmatrix} m & 0 \\ 0 & m \end{bmatrix}; \tag{11}$$

then, the effect of radiative corrections is to shift it by $4m^2(\delta_\mu - \delta_e)$. This is inherently unstable. The other is

$$\mathcal{M} = \begin{bmatrix} m & m' \\ m' & -m \end{bmatrix}; \tag{12}$$

then, the shift is $4m\sqrt{m^2 + m'^2}\,(\delta_\mu - \delta_e)$. This is stable as long as $m \ll m'$ and is easily understood because the $m = 0$ limit corresponds to the existence of an extra global $L_e - L_\mu$ symmetry for the entire theory.

5. TWO-LOOP EXAMPLE

Choose the canonical seesaw mechanism for obtaining neutrino masses. Impose a global $SO(3)$ symmetry so that $(\nu_i, l_i)_L$ and N_{iR} with $i = +, 0, -$ are triples. Invariants are then

$$\begin{aligned} & f[(\bar\nu_+ N_+ + \bar\nu_0 N_0 + \bar\nu_- N_-)\bar\phi^0 \\ & - (\bar l_+ N_+ + \bar l_0 N_0 + \bar l_- N_-)\phi^-] + \text{h.c.} \end{aligned} \tag{13}$$

and

$$M(2N_+N_- - N_0N_0). \tag{14}$$

Assume $SO(3)$ invariance for f to be valid at the electroweak symmetry breaking scale, i.e., no renormalization correction from different ν_i's. Let $m_D = f\langle\bar\phi^0\rangle \ll M$ and $m_0 = m^2_D/M$; then,

$$\mathcal{M}_\nu = \begin{bmatrix} 0 & -m_0 & 0 \\ -m_0 & 0 & 0 \\ 0 & 0 & m_0 \end{bmatrix} \tag{15}$$

in the basis (ν_+, ν_-, ν_0). Now choose $l_+ = e$ so that $\mathcal{M}_{ee} = 0$, and let

$$l_- = c\mu + s\tau, \quad l_0 = c\tau - s\mu, \tag{16}$$

where $c = \cos\theta$, $s = \sin\theta$.

This model [5] differs from the standard model only in the addition of three heavy N's. The effective low-energy theory differs at tree level only in the appearance of three nonzero, but equal, neutrino masses. This degeneracy is then lifted in two loops [13], as illustrated in Fig. 3.

The leading contribution to the above two-loop diagram is universal, but the effects of the charged-lepton masses show up in the propagators, and since m_τ is the largest such mass, the radiative splitting is proportional to m_τ^2. The neutrino-mass matrix of (15) is now corrected to read

$$\mathcal{M}_\mu = \begin{bmatrix} 0 & -m_0 - s^2 I & -scI \\ -m_0 - s^2 I & 0 & scI \\ -scI & scI & m_0 + 2c^2 I \end{bmatrix}, \qquad (17)$$

where

$$I = \frac{g^4}{256\pi^4}\frac{m_\tau^2}{M_W^2}\left(\frac{\pi^2}{6} - \frac{1}{2}\right)m_0 = 3.6\times 10^{-9} m_0, \qquad (18)$$

and the eigenvalues are $-m_0 - s^2 I$, m_0, and $m_0 + (1 + c^2)I$. Let $s^2 \ll 1$; then, ν_e oscillates mostly into ν_μ with

$$P(\nu_e \longrightarrow \nu_e) = \frac{1}{2} + \frac{1}{2}\cos\frac{\Delta m^2 L}{2E}, \qquad (19)$$

where $\Delta m^2 = 2s^2 m_0 I = 7.2 \times 10^{-9} s^2 m_0^2 \sim 10^{-10}$ eV^2 if $s \sim 0.1$ and $m_0 \sim 1$ eV.

This example shows that a minimum splitting of the Majorana neutrino-mass degeneracy in the canonical seesaw model is suitable for the vacuum oscillation solution of the solar neutrino deficit [14]. However, other effects may be larger, such as the renormalization of the $\bar{\nu}_L N_R \bar{\phi}^0$ vertex.

6. ONE-LOOP EXAMPLE I

Choose the heavy scalar triplet ξ for generating small Majorana neutrino masses. Impose a discrete S_3 symmetry, having the irreducible representations $\underline{2}$, $\underline{1}$, and $\underline{1}'$. Let $(\nu_1, \nu_2) \sim \underline{2}$ and $\nu_3 \sim \underline{1}$; then,

$$\begin{aligned}\mathcal{L}_{\text{int}} = \xi^0[f_0(\nu_1\nu_2 + \nu_2\nu_1) + f_3\nu_3\nu_3] \\ + \mu\bar{\xi}^0\phi^0\phi^0 + \dots .\end{aligned} \qquad (20)$$

Let $\langle\xi^0\rangle = u = -\mu\langle\phi^0\rangle^2/m_\xi^2$; then,

$$\mathcal{M}_\nu = \begin{bmatrix} 0 & m_0 & 0 \\ m_0 & 0 & 0 \\ 0 & 0 & m_3 \end{bmatrix}, \qquad (21)$$

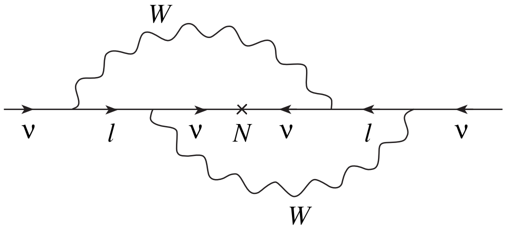

Fig. 3. Two-loop radiative breaking of neutrino mass degeneracy.

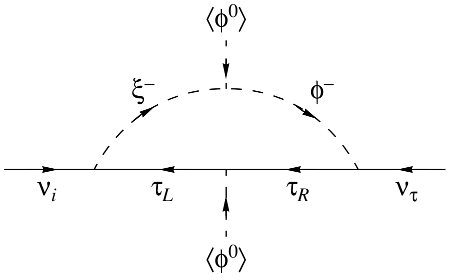

Fig. 4. One-loop radiative breaking of neutrino mass degeneracy.

where $m_0 = 2f_0u$ and $m_3 = 2f_3u$. Now choose $\nu_1 = \nu_e$, so that again $\mathcal{M}_{ee} = 0$, and let $\nu_2 = c\nu_\mu - s\nu_\tau$, $\nu_3 = c\nu_\tau + s\nu_\mu$.

This model [6] allows the radiative splitting of the twofold neutrino mass degeneracy to occur in one loop, as illustrated in Fig. 4.

Hence $\mathcal{M}_\nu$ of (21) becomes

$$\mathcal{M}_\nu = \begin{bmatrix} 0 & m_0(1 + s^2 I) & -scm_0 I \\ m_0(1 + s^2 I) & 0 & -scm_3 I \\ -scm_0 I & -scm_3 I & m_3(1 + 2c^2 I) \end{bmatrix}, \qquad (22)$$

whose eigenvalues are $m_3(1 + 2c^2 I)$, and

$$\mp m_0(1 + s^2 I) \mp \frac{s^2c^2(m_0 \mp m_3)^2 I^2}{2(m_0 \pm m_3)}, \qquad (23)$$

with

$$I = \left(\frac{1}{4\pi^2} - \frac{1}{16\pi^2}\right)\frac{G_F m_\tau^2}{\sqrt{2}}\ln\frac{m_\xi^2}{M_W^2}, \qquad (24)$$

where the second term inside the parentheses comes from the shift of the neutrino wave-function renormalization from m_ξ to M_W. Numerically, $I^2 \ll (m_0 - m_3)^2/(m_0 + m_3)^2$; hence,

$$\Delta m_{12}^2 \simeq \frac{8s^2c^2 I^2 m_\nu^4}{m_0^2 - m_3^2}, \qquad (25)$$

where $m_\nu \simeq m_0 \simeq m_3$ has been used. Thus, a simple connection between atmospheric [15] and solar-neutrino vacuum oscillations is obtained:

$$\frac{(\Delta m^2)_{\mathrm{sol}}(\Delta m^2)_{\mathrm{atm}}}{m_\nu^4(\sin^2 2\theta)_{\mathrm{atm}}} = 2I^2 = 4.9\times 10^{-13}\left(\ln\frac{m_\xi^2}{M_W^2}\right)^2. \quad (26)$$

This equality holds for the sample values of m_ν = 0.6 eV, $(\sin^2 2\theta)_{\mathrm{atm}} = 1$, $m_\xi = 1$ TeV, $(\Delta m^2)_{\mathrm{sol}} = 4\times 10^{-10}$ eV^2, and $(\Delta m^2)_{\mathrm{atm}} = 4\times 10^{-3}$ eV^2. If $m_\xi = 10^{13}$ GeV, then $m_\nu \sim$ 0.2 eV.

This example shows that it is possible to have a one-loop effect, but which appears only in second order because of nondegenerate ($m_0 \neq m_3$) perturbation theory. In the previous example, the effect is two-loop, but it occurs in first order because of degenerate perturbation theory.

7. ONE-LOOP EXAMPLE II

This model [7] is a variation of Example I, with $\nu_1\nu_1 + \nu_2\nu_2$ as an invariant, say, under $SO(2)$. Hence,

$$\mathcal{M}_\nu = \begin{bmatrix} m_0 & 0 & 0 \\ 0 & m_0(1+2c^2I) & -sc(m_0+m_3)I \\ 0 & -sc(m_0+m_3)I & m_3(1+2s^2I) \end{bmatrix}, \quad (27)$$

where $\nu_1 = \nu_e$, $\nu_2 = c\nu_\tau - s\nu_\mu$, $\nu_3 = c\nu_\mu + s\nu_\tau$. Now rotate ν_1 and ν_2 slightly by θ'; then, the small-angle matter-enhanced solution to the solar neutrino deficit works for $\sin^2 2\theta' \simeq (2\text{–}10)\times 10^{-3}$ and

$$(\Delta m^2)_{12} = 4c^2 I m_0^2 \simeq (3\text{–}10)\times 10^{-6}\ \mathrm{eV}^2. \quad (28)$$

For $c^2 = 0.7$, i.e., $(\sin^2 2\theta)_{\mathrm{atm}} = 0.84$, and $m_\xi = 10^{14}$ GeV, this implies

$$0.20 < \mathcal{M}_{ee} < 0.36\ \mathrm{eV}. \quad (29)$$

Experimentally, the most recent Heidelberg–Moscow result [9] is $\mathcal{M}_{ee} < 0.2$ eV, but the expected sensitivity is only 0.38 eV, both at 90% C.L. More data may see something or rule out the above prediction.

8. CONCLUSION

Neutrino mass is equally natural coming from the seesaw mechanism or a heavy scalar triplet.

If $\nu_{e,\mu,\tau}$ are nearly mass-degenerate, their radiative splitting may be suitable for solar neutrino oscillations. Details depend on the specific model, but the smallness of vacuum $(\Delta m^2)_{\mathrm{sol}}$ is only obtained in certain special cases.

ACKNOWLEDGMENTS

I thank Sergey Kovalenko and everyone associated with the organization of NANP-99 for their great hospitality. This work was supported in part by the U.S. Department of Energy under grant no. DE-FG03-94ER40837.

REFERENCES

1. E. Ma, Phys. Rev. Lett. **81**, 1171 (1998).
2. M. Gell-Mann, P. Ramond, and R. Slansky, in *Supergravity*, Ed. by P. van Nieuwenhuizen and D. Z. Freedman (North-Holland, Amsterdam, 1979), p. 315; T. Yanagida, in *Proceedings of the Workshop on the Unified Theory and the Baryon Number in the Universe, Tsukuba, Japan, 1979*, Ed. by O. Sawada and A. Sugamoto, 1979, Report of KEK No. 79-18, p. 95; R. N. Mohapatra and G. Senjanovic, Phys. Rev. Lett. **44**, 912 (1980).
3. E. Ma and U. Sarkar, Phys. Rev. Lett. **80**, 5716 (1998).
4. E. Ma, hep-ph/9907400.
5. E. Ma, Phys. Lett. B **456**, 48 (1999).
6. E. Ma, hep-ph/9902392.
7. E. Ma, Phys. Lett. B **456**, 201 (1999).
8. S. Weinberg, Phys. Rev. Lett. **43**, 1566 (1979).
9. L. Baudis *et al.*, hep-ex/9902014.
10. L. Wolfenstein, Phys. Rev. D **17**, 2369 (1978); S. P. Mikheev and A. Yu. Smirnov, Yad. Fiz. **42**, 1441 (1985) [Sov. J. Nucl. Phys. **42**, 913 (1985)].
11. J. Ellis and S. Lola, hep-ph/9904279; J. A. Casas, J. R. Espinosa, A. Ibarra, and I. Navarro, hep-ph/9904395; hep-ph/9905381; hep-ph/9906281.
12. R. Barbieri, G. G. Ross, and A. Strumia, hep-ph/9906470; N. Haba and N. Okamura, hep-ph/9906481.
13. K. S. Babu and E. Ma, Phys. Rev. Lett. **61**, 674 (1988).
14. R. Davis, Prog. Part. Nucl. Phys. **32**, 13 (1994); P. Anselmann *et al.*, Phys. Lett. B **357**, 237 (1995); erratum: **361**, 235 (1995); J. N. Abdurashitov *et al.*, Phys. Lett. B **328**, 234 (1994); Y. Fukuda *et al.*, Phys. Rev. Lett. **77**, 1683 (1996); **81**, 1158 (1998); **82**, 1810 (1999); **82**, 2430 (1999).
15. Y. Fukuda *et al.*, Phys. Lett. B **433**, 9 (1998); **436**, 33 (1998); Phys. Rev. Lett. **81**, 1562 (1998); **82**, 2644 (1999).

Physics of Atomic Nuclei, Vol. 63, No. 6, 2000, pp. 979–983. From Yadernaya Fizika, Vol. 63, No. 6, 2000, pp. 1054–1058.
Original English Text Copyright © 2000 by Huzita.

NEUTRINO PHYSICS

The Precious Information from Supernova LMC-87A on the Neutrino Masses and Neutrino Mixing Angles among the Flavor States and the Mass States*

H. Huzita
Istituto Nazionale di Fisica Nucleare, Padova, Italy

Abstract—This note relies on a paper published 12 years ago, in which only the result of an analysis of the experimental data of neutrino from SN-87A without any explicit description of the logical steps towards the conclusion is presented. The process was evident, and it was thought that a demonstration was not necessary explicitly. Probably for this reason, the paper was ignored by the majority of physicists. This is the reason to rewrite it now with all the logical steps. Moreover, some possible interpretation of the results have been added. *© 2000 MAIK “Nauka/Interperiodica”.*

1. INTRODUCTION

There are some apparent disagreements between the theoretical expectation and the observations of the neutrinos from the Supernova LMC-87A [1].

Supernova experts expected that all kinds of neutrino flavors (supposed three) are produced in the supernova LMC-SN-87A possibly in a little different energy spectrum, but passing through the entire dense material of the supernova, they would be mixed up almost completely by the MSW phenomena due to the oscillation (mass) and the interaction (flavor).

This article is not, obviously, searching for the oscillation phenomena that need the knowledge of the change of flavor components in two different places or times, initial and final, but trying to analyze the data of neutrinos observed at the Earth after a long distance trip of about 170000 light years in excellent vacuum.

About the Supernova of February 23, 1987, theorists predicted that the neutrino emission takes place in few seconds with average energy 10 to 15 MeV [2, 3].

At the Kamiokande [4] apparatus, the time duration of the event was more than 12 s; at IMB [5], more than 5 s; and, at Baksan [6], more than 9 s. This is one of the points in strong contrast to the theoretical prediction. The neutrino emission at the supernova appears to have a much larger scale than the expected (Figs. 1 and 2).

In the above theoretical papers, there is an estimate of the neutrino flux and of the number of events: about 50 events with energy more than 10 MeV at Kamiokande (3 kt of water). The events observed in Kamiokande were 12 in total, and only seven of them had energy more than 10 MeV. This is another point of strong disagreement between the prediction and the observation, and since the Kamiokande threshold energy is fairly low (about 6 MeV), its efficiency at more than 10 MeV should be already good. This seems to indicate that the real neutrino emission has a much smaller scale than expected, in an opposite sense compared to the disagreement of the time duration.

The observed spectrum of the event energy and therefore its average value should be sensitive to the experimental threshold energy and also to its efficiency in event detection.

The average energy of Kamiokande events is 14.5 MeV, while at Baksan it is 19.1 MeV and at IMB it is 32.5 MeV. In fact, the lowest energy of events at Kamiokande is 6.3, 12 MeV at Baksan, and 20 MeV at IMB. The estimation can be considered in a fairly good accordance with the observation considering the relatively low threshold at Kamiokande and the high threshold energy especially for the IMB detector. Therefore the real average energy should be a little lower than that of Kamiokande, much lower than the Baksan’s, and very much lower than that of the IMB.

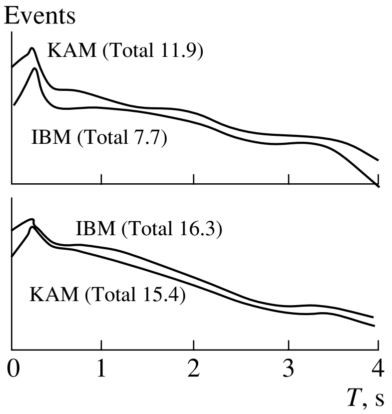

Fig. 1. Theoretically expected time distribution of the neutrinos leaving Supernova LMC-87A under some hypothesis.

---

* This article was submitted by the author in English.

1063-7788/00/6306-0979$20.00 © 2000 MAIK “Nauka/Interperiodica”

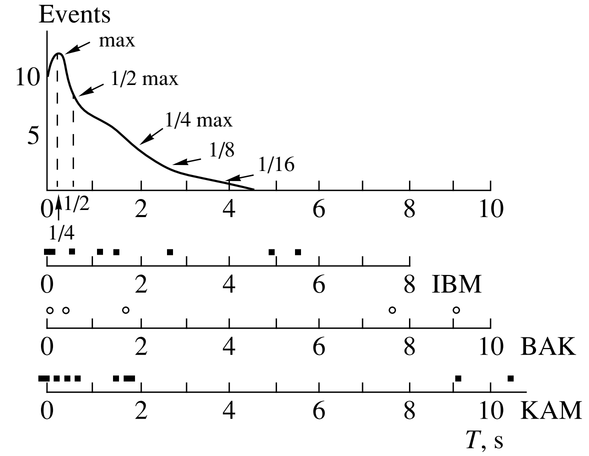

Fig. 2. Comparison of the time distributions observed at IMB, BAK, and KAM with the expected one.

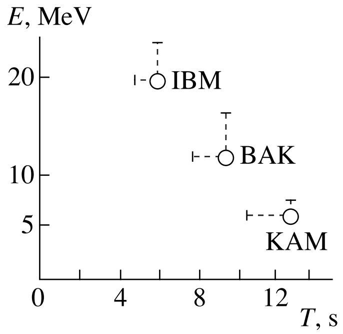

Fig. 3. Relation between the time spread of neutrino events and the threshold energy of detectors.

We have neutrino interaction signals only with electronic channel. This is due to the low energy neutrino spectrum, not high enough to produce muon or tauon in CC interaction. In the data, energies are measured with relatively large error (10 to 30%), while their arrival times are known with an extreme precision, less than millisecond.

According to the estimations the majority of events should be within one second; only a negligible fraction is expected after a few seconds. The disagreement with data is enormous.

The observed spread of event arriving times, which is much wider than expected, suggests to us not only a bigger scale for the emission source but also a possible effect of a nonzero neutrino mass. If neutrino mass is nonzero, the lower energy neutrinos will arrive much later at the Earth, and as a consequence, the arriving times would be spread much wider than time of the emission. The neutrinos spread time where they have left the Supernova can be observed as exactly the same on the Earth only if all the neutrino masses are identically zero so that every neutrino propagates with the velocity of the light. For this purpose, to make a comparison among the data collected by different detectors is better than to compare them with the theoretical estimations. The fact that spread of the arriving time in the IMB, which cannot observe low-energy neutrinos, is much shorter than that observed with Kamiokande (less than 1/2) supports the hypothesis of nonzero neutrino mass. For the zero-mass neutrinos, these time spreads should be equal. Due to the very limited statistics, large fluctuations are expected, but this is not enough to interpret this large discrepancy in time spread. This is logically a much stronger information for the nonzero mass neutrino, since it does depend only on the observed phenomena.

Furthermore, the Baksan data, where the threshold energy is about a halfway between IMB and Kamiokande, give the spread time also in the middle:

	Lowest energy, MeV	Spread time, s
Kamiokande	6.3	12.4
Baksan	12	9.1
IMB	20	5.6

This effect is shown in Fig. 3. The errorlike bars are constructed using the next lowest energy event and the next last arriving event of each detector. This demonstrates that the event time spread is smoothly and systematically varying wider with the lower energy threshold of an apparatus.

It should be noticed that the time duration of the neutrino signals is independent of the mechanism of observation and of the dimension of a detector.

2. SEARCH FOR POSSIBLE NEUTRINO MASSES

Now let us look at the arriving times with a finer process. The time necessary to arrive at the Earth is the same for all neutrinos if their masses are exactly equal to zero

$$T_0 = L_{\mathrm{SN}}/c = 1.7\times 10^5\ \mathrm{yr}.$$

However if the mass is nonzero,

$$T_m = \frac{L_{\mathrm{SN}}}{c\sqrt{1-(m/E)^2}} \sim \frac{L_{\mathrm{SN}}}{c}\left\{1+\frac{1}{2}\left(\frac{m}{E}\right)^2\right\}.$$

The time delay of a nonzero-mass neutrino relative to a zero-mass neutrino is

$$dT_m = T_m - T_0 = \frac{1}{2}\left(T_0\frac{m^2}{E^2}\right).$$

As an example, the neutrino with energy 5 MeV and mass 3 eV should retard one second, and 5-MeV neutrino with 10 eV mass arrives at the Earth 10 s later, relative to the arriving time of a zero-mass neutrino.

The best way to see if the mass effect exists would consist in plotting the arriving time T or δT (from the first event arriving) versus $1/E^2$, since the mass effect arranges data points along a straight line that passes near the origin, a little bit before the first arriving event, which corresponds to the arriving time of a zero-mass particle. The slope (tangent) of this line should be proportional to m^2. This relative delay from the first arriving event does not influence the result in linear scale in δT vs $1/E^2$. In fact,

$$X + (T_n - T_1) = \frac{1}{2}\left(T_0\frac{m^2}{E^2}\right).$$

Here, T_1 and T_n are the first and nth arriving times, and X is the arriving time of a zero-mass neutrino and has an ambiguity for the emission time width. X and m^2 are unknown parameters for the linear fit in this diagram.

Therefore, the angular distribution around the origin of the plot should make roughly a mass distribution knowing the value of X. In Fig. 4, these mass distributions both for Kamiokande and IMB data are shown with $X = -0.2$ s as obtained by the linear fit of the Kamiokande data. In Fig. 5 are shown all the data of the three detectors. All the data points are completely consistent except the effect of the different threshold energy in each detector. One can see clearly two separate event groups. Both of them well along a straight line crossing the time axis a bit before the time of the first arriving event ($T = 0$). Obviously, these two groups correspond to two different masses.

The consistency within the three detectors is, however, only one direction, from the data of Kamiokande. In comparison with this data, the other detectors are blind for the important lower energy region. This is really thanks to the Kamiokande people who continued an enormous effort to purify the water to obtain a very good transparency.

The linear fit of the Kamiokande events in each group gives the masses

$$m_1 = 3.4 \pm 0.6 \text{ eV} \quad \text{and} \quad m_2 = 22.0 \pm 4.0 \text{ eV}.$$

It is important that the ambiguity on the position of the unknown X and also the efficiency of the apparatus, even if it is very bad, obviously should not influence the result. There is an argument: even if lower energy neutrino from a supernova arrives at the Earth later than higher energy one, this could not indicate uniquely the effect of nonzero-mass neutrino, since the slow cooling-down effect of the supernova could produce the same effect. However, this two mass appearance can exclude completely this interpretation of the phenomenon.

2.1. How Good Is the Confidence Level of This Nonzero Mass Appearance?

There is a simple but very sensitive mathematical method to obtain such level—order statistics. Here, two variables are put in comparison with each other to obtain how well these two orders are meaningfully related. In this case, two orders are the order of arriving time of event that is extremely precise and the order of event energy which is known at a level of 10–30%. The result is that they are correlated at a 95% confidence level.

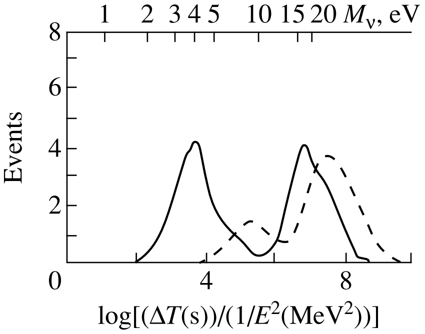

Fig. 4. Expected mass distribution by ΔT vs. $1/E^2$ plot KAM and IMB events.

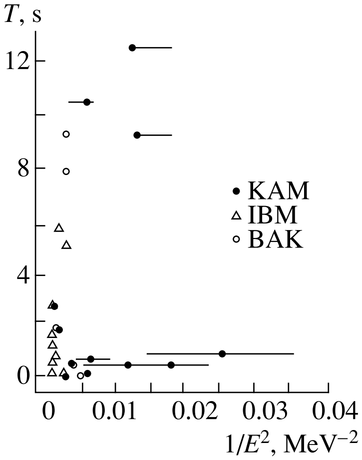

Fig. 5. Arriving T vs. $1/E^2$ plot.

However, this is a result of the first rough test which checks only the regularity between the above-mentioned two orders without any other considerations, e.g., errors. In realty, there are many other additive, clearly observed facts we have to take into account that increase considerably the confidence level for the mass appearance.

1. Which order? In order of increasing energy or decreasing? This reduces the remaining ambiguity to about a half from the above estimation and increases the confidence.

2. The energy of event has a large error in comparison with the arriving time, and this can turn over the good order by the imprecision of the measurement. The order statistics does not consider the experimental error and any of such possibilities. This could increase very much the level of the confidence.

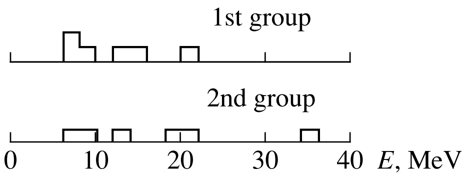

Fig. 6. Each energy distribution separated in two mass groups of KAM events.

3. The very good fit in the linearity in T vs. $1/E^2$ diagram is not considered here. The order statistics does not matter for any kind of curves but only for the monotony. This good linearity increases also to some extent the confidence.

4. The other necessary condition for the existence of the neutrino mass consists is the fact that each fitted line should cross axis about the zero time or, better, a little bit earlier than the arriving time of the first event. This increases the confidence level to a big factor (more than one order of magnitude) for both mass groups independently.

So far, two mass groups are considered separately. However, we have to consider further consistency between the independent results which could increase the confidence much more.

1. The two linear fits are not only good by themselves as mentioned above, but both behave exactly the same way except for their mass parameter. Moreover all the events are only along these lines.

2. Until here, Kamiokande events are used. We have to consider also, finally, the excellent agreement with the result of IMB data even if the low-energy efficiency is very much poorer. This can explain well why in the IMB data the first mass group is almost completely missing. This consistency between the independent observations could significantly further increase the level of confidence.

Furthermore the Baksan group, due to the small size of the detector and higher threshold, has small statistics (five events). The data are not enough by themselves, but when analyzed with all the others in the δT vs. $1/E^2$ plot, they clearly show two events in the first mass group and three events in the second mass group. Then, they all appear consistent with Kamiokande's and IMB's events even with the ambiguities due to time-zero and systematic errors (Fig. 5).

Taking into account all these facts, the total confidence level should be more than 99.99%. Therefore, the mass appearance cannot be interpreted as a purely accidental phenomenon.

The starting point was the apparent disagreement between the neutrino emission time in the theoretical preview and the observation, which appeared as much longer. The conclusion is in the other sense. The good linear fits of two masses make, indeed possible, the conclusion that the real time duration of the neutrino emission at the SN-87A is not a few seconds as estimated by theorists and not as long as more than ten seconds as observed at the Earth, but it should be a fraction of second, about 1/10 of second.

We started with the question why the observed neutrino emission time appeared to be so much longer than the theoretical estimates and understood with why the real local emission time in the Supernova is so short comparing to the theoretical estimates of neutrino emission time. This could indicate that the Supernova was much in smaller scale. This seems also consistent with the number of observed events, which is much smaller (about 1/7) than expected.

2.2. *The Third Mass*

We have observed two nonzero masses. Then, what about the third neutrino mass? Is it equal to zero or nonzero? Consider that there are three neutrino flavor states and three neutrino mass states. Supposing that the third mass is clearly visible, then all the unknown parameters of neutrinos, three masses and three mixing angles (only five are independent), could be obtained even if the error could be large. It is a really a great pity that there was not a visible third mass.

The fact that only two masses made their visible appearances in the plot creates a big ambiguity instead of a clear decisive conclusion from Kamiokande data. We are obliged to suspect and to speculate.

1. If the third mass is zero and if the corresponding neutrino interacts in the electronic flavor channel, it cannot escape the observation, since, in this case, events of this neutrino should be concentrated a little before the time zero or near the first arrived event. This cannot be lost experimentally. Therefore, this possibility can be rejected except the one case (see below, 3a).

2. Assume the third mass is very large (about 100 eV); then, their event arriving times would be spread in a very wide range, one to two minutes, so that to distinguish the Supernova signals from the background events would become very hard or impossible. Prof. Koshiba said, “we cannot say that there is not a third mass signal, neither that it could be there but not distinct from the background.”

3. There are also other possible or probable reasons to make the third mass physically invisible:

(a) This mass state, assuming it exists, could have a mixing angle with the electronic flavor state roughly 90 (i.e., a very small component of electronic flavor state), and therefore these neutrinos cannot interact and produce any visible electronic event, while, for the other flavor channels, these neutrinos do not have enough energy to produce muon (105.66 MeV) of very much heavier tauon (1784.2 MeV). In fact, we have to remember the maximum energy of signals obtained is 35.4 MeV in Kamiokande, 23.3 MeV in Baksan, and 40 MeV in IBM detector, which is very far from the possibility of producing charged lepton except electron, and all the events observed are all electronic flavor both in Kamiokande and IMB. Theoretical estimation of the neutrino energy from the SN-87A also excludes such high-energy neutrinos.

(b) The third mass is very near, within the error of the linear fit, to one of the observed masses, the first group or the second one, and therefore we are not able to discriminate these two masses.

Even if there is a wide ambiguity on the third mass possibility, the last case (b) seems a most reasonable hypothesis, that is,

$$m_1 \approx m_3 \quad \text{or} \quad m_2 \approx m_3.$$

2.3. A Possible Evaluation of the Mixing Angles between Neutrino Mass States and Flavor States

The other observed fact is that these two mass groups consist of almost the same number of events: in Kamiokande data in the first mass group six or five events are observed and six events in the second and two and three, respectively, in the Baksan data. Even if the statistics are very small, this should not be ignored but should be considered as a clear experimental fact. This indeed could show that each of these observed two mass states has roughly the same mixing angle with the electronic flavor state, since the energy spectrum of events in each mass group is roughly consistent (Fig. 6) and the average cross section of the electronic interaction in both groups has nearly the same value. This would be the effect of oscillations in the dense matter of the Supernova itself. Then, these mixing angles should be fairly big or about maximal (roughly around 45° or 135°).

If one observed mass is a superposition of two masses (one of them is the third mass), the sum of the events of these mass states is roughly the same as the others. For example, the third mass is in the second mass group, and also assuming it represents exactly half of the events in the group, then one can give a geometrical example (not unique, here only easy case):

$$\theta_{nf} = \begin{pmatrix} 45^\circ & 90^\circ & 135^\circ \\ 60^\circ & 45^\circ & 60^\circ \\ 60^\circ & 135^\circ & 60^\circ \end{pmatrix},$$

where n and f indicate mass states and flavor states. This is really not a good example, since the mixing angle $(1 - \mu)$ is 90°, too much particular. In reality, there is a big ambiguity due to the missing of visible distinguished third mass.

The analysis we used is very simple, almost childish, but it comes directly from the phenomenology. Every parameter corresponds to one apparent phenomenon and is independent from others, and there is no delicacy or complication of interdependence of more than one parameter like the oscillation phenomena. Independence from any Monte Carlo computation and also from any kind of theoretical model makes the conclusion more convincing.

3. SUMMARY

Some theoretical predictions of the time structure of neutrino emission and the total number of events strongly disagrees with observations. These disagreements could be logically of opposite sense and inconsistent with each other.

The arriving time spreads of three independent observations are quite different from each other but seem systematically and smoothly dependent on the threshold energy of each detector. This is not so for massless neutrinos.

The simple but best way to check a possible mass effect of neutrinos shows the consistency among three independent observations and clearly the existence of the masses: one about 3 eV and the other about 20 eV by the data of Kamiokande. This mass appearance has a very high confidence level and two disagreements of opposite sense between the observation and the theoretical predictions could become one possible reason only: the Supernova was a smaller scale then the expected. This two mass appearance excludes completely the other possible interpretation: the cooling-down effect of the Supernova to show a reason of the wide time spread of events. Only the mass effect can interpret the phenomenon of division into two groups in the wide time spread of events.

The third mass of neutrino is not apparently visible. A very probable suspect would be that they are mixing in one of the two observed mass groups, as mass difference between them is smaller than the statistical error of the line fit for the masses. These masses would be consistent with the value requested from the dark matter phenomena.

As has been seen clearly, to make threshold energy as low as possible is the essential key point to observe fully low-energy neutrinos from supernovas. A well-controlled world standard clock should be helpful to combine together data of detectors in different places scattered in world wide.

REFERENCES

1. H. Huzita, Mod. Phys. Lett. A **12**, 905 (1987).
2. J. N. Bahcall, A. Dar, and T. Piran, Nature **326**, 135 (1987) and references therein.
3. M. Goldhaber, *Introductory Talk of the Conference "Neutrino Telescope," Venice, Italy, 1999*.
4. K. Hirata *et al*., Phys. Rev. Lett. **58**, 1490 (1987); K. Hirata *et al*., Phys. Rev. D **38**, 448 (1988).
5. R. M. Bionta *et al*., Phys. Rev. Lett. **58**, 1494 (1987); C. B. Bratton *et al*., Phys. Rev. D **37**, 3361 (1988).
6. E. N. Alexeyev *et al*., Phys. Lett. B **205**, 209 (1988).

Physics of Atomic Nuclei, Vol. 63, No. 6, 2000, pp. 984–988. From Yadernaya Fizika, Vol. 63, No. 6, 2000, pp. 1059–1063.
Original English Text Copyright © 2000 by Dorman.

NEUTRINO PHYSICS

Solar-Neutrino Variations: A Manifestation of Nonzero Neutrino Mass and Magnetic Moment, and Mixing*

L. I. Dorman**

Technion, Haifa, Israel Cosmic Ray Center and Emilio Segrè Observatory of TAU, Tel Aviv, Israel

Abstract—Time variations of solar neutrino flux are investigated on the basis of available Homestake experimental data for more than two solar cycles (1970–1994). At first, we determine (with the weight-time function by taking into account ^{37}Ar decay), for each solar neutrino run n, the effective Earth's heliolatitude $L_{\text{eff}}(n)$, the effective Zurich sunspots number $Z_{\text{eff}}(n)$, the effective latitude of sunspots distribution $\Lambda_{\text{eff}}(n)$, and the effective surfaces of sunspots in different heliolatitude belts. Then, we consider the correlation of solar-electron-neutrino fluxes with these parameters for different periods of solar activity. It is found that correlation coefficients change sign in different periods of solar activity, so that for total period 1970–1994 the correlation coefficient is very small. The obtained information indicates that a neutrino should have nonzero mass and nonzero magnetic moment. *© 2000 MAIK "Nauka/Interperiodica".*

1. THE PROBLEM OF SOLAR NEUTRINO TIME VARIATIONS

On the base of Homestake experimental data, many authors investigated the solar neutrino time variability connected with solar activity and galactic cosmic ray intensity variations [1–14]. Until now, many scientists did not believe in the reliability of solar neutrino time variations. A possible cause can be found in the large fluctuations of Homestake data which decrease the reliability of the obtained correlation coefficients. A second cause is that, in contradiction with Homestake experiment, Kamiokande data do not show any significant time variations [15]. Recently, the reliability of solar neutrino flux time variations and their connection with solar activity appeared to be even lower after obtaining Homestake's data for the period 1990–1994, when the correlation with solar activity changed sign (became positive) and the total correlation for 1970–1994 became very weak [16].

To make the analysis more reliable, we will determine, with the weight-time function by taking into account ^{37}Ar decay, for each solar neutrino run n the following parameters: the effective heliolatitude of the Earth $L_{\text{eff}}(n)$, the effective Zurich sunspots number $Z_{\text{eff}}(n)$, the effective latitude of sunspots distribution $\Lambda_{\text{eff}}(n)$, and the effective surfaces of sunspots in different intervals of heliolatitudes (in units 10^{-6} of solar disc surface): $\Sigma 5_{\text{eff}}(n)$ (includes three zones from –7.5° to –2.5°, from –2.5° to +2.5°, and from +2.5° to +7.5°), $\Sigma 10_{\text{eff}}(n)$ (includes five zones from –12.5° to + 12.5°), $\Sigma 15_{\text{eff}}(n)$ (includes seven zones from –17.5° to +17.5°), $\Sigma 20_{\text{eff}}(n)$ (includes nine zones from –22.5° to +22.5°), and total effective surface of sunspots $\Sigma 50_{\text{eff}}(n)$ (includes 21 zones from –52.5° to +52.5°). Then, we consider the correlation of solar electron neutrino fluxes with these parameters for different periods of solar activity.

2. DETERMINATION OF EARTH'S EFFECTIVE HELIOLATITUDE AND EFFECTIVE SOLAR ACTIVITY PARAMETERS FOR EACH SOLAR NEUTRINO RUN

For determining the Earth's effective heliolatitude $L_{\text{eff}}(n)$, we take into account the change $L(T)$ of the Earth's heliolatitude during the run from the start time $T_S(n)$ up to the end of run $T_E(n)$, and the weight-time function $\exp(-\lambda T)$, where $\lambda = (0.1356\ \text{year})^{-1}$ corresponds to $T_{1/2} = 35.04$ d of ^{37}Ar decay:

$$\lambda_{\text{eff}}(n) = 7.25^\circ \int\limits_{T_S(n)}^{T_E(n)} e^{-\lambda(T - T_S(n))}\cos(2\pi(T - T_{\max}))dT \times \left[\int\limits_{T_S(n)}^{T_E(n)} e^{-\lambda(T - T_S(n))}dT\right]^{-1}. \tag{1}$$

The time T is in years and $T_{\max}$ for each year corresponds to September 5, when the Earth reaches the maximum heliolatitude +7.25° North. For each run n, the effective value $X_{\text{eff}}(n)$ of some solar activity parameter X can be determined as

$$X_{\text{eff}}(n) = \int\limits_{T_S(n)}^{T_E(n)} e^{-\lambda(T - T_S(n))}X(T)dT \times \left[\int\limits_{T_S(n)}^{T_E(n)} e^{-\lambda(T - T_S(n))}dT\right]^{-1}, \tag{2}$$

---

* This article was submitted by the author in English.

** On leave from IZMIRAN, Troitsk, Russia;
e-mail: lid@physics.technion.ac.il, lid1@ccsg.tau.ac.il

1063-7788/00/6306-0984$20.00 © 2000 MAIK "Nauka/Interperiodica"

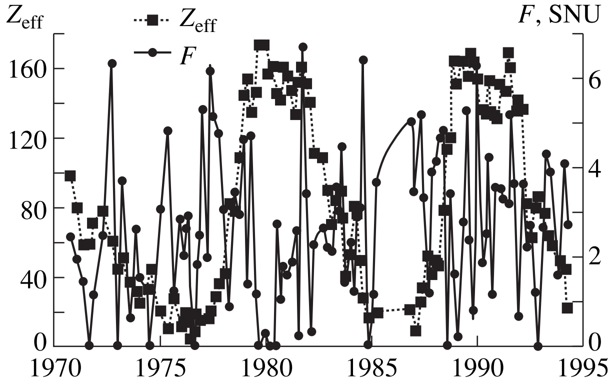

Fig. 1. Comparison of solar neutrino fluxes $F(T_{eff})$ according to Homestake experiment [18] and effective sunspot numbers $Z_{eff}(T_{eff})$ calculated according to (2).

where $X(T) \equiv Z(T)$, $\Lambda_{av}(T)$, $\Sigma5(T)$, $\Sigma10(T)$, $\Sigma15(T)$, $\Sigma20(T)$, $\Sigma50(T)$. The average latitude of sunspots distribution $\Lambda_{av}(T)$ will be

$$\Lambda_{av}(T) = \int_{-\pi/2}^{\pi/2} |\Lambda|\Sigma(\Lambda, T)d\Lambda\left[\int_{-\pi/2}^{\pi/2} \Sigma(\Lambda, T)d\Lambda\right]^{-1}, \quad (3)$$

where $\Sigma(\Lambda, T)$ is the heliolatitude distribution of sunspots surfaces on the solar disc at the time T. In this analysis here and in a following study [17], we will use $L_{eff}(n)$ determined by (1) and $Z_{eff}(n)$, $\Lambda_{eff}(n)$, $\Sigma5_{eff}(n)$, $\Sigma10_{eff}(n)$, $\Sigma15_{eff}(n)$, $\Sigma20_{eff}(n)$, and $\Sigma50_{eff}(n)$ determined by (2) for 108 available runs in Homestake experiment, as well as effective times $T_{eff}(n)$ and measured rates $F(n)$ of production ^{37}Ar atoms per day according to [18], recalculated in units SNU.

3. TIME SERIES OF SOLAR ELECTRON NEUTRINO RATE AND EFFECTIVE SOLAR ACTIVITY PARAMETERS

Figure 1 shows series of solar electron neutrino rate $F(T_{eff})$ (in SNU) and effective sunspots number $Z_{eff}(T_{eff})$. To decrease fluctuations of data, we show in Fig. 2 the observed time variations of 3-run moving averages of neutrino flux $F3(T_{eff}3)$ in comparison with effective sunspot number $Z_{eff}3(T_{eff}3)$. In Fig. 2, we also show the time variations of the parameter $Z_{eff}3(T_{eff}3)/\Lambda_{eff}3(T_{eff}3)$ (we expect that the influence of $Z_{eff}3$ on $F3$ will increase with decreasing $\Lambda_{eff}3$ because detected neutrinos mainly propagate not far from the solar equator). From Fig. 2, it can be seen that there are significant delays between maximums of $Z_{eff}3(T_{eff}3)/\Lambda_{eff}3(T_{eff}3)$ and maximums of $Z_{eff}3(T_{eff}3)$. This effect can be important for determining, by solar neutrino data, the time delay between MHD processes in convective zone and solar activity on the surface. In Fig. 3, we compare the observed time variations of solar neutrino flux $F3(T_{eff}3)$ with the effective sunspot surfaces in different heliolatitude belts ±52.5°, ±22.5°, ±17.5°, ±12.5° and ±7.5°. We note that, for the investigated period 1970–1994, $Z_{eff}(T_{eff})$ and $\Sigma50_{eff}(T_{eff})$ are in good connection with correlation coefficient 0.846 ± 0.018, without significant time lag. For the connection between $Z_{eff}3(T_{eff}3)$ and $\Sigma50_{eff}3(T_{eff}3)$, the correlation coefficient reaches the value 0.917 ± 0.010. A different

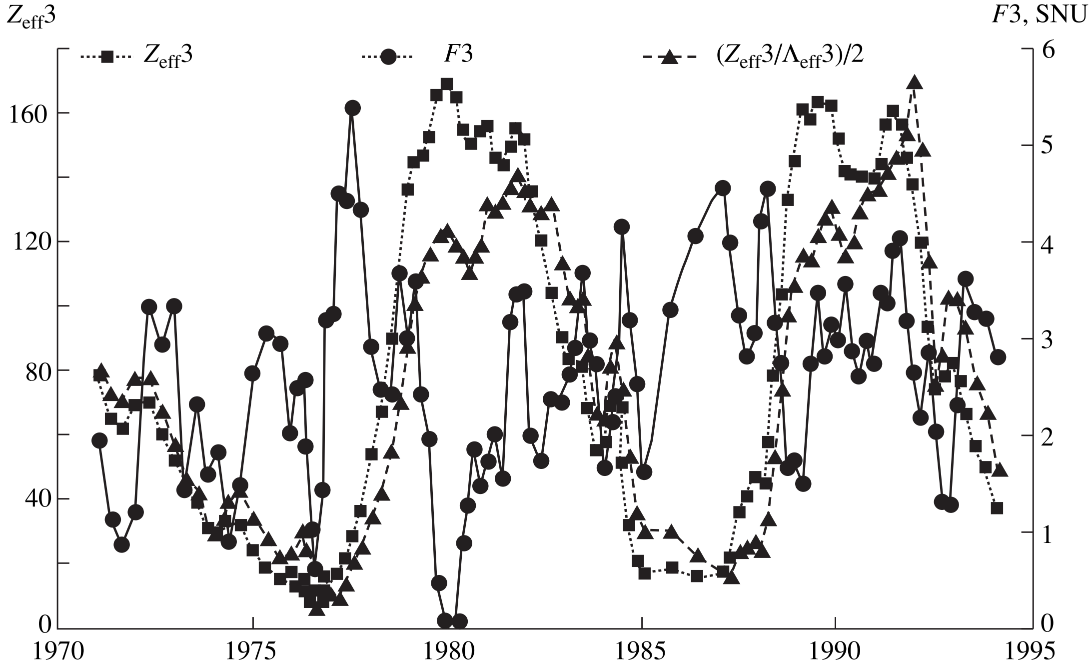

Fig. 2. Comparison of time series of $Z_{eff}3$ ($T_{eff}3$) and $Z_{eff}3/\Lambda_{eff}3(T_{eff}3)$ with $F3(T_{eff}3)$.

situation is observed for smaller heliolatitude intervals: the time lag increases with decreasing heliolatitude interval; this is caused by the movement of sunspot areas from high to low latitudes during the solar cycle development (Fig. 3). This can be clearly seen in Fig. 4 for time series $F3(T_{\text{eff}}3)$, $\Sigma 50_{\text{eff}}3(T_{\text{eff}}3)$ and $\Sigma 15_{\text{eff}}3(T_{\text{eff}}3)$. From all figures, it can be seen that the character of the connection of solar neutrino flux with solar activity parameters is different in periods of increasing and decreasing of solar activity, and changes from one solar cycle to another.

4. ON THE CORRELATION BETWEEN SOLAR ELECTRON NEUTRINO RATE AND SOLAR ACTIVITY PARAMETERS IN DIFFERENT PHASES OF SOLAR CYCLE AND DIFFERENT SOLAR CYCLES

In Table 1, we show the correlation coefficients between $F(T_{\text{eff}})$ and effective solar activity parameters determined by (2), and in Table 2 the correlation coefficients between 3-run moving averages of neutrino

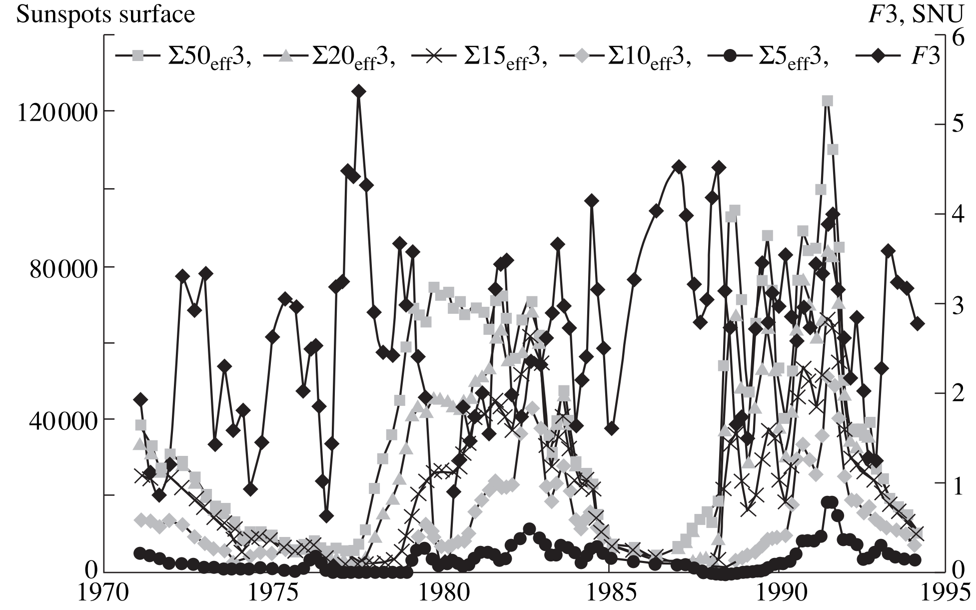

Fig. 3. Comparison of time series of $\Sigma 50_{\text{eff}}3(T_{\text{eff}}3)$, $\Sigma 20_{\text{eff}}3(T_{\text{eff}}3)$, $\Sigma 15_{\text{eff}}3(T_{\text{eff}}3)$, $\Sigma 10_{\text{eff}}3(T_{\text{eff}}3)$, and $\Sigma 5_{\text{eff}}3(T_{\text{eff}}3)$ with $F3(T_{\text{eff}}3)$.

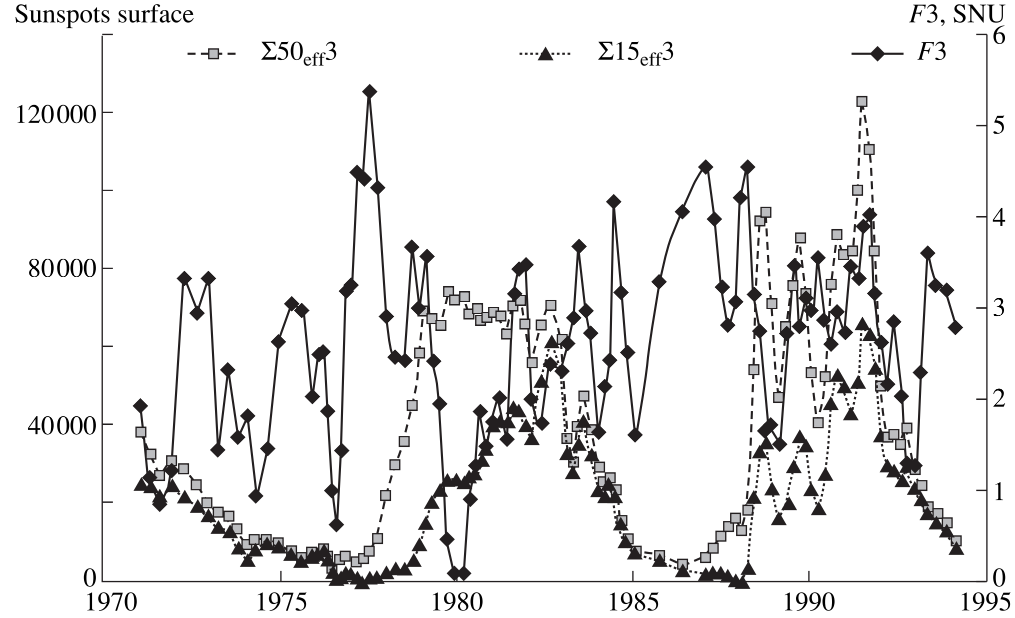

Fig. 4. Comparison of time series of $\Sigma 50_{\text{eff}}3(T_{\text{eff}}3)$ and $\Sigma 15_{\text{eff}}3(T_{\text{eff}}3)$ with $F3(T_{\text{eff}}3)$.

Table 1. Correlation coefficients of solar neutrino flux $F(T_{\text{eff}})$ with solar activity parameters in different time periods

Period	Z_{eff}	$Z_{\text{eff}}/\Lambda_{\text{eff}}$	$\Sigma 50_{\text{eff}}$	$\Sigma 20_{\text{eff}}$	$\Sigma 15_{\text{eff}}$	$\Sigma 10_{\text{eff}}$	$\Sigma 5_{\text{eff}}$
1970–1994	–0.11 ± 0.06	–0.06 ± 0.06	–0.05 ± 0.06	–0.03 ± 0.06	–0.05 ± 0.06	0.08 ± 0.06	0.12 ± 0.06
1970–1979	–0.14 ± 0.10	–0.18 ± 0.10	–0.18 ± 0.10	–0.23 ± 0.10	–0.29 ± 0.10	–0.18 ± 0.10	–0.03 ± 0.11
1980–1989	–0.33 ± 0.09	–0.26 ± 0.09	–0.22 ± 0.09	–0.15 ± 0.10	–0.16 ± 0.10	0.01 ± 0.10	–0.02 ± 0.10
1970–1974	0.23 ± 0.17	0.26 ± 0.16	0.15 ± 0.17	0.16 ± 0.17	0.13 ± 0.18	0.12 ± 0.18	0.06 ± 0.18
1975–1979	–0.23 ± 0.12	–0.25 ± 0.12	–0.27 ± 0.12	–0.30 ± 0.12	–0.38 ± 0.11	–0.20 ± 0.13	–0.02 ± 0.13
1980–1984	–0.21 ± 0.13	0.05 ± 0.13	–0.01 ± 0.13	0.19 ± 0.13	0.24 ± 0.12	0.30 ± 0.12	0.15 ± 0.13
1985–1989	–0.41 ± 0.13	–0.43 ± 0.13	–0.35 ± 0.13	–0.34 ± 0.14	–0.48 ± 0.12	–0.29 ± 0.14	0.16 ± 0.15
1990–1994	0.24 ± 0.13	0.18 ± 0.13	0.25 ± 0.13	0.20 ± 0.13	0.14 ± 0.14	0.21 ± 0.13	0.29 ± 0.13

Table 2. Correlation coefficients of 3-run moving averages of neutrino flux $F3(T_{\text{eff}}3)$ and corresponding 3-run averages of effective solar activity parameters

Period	$Z_{\text{eff}}3$	$Z_{\text{eff}}3/\Lambda_{\text{eff}}3$	$\Sigma 50_{\text{eff}}3$	$\Sigma 20_{\text{eff}}3$	$\Sigma 15_{\text{eff}}3$	$\Sigma 10_{\text{eff}}3$	$\Sigma 5_{\text{eff}}3$
1970–1994	–0.16 ± 0.06	–0.15 ± 0.06	–0.10 ± 0.06	–0.10 ± 0.06	–0.10 ± 0.06	0.04 ± 0.06	0.06 ± 0.06
1970–1979	–0.18 ± 0.10	–0.29 ± 0.09	–0.21 ± 0.10	–0.32 ± 0.09	–0.44 ± 0.08	–0.38 ± 0.09	–0.34 ± 0.09
1980–1989	–0.51 ± 0.07	–0.49 ± 0.08	–0.48 ± 0.08	–0.42 ± 0.08	–0.37 ± 0.09	–0.15 ± 0.10	–0.13 ± 0.10
1970–1974	0.08 ± 0.18	0.08 ± 0.18	0.02 ± 0.18	0.01 ± 0.18	0.05 ± 0.18	0.00 ± 0.18	–0.18 ± 0.17
1975–1979	–0.26 ± 0.12	–0.32 ± 0.12	–0.29 ± 0.12	–0.35 ± 0.11	–0.49 ± 0.10	–0.41 ± 0.11	–0.34 ± 0.12
1980–1984	–0.47 ± 0.10	–0.23 ± 0.12	–0.43 ± 0.11	–0.14 ± 0.13	0.04 ± 0.13	0.34 ± 0.12	0.27 ± 0.12
1985–1989	–0.49 ± 0.12	–0.51 ± 0.11	–0.48 ± 0.12	–0.48 ± 0.12	–0.48 ± 0.12	–0.38 ± 0.13	0.12 ± 0.15
1990–1994	0.39 ± 0.12	0.28 ± 0.13	0.45 ± 0.11	0.37 ± 0.12	0.34 ± 0.12	0.42 ± 0.11	0.44 ± 0.11

fluxes $F3(T_{\text{eff}}3)$ and corresponding 3-run averages effective solar activity parameters.

From Table 1, it can be seen that in the total period 1970–1994 the correlations of observed solar neutrino rate with solar activity parameters are not reliable, in good agreement with recent results of [16]. If we separate the total period in three periods, 1970–1979 and 1980–1989 (both with negative correlation coefficients), and 1990–1994 (with positive correlation coefficients), negative and positive correlations mostly compensated and as a result we obtain very weak correlation for 1970–1994. The same situation we have for 3-run moving average values (Table 2).

Comparison of Table 1 and Table 2 shows that the use of 3-run moving averages leads to some increase of correlation coefficients. We note that for the period 1970–1979 correlation coefficients have a maximum value for $\Sigma 15_{\text{eff}}$ (r = –0.29 ± 0.10) and $\Sigma 15_{\text{eff}}3$ (r = –0.44 ± 0.08). This is mainly caused by the period of raising solar activity in 1975–1979 (maximum r = –0.38 ± 0.11 for $\Sigma 15_{\text{eff}}$ and maximum r = –0.49 ± 0.10 for $\Sigma 15_{\text{eff}}3$). This is confirmed by the next period of raising solar activity in 1985–1989, in which we observe the same effect: maximum r = –0.48 ± 0.12 for both $\Sigma 15_{\text{eff}}$ and $\Sigma 15_{\text{eff}}3$. For smaller latitude intervals, correlation coefficients are found to decrease due to the increase in fluctuations. For larger latitude intervals, correlation coefficients also decrease because high latitude regions of solar activity do not reflect the situation in convection zone at low latitudes where solar electron neutrinos, detected in Homestake experiment, cross the Sun interior.

5. DISCUSSION AND CONCLUSION

From Tables 1 and 2, it can be seen that the connection between solar activity parameters and solar neutrino flux, according to Homestake measurements in 1980–1989, was more evident than in 1970–1979. This difference can be understood if we consider the correlation separately for 1970–1974, 1975–1979, 1980–1984, and 1985–1989. Correlation in 1970–1974 was positive, but in 1975–1979 it was negative; therefore, in the total period 1970–1979 correlation became very weak. In both periods 1980–1984 and 1985–1989 correlation was negative; as a result this gives in 1980–1989, much better negative correlation than in 1970–1979. It is important to note that in 1990–1994 (after about two solar cycles) correlation again becomes positive. These two periods with positive correlation (1970–1974 and 1990–1994) decrease very much the total negative correlation coefficient for 1970–1994 and make it very small (this can be a cause why many people do not believe in real existence of solar neutrino time variations and in their connection with solar activity).

In odd solar cycle 21 yr, in both parts of cycle, we have negative correlation of solar activity with solar electron neutrino flux. It means that in odd cycle correlation between magnetic field in convection zone (in which some part of electron neutrinos are transformed in other types of neutrinos not detected in Homestake experiment, leading to a decrease in the observed neutrino counting rate) and solar activity is positive: increase of solar activity reflects an increase of internal magnetic field in convection zone and a decrease of electron neutrino flux. A more complicated situation is observed in even solar cycles 20 and 22 yr: in periods of increasing solar activity the character of correlation between solar activity and electron neutrino flux is the same as in the odd cycle (negative correlation), but in periods of decreasing solar activity the character of this correlation is opposite in comparison with odd cycle (positive correlation). It means that in even solar cycles there is positive correlation between magnetic field in convection zone and solar activity on the Sun's surface in periods of increasing solar activity and negative correlation in periods of decreasing solar activity (solar activity decreases after reaching the maximum, but the magnetic field in the convection zone still increases in the region around the equatorial plane where neutrinos, detected on the Earth, cross the convection zone). The obtained results can be considered as peculiar features of 22-yr variations in convection zone, which can be connected to 22-yr variations of solar activity on the Sun's surface, as well as to the observed time lag between changes of magnetic fields in the convection zone and solar activity variations. On the other hand, the connection of solar neutrino time variations with solar activity and variable magnetic fields in the convection zone can be considered as manifestation of nonzero neutrino mass and magnetic moment (in the frame of the theory of magnetic neutrino resonant spin-flavor precession [12, 13]).

ACKNOWLEDGMENTS

The author thanks V. Berezinsky, R. Davis, V. Obridko, A. Rez, V. Semikoz, and A.W. Wolfendale for interesting discussions and G. Villoresi and V. Bednyakov for useful comments. This research was partly supported by Physics Department of Technion and by Israel Cosmic Ray Center and Emilio Segré Observatory, affiliated to Tel Aviv University.

REFERENCES

1. G. A. Bazilevskaya *et al*., Yad. Fiz. **39**, 856 (1984) [Sov. J. Nucl. Phys. **39**, 543 (1984)].
2. R. Davis *et al*., Annu. Rev. Nucl. Part. Sci. **39**, 467 (1989).
3. J. N. Bahcall, *Neutrino Astrophysics* (Cambridge Univ. Press, Cambridge, 1989).
4. L. I. Dorman and A. W. Wolfendale, J. Phys. G **17**, 769 (1991); in *Proceedings of 22th International Cosmic Ray Conference, Dublin, 1991*, Vol. 3, pp. 736, 740.
5. J. N. Bahcall and W. N. Press, Astrophys. J. **370**, 730 (1991).
6. V. Gavryusev *et al*., Sol. Phys. **133**, 161 (1991).
7. S. Massetti and M. Storini, Report No. CNR/IFSI-92-18 (1992).
8. L. I. Dorman *et al*., in *Proceedings of 23rd International Cosmic Ray Conference, Calgary, 1993*, Vol. 3, p. 873; L. I. Dorman *et al*., in *Proceedings of 24th International Cosmic Ray Conference, Rome, 1995*, Vol. 4, p. 1239.
9. Yu. R. Rivin, Astron. Rep. **37**, 202 (1993); Yu. R. Rivin and V. N. Obridko, Astron. Rep. **41**, 76 (1997).
10. S. Massetti *et al*., in *Proceedings of 24th International Cosmic Ray Conference, Rome, 1995*, Vol. 4, pp. 1243, 1247; S. Massetti, in *Proceedings of 24th International Cosmic Ray Conference, Rome, 1995*, Vol. 4, p. 1251.
11. D. S. Oakley and H. B. Snodgrass, Astropart. Phys. **7**, 297 (1997).
12. E. Kh. Akhmedov and O. V. Bychuk, Zh. Éksp. Teor. Fiz. **95**, 442 (1989).
13. V. B. Semikoz *et al*., in *Proceedings of EU-Conference "New Trends in Neutrino Physics," Ringberg, Germany, 1998*.
14. P. A. Sturrock *et al*., Astrophys. J. **507**, 978 (1998).
15. P. Raychaudhuri, Mod. Phys. Lett. A **6**, 2003 (1991).
16. G. Walther, Astrophys. J. **513**, 990 (1999).
17. L. I. Dorman, Yad. Fiz. **63**, 1064 (2000) [Phys. At. Nucl. **63**, 989 (2000)].
18. B. T. Cleveland *et al*., Astrophys. J. **496**, 505 (1998).

Physics of Atomic Nuclei, Vol. 63, No. 6, 2000, pp. 989–992. From Yadernaya Fizika, Vol. 63, No. 6, 2000, pp. 1064–1067.
Original English Text Copyright © 2000 by Dorman.

The Asymmetry of Solar-Neutrino Fluxes*

L. I. Dorman**

Technion, Haifa, Israel Cosmic Ray Center and Emilio Segre' Observatory of TAU, Tel Aviv, Israel

Abstract—With effective heliolatitude $L_{\text{eff}}(n)$ for each solar-neutrino run n we separate all available Homestake experimental data for more than two solar cycles (1970–1994) on three zones SOUTH, EQUATORIAL, and NORTH in dependence on the heliolatitude (where detected neutrinos cross the Sun's surface). For each latitudinal zone, we determine the average solar electron neutrino flux and correlations with effective solar-activity parameters for asymmetrical latitudinal belts. The obtained results indicate that neutrino should have nonzero mass and nonzero magnetic moment. *© 2000 MAIK "Nauka/Interperiodica".*

1. THE LATITUDINAL DEPENDENCE OF SOLAR-NEUTRINO FLUX AND CORRELATION COEFFICIENTS

On the base of Homestake experimental data, this problem was considered in [1–4]. Here, we will use the following effective parameters, calculated with the weight-time function by taking into account ^{37}Ar decay for each solar-neutrino run n according to (2) in [4]: effective Earth's heliolatitude $L_{\text{eff}}(n)$, effective Zurich sunspots number $Z_{\text{eff}}(n)$, and effective latitude of sunspots distribution $\Lambda_{\text{eff}}(n)$, as well as effective surfaces of sunspots in different heliolatitude belts $\Sigma 5_{\text{eff}}(n)$ in ±7.5°, $\Sigma 10_{\text{eff}}(n)$ in ±12.5°, $\Sigma 15_{\text{eff}}(n)$ in ±17.5°, $\Sigma 20_{\text{eff}}(n)$ in ±22.5°, and $\Sigma 50_{\text{eff}}(n)$ in ±52.5°. On the basis of data set of effective heliolatitude of the Earth $L_{\text{eff}}(n)$ in each run, we will separate the whole set of 108 runs of Homestake measurements into three latitude sets of 36 runs for each latitude zone SOUTH, EQUATOR, and NORTH. To control the reliability of solar magnetic fields influence on solar-electron-neutrino flux and their connection with solar activity, as well as the reliability of NORTH–SOUTH asymmetry in solar-neutrino flux and correlation coefficients, we calculate sunspots surfaces separately for south and north latitudinal belts: $\Sigma S05_{\text{eff}}(n)$ and $\Sigma N05_{\text{eff}}(n)$ (from 0° to –7.5° and from 0° to +7.5°, respectively), $\Sigma S510_{\text{eff}}(n)$ and $\Sigma N510_{\text{eff}}(n)$ (from –2.5° to –12.5° and from +2.5° to +12.5°), $\Sigma S515_{\text{eff}}(n)$ and $\Sigma N515_{\text{eff}}(n)$ (from –2.5° to –17.5° and from +2.5° to +17.5°), $\Sigma S520_{\text{eff}}(n)$ and $\Sigma N520_{\text{eff}}(n)$ (from –2.5° to –22.5° and from +2.5° to +22.5°), $\Sigma S1015_{\text{eff}}(n)$ and $\Sigma N1015_{\text{eff}}(n)$ (from –7.5° to –17.5° and from +7.5° to +17.5°), $\Sigma S1020_{\text{eff}}(n)$ and $\Sigma N1020_{\text{eff}}(n)$ (from –7.5° to –22.5° and from +7.5° to +22.5°).

2. SEPARATION OF HOMESTAKE DATA AND EFFECTIVE SOLAR-ACTIVITY PARAMETERS ACCORDING TO LATITUDINAL ZONES

Figure 1 shows the time variations of $L_{\text{eff}}(n)$. We use these data to separate solar-neutrino fluxes and effective solar-activity parameters described above into three latitudinal zones SOUTH, EQUATOR, and NORTH (36 runs in each zone). In Table 1, we report for each latitudinal zone the average values $\langle L_{\text{eff}}\rangle$, $\langle F\rangle$, and $\langle Z_{\text{eff}}\rangle$.

3. LATITUDINAL-SOLAR-ACTIVITY DEPENDENCES OF SOLAR-NEUTRINO FLUX

3.1. The NEAR–FAR Effect and NORTH-SOUTH Asymmetry in the Solar-Neutrino Flux for the Total Period

We consider the average values of Earth's effective heliolatitude $\langle L_{\text{eff}}\rangle$, neutrino flux $\langle F\rangle$, and effective sunspots number $\langle Z_{\text{eff}}\rangle$ for each latitudinal zone (Table 1). It can be seen that $\langle L_{\text{eff}}\rangle_{\text{SOUTH}} = -5.26° \pm 0.17°$, $\langle L_{\text{eff}}\rangle_{\text{EQUAT}} = -0.27° \pm 0.31°$, and $\langle L_{\text{eff}}\rangle_{\text{NORTH}} = +5.29° \pm 0.20°$. The angle distance between NEAR (EQUATOR zone) and FAR (SOUTH + NORTH zones) is about the dimension of detected solar-neutrino source in chlorine experiment. Therefore, if the magnetic conditions averaged for many years are a little different in regions NEAR and FAR, one can expect some difference of solar-neutrino fluxes in NEAR and FAR in the frame of the theory of magnetic neutrino resonant spin-flavor precession. From Table 1, it can be seen that the differences in $\langle F\rangle$ are small, inside 1σ. We can see only some

Table 1. Separation of Homestake runs according to latitudinal zones SOUTH, EQUATOR, and NORTH

Zone	$\langle L_{\text{eff}}\rangle$, deg	$\langle F\rangle$, SNU	$\langle Z_{\text{eff}}\rangle$
SOUTH	–5.26 ± 0.17	2.57 ± 0.25	76.7 ± 8.4
EQUATOR	–0.27 ± 0.31	2.71 ± 0.27	86.3 ± 9.8
NORTH	5.29 ± 0.20	2.50 ± 0.34	92.0 ± 9.1

---

* This article was submitted by the author in English.

** On leave from IZMIRAN, Troitsk, Russia;
e-mail: lid@physics.technion.ac.il, lid1@ccsg.tau.ac.il

1063-7788/00/6306-0989$20.00 © 2000 MAIK "Nauka/Interperiodica"

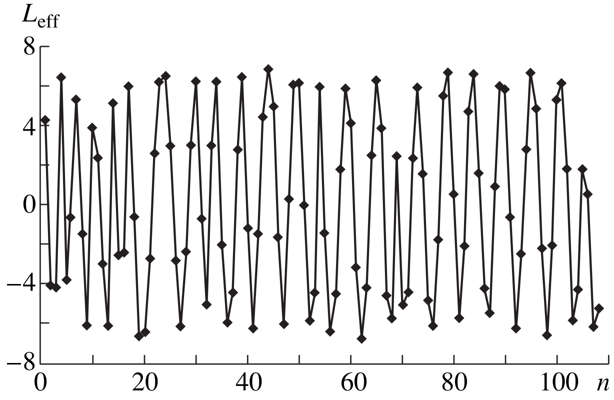

Fig. 1. Variation of effective heliolatitude $L_{\mathrm{eff}}(n)$ in dependence of run number n.

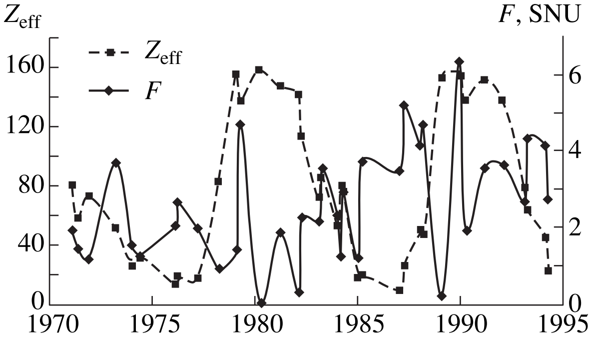

Fig. 2. Comparison of solar-neutrino fluxes $F(T_{\mathrm{eff}})$ in SNU according to Homestake experiment [5] and effective sunspot numbers $Z_{\mathrm{eff}}(T_{\mathrm{eff}})$ according to Table 1 for the SOUTH zone.

tendency of little bigger neutrino flux $\langle F\rangle$ in EQUATOR zone by about 7% in comparison with SOUTH and NORTH zones. This NEAR–FAR effect cannot be caused by the negligible difference in $\langle Z_{\mathrm{eff}}\rangle$: for NEAR (= EQUATOR zone) $\langle Z_{\mathrm{eff}}\rangle_{\mathrm{NEAR}} = 86.3 \pm 9.8$, and for FAR (= (SOUTH + NORTH)/2) $\langle Z_{\mathrm{eff}}\rangle_{\mathrm{FAR}} = 84.4 \pm 8.7$. If the NEAR–FAR effect in solar-neutrino flux is real, the little smaller average magnetic field near EQUATOR plane than at bigger angle distances is expected in the frame of theory of magnetic neutrino resonant spin-flavor precession. On the other hand, the small deficit of $\langle F\rangle$ in NORTH zone in comparison with SOUTH zone can be caused by the smaller value of $\langle Z_{\mathrm{eff}}\rangle$ in SOUTH zone than in NORTH zone: $\langle Z_{\mathrm{eff}}\rangle_{\mathrm{SOUTH}} = 76.7 \pm 8.4$ and $\langle Z_{\mathrm{eff}}\rangle_{\mathrm{NORTH}} = 92.0 \pm 9.1$. Therefore we can reasonably assert that, as an average for total period of 23 yr, there is no significant North–South asymmetry in solar-neutrino flux.

3.2. Latitudal Dependencies of the Solar-Neutrino Flux in Periods of Low, Medium, and High Solar Activity

On the basis of effective sunspots numbers $Z_{\mathrm{eff}}(n)$, we separate each latitudinal zone SOUTH, EQUATOR, and NORTH into three equal groups of LOW, MEDIUM, and HIGH solar-activity level. Results are shown in Table 2, from which it follows:

1. In SOUTH zone, there is tendency of decreasing solar-neutrino flux with increasing solar activity, but in NORTH zone the tendency is opposite.

2. The biggest decrease of solar-neutrino flux with increasing solar activity from LOW ($\langle Z_{\mathrm{eff}}\rangle \approx 22$) to HIGH ($\langle Z_{\mathrm{eff}}\rangle \approx 156$) is observed in EQUATOR zone: from 3.6 ± 0.5 SNU to 2.1 ± 0.4 SNU.

3. The biggest NEAR–FAR effect is observed in periods of LOW solar activity: 3.6 ± 0.5 SNU in NEAR zone and 2.5 ± 0.5 SNU in FAR zone; this effect decreases with increasing solar activity and disappears in periods of MEDIUM and HIGH solar activity.

4. The biggest NORTH–SOUTH asymmetry also is observed in periods of LOW solar activity: 2.1 ± 0.6 SNU in NORTH zone and 2.9 ± 0.4 SNU in SOUTH zone.

4. CORRELATION OF SOLAR-NEUTRINO FLUX WITH DIFFERENT PARAMETERS OF SOLAR ACTIVITY: LATITUDINAL DEPENDENCES

4.1. Solar-Neutrino-Flux Variations in Connection with Effective Sunspot Numbers Separately for SOUTH, EQUATOR and NORTH Zones; Asymmetry in Correlation Coefficients

In Figs. 2–4, time series of solar-neutrino flux $F(T_{\mathrm{eff}})$ and effective sunspots numbers $Z_{\mathrm{eff}}(T_{\mathrm{eff}})$ for

Table 2. Average values of solar-neutrino flux $\langle F\rangle$ of effective latitude $\langle L_{\mathrm{eff}}\rangle$, and of effective sunspots number $\langle Z_{\mathrm{eff}}\rangle$ in different latitudinal zones and different groups of solar-activity (SA) levels

Zone	Parameter	Low SA	Medium SA	High SA
SOUTH	$\langle F\rangle$, SNU	2.9 ± 0.4	2.4 ± 0.3	2.5 ± 0.6
	$\langle L_{\mathrm{eff}}\rangle$, deg	–5.5 ± 0.3	–4.9 ± 0.3	–5.5 ± 0.2
	$\langle Z_{\mathrm{eff}}\rangle$	23.9 ± 3.3	67.8 ± 3.6	138.6 ± 6.1
EQUATOR	$\langle F\rangle$, SNU	3.6 ± 0.5	2.5 ± 0.4	2.1 ± 0.4
	$\langle L_{\mathrm{eff}}\rangle$, deg	–0.2 ± 0.7	0.0 ± 0.5	–0.6 ± 0.5
	$\langle Z_{\mathrm{eff}}\rangle$	21.7 ± 3.5	80.8 ± 8.5	156.3 ± 3.5
NORTH	$\langle F\rangle$, SNU	2.1 ± 0.6	2.8 ± 0.5	2.7 ± 0.6
	$\langle L_{\mathrm{eff}}\rangle$, deg	5.0 ± 0.4	5.4 ± 0.3	5.5 ± 0.3
	$\langle Z_{\mathrm{eff}}\rangle$	29.4 ± 3.7	91.7 ± 7.5	154.7 ± 3.1

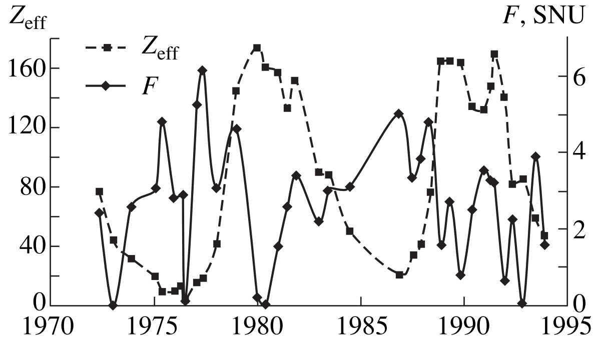

Fig. 3. The same as in Fig. 2, but for the EQUATOR zone.

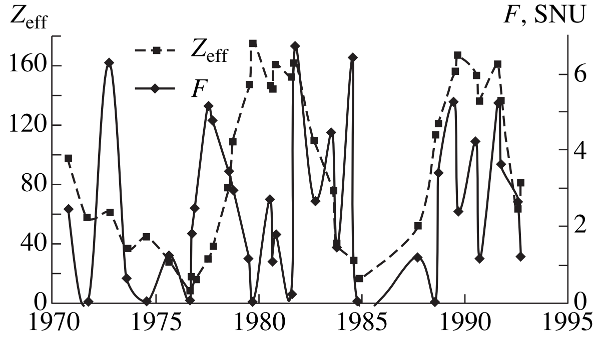

Fig. 4. The same as in Fig. 2, but for the NORTH zone.

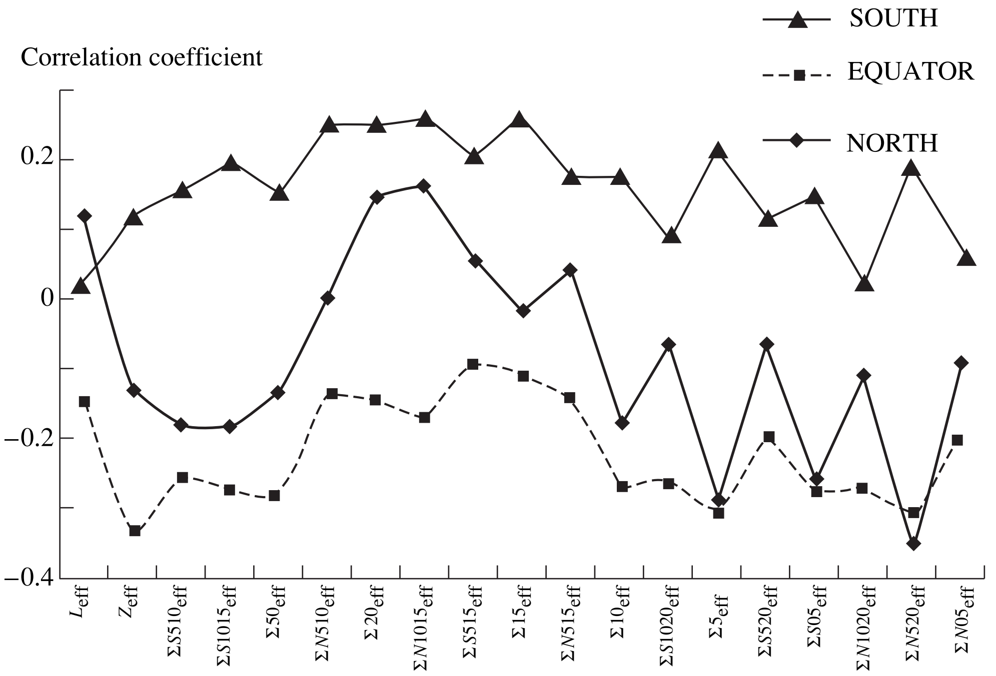

Fig. 5. Correlation coefficients for connection of solar-neutrino fluxes $F(T_{\rm eff})$ according to Homestake experiment [5] with $L_{\rm eff}(T_{\rm eff})$ and different solar-activity parameters based on data in symmetric and asymmetric latitudinal belts separately for SOUTH, EQUATOR, and NORTH zones.

SOUTH, EQUATOR, and NORTH zones are shown. The connection between $F(T_{\rm eff})$ and $Z_{\rm eff}(T_{\rm eff})$ for SOUTH zone is characterized by correlation coefficient $R_S = -0.14 \pm 0.11$, for EQUATOR zone by $R_E = -0.35 \pm 0.10$, and for NORTH zone by $R_N = +0.12 \pm 0.11$. Therefore, in correlation coefficients there is a significant NEAR–FAR effect and a great NORTH–SOUTH asymmetry (with opposite signs in correlation coefficients). For EQUATOR zone, characterized by the highest correlation coefficient, the regression equation will be

$$F = 3.52 - 0.0094 Z_{\rm eff}\ (\mathrm{SNU}), \tag{1}$$

which gives for $Z_{\rm eff} \longrightarrow 0$ an expected flux $F_{\max} = 3.52$ SNU, in good agreement with Table 2.

4.2. Correlation of Solar-Neutrino Flux with Different Effective Parameters of Solar Activity in SOUTH, EQUATOR and NORTH Zones

In Fig. 5, we show correlation coefficients, for connection in SOUTH, EQUATOR and NORTH zones, of the solar-neutrino flux $F(T_{\rm eff})$, according to Homestake experimental data, with $L_{\rm eff}(T_{\rm eff})$ and with following solar-activity parameters: $Z_{\rm eff}(T_{\rm eff})$, $\Sigma 50_{\rm eff}(T_{\rm eff})$, $\Sigma 20_{\rm eff}(T_{\rm eff})$, $\Sigma 15_{\rm eff}(T_{\rm eff})$, $\Sigma 10_{\rm eff}(T_{\rm eff})$, $\Sigma 5_{\rm eff}(T_{\rm eff})$, $\Sigma S05_{\rm eff}(T_{\rm eff})$, $\Sigma N05_{\rm eff}(T_{\rm eff})$, $\Sigma S510_{\rm eff}(T_{\rm eff})$, $\Sigma N510_{\rm eff}(T_{\rm eff})$, $\Sigma S515_{\rm eff}(T_{\rm eff})$, $\Sigma N515_{\rm eff}(T_{\rm eff})$, $\Sigma S520_{\rm eff}(T_{\rm eff})$, $\Sigma N520_{\rm eff}(T_{\rm eff})$, $\Sigma S1015_{\rm eff}(T_{\rm eff})$, $\Sigma N1015_{\rm eff}(T_{\rm eff})$, $\Sigma S1020_{\rm eff}(T_{\rm eff})$, $\Sigma N1020_{\rm eff}(T_{\rm eff})$. The main features of observed correlations are as following:

1. The correlation with $L_{\mathrm{eff}}(T_{\mathrm{eff}})$ is negative in EQUATOR zone and positive in SOUTH zone; it means that maximum of $F(T_{\mathrm{eff}})$ is expected near the boundary between SOUTH and EQUATOR zones.

2. Correlations with solar-activity parameters based on the data in symmetrical latitudinal belts $Z_{\mathrm{eff}}(T_{\mathrm{eff}})$, $\Sigma 50_{\mathrm{eff}}(T_{\mathrm{eff}})$, $\Sigma 20_{\mathrm{eff}}(T_{\mathrm{eff}})$, $\Sigma 15_{\mathrm{eff}}(T_{\mathrm{eff}})$ are characterized by the biggest correlation coefficients for EQUATOR zone, but for this zone the correlation with parameters in the narrower zones $\Sigma 10_{\mathrm{eff}}(T_{\mathrm{eff}})$ and $\Sigma 5_{\mathrm{eff}}(T_{\mathrm{eff}})$ are very weak; correlation coefficients for SOUTH and NORTH zones have opposite signs not only for $Z_{\mathrm{eff}}(T_{\mathrm{eff}})$ (as it was shown above), but also for other solar-activity parameters based on data in symmetrical latitudinal belts.

3. Correlations with solar-activity parameters based on the data in south and north latitudinal belts $\Sigma S515_{\mathrm{eff}}(T_{\mathrm{eff}})$, $\Sigma N515_{\mathrm{eff}}(T_{\mathrm{eff}})$, $\Sigma S520_{\mathrm{eff}}(T_{\mathrm{eff}})$, $\Sigma N520_{\mathrm{eff}}(T_{\mathrm{eff}})$, $\Sigma S1015_{\mathrm{eff}}(T_{\mathrm{eff}})$, $\Sigma N1015_{\mathrm{eff}}(T_{\mathrm{eff}})$, $\Sigma S1020_{\mathrm{eff}}(T_{\mathrm{eff}})$, and $\Sigma N1020_{\mathrm{eff}}(T_{\mathrm{eff}})$ are characterized by very important features: for the SOUTH zone we observe much better negative correlation with solar-activity parameters based on the data in south latitudinal belts, and for NORTH zone, in north latitudinal belts. For example, for SOUTH zone, correlation coefficient of $F(T_{\mathrm{eff}})$ with $\Sigma S515_{\mathrm{eff}}(T_{\mathrm{eff}})$ is three times bigger than with $\Sigma N515_{\mathrm{eff}}(T_{\mathrm{eff}})$, with $\Sigma S520_{\mathrm{eff}}(T_{\mathrm{eff}})$ is 4.8 times bigger than with $\Sigma N520_{\mathrm{eff}}(T_{\mathrm{eff}})$, with $\Sigma S1015_{\mathrm{eff}}(T_{\mathrm{eff}})$ is 2.4 times bigger than with $\Sigma N1015_{\mathrm{eff}}(T_{\mathrm{eff}})$, and with $\Sigma S1020_{\mathrm{eff}}(T_{\mathrm{eff}})$ is 3.9 times bigger than with $\Sigma N1020_{\mathrm{eff}}(T_{\mathrm{eff}})$. This feature shows that the correlations of $F(T_{\mathrm{eff}})$ with solar-activity parameters are not accidental and they are connected to the interaction of magnetic electron neutrino with strong internal magnetic fields variable with solar activity (in the frame of the theory of magnetic neutrino resonant spin-flavor precession).

5. CONCLUSION

The main results that characterize the latitudinal dependences of solar-neutrino fluxes and their correlation with parameters of solar activity, the NEAR–FAR effect, and NORTH–SOUTH asymmetry can be summarized as following:

1. Homestake experimental data of solar-neutrino fluxes for about 24 years show the existence of NEAR–FAR effect; this effect increases significantly in periods of LOW solar activity, when a significant NORTH–SOUTH asymmetry is also observed.

2. The biggest decrease of solar-neutrino flux with increasing solar activity was observed in EQUATOR zone; in this zone the maximum solar-neutrino flux at zero solar activity is expected to be 3.5 SNU.

3. Correlation coefficients of solar-neutrino flux with solar activity for SOUTH and NORTH zones have opposite signs for sunspots numbers, as well as for sunspots surfaces, taken in symmetrical latitudinal belts.

4. We show that there are reliable NORTH–SOUTH asymmetry in fluxes and correlation coefficients and that neutrino flux in SOUTH zone F_S better correlates with sunspots surfaces ΣS than with ΣN, and neutrino flux F_N better correlates with sunspots surfaces ΣN than with ΣS. Neutrino fluxes in SOUTH zone are controlled mainly by solar activity in south latitude belts (correlation coefficients for south latitude belts are in 2–4 times bigger than for north latitude belts), and fluxes in NORTH zone are controlled by solar activity in north latitude belts.

5. Neutrino fluxes in EQUATOR zone are controlled mainly by solar activity in symmetrical latitudinal belts.

The smaller time variations in Kamiokande experiment in comparison with Homestake experiment can be understood if we take into account that about 1/3 part of $\bar{\nu}_e$ (as a result of magnetic ν_e transformation in the neutrino interaction with Sun's internal magnetic fields, see in [2]) will be detected by Kamiokande experiment and not detected by Homestake experiment.

Dependences of solar-neutrino fluxes and of correlation coefficients on the position of the region where neutrino crosses the solar surface give additional arguments to support the conclusion [4] that the interpretation of obtained results can be based on the standard solar model of electron neutrino generation in thermonuclear processes; their propagation through 22-yr variable strong magnetic fields in the convection zone, connected with solar activity magnetic cycle; and theory of magnetic neutrino resonant spin-flavor precession (see [6, 7]).

ACKNOWLEDGMENTS

The author thanks V. Berezinsky, R. Davis, V. Obridko, A. Rez, V. Semikoz, and A.W. Wolfendale for interesting discussions and G. Villoresi and V. Bednyakov for useful comments. This research was partly supported by Physics Department of Technion and by Israel Cosmic Ray Center and Emilio Segre Observatory, affiliated to Tel Aviv University.

REFERENCES

1. L. I. Dorman and A. W. Wolfendale, J. Phys. G **17**, 769 (1991); in *Proceedings of 22th International Cosmic Ray Conference, Dublin, 1991*, Vol. 3, pp. 736, 740.
2. L. I. Dorman *et al.*, in *Proceedings of 23rd International Cosmic Ray Conference, Calgary, 1993*, Vol. 3, p. 873; L. I. Dorman *et al.*, in *Proceedings of 24th International Cosmic Ray Conference, Rome, 1995*, Vol. 4, p. 1239.
3. S. Massetti *et al.*, in *Proceedings of 24th International Cosmic Ray Conference, Rome, 1995*, Vol. 4, pp. 1243, 1247; S. Massetti, in *Proceedings of 24th International Cosmic Ray Conference, Rome, 1995*, Vol. 4, p. 1251.
4. L. I. Dorman, Yad. Fiz. **63**, 1059 (2000) [Phys. At. Nucl. **63**, 984 (2000)].
5. B. T. Cleveland *et al.*, Astrophys. J. **496**, 505 (1998).
6. E. Kh. Akhmedov and O. V. Bychuk, Zh. Éksp. Teor. Fiz. **95**, 442 (1989).
7. V. B. Semikoz *et al.*, in *Proceedings of EU-Conference "New Trends in Neutrino Physics," Ringberg, Germany, 1998.*

Physics of Atomic Nuclei, Vol. 63, No. 6, 2000, pp. 993–1001. From Yadernaya Fizika, Vol. 63, No. 6, 2000, pp. 1068–1076.
Original English Text Copyright © 2000 by Busenitz.

Reactor Neutrinos—Present and Future*

J. Busenitz**
University of Alabama, USA

Abstract—The main characteristics of experimental searches for neutrino oscillations at nuclear reactors are reviewed. We then describe the Chooz and Palo Verde experiments and report their results to date. We also describe the KamLAND experiment, presently under construction in the Kamioka laboratory in Japan, which is designed to extend the sensitivity to $\nu_e \rightleftarrows \nu_X$ oscillations by two orders of magnitude in Δm^2. In particular, this experiment expects to be able to carry out a terrestial test of the large-angle MSW solution to the solar neutrino problem. © *2000 MAIK "Nauka/Interperiodica".*

1. NEUTRINO OSCILLATION SEARCHES AT REACTORS

Nuclear reactors, as copious $\bar{\nu}_e$ sources, have played and important role in the experimental study of neutrinos, beginning in the 1950s with the first observation of neutrinos by Cowan and Reines at the Savannah River reactor. In this paper, we describe present efforts and future plans to exploit reactors to search for neutrino oscillations, which occur if neutrino masses are nondegenerate and the weak interaction eigenstates do not coincide with mass eigenstates. We focus on the Chooz and Palo Verde experiments in the present generation and the KamLAND experiment in the next generation. Given our focus, this paper is by no means a comprehensive review of current reactor neutrino experiments or ideas and plans for the future. For a description of other reactor experiments currently taking data or under consideration, see the papers by Mikaelyan, Sinev, and Martemyanov in these proceedings. Results from earlier oscillation searches at reactors may be found in the literature [1].

In the simplest case, which nonetheless serves well to describe its main characteristics, a reactor oscillation search experiment consists of a $\bar{\nu}_e$ detector with target mass M at a distance (baseline) L from a reactor core. Given that reactors are essentially pure $\bar{\nu}_e$ sources, $\nu_e \rightleftarrows \nu_X$ oscillations would be made manifest by a deficit in the number of $\bar{\nu}_e$'s detected relative to that expected for no oscillations. To control backgrounds, the detector is typically mounted in an underground laboratory, constructed from materials selected for low radioactivity, equipped with an active cosmic muon veto, and includes components to shield the central detector from background-producing neutrons and gammas originating from the outer detector components and laboratory walls. The following paragraphs describe the $\bar{\nu}_e$ detection, background control and estimation, and experimental sensitivity in more detail.

Beta decay of the unstable daughters of fission fragments is the source of the $\bar{\nu}_e$ flux from reactors. The flux at the detector falls off as L^{-2} under the usual assumption that it is isotropic. The production rate for $\bar{\nu}_e$'s with energy greater than ~2 MeV is about 2×10^{20} per GW of thermal power. By tracking the reactor power and having a good understanding of the contributions of the various fissioning isotopes to the total reactor power, the total production rate can be determined with an uncertainty less than 2% [2]. As a function of energy, the antineutrino production rate decreases monotonically, becoming negligible above 10 MeV. For this range of neutrino energies, kinematics allows the charged current interaction only for the electron flavor. This clearly accounts for why reactor experiments are designed as $\bar{\nu}_e$ detectors and look for the "disappearance" of $\bar{\nu}_e$s as the signature of neutrino oscillations.

The signal reaction for $\bar{\nu}_e$ is inverse beta decay: $\bar{\nu}_e + p \longrightarrow e^+ + n$. The event rate is proportional to the mass M of the target or, more precisely, to the number of free protons. The positron kinetic energy is very nearly 1.8 MeV less than that of the neutrino. The cross section is an increasing function of energy so that the convolution of the neutrino flux and cross section results in an interaction rate which peaks around 4 MeV in neutrino energy.

Both the positron and the neutron are detected, the positron by the deposit of its kinetic energy and the energy from its annihilation with an atomic electron and the neutron by its capture after thermalization. The positron energy deposition is practically prompt, while the mean neutron capture time ranges from tens of microseconds to hundreds of microseconds, depending on the target material. A delayed coincidence is required in order to help suppress backgrounds.

---

* This article was submitted by the author in English.

** e-mail: busenitz@bama.ua.edu

1063-7788/00/6306-0993$20.00 © 2000 MAIK "Nauka/Interperiodica"

Backgrounds may be categorized as "correlated" and "uncorrelated." Correlated backgrounds are those in which both the prompt and delayed parts of the event are due to the same process. The main such background source is fast neutron production by muon spallation in the earth near the detector: the fast neutron is transported into the central detector, produces recoil protons which fake the positron signal, and is then captured. Uncorrelated background events are those due to the random delayed coincidence between two independent processes. The dominant source of such background is natural radioactivity.

The following measures are typically taken to control backgrounds:

Use of an underground site so that the earth overburden removes the hadronic component of cosmic rays and attenuates the μ component.

An active cosmic veto surrounding the detector to remove events produced by muons passing through the detector.

A layer of shielding immediately outside the central detector to attenuate gammas and neutrons originating from the lab walls and outer detector components.

Selection of laboratory and detector materials low in natural radioactivity.

Design of central detector material to reduce the neutron capture time so that the window for the delayed coincidence can be narrowed.

Uncorrelated backgrounds may be estimated and subtracted by looking at events with the wrong-sign delayed coincidences, i.e., the neutron capture candidate preceding the positron candidate, or at events with delayed coincidence time long compared to the mean neutron capture time. Correlated backgrounds can be estimated and subtracted by studying the correlation of the event rate with reactor power after the uncorrelated background has been subtracted. The correlated background component will be independent of the reactor power. For the simplest case of a single reactor, the event rate with the reactor off for refueling is the correlated background event rate. For the case of multiple reactors at various distances from the detector, unfolding backgrounds while allowing for the possibility of neutrino oscillations is technically more involved, but the principle is the same.

The sensitivity of an experiment to neutrino oscillations may be expressed in terms of the region of parameter space excluded were the observed signal rate consistent with no $\bar{\nu}_e$ disappearance between the reactor and the detector. For simplicity, it is usual practice to assume that two-flavor oscillations are dominant, in which case the probability that the $\bar{\nu}_e$ survives to the detector is given by

$$P(\bar{\nu}_e \longrightarrow \bar{\nu}_e)$$
$$= 1 - \sin^2 2\theta \sin^2\left[\frac{1.27\Delta m^2\ (\mathrm{eV}^2) L\ (\mathrm{m})}{E_{\bar{\nu}}\ (\mathrm{MeV})}\right],$$

where θ is the mixing angle between the two flavors and Δm^2 is the difference between the square of the masses.

On a plot of Δm^2 versus $\sin^2 2\theta$, the interval in $\sin^2 2\theta$ excluded as a function of decreasing Δm^2 is roughly constant for $\Delta m^2 \gg L^{-1}$ and then gradually narrows toward $\sin^2 2\theta = 1$. The minimum Δm^2 excluded at large mixing angle is given by

$$\Delta m^2\ (\mathrm{eV}^2) \sim \frac{1}{L\ (\mathrm{m})},$$

while the minimum $\sin^2 2\theta$ excluded (90% C.L.) at large Δm^2 obeys

$$\sin^2 2\theta \sim \text{few} \times \text{fractional experimental error.}$$

The experimental error includes the uncertainties in the $\bar{\nu}_e$ production rate, the cross section for inverse beta decay, estimate of the detection efficiency, background subtraction, event statistics, etc. If, for instance, the fractional experimental error were 0.06, that is, the convolution of the uncertainties in the observed number of events and expected number of events were 6% of the expected number of events, the minimum $\sin^2 2\theta$ excluded would be about 0.2. The contributions to the experimental error from the uncertainties in quantities such as $\bar{\nu}_e$ production rate, cross section, and detection efficiency can be reduced by carrying out measurements at different values of L with essentially the same detector.

To obtain sensitivity to lower values of Δm^2, the baseline must be increased. The cost of increasing the baseline, of course, is a reduction in flux which falls off as L^{-2}. To compensate for this, the detector mass M must be increased and stronger measures taken to control backgrounds in order to achieve useful event rates and an acceptable signal-to-background ratio.

2. THE CHOOZ AND PALO VERDE EXPERIMENTS

Measurements made by the Kamiokande experiment [3] of the neutrinos produced in cosmic ray showers indicated a lower-than-expected ratio for ν_μ/ν_e. These data can be explained in terms of $\nu_\mu \rightleftarrows \nu_X$ oscillations with mixing parameters in the region $\sin^2 2\theta > 0.6$, $0.003 < \Delta m^2 < 0.1$ eV^2. The possibility that $X = e$ with $\Delta m^2 > 0.01$ eV^2 was already excluded by the Krasnoyarsk, Bugey 3, and Goesgen experiments [1]. For a reactor experiment to explore with high sensitivity the full region of parameter space allowed assuming $\nu_\mu \rightleftarrows \nu_e$ oscillations, a baseline $L \sim 1000$ m was needed. This provided the primary motivation for mounting the Chooz and Palo Verde experiments. Figure 1 shows an example for the Palo Verde experiment of how the kinetic energy spectrum for the detected positrons would be distorted by oscillations with parameters allowed by the Kamiokande data.

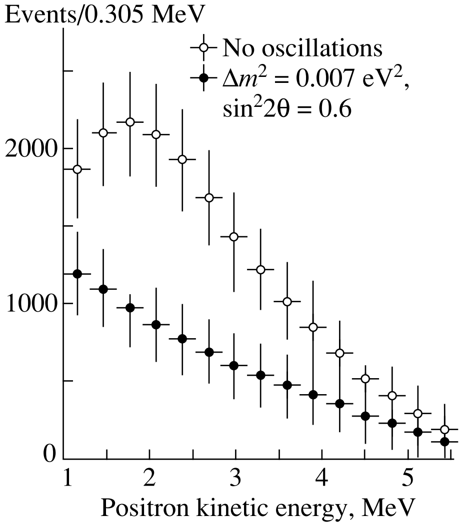

Fig. 1. Expected positron energy spectra (after background subtraction) at the Palo Verde experiment for the case of no oscillations and for two-flavor oscillations with the parameters indicated. The errors are statistical only, corresponding to a running period of approximately 2 yr with a S/B ratio of 3 : 1.

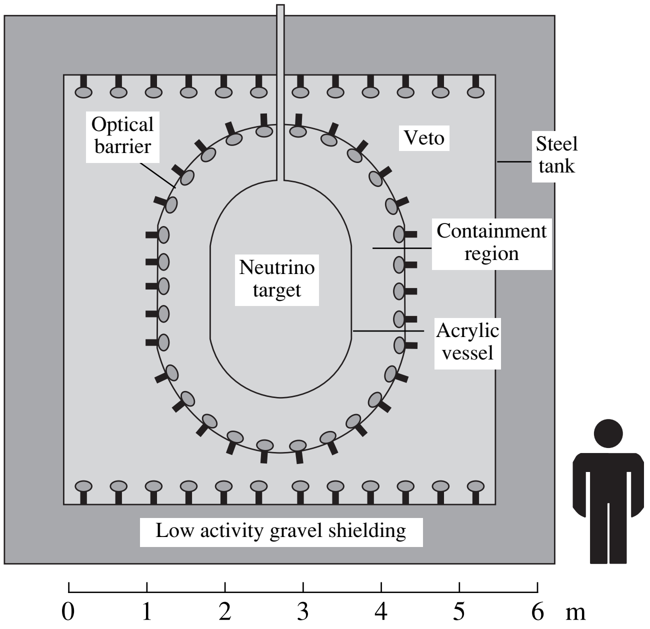

Fig. 2. Schematic view of the Chooz detector.

To introduce the experiments, we show their main characteristics in Table 1. A striking difference between the two experiments is the amount of overburden, which may be viewed as the main factor responsible for how the experiments compare on detector design, event rate, and signal-to-background (S/B). As a relatively shallow experiment, the Palo Verde detector is segmented in order to control backgrounds due to cosmics. Detector segmentation comes at a cost in detection efficiency, and moreover there is more deadtime from the cosmic muon veto because of the higher muon flux at 32 mwe. This explains why the event rates at full power for the two experiments are similar although the total reactor power and target mass are greater, and the baselines shorter, for Palo Verde. Both experiments use Gd-loaded scintillator. The Gd loading reduces the mean n capture time from ~200 μs (capture on hydrogen only) to about 30 μs. A further advantage is that the energy of the gamma cascade constituting the capture signature is about 8 MeV, well above most backgrounds due to natural radioactivity. It is, however, very difficult to make and use Gd-loaded liquid scintillator which has good long-term stability. Both experiments ultimately succeeded, pursuing independent efforts in meeting this challenge [4, 5].

We now describe each experiment in more detail and present its results. The Chooz experiment has been carried out by a collaboration of French, Italian, American, and Russian physicists at the Chooz nuclear power station near the French–Belgian border. A schematic of the detector is shown in Fig. 2. The central detector (target) consists of 5 t of Gd-loaded liquid scintillator contained in a transparent acrylic vessel. This region is viewed by 192 8-inch PhotoMultiplier Tubes (PMT's) separated from the central detector by 70 cm of liquid scintillator (containment region). The purpose of the containment region is to shield the target from gammas emitted from the PMT's and to contain the gammas from n capture. Surrounding the central target and containment region, and optically isolated from them, is the muon veto comprised of 90 t of liquid scintillator viewed by 48 PMT's. Finally, to shield the experiment from natural radioactivity and spallation of fast neutrons in the surrounding rock, there is a 75-cm layer of low-radioactivity sand and 14 cm of cast iron.

Table 1. Main characteristics of the Chooz and Palo Verde experiments

	Chooz (France)	Palo Verde (Arizona)
Number of reactors	2	3
Total thermal power, GW	8.5	11
Baselines, m	998, 1115	890, 750, 890
Overburden, mwe	300	32
Target mass, t	5	11
Target material	Liq. scint. (0.09% Gd)	Liq. scint. (0.1% Gd)
Detector design	Homogeneous	Segmented
Detected $\bar{\nu}_e$ rate, d^{-1}*	~25	~25
S/B	~20 : 1	~1 : 1

* At full power.

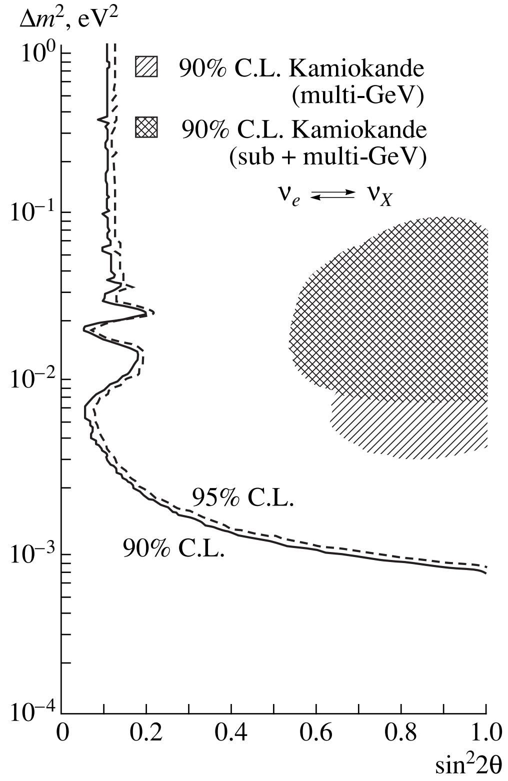

Fig. 3. Regions of $\nu_e \rightleftarrows \nu_X$ oscillation parameter space excluded by the Chooz experiment. Also shown are the regions allowed by the Kamiokande data.

The experiment trigger has two levels of requirements. The first level requires an energy deposit greater than 1.3 MeV ($L1_{\rm low}$) or greater than 3.3 MeV ($L1_{\rm high}$). The second level (L2) requires a delayed coincidence between $L1_{\rm low}$ and $L1_{\rm high}$ within 100 μs. Readout is initiated by L2 if there was no μ veto hit in the preceding 1 ms.

The output of each PMT is digitized by multihit TDC's and two banks of ADC's (one for the positron candidate and the other for the neutron capture candidate). The PMT outputs are also summed in groups of eight and digitized by fast and slow waveform digitizers and two banks of multihit VME ADC's gated by $L1_{\rm low}$.

Detector calibration and monitoring has been carried out using a laser flasher system and radioactive sources.

Selection of $\bar{\nu}_e$ candidates imposes appropriate energy cuts on the "positron" and "neutron capture" components of the event and requires that they be correlated in space and well separated from the PMTs. Further detail on the event selection as well as on the data acquisition system can be found in publications from the experiment [5, 6]. The experiment background has been estimated in several ways. The first is simply to measure the event rate with both reactors off. The second is essentially to measure the event rate at different levels of reactor power; a fit to the event rate versus total reactor power extrapolated to zero power gives the background contribution. The third way is to measure the correlated and uncorrelated components separately and take the sum. The uncorrelated component is estimated from the wrong-sign combinations of $L1_{\rm low}$ and $L1_{\rm high}$. The correlated component is estimated by assuming that the event rate with "positron" energy greater than 8 MeV is entirely due to fast neutrons from muon spallation and by extrapolating this rate into the energy range used for the positron candidate selection. All three methods agree, giving a total background rate of about 1 event/d.

Subtracting the background, the Chooz experiment has found that the integral event rate as well as the distribution of the events in positron energy to be in agreement with that expected for no oscillations. With respect to the integral rate, the ratio of the observed to expected (no osc.) is 1.01 ± 0.028 (stat.) $\pm\, 0.027$ (syst.). The regions of oscillation parameter space excluded at the 90 and 95% confidence levels are shown in Fig. 3.

The Chooz experiment also acquired data with the first reactor on and the second reactor off and vice versa, which is equivalent to carrying out the experiment at two different distances from a reactor since the two reactors are practically identical. The analysis of these data and its results may be found in [6].

We turn next to the Palo Verde experiment, which is being carried out at the Palo Verde Nuclear Generating Station, a three-reactor power plant 70 km west of Phoenix, Arizona. The collaborating institutions are the California Institute of Technology, Stanford University, University of Alabama, and Arizona State University. It began taking data in Summer 1998.

A schematic view of the detector is shown in Fig. 4. The central detector is an 11×6 matrix of cells. Each cell is 9 m long, subdivided into a 740-cm central section filled with liquid scintillator and an 80-cm section of mineral oil at either end. The cell is viewed at each end by a 5-inch PMT. Surrounding the central detector along the long sides are tanks providing a layer of water shielding 1 m thick. The water and mineral oil shielding sections attenuate gammas and neutrons emitted from the laboratory walls and outer components of the detector, e.g., the glass of the PMT's. The detector is fully enclosed by liquid scintillator detectors used to veto cosmic muons.

The central detector is segmented in order to improve the discrimination between positrons from inverse beta decay and electrons, gammas, and recoil protons. The experimental signature required for a positron is an energy deposit in one cell greater than ~1 MeV (kinetic energy of the positron) and energy deposits in adjacent cells consistent with those expected from back-to-back 511 keV annihilation gammas.

The event trigger is based on a so-called triple. For triggering, the anode output of the PMT is split and sent to two sets of discriminators, one set having a threshold corresponding to an energy deposit of ~50 keV (LO) in the cell and the other set having a threshold corresponding to ~500 keV (HI). The discriminator outputs are fed into a fast trigger processor which generates a triple if there is a coincidence between at least 3 LOs and 1 HI in any 5×3 cell submatrix in the detector. The occurrence of a triple initiates digitization of the associated event. Readout is carried out if two triples occur within 450 μs of each other. Given the proximity on time of the "prompt" and "delayed" part of a candidate event, two banks of Fastbus ADCs and TDCs must be used for digitization.

The muon veto hit rate is about 2 kHz. A hit in the veto generates 5 μs of deadtime for the triple trigger processor. Otherwise, muon hits are only clocked and latched for readout, and the main μ veto cuts are applied off-line.

Detector calibration for energy and position reconstruction is carried out using γ point sources, blue LEDs, and a fiberoptic flasher system. The detector simulation program used to estimate the triple trigger efficiencies is tuned and checked against data taken with ^{22}Na and ^{68}Ge sources for the case of positrons and with a ^{252}Cf source and a tagged Am–Be source for the case of neutron capture. Detector stability between calibrations is monitored using the LEDs and fiberoptic flasher system.

A measurement of the $\bar{\nu}_e$ event rate has been carried out using data taken in late 1998. The integrated data taking time for this measurement is 60 d and includes 30 d during which one of the reactors at 890 m was off for refueling.

Event candidates were selected by the applying the cuts listed below. (The subscript "1" refers to the prompt triple, and "2" to the delayed triple. The superscript (i) labels the *i*th most energetic cell energy. Averages over cell row number, cell column number, the position *z* along length of the central detector, etc., are weighted by cell energy.)

The two triples are correlated in time: $5 < t_2 - t_1 < 200$ μs.

The two triples are spatially correlated: $|\bar{z}_2 - \bar{z}_1| < 100\,\text{cm}$, $|\overline{\text{row}_2} - \overline{\text{row}_1}| < 1.5$, $|\overline{\text{column}_2} - \overline{\text{column}_1}| < 2.5$.

No μ veto hit in the interval $t_1 - 150\ \mu\text{s} < t < t_2$.

$E_1^{\text{tot}} > 3$ MeV or $E_2^{\text{tot}} > 3$ MeV.

e^+ cuts: $0.5 < E_1^{(1)} < 8$ MeV; $E_1^{\text{tot}} - E_1^{(1)} < 1.2$ MeV; $E_1^{(2)} < 0.6$ MeV; $E_1^{(3)} > 0.03$ MeV.

Excluding the effects of the μ veto cuts and data acquisition deadtime, the efficiency for inverse beta decay events to trigger the detector and survive the above cuts is about 17%.

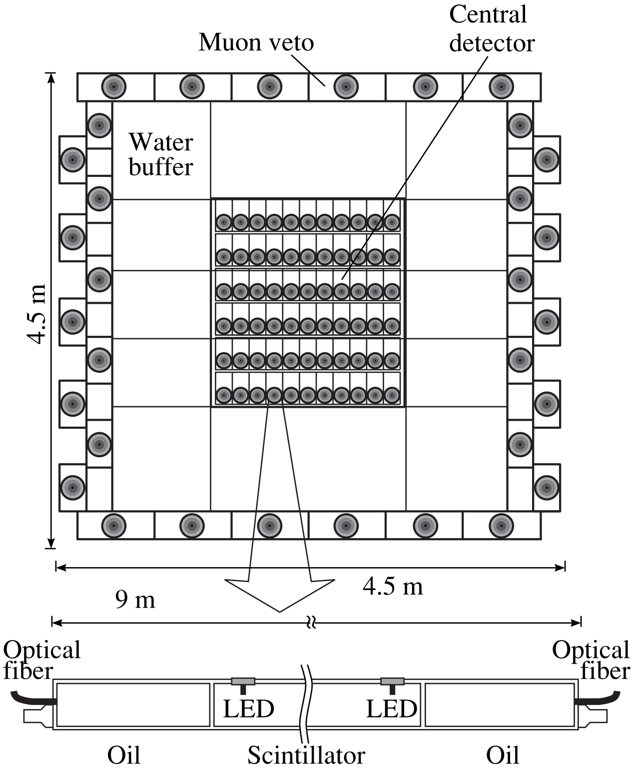

Fig. 4. Schematic view of the Palo Verde detector.

The event rate after applying the above cuts is (39.1 ± 1.0 (stat.))/d for all reactors at full power and (32.6 ± 1.0 (stat.))/d when one reactor is off. The difference between the two rates is (6.5 ± 1.4 (stat.))/d and corresponds to the contribution to the full power rate by the reactor that was off for refueling. From these numbers, one can estimate the signal-to-background (correlated and uncorrelated combined) ratio assuming no oscillations. If no oscillations are occurring, then the reactor which was off for refueling accounts for 30% of the total detected inverse beta decay event rate. Thus the total $\bar{\nu}_e$ rate at full power is (21.7 ± 4.7 (stat.))/d, which indicated S/B ~ 1 : 1 when compared to the full power event rate of (39.1 ± 1.0 (stat.))/d.

Correcting for detection efficiency and including the effect of systematics, the interaction rate of $\bar{\nu}_e$'s in the detector from the refueled reactor is (77 ± 17 (stat.) ± 11 (syst.))/d. The rate which is expected for no oscillations in (59 ± 2)/d. The rates as a function of positron energy are also in agreement. The region of oscillation parameter space excluded by these results is shown in Fig. 5. Most of the Kamiokande-allowed region for the $\nu_e \rightleftarrows \nu_\mu$ hypothesis is excluded at the 90% C.L.

The Palo Verde experiment is continuing to take data to increase statistics over 1998 by at least a factor of ten and to include several more reactor-off periods to improve the accuracy of the background subtraction. To

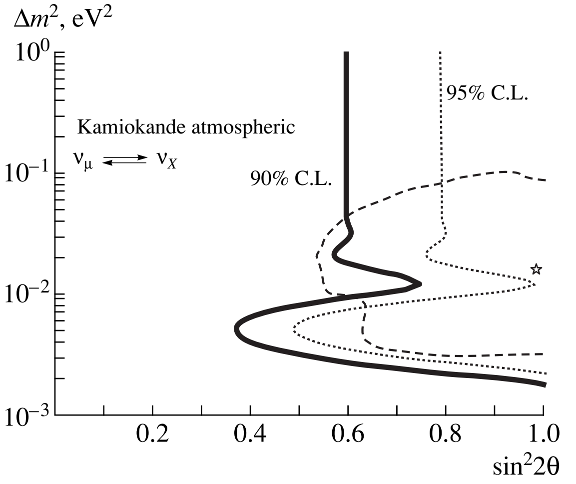

Fig. 5. Regions of $\nu_e \rightleftarrows \nu_X$ oscillation parameter space excluded by the Palo Verde experiment after 70 days of data taking. The solid line corresponds to the 90% C.L. and the dotted line to the 95% C.L. The dashed line bounds the region allowed by the Kamiokande experiment at the 90% C.L. with the star indicating the parameters for the best fit.

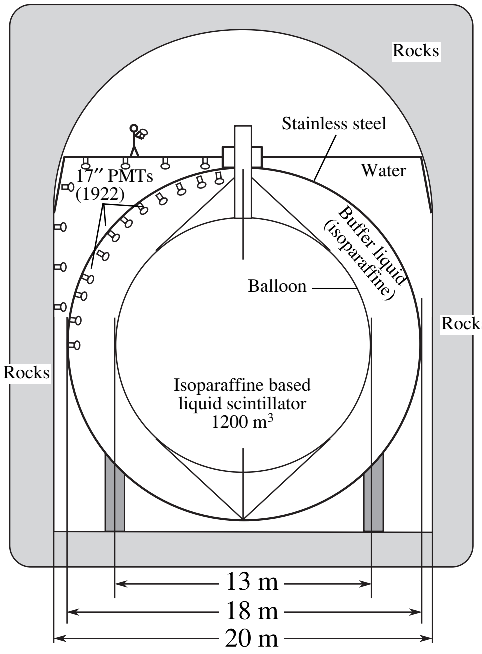

Fig. 6. Schematic view of the KamLAND detector.

further reduce the uncertainty in the background estimation, the analysis is being refined with the goal of improving the S/B ratio while maintaining detection efficiency, and alternate methods of background subtraction are being explored which do not depend wholly on reactor-off data.

To close this review of the Chooz and Palo Verde experiments, the results which they have reported and the more precise atmospheric ν measurements carried out by the Super-Kamiokande experiment indicate that oscillations involving the electron flavor do not largely account for the atmospheric neutrino anomaly. However, some analyses of the neutrino data in terms of three-flavor oscillations favor or allow $P(\bar{\nu}_e \longrightarrow \bar{\nu}_e) =$ 0.90–0.95 in the range of 10^{-2}– 10^{-3} eV^2 for Δm^2 [7]. To be sensitive to $P(\bar{\nu}_e \longrightarrow \bar{\nu}_e)$, a little less than unity is a challenge for future reactor experiments.

3. THE KAMLAND EXPERIMENT

A significant discrepancy between the measured solar ν_e flux at the earth and the flux expected according to standard solar models is now well established. Based on the solar neutrino measurements to date, one of the strongest contenders to resolve this discrepancy is matter-enhanced neutrino oscillations. A fit of this hypothesis for two-flavor oscillations to the neutrino data gives a local minimum with acceptable χ^2 at $\sin^2 2\theta \sim 0.75$ and $\Delta m^2 \sim 2 \times 10^{-5}$ eV^2, which is commonly referred to as the large-angle MSW solution.

Given the large mixing angle of this solution, one can consider the possibility of testing it with a reactor neutrino experiment. Such an experiment would have the clear advantage of being entirely a terrestial experiment with the particularly attractive feature that the source is well understood. Such an experiment would require a baseline on the level of 100 km (10^5 m) or more to have sufficient reach in Δm^2. To offset the strong reduction of L^{-2}, this experiment would require a high level of reactor power, a large target mass, and very good control of backgrounds.

The KamLAND experiment, being mounted by a collaboration of physicists from Japan, United States, and Hungary, is such an experiment designed to provide a test of the large-angle MSW solution. It will be situated in the old Kamiokande cavern so that it is well shielded (2700 mwe) from cosmic rays. The central detector will consist of 1000 t of high-purity liquid scintillator. Within a 400 km radius, there is a large number of Japanese power plants having a total thermal power of ~100 GW; the mean distance of the reactors from the experiment, weighted by their flux, is about 160 km. The KamLAND experiment also aims to carry out measurements of the $\bar{\nu}_e$'s from terrestial radioactivity, searches for astrophysical $\bar{\nu}_e$ sources, and measurement of solar ν_e's directly, but their descriptions are outside the scope of this paper.

A cross-sectional view of the detector is shown in Fig. 6. The central detector consists of 1000 t of liquid scintillator enclosed in a transparent balloon designed to have low permeability to radon. The central detector is viewed by ~1900 17-inch PMTs mounted on a stainless steel sphere. The PMTs cover 30% of the total solid angle; for this coverage combined with the light yield and transparency of the scintillator,

>150 photoelectrons/MeV are expected for energy deposits at the center of the detector. The faces of the PMTs are separated from the central detector by 2 m of isoparaffin, which provides shielding against natural radioactivity in the PMTs, stainless steel sphere, and rock as well as against fast neutrons produced by muon spallation in the rock. Not shown is an acrylic spherical shell just in front of the PMT faces to provide a diffusion barrier to radon emanating from the PMT faces. The stainless steel sphere is immersed in a tank of pure water viewed by PMTs; muons passing through the experiment are detected by the Cerenkov light they produce in this detector.

As usual for reactor neutrino experiments, $\bar{\nu}_e$'s will be detected via inverse beta decay. The experimental signature will be a prompt energy deposit—the positron kinetic energy and annihilation energy—and a 2.2 MeV energy deposit, delayed by an average of ~200 μs, from capture of the neutron on a proton. The average event rate in the case of no oscillations is expected to be 2.2/d for a positron energy threshold of 1 MeV. (The average event rates for several sets of oscillation parameters are given in Table 2.) Obviously backgrounds in the large detector must be tightly controlled.

We review here the main sources of background, the measures being taken in the design and construction of the detector to control these backgrounds, and an estimate of the background rates the experiment expects to see. We then discuss how the backgrounds can be experimentally measured and how the sensitivity of the experiment depends on the accuracy to which the background is known.

As with the other reactor experiments we have discussed, the main background sources are cosmic ray muons and natural radioactivity. Besides the production of fast neutrons in the earth surrounding the detector by muon spallation, one must also reckon with the backgrounds due to isotope activation by muons passing through the large detector (cosmogenesis). The backgrounds due to natural radioactivity arise mainly from (a) the decay chains of ^{238}U, ^{232}Th, and ^{40}K naturally present in the surrounding rock and detector materials and (b) decays of ^{60}Co added to stainless steel in manufacturing for quality control.

The measures—some of which have already been mentioned—that KamLAND will take to control backgrounds are as follows. The overburden of 2700 mwe equivalent strongly suppresses the muon flux; to give an idea of this suppression, the rate at which muons pass through the detector is expected to be about 0.3 Hz. The water Cerenkov detector constituting the outer layer of the experiment will efficiently tag muons that pass through the detector. Radioassay is being used to select detector materials which are low in radioactivity. The 2.5 m of isoparaffin between the stainless steel sphere and the balloon, as well the water in the muon veto detector, will help attenuate background-producing gammas and neutrons emanating from the rock and outer detector components. Diffusion of radon, product of natural radioactivity in the PMT glass, into the central detector, will be retarded by the acrylic shell and a balloon made from materials relatively impermeable to radon. The scintillator will be recirculated to remove radiocontaminants. Of course, event selection will also play an important role in suppressing backgrounds. Requiring the sequential prompt and delayed parts of the candidate event to be correlated to space as well as in time will reduce uncorrelated backgrounds, and the experiment intends to use Pulse Shape Discrimination (PSD) to distinguish events induced by fast neutrons. If necessary, the backgrounds can be further reduced by increasing the effective thickness of the buffer by restricting the fidcuial volume. A detailed detector simulation has been carried out to estimate the singles and delayed coincidence (500 μs window) rates after all control measures except PSD have been taken. The estimated singles rate is dominated by natural radioactivity in the detector materials and rock. The individual contributions as well as the assumed concentrations of radio-contaminants are listed in Table 3. It is worth noting that all these radio-contaminant levels can be readily achieved with present-day technology. The delayed coincidence rates are summarized in Table 4. The conclusion one can draw from these results is that the singles rate will be very manageable for the data

Table 2. Average event rates for $\sin^2 2\theta = 0.7$

Δm^2, eV^2	Rate, d^{-1}
1×10^{-4}	1.4
2×10^{-5}	1.2
1×10^{-5}	1.7

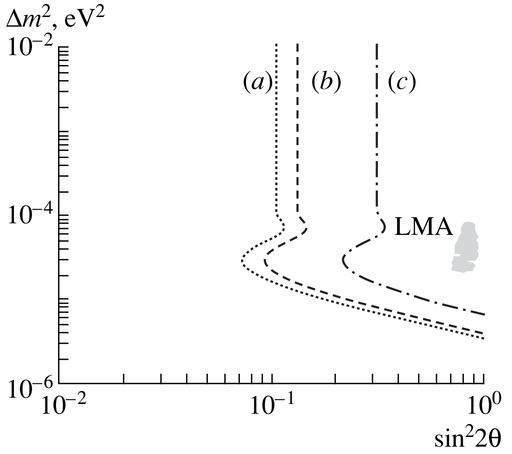

Fig. 7. Expected sensitivity of the KamLAND experiment after 3 yr of data taking: (*a*) No background; (*b*) S/B = 10 : 1 with background known to ±25%; (*c*) S/B = 10 : 1 with background determined from modulation of reactor power only.

Table 3. Singles rates above 1 MeV for all materials and radon

Material	Mass, t	Isotope	Purity, ppb	1-kt backgr., Hz	600-t backgr., Hz
Scint.	920	^{238}U	10^{-5}	0.287	0.191
		^{232}Th	10^{-5}	0.106	0.075
		^{40}K	10^{-5}	0.453	0.334
		Radon	1 μBq/m^3	0.002	0.001
Buffer oil	1523	^{238}U	10^{-5}	0.003	0.0
		^{232}Th	10^{-5}	0.001	0.0
		^{40}K	10^{-5}	0.009	0.0
		Radon	10 mBq/m^3	0.030	0.0
Steel tank	31	^{238}U	1	0.001	0.0
		^{232}Th	1	0.004	0.0
		^{40}K	1	0.010	0.0
		^{60}Co	10^{-9}	0.005	0.0
PMT	7.2	^{238}U	400	0.503	0.003
		^{232}Th	300	0.137	0.0004
		^{40}K	180	0.046	0.0002
Rock	627	^{238}U	73 000	0.199	0.001
		^{232}Th	200 000	0.059	0.0002
		^{40}K	4600	0	0
Total				1.855	0.606

Table 4. Delayed coincidence rates from backgrounds

Source	1-kt backgrounds	600-t backgrounds
Fast neutrons from spallation	0.1 d^{-1}	0.07 d^{-1}
Natural radioactivity (random coincidence)	0.15 d^{-1}	0.02 d^{-1}
Natural radioactivity (correlated)	0.005 d^{-1}	0.003 d^{-1}
All	0.25 d^{-1}	0.09 d^{-1}

acquisition system and the S/B ratio for neutrino candidates will be about 10 : 1. At the least, the correlated background can be measured with sufficient accuracy by correlation of the event rate with thermal powers of the various reactors. The thermal power as a function of time varies by 30%, peaking as expected in the summers and winters when energy demands are greatest. Additional constraints on the correlated background can be obtained by (a) by investigating the spatial distribution of events (signal events should be distributed uniformly throughout the detector volume while backgrounds from external sources will be preferentially distributed toward the wall) and (b) selecting neutron-induced events on the basis of PSD and studying their properties. The uncorrelated background rate can be estimated using the familiar techniques of looking at events with the wrong-sign time correlation or at right-sign events for delayed coincidence times long compared to the mean neutron capture time.

Figure 7 shows the expected sensitivity of the KamLAND experiment for different assumptions on the background rate and the accuracy to which it is known. It can be seen that, even in the case where the background is determined only from the modulation of the reactor power, the region of sensitivity encompasses well the region comprising the large-angle MSW solution to the solar neutrino problem. The KamLAND experiment is being funded by the Japanese Ministry of Education and the US Department of Energy. Design and construction of the experiment is well underway. Data taking is scheduled to begin in April 2001.

4. SUMMARY

To the question of whether or not neutrino oscillations involving the electron flavor are mainly responsible for the atmospheric neutrino anomaly, the answer from the Chooz experiment is definitely no. The initial results from the Palo Verde experiment are also consistent with a nondominant role for electron neutrinos, but these results are statistics limited and the Palo Verde experiment continues to take data. In order for a reactor experiment to definitively address the question of whether or not ν_e oscillations with a few percent mixing are taking place at $\Delta m^2 = 10^{-3}$–10^{-2} eV^2, very tight controls on systematic errors will be required.

The KamLAND experiment will extend the sensitivity to $\nu_e \rightleftarrows \nu_X$ oscillations by two orders of magnitude in Δm^2 at large mixing angles. In so doing, it will be able to carry out a terrestial test of the large-angle MSW solution to the solar neutrino problem.

ACKNOWLEDGMENTS

I would like to thank my collaborators on the Palo Verde and KamLAND experiments for many interesting and informative discussions on searches for neutrino oscillations in reactor experiments. I also would like to thank Prof. B. Dieterle and L. Mikaelyan for providing information about the Chooz experiment.

REFERENCES

1. G. Zacek *et al*., Phys. Rev. D **34**, 2621 (1986); G. S. Vidyakin *et al*., Pis’ma Zh. Éksp. Teor. Fiz. **59**, 364 (1994) [JETP Lett. **59**, 390 (1994)]; B. Achkar *et al*., Nucl. Phys. B **434**, 503 (1995); Z. D. Greenwood *et al*., Phys. Rev. D **53**, 6054 (1996).
2. B. Achkar *et al*., Phys. Lett. B **374**, 243 (1996).
3. Y. Fukuda *et al*., Phys. Lett. B **335**, 237 (1994).
4. A. Piepke, S. Moser, and V. Novikov, Nucl. Instrum. Methods Phys. Res. A **432**, 392 (1999).
5. M. Apollonio *et al*., Phys. Lett. B **420**, 397 (1998).
6. M. Apollonio *et al*., hep-ex/9907037.
7. See, for example, V. Barger and K. Whisnant, hep-ph/9812273.